Computational modelling of full aperture easy open ends for improved can end design.

Taylor, Daryn

Swansea University
Prifysgol Abertawe

Computational Modelling of Full Aperture Easy Open Ends for Improved Can End Design

Daryn Taylor

Thesis Submitted to Swansea University in candidature for the degree of an Engineering Doctorate

Swansea University

September 2011

ProQuest LLC.
789 East Eisenhower Parkway
P.O. Box 1346
Ann Arbor, MI 48106 – 1346

Declaration

(i) This work has not previously been accepted in substance for any degree and is not being concurrently submitted in candidature for any degree.

Candidate ..

Date 15th June 2012

(ii) This thesis is the result of my own investigation, except where otherwise stated. Other sources have been acknowledged by giving explicit references. A bibliography is appended.

Candidate.....

Supervisor....

Date 15th June 2012

(iii) I hereby consent for my thesis, if accepted, to be available for photocopying and inter-library loan, and for the title and summary to be made available to outside organizations.

Candidate.....

Date 15th June 2012

I dedicate this thesis to my late mother

Winifred Anne Taylor who passed away in March 2010

I miss her dearly and think of her everyday

Acknowledgements

I would like to express my sincere thanks and gratitude to both of my EngD supervisors, my industrial supervisor, Dr Géza Nagy of Tata Steel and my academic supervisor, Professor Roger Owen of Swansea University, both supervisors have provided me with guidance, enthusiasm, and constant support, all of which has been given freely over the duration of this research.

Since September 2006, I've been lucky enough to receive lots of help and assistance, not to mention encouragement, from many different sources, including people from various organisations, therefore, I'd like to take this opportunity to thank everyone at Tata Steel and everyone associated with the EngD scheme at Swansea University.
I would also like to thank all of the staff at Rockfield Software, Swansea, for all of their help, advice and assistance, again provided without cost over a long period of time. So a big thank you to everyone who's helped me along the way, you all know who you are.

Finally, and most of all I'd like to acknowledge and thank my family, without who's enduring love and patience I would not have been able to achieve very much at all.

To my partner, Valerie, my sons, Kelan and Ewan, thank you.
I love you all very much, more than you'll ever know.

Abstract

Easy-Open-End's *(EOE)* in can design are increasing within the can making industry, drink can EOE's known as pouring aperture's are now widely used because of their consumer friendliness.
Following this trend manufacturers are developing EOE's with near full aperture opening, for use in the food can market, known as Full-Aperture-Easy-Open-Ends *(FAEOE)* they eliminate the need for can opening devices.

FAEOE's are manufactured from metals such as aluminium and increasingly steel, all incorporate a shared design feature whereby the can end incorporates a circumferential score with integral pull-tab that enables the consumer to easily gain access by lifting the tab to initiate a fracture that then propagates around the circumferential score. For competitiveness, the steel end manufacturer needs to use a thinner gauge whilst at the same time refining the design to improve opening performance. Traditionally, end optimisation is a long-drawn-out process, but now, modern computational methods may have the potential to allow end optimisation to be modelled accurately.

The damage and fracture mechanisms that lead to crack initiation and propagation in the opening process are not fully understood, therefore optimisation of easy open end scores is largely based on trial and error.

This thesis presents an experimental analysis that concentrates on the combined shear and bending forces as applied to the particular industrial method concerning full aperture easy open ends, together with a computational analysis that concentrates on the simulation of score forming and the damage that accumulates as a punch is pressed into thin steel sheet.

The use of damage models within simulation is steadily increasing along with having greater accuracy in tension, however, descriptions of performance in compression and shear are relatively hard to find.

Damage simulation of score forming should help provide better knowledge of the mechanisms present when opening easy open ends and give additional understanding of the novel experiments that have been undertaken for dissimilar loading modes; this understanding will eventually lead to the development of a complete multi-mode model for can end optimisation.

The influence of a gradually increasing gap on traditional groove geometries and depths are examined for modern packaging steels.
Earlier studies have shown that the complete opening cycle depends on fracture modes I, II and III as well as their combination.
Experimental results for modes I II and III will be presented, however, attention will focus on the behaviour of the initial fracture point whereby prior investigations have shown it to be influenced primarily by mode II shearing.

After initial specimen manufacture, where the score is formed by pressing a punch into a thin steel sheet, the predeformed scored specimens are loaded in shear to simulate the local stress field found during the initial opening phase. Experiments have been completed using a novel mode II experimental technique that has been designed for use in the majority of commercially available tensile test machines.

Experimental results indicate that opening forces can change radically with different gap sizes and that there is considerable potential for the industrialised process of can end manufacture to be optimised through the efficient management and control of the can ends dimensional parameters

Contents

List of Figures

List of Tables

Chapter 1

Introduction

1.1 Aim and Motivation

In the packaging industry convenience is key, as increasingly packaging has to adapt to busier lifestyles with less time for food preparation and consumption.[1] Canned foods can save up to 50% of the time of preparing a meal and increasingly consumers are aware of and appreciate consumer friendly opening systems and are prepared to pay an additional 8% for the benefits of easy opening, which confirms that making cans easier to open constitutes a major benefit for brand owners in terms of potential sales.

One consumer friendly opening system is the Full Aperture Easy Open End (FAEOE), and its use in food cans has steadily been increasing since 1990 with predictions indicating further growth [4]. Maintaining this success, however, means that further advances are required in lowering the opening forces whilst still ensuring the cans overall integrity, this may be achieved through optimisation of the design of the FAEOE using computational techniques [11].

[1] *Time spent cooking in the UK has fallen from 60min in 1980 to 13min in 2002* [3]

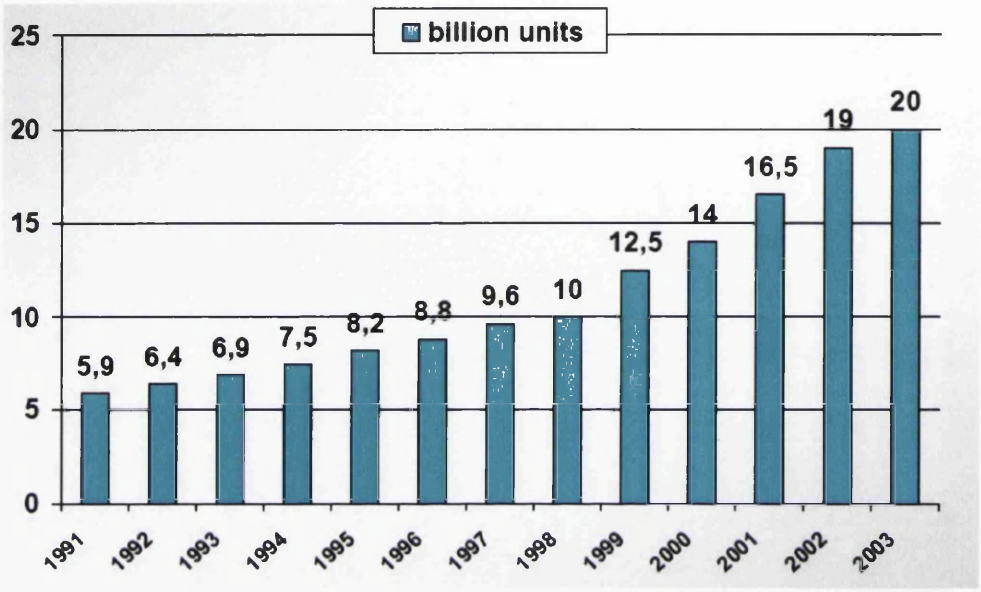

Figure 1.1: European Growth of EOE's

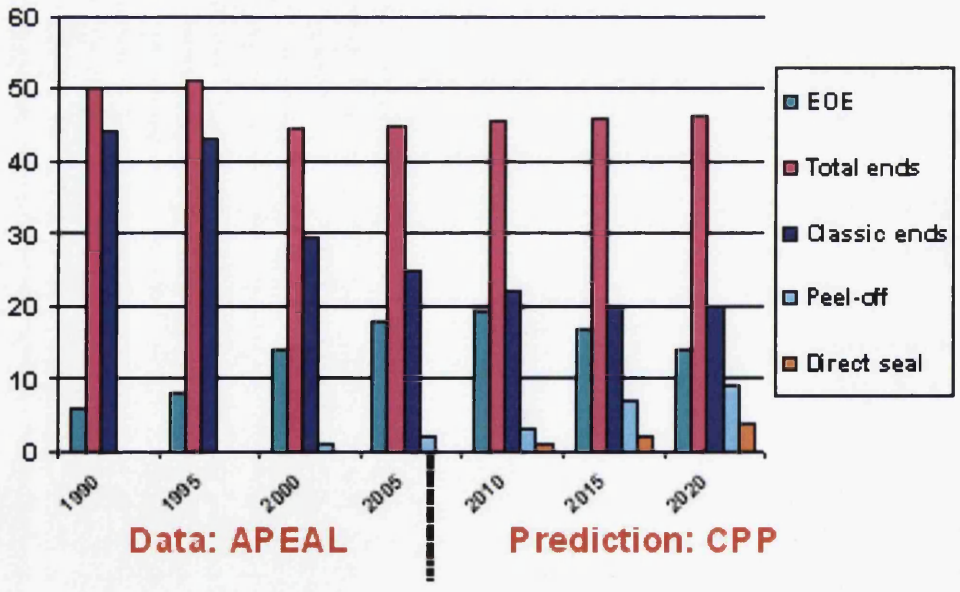

Figure 1.2: Growth Prediction of EOE's

FAEOE's are manufactured using blanking and forming processes and subsequent opening by the consumer involves separation of the material by generating macroscopic cracks that propagate down a predetermined path, however predicting the onset and progression of failure accurately is presently a difficult task for many forming operations.

The dominant failure mode in sheet metal forming is necking, and some tools and methods exist that can be used to predict its onset, but each method has its inherent advantages and disadvantages. Forming Limit Curves (FLC's) have been successfully used to evaluate the likelihood of failure processes where a plane stress condition is present, i.e. major and minor strains are both positive and M1, M2 $>$ 0 like biaxial stretching, or the absolute value of the negative minor strain is small compared to the positive major strain $\frac{M1}{2} - M2$ i.e. uniaxial tension.

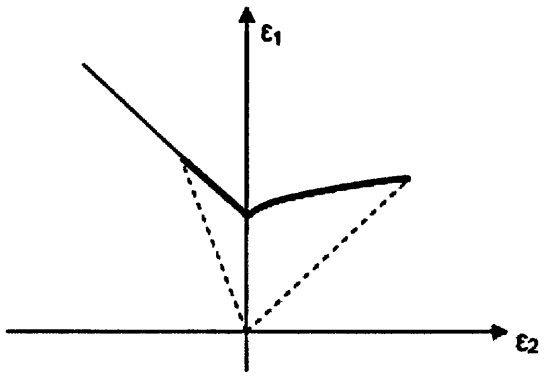

Figure 1.3: FLC Predicts Failure between Uniaxial & Biaxial Tension

In other ratios, such as, deep drawing, where M1 = -M2, the FLC does not form a deterministic limit and other quantities, such as the Limiting Draw Ratio (LDR) of the material has to be determined. Furthermore, shear induced fracture can not be predicted with FLC's, and FLC's are not defined for compression. Additionally, FLC's are limited to straight strain paths, which means that the FLC approach can not be used for complex forming processes, also thermal and rate effects are not included in FLC's.

Increasingly, damage is being used as a parameter to identify the limits of failure and because damage is an accumulated quantity, it may well be suitable for complex processes. Effects such as; anisotropy, thermal and rate effects may also be incorporated into the damage formulation, however most current damage formulations are limited in use to plane stress. Generalised damage however does not have this limitation.

Damage can take many forms such as cracks and voids, which result in the overall deterioration of the structure, therefore predicting the implications of this deterioration can be thought of as the ultimate goal of damage mechanics. Presently damage is relatively well understood under tensile loading, but reports on compression [57],[56] and shear [1], [24],[29] deformation and fracture behavior are relatively hard to find.

One long term objective is to integrate the recent advances in damage and fracture mechanics into a working Finite Element model that describes the opening behavior of easy open ends, however, in order to accomplish this the important aspects of the physics of the failure of scoring must be included, but must remain extremely selective in order to reduce or eliminate any complexities. It is therefore essential to understand the underlying phenomena of scoring and opening on the many scales that are involved.

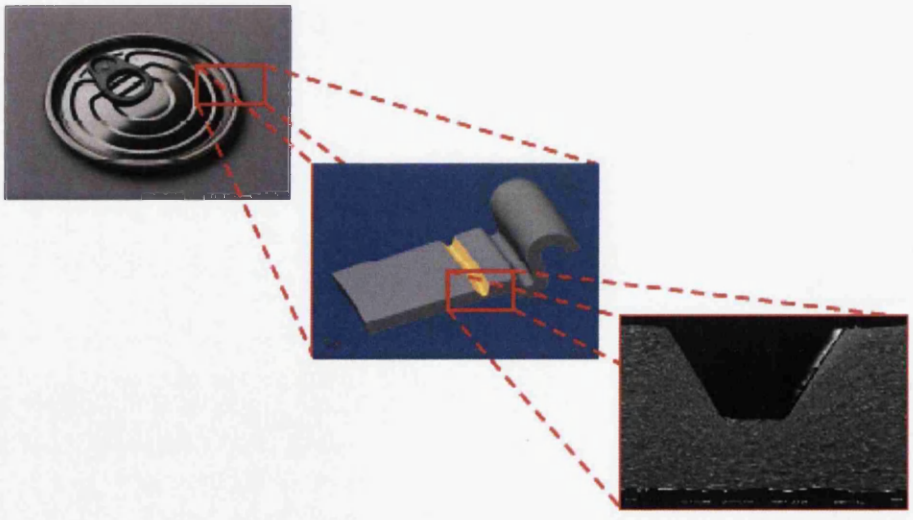

Figure 1.4: Scoring is a Multi-Scale Process

Computational methods now have the ability to predict the formulation and evolution of cracks, which can be used to model the manufacturing process used for creation and fabrication together with modelling of the completed product. This enables manufacturers to optimise a product and its key factors such as final shape, manufacturability and fabrication method, which in turn has a direct result on savings in time and cost and therefore profitability.

Known as virtual manufacturing, fabrication and testing methods can be simulated realistically, which reduces the need to produce physical prototypes. As numerical analysis can be repeated relatively cheaply and as many times as necessary, the final product can be produced in a right first time environment, which gives manufacturers greater confidence in their ability to produce products of the right quality, on time and on budget. Controlling the development of damage and cracks using computational methods has over recent years become known as Damage Engineering, [53].

This Thesis[1] provides an insight into the void growth and ductile failure mechanisms found in single phase packaging steels under plane stress and plane strain compression and shear. Relevant state-of-the-art constitutive models are discussed as the knowledge gained herein is required for the further development of quantitatively accurate constitutive relations for porous metals.

[1]Thesis was written and produced with LaTeX 2_ε.

1.2 Outline

The thesis is divided into eight chapters, beginning with the introduction, which discusses the projects aims and motivations, then:-

Chapter 2 Here, the background of the project is explained, followed by a brief history of can development and the origin of the Easy Open End. Material selection is discussed, together with the tooling requirements for sample manufacture and the testing plan.

Chapter 3 This chapter discusses the experimental work undertaken together with the results, firstly, the universal tensile tooling is explained followed with the testing and results for Mode III, Mode I, and Mode II. A discussion on folding side constraint conditions closes the chapter.

Chapter 4 Factorial Analysis is now used in many engineering applications, this chapter introduces the methodology of Design of Experiments, which is then applied to analyse the results for all fracture modes, i.e. Modes I, II, and III, the conclusions and outcomes for each mode are then presented.

Chapter 5 The subject of this chapter is Micrography, after a brief introduction, sample preparation and investigation procedures are reviewed, followed by the initial outcomes. Further experiments are discussed with initial void and element analysis and damage evolution in the bulk, failure in shear is reviewed as well as the results of macroscopic tests, deformation at multiple scales is looked at, together with an analysis of internal microscopic cracks and their effects.

Chapter 6 This chapter begins with an overview of damage mechanics and the effects of physical damage in solids, this is followed with the classification of damage models, which leads into continuum damage mechanics and the Lemaitre damage model. Crack closure is discussed, followed finally by the characterisation of stress states.

Chapter 7 Here, finite element analysis is briefly reviewed, which leads into the modelling of a single element, scoring follows, beginning with uncoupled damage, model outlines and the coupled Lemaitre damage model. Finally, the model outcomes are reviewed in a comparative analysis.

Chapter 8 This final chapter discusses the projects conclusions followed with with some suggestions for possible future work.

In addition to the above, a number of appendices are included.

Appendix A Here, the full tooling production drawings are detailed for all tooling used in the project.

Appendix B Contains a complete worked example detailing the calculations for biaxial deformation.

Appendix C All the results from the factorial analysis of chapter 4.

Appendix D Complete set of contour plot images for damage, strain, stress and triaxiality.

In addition, part of the research work provided in this thesis has been presented at the following conferences and can be found in the following references;
[42], [88], [89], [91], [90].

Chapter 2

Materials and Tool Design

2.1 Project Background

Development of a Computer Model for FAEOE's

Tata Steel packaging is a customer facing business that works closely with its clients, so the development of a computer model for FAEOE design will help TATA improve its understanding of the effects of changeable variables like score geometry and material properties, it will also help reduce the need to manufacture physical prototypes and perform physical tests.

This increased understanding in turn will allow TATA to improve its technical support and advice and provide a higher quality service to its customers.

Crack Propagation and Opening

It is well understood, [92], that opening a FAEOE involves the separation of the material by generating cracks that propagate down a predetermined path, i.e. the score, see figure 1.4. It is also known, [97], that opening a FAEOE happens in four phases with a number of forces identified.

1. Pop Force - force required to initiate cracking of the score.
2. Maximum Tear Force - peak force generated during opening of the end.
3. Average Tear Force - average force measured after the peak force.
4. Tear off force - force generated by separating the end from the can body.

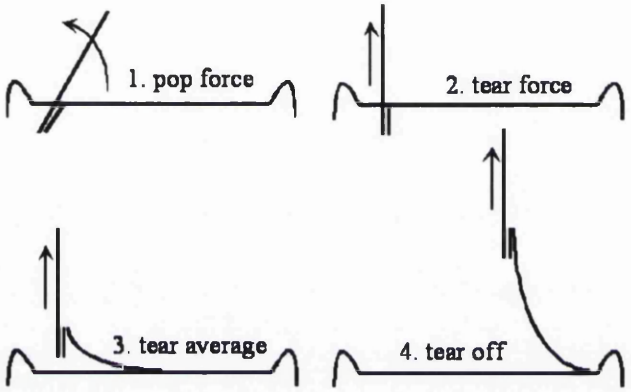

Figure 2.1: Schematic Diagram showing the Four Phases of Opening

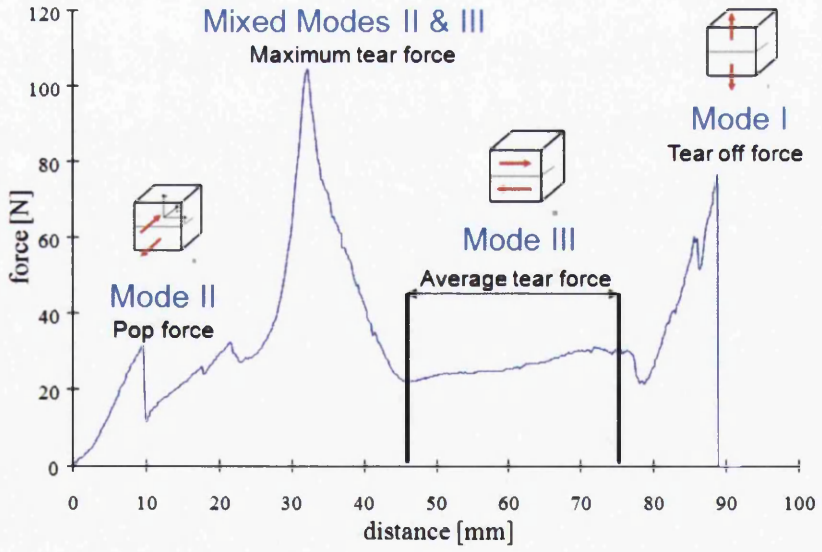

Figure 2.2: Phases and Forces generated when Opening a FAEOE

Forces Generated During Opening

Can manufacturers have previously stated, [96], that a reduction in tear force of around 5N would be regarded as a significant improvement, present thinking suggests that lowering or leveling the peaks found in a typical FAEOE opening force graph, shown in figure 2.2, would also bring about large benefits and improve the EOE opening experience.

It is also suspected that each peak is directly related to one or more opening modes i.e. pop force is likely to be linked to mode II whereas the maximum tear force peak is more probably a mixture of mode II and mode III. Also clear is that the average tear force represents mode III opening and that the final peak force generated by tear off is primarily mode I.

Fracture Modes I, II and III

It is universally acknowledged, [76], [2], that cracks propagate in fracture modes or a combination of fracture modes. Three types of mode are recognized, and are known respectively as:-

- Mode I
- Mode II
- Mode III

It is now thought that by separating and analysing each fracture mode individually, eventually, all the information will be in place to allow for a complete formulation of a full computational opening model for FAEOE's.

Previously Completed Work

Tata RD&T have previously completed a number of tests, developed by Boers, [9], which have been used to measure the forces generated for a number of different fracture modes.

Mode I Test

This test, attempts to simulate failure due to internal pressure or burst pressure, as it was believed that the score is subject to a plain strain condition with no strains occurring in the circumference of the can.

It is now also suspected that this mode is likely to relate to the tear off phase generated when separating the end from the can body.

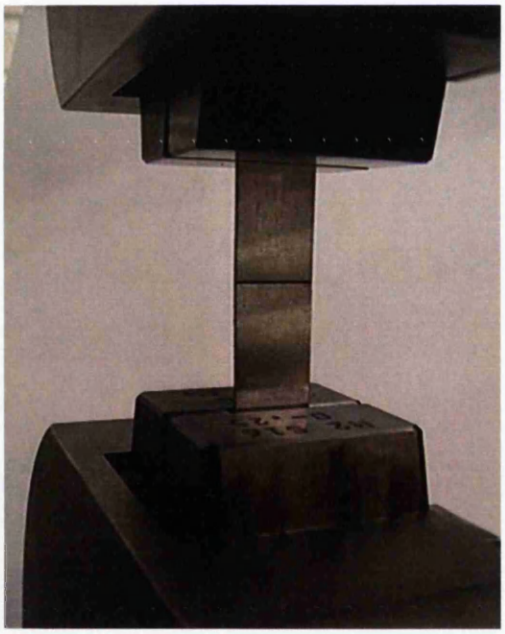

(a) Mode I Test.

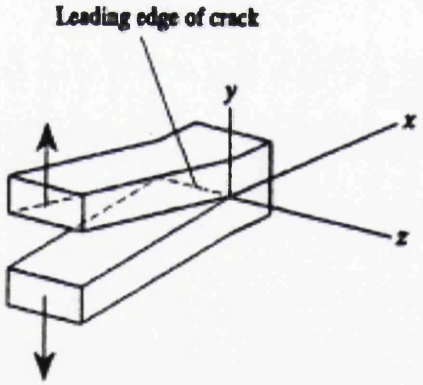

(b) Mode I Schematic.

Figure 2.3: Mode I Test

Mode III Test

This test, again developed by Boers, [9], but this time to simulate the out of plane forces thought to be present during the normal opening or average tearing of a FAEOE. Testing of the Mode III double scored samples, shown in figure 4.13(a), differed in that the Mode III test device, figure 4.13(b),was used to tear the double scored samples apart, once more recording both force and displacement, a typical result graph is shown in figure 4.13(d).

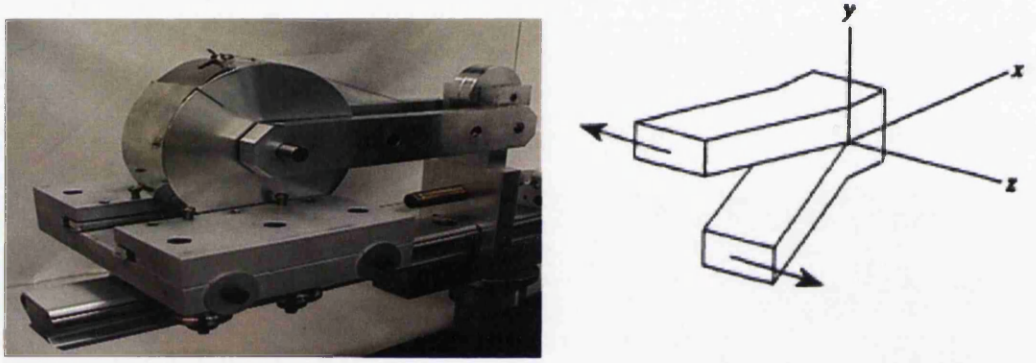

(a) Mode III Test.

(b) Mode III Schematic.

Figure 2.4: Mode III Test

However, this test method is subject to a number of limitations, such as;

- When samples are scored in the *Minster Press* for subsequent testing in the *Tram Rail* device the evolution of damage concentrated in the score is heavily dependant upon the boundary conditions present at the time of manufacture in the press.
- Due to the design of the *Tram Rail* device it is believed that the mode of fracture is not entirely pure mode III, i.e. there is a wave front occurring ahead of the crack together with residual bending taking place in the score.

2.2 Brief History of Food Can Development

Historically can development can be traced back for over 200 years to when Napoleon offered a considerable 12,000 franc reward to the person who could successfully develop a method for preserving food for his army.

In 1810 this reward was collected by French confectioner, Nicolas Appert, who was successful due to his experiments with food preservation through sterilisation. Around about the same time an Englishman called Peter Durand was awarded a patent by King George III for developing a tin plated iron can for food containment, but the catch was that even the most highly skilled craftsmen could only produce about 60 cans a day.

1900 Europe, a more sanitary open-top food can was developed, increasing the speed of the manufacturing process, can ends still soldered by hand.

1963 Ernie Fraze of Dayton Reliable Tool Company, with Alcoa, invented the aluminium easy-open end.

1983 Three European steel producers form tri-party technical agreements for steel easy open end development.

1993 Eco-top steel ends became available in the UK.

1998 Development of Full Aperture Easy Open End patent by Wilson [99]. This is considered in more detail in section 2.4.

2.3 Origin of Easy Open End

The origin of the easy open end for cans began with an American named Ermal Fraze, known as *Ernie* he was born in 1913, and in 1949, he formed a machine tool business called the Dayton Reliable Tool Company, in Dayton, Ohio.

The company manufactured tools and machinery for various industries and among its clients were companies such as Alcoa, Chrysler, General Electric, Ford, and NASA. At a picnic in 1959, Fraze forgot his *church key*, this was the local name given to the separate opener that had to be purchased to open a beverage can at that time, and Fraze ended up using a car bumper to open drinks for his guests. The problem must have started Fraze thinking, as later in that same year, he developed a can with an integral lever opener, but regrettably the design produced a sharp aperture that could potentially injure the consumer.

In 1963, in conjunction with ALCOA, Fraze developed a new can design known as the *pull-top*, and it was this design that incorporated a removable tab that the consumer had to pull to gain access to the beverage. Although Fraze did not receive a patent for this invention until October 1967, by 1965, 75% of beer brewers in America had adopted Fraze's can design, with the Pittsburgh Brewing Company in Pittsburgh, Pennsylvania being the first company to use Fraze's design. Fraze's pull-top can proved to be a major improvement in beverage packaging, allowing drinkers quick and easy access to their drink, but pull-top cans caused an number of problems, first an increase in littering, as most people just threw away the tab, and injury, as others placed the tab inside the can and then injured themselves by swallowing it or cutting themselves with it as they took a drink.

To solve these issues, in 1977, Fraze patented the first push-in and fold-back tab, this tab remained attached to the can, and it is the principal design still used on canned beverages today. By 1980, Fraze's new tab design and machinery to manufacture the can was earning the Dayton Reliable Tool and Manufacturing Company, Inc., over 500 million dollars per year.

Fraze died in 1989 and the Dayton Reliable Tool and Manufacturing Company, was sold to the business's managers, were it still remains in operation in Dayton today.

2.4 Wilson's Patent

The Full Aperture Easy Open End (FAEOE) is a variation of Fraze's traditional Easy Open End (EOE) designed specifically for containing food; only here the majority of the end is removed to give greater and easier access to the cans contents. Recent papers on can end research [11], [63], cite Wilson as developing the patent for Full Aperture Easy Open Ends in December 1998.
Wilson's patented design for Full Aperture Easy Open End is shown below.

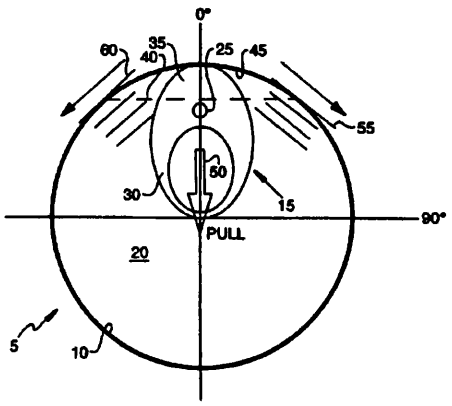

Figure 2.5: Plan View of Wilson's Full Aperture Easy Open End

The patented FAEOE design incorporates the following main features:-

- A Central Panel - 20
- A Circumferential Score - 10
- A Tab - 15

The tab is riveted to the central panel, so the nose of the tab (35) is positioned directly above the score. At first opening the score is broken along an arc (45) that has a specific chord length (40). The steel grain of the end is aligned to a tangent of one end of the chord (40) and the preferred embodiment is that at the grain tangent the circumferential score is at its minimum thickness *(Score Residual)*. Full opening of an EOE is achieved by initiating a crack and then forcing the crack to propagate down a predetermined path or score; it is this mechanism that the EOE design relies upon for its success.

2.5 Material Selection

The initial testing plan proposed to manufacture samples from seven different steel packaging grades; however this was revised and reduced to two steel grades as it became apparent that it was not going to be possible to manufacture samples for seven steel grades within the allocated timeframe.

Two materials were finally chosen because they are both used in the production of FAEOE's. Table 2.1 below details the materials finally selected.

Material Code	Temper	Storage Code	Width	Gauge
TH435	T65CA	20080234	816mm	0.21mm
TH550N	DR550N	20080247	802mm	0.21mm

Table 2.1: Final Material Table

Sheet materials were located in RD&T's material storage area, the selected sheets were unpacked then cut to size using a pneumatic guillotine. Two types of sample were produced with the following dimensions:-

(i) 12.5mm Score Sample - Dimensions - 12.5mm x 150mm[1]

(ii) Double Score Sample - Dimensions - 140mm x 100mm

Both types of unscored sample are shown in figure 2.6, followed by a scored, double score sample in figure 2.7

[1] 12.5mm samples were manufactured to dimensions outlined in standard BSEN10002-1

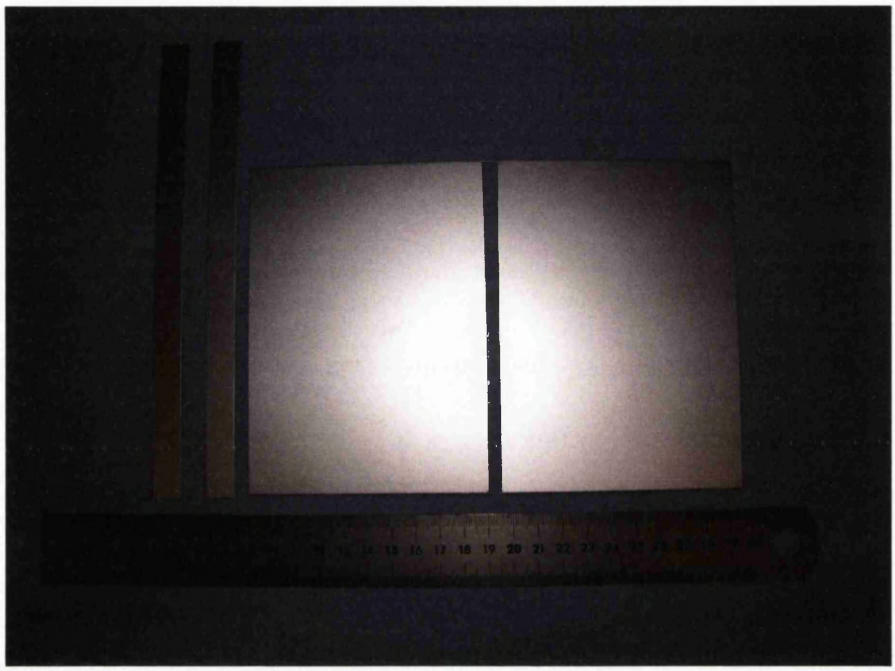

Figure 2.6: 12.5mm & Double Score Blank Samples *(Unscored)*

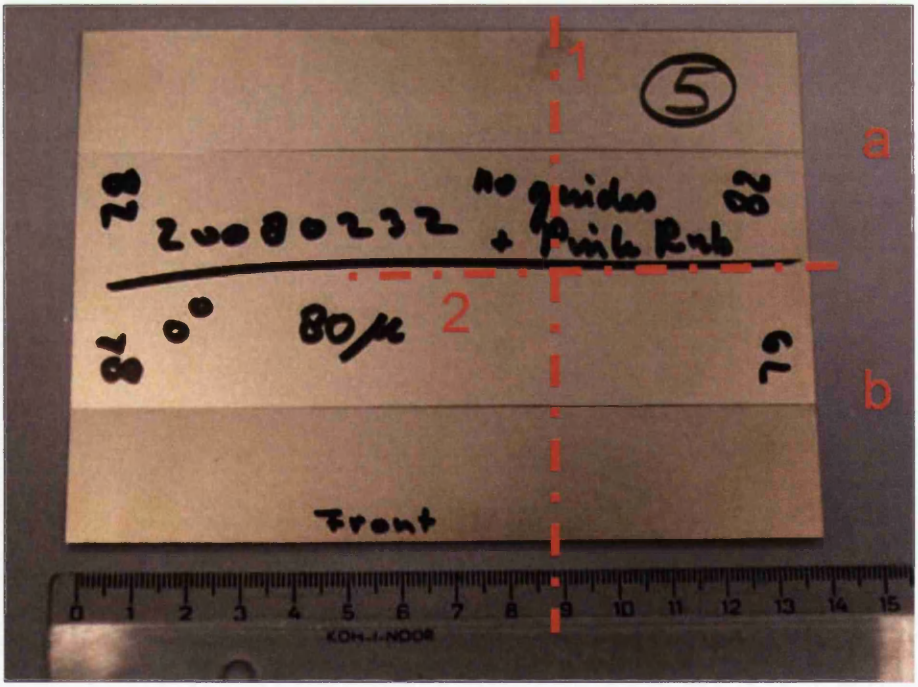

Figure 2.7: Double Score Sample for SEM *(Scored)*

2.6 Tram Rail Tooling

The original *Tram Rail* tooling was designed by Hoogovens Staal in October 1999 and originally specified in the following Minster Press tooling drawings supplied by Tata. Each of the existing *Tram Rail* score tools employed the exact same score profile consisting of a 60°included angle and a 60μm flat plateau.

It was decided that for the planned IJmuiden secondment, that additional tram rail experiments using tooling with subtly different score geometry would be undertaken and for this purpose extra tooling was required to be designed.[1]

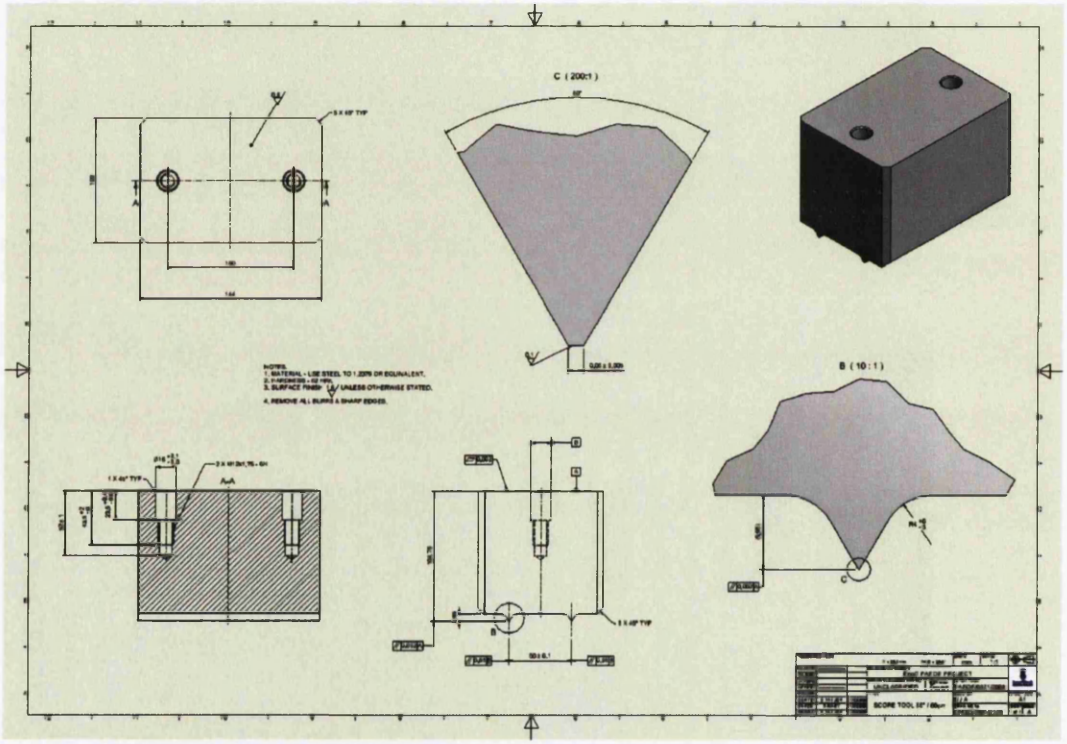

Figure 2.8: Production Drawings for New 60-60 Tool

[1] Appendix A contains drawings for the Tram Rail & Sample Holder Tooling.

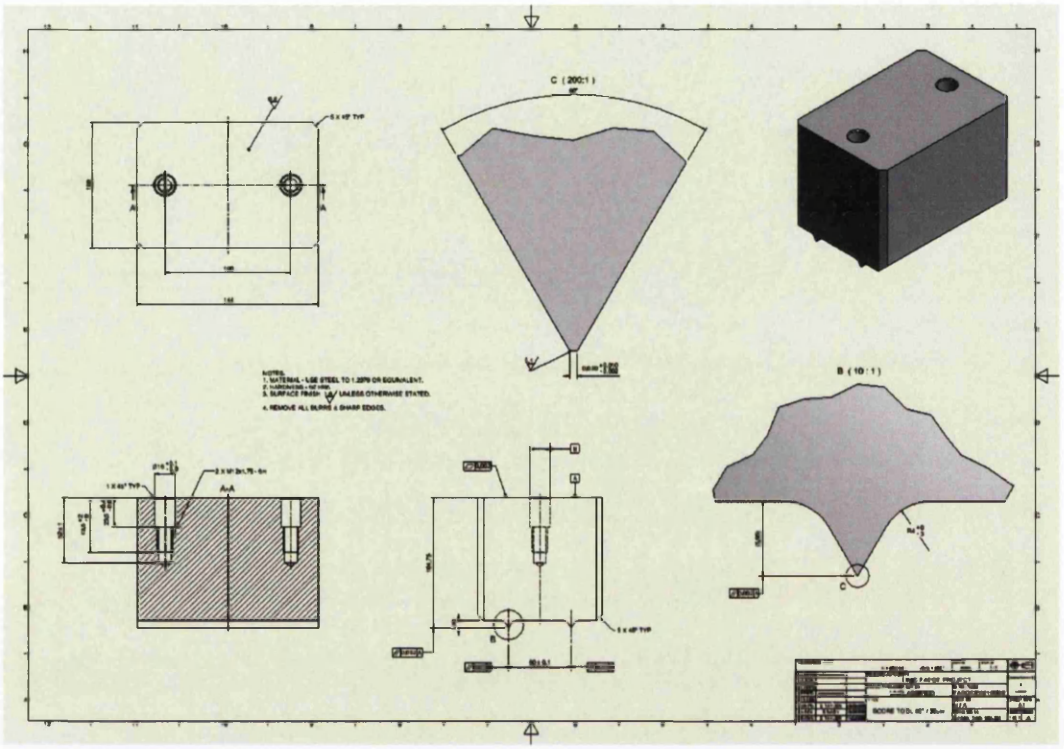

Figure 2.9: Production Drawings for New 60-30 Tool

Using the original drawings as a basis for the design, 3D CAD was employed to construct a Model of the *Tram Rail* tooling with subtly different score profiles. The new score profiles decided upon were:-

- 60°included angle with a 30μm flat plateau.
- 40°included angle with a 30μm flat plateau.

After successful construction of the 3D CAD models, engineering drawings[1] were produced that were used to provide detailed manufacturing instructions for the toolmaker to produce the required *Tram Rail* tooling.

[1]See Appendix A for larger versions of all Tooling Drawings

2.7 Mode II Tool Design

It was realised early on in the project that much design work was necessary, varied amounts of tooling had to adapted, better understood and finally manufactured, including a specific device required to enable Mode II testing.

The majority of this work could be termed design and the amount of work undertaken was enough to complete a design project on its own merit.
Not all of the design work work is included here, however, all of the manufacturing drawings produced for the project can be found in Appendix A.

The following describes the design process up to the successful manufacture and delivery of the tooling that became known as the *Mode II device.*

Shigley and Mischke [84] that;

"Engineering and Design are two sides of the same profession and that engineering is a profession primarily concerned with the application of a certain body of knowledge, set of skills, and point of view in the creation of devices, structures, and processes used to transform resources to forms which satisfy the needs of society".

All design starts or should start with the identification of need; from here a Product Design Specification (PDS) is devised that becomes the specification of the product that is being designed.

Product Design Specification

The product design specification (PDS) is a document that sets out in detail the exact requirements of a product, before it is designed,
The PDS for the Mode II device is detailed below.

Function

- Device to provide a method of shear testing pre-scored samples.
- Device to provide an adjustable gap, to mimic variation in tab distance.
- Design to be capable of testing to within a 20 - 40μm tolerance.
- Centre placement for a balanced load test.
- Edge placement to enable in-situ microscopy later on.
- Symmetry of design - Rotational clamping blocks for changes in clearance.
- Universal set up - Tooling to be used in any standard tensile test machine.

Loading

- Device to safely support all parts when in use.
- All forces acting on the device to be taken into consideration during design.

Manufacturing

- All components to be manufactured in high precision Toolroom.
- Materials - Commercially available steels, EN24, M2 Tool Steel.
- Non standard components to be kept to a minimum.
- Assembly - Hand assembly of all components.
- Protective coating - Light oil.

Safety

- Safety assessment required.
- Project risk assessment required.

Quality

- Certificate of Conformity to be issued by Tool Manufacturer.

Timing

- Design drawings to Toolmaker by 22nd July 2009.
- Mode II Assembly to be received by end March 2010.

Ergonomic

- Ease of assembly and positioning.
- Ease of access for removal of parts.
- Ease of operation.

Operation

- To meet all requirements when used as specified.

Maintenance

- Routine visual inspection
- Light lubrication of all moving parts on assembly.
- Tool to be stored in purpose build box when not in use.

Concept Design

Concept design is concerned with the generation of solutions by linking separate elements into a connected whole that meets the required need by generating ideas and potential solutions. The two main capabilities, required by the device were:-

1 Ability to shear a sample made from 0.21mm thick packaging steel.

2 An adjustable *Gap*, i.e. to mimic the distance between score & tab.

A number of different concepts were generated for the Mode II design, these concepts are shown in figure 2.10.

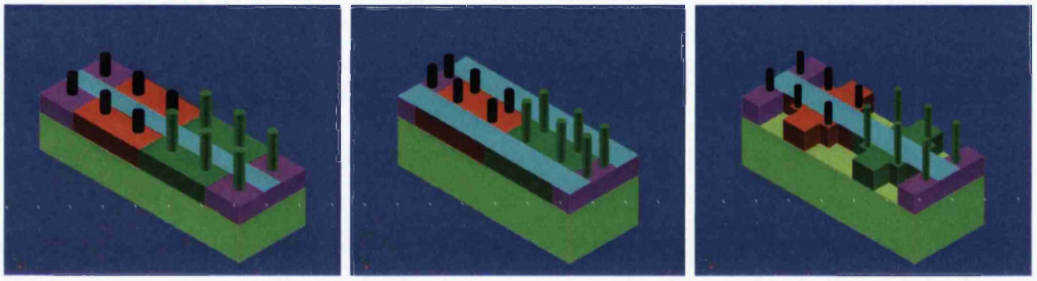

(a) Single Middle Strip (b) Double Edge Strip (c) Shaped Rotational Blocks

Figure 2.10: Evaluation Concept Designs for Mode II Device

The concepts evaluated different functions as specified in the PDS.

Outcome

Refinement of the results from the concept design phase, enabled a 3D CAD model to be produced that lay the foundations for the start of the detailed design phase.

Detail Design

In reality, detailed design and analysis take place continuously; going back and forth as the design evolves, this was the case with the Mode II Device.

After evaluating each concept it was decided that the completed design should have the following capabilities:-

- The device should be able to hold the sample in such a way that it gave the opportunity to view the sample as it was being sheared, either with a microscope or camera. This meant locating the sample at the edge of the device in order to position the viewing equipment, this sample position, however, meant that the device was unbalanced as the shearing would be unsymmetrical. One idea was to place two samples into the device to even out the forces, but it was realised that for the majority of its use the device would be used to shear a single sample.
  In the final design, the solution was to provide locating pins that could be moved, which meant that the device could be set-up to shear a single sample located in the middle of the device or alternatively, set up to shear two samples located at each side.

- Another problem was how to locate the sample precisely and exactly in the centre of the device, as this was critical to providing accurate results. The answer was to use a method commonly used in engineering for accurate holding and positioning, i.e. a taper. The preformed score had a tapered profile, so by using a centering tool with the exact same profile, the sample could be located accurately and held in position as end clamps were fitted. The centering tool could then be removed, then the rotational clamping blocks could be fitted to give a precise, but controllable distance between the score and the edge of the blocks, this enabled the simulation of varying tab distances as found in a real can end.

- Finally, a lifting assembly, was fastened to the device, located in a tensile test machine, the device could be precisely raised to shear the sample whilst simultaneously recording both force and displacement until sample failure.

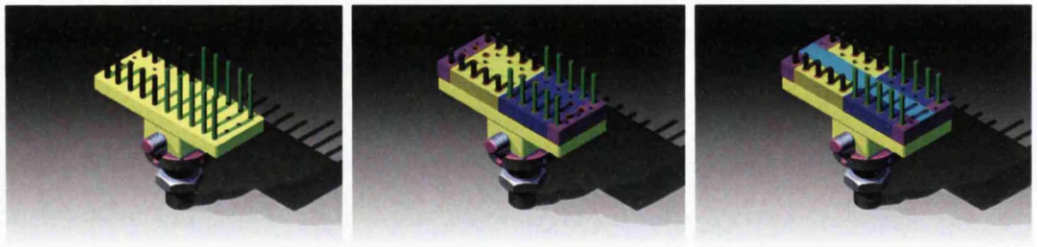

(a) Base with Pins (b) Lower Blocks (c) Single Strip Sample

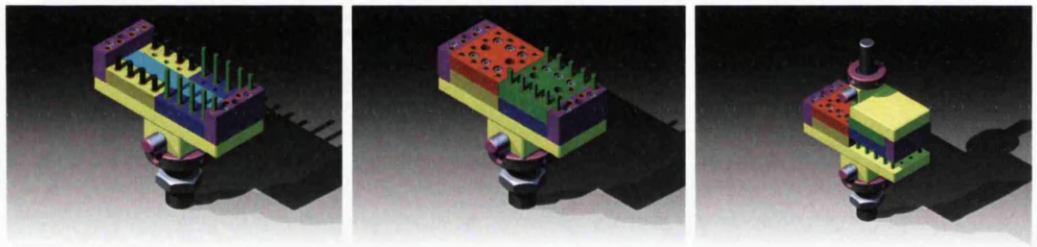

(d) End Clamp Blocks (e) Upper Blocks (f) Sheared Sample

Figure 2.11: Mode II Device - Middle Sample Location

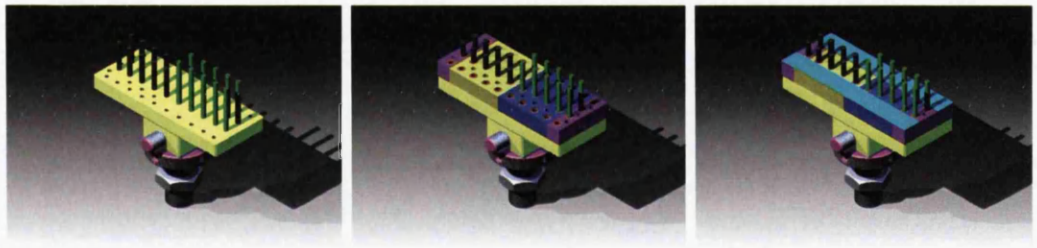

(a) Base with Pins (b) Lower Blocks (c) Double Strip Samples

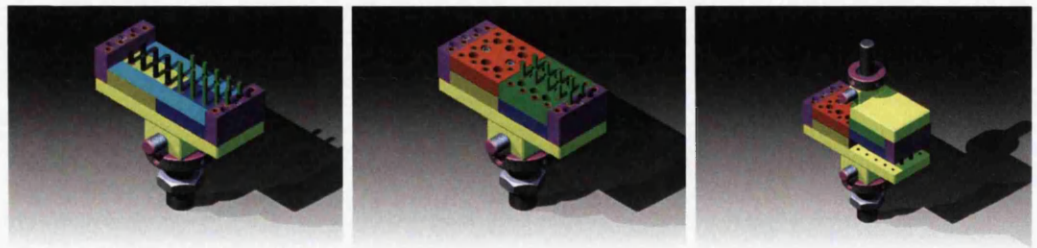

(d) End Clamp Blocks (e) Upper Blocks (f) Sheared Samples

Figure 2.12: Mode II Device - Edge Sample Location

Load Paths

When the tooling was first used, it was realised, that due to the positioning of the lifter assembly, a slight bending moment was induced into the side of the device being raised, this in turn caused slightly more friction, which meant that the force of the device itself had to be recorded before each test. The results could then be adjusted to try to cancel out this effect.

It was known, however, that as the sample reached its elastic limit, due to the nonlinearity, the principle of superposition would no longer apply, so canceling out the effect of the device from the results would no longer be possible. Although this problem did cause some concern, in the actual test, primary interest was focused on the linear part of the results.

Cost

Cost in design is primarily caused through complexity, cost reductions can be achieved by focusing on simplicity. Pugh [80] quotes Carroll & Bellinger who state:-

"Perhaps the major single contributor to operating reliability is simplicity" and *"The superior design is one which encompasses the necessary operating and protective functions with the absolute minimum number of components and connections"*

The cost of the Mode II tooling was as follows:-

Qty	Description	Total £
1 off	Mode II Score Tool	£3100.00

Table 2.2: Mode II Tooling - Manufacturing Costs

All score blocks and anvils were manufactured from M2, 60-62Rc, tool steel, and all shafts and locking rings from EN24T.

Manufacture

After the concept and detailed design phases were complete, it became necessary to fully document the design as a fully functional 3D CAD model, this was successfully achieved using Autodesk Inventor CAD software. However, this did not mean that the design process was over, as with any mechanical device requiring manufacture, a full set of production drawings had to be drafted in order for the toolmaker to be able to successfully manufacture and assemble the tooling.

The toolmaker selected to produce the tooling was NPE-Innotek Ltd based in Neath, the reason, was due not only to their general experience in precision engineering, but also their extensive experience gained in manufacturing tooling specifically for the can industry, as originally the Toolmakers was formed in 1937 to provide support for the can making industry in Neath, becoming independent as NPE in 1987. Some of their capabilities were:-

- Turning and Milling - Both manual and CNC controlled.
- Wire Erosion, Grinding - CNC erosion cells, CNC jig, universal & surface.
- Spark Erosion and Hard Turning - CNC erosion cells, high tolerance turning.
- Inspection - CMM inspection in temp controlled environment.

Prototype drawings were delivered to the Toolmaker on the 22nd July 2009 for quotation. The final completed Mode II Tool Assembly was received back from the Toolmaker on the 23rd March 2010.

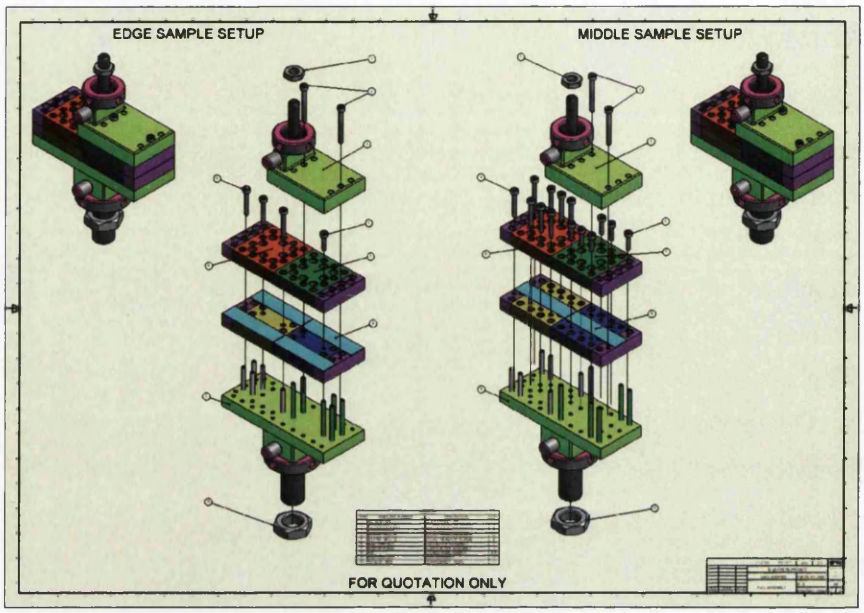

(a) Full Assembly Drawing

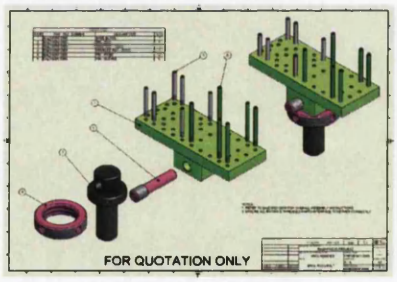

(b) Base Assembly

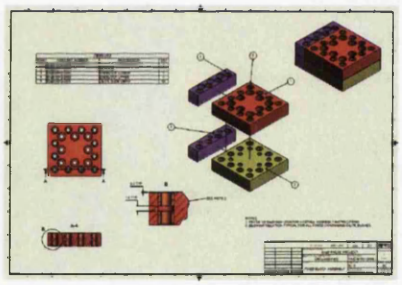

(c) Fixed Block Assembly

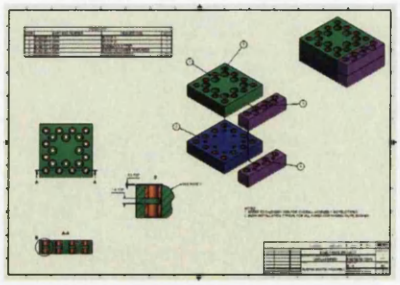

(d) Sliding Block Assembly

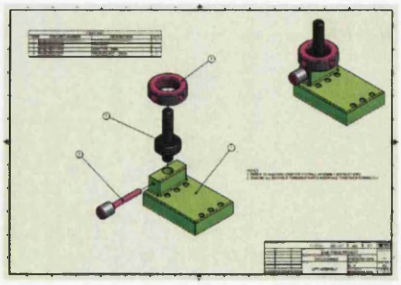

(e) Lift Assembly

Figure 2.13: Mode II Device - Manufacturing Drawings

Standards

After many years of experience, working to a plethora of standards becomes normal practice, however, it would be pointless to try to name all of the standards used within the context of modern design, as there are hundreds, maybe thousands that can be called upon depending upon the individual design or project involved, one standard, however, used constantly with every design is:-

BS 8888:2004 - Technical Product Documentation
Defining, specifying and graphically representing products

This British Standard supersedes BS308-1:1993, BS308-2:1985 and BS308-3:1990, which are all withdrawn. Drawing conventions which applied to BS 308-1,2, and 3 in general also apply to the European Standards referenced in BS 8888, the standard is provided to unify all of the recently implemented ISO and EN ISO standards related to Technical Product Documentation.

BS 8888 references standards covering all aspects of technical product documentation including:-

- Engineering Flow Diagrams
- Representation of Engineering components
- Lettering
- Units/ quantities
- Tolerancing
- Geometric Product Specifications
- Orthographic/Isometric representation
- Handling of Computer based information
- Metrology

2.8 Minster Press and Tram Rail Tooling

During the secondment to Tata RD&T in IJmuiden, all the scored test samples were produced on a mechanical press known locally as the *Minster Press*, named after its manufacturer. Both the 12.5mm and Double Score samples shown in figure 2.6, were manufactured on this press, but as the 12.5mm samples only required the production of a single score, a dedicated holder was required to be designed and manufactured so that the existing tram rail tooling could be utilised; this saved the significant cost of producing further tram rail tooling with a single score and the same score profile geometry.

Using the complete set of original *Minster Press* drawings a comprehensive 3D mechanical model was built to provide a platform to begin the concept and detailed design of a dedicated holder for the Euro-norm tensile test specimens. The process of designing the 3D model also had an additional benefit of providing a much better understanding of the *Minster Press* set up before the secondment to Tata RD&T began.

2.9 Sample Holder

The secondment with Tata began after arriving in Holland on Sunday 7th Sept 2008, and commenced the following day at Tata RD&T at IJmuiden Steelworks. The first technical problem to be addressed was to conclude the design and manufacture of the sample holder. The holder design began with a sketch to see how all the existing parts interacted at the anvil interface with the design concept based on what was thought to be the simplest design that would work, for the lowest amount of cost.

As mentioned, it was hoped that the tensile test samples could be produced using the double tram rail tooling to save cost, but that meant that the maximum length between the scores could only be a maximum of 50mm, as this was the fixed distance between the score knife edges. Working to standard EN10002-1-Annex B, it was unlikely that it would be possible to use the 20mm wide type 2 samples, as it was doubtful that they would provide enough material to have a parallel length of 120mm, as per the standard.

Additionally, with 20mm samples, the maximum amount that could be produced at the same time was three, due to the gap between the dowels being 65mm.
It was, however, possible to produce the 12.5mm wide type 1 samples, as per the standard.
Type 1:-

- 50mm Original gauge length
- 75mm Parallel length
- 87.5mm Free length

Also because of the reduction in width, it was possible to produce four samples simultaneously instead of three.

Figure 2.14 shows the 3D model for four 12.5mm wide samples.

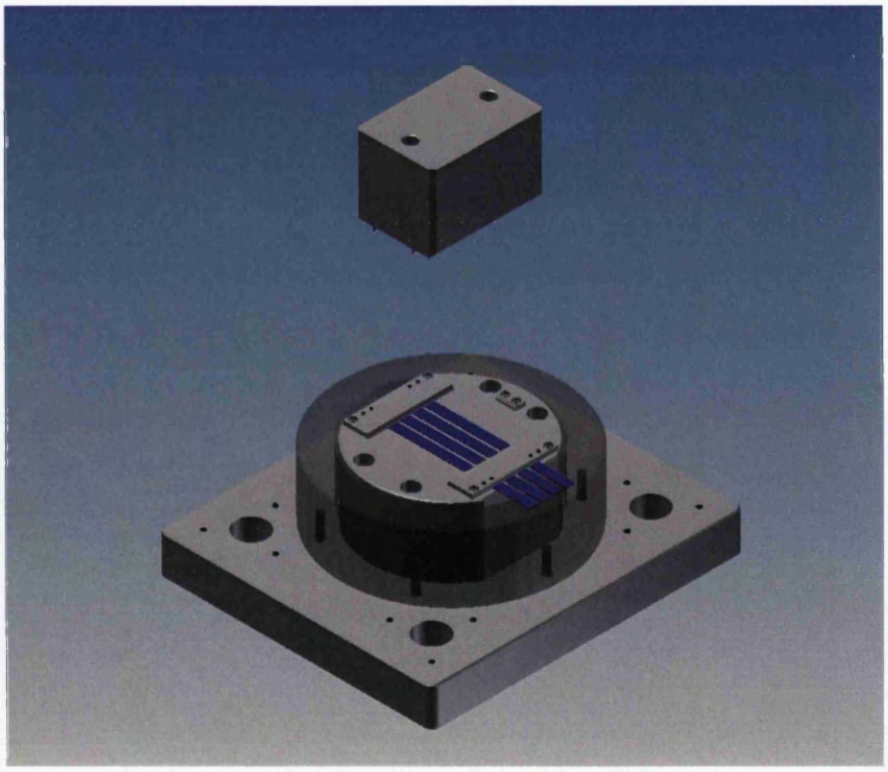

Figure 2.14: Sample Holder 3D Model

2.10 Final Testing Plan

The initial testing plan turned out to be far too ambitious to be able to produce the amount of samples within a reasonable timeframe, so eventually on the 25th November 2008, after going through a number of iterations, the final plan as detailed in figure 2.15 was agreed.

Testing Plan

Tool	Samples	Material	Depth	Material Direction	Qty	Test no
60/60	Tramrail	TH550	80	0°	4	1
60/60	Tramrail	TH550	80	90	4	2
60/60	Tramrail	TH550	60	0	4	3
60/60	Tramrail	TH550	60	90°	4	4
60/60	Tramrail	TH435	80	0°	4	5
60/60	Tramrail	TH435	80	90	4	6
60/60	Tramrail	TH435	60	0	4	7
60/60	Tramrail	TH435	60	90°	4	8
60/60	Strips	TH550	80	0°	16 = 4 Strokes	9
60/60	Strips	TH550	80	90	16 = 4 Strokes	10
60/60	Strips	TH550	60	0°	16 = 4 Strokes	11
60/60	Strips	TH550	60	90	16 = 4 Strokes	12
60/60	Strips	TH435	80	0°	16 = 4 Strokes	13
60/60	Strips	TH435	80	90	16 = 4 Strokes	14
60/60	Strips	TH435	60	0°	16 = 4 Strokes	15
60/60	Strips	TH435	60	90	16 = 4 Strokes	16
Tool	**Samples**	**Material**	**Depth**	**Material Direction**	**Qty**	**Test no**
60/30	Tramrail	TH550	80	0°	4	17
60/30	Tramrail	TH550	80	90	4	18
60/30	Tramrail	TH550	60	0	4	19
60/30	Tramrail	TH550	60	90°	4	20
60/30	Tramrail	TH435	80	0°	4	21
60/30	Tramrail	TH435	80	90	4	22
60/30	Tramrail	TH435	60	0	4	23
60/30	Tramrail	TH435	60	90°	4	24
60/30	Strips	TH550	80	0°	16 = 4 Strokes	25
60/30	Strips	TH550	80	90	16 = 4 Strokes	26
60/30	Strips	TH550	60	0°	16 = 4 Strokes	27
60/30	Strips	TH550	60	90	16 = 4 Strokes	28
60/30	Strips	TH435	80	0°	16 = 4 Strokes	29
60/30	Strips	TH435	80	90	16 = 4 Strokes	30
60/30	Strips	TH435	60	0°	16 = 4 Strokes	31
60/30	Strips	TH435	60	90	16 = 4 Strokes	32

Figure 2.15: Final Testing Plan

The plan was made up of 32 individual experiments and was colour coded to highlight the final two materials chosen, with red representing TH550N and blue representing TH435.

Chapter 3

Experimental Work and Results

3.1 Universal Tensile Tooling

Before any actual testing could take place an examination into the different tensile test equipment that was available at both Tata RD&T and Swansea University was completed.[1] This investigation made clear that there were a number of tensile test machines available for research use between the facilities.
Mode III testing was the first to be completed at Tata RD&T facilities in IJmuiden, Holland, due to the Mode III samples being the first to be manufactured on the *"Minster Press"*.

Following this, all Mode I and Mode II experiments were then completed at Swansea University, due mainly to the following reasons:-

- The tensile machine was available throughout August and September 2009.
- The machine was calibrated and all software was up to date.
- Load cells were available with 10KN, 1KN and 100N capacities.
- A temperature controlled cabinet was attached and available if required.

[1] Appendix A has more detail on the selection of the Tensile Test equipment.

3.2 Mode III Testing and Results

The first testing to be completed was Mode III, which took place during the secondment to Tata's RD&T facilities in IJmuiden, Holland, mainly due to the Mode III samples being the first to be *Scored* on the *Minster Press*.

Sixteen Mode III tests were performed, with each test being repeated three times to give a total of 48 results. The test numbers for Mode III correspond with the final plan as shown in Chap 2, figure 2.15, numbered 1 thru 8 and 17 thru 24 and type labeled *Tramrail*.

However, a more comprehensive work plan that details the Mode III experimental work can be seen in figure 3.1 below.

Mode III Experimental Work

Mode Type	Test Number	Tool Profile	Type	Material	Residual	RD	ID No
	MODE III TEAR						
MODE III TEAR	1	60/60	Tramrail	TH550	80	0°	20080247
	2					90°	
	3				60	0°	
	4					90°	
	5			TH435	80	0°	20080234
	6					90°	
	7				60	0°	
	8					90°	
	17	60/30		TH550	80	0°	20080247
	18					90°	
	19				60	0°	
	20					90°	
	21			TH435	80	0°	20080234
	22					90°	
	23				60	0°	
	24					90°	

Figure 3.1: Mode III Experimental Work Plan

A typical result graph for Mode III is shown in figure 3.2 below, which shows a force v displacement graph detailing the three test results.

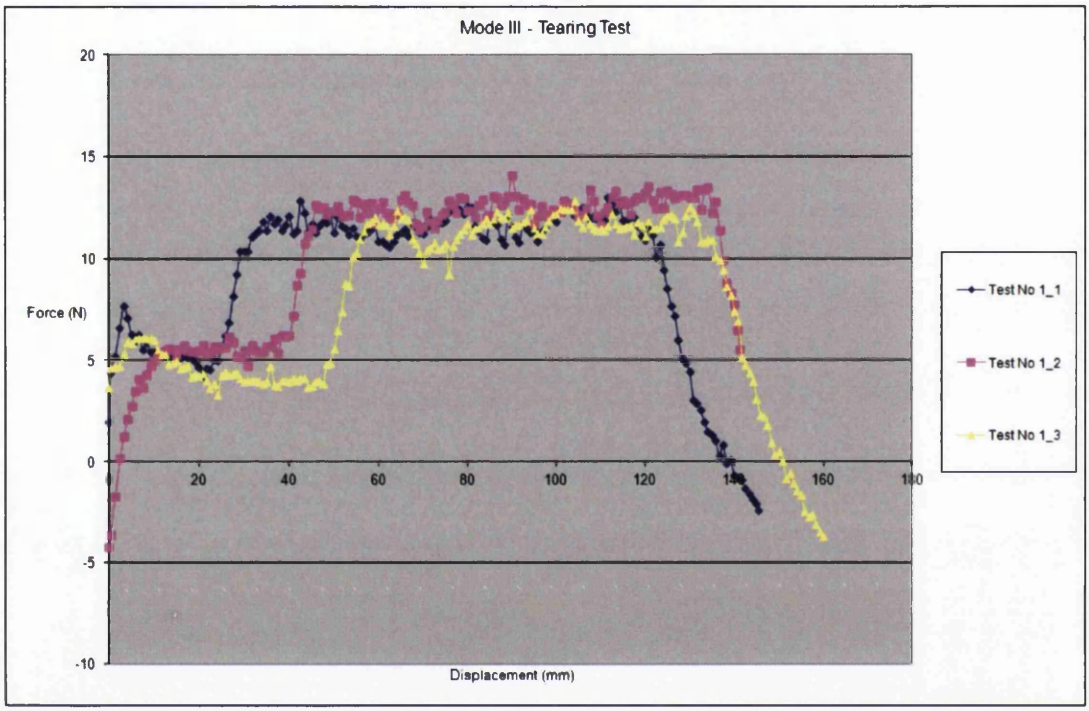

Figure 3.2: Typical Mode III Result Graph

A further more detailed analysis that considers the meaning behind the results is the next topic of discussion and follows in Chapter 4, Factorial Analysis[1].

[1] A complete and comprehensive set of result data, that details all of the Mode III experiments can be found on the DVD included with this Thesis

3.3 Mode I Testing and Results

Some time after returning from the IJmuiden secondment, the pre scored 12.5mm strip samples were delivered to Swansea University's Materials department, which meant that the Mode I testing could begin.

As with the Mode III tests, sixteen Mode I tests were performed, once again with each test being repeated three times to give a total of 48 results. The test numbers for Mode I again corresponded with the final plan as shown in Chap 2, figure 2.15, this time numbered 9 thru 16 and 25 thru 32 respectively and type labeled *Strip*.

Again, a more comprehensive work plan detailing the Mode I experimental work is shown in figure 3.3 below.

Mode I Experimental Work

Mode Type	Test No	Tool Profile	Type	Material	Residual	Measured	RD	ID No
MODE I TENSILE								
MODE I TENSILE	9	60/60	Tensile Strip	TH680	80	80 80 80	90°	20080247
	10					80 80 80	0°	
	11				60	61 61 61	0°	
	12					60 58 59	90°	
	13	60/60	Tensile Strip	TH435	80	82 82 81	90°	20080234
	14					82 82 82	0°	
	15				60	64 66 67	0°	
	16					62 63 62	90°	
	25	60/30	Tensile Strip	TH550	80	79 82 79	90°	20080247
	26					82 81 80	0°	
	27				60	62 62 60	0°	
	28					58 52 62	90°	
	29	60/30	Tensile Strip	TH435	80	79 84 82	90°	20080234
	30					78 77 79	0°	
	31				60	62 64 62	0°	
	32					60 61 63	90°	

Figure 3.3: Mode I Experimental Work Plan

A typical result graph for Mode I can be seen in figure 3.4, which shows a typical force v displacement graph detailing the three test results.

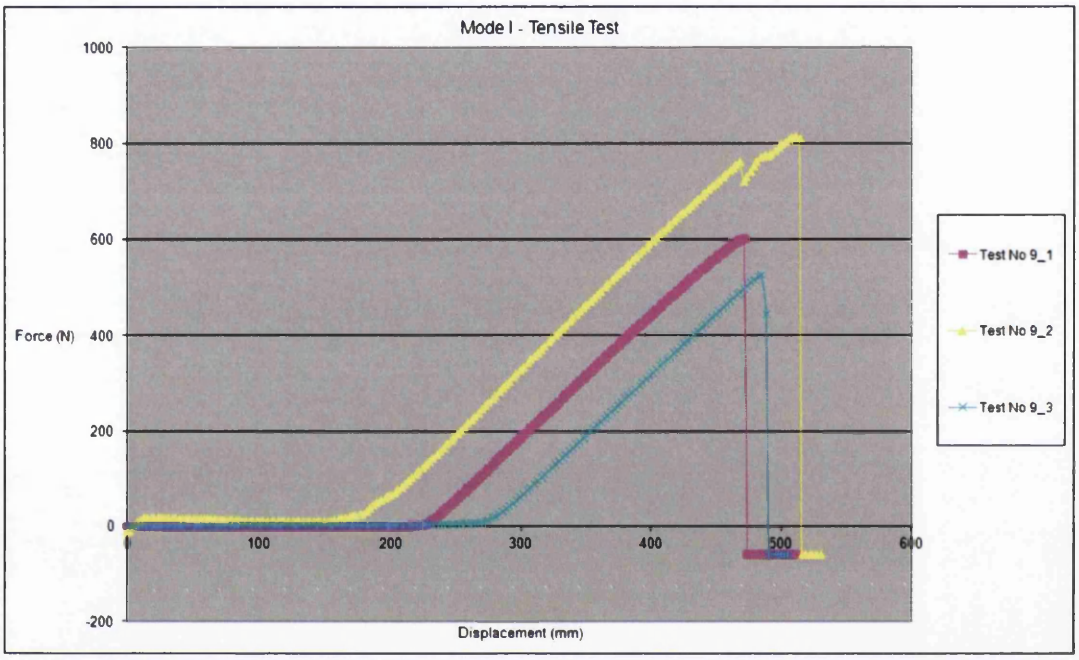

Figure 3.4: Typical Mode I Result Graph

Once more, a detailed analysis that considers the meaning behind the results is the next topic of discussion and follows in Chapter 4, Factorial Analysis.

3.4 Mode II Testing and Results

The Mode II experiments were the final set of tests to be completed, *(Testing began in April 2010)*, which was due in no short part to the time taken designing, developing and manufacturing the tooling known as the *Mode II Tooling* or *Mode II Device*, discussed in section 2.7. This tooling had been developing iteratively since March 09 and the complete set of manufacturing drawings were delivered to the toolmaker in July 09.

As with the other Mode tests described previously, sixteen Mode II tests were performed, however, each test had to be repeated for 8 individual clearances, which gave 128 tests and as before each test was repeated three times, giving a total of 384 results[1].

Mode II Experimental Work

Mode Type	Test No	Clearance / (Actual)	Tool Profile	Type	Material	Residual	Measured	RD	ID No
MODE II SHEAR									
MODE II SHEAR	9_1	0.18	60/60	Shear Strip	TH550	80	79	90°	20080247
							81		
	10_1						81	0°	
							81		
							82		
							83		
	11_1					60	59	0°	
							59		
							60		
	12_1						58	90°	
							59		
							60		
	13_1				TH435	80	80	90°	20080234
							81		
							82		
	14_1						84	0°	
							84		
							84		
	15_1					60	58	0°	
							59		
							60		
	16_1						60	90°	
							60		
							60		
	25_1		60/30		TH550	80	79	90°	20080247
							79		
							79		
	26_1						80	0°	
							80		
							82		
	27_1					60	59	0°	
							60		
							60		
	28_1						57	90°	
							58		
							61		
	29_1				TH435	80	79	90°	20080234
							79		
							80		
	30_1						80	0°	
							82		
							83		
	31_1					60	62	0°	
							63		
							64		
	32_1						62	90°	
							62		
							64		

Figure 3.5: Mode II Experimental Work Plan

[1]Figure 3.5 details the experimental plan for just 1 clearance, out of a total of 8

Furthermore, an additional test had to be performed after each set of samples had sheared, which was done in order to be able to measure the effect of the *Mode II Device* itself and was required so that the effect of the tooling could be taken into account and if possible removed from the test results. *(See section 2.7 for further discussion)*

Once again the test numbers for Mode II correspond with the final plan shown in figure 2.15, again numbered 9 thru 16 and 25 thru 32 and type labeled *Strips*. A more detailed work plan was then developed to cover the Mode II experimental work and this can be can be found in figure 3.5. A typical result graph for Mode II can be seen in figure 3.6, which shows a force v displacement graph detailing the three test results together with the result showing the effect of the *Mode II Tooling*.

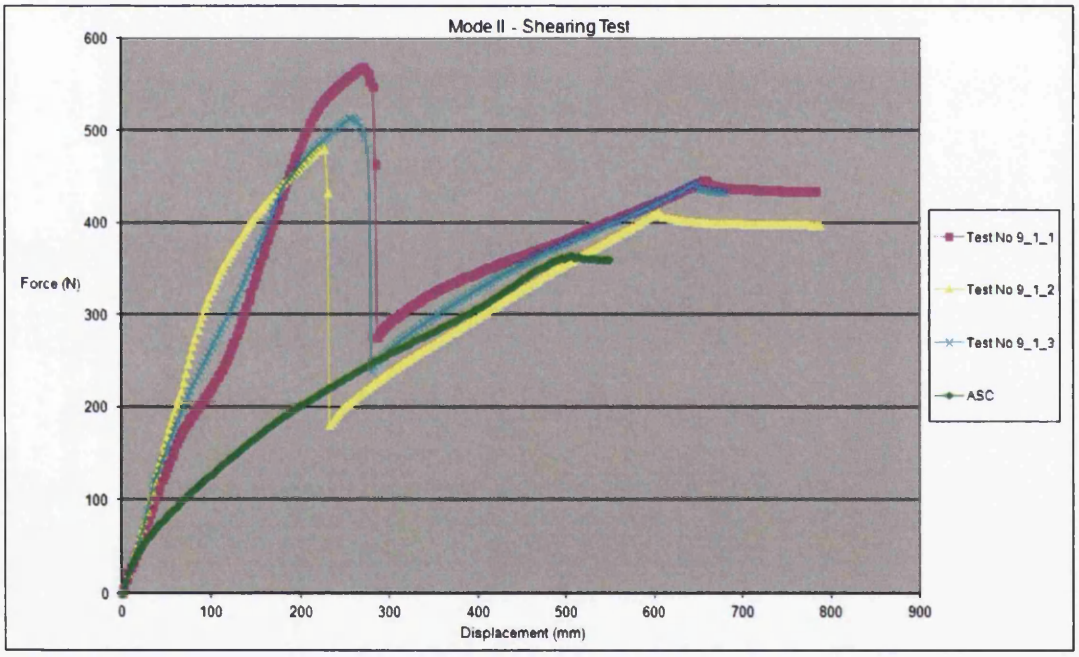

Figure 3.6: Typical Mode II Result Graph

3.5 Folding Side - Constraint Conditions

Initial double score sample production showed that the samples were not only scored, but also deformed, in that both sides were folded up, this was observed previously in [9]. An investigation was completed, which is reported fully in [89], however, the conclusions found are repeated here for completeness.

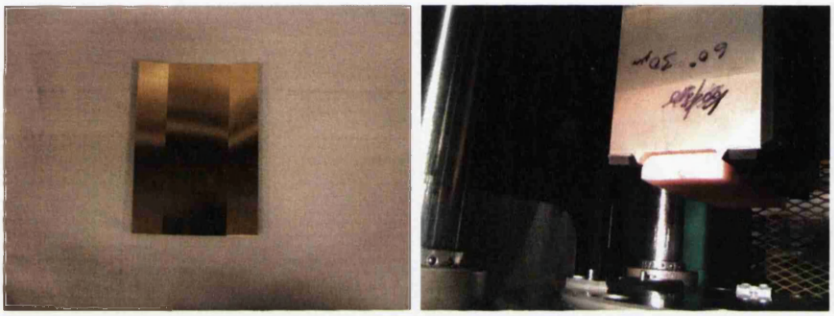

(a) Folded Sample (b) Edge, Middle Foams & Guides

Figure 3.7: Folded Samples and Foam Solution

Further samples were produced using a set-up with two different foams, then, different configurations were used to help decide what particular set up would, in our view, best represent the real life configuration at a can-making plant.

Code	Edge Foam	Middle Foam	Guides
NNN	No	No	No
NNY	No	No	Yes
YNN	Yes	No	No
YNY	Yes	No	Yes
YYN	Yes	Yes	No
YYY	Yes	Yes	Yes

Table 3.1: Foam Constraint Configurations

Two configurations, YYN and YYY, seemed to best represent the actual constraint conditions found on a real *Can End* production line, after a final review, [43], YYN, was eventually selected to produce all further samples.

Chapter 4

Factorial Analysis

4.1 Introduction to Design of Experiments

In science and engineering normal practice undertaken when trying to find something out about a particular system or process is to undertake experiments or tests, put more formally an experiment can be defined as;

"A test or series of tests where predetermined changes are made to the input variables of the system or process, so that the reasons for the changes can be observed and identified in the output response". [67]

Many experiments involve the study of the effects of two or more factors and in general, factorial designs are the most efficient for this type of experiment. Factorial design means that for each complete trial or replication of the experiment all possible combinations of the levels of the factors are investigated. i.e. if there are a levels of factor A, and b levels of factor B, each replicate contains all ab combinations.

Factorial designs are now widely used for experiments where it is necessary to study the joint effect of various factors upon a response, several cases of special factorial design are important and are commonly used in research, also because they form the basis of other designs that are of considerable practical value.

The most important special case of factorial design is known as k factor design with each factor having only two levels. The level could be **Quantitative**, such as two values of temperature, pressure, or time; or **Qualitative**, such as two machines, two operators or even *high* and *low* levels of a factor, this is the method that has been used here. A complete replicate of such a design requires 2 x 2 x...x 2 = 2^k observations and is known as a $\mathbf{2^k}$ **factorial design.**
For this class of design it is assumed that;

1. All factors are fixed
2. The designs are completely randomised
3. Usual normality assumptions apply

$\mathbf{2^k}$ design is very useful in the early stages of experimental work when many factors are being investigated, as it provides the smallest number of runs with which k factors can be studied for a complete factorial design.

Consequently, these designs are also widely used in factor screening experiments, as there are only two levels for each factor, it is assumed that the response is approximately linear over the range of the factor levels chosen. In many factor based experiments, as the study is beginning, this is often quite a reasonable assumption to make.

Experiments for Factorial Analysis

The experiments for all loading Modes consisted of a number of factors, each set at two levels, one low (-1) and one high (+1).
The following five factors were considered:-

A - Tool Profile

B - Material

C - Score Residual

D - Rolling Direction

E - Gap

Figure 4.1, shows a physical representation of factors A, B, C, D & E.

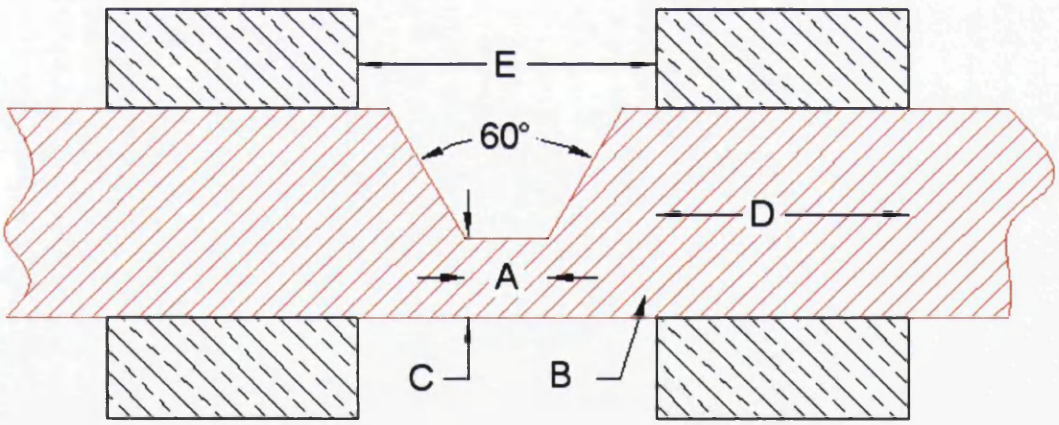

Figure 4.1: Schematic showing a Physical Representation of all Five Factors

Figure 4.2 lists each factor together with their values of low and high levels.

Factor	A	B	C	D	E
Level	Tool Width	Material	Score Residual	Rolling Direction	Gap
-1	60°/30µm	TH435	60µm	0°	0.18mm
+1	60°/60µm	TH550N	80µm	90°	0.40mm

Figure 4.2: High and Low Levels for each Factor

Factor E - Gap, was only valid for the Mode II experiments, which meant that all factorial analysis for Modes I and III were 2^4 factorial, whereas the factorial analysis for Mode II was 2^5 factorial.

In order to best understand factorial analysis, the following sections present the methodology used for a typical 2^4 analysis as used for Modes I and III, followed by a 2^5 analysis as used in Mode II.

2^4 Factorial Design

Each Mode I and Mode III loading experiment produced 16 results, these were then used to perform factorial analysis based on the four factors applicable to the testing, the following example demonstrates the method undertaken to perform a complete 2^4 factorial analysis.

Using the 16 results generated, it becomes possible to estimate the effect of each factor and the effect of each interaction, a typical design matrix for a 16 results analysis is shown in figure 4.3.

Mode I - Factorial Analysis - Displacement Results

Run Number	Factors A	B	C	D	Run Label	Factors A	B	C	D	Test Number	Test Order	Run No	Disp (mm)	
1	-	-	-	-	(1)	60/30	TH435	60	0°	31	15	1	416.00	(1)
2	+	-	-	-	a	60/60	TH435	60	0°	15	7	2	542.50	a
3	-	+	-	-	b	60/30	TH550	60	0°	27	11	3	508.67	b
4	+	+	-	-	ab	60/60	TH550	60	0°	11	3	4	385.25	ab
5	-	-	+	-	c	60/30	TH435	80	0°	30	14	5	457.50	c
6	+	-	+	-	ac	60/60	TH435	80	0°	14	6	6	648.50	ac
7	-	+	+	-	bc	60/30	TH550	80	0°	26	10	7	476.25	bc
8	+	+	+	-	abc	60/60	TH550	80	0°	10	2	8	456.25	abc
9	-	-	-	+	d	60/30	TH435	60	90°	32	16	9	389.75	d
10	+	-	-	+	ad	60/60	TH435	60	90°	16	8	10	545.50	ad
11	-	+	-	+	bd	60/30	TH550	60	90°	28	12	11	418.75	bd
12	+	+	-	+	abd	60/60	TH550	60	90°	12	4	12	410.00	abd
13	-	-	+	+	cd	60/30	TH435	80	90°	29	13	13	484.25	cd
14	+	-	+	+	acd	60/60	TH435	80	90°	13	5	14	643.50	acd
15	-	+	+	+	bcd	60/30	TH550	80	90°	25	9	15	515.25	bcd
16	+	+	+	+	abcd	60/60	TH550	80	90°	9	1	16	482.25	abcd
												Average Max Load (N) =	486.26	

Figure 4.3: Design Matrix for typical 2^4 Analysis *(16 Results)*

Main factors are found using the following equations[1];

$$A = \frac{1}{8n}[a+ab+ac+abc+ad+abd+acd+abcd\ -(1)-b-c-bc-d-bd-cd-bcd] \tag{4.1}$$

$$B = \frac{1}{8n}[b+ab+bc+abc+bd+abd+bcd+abcd\ -(1)-a-c-ac-d-ad-cd-acd] \tag{4.2}$$

$$C = \frac{1}{8n}[c+ac+bc+abc+cd+acd+bcd+abcd\ -(1)-a-b-ab-d-ad-bd-abd] \tag{4.3}$$

$$D = \frac{1}{8n}[d+ad+bd+abd+cd+acd+bcd+abcd\ -(1)-a-b-ab-c-ac-bc-abc] \tag{4.4}$$

[1]Where n represents the replicates i.e. the number of times the experiment was run.

With two way interactions defined by;

$$AB = \frac{1}{8n}[(1)+ab+c+abc+d+abd+cd+abcd\ -a-b-ac-bc-ad-bd-acd-bcd] \tag{4.5}$$

$$AC = \frac{1}{8n}[(1)+b+ac+abc+d+bd+acd+abcd\ -a-ab-c-bc-ad-abd-cd-bcd] \tag{4.6}$$

$$AD = \frac{1}{8n}[(1)+b+c+bc+ad+abd+acd+abcd\ -a-ab-ac-abc-d-bd-cd-bcd] \tag{4.7}$$

$$BC = \frac{1}{8n}[(1)+a+bc+abc+d+ad+bcd+abcd\ -b-ab-c-ac-bd-abd-cd-acd] \tag{4.8}$$

$$BD = \frac{1}{8n}[(1)+a+c+ac+bd+abd+bcd+abcd\ -b-ab-bc-abc-d-ad-cd-acd] \tag{4.9}$$

$$CD = \frac{1}{8n}[(1)+a+b+ab+cd+acd+bcd+abcd\ -c-ac-bc-abc-d-ad-bd-abd] \tag{4.10}$$

Three way interactions by;

$$ABC = \frac{1}{8n}[a+b+c+abc+ad+bd+cd+abcd\ -(1)-ab-ac-bc-d-abd-acd-bcd] \tag{4.11}$$

$$ABD = \frac{1}{8n}[a+b+ac+bc+d+abd+cd+abcd\ -(1)-ab-c-abc-ad-bd-acd-bcd] \tag{4.12}$$

$$ACD = \frac{1}{8n}[a+ab+c+bc+d+bd+acd+abcd-(1)-b-ac-abc-ad-abd-cd-bcd] \tag{4.13}$$

$$BCD = \frac{1}{8n}[b+ab+c+ac+d+ad+bcd+abcd\ -(1)-a-bc-abc-bd-abd-cd-acd] \tag{4.14}$$

And finally the last remaining four way interaction by;

$$ABCD = \frac{1}{8n}[(1)+ab+ac+bc+ad+bd+cd+abcd\ -a-b-c-abc-d-abd-acd-bcd] \tag{4.15}$$

2^4	A	B	AB	C	AC	BC	ABC	D	AD	BD	ABD	CD	ACD	BCD	ABCD
(1)	-1	-1	1	-1	1	1	-1	-1	1	1	-1	1	-1	-1	1
a	1	-1	-1	-1	-1	1	1	-1	-1	1	1	1	1	-1	-1
b	-1	1	-1	-1	1	-1	1	-1	1	-1	1	1	-1	1	-1
ab	1	1	1	-1	-1	-1	-1	-1	-1	-1	-1	1	1	1	1
c	-1	-1	1	1	-1	-1	1	-1	1	1	-1	-1	1	1	-1
ac	1	-1	-1	1	1	-1	-1	-1	-1	1	1	-1	-1	1	1
bc	-1	1	-1	1	-1	1	-1	-1	1	-1	1	-1	1	-1	1
abc	1	1	1	1	1	1	1	-1	-1	-1	-1	-1	-1	-1	-1
d	-1	-1	1	-1	1	1	-1	1	-1	-1	1	-1	1	1	-1
ad	1	-1	-1	-1	-1	1	1	1	1	-1	-1	-1	-1	1	1
bd	-1	1	-1	-1	1	-1	1	1	-1	1	-1	-1	1	-1	1
abd	1	1	1	-1	-1	-1	-1	1	1	1	1	-1	-1	-1	-1
cd	-1	-1	1	1	-1	-1	1	1	-1	-1	1	1	-1	-1	1
acd	1	-1	-1	1	1	-1	-1	1	1	-1	-1	1	1	-1	-1
bcd	-1	1	-1	1	-1	1	-1	1	-1	1	-1	1	-1	1	-1
abcd	1	1	1	1	1	1	1	1	1	1	1	1	1	1	1

Figure 4.4: Contrast Constraints for a 2^4 Design

The Sum of Squares for each main effect and interactions are calculated next, for a 2^4 analysis, the contrasts that have already been calculated in equations 4.1 thru 4.15 are reused, i.e. for main effect A the contrast is equal to:-

$$Contrast_A = [a+ab+ac+abc+ad+abd+acd+abcd\ -(1)-b-c-bc-d-bd-cd-bcd] \tag{4.16}$$

The exact same result determined by equation 4.16 can also be found from column A of figure 4.4, which means that the contrasts for all the other main effects and interactions can be determined in exactly the same manner.
With the contrasts available the Sum of Squares can now be calculated using:-

$$SS_A = \frac{[a + ab + ac + abc + ad + abd + acd + abcd - (1) - b - c - bc - d - bd - cd - bcd]^2}{8n} \tag{4.17}$$

or more concisely:-

$$SS = \frac{[Contrast]^2}{8n} \tag{4.18}$$

With the main effects, contrasts and sum of squares available, further simple calculations can be made to find the following:-

- Contrast squared and (%) percentage contribution.
- Sum of (+) positive effects and averaged sum of (+) positive effects.
- Sum of (-) negative effects and averaged sum of (-) negative effects.

In reality, calculations are best performed using a spreadsheet, figure 4.5 below details the values generated from the results of a typical 2^4 factorial analysis.

Model Term	A	B	AB	C	AC	BC	ABC	D	AD	BD	ABD	CD	ACD	BCD	ABCD
(1)	-416	-416	416	-416	416	416	-416	-416	416	416	-416	416	-416	-416	416
a	543	-543	-543	-543	-543	543	543	-543	-543	543	543	543	543	-543	-543
b	-509	509	-509	-509	509	-509	509	-509	509	-509	509	509	-509	509	-509
ab	385	385	385	-385	-385	-385	-385	-385	-385	-385	-385	385	385	385	385
c	-458	-458	458	458	-458	-458	458	-458	458	458	-458	-458	458	458	-458
ac	649	-649	-649	649	649	-649	-649	-649	-649	649	649	-649	-649	649	649
bc	-476	476	-476	476	-476	476	-476	-476	476	-476	476	-476	476	-476	476
abc	456	456	456	456	456	456	456	-456	-456	-456	-456	-456	-456	-456	-456
d	-390	-390	390	-390	390	390	-390	390	-390	-390	390	-390	390	390	-390
ad	546	-546	-546	-546	-546	546	546	546	546	-546	-546	-546	-546	546	546
bd	-419	419	-419	-419	419	-419	419	419	-419	419	-419	-419	419	-419	419
abd	410	410	410	-410	-410	-410	-410	410	410	410	410	-410	-410	-410	-410
cd	-484	-484	484	484	-484	-484	484	484	-484	-484	484	484	-484	-484	484
acd	644	-644	-644	644	644	-644	-644	644	644	-644	-644	644	644	-644	-644
bcd	-515	515	-515	515	-515	515	-515	515	-515	515	-515	515	-515	515	-515
abcd	482	482	482	482	482	482	482	482	482	482	482	482	482	482	482
Contrast	447	-373	-331	547	147	-191	11	-7	99	1	104	175	-157	65	-31
contrast Squared	200104	225464	668584	299570	21659	17601.3	124.769	2.7889	9834.69	1.7689	10851.4	30684.5	35596.4	7253.93	4444.89
Effect Estimate	55.9163	-59.384	-102.21	68.4163	18.3963	-16.584	1.39625	-0.2088	12.3963	0.16625	13.0213	21.8963	-28.584	10.6463	-8.3338
Sum of Squares	12506.6	14091.5	41786.5	18723.1	1353.69	1100.08	7.79806	0.17431	614.668	0.11056	678.212	1917.78	2224.77	453.371	277.806
% Contribution	13.0636	14.7191	43.6476	19.557	1.41398	1.14908	0.00815	0.00018	0.64204	0.00012	0.70842	2.0032	2.32386	0.47356	0.29018
Calculations for main effects ΣYA+	4113.75	3652.67	3481.25	4163.75	3963.67	3823.75	3895.67	3889.25	3939.67	3890.75	3942.17	3977.67	3798.75	3932.67	3856.75
ΣYA+/8	514.219	456.584	435.156	520.469	495.459	477.969	486.959	486.156	492.459	486.344	492.771	497.209	474.469	491.584	482.094
ΣYA-	-3656.47	-4127.5	-4298.03	-3616.42	-3816.5	-3956.42	-3984.5	-3950.92	-3940.05	-4089.42	-3938	-3802.5	-3984.47	-3867.5	-3924.53
ΣYA-/8	-456.3	-515.94	-537.37	-452.05	-477.06	-494.55	-498.06	-493.87	-492.56	-486.18	-492.25	-475.31	-498.06	-483.44	-490.57

Figure 4.5: Spreadsheet Generated Values for a Typical 2^4 Factorial

After the results are collected and all calculations are complete, the next step is to produce a probability plot that arranges the main effects and interactions in order of rank and probability, from this table a graph can then be produced that visually ranks each main effect and interaction in order of its probability.

Probability Plot				
Term	Effect	Rank	CP	ZI
AB	-102.2088	1	3.33333	-1.83391
B	-59.35375	2	10	-1.28155
ACD	-23.58375	3	16.6667	-0.96742
BC	-16.58375	4	23.3333	-0.72791
ABCD	-8.33375	5	30	-0.5244
D	-0.20875	6	36.6667	-0.34069
BD	0.16625	7	43.3333	-0.16789
ABC	1.39625	8	50	-1.4E-16
BCD	10.64625	9	56.6667	0.16789
AD	12.39625	10	63.3333	0.34069
ABD	13.02125	11	70	0.5244
AC	18.39625	12	76.6667	0.72791
CD	21.89625	13	83.3333	0.96742
A	55.91625	14	90	1.28155
C	68.41625	15	96.6667	1.83391

(a) Probability Table

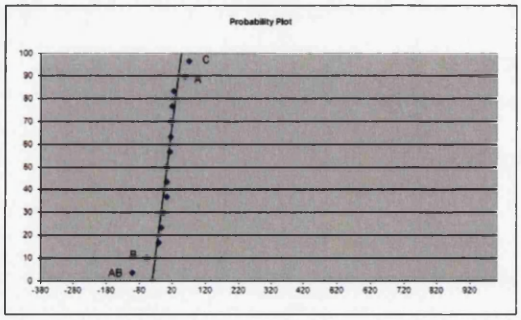

(b) Probability Plot

Figure 4.6: Typical 2^4 Probability Table & Graph

The probability table and graph for a typical 2^4 analysis is detailed in figure 4.6, however, results for each individual Mode will be discussed in more detail under the relevant section.

Using the results from the probability plot, further plots are then produced of all the main effects and interactions that are not positioned on the straight line that links each factor and interaction, this can be seen on plot in figure 4.6.

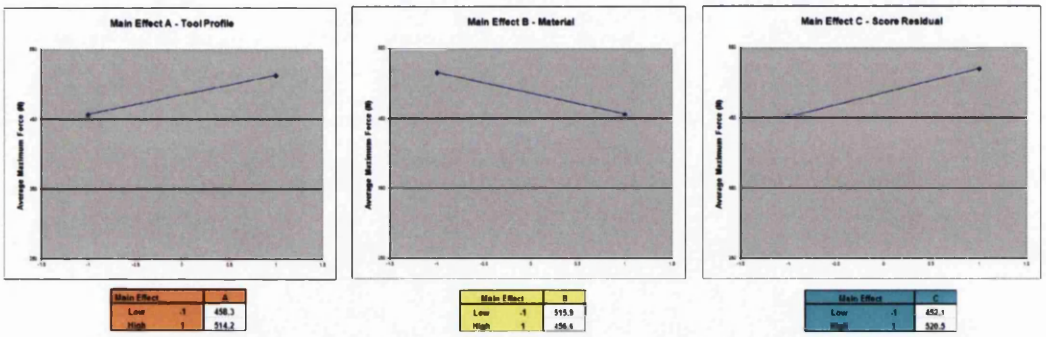

(a) Main Effect A (b) Main Effect B (c) Main Effect C

Figure 4.7: Main Effects from a typical 2^4 Analysis

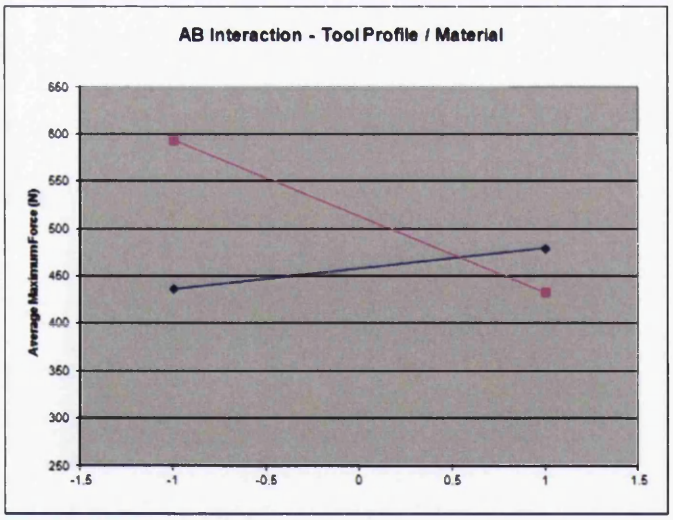

A-B Interaction		B Low	B High
-1	A Low	436.9	479.7
1	A High	595.0	433.4

Figure 4.8: Two Way Interaction from a typical 2^4 Analysis

It is these factors and interactions that do not lie on the straight line that are most likely to have the greatest influence on the results.

2^5 Factorial Design

For the Mode II experiments, an additional factor was introduced called *Gap* and given the label E, which meant that the factorial design for Mode II increased to a 2^5 design. The main difference between a 2^4 and a 2^5 factorial, is that the 2^5 doubles in size in comparison to the 2^4, i.e. 32 results, as opposed to 16.
Figure 4.9 shows the difference in size, compared with the 2^4 factorial of fig 4.3.

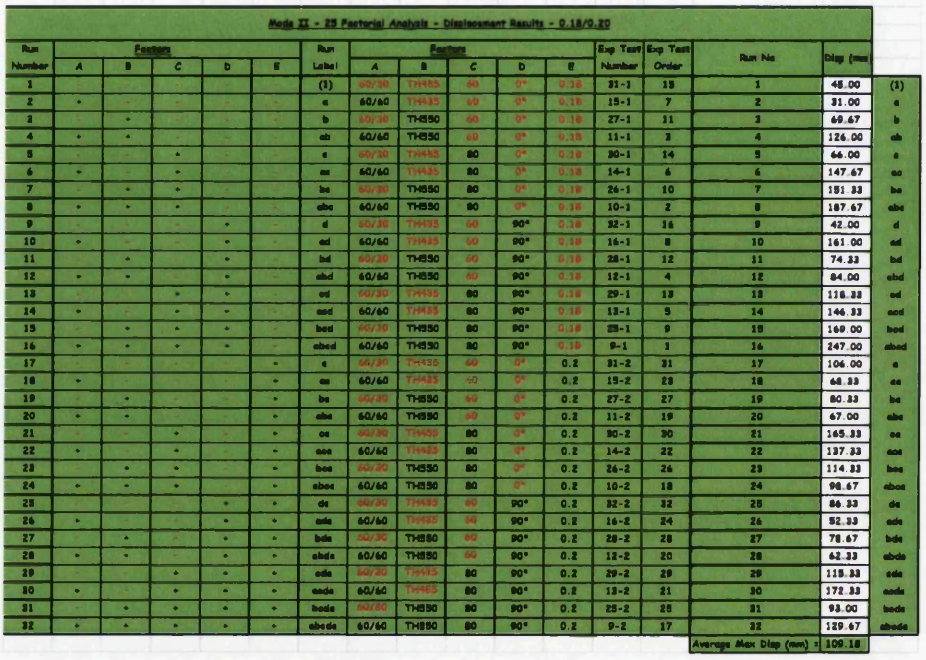

Run Number	Factors A	B	C	D	E	Run Label	Factors A	B	C	D	E	Exp Test Number	Exp Test Order	Run No	Disp (mm)	
1						(1)	60/30	TH455	60	0°	0.15	31-1	15	1	45.00	(1)
2	+					a	60/60	TH435	60	0°	0.15	15-1	7	2	31.00	a
3		+				b	90/30	TH550	60	0°	0.15	27-1	11	3	69.67	b
4	+	+				ab	60/60	TH550	60	0°	0.15	11-1	3	4	126.00	ab
5			+			c	60/30	TH455	80	0°	0.15	30-1	14	5	66.00	c
6	+		+			ac	60/60	TH435	80	0°	0.15	14-1	6	6	147.67	ac
7		+	+			bc	90/30	TH550	80	0°	0.15	26-1	10	7	151.33	bc
8	+	+	+			abc	60/60	TH550	80	0°	0.15	10-1	2	8	187.67	abc
9				+		d	60/30	TH455	60	90°	0.15	32-1	16	9	42.00	d
10	+			+		ad	60/60	TH435	60	90°	0.15	16-1	8	10	161.00	ad
11		+		+		bd	90/30	TH550	60	90°	0.15	28-1	12	11	74.33	bd
12	+	+		+		abd	60/60	TH550	60	90°	0.15	12-1	4	12	84.00	abd
13			+	+		cd	60/30	TH455	80	90°	0.15	29-1	13	13	116.33	cd
14	+		+	+		acd	60/60	TH435	80	90°	0.15	13-1	5	14	146.33	acd
15		+	+	+		bcd	90/30	TH550	80	90°	0.15	25-1	9	15	169.00	bcd
16	+	+	+	+		abcd	60/60	TH550	80	90°	0.15	9-1	1	16	247.00	abcd
17					+	e	60/30	TH435	60	0°	0.2	31-2	31	17	106.00	e
18	+				+	ae	60/60	TH435	60	0°	0.2	15-2	23	18	68.33	ae
19		+			+	be	90/30	TH550	60	0°	0.2	27-2	27	19	80.33	be
20	+	+			+	abe	60/60	TH550	60	0°	0.2	11-2	19	20	67.00	abe
21			+		+	ce	60/30	TH435	80	0°	0.2	30-2	30	21	165.33	ce
22	+		+		+	ace	60/60	TH435	80	0°	0.2	14-2	22	22	137.33	ace
23		+	+		+	bce	90/30	TH550	80	0°	0.2	26-2	26	23	114.33	bce
24	+	+	+		+	abce	60/60	TH550	80	0°	0.2	10-2	18	24	98.67	abce
25				+	+	de	60/30	TH455	60	90°	0.2	32-2	32	25	86.33	de
26	+			+	+	ade	60/60	TH435	60	90°	0.2	16-2	24	26	52.33	ade
27		+		+	+	bde	90/30	TH550	60	90°	0.2	28-2	28	27	78.67	bde
28	+	+		+	+	abde	60/60	TH550	60	90°	0.2	12-2	20	28	62.33	abde
29			+	+	+	cde	60/30	TH475	80	90°	0.2	29-2	29	29	115.33	cde
30	+		+	+	+	acde	60/60	TH465	80	90°	0.2	13-2	21	30	172.33	acde
31		+	+	+	+	bcde	90/30	TH550	80	90°	0.2	25-2	25	31	93.00	bcde
32	+	+	+	+	+	abcde	60/60	TH550	80	90°	0.2	9-2	17	32	129.67	abcde
														Average Max Disp (mm) =	109.18	

Figure 4.9: Design Matrix for typical 2^5 Analysis *(32 Results)*

Once again the main effects are found using the same procedure as before, however notice how much larger equation 4.19 becomes for the 2^5 factorial compared with equation 4.1 for a 2^4, i.e. the number of R.H.S. terms effectively doubles.

$$A = \frac{1}{8n}[a + ab + ac + abc + ad + abd + acd + abcd + ae + abe + ace$$
$$+abce + ade + abde + acde + abcde - (1) - b - c - bc - d - bd - cd - bcd$$
$$-e - be - ce - bce - de - bde - cde - bcde] \tag{4.19}$$

This increase in size can also be seen when comparing the contrast table for the 2^4 analysis, figure 4.4, with figure 4.10 below for the 2^5 factorial.

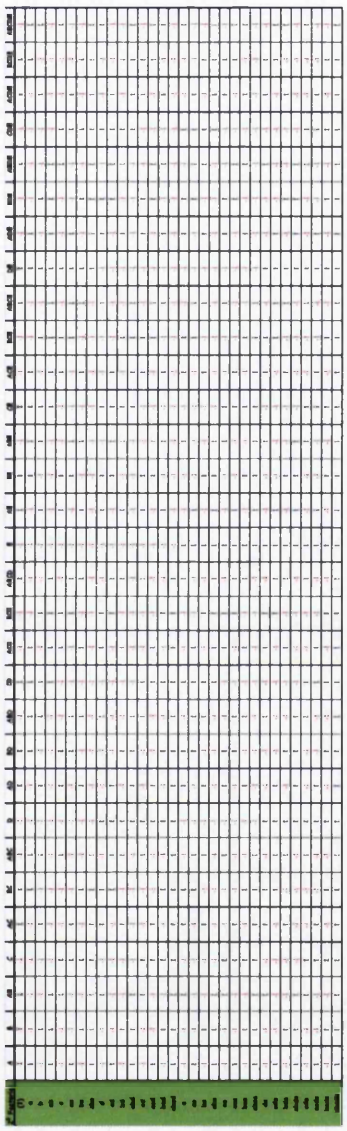

Figure 4.10: Contrast Constraints for a 2^5 Design

All three opening modes were tested using a standard calibrated bench mounted tensile tester and the results for each analysis, i.e. Mode I, II & III are discussed further in the following sections.

4.2 Mode I

Both Mode I and Mode III had been investigated previously by others, [66], [10], [11], [65], & [63], however, the main reason behind repeating the experiments was to generate a comprehensive data set for both selected materials with the 60°/60μm and 60°/30μm tooling at two score residual depths of 60μm and 80μm.

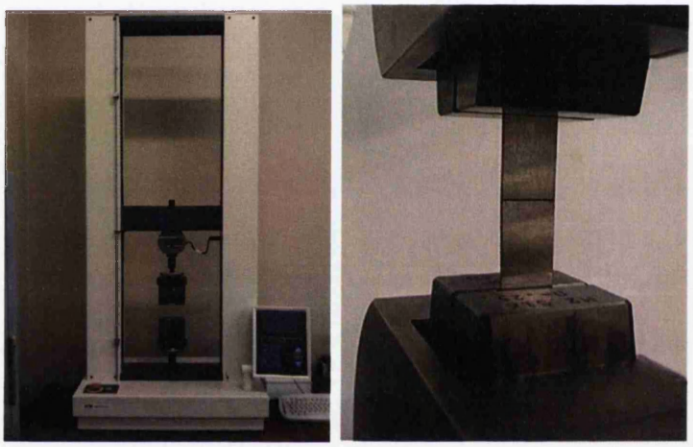

(a) Tensile M/C (b) Mode I Experiment

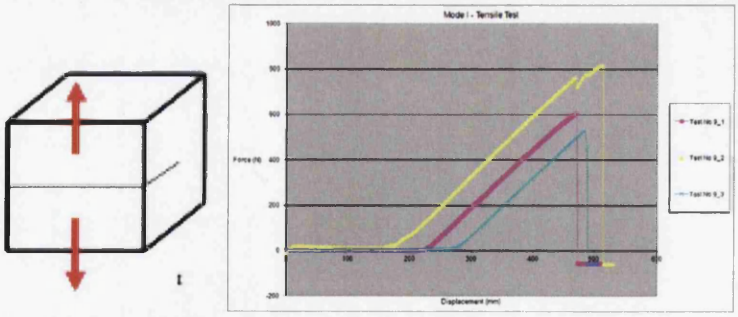

(c) Mode I Loading (d) Mode I Load-Disp Graph

Figure 4.11: Mode I Experiment, Loading Mode and Result Graph

The 12.5mm strip samples used for Mode I were placed directly into the jaws of the machine as shown in 4.11(b) and pulled apart whilst recording both force and displacement, a typical result graph can be seen in 4.11(d).

Using four combinations of factors for analysis, [67], meant that 16 tests were completed, however, each test was duplicated 3 times to give 48 runs, then each result was averaged to give the final 16 results used for the Mode I analysis.

Level	A - Tool Profile	B - Material	C - Score Residual	D - Roll Direction
-1	60°/30μm	TH435	60μm	0°
+1	60°/60μm	TH550	80μm	90°

Table 4.1: Mode I - Experimental Factors and Levels

The force and displacement results generated were used to calculate results for stress, then all three separate sets of results were used for a complete factorial analysis for Mode I. Initially, all analysis was completed using an Excel^{TM}spreadsheet, however it soon became apparent that using the commercial statistics package Minitab^{TM}, would be beneficial as it would not only help speed up the time required to complete an analysis, but it could also be used as a double check with the Excel^{TM}analysis.
The following details the complete set of factorial analysis completed for Mode I[1].

1. Force Results
   (a) Minitab^{TM}
   (b) Excel^{TM}
2. Displacement Results
   (a) Minitab^{TM}
   (b) Excel^{TM}
3. Stress Results
   (a) Minitab^{TM}
   (b) Excel^{TM}

[1]Appendice C, figures C.1 thru C.6, contain details of all of the results generated for each Mode I analysis, presented firstly in Minitab^{TM}, followed by Excel^{TM}

Conclusions - Mode I

For all three sets of results, i.e. Force, Displacement and Stress, each normal plot shows that for Mode I, Factors A - Tool Profile, and C - Score Residual, were positively significant, which means that as both these factors increase i.e. go from the low level (-1), to the high level (+1), the force, the displacement and the stress required to break the sample increases as well.

More subtly, the results also seem to indicate that Factor B - Material and Interaction AB - Tool Profile / Material also has some significance throughout all three sets of results, however, it is thought that the very large pre-deformations produced by the initial scoring process probably annihilate or mask the differences in the base materials and this is likely to be the reason why Factor B - Material, shows minor significance in Mode I.

Although the results held no real surprises, they did provide confirmation of what was expected, which in turn gave confidence in the methods used with the factorial analysis, however, these results still have value, as they are now available to provide for future validation with the further development of a multistage numerical model.

4.3 Mode II

Mode II testing, as applied to FAEOE's, according to the authors best knowledge, has never been recognised either experimentally or numerically, therefore this opening Mode became the main focus of the project.

Firstly, a tool had to be developed, that could hold, then shear a 12.5mm strip with variable clearance, additionally, the tool required ease of manufacture and use and cost within the available budget.

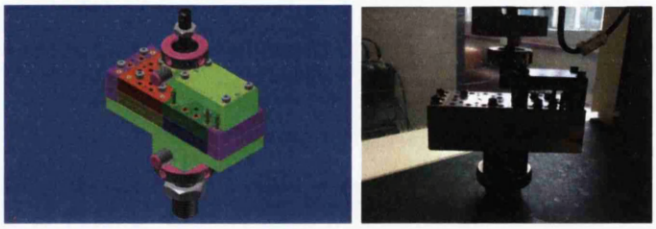

(a) Mode II 3D Model (b) Mode II Experiment

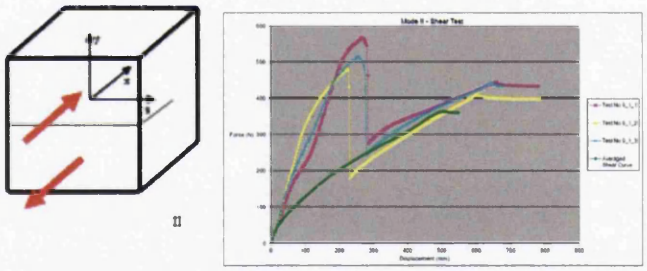

(c) Mode II Loading (d) Mode II Load-Disp Graph

Figure 4.12: Mode II Experiment, Loading Mode & Result Graph

As discussed in section 2.7, the final Mode II tool design was selected after going through a number of different concepts.
The finished tool was delivered with the following functions:-

- Accuracy - Capable of testing to within a 20μm - 40μm tolerance
- Placement - Centre placement for shear, edge placement for microscopy
- Design Symmetry - Adjustable blocks, to allow many variations in clearance
- Universal set up - Used in any standard tensile test machine 4.12(b)

The 12.5mm strip samples were placed directly onto the lower blocks, a centre finder then centrally positioned the sample by locating in the predeformed score, with the sample centred correctly it was clamped and the centre finder removed, the remaining upper blocks are slid into position, which sandwiches and clamps the 12.5mm sample securely. With the tool located in the tensile machine, one half remains free to slide upwards, shearing the sample in half, again both force and displacement were recorded with a typical result graph shown in 4.12(d).

As the Mode II tests contain five combinations of factors, 32 tests were required, each test was completed 3 times, giving 96 runs, however, after the third test was completed the tool was reset without removing the sheared sample and the test rerun, this allowed for the force of the tooling to be recorded, this could then be used to estimate the force of the Mode II Tool, in order to try to remove its influence from the results and establish a final result.

Overall 128 runs were completed for each of the 8 clearances, which gave a total of 1024 runs for the whole of the Mode II experiment.

Level	A - Tool Profile	B - Material	C - Score Res	D - Roll Dir	E - Gap
-1	60°/30μm	TH435	60μm	0°	0.18mm
+1	60°/60μm	TH550	80μm	90°	0.40mm

Table 4.2: Mode II - Experimental Factors and Levels

Five factors combinations are shown in Table 4.2, but for Factor E - Gap, the following eight values were used, 0.18, 0.2, 0.22, 0.24, 0.28, 0.32, 0.36 & 0.4mm, these clearances provided the variation, which enabled a thorough investigation of two level factorial analysis to be completed.

For Mode II, both force and displacement results were generated, a full 2^5 factorial analysis for Mode II was then completed using these results.

After the experience gained with the Mode I analysis it was decided that because of the large amount of analysis required for Mode II it would be easier and faster to complete the analysis using the commercial statistics package Minitab^{TM}, however it was decided that for both sets of results to also complete an Excel^{TM}analysis for the first and last set of clearances in order to act as a double check.

The following details the complete set of factorial analysis for Mode II.[1]

1. Force Results
   (a) Minitab™: 0.18 - 0.20
   (b) Excel™: 0.18 - 0.20
   (c) Minitab™: 0.18 - 0.22
   (d) Minitab™: 0.18 - 0.24
   (e) Minitab™: 0.18 - 0.28
   (f) Minitab™: 0.18 - 0.32
   (g) Minitab™: 0.18 - 0.36
   (h) Minitab™: 0.18 - 0.40
   (i) Excel™: 0.18 - 0.40
2. Displacement Results
   (a) Minitab™: 0.18 - 0.20
   (b) Excel™: 0.18 - 0.20
   (c) Minitab™: 0.18 - 0.22
   (d) Minitab™: 0.18 - 0.24
   (e) Minitab™: 0.18 - 0.28
   (f) Minitab™: 0.18 - 0.32
   (g) Minitab™: 0.18 - 0.36
   (h) Minitab™: 0.18 - 0.40
   (i) Excel™: 0.18 - 0.40

[1]Appendice C, figures C.7 thru C.24, details the results for each 2^5 factorial completed for Mode II, with the first and last analysis i.e. clearance 0.18 - 0.20 and clearance 0.18 - 0.40 repeated in Excel™

Conclusions - Mode II

Gap	Positive Significant Effects									Negative Significant Effects			
0.18-0.20		B	C	E						AE	BE		
0.18-0.22	A	B	C			AC	BC		ACE		BE		
0.18-0.24	A	B	C	E							BE	ABE	BCE
0.18-0.28	A	B	C		AB					AE	BE		
0.18-0.32	A	B	C	E				CE			BE		
0.18-0.36		B	C					CE			BE		
0.18-0.40			C		AB						BE		
Qty	4	6	7	3	2	1	1	2	1	2	7	1	1

Table 4.3: Mode II - Significant Effects and Interactions - Force Results

The results shown in table 4.3 were generated using the load response, for positive significant effects, what can be seen instantly regarding the main factors is that;

Factor C - Score residual, seems to have the most influence over the whole range, closely followed by Factors B - Material, A - Tool Profile and E - Gap, however for the range 0.18 - 0.40 a number of results had to be recorded as zero as some of the samples were very brittle and had broken in half, leaving an insufficient amount to complete the tests. However, when averaged results replace the zero in a *"what if"* analysis, Factor E reappears in the results, indicating that it may have more significance than first appears in table 4.3.

Regarding positive interactions, the results indicate that over the majority of the ranges interactions are low, i.e. either zero or one interaction per range; however, one exception is the range 0.18 - 0.22, which shows three separate interactions, it will be interesting to discover exactly what is going on here and it is hoped that further future numerical analysis, will help to provide an explanation.

Concerning negative significant effects, it is immediately clear that all the effects are interactions, the most significant of which is the interaction between Factors B - Material and E - Gap that appears over the complete set of ranges,

additionally, it is also worth noting that Factor E is prevalent on every negative interaction, which seems to indicate that gap or clearance variation does indeed have a considerable effect for Mode II opening.

As discussed previously, the initial scoring process introduces very large pre-deformations, which are probably large enough to annihilate any differences in the base materials. Hardening at very high equivalent strain levels is likely to become saturated to similar intensity for both tested material grades, which are of a same class of low carbon steels and this may well be the reason why both materials show minor significant effects in Mode I and III, however, the Mode II test is deliberately designed to allow bending of the sample, therefore a material influence is to be expected.

Gap	**Positive Significant Effects**											**Negative Significant Effects**			
0.18-0.20	A	C											AE	BE	
0.18-0.22	A	C				AC								BE	
0.18-0.24		C	D	E				CE					AE	BE	
0.18-0.28		C										E		BE	
0.18-0.32	A	C	D	E			BC	CE		BCD	BDE			BE	BCE
0.18-0.36	A	C						CE						BE	BCE
0.18-0.40	A	C			AB				ABE					BE	
Qty	5	7	2	2	1	1	1	3	1	1	1	1	2	7	2

Table 4.4: Mode II - Significant Effects and Interactions - Displacement Results

The results shown in table 4.4 were generated this time by the displacement response, regarding the main factors for positive significant effects, once again; Factor C - Score residual, seems to have the most influence over the whole range, this is followed closely by Factor A - Tool Profile, Factor D - Rolling Direction and Factor E - Gap, however, appear only twice. A fundamental difference in the displacement results compared with the force results is that Factor B - Material seems to disappear, the reasons for this, however, are presently not fully understood, and again it is hoped that future numerical analysis, will help provide an explanation and discover exactly what is going on.

With regards to the remaining positive interactions, the results again indicate that the interactions are low, i.e. either zero or one interaction per range; however, one exception is the range 0.18 - 0.32, which shows a number of two way and three way interactions, again here, further numerical analysis may help to provide an explanation.

As previously shown with the force analysis, regarding the negative significant effects, all effects bar one are interactions, again the most significant is the interaction between Factors B - Material and E - Gap, which again appears over the complete set of ranges, as with the force results, Factor E is prevalent on every negative interaction, therefore indicating that a variation in clearance does have a considerable effect for Mode II opening.

4.4 Mode III

As with the Mode I analysis, Mode III had been investigated previously, [66], [10], [11], [65], and [63], again the main reason behind repeating the experiments was to generate a comprehensive data set for both selected materials with the $60°/60\mu m$ and $60°/30\mu m$ tooling and score residual depths of $60\mu m$ and $80\mu m$.

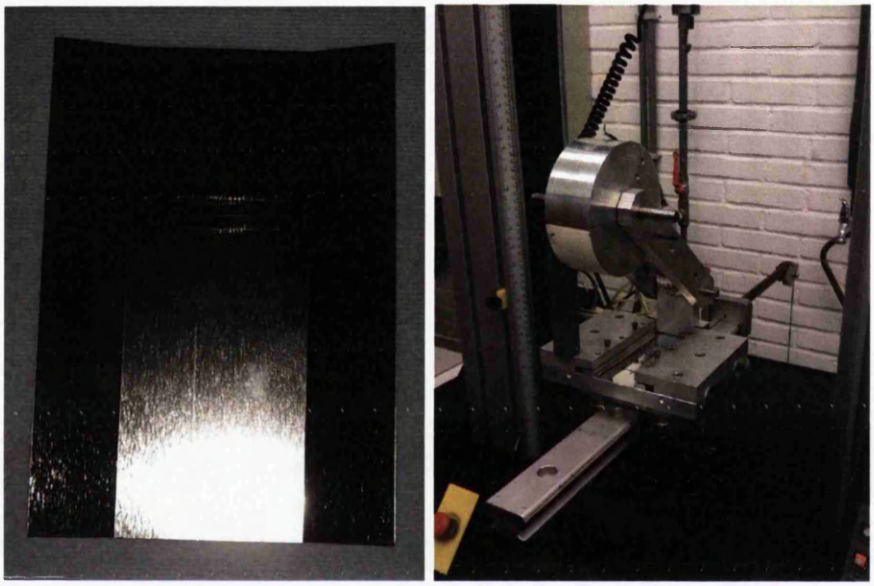

(a) Mode III Double Score Sample (b) Mode III Experiment

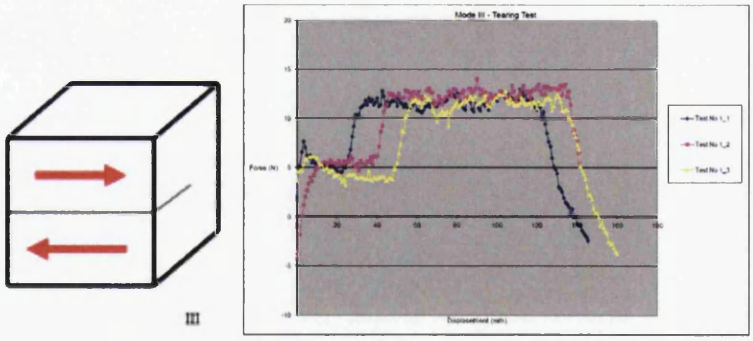

(c) Mode III Loading (d) Mode III Load-Disp Graph

Figure 4.13: Mode III Experiment, Loading Mode and Result Graph

Factorial analysis [67], using four combinations of factors was completed, requiring 16 tests, duplicated 3 times, giving a total of 48 runs. Once more each result was averaged to give the final 16 results used for the Mode III analysis.[1]

Level	A - Tool Profile	B - Material	C - Score Residual	D - Roll Direction
-1	60°/30μm	TH435	60μm	0°
+1	60°/60μm	TH550	80μm	90°

Table 4.5: Mode III - Experimental Factors and Levels

Due to the way that the Mode III results were generated, meant that it was not possible to use the displacement results in the analysis, it was also not possible to calculate accurate results for stress, which meant that the only results available were the force results. Again, the analysis was completed using Excel^{TM}and repeated using Minitab^{TM}.

[1] Appendice C, figures C.25 and C.26, detail all results for the Mode III analysis

Conclusions - Mode III

The normal plot for Mode III shows that here, Factor C - Score Residual and Interaction AC - Tool Profile/Score Residual, are positively significant; i.e. when the score residual increases the breaking load rises. The interaction of A and C however, means that although the tool profile is not regarded as significant on its own, its interaction with C does cause a positive increase in the load required to break the sample.

As with Mode I, more subtly, the results also seem to indicate that the following factors, interactions and even a three way interaction, do show some influence on the results.

- Factor B - Material
- Interaction BC - Material/Score Residual
- Interaction BD - Material/Rolling Direction
- Interaction ABD - Tool Profile/Material/Rolling Direction

However, caution should be exercised regarding these more subtle results as they do not have the benefit of being backed up by additional factorial analysis as was the case for Mode I, here the only results analysed were for force.

Again, as was described for Mode I, the very large pre-deformations produced by the initial scoring process are thought to somehow annihilate or mask the differences in the base materials and this may be the reason why Factor B shows minor significance in Mode III.

As was the case for Mode I, the results provide no real surprises, but do provide confirmation of what was expected, once more these results are still valuable, in that they also can be used to provide further validation for a future multistage development of a numerical model.

Chapter 5

Micrography

5.1 Introduction

The work in this chapter is based on work carried out by Reseacher's from Tata Steel's Research, Development and Technology Department; *(formerly Corus RD&T).*

In particular I would like to thank Dr Monika Krugla for the work that she completed on my behalf during the period, Sept 2008 - March 2009, her efforts have really helped with the development of a more complete understanding of the microstructure of damaged scored materials and the processes and procedures used as necessary to develop this knowledge. I would also like to thank Dr Steven Celotto for allowing this work to be completed in a department that was already very busy supporting the demands from Tata's international business.

Finally, I would also like to once again thank my Industrial Supervisor Dr Géza Nagy, for allowing me to use additional information developed from a study that he completed within the Dutch Knowledge Workers scheme, innvestigating the evolution of damage in packaging steels during scoring of Easy Open Ends (EOE), completed in conjunction with Eindhoven University of Technology (TU/e).

5.2 Summary

In order to begin to determine damage occurring in a material during score forming, several steps were required.

- An investigation using Scanning Electron Microscopy (SEM) on samples with different surface states.
- Observation of voids and cracks in the as-polished samples.
- Nital etching, to provide additional information about the microstructure.
- Marshall reagent, to reveal the grain boundaries in the deformed area.

The influence of side effects of both reagents, *(i.e. etched out inclusions)* are also discussed.

5.3 Sample Preparation

To determine the state of the material after score forming, a series of scored samples were examined using SEM, see figure 2.7.

Each double score sample was first cut along line 1, using plate shears, then, to prevent further deformation, the samples were supporter by rubber and cut approximately 50mm in from the investigated edge of the sample *(RH edge, as shown in Figure 2.7)*, then a cut was made along line 2.

The sample was cold mounting using, *Epofix, Struers*, as this avoided both the shrinkage of the mounting material away from the specimen edges and helped eliminate the effects of any heat on the samples, the mounted samples were then ground and polished to 1 μm.

5.4 Investigation Procedure

To determine the damage which occurs in the material during score forming, samples were investigated in three different states:

- Mechanically polished samples
- Nital etched samples
- Marshall etched samples

Each state aimed to obtain different types of information about the damage and deformation of the microstructure.

Mechanically Polished Samples

Samples were mechanically diamond polished (DP) with 600 grit, followed by 1000 grit. Soft and ductile materials then require a final polish for optimum quality, here, oxide polishing (OP) is used. Colloidal silica, with a grain size of approximately 0.04 μm and a pH of about 9.8, shows remarkable results.

The combination of chemical activity and fine, gentle abrasion produces absolutely scratch-free, deformation-free specimen. Observations from the mechanically-polished samples did not reveal a lot of information about the microstructure *(i.e. ferrite grain boundaries and cementite particles)*, however, it did ensure that etching artifacts were not confused with voids generated by damage, correlations between voids and microstructure can then be made by using comparisons of the same regions, before and after etching.

Additionally, another advantage of observations before etching is that the tin layer can be observed after score forming.

Nital Etched Samples

One of the basic etchants used in metallography is Nital. It consists of a solution of 0.5-10% nitric acid in ethanol. Nital is used to reveal ferrite grain boundaries and martensite phase in most carbon and low-alloy steels as well as in cast irons. It is also employed for etching bainitic and pearlitic steels. During the etching process, Nital chemically attacks and dissolves ferrite. The dissolution rate of the ferrite depends on the crystallographic orientation and the strain in the bonds between the atoms, thus the etching process causes stress relief on the specimen.

In ferrite-martensite microstructure the grain boundaries can be visualised because most of the time they are standing out of the surface and therefore, causing pronounced light scattering. It is also possible to observe the carbides and inclusions in the microstructure since they are not affected by Nital. They can be easily detected because they appear as protruding irregularities, as Nital tends to rapidly open up cracks and holes in the material.

In previous investigations of damage caused by scoring, all the samples were etched with Nital, which revealed the ferrite grain boundaries, cementite, inclusions and some deformation features such as slip bands, these features are revealed because Nital is a *selective* etchant, in that the ferrite is dissolved at a rate dependent on the crystal orientation or by how strained the bonds are between atoms *e.g. dislocation cores.* The phases that are carbon-rich are less attached and so carbides stand proud of the ferrite matrix.

One unfortunate effect of etching with Nital is that inclusions and cementite particles can fall out of the ferrite matrix, so that voids seen in (b) of Figure 5.1, are not visible when compared with the same non-etched sample (c).

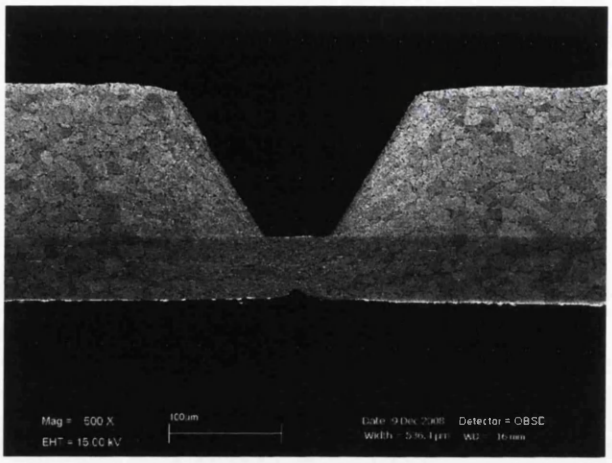

(a) 5A - Nital - QBSD

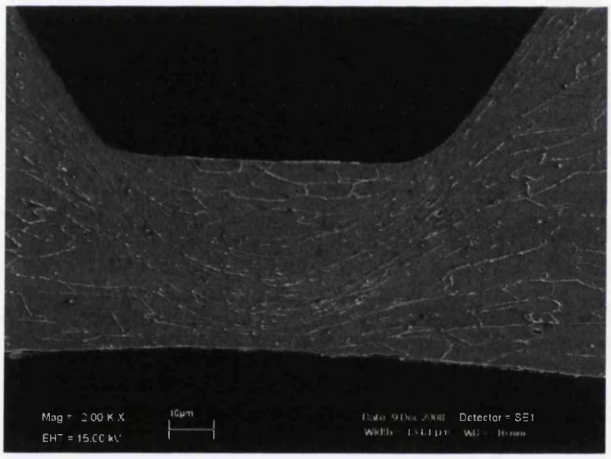

(b) 5B - Nital - SE1

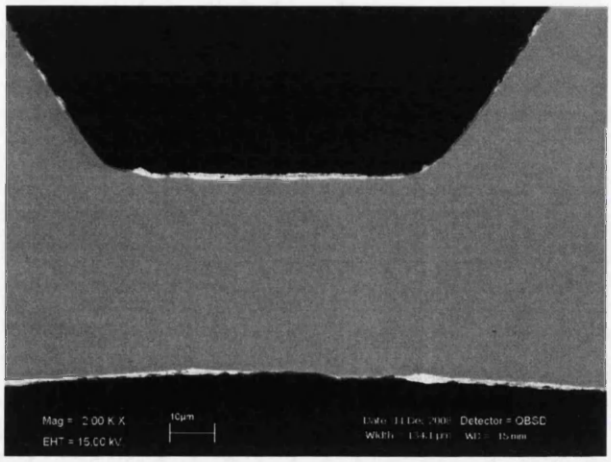

(c) 5B - QBSD Detector

Figure 5.1: Cross Sections with and without Etching

Nital Micrographs also show that although the deformation of the grains and slip bands can be seen, the grain boundaries cannot easily be distinguished in the deformed area.
This effect can be seen quite clearly in Figure 5.2.

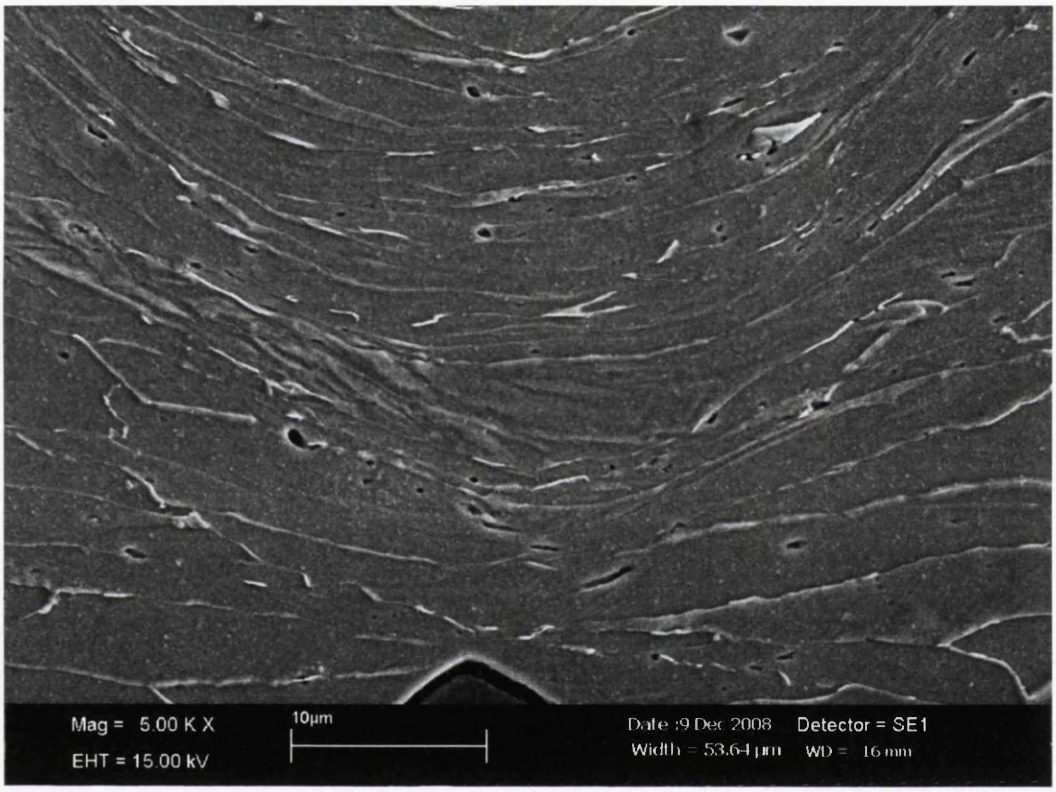

Figure 5.2: Cross Section of Sample etched with Nital

Marshall Etched Samples

This solution simultaneously smooths and etches the metallic sample, resulting in a bright finish in which a wide variety of microstructural detail can be observed. Composed of 8g oxalic acid and 5ml concentrated sulphuric acid in 100ml water mixed with an equal volume of 30% hydrogen peroxide, this chemical polishing technique reduces the extent of plastic deformation during sample preparation.

Unlike other chemical polishing processes that result in a dull surface finish, Marshall is suitable for selective etching of steel surfaces to reveal details of the microstructure for which other techniques are inadequate. Marshall reagent is often used with Interstitial Free (IF) steels to reveal the ferrite grain structure, primarily because Nital doesn't show all of the grain boundaries due to the similarities in the orientation of most of the grains. Marshall reagent doesn't attack the bulk ferrite grain, but instead it attacks the boundaries, *(It can be thought of as the reverse of Nital).* However, not only are the ferrite grain boundaries attacked, but also those between the matrix and any inclusion, consequentially, more particles fall out, or are dissolved in this reagent than is the case with Nital.

Unfortunately, this can give the impression of the presence of a large amount of voids in the material, see (a) from Figure 5.3, the Marshall reagent was used only in order to reveal the grain boundaries in the deformed part of the sample, as shown in (b) and (c), this wasn't possible using Nital etching.

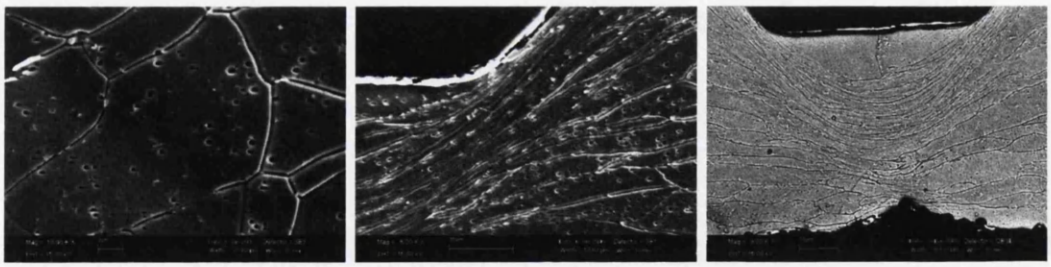

(a) 6A - Marshall - SE1 (b) 6B - Marshall - SE1 (c) 5A - Marshall - QBSD

Figure 5.3: Cross Sections of Samples etched with Marshall

5.5 Outcomes

A preliminary investigation of the cross sections of the scores showed that a three step procedure was required to get the best overview of both the microstructure and damage in thin packaging steel materials.

- Observations after polishing, but without etching were completed, this established the presence of voids without the risk of confusion with etching defects, also observation of the tin layer were made see (a) of Figure 5.4.
- Observations after etching with Nital - the microstructure of the undeformed regions are best revealed, heavily deformed region less so. Inclusions are also revealed with some voids detected. After comparison with the same sample in as-polished state it's clear they were caused through etching, see (b).
- Finally, etching with Marshall reagent - reveals the grain boundaries in the deformed area, however, because of the aggressiveness of this etchant along the grain boundaries, the inclusions become etched out.
  The amount of voids is high when compared with the two previous states, see (c).

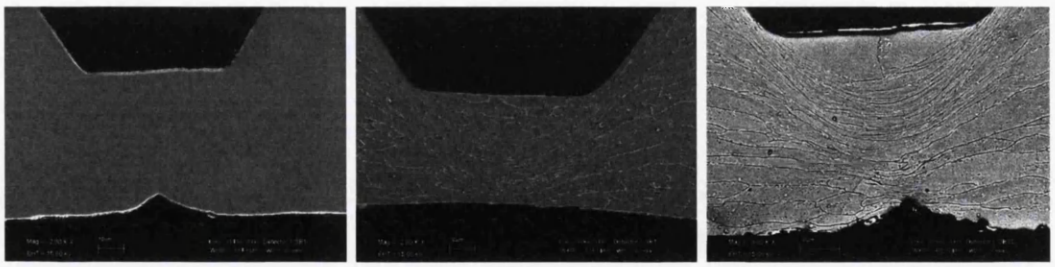

(a) 6A without Etching (b) 5B Nital SE1 (c) 6A Marshall QBSD

Figure 5.4: Cross Sections with and without Etching

5.6 Further Experiments

As mentioned in section 5.1, further investigation into the evolution of damage in packaging steels during scoring of Easy Open Ends (EOE) was completed by Dr Géza Nagy, in conjunction with Eindhoven University of Technology (TU/e).

During scoring of Easy Open Ends the usual 0.21mm gauge material is reduced in thickness to approximately 0.08mm. This process induces very high compressive and shear strains into the material, which has to withstand these very large deformations without sustaining premature damage.

One assumption is that the scoring process influences the opening characteristics, this implies that if the response of the material to scoring can be better understood, then the response to opening itself may also be improved.

As shown previously, when the experiments were complete, each sample was cross-sectioned for further micrographic analysis of the bulk.

5.7 Picral Etching

Following on from the work described in section 5.4, more attention was given to find a suitable etch technique in order to follow the damage in the form of micro-cracks and voids, see figure 5.5.

Each of the methods discussed earlier were used, but an additional method, known as Picral etching, was also investigated. Out of these four methods, Picral etching proved to have the most potential, due to the partial closure of the cracks and voids being observed at the surface of mechanically polished specimen, and that Nital and Marshall etch, as discussed in section 5.4, tended to open up voids, in extreme cases causing carbide particles to fall out from the microstructure.

Picral is also a standard etchant used in steels to reveal the microstructure, it contains 4g of picric acid dissolved in 100ml of ethanol. This etchant is used to reveal carbon-rich phases such as cementite, pearlite, martensite or bainite. Picral mainly attacks the interfaces between the carbon-rich phases and ferrite. The ferrite is dissolved irrespective of crystallographic orientation or other features. Therefore, etching with Picral does not allow for the sharp visualisation of the

boundaries between ferrite grains, also the etching time for Picral is longer than that for Nital, this allows for better control over the entire process.

Picral also has the advantage of being a more gentle process, revealing voids, but leaving any surrounding cementite particles mostly intact. Commonly, cementite particles are the usual suspects that initiate damage by acting as stress concentrations, therefore it is important to visualise them with their immediate vicinity. A disadvantage of Picral is that it does not give a contrast-rich image over grains and grain boundaries. However, the quality of Picral-etch SEM images were found to be satisfactory.

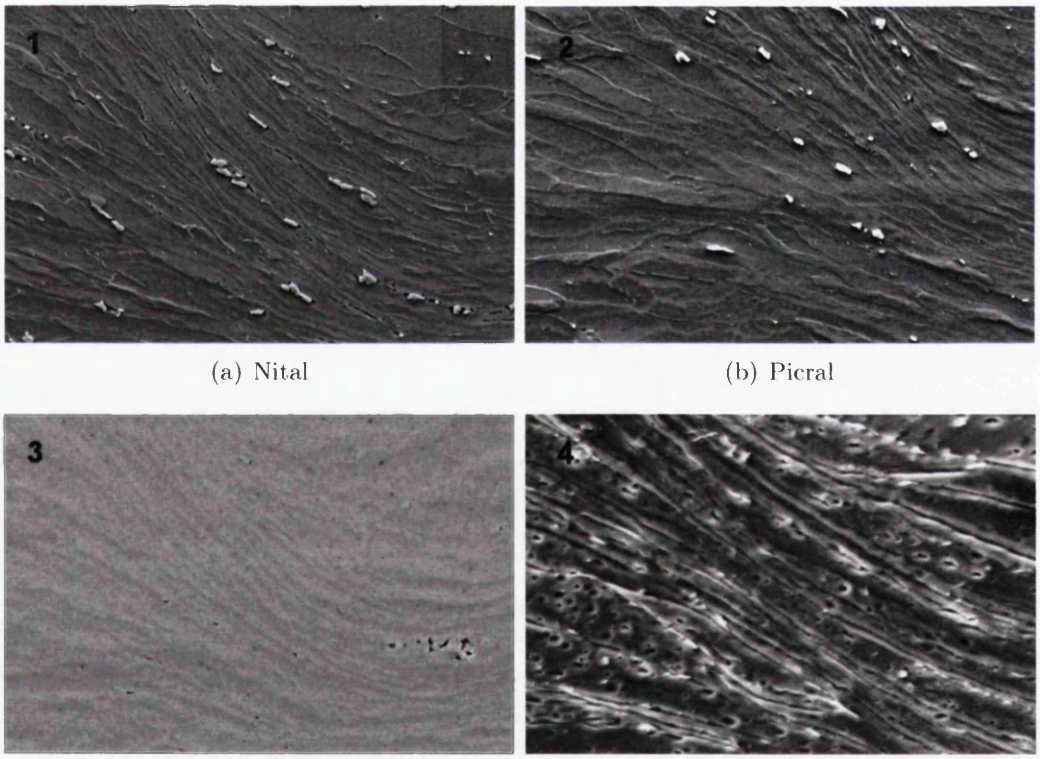

(a) Nital (b) Picral

(c) OP Polishing (d) Marshall *(not to scale)*

Figure 5.5: Various Surface Preparations showing Grains, Voids & Cementite

5.8 Microscopy of the Specimen Surface

Microscopy shows damage progression as the score depth increases, a crack may develop that propagates from the surface inwards, see (a) of fig 5.6. This is mainly caused by the materials sensitivity to the uneven cut edge acting as a stress concentration. However, a surface crack like this is rarely deep and is normally arrested by a smiley-like tip.

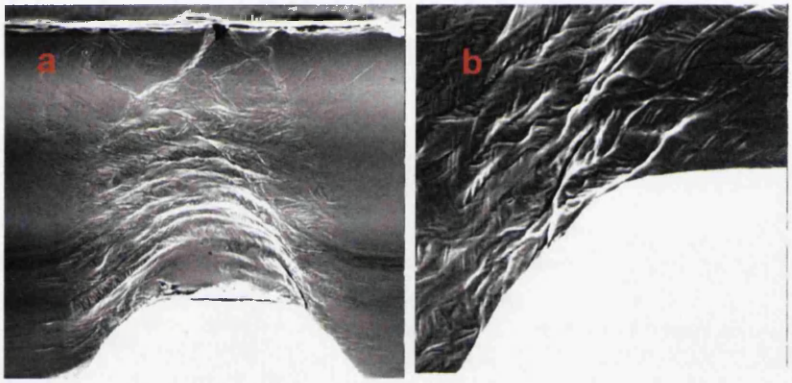

(a) Large Root Crack (b) Inclusion - σ Concentration

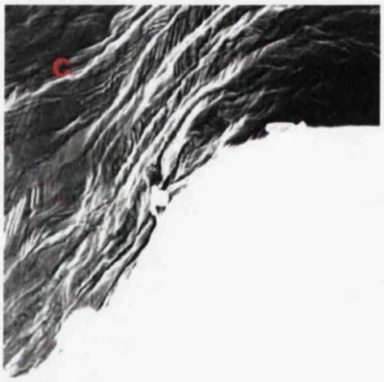

(c) Excessive Cracking

Figure 5.6: Crack Initiated from the Outside Surface

Later, interior cracks develop in the areas where high shear is present, see (b) of fig 5.6. These cracks are not yet connected and typically end in a shear band, which gives them an s-shape.

As the Scoring tool presses deeper into the material, a complex system of cracks begin to develop through Y-branching and X-branching, following slip-lines, see fig 5.7.

A dead-zone of deformation can be observed under the trapezoidal tool tip, this region is in a state of high hydrostatic stress with little or no deviatoric stresses. Eventually, an external root crack propagates from the edge of the tooling at the location of the sharpest edge or most critical stress concentration. This large and ever growing crack joins with the existing system of cracks through coalescence, which eventually causes failure.

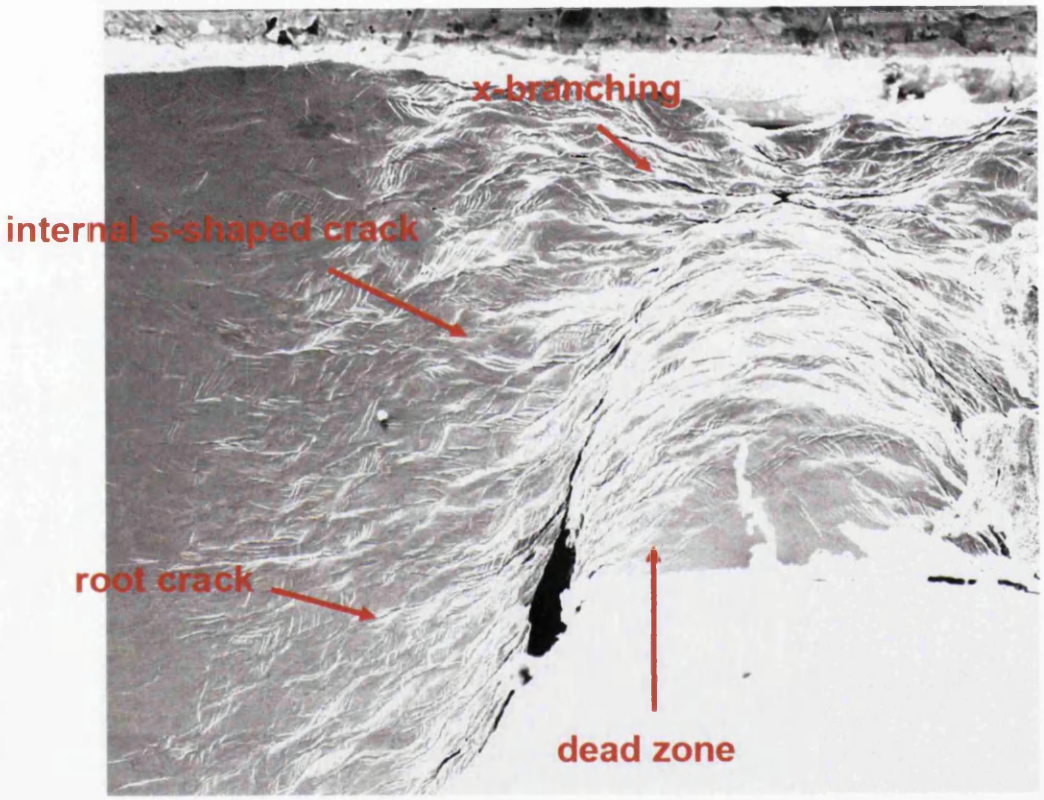

Figure 5.7: Propagation of Surface Cracks, typical pattern for packaging Steels

For stress states, where the material is loaded in tension the presence of an inclusion in a growing void is not very relevant. It is well known that packaging steel contains inclusions, and it is currently thought that under compression and shear, an inclusion prevents the flattening and closure of a void.

Important theoretical work has been completed, see [25, 70, 74, 93, 95], whereby internal pressure inside the void is simulated, which prevents the void from closing. Then, under shear loading, voids flatten out to micro-cracks, which rotate and elongate until their interaction with surrounding micro-cracks gives coalescence. This means that in shear, ductile failure still occurs due to the deformation of voids and their interaction with other voids, but in shear, the mechanism is very different from the well-known void growth to coalescence mechanism found under tensile loading.

Although Tvergaard, [95], did not use a particle inside the void, the method of simulating internal pressure can also be thought of as representing the presence of an particle within the void.

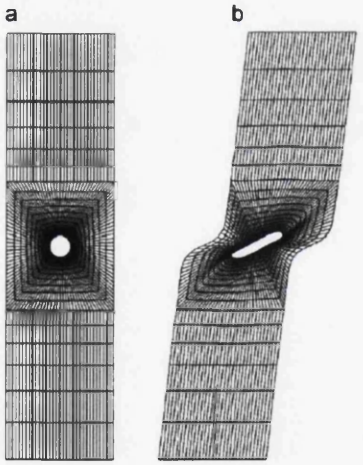

Figure 5.8: Void Rotation and Elongation under Shear

Small voids in the shear zone tend to rotate first to the direction of the shear band then eventually grow by tension, fig 5.9.

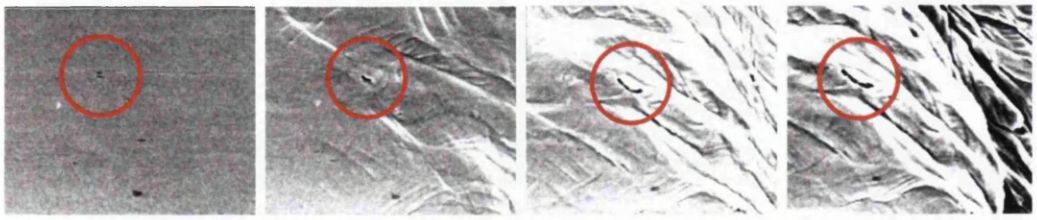

Figure 5.9: Evolution of a Void in the Shear Zone

Similar phenomenon can be observed around a single large inclusion, located in the compression zone under the tool tip, fig 5.10. Although the overall stress state in the plane is compressive, the void can not flatten and close because of the hard particle, so local shear and tensile stresses develop and the void is able to grow.

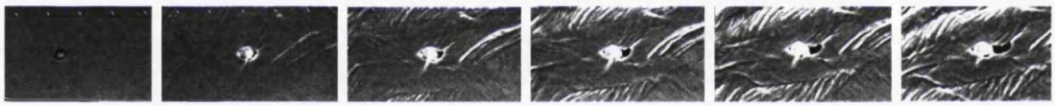

Figure 5.10: Evolution of a Void with Hard Inclusion in Compression Zone

The birth of a void due to localisation can be observed on a face, fig 5.11, where several grain boundaries meet. Shear stress concentration is likely to develop which assists crack initiation, the crack then grows due to shear and tension.

Figure 5.11: Birth of a Crack at Multiple Grain Boundaries

5.9 Initial Void and Element Analysis

Observations of undeformed material reveal a small number of initial voids in all samples, fig 5.12. Although packaging steels are relatively clean steels, the material always contains some natural precipitates or inclusions that can not be avoided. Voids are naturally present around inclusions as there is a weak bond between the hard particle and the surrounding ferrite matrix, due to incompatibilities in their atomic structure.

In packaging steels voids are almost always located around inclusions or carbide particles, fig 5.13, clusters of carbide particles, fig 5.14, or bands of carbide particles, fig 5.15. Cementite is a hard brittle iron carbide of Fe_3C, however, the cementite in steel is in a form that is not so brittle, due in part to its small size and the fact that it is surrounded by ductile ferrite. The spheroidal carbide would be in compression, when the surrounding matrix material is under low tension.

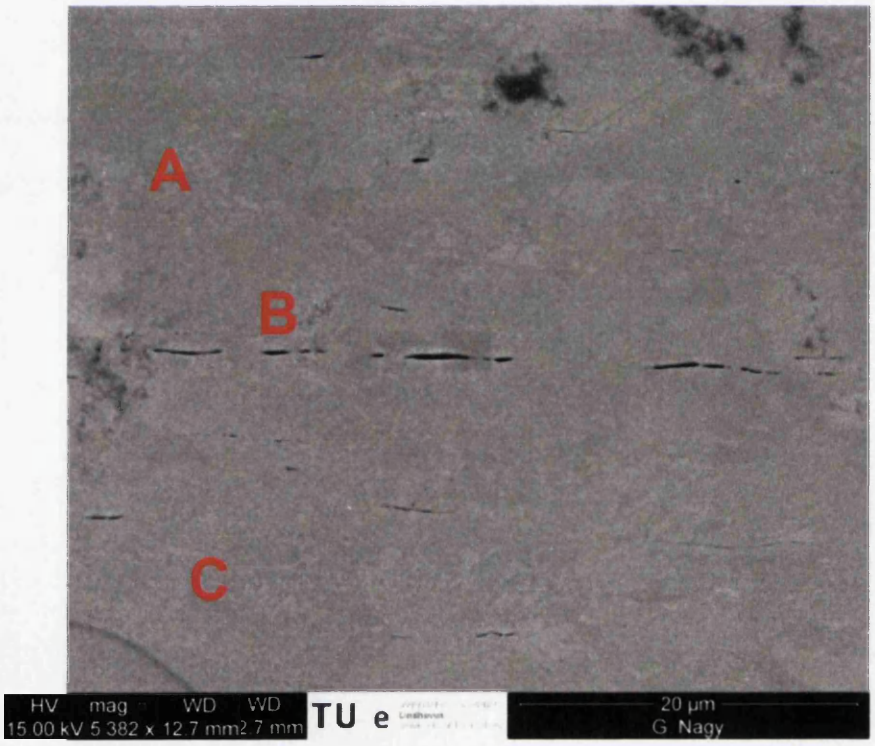

Figure 5.12: Typical Voids in the As Supplied Material

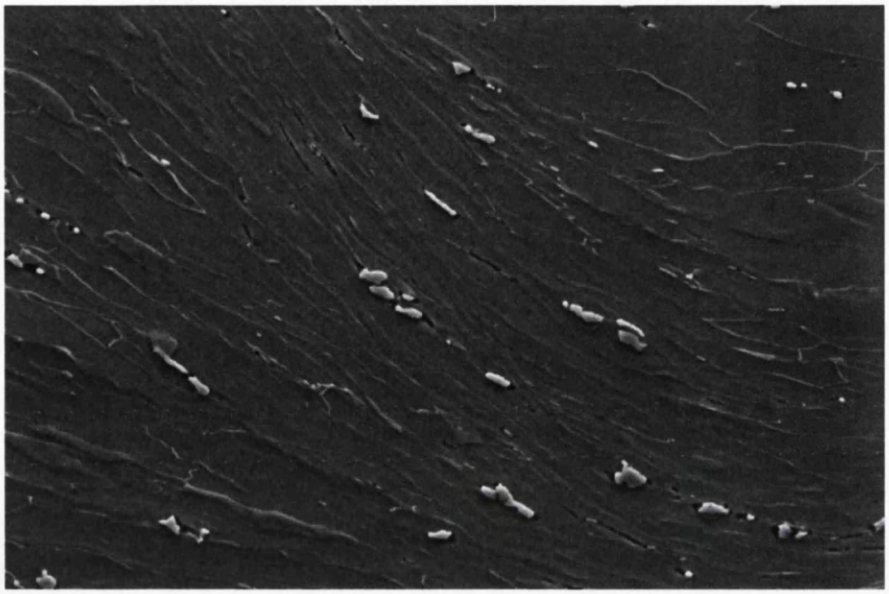

Figure 5.13: Voids around Large Cementite Particles

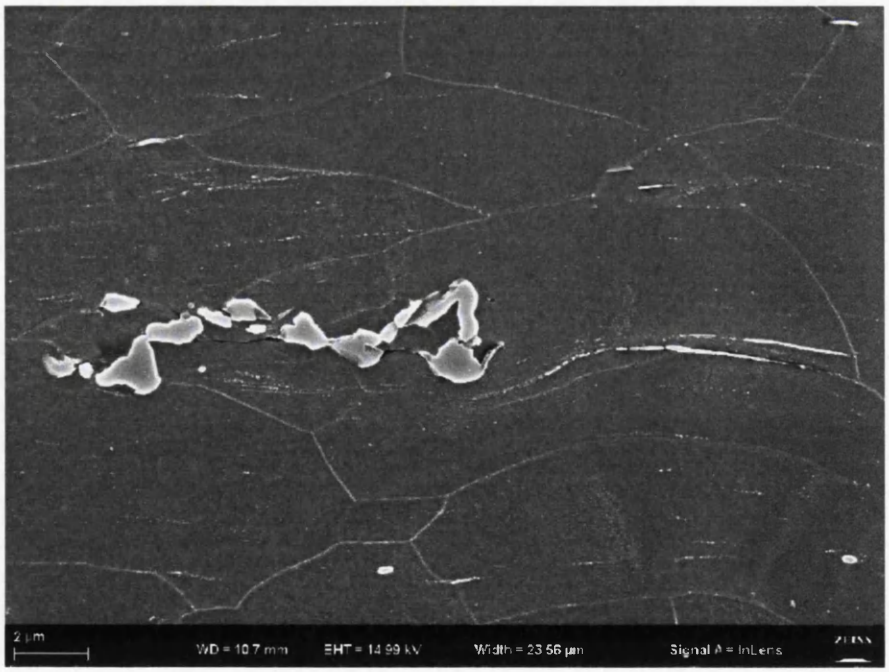

Figure 5.14: Voids around a Cluster of Cementite Particles

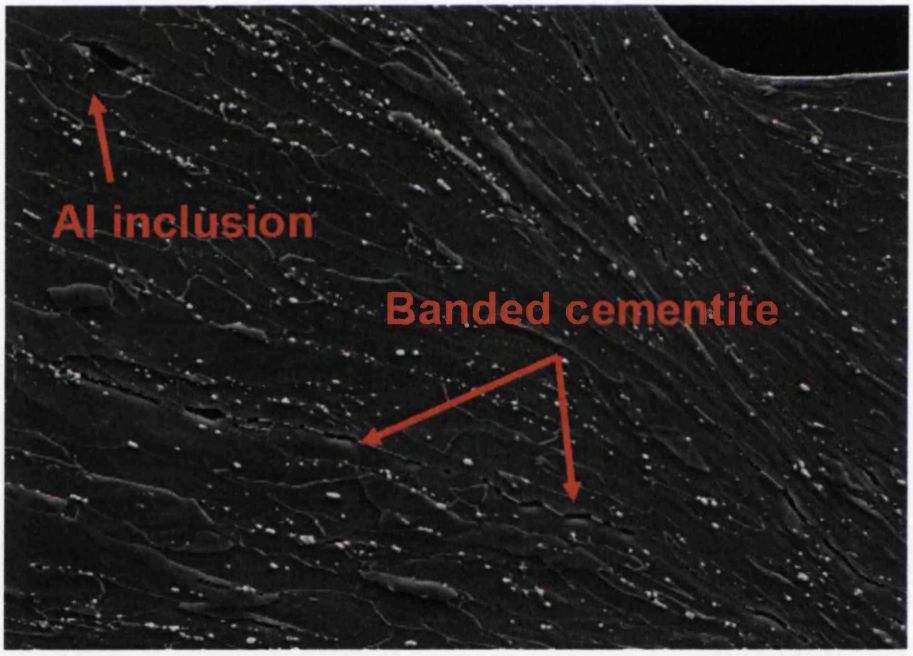

(a) Fig 10

Figure 5.15: Crack propagating though a Band of Cementite Particles

Three distinct shapes of voids can be found in packaging steels, fig 5.16, small, almond shaped holes not larger then 2μm, (A), which usually contain one or two carbide particles. Large elongated cracks of up to 10μm, (B), running through bands of carbide particles. Flat, thin cracks of approximately 5μm, (C), located around carbide particle clusters or bands of finer carbide.

Element analysis was performed at several locations where a void was found. Fig 5.16 (A) shows a typical result for ferrite matrix. Larger, relatively rare inclusions consist of aluminium, more precisely Al_2O_3, (C), (D). These arise during the de-oxidation of molten steels, they are hard, brittle solids, which in practical terms are unstable at all temperatures. Thin, propagating cracks and voids often contain manganese-sulphide, MnS (B),(E), this common inclusion type is deformable, becoming increasingly so as the temperature falls. Its presence is not particularly damaging in low carbon steels, but it can help assist crack propagation. A hard inclusion may be less harmful if it is surrounded by manganese sulphide. Manganese sulphide particles are semi-coherent with the ferrite matrix while hard inclusions are non-coherent. In the nitrogenised grade smaller carbide-nitride particles are more likely to form, however, future research will try to confirm if this is correct.

From a damage mechanics point of view it is important to realise that the presence of intrinsic faults in the material matrix already exist at the starting point. Initial void fraction is not defined in the current descriptions and the physical role and influence of a hard particle surrounded by a void has yet to be incorporated into most models. The reason for this is that the majority of damage models describe material behavior in tension, while the presence of a particle asserts more influence in shear and compression.

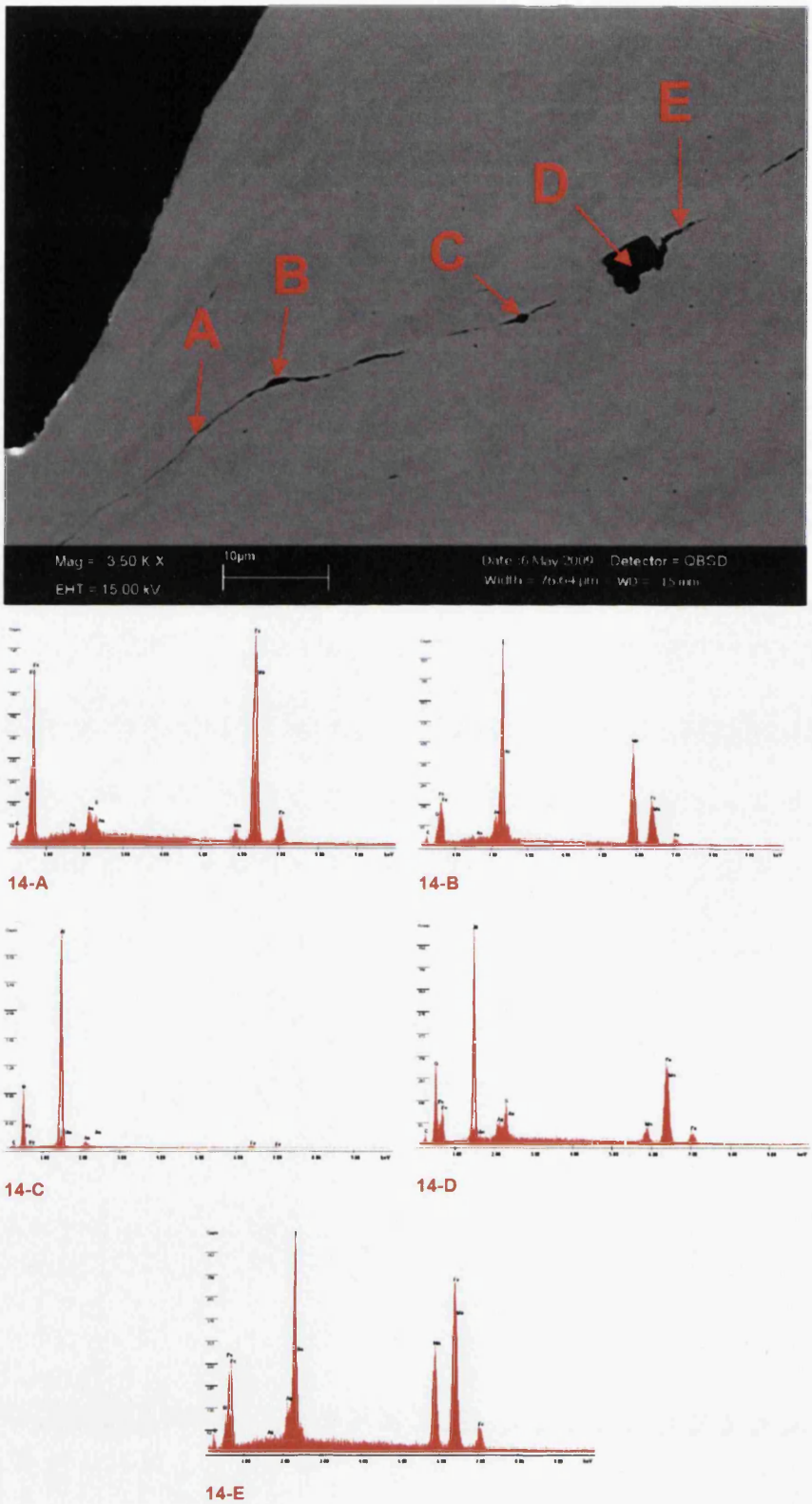

Figure 5.16: Locations of Element Analysis

5.10 Damage Evolution in Specimen Bulk

The most important finding when comparing the bulk *(interior)* with the surface is that the rate of void evolution is very different, fig 5.17, which is due to the fact that a lot less void fraction is developed in the bulk when compared with the surface. This finding, however, is logical, as the triaxiality in the bulk is expected to be much lower, this is because the bulk is in a compressive state of plane strain, while the surface is in plane stress. It is also expected that the third component of negative *(compressive)* stress in plane strain lowers the negative triaxiality even further.

According to damage mechanics, if triaxiality is positive, then there is void growth, but if triaxiality is zero or negative, the material is in a compressive stress state and void growth is not possible, as a hole is unable to grow when it is compressed from all directions. However, it is an important realisation, that while the definition of triaxiality, [12, 13, 57], is generalised to 3D, it is definite only in the 2D state of plane stress, in a truly 3D stress state bifurcations may occur for similar triaxialities. From these findings it is concluded that in future studies on scoring and opening the bulk of the sample shall be observed, i.e. the sample must always be cross-sectioned after scoring by grinding. Up until this point in the experiments, samples were deformed to the extent that they had not reached their ultimate compressive strength, based on the compressive force-displacement curve recorded by the load cell of the test frame. No excessive damage was found in any of the specimens.

For the next stage, fully clamped samples were deformed beyond the ultimate compressive strength, and reduced to a residual thickness of 20μm. Images of cross-sectioned samples, fig 5.18, show significant increase of void fraction in the bulk. However, even the level of damage found in TH620 is not enough to cause catastrophic failure. One possible explanation may be rate dependency, as all tests were performed with a crosshead velocity of 2μm/sec. Whereas in typical production scenarios, scores are produced at a much higher rate, i.e. the full reduction is applied in a fracture of a second.

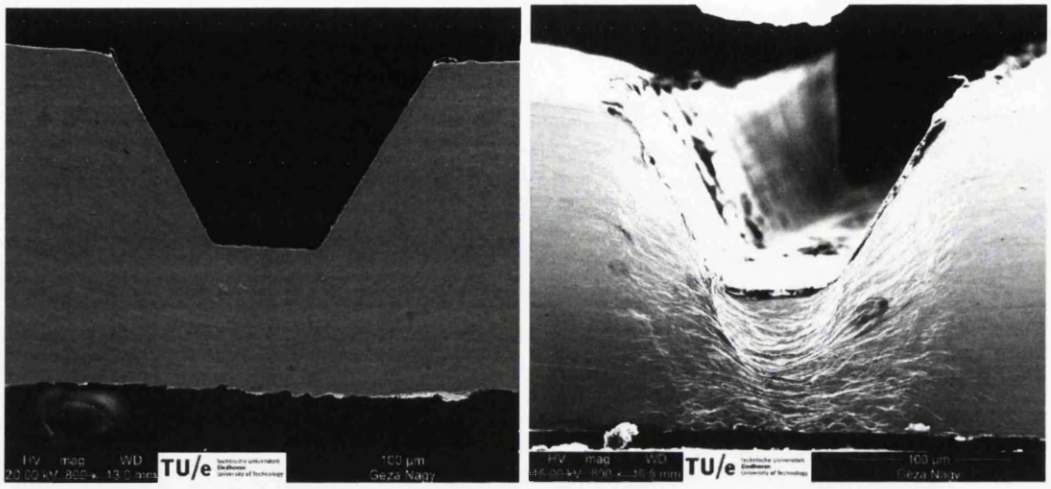

(a) Damage in the Bulk (b) Damage on the Surface

Figure 5.17: Comparison of Bulk v Surface Damage in the Same Sample

Future work recommends that tests are carried out at a much higher rate, in order to reveal any eventual rate dependency. The fundamental question of whether rate dependent damage exists or if the response can be explained exclusively with the rate dependency of the material should also be carefully looked into. Influence of strain rate effects are as yet unknown, but there are plans to extend observations to higher rates in the future. Temperature effects may also have to be considered at higher rates.

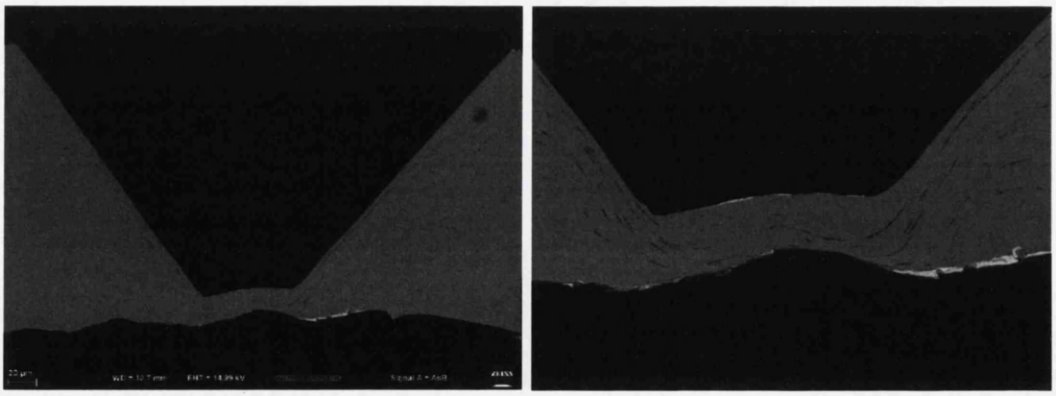

(a) Fully Clamped Sample (b) Exploded View: Excessive Damage

Figure 5.18: Void Number is Insufficient for Catastrophic Failure

5.11 Failure in Shear

It is known that packaging steel is rate dependent, and if rate dependency is important, it may be assumed that final catastrophic failure is a shear-type failure due to the rise of critical tensile stresses in the material matrix already weakened by damage. If there are enough voids in the material, then the loading of the remaining ligaments between the voids becomes increasingly tensile, and eventually will fail in a similar manner to tension. Shear stress failure, therefore, competes with damage. If this is true, then damage and failure in compression may be described by a combination of damage weakening the material matrix and stress-based forming limit, [86].

Also, work done in conjunction with Sheffield University, [28], has shown that the surrounding ferrite matrix is extremely ductile, with strains of up to 600%. Excessive shear is visible and can be see on the grain boundaries in fig 5.19.

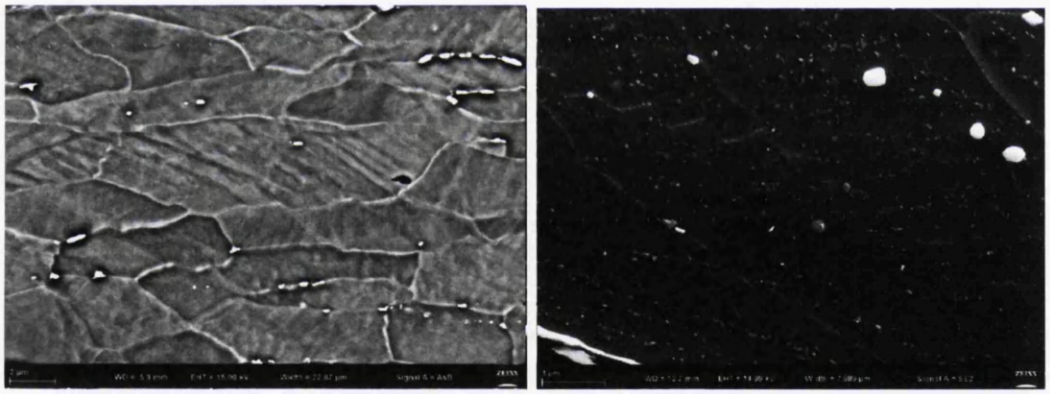

(a) Shear inside a Ferrite Grain (b) Intergranular: Step Like Deformations

Figure 5.19: Severe Shear and Intergranular Shear inside a Ferrite Grain

5.12 Results of Macroscopic Tests

The forces generated during the experiments were recorded[1], fig 5.20, and four unique points were found on the force/crosshead displacement curve, which may represent damage-related changes in the material.

- Point 1 - Dislocations at the elastic limit
- Point 2 - Nano-Scale Damage
- Point 3 - Nano to Macro-Scale Damage
- Point 4 - Macro-Scale UCS *(Current domain of Damage Modelling)*

At all points there is an instantaneous change in the rate of hardening. The first point is the elastic-plastic limit, the second point occurs at about 5% compressive strains, which coincides with the moment when shear bands appear on the full cross section of the compressed area in a form of fine white hair-lines. These shear bands are potentially at the grain boundaries, but many of them are inter-granular. The average grain size of the material, is approximately 10μm. At this early stage of deformation void growth on the micro-scale is definitely not visible, so something must be happening in the material at the nano-scale, which causes a relatively significant drop in the hardening rate.

The question arises over where this effect comes from and whether this should be treated as material damage at a much smaller scale than previously considered. At point 3, the first macroscopic crack appears on the sample surface, then finally, at point 4, the ultimate compressive strength (UCS) is reached and the specimen fails rapidly by crack-through.

Future work will attempt to visualise dislocations in the material by using an Electron Channeling Contrast Imaging (ECCI) technique, a sudden increase of geometrically necessary dislocations density of around 5% strain level, [26], should be expected.

[1] All measured curves were compensated for elastic expansion of the test frame. These are global forces, which include combined effects of tool geometry, friction, material response, etc.

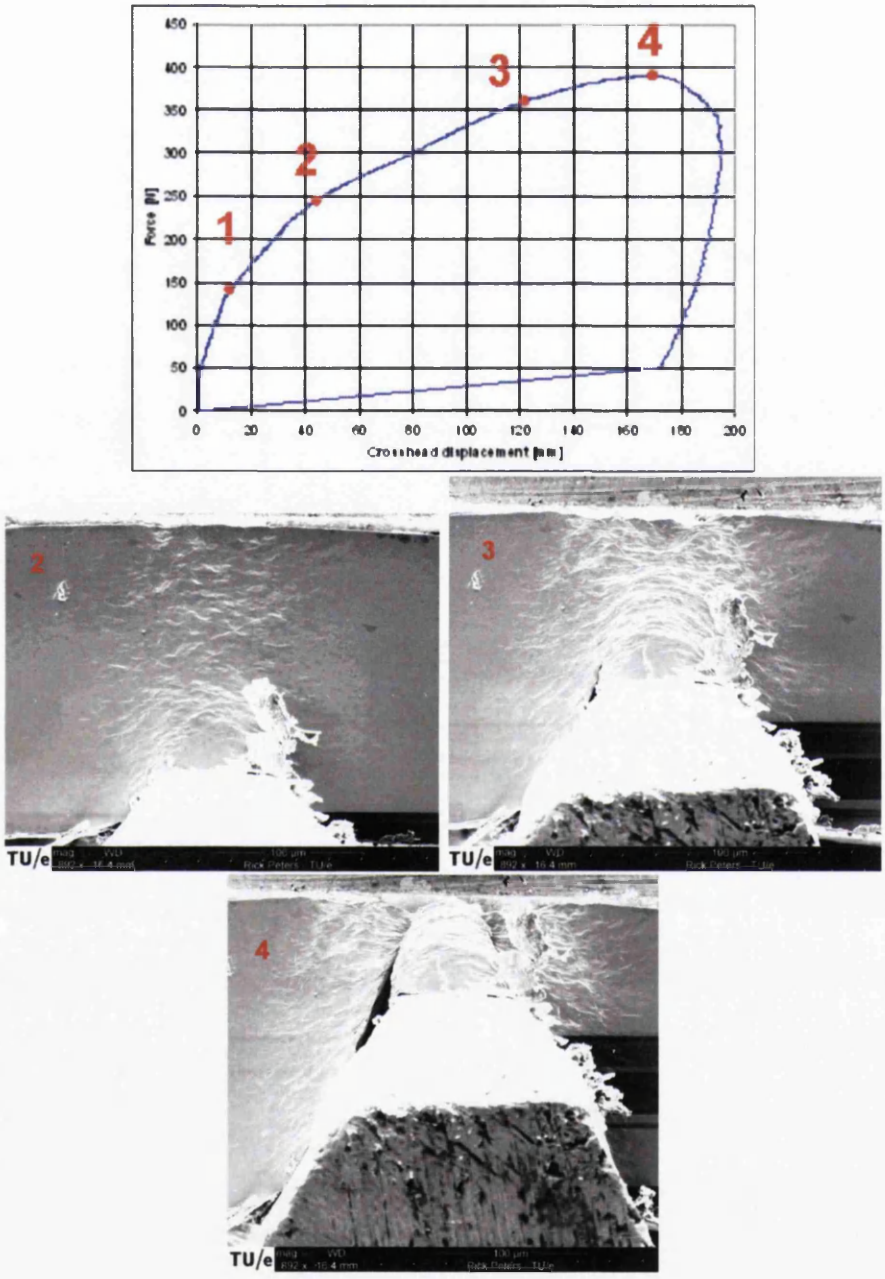

Figure 5.20: Force/Disp Curve with Corresponding Scoring States

A thorough comparison of the measured force-displacement characteristics against the micrographs revealed that the amount dropped after the ultimate compressive strength is related to the accumulated void fraction in the material.

5.13 Deformation at Multiple Scales

In the compression-shear region voids flatten out, due to compression; these cracks then rotate parallel to the direction of the shear and may even stretch and eventually grow through interaction and coalescence, [94]. Shear bands appear on the grain surface at an early stage of stress, while a drop in hardening rate is recorded, which could be interpreted as, geometrically necessary dislocations beginning to initiate some kind of early damage at the crystallographic level. Larger cracks initiate either from the surface or by joining shear cracks that are growing together in the bulk, but small surface cracks that do not join the main crack seem to have no appreciable effect on the global compression deformation behaviour.

5.14 Interior Microscopic Cracks and Effects

Methods of testing of scored cross-sections have now been established. From the results, it is clear that the bulk of the material must be investigated for damage, as tests on the surface, *(plane stress)*, give different results in terms of void density, which does not reflect the response to plane strain deformation. It is advised to observe damage evolution in-situ in the future on cross-sectioned specimens, where the deformation at the centre of the specimen is as close to plane strain as possible as the specimen is constrained along the score knife due to friction. Both fully constrained and unconstrained samples should be tested until a relationship is established between the constraint conditions of the strip tests in comparison with circular ends.

It is also recommended to use a somewhat wider specimen in the future, in order to achieve conditions as near to plane strain as possible at the centre of the sample. Void growth or coalescence is visible, but it appears that voids have no effect before the ultimate compressive strength is reached. Micro-cracks nucleate at pre-crack tips, cavities, inclusions, or other defects where high shear is present and micro-cracks produced in the bulk result in a descending section in the load/displacement curve.

Chapter 6

Damage Mechanics

6.1 Overview of Damage Mechanics

Most modern textbooks that cover the subject, [22, 51, 53, 98], define damage as the presence, creation, growth and evolution of microvoids or microcracks, which have the potential to direct a material towards failure through the loss of its load carrying capability.

For most modern engineering purposes, prediction of mechanical failure is important if not critical, whereas for some applications mechanical failure can cause serious economic impacts, *(Think of a high capacity hot steel mill breaking down mid production run)*, in safety critical industries, such as Nuclear and Aerospace, unexpected failure can have catastrophic effects and consequences that can reach well beyond just economical concerns. In manufacturing, especially where metal forming and composite applications are concerned, a full understanding of failure mechanisms becomes crucial. For some of the more affluent Industries, i.e. Aerospace, the failure of components was based on experience gained through the methodical testing of components or parts to destruction under conditions meant to reproduce actual *"real life"* circumstances, however, this is an expensive process. Conventionally, prediction of failure was based on empirical experience gained over long periods of time.

Our knowledge of the mechanisms that cause internal damage and failure, throughout a large variety of materials is growing fast and it is now possible to have continuum constitutive models that are capable of predicting internal damage and its progression. This development is a relatively new branch of continuum solid mechanics, which has developed into and become known as *Continuum Damage Mechanics*, CDM. Along with other developments in Engineering, such as computational mechanics and finite element methods, computational tools can now offer a realistic alternative, which is presently being successfully adopted by many industries concerned with ongoing design and damage assessment.

6.2 Physical Damage in Solids

Different materials vary considerably when looked at on the microscale, which means that the characterisation of internal damage depends significantly on the specific type of material under consideration, however, damage mechanics can be applied to a wide range of materials, including metals, alloys, polymers, elastomers, composites, and concrete, as each material has more or less the same qualitative behavior when looked at on the meso or macroscales. The progression of damage can be triggered by very different physical mechanisms, which depend significantly on the following factors

- Damage type
- Loading Rate
- Temperature or Thermal effects
- Environmental; i.e. Corrosion/Radiation

For the study of CDM the material-process-environment triad must be taken into consideration. Continuum mechanics, [31, 44, 59, 62], introduces the concept of a Representative Volume Element (RVE) whose properties are represented by homogenized variables. A typical size for the RVE varies from around $(0.1mm)^3$ for metals to around $(100mm)^3$ for concrete. Damage discontinuities are *small* when compared with the size of the RVE, but are of course large in comparison to the materials atomic spacing.

Damage in Metals

Damage in metals can be categorised into the following distinctive groups;

- Brittle
- Ductile
- Fatigue

Brittle damage tends to split or cleave apart the crystallographic planes when undergoing plastic deformation, at low temperatures, brittle behaviour can be seen in many polycrystalline metals. At high temperatures, brittle damage has been linked with the phenomena of creep, but here it is represented by intergranular decohesions at the grain boundaries, accompanied by low stresses and small strains.

Ductile damage[1], however, is normally related to large plastic deformations occurring in the region of localised crystalline defects. Here, interatomic bonds become separated at the interface with particles or inclusions of other alloys or precipitates, which in turn can lead to the creation of microscopic cracks and voids. Any additional localised plastic deformation can cause coalescence of the cracks and voids resulting eventually in separation or division.

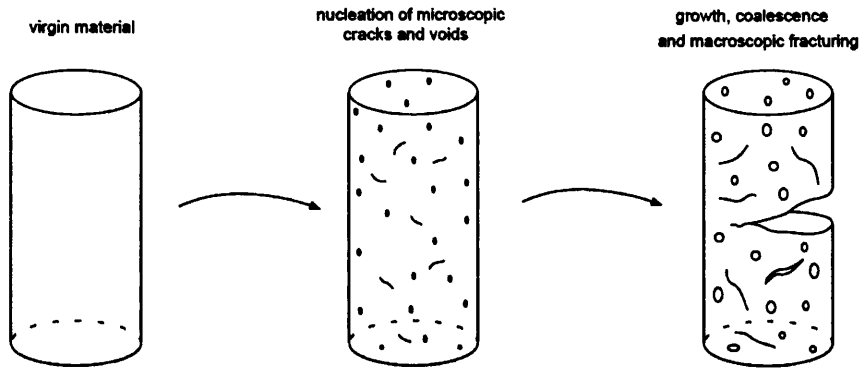

Figure 6.1: Ductile Damage in Metals

[1]Image reproduced with kind permission from [22]

Damage in the majority of metallic materials, is a combination of both brittle and ductile responses, each modes contribution is dependant on the surrounding factors, such as thermal environment, loading rate, etc.

However, fatigue is also an important mode of material deterioration in metals. It often occurs in mechanical parts that are subjected to cyclic loads or temperature gradients and can take place at stress levels significantly below the normal limits for macroscopic plastic yield. Fatigue can be recognised as a build up of dislocations generated by cyclic plastic loading, caused in part through a combination of local stress concentrations and microscopic defects. Fatigue is defined by many complicated interactions that take place beginning with the initial nucleation of cracks up to the total failure of the material.

Under the domain of material science, a full and complete understanding of metal fatigue still remains outstanding, however some of the most important mechanisms regarding material damage have been described by Engel and Klingele [23].

6.3 Classification of Damage Models

There are many criteria for assessing damage and failure initiation in ductile materials. According to most damage models there is a unique dependence between triaxiality and the rate of accumulated damage. Damage models can be arranged into the following main model groups; *(with many subgroups within).*

- Empirical criteria
- Void growth models
- Porosity-type models
- Continuum based models

For models in the first two groups, damage and plasticity are usually decoupled. For the latter two, the elastic-plastic framework and damage can be coupled. The following section presents models in the form that they are implemented into Rockfield Software's ELFEN^{TM}solver.

Empirical Criteria

For empirical models, damage accumulates with equivalent plastic strain weighted on a triaxiality function. Models by Datsko, Latham-Cockroft, Brozzo and Norris are typical examples.

$$\text{Datsko} \qquad \bar{\varepsilon}_p = \int d\varepsilon_p \tag{6.1}$$

$$\text{Latham-Cockroft - } \textit{(Total Plastic Work)} \qquad \int \bar{\sigma} d\varepsilon_p \tag{6.2}$$

$$\text{Brozzo et.al. - } \textit{(Modified Tensile Plastic Work)} \qquad \int \frac{2\sigma_1}{3(\sigma_1 - \sigma_H)} d\varepsilon_p \tag{6.3}$$

$$\text{Norris et.al. - } \textit{(Effective Plastic Strain Rate)} \qquad \dot{\bar{\varepsilon}}_p = \frac{\Delta \bar{\varepsilon}_p}{\Delta t} \tag{6.4}$$

$$\text{MSPW - } \textit{(Maximum Shear Plastic Work)} \qquad \int_0^{\gamma} \tau \delta \gamma_p \tag{6.5}$$

The effective plastic strain criterion, suggested by Datsko, states that ductile fracture in forming processes is governed by a material and operation dependent plastic deformation limit represented by the effective plastic strain.

Total plastic work criteria states that at fracture initiation, the extension is dictated by the amount of plastic energy absorbed, it assumes the existence of a critical value of plastic energy absorbed by unit volume.

The Latham-Cockroft model assumes that the maximum principal stress and the strain history are relevant to fracture initiation, therefore the criterion is defined as the plastic work over the effective plastic strain path.

Brozzo extended the criterion with explicit dependency of the hydrostatic stress. Norris proposed an empirical criterion based on the fact that ductility decreases with hydrostatic stress, the criterion assumes that fracture occurs when the time integrated product of the equivalent plastic strain rate as a function of the effective stress exceed a critical value.

It is also worthwhile mentioning the maximum shear plastic work criterion, as many theoretical models for metal forming assume that large deformation occurs along the shear plane, which is believed to be the main mechanism of separation.

Void Micro Mechanics

Void micro-mechanics models have similar formulation to empirical criteria but they are based on description of micro-void evolution.
Examples are:-

$$\text{Hancock \& Mackensie } \textit{(Simplified McClintock)} \qquad \exp\left(\frac{\sqrt{3}\sigma_H}{\bar{\sigma}}\right)\bar{\varepsilon}_p \tag{6.6}$$

$$\text{Rice \& Tracy} \qquad \int 0.283\exp\left(\frac{\sqrt{3}}{2}\frac{\sigma_H}{\bar{\sigma}}\right)d\varepsilon_p \tag{6.7}$$

$$\text{Atkins} \qquad \dot{\bar{\varepsilon}}_p = \frac{\sqrt{\frac{2}{3}d\varepsilon_{ij} : d\varepsilon_{ij}}}{\Delta t} \tag{6.8}$$

Nucleation, growth and void coalescence are widely accepted as the mechanism that better describes ductile fracture and one of the first relatively successful ductile fracture criterion was presented by McClintock, whose model assumes that the material is divided into regions, each containing two cylindrical holes. Fracture occurs when the holes touch each other or the boundary of the element. The inverse dependence of hydrostatic stress and fracture strain was established within this criterion.

Rice and Tracy modelled the growth of spherical voids in a triaxial stress field, the criterion was originally defined in terms of the ratio of the average strain rate of the sphere radius to the remotely imposed strain rate, the exact form of the equation is only for perfectly plastic materials, however it appears to show a good approximation of cavity growth rates in ferritic steels, the criterion is expressed in an integral form and fracture occurs when the critical value of the non-dimensional void size reaches a critical threshold.

Based on the fact that the criterion of Norris did not adequately described fracture in sheet forming, Atkins modified it by introducing explicit dependency of the damage to the strain path.

Porosity Type

Porosity type models assume that failure is caused by nucleation, growth and coalescence of micro-voids at second phases and inclusion sites inside the material. These evolution steps are modelled by Gurson, and Tvergaard-Needleman.

$$\text{Gurson}\textit{(Nucleation \& Growth)} \qquad \left(\frac{\sigma_h}{\bar{\sigma}}\right)^2 + 2q_1 f \cosh\left(\frac{3q_2\sigma_h}{2\bar{\sigma}}\right) - \left[1 + (q_1 f)^2\right] = 0 \tag{6.9}$$

Continuum Based Models

Computational damage mechanics models estimate damage from the loss of stiffness in the material, ideally forming a consistent thermo-dynamical framework. Such models were first introduced by Lemaitre, however the model by Oyane belongs here too.

$$\text{Oyane } \textit{(Volumetric Strain)} \qquad \int \left[1 + A\frac{\sigma_h}{\bar{\sigma}}\right] d\varepsilon_p \tag{6.10}$$

$$\text{Lemaitre} \qquad \int \left[\frac{2}{3}(1+v) + 3(1-2v)\left[\frac{\sigma_h}{\bar{\sigma}}\right]^2\right] d\varepsilon_p \tag{6.11}$$

Oyane developed a material model for metal powder, which included explicit dependence of the von-Mises yield criterion on the function of hydrostatic stresses, the apparent density of the porous material and the pore-free matrix, the model assumes that fracture occurs when volumetric strains reach a critical level.

Lemaitre proposed a model for isotropic damage based on a continuum damage variable of the concept of effective stress, the model assumes that a damage value ranging from 0 *(undamaged state)* to 1 *(rupture of the element into two parts)* physically represents the corrected area of cracks and cavities per surface unit.

Note:

Approaches based on void growth and coalescence incorporate a dependence on triaxiality, such that, higher triaxiality results in a higher rate of damage progression, thus earlier failure at lower strains. Experimental evidence, however, suggests that failure occurs at a lower strain levels in torsion compared to tension, even though the triaxiality in torsion is zero, which is non-consistent with the models [87], it is suggested that the fracture limit may depend upon the deviatoric stress state as well [18]. Wierzbicki et. al. [6, 7, 8, 58], introduced another normalised deviatoric parameter, based on the third invariant of the stress tensor, that is related to the Lode angle 7.23, and has a consequence of non-uniqueness in the relation between triaxiality and fracture strain.

$$\zeta = \cos(3\theta) = \frac{27}{2}\frac{J_3}{\bar{\sigma}^3} \tag{6.12}$$

It is important to realise that in the classical application of plasticity the most used yield criterion is the von Mises *(J2)* criterion 6.57, which does not account either for the hydrostatic pressure *(I1)* 6.49 or the Lode angle *(J3)* 6.54. With the introduction of two additional stress parameters, 6.55 and 6.12 to describe the fracture locus the failure depends on the three invariants *I1*, *J2*, and *J3*

6.4 Continuum Damage Mechanics

The principal processes that define damage are fundamentally different from those that typify deformation. In elasticity, deformation is connected to reversible changes in interatomic spacing, whilst plasticity is represented by the movement and accumulation of dislocations.

For damage however, it is evident that an irreversible breakdown of the materials atomic bonds lies behind the phenomena. In order to describe the internal deterioration within the theoretical framework of continuum mechanics, new variables inherently related to the process of internal damage have to be introduced into the description of deformation along with the commonly used standard variables, like the strain tensor, plastic strain, etc.

After Kachanov's [36], original work, a significant volume of the literature has been employed with the formulation of constitutive models that describe the internal degradation of solids within the framework of continuum mechanics.

Presently, after many years of development, major progress has been achieved and progressive theory has evolved into what is now commonly refereed to as Continuum Damage Mechanics, CDM [40, 52].

Original Development

Kachanov [36], was the first to propose a CDM model, however, the model was a scalar internal variable developed to model the creep failure of metals under uniaxial tension. Unfortunately this model was without a clear physical meaning for damage. Later, Rabotnov [81], developed a model that reduced the cross-sectional area owing to the formation of microcracks, this gave damage a physical significance and acted as a suitable measure for internal damage. Represented respectively by A and A_0, giving the effective load bearing areas of the virgin and damaged materials, the damage variable D was established as;

$$D = \frac{A - A_0}{A}, \tag{6.13}$$

with $D=0$ representing the undamaged material and $D=1$ representing complete separation of the material i.e complete loss of its load bearing capacity[1].

Kachanov then replaced the observed uniaxial stress σ with the *effective stress* in the standard Norton's Law for creep.

$$\sigma_{\text{eff}} = \frac{\sigma}{1 - D} \tag{6.14}$$

Which meant that the normal uniaxial constitutive equation for the plastic strain rate was replaced using;

$$\dot{\varepsilon}^p = \left(\frac{|\sigma|}{\lambda\,(1 - D)}\right)^N \text{sign}(\sigma), \tag{6.15}$$

this meant that increasing damage *(high D)* produced a clear acceleration in the plastic strain rate.

[1]Kachanov's original development used the *material continuity* or *integrity*, $\omega = 1 - D$, as the variable for internal deterioration.

After the original work by Kachanov and Rabotnov, work began generalising the concept of an internal damage variable to three-dimensions. A great deal of work has been completed, but the work by the following researchers is highlighted:-

- Leckie & Hayhurst [45], used the decrease in effective load bearing area to define a scalar measure for material damage, used to model creep-rupture with multiaxial stress.
- Chaboche [14, 15, 16], suggested a phenomenological theory for creep-damage that was derived from rigorous thermodynamic origins, a result of the hypothesis of *strain equivalence.* As a result of this, for general anisotropy, the damage variable appears as a *fourth order* non-symmetric tensor.
- Murakami & Ohno [68, 69], defined anisotropic damage, in this case a *second rank* symmetric tensor, by applying the effective stress concept to three dimensions.
- Saanouni *et al.* [83], predicted the nucleation and growth of cracks through a non-local procedure.

Theory

Although CDM was developed from research on creep, it has also been used effectively in other areas of solid mechanics to describe internal damage.

Gurson's [30], void growth model for ductile damage considered ball shaped microscopic voids embedded in an elastoplastic matrix, it is well known to be able to represent the behaviour of porous metals.

Lemaitre [47], through a purely phenomenological model, presented a scalar damage variable through the hypothesis of strain equivalence, which states;

"The deformation behaviour of the damaged material is represented by the constitutive laws of the virgin material with true stress replaced by the effective stress"

$$\sigma_{\text{eff}} = E_0\,\varepsilon\,, \tag{6.16}$$

or, equivalently,

$$\sigma = E\,\varepsilon\,, \tag{6.17}$$

where E_0 and

$$E = (1 - D)E_0 \tag{6.18}$$

are the Young's moduli of the undamaged and damaged materials, respectively. This means that the reduction of load carrying area,[1] as defined in the standard definition of damage, was replaced by Lemaitre with a decrease in the Young's modulus under ideal isotropic conditions. This then provides a redefinition of the damage variable to:-

$$D = \frac{E - E_0}{E}\,. \tag{6.19}$$

In the mid 80's Lemaitre extended his model, [48, 49], then added ageing in conjunction with Marquis [61]. In 2000, Lemaitre [55], adapted his original isotropic model to further describe anisotropic damage, compressive loads and the semi-closure of microcracks. Here, damage is a second order tensor linked to the principal directions of the plastic strain rate.

[1] The original definition for load carrying area was never very well defined or easy to quantify

Additional CDM based models can also be found, the following work refers;

- Cordebois & Sidoroff, [20].
- Simo and Ju, [85].
- Armero & Oller, [5].

Different approaches have also been followed by;

- Krajčinović & Fonseka, [27, 38, 39, 41].
- Kachanov, [37].
- Mitchell, [64].

Fatigue modelling for CDM has also been studied, see;

- Janson, [33].
- Lemaitre, [50].

The developments cited above are not elaborated on further here, however, they are more fully described by Chaboche [17], also the book by Lemaitre and Chaboche [52], and more recently, the book by De Sousa Neto et.al. [22], as well as the original referenced literature.

Damage Variable

It is now well known [22], that the success or failure of a CDM model greatly depends on how its internal variables have been specified. Variable definition is a very difficult task, due in part to the diversity that microscopic internal damage can take. Many variables with different mathematical characteristics, *(scalars, vectors, tensors)* and physical representations *(reduction of load bearing area, loss of stiffness, distribution of voids)* have been used to describe damage under many scenarios.

Physical Aspects

The theories behind the models of Continuum Damage Mechanics can broadly be split into two main classes;

- Micromechanical
- Phenomenological

In micromechanical models; internal damage is represented by variables that average the effect of microscopic imperfections. However, even though this method is very appealing, it presently requires a huge amount data accounting as well as the difficult matter of accurately identifying the state of damage. These are the reasons why most micromechanical theories are presently not being used in industrial applications, large scale problems, or engineering design.

Phenomenological models, however, are defined by how internal damage affects the materials macroscopic properties. The materials elastic moduli [19, 32], yield stress, density and electric resistance are all effected by damage. Measurements here are normally much easier than trying to determine the geometric distribution of microscopic imperfections. Lemaitre and Chaboche [52], use the degradation of the elastic moduli as the macroscopic measure of damage. Ideally, under isotropic conditions, the damage variable is a scalar, 6.19, whereas under anisotropy, the damage variable is a second order tensor [55]. Methods to identify damage are described in detail by Lemaitre and Dufailly [54].

6.5 Lemaitre Damage

In 1985, [48, 49], Lemaitre proposed constitutive equations for damage coupled to elasto-plasticity using *"effective stress & hypothesis of strain equivalence"*. The model is used to predict damage in ductile materials by using the progression of damage together with non-linear isotropic and kinematic hardening. The following classification is based on the model provided by Lemaitre in his books, [52]. This specific breakdown however, is as detailed by De Sousa Neto in; [22].

Damage Model

State variables

The theory begins by assuming that the free energy is a function of the state variables, $\{\varepsilon^e, R, \boldsymbol{X}, D\}$;

$$\psi = \psi(\varepsilon^e, R, \boldsymbol{X}, D)\,, \tag{6.20}$$

with ε^e the elastic strain tensor, and R, D representing the *scalar* internal variables of *isotropic hardening* and *isotropic damage*. $\boldsymbol{X}$ is the second order tensor associated with *kinematic hardening*. As discussed in section 6.4, D represents the damage variable and can be understood to represent an indirect measure of the density of microcracks and voids [46]. Here, microscopic imperfections are taken to be isotropically dispersed, which is shown phenomenologically by changes in the elastic modulus. Critical damage is represented by D_c, which defines the initiation of a macrocrack [52]. Hypothetically decoupling the elastic damage from the plastic hardening, arrives at the following equation for specific free energy.

$$\psi = \psi^{ed}(\varepsilon^e, D) + \psi^p(R, \boldsymbol{X})\,, \tag{6.21}$$

Here, ψ^{ed} and ψ^p represent the elastic damage and plastic contribution to the free energy.

Elastic-Damage Potential: Elasticity-Damage Coupling

In Lemaitre's theory the elastic-damage potential is represented by;

$$\bar{\rho}\,\psi^{ed}(\boldsymbol{\varepsilon}^e, D) = \tfrac{1}{2}\,\boldsymbol{\varepsilon}^e : (1-D)\mathbf{D}^e : \boldsymbol{\varepsilon}^e\,, \tag{6.22}$$

where $\mathbf{D}^e$ is the standard isotropic elasticity tensor. The elasticity law for this potential, is then;

$$\boldsymbol{\sigma} = \bar{\rho}\,\frac{\partial \psi}{\partial \boldsymbol{\varepsilon}^e} = (1-D)\mathbf{D}^e : \boldsymbol{\varepsilon}^e\,. \tag{6.23}$$

Equivalently, the above damaged elastic law can be written as;

$$\boldsymbol{\sigma}_{\text{eff}} = \mathbf{D}^e : \boldsymbol{\varepsilon}^e\,, \tag{6.24}$$

where $\boldsymbol{\sigma}_{\text{eff}}$ represents the *effective stress tensor*, which widens the definition of the uniaxial effective stress of given in 6.14;

$$\boldsymbol{\sigma}_{\text{eff}} \equiv \frac{1}{1-D}\,\boldsymbol{\sigma}\,. \tag{6.25}$$

The thermodynamical force conjugate to the damage internal variable is given by;

$$Y \equiv \bar{\rho}\,\frac{\partial \psi}{\partial D} = -\tfrac{1}{2}\,\boldsymbol{\varepsilon}^e : \mathbf{D}^e : \boldsymbol{\varepsilon}^e\,, \tag{6.26}$$

or, using the inverse of the elastic stress/strain law;

$$\begin{aligned} Y &= \frac{-1}{2(1-D)^2}\,\boldsymbol{\sigma} : [\mathbf{D}^e]^{-1} : \boldsymbol{\sigma} \\ &= \frac{-1}{2E(1-D)^2}\left[(1+\nu)\,\boldsymbol{\sigma} : \boldsymbol{\sigma} - \nu\,(\operatorname{tr}\boldsymbol{\sigma})^2\right] \\ &= \frac{-q^2}{2E(1-D)^2}\left[\frac{2}{3}(1+\nu) + 3(1-2\nu)\left(\frac{p}{q}\right)^2\right] \\ &= \frac{-q^2}{6G\,(1-D)^2} - \frac{p^2}{2K\,(1-D)^2}\,, \end{aligned} \tag{6.27}$$

here, E represents Young's modulus related to G, whilst ν is Poisson's ratio associated with K. Also, p gives the hydrostatic stress and q the von Mises effective stress.

Known widely as the *damage energy release rate*, $-Y$ represents the variation of internal energy density due to damage growth at constant stress. It can be thought of as the CDM analogue of the J-integral found in fracture mechanics [2, 82].
The product $-Y\dot{D}$ represents the power thats dissipated through the course of internal deterioration. *(Mostly through the decohesion of interatomic bonds).*

Note:

Stress-strain rule (6.23) has an important experimental consequence. With the elasticity-damage coupling introduced via the hypothesis of strain equivalence *(stated in Section 6.4)*, the *effective* elastic modulus of the material, which can be measured from experiments, is given by;

$$\mathbf{D}_{\text{eff}} = (1 - D)\mathbf{D}^e \,, \tag{6.28}$$

where the damage variable assumes values within the interval $[0, 1]$. In the absence of damage ($D = 0$), the effective modulus equals the modulus $\mathbf{D}^e$ of the virgin material. For a completely damaged state ($D = 1$), $\mathbf{D}_{\text{eff}} = \mathbf{0}$, corresponding to a total loss of stiffness and load bearing capacity of the material. The identification of a generic damaged state, with $D \in [0, 1]$, is then restricted to the measurement of the degradation of the current effective elastic modulus with respect to the virgin state ($D = 0$) as described by Lemaitre [48] and Lemaitre and Chaboche [52].

Isotropic and Kinematic Hardening

The plastic contribution $\psi^p(R, \boldsymbol{X})$ to the free energy is chosen as a sum of an isotropic and a kinematic hardening-related term;

$$\bar{\rho}\,\psi^p(R, \boldsymbol{X}) = \bar{\rho}\,\psi^I(R) + \frac{a}{2}\,\boldsymbol{X} : \boldsymbol{X}\,, \tag{6.29}$$

where a is a material constant and the isotropic hardening contribution, $\psi^I(R)$, is an arbitrary function of the single argument R. The thermodynamical force associated to isotropic hardening is, then, defined as;

$$\kappa \equiv \bar{\rho}\,\frac{\partial \psi^p(R, \boldsymbol{X})}{\partial R} = \bar{\rho}\,\frac{\partial \psi^I(R)}{\partial R} = \kappa(R)\,. \tag{6.30}$$

From (6.29), it follows that the thermodynamic force associated with kinematic hardening, the *back-stress tensor*, $\boldsymbol{\beta}$, is given by;

$$\boldsymbol{\beta} \equiv \bar{\rho}\,\frac{\partial \psi}{\partial \boldsymbol{X}} = a\,\boldsymbol{X}. \tag{6.31}$$

Yield Function

For the *yield function* Φ the following von Mises type form is adopted;

$$\Phi(\boldsymbol{\sigma}, \kappa, \boldsymbol{\beta}, D) = \frac{\sqrt{3\,J_2(\boldsymbol{s} - \boldsymbol{\beta})}}{1 - D} - \sigma_{y_0} - \kappa\,, \tag{6.32}$$

where the material parameter σ_{y_0} is the uniaxial yield stress of the virgin material.

Flow Potential: Internal Variable Evolution

The *flow potential* is assumed to be given by;

$$\Psi = \Phi + \frac{b}{2a}\beta : \beta + \frac{r}{(1-D)(s+1)}\left(\frac{-Y}{r}\right)^{s+1}, \tag{6.33}$$

where a, b, r and s are material constants. The damage evolution constants r and s can be identified by integrating the damage evolution law for particular cases of *(constant)* stress triaxiality rate as described in Section 7.4 of Lemaitre and Chaboche [52]. The constants a and b, associated with the resulting Armstrong-Frederick kinematic hardening law and can be obtained from cyclic loading experiments [52].

The convexity of the flow potential Ψ with respect to the thermodynamical forces for positive constants a, b, r and s ensures that the dissipation inequality is satisfied *'a priori'* by the present constitutive model.

The constitutive equations of Lemaitre's ductile damage model are grouped for convenience below.

(i) Elasto-plastic split of the strain tensor;

$$\boldsymbol{\varepsilon} = \boldsymbol{\varepsilon}^e + \boldsymbol{\varepsilon}^p$$

(ii) Coupled elastic-damage law;

$$\boldsymbol{\sigma} = (1 - D)\mathbf{D}^e : \boldsymbol{\varepsilon}^e$$

(iii) Yield function;

$$\Phi = \frac{\sqrt{3\, J_2(\boldsymbol{s}-\boldsymbol{\beta})}}{1-D} - \sigma_y$$

where $\sigma_y = \sigma_y(R)$.

(iv) Plastic flow and evolution equations for R, $\boldsymbol{\beta}$ and D;

$$\dot{\boldsymbol{\varepsilon}}^p = \dot{\gamma}\, \boldsymbol{N}$$
$$\dot{R} = \dot{\gamma}$$
$$\dot{\boldsymbol{\beta}} = \dot{\gamma}\,(a\, \boldsymbol{N} - b\, \boldsymbol{\beta})$$
$$\dot{D} = \dot{\gamma}\, \frac{1}{1-D} \left(\frac{-Y}{r}\right)^s$$

with Y given by (6.27) and the flow vector;

$$\boldsymbol{N} \equiv \sqrt{\frac{3}{2}}\, \frac{\boldsymbol{s}-\boldsymbol{\beta}}{(1-D)\|\boldsymbol{s}-\boldsymbol{\beta}\|}$$

(v) Loading/unloading criterion;

$$\Phi \leq 0 \qquad \dot{\gamma} \geq 0 \qquad \Phi\, \dot{\gamma} = 0$$

Damage threshold

At low values of accumulated plastic strain, $\bar{\varepsilon}^p$, elastic modulus degradation can hardly be detected by experiment. It can therefore be assumed that damage growth starts only at a critical value, denoted $\bar{\varepsilon}^p_D$. Called the *damage threshold* it can be inserted into the model by redefining the damage evolution law of item (iv) on page 108 to;

$$\dot{D} = \dot{\gamma} \frac{\hat{H}(\bar{\varepsilon}^p - \bar{\varepsilon}^p_D)}{1 - D} \left(\frac{-Y}{r} \right)^s , \tag{6.34}$$

where $\hat{H}$ here denotes the Heavyside step function.[1]

If such a threshold is adopted, then the evolution law for $\bar{\varepsilon}^p$ has to be defined for the model to be complete, we have;

$$\dot{\bar{\varepsilon}}^p = \sqrt{\tfrac{2}{3}} \left\| \dot{\varepsilon}^p \right\| . \tag{6.35}$$

by taking the plastic flow rule for the present model into consideration, the above equation results in the following evolution law for the accumulated plastic strain;

$$\dot{\bar{\varepsilon}}^p = \frac{\dot{\gamma}}{1 - D} . \tag{6.36}$$

[1] Further detailed definitions for all functions and equations can be found in [22].

6.6 Crack Closure Effect

Over the last twenty years the modelling of material damage has continued to make progress, however, even more refinement is needed in order to produce the next generation of models with even greater predictive capability, especially those concerning simulations that involve complex strain paths.

Although models such as the one described in section 6.5, are able to predict damage accurately over simple strain paths, this soon begins to deviate from experiments as the strain paths become more complex. In general, this observation is true not only when modelling damage, but also for all inelastic continuum models and it is well known that constitutive refinement in inelasticity still remains an open issue.

The model of section 6.5, defines damage, D, as the degradation of the elastic modulus due to the evolution of voids and micro-cracks *(see note 6.5, on 105)*,as the elastic law is assumed to remain linear in the presence of damage with equal responses in tension and compression.

Observations of uniaxial tension tests, however, find that the degradation of the elasticity modulus *(caused through the onset of voids and cracks)* is far greater in tension than in compression, due to cracks opening in tension, resulting in loss of load bearing area and associated stiffness, whilst the opposite occurs under compression, i.e. cracks begin to close up, resulting in an increase in load bearing area and stiffness.

Uniaxial crack closure model

The standard Lemaitre model material with damage state D, has an effective Young's modulus;

$$E = (1 - D)\, E_0\,, \tag{6.37}$$

where E_0 is the Young's modulus of the virgin *(undamaged)* material. The uniaxial stress-strain constitutive equation for the damaged material is given by;

$$\sigma = (1 - D)\, E_0\, \varepsilon \qquad \text{or} \qquad \varepsilon = \frac{\sigma}{(1 - D)\, E_0}\,. \tag{6.38}$$

crucially, the definition of the crack closure model assumes that this relationship is valid only when subject to *tensile* stresses ($\sigma \geq 0$). For *compressive* stresses ($\sigma < 0$), the uniaxial stress-strain relation is assumed to take the form;

$$\sigma = (1 - h\, D)\, E_0\, \varepsilon \qquad \text{or} \qquad \varepsilon = \frac{\sigma}{(1 - h\, D)\, E_0}\,, \tag{6.39}$$

where h is an experimentally determined constant which satisfies;

$$0 \leq h \leq 1\,. \tag{6.40}$$

this constant describes the effect of partial microcrack/void closure. A value $h \approx 0.2$ is typically observed in many experiments [51]. Note that for $h = 1$, the behaviour of the original damage model, without crack closure effects is recovered, whereas the other extreme value, $h = 0$, represents full crack closure with $E = E_0$ under compression. Any other value of h describes a partial crack closure effect. The uniaxial stress-strain diagram of figure 6.2 illustrates the behaviour of the model.

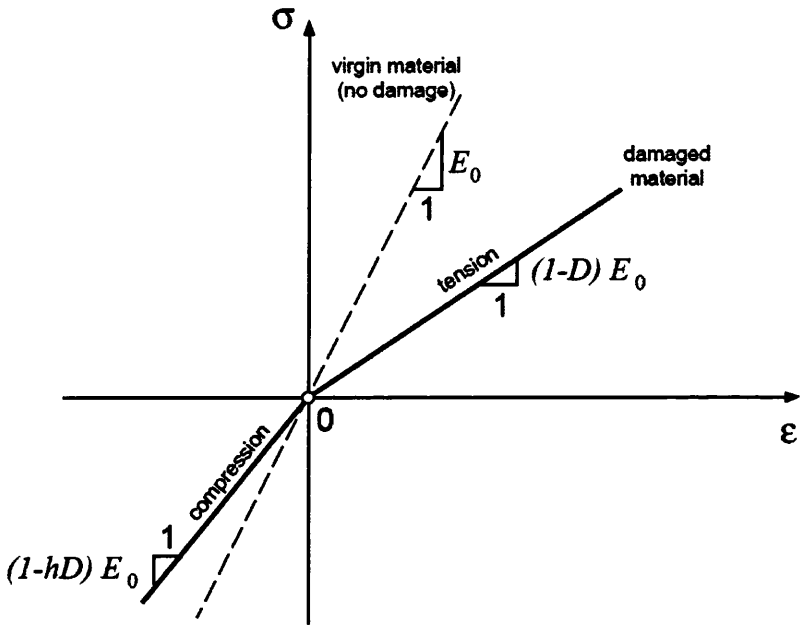

Figure 6.2: Crack Closure

Tensile/compressive split of the uniaxial stress

The constitutive equation of the above uniaxial model can be more elegantly expressed by introducing the following *tensile/compressive split* of the uniaxial stress;:

$$\sigma = \sigma_+ + \sigma_- \,, \tag{6.41}$$

where;

$$\sigma_+ = \langle \sigma \rangle \qquad \text{and} \qquad \sigma_- = -\langle -\sigma \rangle \,, \tag{6.42}$$

are, respectively, the *tensile* and *compressive components* of σ and $\langle\,\rangle$ is the *Macauley bracket*, that is, for any scalar, a,

$$\langle a \rangle = \begin{cases} a & \text{if } a \geq 0 \\ 0 & \text{if } a < 0 \,, \end{cases} \tag{6.43}$$

With the above notation, the uniaxial stress-strain relation for the damaged elastic material crack closure effect can be written simply as;

$$\varepsilon = \frac{1}{E_0}\left(\frac{\sigma_+}{1-D} + \frac{\sigma_-}{1-h\,D}\right). \tag{6.44}$$

The model described previously shows that it is relatively easy to establish a piece-wise linear damaged elastic model capable of accounting for crack closure effects in the uniaxial case. However, extending this simple model to the general three-dimensional situation, is far from trivial. This extension is not described here, however, additional information can be found in the following publications; [22] and [77, 78, 79].

6.7 Characterisation of Stress States

Ductile Steel materials that are subject to plastic deformation suffer from a progressive degradation of the microstructure with further deformation eventually leading to material failure. The physical mechanisms of damage at the microscale are still not completely understood, along with the correct interpretation of damage on a metallurgically sound basis, which means that a full understanding of the mechanism behind this phenomena can still be regarded as being an open matter of research.

Some computational models still have weaknesses in predicting damage evolution up to final fracture as the majority still treat plasticity and damage as being fully decoupled. More advanced models couple the plasticity and damage, meaning that increasing damage influences the plastic behaviour. Implementing and using these more advanced models, however, is more complex, due in part to the inevitable modification of the elasto-plastic framework.

It is well understood that when voids are present in a ductile material undergoing a tensile loading, the voids have a tendency to grow and ductile fracture will occur through the coalescence of voids, which in turn typically leaves a dimpled fracture surface. It is also widely accepted that damage depends greatly on the triaxiality level of the stress tensor.

Stress can be split into its hydrostatic and deviatoric components, with the mean hydrostatic stress tensor or volumetric stress tensor or mean normal stress tensor changing the volume of the body, while the stress deviator tensor distorts the body. The stress deviator tensor is known to be in a state of pure shear.

The deviatoric stress can be determined as:

$$\sigma_{ij} = s_{ij} + \sigma_H \delta_{ij} \tag{6.45}$$

where, σ_{ij} represents the Cauchy Stress Tensor, with s_{ij} representing the Deviatoric component and σ_H the Hydrostatic Stress, δ_{ij} represents the Kronecker delta or unit or identity matrix.

$$\sigma_{ij} = \begin{bmatrix} \sigma_{11} & \sigma_{12} & \sigma_{13} \\ \sigma_{21} & \sigma_{22} & \sigma_{23} \\ \sigma_{31} & \sigma_{32} & \sigma_{33} \end{bmatrix} = \sigma_{ij} \begin{bmatrix} \sigma_{11} - \sigma_H & \sigma_{12} & \sigma_{13} \\ \sigma_{21} & \sigma_{22} - \sigma_H & \sigma_{23} \\ \sigma_{31} & \sigma_{32} & \sigma_{33} - \sigma_H \end{bmatrix} + \sigma_H \begin{bmatrix} 1 & 0 & 0 \\ 0 & 1 & 0 \\ 0 & 0 & 1 \end{bmatrix} \tag{6.46}$$

The Cauchy stress tensor can then be rotated into a coordinate system where the shear components vanish by solving the equation;

$$\sigma_{ij} - \lambda \delta_{ij} = \begin{bmatrix} \sigma_{11} - \lambda & \sigma_{12} & \sigma_{13} \\ \sigma_{21} & \sigma_{22} - \lambda & \sigma_{23} \\ \sigma_{31} & \sigma_{32} & \sigma_{33} - \lambda \end{bmatrix} = 0 \tag{6.47}$$

$$\sigma_{ij} - \lambda \delta_{ij} = -\lambda^3 + I_1 \lambda^2 - I_2 \lambda + I_3 = 0 \tag{6.48}$$

Where λ_i represents $\sigma_1, \sigma_2, \sigma_3$ the principal stresses; I_1, I_2, I_3 the Stress Invariants.

$$I_1 = \sigma_{kk} = \sigma_{11} + \sigma_{22} + \sigma_{33} = \sigma_1 + \sigma_2 + \sigma_3 \tag{6.49}$$

$$I_2 = \sigma_{11}\sigma_{22} + \sigma_{22}\sigma_{33} + \sigma_{33}\sigma_{11} - \sigma_{12}^2 + \sigma_{23}^2 + \sigma_{13}^2 = \sigma_1\sigma_2 + \sigma_2\sigma_3 + \sigma_3\sigma_1 \tag{6.50}$$

$$I_3 = \sigma_{11}\sigma_{22}\sigma_{33} + 2\sigma_{12}\sigma_{23}\sigma_{31} - \sigma_{12}^2\sigma_{33} - \sigma_{23}^2\sigma_{11} - \sigma_{13}^2\sigma_{22} = \sigma_1\sigma_2\sigma_3 \tag{6.51}$$

The stress deviator tensor, which is in the state of pure shear, also has three invariants, these can be derived similarly to the stress invariants.

$$J_1 = S_{kk} = s_1 + s_2 + s_3 = 0 \tag{6.52}$$

$$J_2 = s_1 s_2 + s_2 s_3 + s_3 s_1 = \frac{1}{6}[(\sigma_1 - \sigma_2)^2 + (\sigma_2 - \sigma_3)^2 + (\sigma_3 - \sigma_1)^2] \tag{6.53}$$

$$J_3 = s_1 s_2 s_3 \tag{6.54}$$

Triaxiality is defined as the ratio of hydrostatic stress to the equivalent stress.

$$\eta = \frac{\sigma_h}{\bar{\sigma}} \tag{6.55}$$

where;

$$\sigma_H = \frac{1}{3}(\sigma_1 + \sigma_2 + \sigma_3) = \frac{1}{3}(\sigma_{11} + \sigma_{22} + \sigma_{33}) = \frac{I_1}{3} \tag{6.56}$$

the mean hydrostatic stress σ_H is related to the first invariant I_1 of the stress tensor. In many cases the equivalent stress is the Von Mises stress *(assuming negligible shear stresses)*

$$\bar{\sigma} = \sqrt{\frac{1}{2}[(\sigma_1 - \sigma_2)^2 + (\sigma_2 - \sigma_3)^2 + (\sigma_3 - \sigma_1)^2]} = \sqrt{3J_2} \tag{6.57}$$

The von Mises stress is related to the second invariant J_2.

Also note that for the seven deformation modes discussed herein that;

- Biaxial tension ($\sigma_3 = 0, \sigma_1 = \sigma_2$); $\eta = \frac{2}{3}$
- Biaxial Nonuniform ($\sigma_3 = 0, \sigma_1 = 1\frac{1}{4}\sigma_2$); $\eta = 0.6547$
- Plane Strain ($\sigma_3 = 0, \sigma_1 = 2\sigma_2$); $\eta = 0.5774$
- Uniaxial tension ($\sigma_3 = \sigma_2 = 0$); $\eta = \frac{1}{3}$
- Shear Pure ($\sigma_3 = 0, \sigma_1 = -\sigma_2$); $\eta = 0$
- Shear Nonuniform ($\sigma_3 = 0, \sigma_1 = -\frac{1}{4}\sigma_2$); $\eta = -0.2182$
- Uniaxial compression ($\sigma_3 = \sigma_1 = 0$); $\eta = -\frac{1}{3}$

A yield surface is a five-dimensional surface in the six-dimensional space of stresses, the yield surface is usually convex and the state of stress inside the yield surface is elastic. When the stress state lies on the yield surface the material is said to have reached its yield point and the material is said to have become plastic.

A yield surface, similarly to a fracture surface, may be expressed *(and visualized)* in terms of a three-dimensional principal stress space (R1,R2,R3), a two or three-dimensional space spanned by stress invariants (I1,J2,J3) or a version of the three-dimensional HaighWestergaard stress space.

Therefore, the equation of a yield surface can be written in the following forms;

$f(\sigma_1, \sigma_2, \sigma_3) = 0$ where σ_i are the principal stresses.

$f(I_1, J_2, J_3) = 0$ where I_1 is the first principal invariant of the Cauchy stress and J_2,J_3 are the second and third principal invariants of the deviatoric part of the Cauchy stress.

$f(p, q, r) = 0$ where p,q are scaled versions of I_1 and J_2 and r is a function of J_2,J_3.

$f(\xi, \rho, \theta)$ where ξ, ρ are scaled versions of I_1 and J_2, and θ is the Lode angle.

Any stress states can be represented in the space of principal stresses by using the Haigh-Weestergaard coordinates;

$$\xi = \frac{I_1}{\sqrt{3}} = \sqrt{3\sigma_H} \tag{6.58}$$

$$\rho = \sqrt{2J_2} \tag{6.59}$$

$$\text{Lode Angle} \qquad \theta = \frac{1}{3}\cos^{-1}\left(\frac{3\sqrt{3}}{2}\frac{J_3}{J_2^{\frac{3}{2}}}\right) \tag{6.60}$$

Chapter 7

Computational Modelling

7.1 Finite Element Analysis

Finite element analysis (FEA) was first developed for use in the aerospace and nuclear industries where safety is critical; its growth and current use is down to the ongoing evolution in computer technology. Mathematically, the analysis structure is divided into a mesh of finite sized elements, equations for the strains and stresses are developed in terms of unknown nodal displacements then the equations of equilibrium are put into matrix form, which can then be solved by computer. After applying the appropriate boundary conditions, the nodal displacements are found by solving the matrix stiffness equations, and once the nodal displacements are known, element stresses and strains can be calculated.

FEA Software

The software used for the duration of the project is the Finite Element package created by Rockfield Software Ltd, known as ELFEN^{TM}.

ELFEN^{TM}is a 2D/3D numerical modelling package, which includes the latest Finite Element (FE) and Discrete Element (DE) analysis technology and can be used to solve an extensive range of applications. It has been in constant development by Rockfield since 1986 and it's ongoing evolution draws upon the vast amount of knowledge and experience acquired by Rockfield's senior staff and the company's longstanding collaboration and association with the internationally renowned Civil & Computational Engineering Centre at Swansea University [22, 75, 100].

ELFEN's^{TM}continuous development ensures that state of the art analysis techniques are applied whilst presentation to the user takes the form of a simple, easy to use interface. This arrangement achieves the aim of providing *"Design tools for Engineers"* rather than a FE system for use by expert analysts alone.

ELFEN^{TM}is a general purpose FE/DE system that consists of the following:-

- Pre-processor - model generation, material database, geometry import.
- Processor - implicit and explicit analysis capabilities.
- Post-processor - assessment and visualisation of results.

A Word of Caution

FEA is an extremely powerful method of analysis, but due to the comfort of a convincing contour plot, Engineers can be easily fooled into thinking that an accurate result has been achieved. The quality and accuracy of the result is totally dependent on the quality and accuracy of the analysis model and how it represents the physical problem being investigated as it can only answer the questions asked of it. The well known saying *"Ask a stupid question, get a stupid answer"* is certainly true when applied to FEA, careful planning is the key to a successful analysis.

In Engineering numerous situations present themselves where FE analysis is not required, maybe the problem can be solved analytically with hand calculations or through the use of calculation software such as MathCAD^{TM}. The bottom line is that FEA is not a trivial process and no level of automation can make analysis easy, or more importantly, correct. The key to good analysis is knowledge of the limitations of the method coupled with an understanding of the physical phenomena under investigation.

Over recent years, finite element programs have become common tools for Engineers, but unfortunately many Engineers lack the proper training and understanding of the underlying concepts needed to use these tools correctly. In essence, the use of any FEA analysis session should be to interrogate the solver with many well formed and appropriate questions.

7.2 Single Element Modelling

The finite element package ELFEN^{TM}benefits from a number of uncoupled damage indicator and coupled damage models that are included as standard in the software.

In order to complete a general evaluation of a number of damage indicator models that showed potential for further use in scoring simulations, a comparison was completed using analytical methods to calculate the deformation of a unit cube sized block of steel material. The results were then directly compared with the results from the computational modelling of a single element, this helped to verify and validate element behaviour, as well as damage prediction under common sheet metal forming loading conditions undergoing very large strains, it also provided a better understanding of how the damage models functioned, and how well the results from the computational modelling reflected the analytical results.

Figure 7.3 on page 130, shows that, despite some minor deviations in directional stresses, the single element modelling successfully predicted triaxiality for all conditions of loading.

Modes of Deformation

The analytical results were based on a number of different deformation modes that are commonly found in sheet metal forming, such as;

- Biaxial tension ($\sigma_3 = 0, \sigma_1 = \sigma_2$); $\beta = 1$, $\alpha = 1$; $\eta = \frac{2}{3}$
- Biaxial Nonuniform ($\sigma_3 = 0, \sigma_1 = 1\frac{1}{4}\sigma_2$); $\beta = 0.5$, $\alpha = 0.8$; $\eta = 0.6547$
- Plane Strain ($\sigma_3 = 0, \sigma_1 = 2\sigma_2$); $\beta = 0$, $\alpha = 0.5$; $\eta = 0.5774$
- Uniaxial tension ($\sigma_3 = \sigma_2 = 0$); $\beta = -0.5$, $\alpha = 0$; $\eta = \frac{1}{3}$
- Shear Pure ($\sigma_3 = 0, \sigma_1 = -\sigma_2$); $\beta = -1$, $\alpha = -1$; $\eta = 0$
- Shear Nonuniform ($\sigma_3 = 0, \sigma_1 = -\frac{1}{4}\sigma_2$); $\beta = -1.5$, $\alpha = -4$; $\eta = -0.2182$
- Uniaxial compression ($\sigma_3 = \sigma_1 = 0$); $\beta = -2$, $\alpha = -\infty$; $\eta = -\frac{1}{3}$

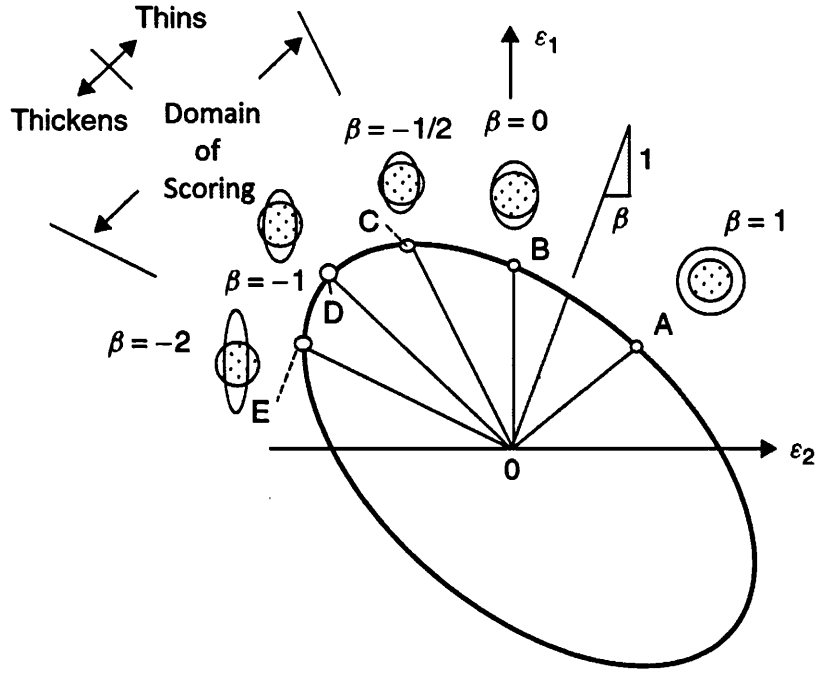

Figure 7.1: Beta Strain Ratios

The ellipse in Figure 7.1 represents a contour of equal effective strain, $\bar{\varepsilon}$, each point represents the strain in a material element with the same flow stress, σ_f. All points are to the left of the right-hand diagonal as shown in figure 7.1, i.e. left of the strain path that represents equal biaxial stretching, where $\beta = 1$.

The principal tension and principal stress in direction 1, will always be tensile or positive, i.e. $\sigma_1 \geq 0$. For the extreme case in which $\sigma_1 = 0$ it is found that, $\alpha = \infty$ and $\beta = -2$, which means that all possible straining paths in sheet forming processes lie between OA and OE in Figure 7.1, i.e. the strain ratio will be in the range $-2 \leq \beta \leq 1$. However, for scoring, the strain paths are represented by the range between OC and OE, i.e. Uniaxial Tension through to Uniaxial Compression, where the triaxiality value begins at the positive value of $\eta = \frac{1}{3}$ and ends negatively at $\eta = -\frac{1}{3}$.

Evidence that these modes dominate scoring can be seen in the contour plots for triaxiality generated by a FE analysis for scoring, found in appendix D beginning on page 256.

Deformation of a Unit Cube

Analytical results were obtained using similar methods to those detailed in Chap 2 of [60], the following describes the equations required, then the same methodology was used to calculate the results for all the other deformation modes commonly found in sheet metal forming, as discussed in section 7.2.

A complete worked example of the procedure used to calculate results for the deformation of a unit cube of steel material undergoing equal biaxial stretching, can be found in Appendix B,

Principal Strains

The Principal strains were calculated using the following equation;

$$\varepsilon = \int \mathrm{d}\varepsilon = \int_{lo}^{l} \frac{\mathrm{d}l}{l} = \ln \frac{l}{lo} \tag{7.1}$$

which can then be further split into the three principle strains directions; i.e.

$$\varepsilon_1 = \ln \frac{l}{lo} \qquad \varepsilon_2 = \ln \frac{w}{wo} \qquad \varepsilon_3 = \ln \frac{t}{to} \tag{7.2}$$

Strain and Stress Ratios

For a proportional process, i.e. where both the stress and strain ratios are constant, then it is usual practice to describe the deformation of an element, as detailed in figure 7.2. Normal convention is to define the principal directions so that $\sigma_1 > \sigma_2$ and the third direction is perpendicular to the surface where $\sigma_3 = 0$.

For Strains;

$$\varepsilon_2 = \beta\varepsilon_1 \qquad \varepsilon_3 = -(1+\beta)\varepsilon_1 \tag{7.3}$$

For Stresses;

$$\sigma_2 = \alpha\sigma_1 \qquad \sigma_3 = 0 \tag{7.4}$$

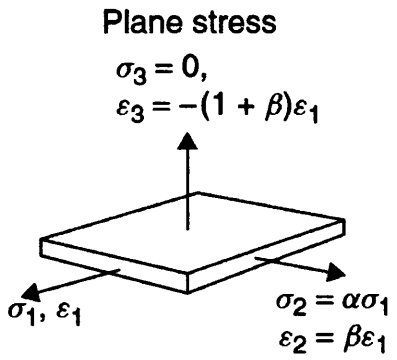

Figure 7.2: Principal Stress and Strain in a Plane Stress Process

The following relationship between the stress and strain ratios also exist;

$$\alpha = \frac{2\beta + 1}{2 + \beta} \qquad \beta = \frac{2\alpha - 1}{2 - \alpha} \tag{7.5}$$

These equations arise from the *Levy-Mises Flow Rule*, which is not discussed here, however, more detail can be found in [60].

Effective Strain

The effective or equivalent strain was calculated using the following;

$$\bar{\varepsilon} = \sqrt{\frac{4}{3}(1 + \beta + \beta^2)\varepsilon_1} \tag{7.6}$$

Other equations, such as;

$$\bar{\varepsilon} = \sqrt{\frac{2}{3}(\varepsilon_1^2 + \varepsilon_2^2 + \varepsilon_3^2)} \tag{7.7}$$

or;

$$\bar{\varepsilon} = \sqrt{\frac{2}{9}[(\varepsilon_1 - \varepsilon_2)^2 + (\varepsilon_2 - \varepsilon_3)^2 + (\varepsilon_3 - \varepsilon_1)^2]} \tag{7.8}$$

are also useful.

The effective strain increment, *(required to determine damage)* was calculated by subtracting the current incremental value of $\bar{\varepsilon}$ from the previous incremental value of $\bar{\varepsilon}$.

Effective Stress

If tensile test data is available for the material, then this can be generalised using the following effective stress function;

$$\bar{\sigma} = \sqrt{\frac{1}{2}[(\sigma_1 - \sigma_2)^2 + (\sigma_2 - \sigma_3)^2 + (\sigma_3 - \sigma_1)^2]} \tag{7.9}$$

or for plane stress;

$$\bar{\sigma} = \sqrt{\sigma_1^2 - \sigma_1\sigma_2 + \sigma_2^2} = (\sqrt{1 - \alpha + \alpha^2})\sigma_1 \tag{7.10}$$

For numerical models, the actual stress strain curve can be used, but for an analytical mechanics model, common practice is to approximate the data by using a simple empirical power law, such as;

$$\bar{\sigma} = K(\varepsilon_0 + \bar{\varepsilon})^n \tag{7.11}$$

The stress strain laws for both material used in this project were;

TH435

$$\bar{\sigma} = 744(0.16 + \bar{\varepsilon})^{0.27} \tag{7.12}$$

TH550N

$$\bar{\sigma} = 850.46(0.0768 + \bar{\varepsilon})^{0.1768} \tag{7.13}$$

Principal Stress

Principal stress can be found from the effective stress using;

$$\sigma_1 = \frac{\bar{\sigma}}{\sqrt{1 - \alpha + \alpha^2}} \tag{7.14}$$

then;

$$\sigma_2 = \alpha\sigma_1 \tag{7.15}$$

Hydrostatic Stress

The Hydrostatic stress is then;

$$\sigma_h = \frac{\sigma_1 + \sigma_2 + \sigma_3}{3} \tag{7.16}$$

Deviatoric Stresses

The Deviatoric stresses are then;

$$\sigma_1^{/} = \sigma_1 - \sigma_h \qquad \sigma_2^{/} = \sigma_2 - \sigma_h \qquad \sigma_3^{/} = \sigma_3 - \sigma_h \tag{7.17}$$

Flow Rule

The flow rule can then be checked by;

$$= \frac{\varepsilon_1}{\sigma_1^{/}} \qquad = \frac{\varepsilon_2}{\sigma_2^{/}} \qquad = \frac{\varepsilon_3}{\sigma_3^{/}} \tag{7.18}$$

Plastic Work

The plastic work of deformation can be found using;

$$\frac{W}{vol} = \int_0^{\bar{\varepsilon}} \bar{\sigma}\bar{\varepsilon} \tag{7.19}$$

Pressure Triaxiality

Pressure Triaxiality is then;

$$= \frac{\sigma_h}{\bar{\sigma}} \tag{7.20}$$

Product Triaxiality

Product Triaxiality is;

$$= \frac{\sigma_1 \times \sigma_2}{\bar{\sigma}^3} \tag{7.21}$$

Deviatoric Triaxiality

And the Deviatoric Triaxiality is;

$$= \frac{\sigma_1^{/} \times \sigma_2^{/} \times \sigma_3^{/}}{\bar{\sigma}^3} \tag{7.22}$$

Lode Angle

Finally the Lode Angle can be calculated using;

$$\theta = \frac{1}{3}\cos^{-1}\left(\frac{3\sqrt{3}}{2}\frac{J_3}{J_2^{\frac{3}{2}}}\right) \tag{7.23}$$

Damage Indicator Models

As a precursor to full score modelling, which follows in section 7.3, the uncoupled or damage indicator models, as discussed in section 6.3, were first used to evaluate the level of damage in a single element, this not only helped with the understanding of exactly how the uncoupled damage models evaluated damage, but also, with the Oyane and Generalised Lemaitre models, it helped with the understanding of the effect of the parameters, i.e. parameter *(A)* for the Oyane model and parameter *(So)* for the Generalised Lemaitre model.

Oyane Damage Indicator

The uncoupled Oyane Damage Indicator model;

$$= \int \left[1 + A\frac{\sigma_h}{\bar{\sigma}}\right] d\varepsilon_p \tag{7.24}$$

Generalised Lemaitre Damage Indicator

The uncoupled Generalised Lemaitre Damage Indicator model;

$$= \int \bar{\sigma}^{2So} \left[\frac{2}{3}(1+v) + 3(1-2v)\left[\frac{\sigma_h}{\bar{\sigma}}\right]^2\right]^{So} d\bar{\varepsilon} \tag{7.25}$$

Rice & Tracy Damage Indicator

The uncoupled Rice & Tracy Damage Indicator model;

$$= \int 0.283 \exp\left[\sqrt{\frac{3}{2}}\frac{\sigma_h}{\bar{\sigma}}\right] d\bar{\varepsilon} \tag{7.26}$$

Lemaitre Damage Indicator

And finally the uncoupled Lemaitre Damage Indicator model;

$$= \int \left[\frac{2}{3}(1+v) + 3(1-2v)\left[\frac{\sigma_h}{\bar{\sigma}}\right]^2\right] d\bar{\varepsilon} \tag{7.27}$$

Uncoupled Damage Indicator Analysis

For all results, the equivalent strain was kept constant, secondly, although the analysis was completed for both materials under investigation, i.e. TH435 and TH550N, only the results for TH550N will be discussed, as the outcomes for TH435 were similar, but with different values.

The following figure shows firstly a table, (a), that compares the analytical results against the simulated results, then (b) and (c), which show plots of triaxiality against the α and β Stress-Strain ratios.

Figure 7.4, again plots analytical results against simulated results, this time for damage against triaxiality for the uncoupled Oyane, Rice & Tracy and Lemaitre damage models.

Calculated Results											Oyane		Rice & Tracy		Lemaitre	
Deformation Mode	eps_1 princ	eps_2 princ	eps_3 princ	β strain ratio	α stress ratio	eps eff	sig eff	sig_1 princ	sig_2 princ	pressure Triaxiality	D_Incre	D_Total	D_Incre	D_Total	D_Incre	D_Total
Biaxial	0.250	0.250	-0.500	1.0	1.0	0.500	771.619	771.619	771.619	0.6667	0.0720	1.8000	0.0101	0.2521	0.028	0.7000
Biaxial - Nonuniform	0.327	0.164	-0.491	0.5	0.8	0.500	771.619	841.906	673.525	0.6547	0.0711	1.7768	0.0100	0.2494	0.0276	0.6906
Plane Strain	0.433	0.000	-0.433	0.0	0.5	0.500	771.619	890.989	445.495	0.5774	0.0650	1.6258	0.0093	0.2333	0.0253	0.6333
Uniaxial Tension	0.500	-0.250	-0.250	-0.5	0.0	0.500	771.619	771.619	0.000	0.3333	0.0460	1.1500	0.0076	0.1889	0.0200	0.5000
Shear - Constant	0.433	-0.433	0.000	-1.0	-1.0	0.500	771.619	445.495	-445.495	0.0000	0.0200	0.5000	0.0057	0.1415	0.0173	0.4333
Shear - Nonuniform	0.327	-0.491	0.164	-1.5	-4.0	0.500	771.619	168.381	-673.525	-0.2182	0.0030	0.0746	0.0047	0.1171	0.0186	0.4619
Uniaxial Compression	0.250	-0.500	0.250	-2.0	-1000.0	0.500	771.619	0.771	-771.234	-0.3328	-0.0060	-0.1490	0.0042	0.1061	0.0200	0.4998
Numerical Results											Oyane (100, 0.25		Rice & Tracy (100, 0)		Lemaitre (100, 0)	
Biaxial	0.250	0.250	-0.497	1.0	1.0	0.498	770.354	770.518	770.518	0.6666		1.7814		0.2494		0.6927
Biaxial - Nonuniform	0.327	0.164	-0.488	0.5	0.8	0.498	770.398	834.906	683.704	0.6571		1.7565		0.2469		0.6834
Plane Strain	0.433	0.000	-0.430	0.0	0.5	0.499	770.492	889.970	444.805	0.5775		1.6097		0.2310		0.6271
Uniaxial Tension	0.500	-0.249	-0.249	-0.5	0.0	0.499	770.750	771.305	0.598	0.3338		1.1415		0.1875		0.4963
Shear - Constant	0.433	-0.433	0.000	-1.0	-1.0	0.500	771.148	424.121	-459.819	-0.0154		15.8956		1043.9050		45.0759
Shear - Nonuniform	0.327	-0.491	0.162	-1.5	-4.0	0.500	772.548	-58.187	-900.109	-0.3703		0.0859		0.1192		0.4713
Uniaxial Compression	0.249	-0.500	0.249	-2.0	-1000.0	0.500	770.736	-0.666	-771.402	-0.3336		-0.1489		0.1053		0.4964

(a) Comparison of Calculated v Simulated Results

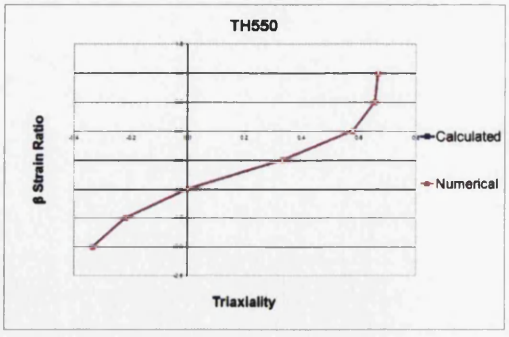

(b) β v Triaxiality

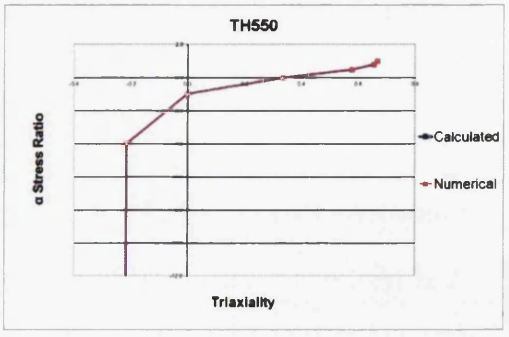

(c) α v Triaxiality

Figure 7.3: Results for TH550N with 7 Deformation Modes

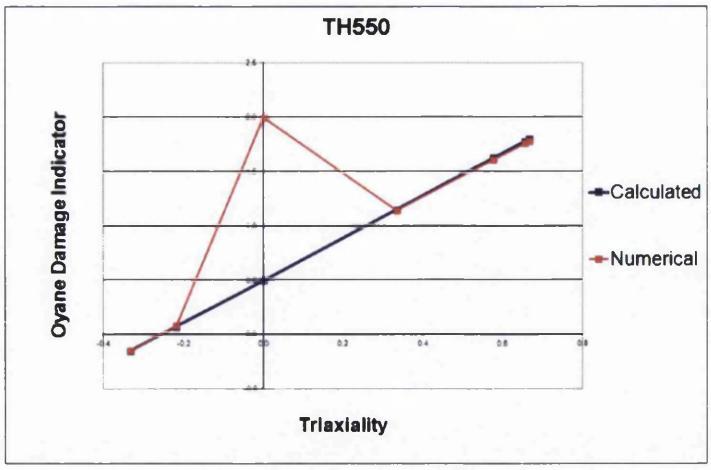

(a) Oyane v Triaxiality

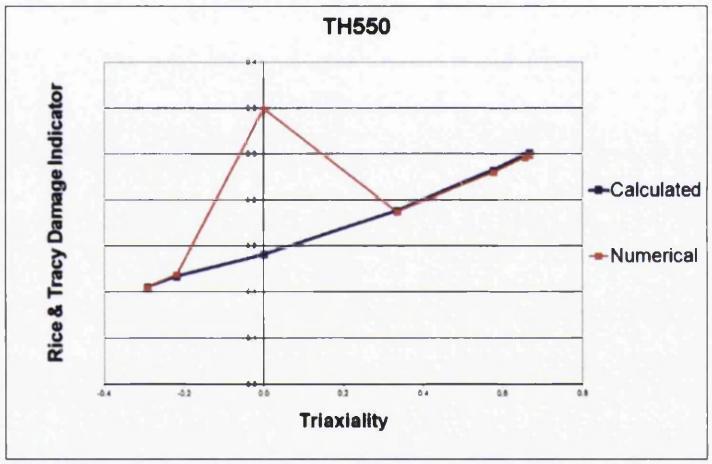

(b) R&T v Triaxiality

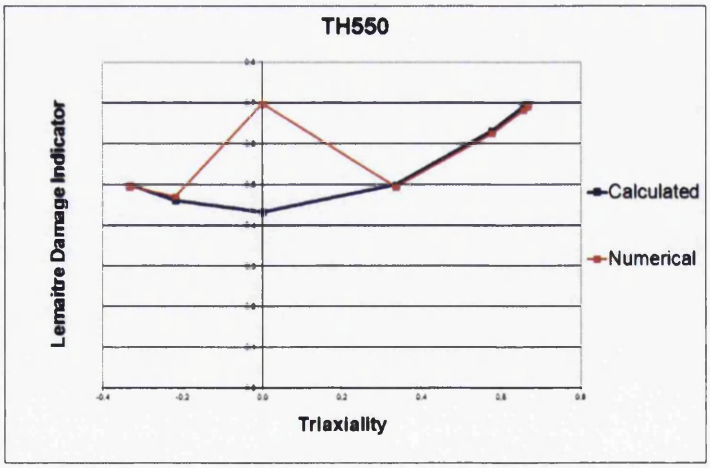

(c) Lemaitre v Triaxiality

Figure 7.4: Results for TH550N with Damage Indicator Models

Outcomes

What can be seen from these results, is that in figure 7.3, for both stress and strain ratios, the numerical results very closely match the analytical values for all deformation modes.

Regarding figure 7.4, the damage indicator plots, again the numerical results very closely match the analytical values for all deformation modes, but with one exception, the highlighted values for pure shear were much higher than the calculated values. The reason behind this is thought to be that pure shear is very sensitive to triaxiality, so, the highlighted values indicate that the single element shows a weaker performance in this mode.

What can also be seen from figure 7.4 is that triaxiality, and hence the damage value, differs for individual strain ratios, which in turn means that as score forming covers the domain of multiple strain ratios, therefore, damage needs to be fitted over the full range applicable.

The literature, however, shows that although there are possibilities to fit damage parameters to a single strain ratio, *(linear proportional loading)*, parameter fitting for multiple strain ratios is altogether a much more difficult thing to achieve.

Further Uncoupled Analysis

Due to the results seen previously, it was decided to repeat the analysis, but this time to include extra additional in-between modes. The deformation modes increased from the seven well-known modes discussed in section 7.2 to eleven modes, i.e. four extra in-between modes.

Calculated Results											Oyane		Rice & Tracy		Lemaitre	
Deformation Mode	eps_1 princ	eps_2 princ	eps_3 princ	β strain ratio	α stress ratio	eps eff	sig eff	sig_1 princ	sig_2 princ	pressure Triaxiality	D_Incre	D_Total	D_Incre	D_Total	D_Incre	D_Total
Biaxial	0.250	0.250	-0.500	1.000	1.00	0.500	771.619	771.619	771.619	0.6667	0.0720	1.8000	0.0101	0.2521	0.026	0.7000
Biaxial - Nonuniform	0.327	0.164	-0.491	0.500	0.80	0.500	771.619	841.906	673.525	0.6547	0.0711	1.7766	0.0100	0.2494	0.027619	0.6905
Plane Strain	0.433	0.000	-0.433	0.000	0.50	0.500	771.619	890.989	445.495	0.5774	0.0650	1.6258	0.0093	0.2333	0.025333	0.6333
Uniaxial Tension	0.500	-0.250	-0.250	-0.500	0.00	0.500	771.619	771.619	0.000	0.3333	0.0460	1.1500	0.0076	0.1899	0.02	0.5000
Between UT & S-C	0.480	-0.360	-0.120	-0.750	-0.40	0.500	771.620	617.788	-247.118	0.1601	0.0325	0.8122	0.0085	0.1625	0.017949	0.4487
Between UT & S-C_2	0.435	-0.431	-0.004	-0.990	-0.97	0.500	771.619	462.194	-438.762	0.0058	0.0205	0.5113	0.0057	0.1422	0.017334	0.4334
Shear - Constant	0.433	-0.433	0.000	-1.000	-1.00	0.500	771.619	445.495	-445.495	0.0000	0.0200	0.5000	0.0057	0.1415	0.017333	0.4333
Between S-C & S-N_2	0.431	-0.435	0.004	-1.010	-1.03	0.500	771.619	438.829	-452.127	-0.0057	0.0196	0.4888	0.0056	0.1408	0.017334	0.4334
Between S-C & S-N	0.378	-0.472	0.094	-1.250	-2.00	0.500	771.619	291.645	-583.289	-0.1260	0.0102	0.2543	0.0051	0.1269	0.017714	0.4429
Shear - Nonuniform	0.327	-0.491	0.164	-1.500	-4.00	0.500	771.619	188.381	-673.525	-0.2182	0.0030	0.0745	0.0047	0.1171	0.018476	0.4619
Uniaxial Compression	0.250	-0.500	0.250	-2.000	-1000.0	0.500	771.619	0.771	-771.234	-0.3328	-0.0060	-0.1490	0.0042	0.1061	0.019992	0.4998
Numerical Results											Oyane (100, 0.2584)		Rice & Tracy (100, 0)		Lemaitre (100, 0)	
Biaxial	0.250	0.250	-0.497	1.00	1.00	0.498	770.354	770.518	770.518	0.6666		1.7814		0.2496		0.6927
Biaxial - Nonuniform	0.327	0.164	-0.488	0.50	0.80	0.498	770.398	834.908	683.704	0.6571		1.7585		0.2469		0.6834
Plane Strain	0.433	0.000	-0.430	0.00	0.50	0.499	770.492	889.970	444.805	0.5775		1.6097		0.2310		0.6271
Uniaxial Tension	0.500	-0.248	-0.249	-0.50	0.00	0.499	770.720	771.305	0.586	0.3338		1.1416		0.1875		0.4963
Between UT & S-C	0.480	-0.360	-0.120	-0.75	-0.40	0.500	772.936	364.434	-523.357	-0.0988		0.8195		0.1661		0.4624
Between UT & S-C_2	0.435	-0.431	-0.005	-0.99	-0.97	0.500	773.416	182.888	-879.125	-0.2228		0.5237		0.1457		0.4516
Shear - Constant	0.433	-0.433	0.000	-1.00	-1.00	0.500	771.146	424.121	-459.819	-0.0164		15.8966		1043.9060		45.0758
Between S-C & S-N_2	0.431	-0.435	0.003	-1.01	-1.03	0.500	773.420	149.951	-697.469	-0.2317		0.5016		0.1443		0.4515
Between S-C & S-N	0.378	-0.472	0.093	-1.25	-2.00	0.500	773.094	15.994	-759.745	-0.3164		0.2672		0.1298		0.4577
Shear - Nonuniform	0.327	-0.491	0.162	-1.50	-4.00	0.500	772.548	-58.167	-800.109	-0.3703		0.0859		0.1192		0.4713
Uniaxial Compression	0.249	-0.500	0.249	-2.01	610.06	0.500	770.736	-0.666	-771.402	-0.3339		-0.1489		0.1053		0.4964

(a) Recomparison of Calculated v Simulated Results

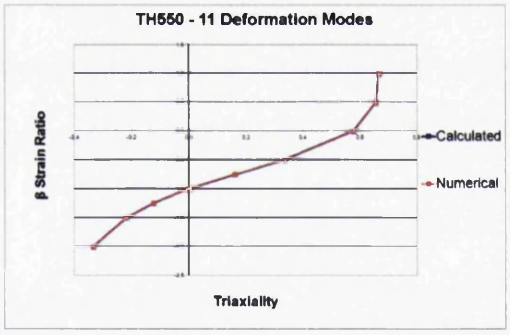

(b) β v Triaxiality

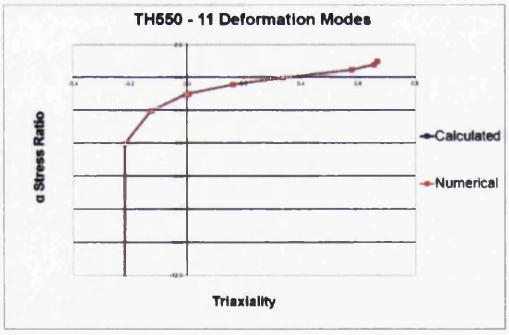

(c) α v Triaxiality

Figure 7.5: Results for TH550N with 11 Deformation Modes

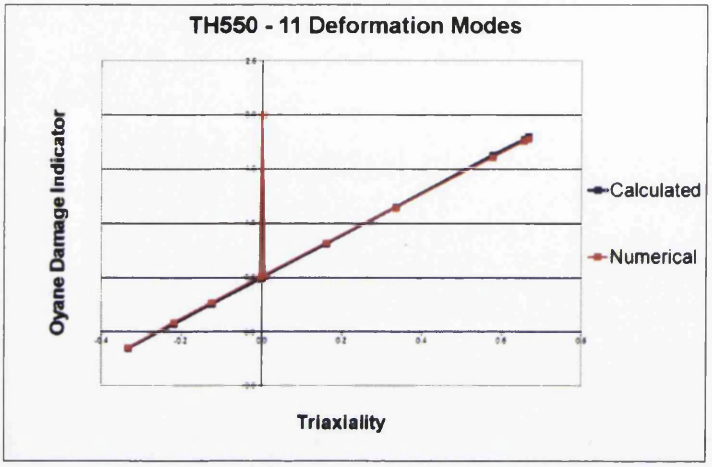

(a) Oyane v Triaxiality

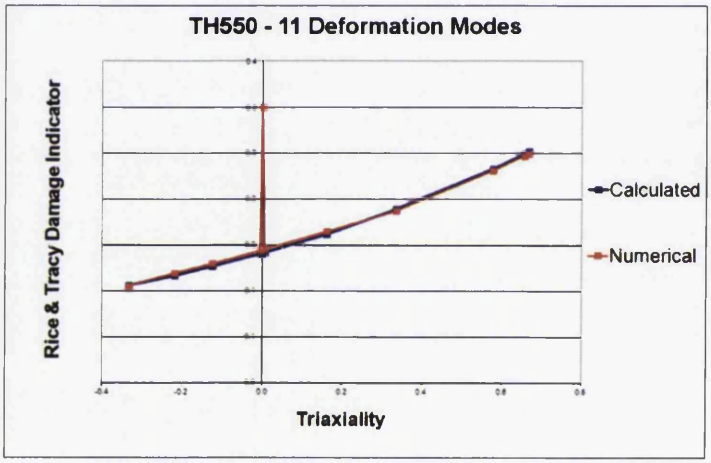

(b) R&T v Triaxiality

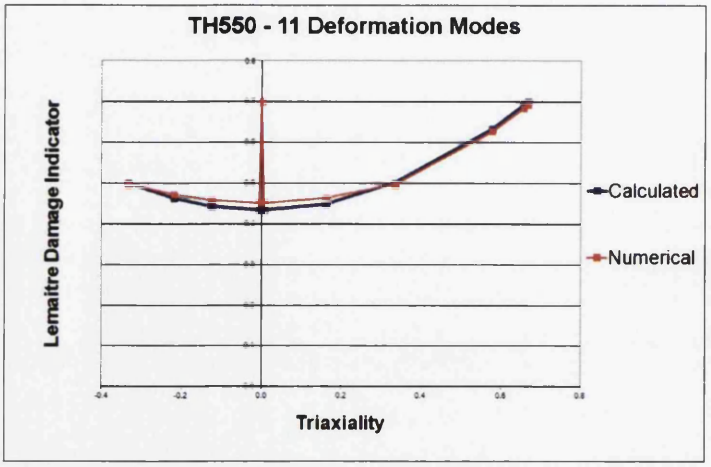

(c) Lemaitre v Triaxiality

Figure 7.6: Results for TH550N with Damage Indicator Models

Further Outcomes

Once more, from these results, it can be seen that in figure 7.5, regarding both stress and strain ratios, the numerical results, again very closely match the analytical values.

This time however, the damage indicator plots of figure 7.6, show that with the additional in-between modes added to the analysis, the element performance only differs from the analytical values when the element is precisely in the mode of pure shear, i.e. when the triaxiality exactly measures zero.

This confirms, that most likely in a *"real life"* FE analysis, the elements will rarely enter this exact and precise mode of deformation, which means that overall, element performance for full score modelling should not be something to be particularly concerned about.

Oyane - *A* Parameter Effect

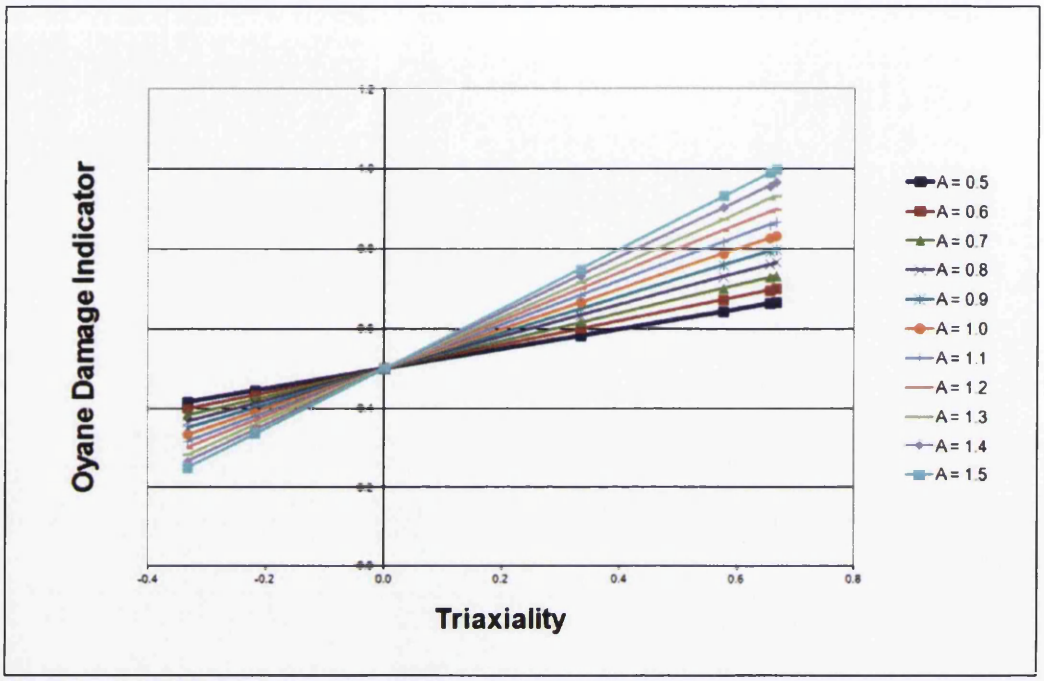

Figure 7.7: Oyane - Effect of Increasing A Parameter

Figure 7.7, graphically shows the effect of increasing parameter A, in this case from 0.5 to 1.5. It can be seen that for positive levels of triaxiality the level of damage increases, whilst at the same time, for negative levels of triaxiality, the damage decreases. Over the whole domain of triaxiality, Oyane damage plots as a straight line, which tends to rotate around the value of the effective strain. As parameter A increases, the line rotates anticlockwise and when parameter A deceases, the line line rotates clockwise. Put together with the triaxiality plots, this behaviour can help explain, the results reported in section 7.6.

Generalised Lemaitre - So Parameter Effect

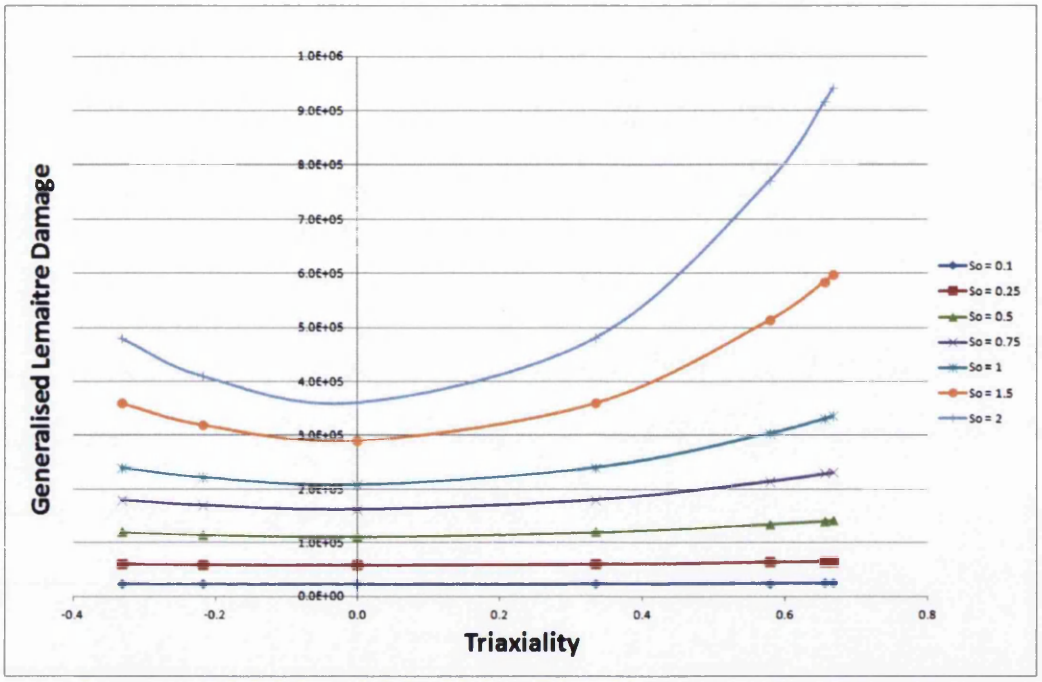

Figure 7.8: Generalised Lemaitre - Effect of Increasing s Parameter

Figure 7.8, again shows graphically the effect of raising the s exponent, the C shaped curve is similar to that seen in the other Uncoupled Lemaitre model, figure 7.6(c), but the whole curve rises up the scale as expected. From this graph, it appears that lower levels of the s exponent are straight lines, but this is just an outcome of the scaling effect of the graph, when looked at individually, all values of exponent s return a similar shaped C curve.

Coupled Lemaitre - Single Element

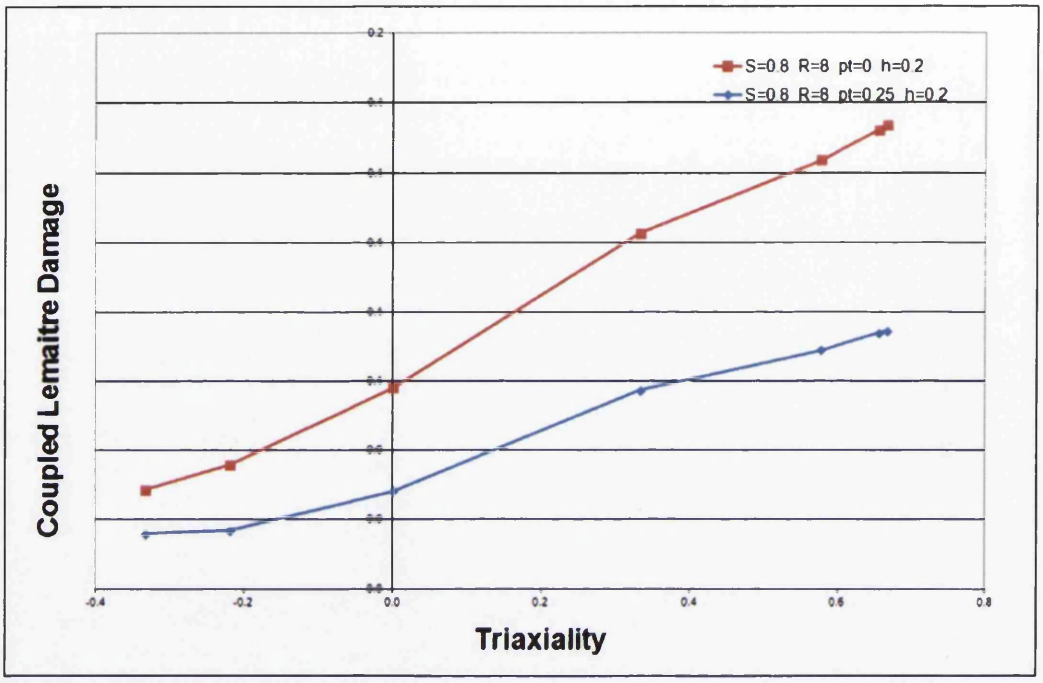

Figure 7.9: Coupled Lemaitre - Single Element Responce

Figure 7.9 shows graphically the effect of the coupled Lemaitre model using the final selected parameters, discussed in section 7.5, however, the values for the *pt* parameter had to be lowered to within the parameters used for the single element, i.e. a constant effective strain of 0.5, future extensions to the single element model should provide final verification for the coupled Lemaitre parameters.

7.3 Scoring - Uncoupled Damage Models

The next step in the numerical analysis was to carry out a full uncoupled damage model analysis for the full scoring model, using the following uncoupled models:-

- Oyane Model *(7.24)*
- Generalised Lemaitre Model *(7.25)*
- Rice & Tracy Model *(7.26)*
- Uncoupled Lemaitre Model *(7.27)*

Also known as *Damage Indicator* models, and classified in section 6.3, the Oyane and Generalised Lemaitre models were run with varying parameters, after all models had successfully completed, contour plot images were captured for;

- Damage
- Strain *(XX YY XY)*
- Stress *(XX YY XY)*
- Triaxiality

The results for the uncoupled analysis are not presented here as a full comparative analysis of the uncoupled results against the coupled results, including micrographic images of cross-section taken at varying score residual thicknesses is presented in section 7.6.[1]

[1] A complete set of all model data is included on the disk attached to this Thesis and a full set of all relevant contour plot images are presented in Appendix D

7.4 Scoring Model - Outline

All scoring models were based on the following geometry with slight variations depending on the tool profile.

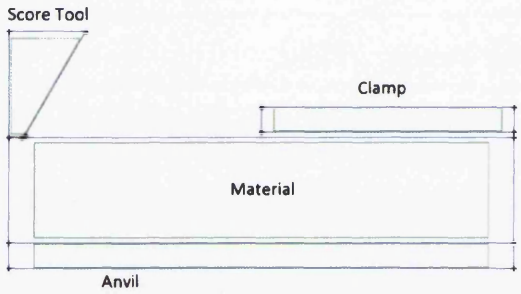

(a) Half Model - Geometry

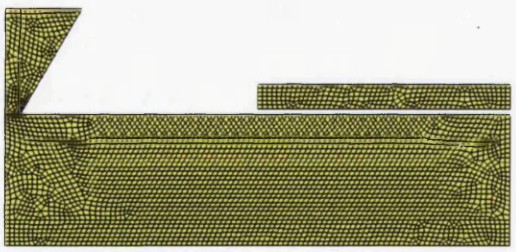

(b) Half Model - Mesh

Figure 7.10: Scoring Model Geometry

7.5 Scoring - Coupled Lemaitre Damage Model

After running all of the uncoupled models and recording the results, the next step was to set up further FE analysis to run the fully coupled Lemaitre model as described in Chapter 6, section 6.5, in order for a comparison to be made from both sets of results.

However, in order to accomplish this, and before being able to run the fully coupled model, the following parameters from equations 6.33 and 6.44, reproduced below, had to be successfully selected for the materials being simulated.

$$\Psi = \Phi + \frac{b}{2a}\beta : \beta + \frac{r}{(1-D)(s+1)}\left(\frac{-Y}{r}\right)^{s+1}$$

- Exponent: s
- Denominator: r

$$\varepsilon = \frac{1}{E_0}\left(\frac{\sigma_+}{1-D} + \frac{\sigma_-}{1-h\,D}\right).$$

- Closure Effect: h

Finally, a parameter that described the plastic threshold for damage evolution was required.

- Plastic Threshold: pt

Up until this point, all the uncoupled models had run successfully and produced results, however, there was a problem in determining how to be sure that the results gave an accurate description of damage in scoring. This was because, and as could already be shown, with different values for the A parameter, the Oyane model produced different results for damage, additionally, the Generalised Lemaitre model also produced different results for damage when the exponent parameter s was altered, therefore, faced with running the fully coupled model, how could so called *"accurate"* parameters be selected for the materials?.

As discussed briefly in section 6.5, methods to identify damage evolution constants had been developed by Lemaitre and Chaboche [52], in fact, in more recent books by Lemaitre [51], and Lemitre and Desmoratrat [53], methods for identifying parameters had been further expanded upon with detailed instructions and even practical examples.

The problem however, with all published methods for identifying damage parameters, is that it was assumed that it was possible to produce test samples out of the same materials, including samples for cyclic fatigue testing. However, in this case, this assumption presented itself as a problem, as the materials used for can ends are on average 0.21mm thick. *(Examples are shown in fig 2.6)*
This meant that specimens for standard S-N cyclic fatigue tests could not be produced, in fact, the best that Tata's own in-house test facility could offer on materials of this thickness, was a test known as a tension-tension test, but unfortunately, this test was not only expensive to complete, but researchers at Tata had little confidence in the tests ability to produce *"good"* useable results.

There was however, a method, that could be employed as a starting point for establishing suitable parameters for the fully coupled model, in fact, Lemaitre had produced a paper discussing numerous methods of measuring damage [54], and this method was included, therefore, the method of physically measuring the amount of voids or void fraction present in the material after scoring was used. This was achieved by using a very high powered electron microscope to analyse the scored samples in order to quantify the amount of voids or void fraction present, the methods used are discussed further in section 7.5, that follows.

Parameter Validation

As mentioned, Tata used SEM techniques to quantify the amount of voids or void fraction present in pre-scored samples, this has been completed on samples with decreasing score residual thickness, shown in table 7.1.[1] The resulting values for void fraction were then organised into a graph that shows the relationship between the increasing void fraction against the decreasing score residual thickness, the resulting graph is shown in figure 7.12(a).

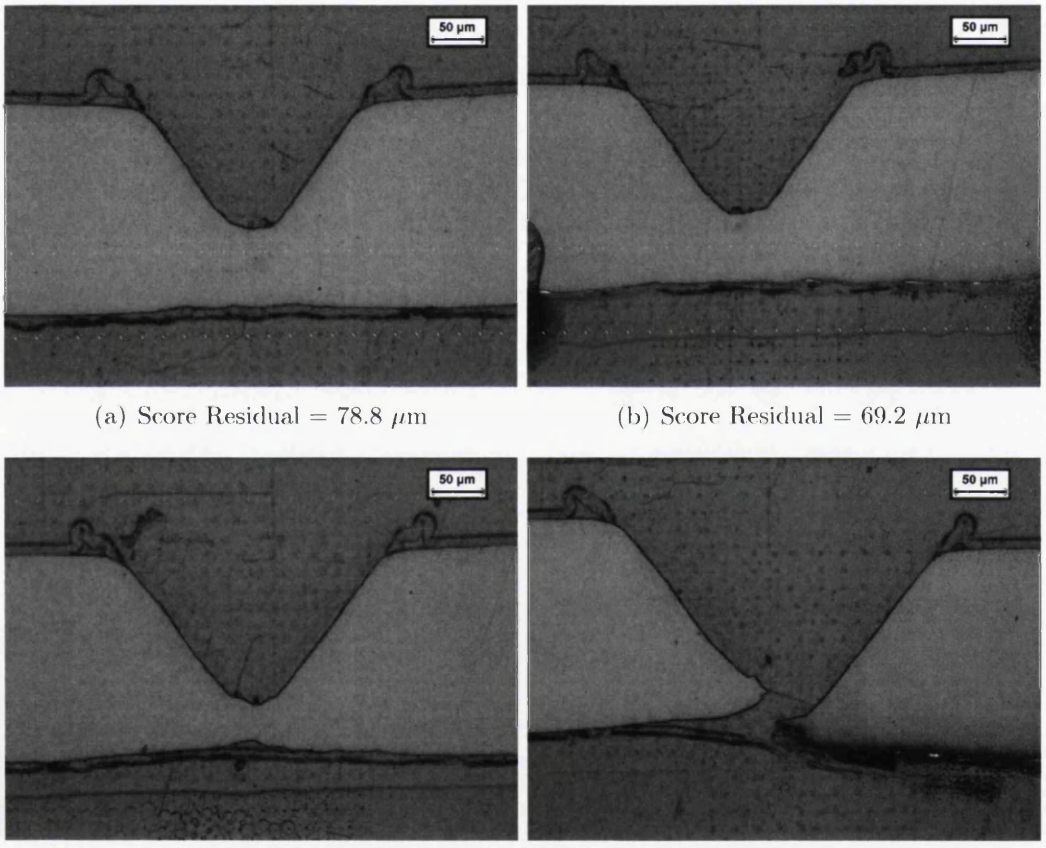

(a) Score Residual = 78.8 μm

(b) Score Residual = 69.2 μm

(c) Score Residual = 35.2 μm

(d) Score Residual = 23.3 μm

Figure 7.11: Void Analysis Images

[1] Identifer tag PL4 was meant to follow PL3, but was placed in front due to an error, this order was left as it was, so to avoid further confusion when arranging the data.

		Void Fraction	
Identifier	**Score Res**	**Middle**	**Edge**
PL1	78.8 μm	0.04	0.03
PL2	69.3 μm	0.02	0.04
PL4	35.2 μm	0.18	0.07
PL3	23.3 μm	0.19	0.1

Table 7.1: Void Fraction Progression

With physical results for void fraction against score residual now available, the fully coupled Lemaitre model could now be run in order to begin to make a comparison between the results. At this point however, parameters were not known, so it was decided as a starting point to use the last set of parameters that had run successfully and in the first instance plot those results against the void fraction measurements to see where those parameters where in relation to the measured results.

Exponent: s

It was known from [52], that some of the parameters would have to be within a certain range, for instance it was likely that the exponent s would have a value of around 1, this had been discussed and agreed with the project supervisors and was also justified by work completed by Pires [77].

Denominator: r

The denominator r controls the damage rate, i.e. how quickly damage grows after initiation, so the larger the number, the slower damage evolves. It was known again, from other work, such as [77], that for steel this figure would be around 11, but it was decided that in the first instance to play safe and set the denominator r to 50.

Plastic Threshold: *pt*

For TH550N, the value for plastic threshold is difficult to assess, to set an initial value means finding the UTS point on the materials engineering stress strain curve, then follow the elastic slope back to the X axis to give the corresponding strain value, this value can then be used as a start point for the plastic threshold. However, the engineering stress strain curve for TH550N is very flat, as the material has already been double reduced during its production, this makes pinpointing the UTS and subsequently the starting value for plastic threshold difficult, a value of 0.6 seemed reasonable and this was chosen.

Crack Closure: *h*

It's widely known that a reasonable value for Lemaitre's crack closure parameter was 0.2, evidence for this can be found in many papers throughout the literature and also in the books by Lemaitre [51, 52, 53] and more recently by De Sousa Neto et.al.[22].

Exp = s	**Den = r**	**Plastic Thres = pt**	**Crack Closure = h**
1	50	0.6	0
1	50	0.6	0.2

Table 7.2: Coupled Lemaitre - Starting Parameters

The first model was run with the parameters of table 7.2, with the results plotted on figure 7.12(b). It was quickly decided to add the crack closure parameter of 0.2 and the model was run again, these results are plotted in figure 7.12(c). The results showed that the initial values were a little off the mark, but as parameters s and h were close to proven values, it left parameters r and pt open to adjustment. Parameter r was known to be high, so it was decided that for the next step, it would be logical to see what the effect of lowering parameter r would do.

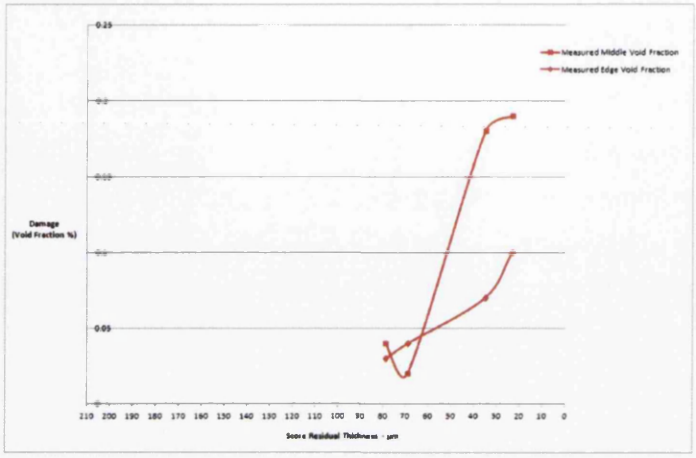

(a) Original Void Fraction Measurements

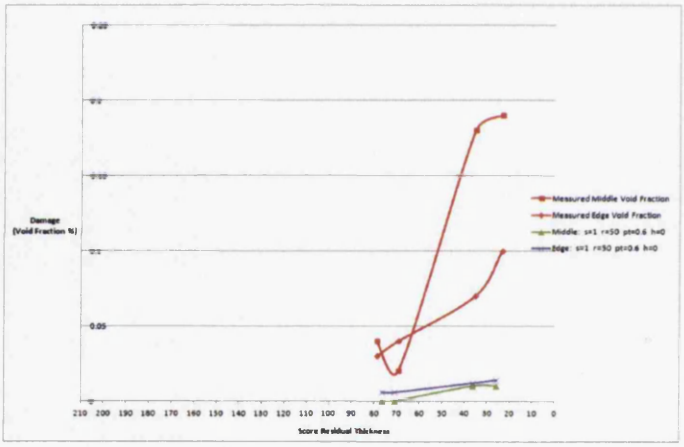

(b) Results for s=1 r=50 pt=0.6 h=0

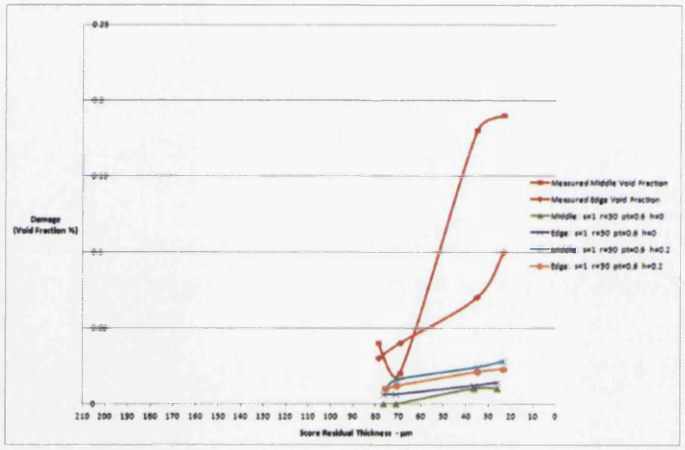

(c) Results for s=1 r=50 pt= 0.6 h=0.2

Figure 7.12: Void Measurements v Initial Parameters

Effect of Lowering r Parameter

Models were then run with parameter r being steadily lowered in value. Table 7.3 below shows the values of the parameters that were used.

Exp = s	Den = r	Plastic Thres = pt	Crack Closure = h
1	40	0.6	0.2
1	30	0.6	0.2
1	20	0.6	0.2
1	10	0.6	0.2
1	8	0.6	0.2
1	6	0.6	0.2

Table 7.3: Coupled Lemaitre - Lowering the r Parameter

The effects of lowering the r parameter can clearly be seen in figure 7.13. As r drops in value, the damage results begin to rise up into the domain of the void fraction measurements, at around $r = 6$ the results begin to rise above the threshold, a value of $r = 8$ was decided on as being the best fit.

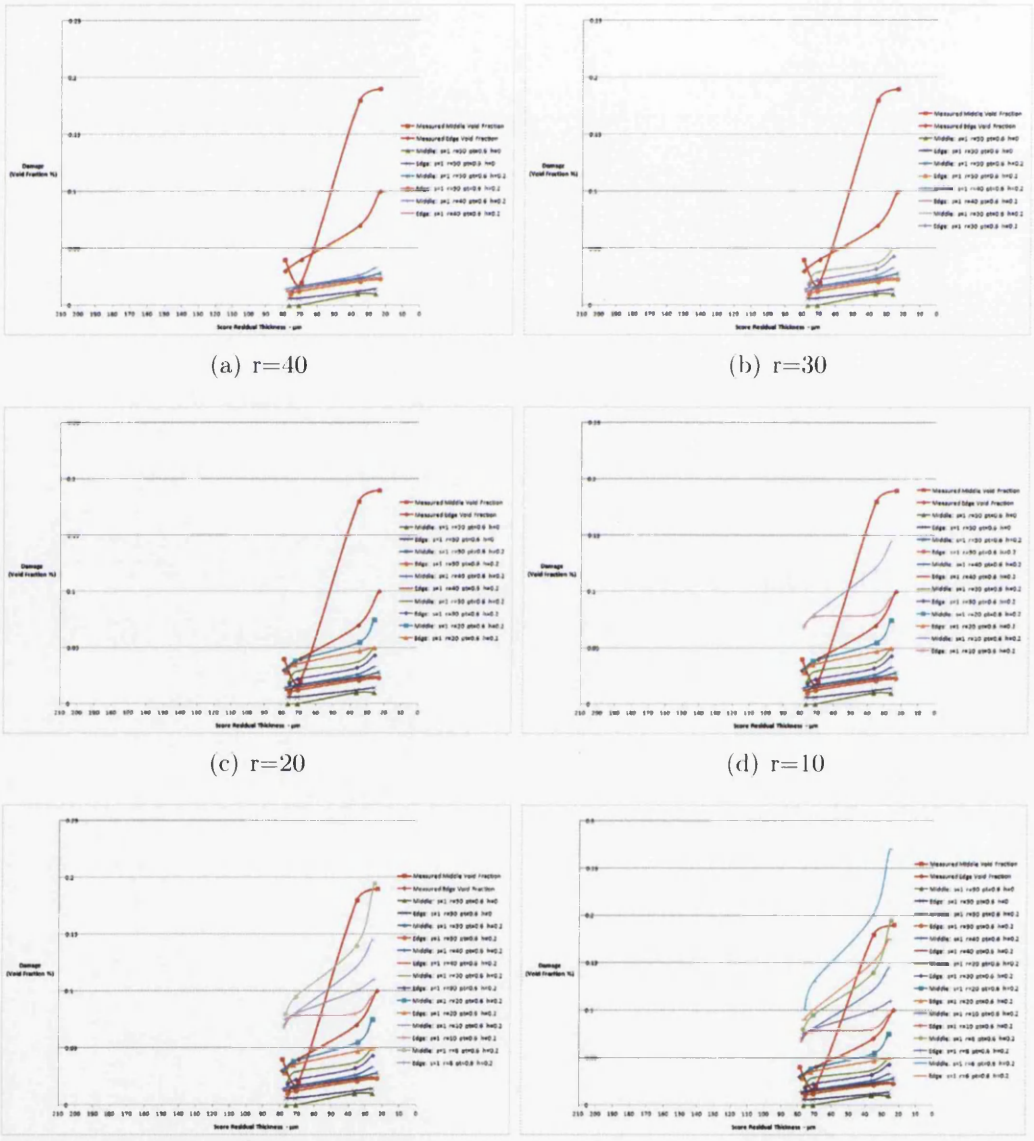

(a) r=40

(b) r=30

(c) r=20

(d) r=10

(e) r=8

(f) r=6

Figure 7.13: Effect of Lowering r Parameter

Effect of Raising Plastic Threshold Parameter

The next iteration saw the adjustment of the plastic threshold parameter *pt*. A number of models were run where *pt* was incrementally raised in value, table 7.4 below shows the values used.

Exp = s	**Den = r**	**Plastic Thres = pt**	**Crack Closure = h**
1	8	0.6	0.2
1	8	0.8	0.2
1	8	1	0.2
1	8	1.2	0.2
1	8	1.4	0.2
1	8	1.1	0.2

Table 7.4: Coupled Lemaitre - Raising the Plastic Threshold *pt*

The effect of increasing the plastic threshold parameter on the modelling results can clearly be seen in figure 7.14. At $pt = 0.6$ the results are in the domain of the measured results, but the fit seems too high, but as *pt* is raised, first to 0.8, then 1 and greater, the modelling results begin to match the measured results better and better, finally, the best fit seemed to be for $pt = 1.1$.

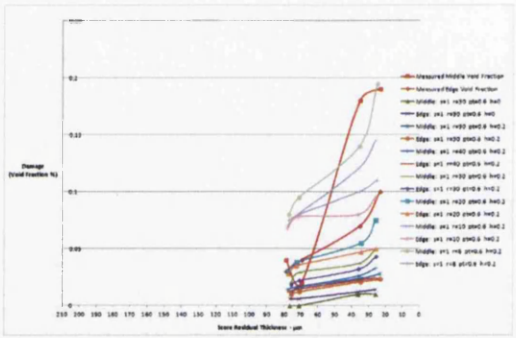

(a) pt=0.6

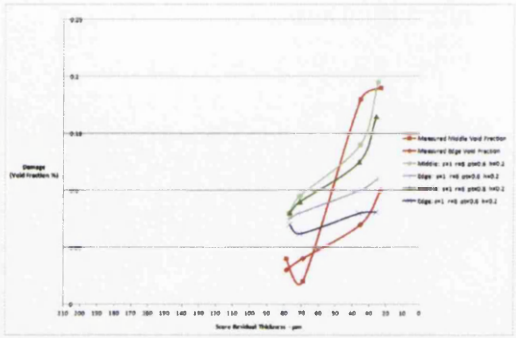

(b) pt=0.8

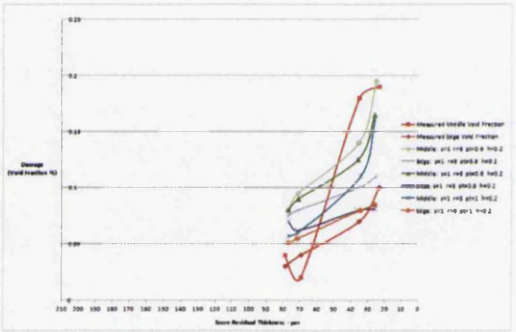

(c) pt=1

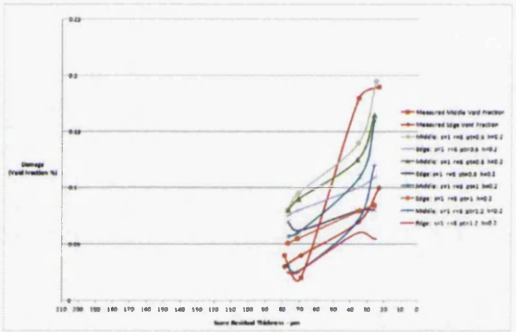

(d) pt=1.2

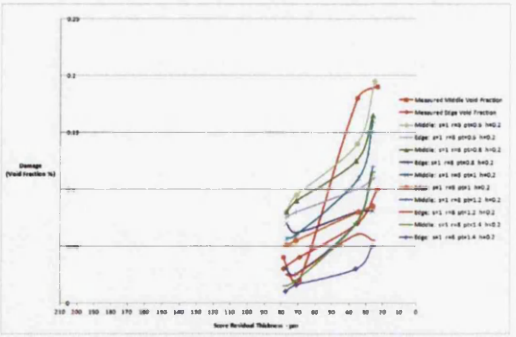

(e) pt=1.4

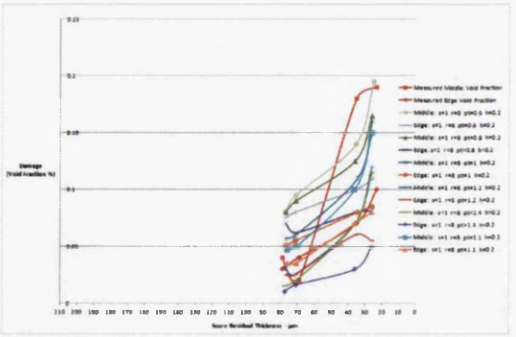

(f) pt=1.1

Figure 7.14: Effect of Raising Plastic Threshold from 0.6 to 1.4

Effect of Raising Crack Closure Parameter

Although the crack closure parameter h, was currently set to the suggested value of 0.2, engineering curiosity saw us increase the parameter to see what effect that would have, table 7.5 below details the values for h that were used.

Exp = s	**Den = r**	**Plastic Thres = pt**	**Crack Closure = h**
1	8	1.1	0.2
1	8	1.1	0.4
1	8	1.1	0.6
1	8	1.1	0.8

Table 7.5: Coupled Lemaitre - Raising the Crack Closure Parameter h

Figure 7.15, shows immediately what the effects of increasing parameter h has on the modelling results, almost instantaneously the modelling results begin to rise through the domain of the measured results, when h= 0.8, the results are already far to high. This result seems to confirm that 0.2, is, for steel at least, a reasonable starting point for the crack closure parameter h.

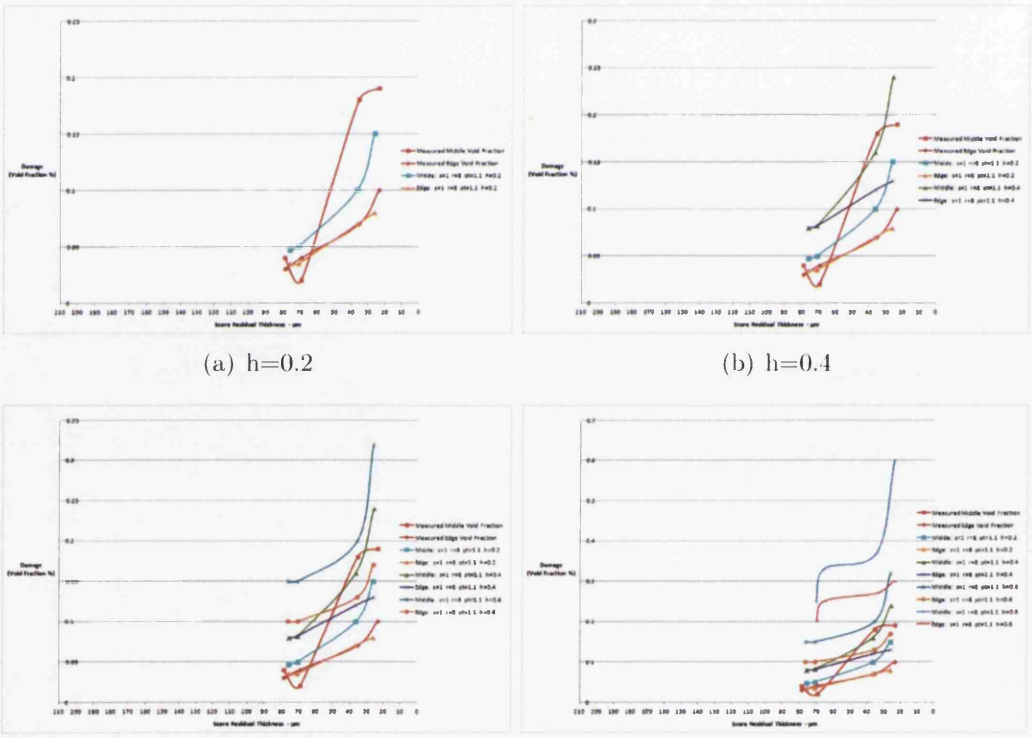

(a) h=0.2 (b) h=0.4

(c) h=0.6 (d) h=0.8

Figure 7.15: Crack Closure raised from 0.6 to 0.8

Effect of Lowering s Parameter

The final parameter left to *"play with"* so to say, was the exponent s, this was currently set to 1, as this value was in agreement with results by Pires [77], De Souza Neto [22], as well as Lemaitre [53]. Table 7.6 that follows shows the values of s that were trialled.

Exp = s	**Den = r**	**Plastic Thres = pt**	**Crack Closure = h**
1	8	1.1	0.2
0.8	8	1.1	0.2
0.4	8	1.1	0.2
0	8	1.1	0.2
-0.4	8	1.1	0.2
-0.8	8	1.1	0.2

Table 7.6: Coupled Lemaitre - Lowering the Exponent s

Again, figure 7.16 shows that it immediately became clear what happened when the exponent s was lowered in value. When $s = 0.8$, the fit improved, but as s reduced to even lower values, so the result domain rapidly increased above and beyond the domain of the measured results. From this trial it seemed that $s = 1$ was a good fit, but $s = 0.8$ was even better.

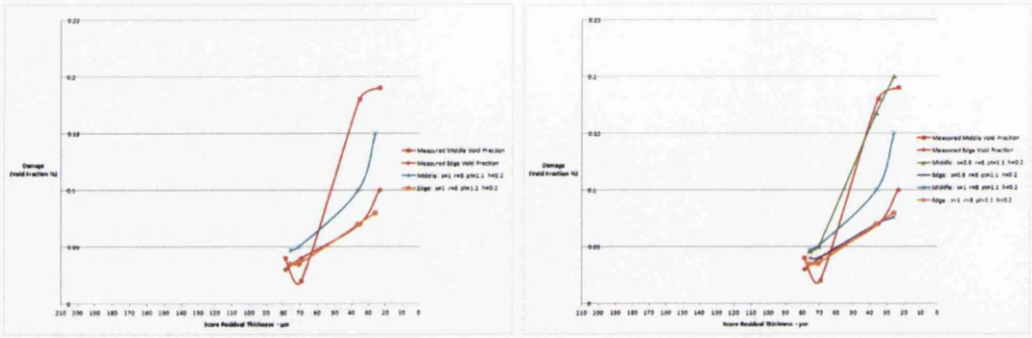

(a) s=1

(b) s=0.8

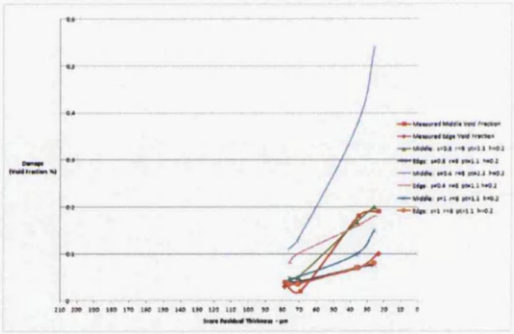

(c) s=0.4

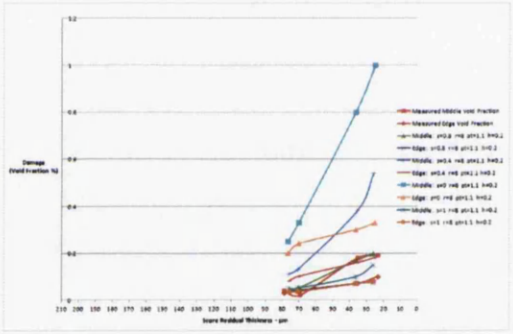

(d) s=0

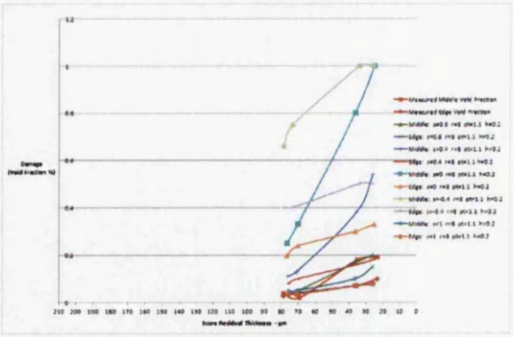

(e) s=-0.4

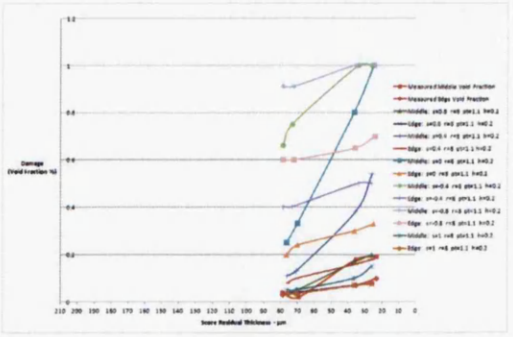

(f) s=-0.8

Figure 7.16: Exponent s Lowered from 1 to -0.8

Final Selected Parameters

Two sets of parameters for the fully coupled Lemaitre models were finally selected, these are shown in table 7.7 below;

Exp = s	**Den = r**	**Plastic Thres = pt**	**Crack Closure = h**
0.8	8	1.1	0.2
1	8	1.1	0.2

Table 7.7: Coupled Lemaitre - Final Parameters

Figure 7.17, on page 156, shows both parameter fits alongside the measured void fraction data, both fits seem reasonable, but $s = 0.8$ seems to be slightly better. Looking at the final value of the selected parameters, it seems that they are not to far away from values for steel found in the literature, similar values can be found in [77], for instance and also examples used in [22].

The technique used here to find the parameters seems to work, however, it is slightly subjective and better, more precise methods will require development as experience is gained, however, the technique used, definitely established the trends in the data, so this method does indeed show potential for establishing material parameters for computational modelling of scoring.

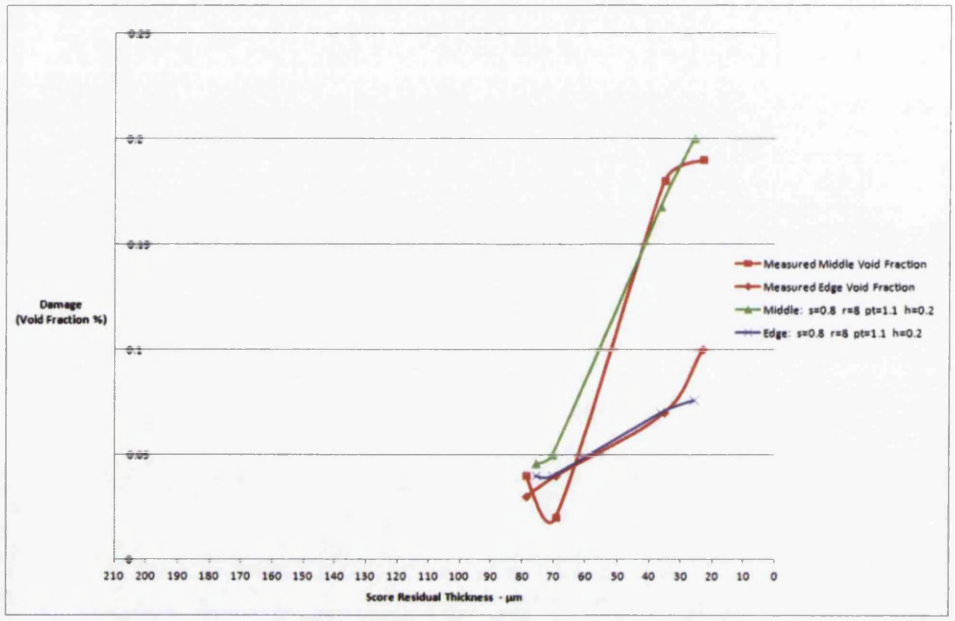

(a) Results for s=0.8 r=8 pt=1.1 h=0.2

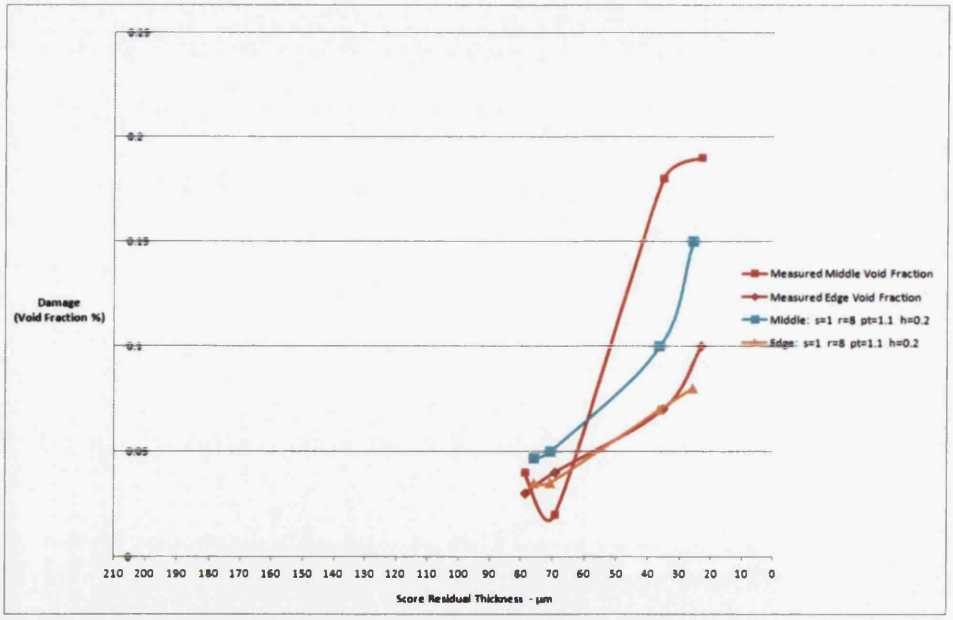

(b) Results for s=1 r=8 pt=1.1 h=0.2

Figure 7.17: Fully Coupled Lemaitre Model - Final Parameters

7.6 Comparative Analysis

Micrographic Images v Coupled Damage

Figure 7.18, that follows shows a comparison of the micrographic images against contour plots for damage progression taken at approximately the same score residual thickness. The score residuals of the comparison are given in table 7.8 below.

Micrograph	Score Residual	Contour Plot	Score Residual
PL1	78.8 μm	7.18(b)	78 μm
PL2	69.3 μm	7.18(d)	68 μm
PL4	35.2 μm	7.18(f)	36 μm
PL3	23.3 μm	7.18(h)	26 μm

Table 7.8: Micrographs v Coupled Damage Contour Plots

What can be seen clearly for all images, is that the contour plots capture the geometric changes accurately right the way through the score progression. It can be seen that the analysis picks up both the rounding of the material at the top of the score as well as the geometry around the tool tip. Additionally, it can also be seen that the analysis captures the start of necking in the TH550N material that begins quite late in the process, at around a score residual thickness of 35.2μm. This can be clearly be seen when comparing image 7.18(e) with contour plot 7.18(f).

Also important, is the location of damage, at 78μm damage is greater around the tip of the tool, and this location doesn't change as damage progresses to 68μm, however by 36μm it can be seen that the damage is beginning to progress to directly beneath the scoring tool and at 26μm the damage directly under the score tool is now strong, in fact in reality as can be seen from image 7.18(g), at 23.3μm the material has already failed and separated into two pieces.

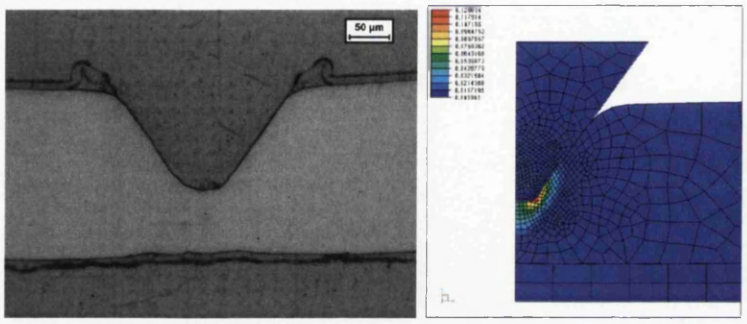

(a) Score Residual = 78.8 μm (b) Score Residual = 78 μm

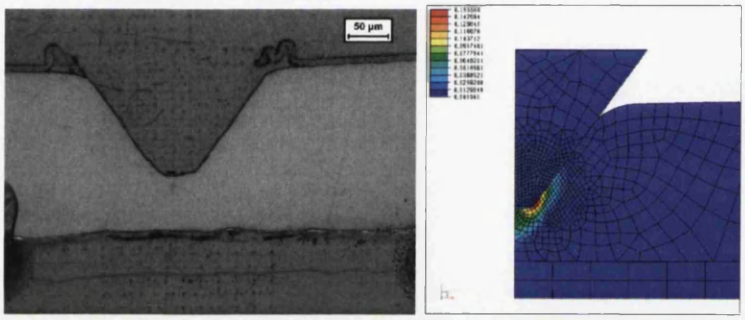

(c) Score Residual = 69.2 μm (d) Score Residual = 68 μm

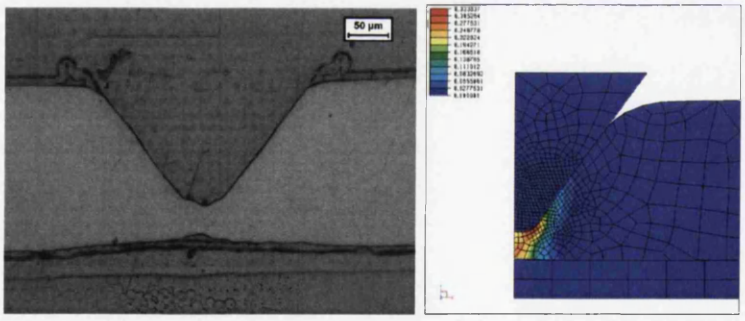

(e) Score Residual = 35.2 μm (f) Score Residual = 36 μm

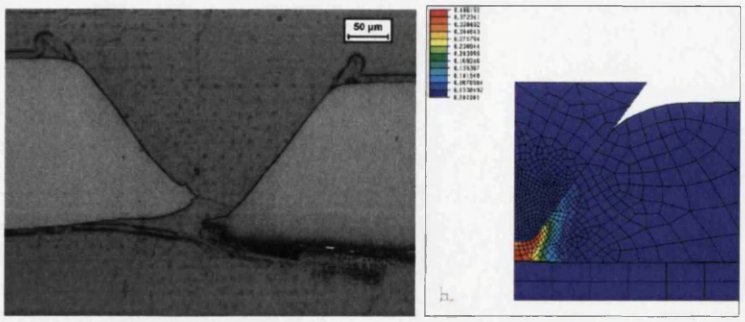

(g) Score Residual = 23.3 μm (h) Score Residual = 26 μm

Figure 7.18: Micrographic Images v Coupled Damage

Coupled Lemaitre s=0.8 v Coupled Lemaitre s=1

In the following figure 7.19, contour plots for the Coupled Lemaitre Model using the final sets of parameters shown in figure 7.17, and given again below, in table 7.9, are compared against each other.

Model	**Exp = s**	**Den = r**	**Plastic Thres = pt**	**Crack Closure = h**
L/H	0.8	8	1.1	0.2
R/H	1	8	1.1	0.2

Table 7.9: Coupled Model Parameters, s=0.8 v s=1

It can be see that for all score residual thickness, damage location is similar in both coupled models, but values are lower, however, this is to be expected as the only parameter to change is the damage exponent s, which measured 0.8 in the left-hand images, and 1 in the right-hand images.

In both models, the damage location tends to move from the tool tip, to below the tool, as the tool progresses into the material.

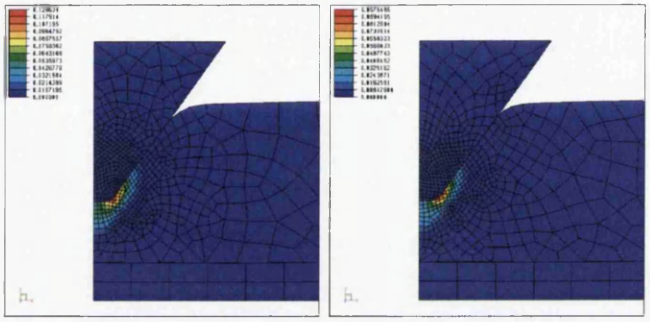

(a) SR = 78 μm: s=0.8 (b) SR = 78 μm: s=1

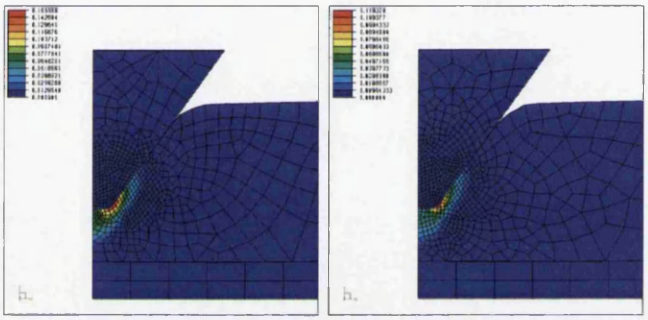

(c) SR = 68 μm s=0.8 (d) SR = 68 μm s=1

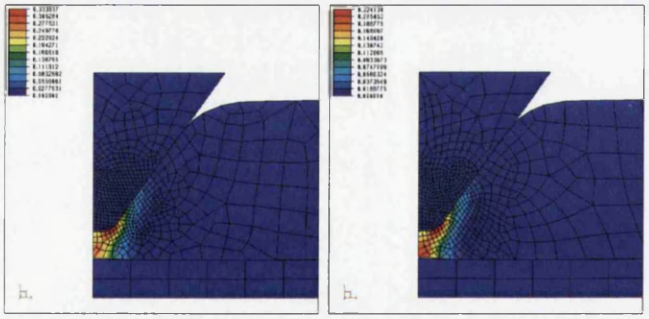

(e) SR = 36 μm s=0.8 (f) SR = 36 μm s=1

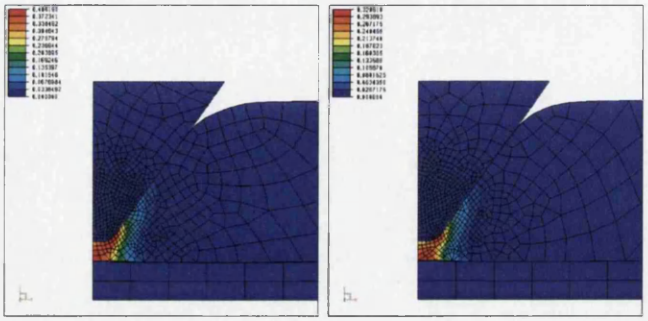

(g) SR = 26 μm s=0.8 (h) SR = 26 μm s=1

Figure 7.19: Coupled Lemaitre s=0.8 v Coupled Lemaitre s=1

Oyane v Coupled Lemaitre

This section compares outputs from the Uncoupled Oyane damage model, with the Coupled Lemaitre model. The Oyane model was run numerous times with its A parameter having values that varied from 0.5 to 1.
The following details the values used;

- A = 0.5 A = 0.6 A = 0.7 A = 0.8 A = 0.9
- A = 1.0 A = 1.1 A = 1.2 A = 1.3 A = 1.4

The contour plots generated from the analysis are shown in figure 7.20, what can be noticed, is at score residuals of 78μm, with A is set to 0.5, the highest damage location seems to settle around the tool tip, whereas, when A is set to 1.4 the location of the highest damage moves directly underneath the tool tip. Additionally, when A= 0.5, the level of damage is almost double the value of when A= 1.4, meaning that as the value of A increases, the level of damage reduces, this pattern is still the case at a score residual of 68μm. At 36μm, with $A = 0.5$, the Oyane model shows damage at the tool tip now beginning to move under the tool and link up, whereas, when $A = 1.4$, highest damage is located under the tool tip alone, finally at a score residual of 26μm, Oyane with $A = 0.5$ has linked the damage from the tool tip to the bottom of the material directly under the tool tip, and at $A = 1.4$, damage remains at the bottom of the material, directly below the score tool.

For Scoring, the Oyane damage model seem to show that lower values of A better predict the damage location, but the value of the damage is high, whereas higher levels of A show lower values for damage, but the location is incorrect. Further understanding of what is happening here can be gained when the results are compared with the graph of figure 7.7, and statement of section 7.2.

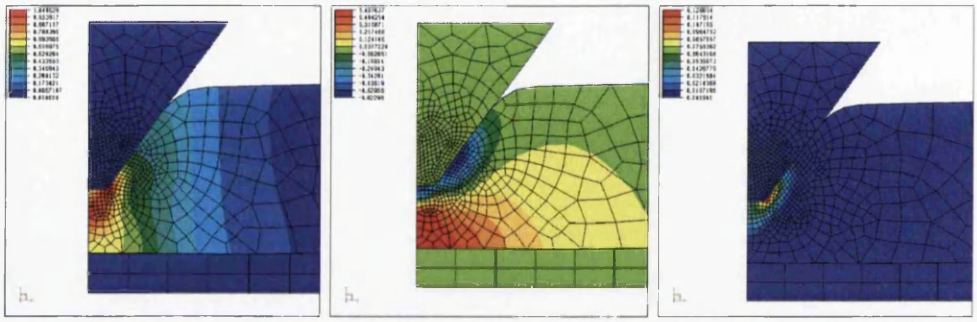

(a) A = 0.5 (b) A = 1.4 (c) SR = 78 μm: s=0.8

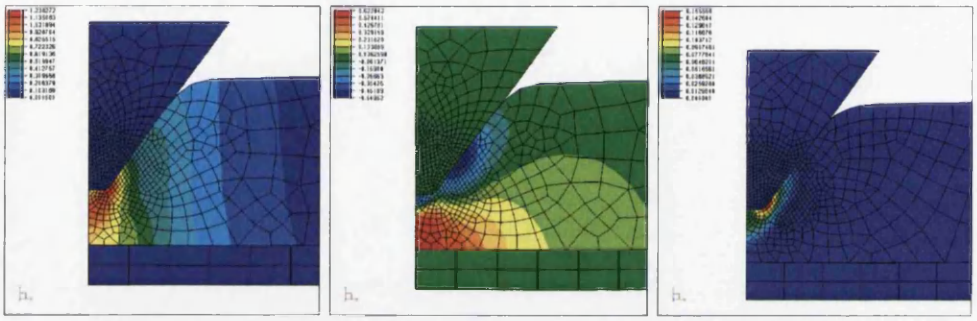

(d) A = 0.5 (e) A = 1.4 (f) SR = 68 μm: s=0.8

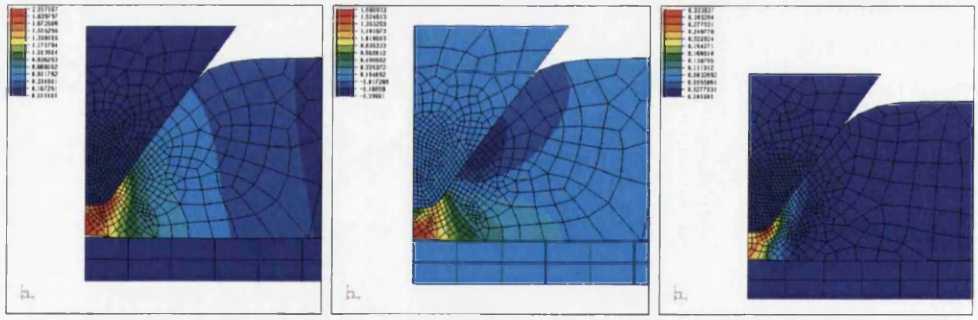

(g) A = 0.5 (h) A = 1.4 (i) SR = 36 μm: s=0.8

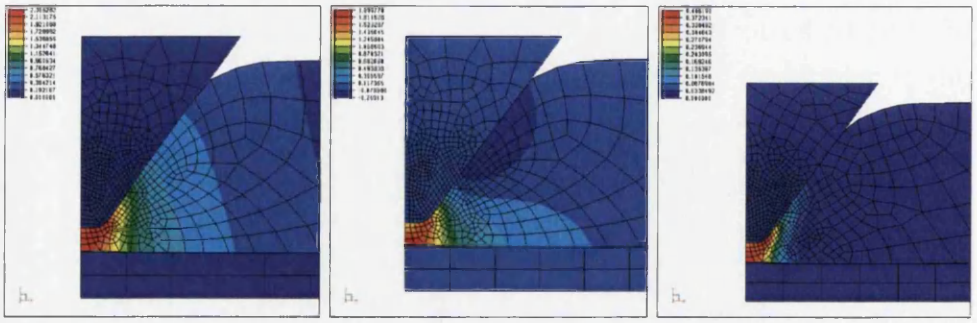

(j) A = 0.5 (k) A = 1.4 (l) SR = 26 μm: s=0.8

Figure 7.20: Oyane Damage v Coupled Lemaitre

Generalised Lemaitre v Coupled Lemaitre

The Generalised Lemaitre model shown in figure 7.21 was also run with varying values for exponent s, using values between 0.1 to 2.
The following details the values that were used;

- s = 0.1 s = 0.25 s = 0.5 s = 0.75
- s = 1.0 s = 1.5 s = 2.0

At 78μm, with $s = 0.1$, the Uncoupled Generalised Lemaitre model seems to show damage that shows has some agreement with the Coupled Lemaitre position, but its value is too high. As s increases to 2, the damage location moves to the side of the tool and also increases in value. At all other score residual values i.e 68μm 36μm and 26μm, when $s = 0.1$, damage seems to show good position at the tip of the tool, but as previously, as s increases to 2, damage moves up onto the side of the tool and increases to much higher values.

It certainly seems that at low levels of the exponent s, damage appears in locations similar to the Coupled Lemaitre model, but the actual value for damage is lower.

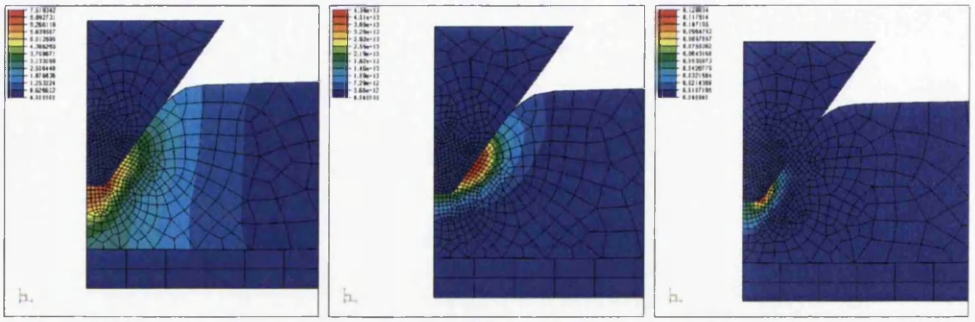

(a) So = 0.1 (b) So = 2 (c) SR = 78 μm: s=0.8

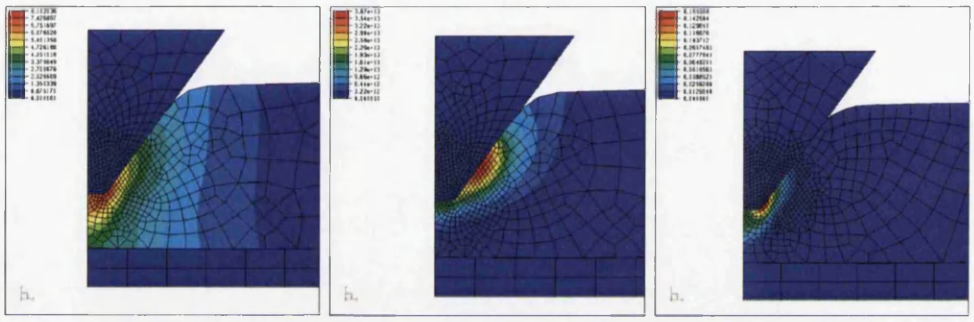

(d) So = 0.1 (e) So = 2 (f) SR = 68 μm: s=0.8

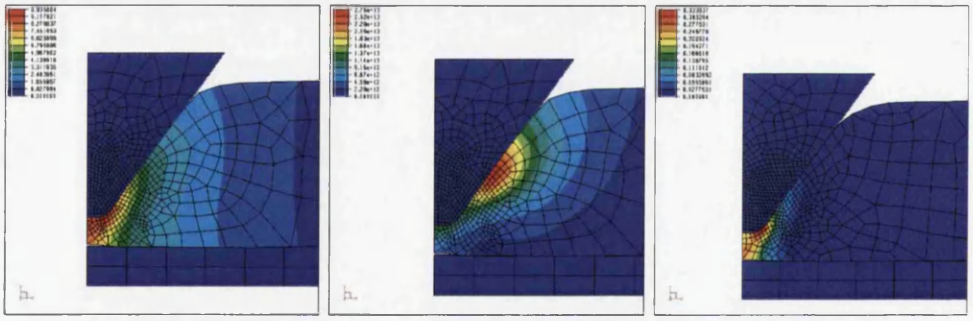

(g) So = 0.1 (h) So = 2 (i) SR = 36 μm: s=0.8

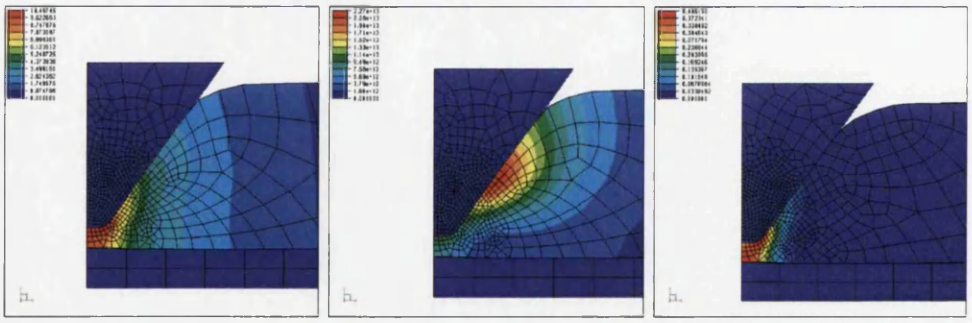

(j) So = 0.1 (k) So = 2 (l) SR = 26 μm: s=0.8

Figure 7.21: Generalised Lemaitre v Coupled Lemaitre

Rice and Tracy v Coupled Lemaitre

The Uncoupled Rice and Tracy damage model, of figure 7.22, does not have any parameters that can be changed with the FE analysis, so with regards to the output, you have no control over what you get out.

That said, the following images show that in actual fact the Rice and Tracy model isn't too far away with its predictions of damage location and damage value, which seems to be just over double the amount that the Coupled Lemaitre model predicts. This trend stays the same throughout all the score residual thicknesses, and overall counts as a positive result.

It may prove that if some type of scaling factor could be applied to this model, its ability to predict damage in scoring might be improved and made more accurate.

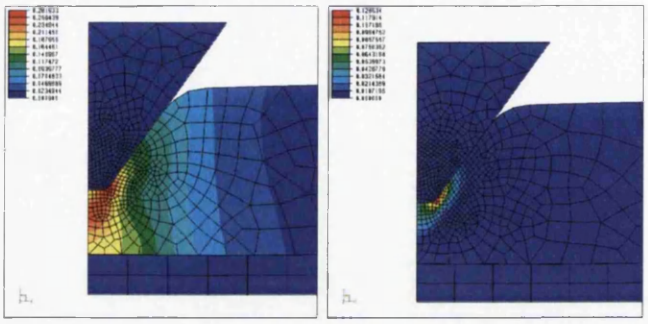

(a) SC = 78.4 μm (b) SR = 78 μm: s=0.8

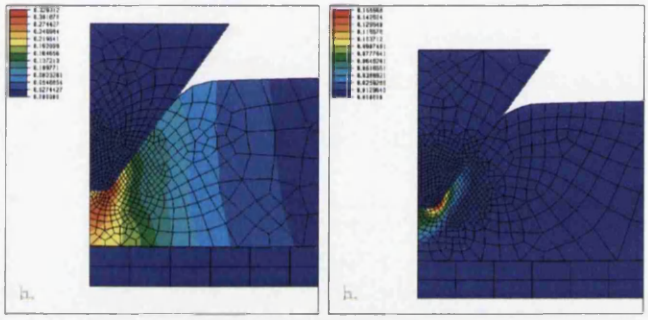

(c) SC = 68 μm (d) SR = 68 μm: s=0.8

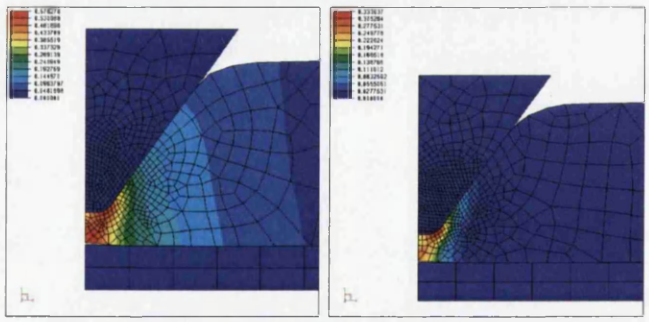

(e) SC = 36.3 μm (f) SR = 36 μm: s=0.8

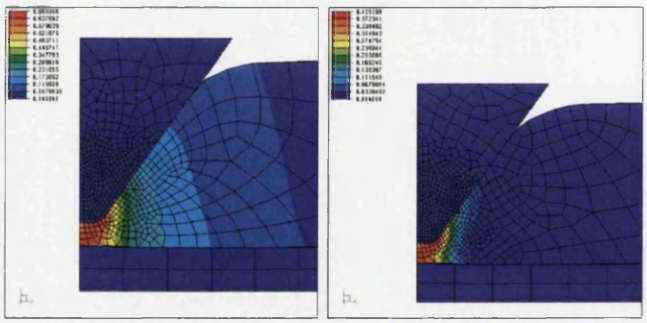

(g) SC = 25.9 μm (h) SR = 26 μm: s=0.8

Figure 7.22: Rice & Tracy v Coupled Lemaitre

Uncoupled Lemaitre v Coupled Lemaitre

As with the Rice and Tracy model described previously, results for the Uncoupled Lemaitre damage model, shown in figure 7.23, also do not have any parameters that can be altered in the FE analysis, giving again, no influence over the output.

For this comparison, the value of the Uncoupled Lemaitre damage seems to be a lot higher than the Coupled model, additionally, the damage seems to be spread over a larger area including the side of the tool.

Finally, as the score residual thickness decreases from 78μm down to 26μm, in the Uncoupled Lemaitre model, damage actually decreases in value, whereas in the Coupled model, damage increases.

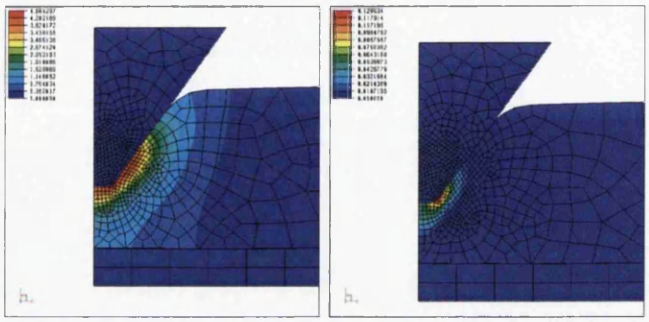

(a) SC = 78.4 μm (b) SR = 78 μm: s=0.8

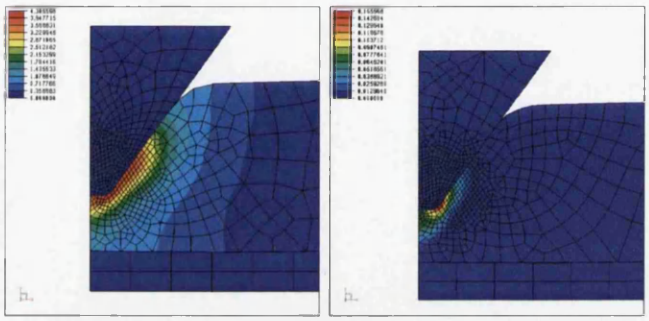

(c) SC = 68 μm (d) SR = 68 μm s=0.8

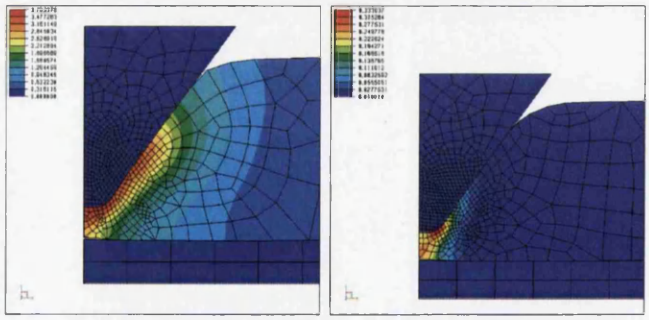

(e) SC = 36.3 μm (f) SR = 36 μm s=0.8

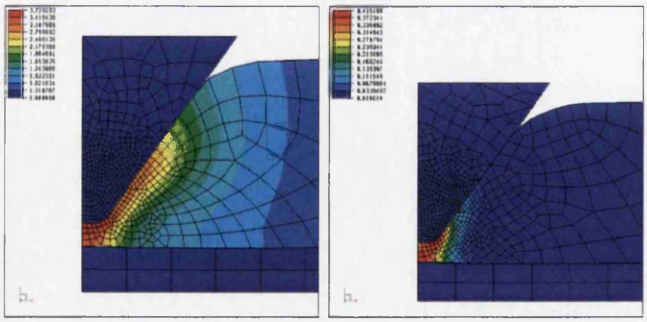

(g) SC = 25.9 μm (h) SR = 26 μm s=0.8

Figure 7.23: Uncoupled Lemaitre v Coupled Lemaitre

Uncoupled Strain v Coupled Strain

As expected, there is very little differences in the strain values, when the uncoupled model and the coupled model are directly compared. The effective strain plots show slightly higher values for the coupled model, so some localisation of strains as the material begins to soften.

Most probably, the apparent localisation is most likely to be caused by the pt parameter.

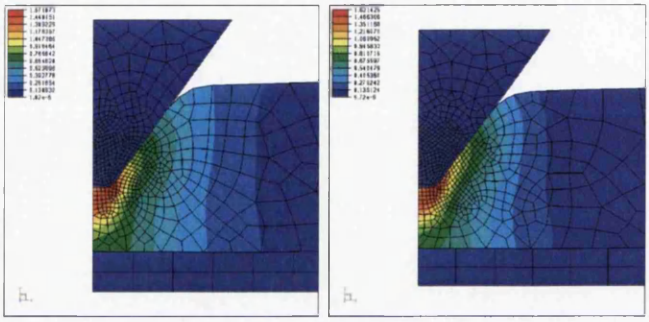

(a) SC = 78.4 μm (b) SR = 78 μm

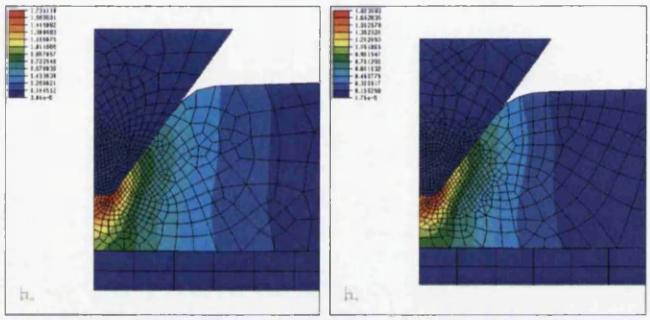

(c) SC = 68 μm (d) SR = 68 μm

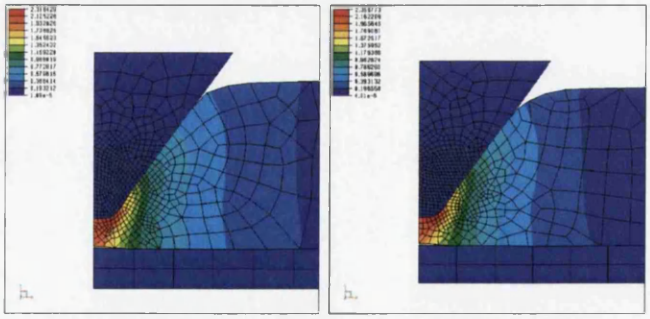

(e) SC = 36.3 μm (f) SR = 36 μm

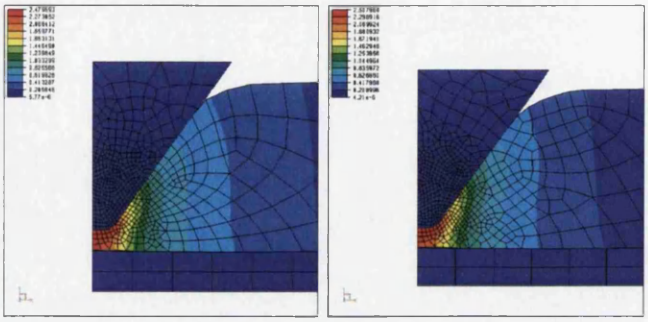

(g) SC = 25.9 μm (h) SR = 26 μm

Figure 7.24: Uncoupled Effective Strain v Coupled Effective Strain

Uncoupled Stress v Coupled Stress

At a score residual of 78μm, the stress in the uncoupled model is slightly lower than the coupled model, this ratio remains around the same level as the score residual decreases to 68μm, but here he gap between models has closed slightly, which is most likely due to the material starting to soften in the coupled model.

As was expected, by the time the score residual reaches a thickness of 36μm, the stress in the coupled model is now much lower than the uncoupled model, which is a clear sign of the response to material softening in the coupled model.

Finally, at a score residual depth of around 26μm, the stress in the coupled model is much lower that the level in the uncoupled model, again a clear sign of the material softening response in the coupled model.

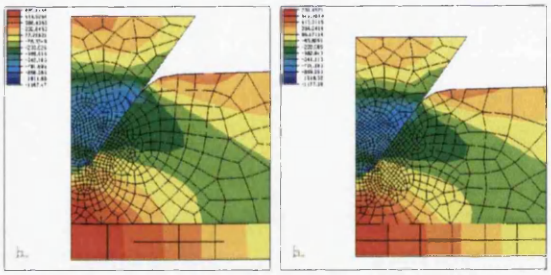

(a) SC = 78.4 μm (b) SR = 78 μm

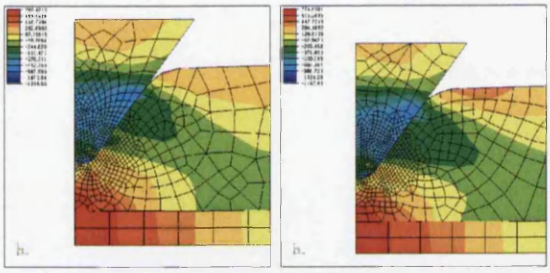

(c) SC = 68 μm (d) SR = 68 μm

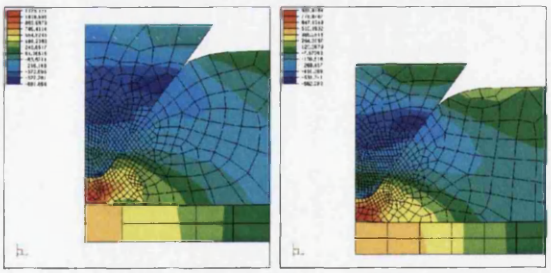

(e) SC = 36.3 μm (f) SR = 36 μm

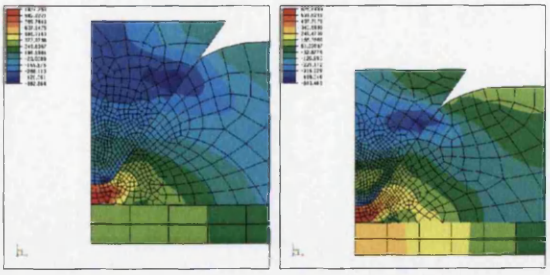

(g) SC = 25.9 μm (h) SR = 26 μm

Figure 7.25: Stress XX

Uncoupled Triaxiality v Coupled Triaxiality

With the triaxiality results , it was expected that both models should show near identical or very similar results, and this is exactly what the following contour plots, figs 7.26,7.27,7.28 and 7.29 show for each score residual thickness.

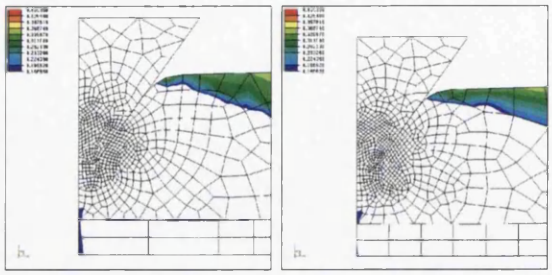

(a) Uniaxial Tension = 0.3333 (b) SR = 78 μm

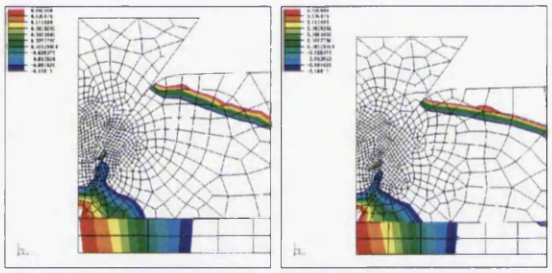

(c) Shear Pure = 0 (d) SR = 78 μm

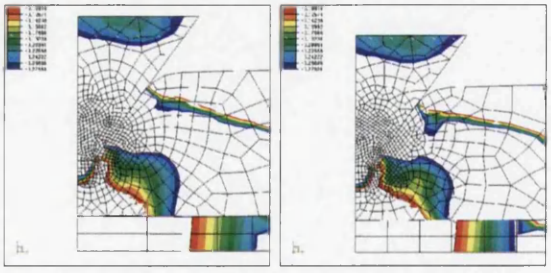

(e) Shear NU = -0.2182 (f) SR = 78 μm

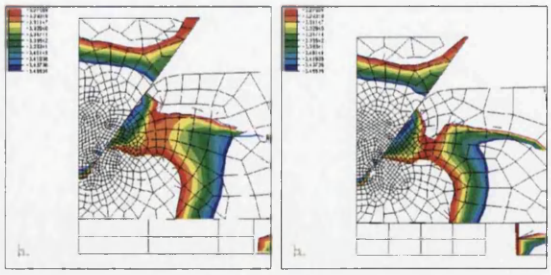

(g) Uniaxial Comp = -0.3328 (h) SR = 78 μm

Figure 7.26: PL1 - Triaxiality : with Score Residual at 78.4 μm

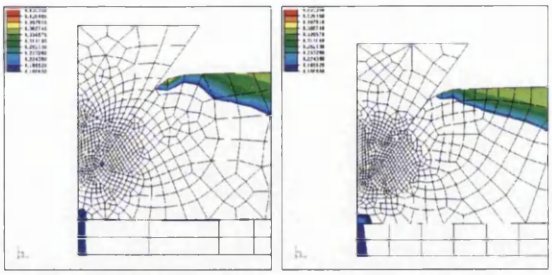

(a) Uniaxial Tension = 0.3333 (b) SR = 68 μm

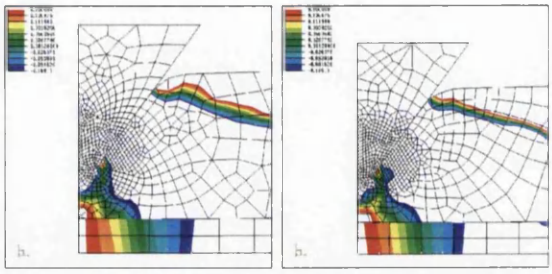

(c) Shear Pure = 0 (d) SR = 68 μm

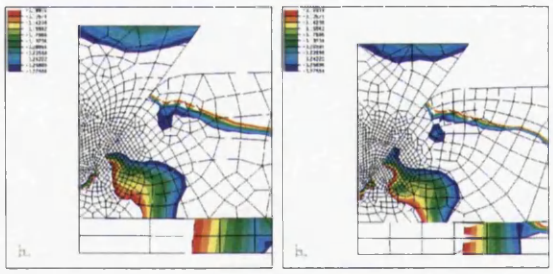

(e) Shear NU = -0.2182 (f) SR = 68 μm

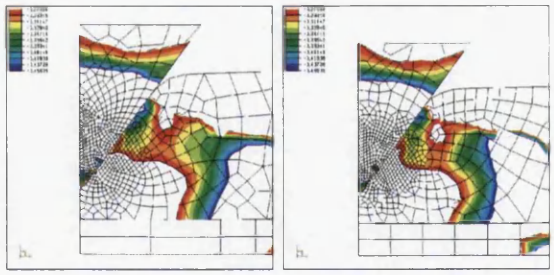

(g) Uniaxial Comp = -0.3328 (h) SR = 68 μm

Figure 7.27: PL2 - Triaxiality : with Score Residual at 68 μm

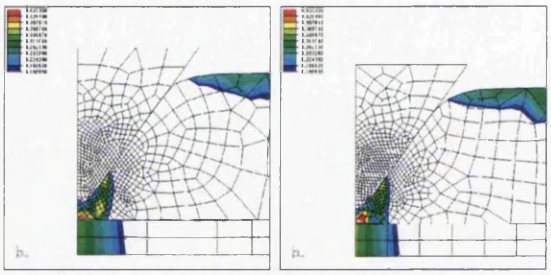

(a) Uniaxial Tension = 0.3333 (b) SR = 36 μm

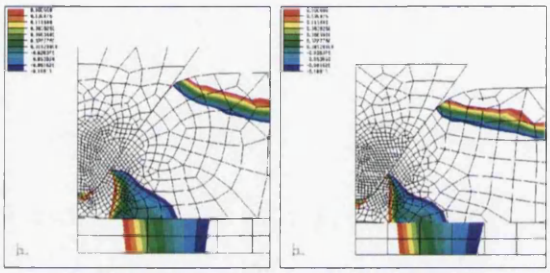

(c) Shear Pure = 0 (d) SR = 36 μm

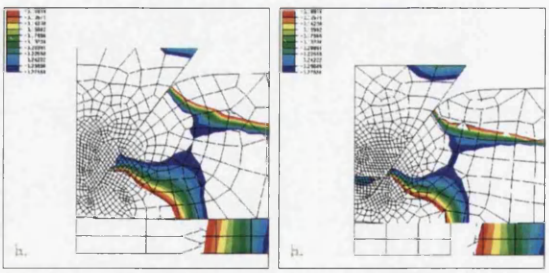

(e) Shear NU = -0.2182 (f) SR = 36 μm

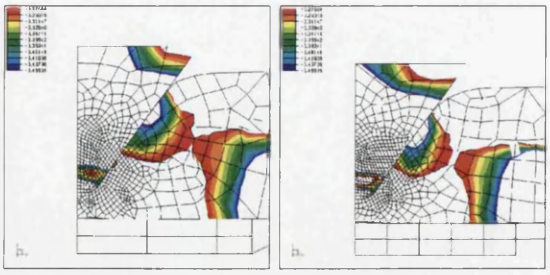

(g) Uniaxial Comp = -0.3328 (h) SR = 36 μm

Figure 7.28: PL4 - Triaxiality : with Score Residual at 36.3 μm

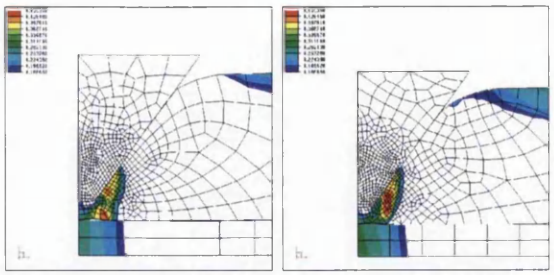

(a) Uniaxial Tension = 0.3333 (b) SR = 26 μm

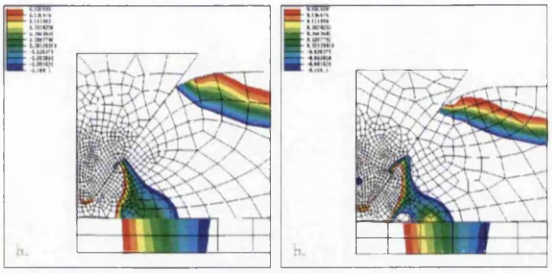

(c) Shear Pure = 0 (d) SR = 26 μm

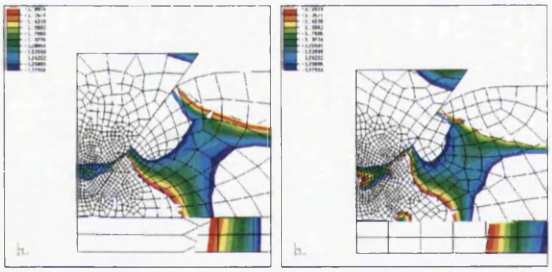

(e) Shear NU = -0.2182 (f) SR = 26 μm

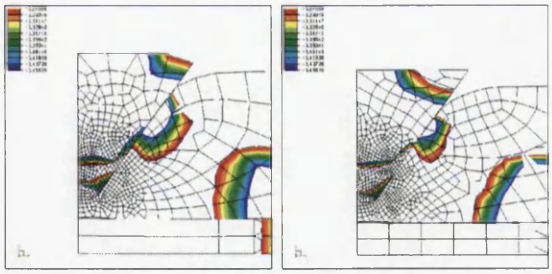

(g) Uniaxial Comp = -0.3328 (h) SR = 26 μm

Figure 7.29: PL3 - Triaxiality : with Score Residual at 25.9 μm

Chapter 8

Conclusions

The project began, with the belief that it was possible to develop a complete computational model to simulate the opening of a FAEOE over the projects four year duration, with an aim to verify the modeling through the testing, however, it was soon realised that no comprehensive data set existed, which could be used to verify the modelling, so, in the first instance, establishing a full set of reliable and consistent data, had to become the priority.

After researching the previous work on scoring of FAEOE's, it became apparent that opening an FAEOE was a product of the combination of all the fracture modes, i.e. a truly mixed mode process, so, before the problem as a whole could be addressed, each mode would have to dealt with individually. This approach had been initiated, see [9], but a comprehensive data set using current, modern packaging steel materials was still yet to be established.

Testing Methods for Mode I and III had been developed, but nothing existed for Mode II, in fact Mode II had not been researched at all, therefore, establishing a functional test to generate test results for Mode II became the priority.

After sample production and testing was completed, the project turned to developing a better understanding of implementing and using damage models within a commercial FE code, the first phase of the modelling was to develop a scoring model that accurately simulated the influence of damage through the scoring process, but, as the knowledge and understanding of damage modelling grew, so did the realisation that using the traditional method of establishing

damage parameters would not be an option due to the nature of the material i.e. very thin, 0.21mm, steel sheet, which meant that another method was required.

Establishing damage parameters for measured void analysis became the strategy that was followed, usually the focus for damage is for uniaxial or tension applications, here, damage models for multiple stress states where compared with experimental results. A working model for scoring was developed and verified, giving good comparisons to experimental results, however complete verification for full Mode II opening still remains open, as currently available models do not contain solutions for damage based crack initiation and propagation.

With a verified model for damage progression in scoring now available, the next step is to verify second stage opening for all Modes i.e. I, II and III, however, this will require the simulation of crack initiation and fracture, which in turn will require the implementation of a damage based fracture model.

8.1 Further Work

Mode I

As discussed in section 4.2, p54, the Mode I results remain valuable for further research, in that they can now be used to assist the development and validation of a 2D multistage numerical model.

Mode II

A fundamental difference found in the displacement results compared with the force results was that Factor B - Material, disappeared from the results, see section 4.3, p58, additionally, further numerical analysis may help to explain why interactions in the range 0.18 - 0.32, show a number of two way and three way interactions, p59.

The reasons behind these results are presently not fully understood, again here, further numerical analysis, may help provide an explanation along with the development and validation of a 2D multistage model..

Mode III

Again, as discussed in section 4.4, p63, the Mode III results also remain valuable, these can also be used further to help with development and validation, this time however, for a 3D multistage numerical model.

Mesh Splitting, Crack Simulation & Triaxiality in 3D

Although modelling of Mode I and II can begin quickly as these remain 2D models, Mode III will require a 3D analysis, and presently, problems remain with 3D meshing and crack simulation methods, in addition, triaxiality in 3D requires further development and verification to provide for a better understanding. Element removal and separation routines also require further development, such as those currently in development by Javani [34, 35] at Eindhoven.

Nitrogenised Steel Grades

Discussed in section 5.9, p78, nitrogenised grades are likely to contain very fine carbide-nitride particles that happen to arrange themselves in chains, it is suspected that the size and distribution of these particles will have an effect on damage evolution, which means that any damage modelling undertaken, should have the ability to capture these events.

Anisotropy

It is also known that damage shows a directional dependency or anisotropic behaviour, however it currently not clear if this anisotropy initiates from the material or whether the anisotropy actually comes from nature of damage itself, again additional work in this field is necessary, with some methods currently in development by Niazi [71, 72, 73] at Twente.

Rate Dependency

In section 5.10, p84, recommendations are made that future tests are completed at much higher rates, this is necessary in order to reveal any rate dependency. A fundamental question of whether rate dependent damage exists or if the response can be explained exclusively with the rate dependency of the material should also be carefully considered.

Influence of strain rate effects are as yet unknown, so efforts should be made to extend observations to higher rates in the future, additionally, temperature effects may also have to be considered at higher rates.

Improvement of Imaging Methods

Section 5.12, p86, shows that future work is necessary in order to look at dislocations in the material, current methods investigate materials on the meso or continuum scale, however, its most likely that damage first begins on the micro or nano scales, which means that the links between these multiscale events require a much better understanding than currently exists.

Future Observation of Damage

It is mentioned in section 7.5, p155, that methods of testing of scored cross-sections have now been established and that it is advised to observe damage evolution in-situ in the future on cross-sectioned specimens, also, both fully constrained and unconstrained samples should be tested until a relationship is established between the constraint conditions of the strip tests in comparison with circular ends. A wider specimen is recommended for future use, in order to achieve conditions as near to plane strain as possible at the centre of the sample.

Coupled Lemaitre Parameters

Two sets of parameters for the fully coupled Lemaitre model were finally selected, see section 7.5, p155.

It is proven that the technique used to find the parameters does produce results, however, it is slightly subjective, therefore, in future, better, more precise methods of identifying the parameters will require development as additional experience is gained.

Single Element Numerical Model

In the future, the single element model discussed in section 7.2, will require extension, this will help to provide additional verification of the coupled Lemaitre parameters.

Harmonic Pattern

For all Mode II results, when either displacement or force were plotted against the variable parameter, Gap, a harmonic pattern emerged, see figure 8.1.

Although, for this project, this trend was not investigated further, a future investigation into this phenomena may provide additional insight and possibly help with further optimisation of various parameters.

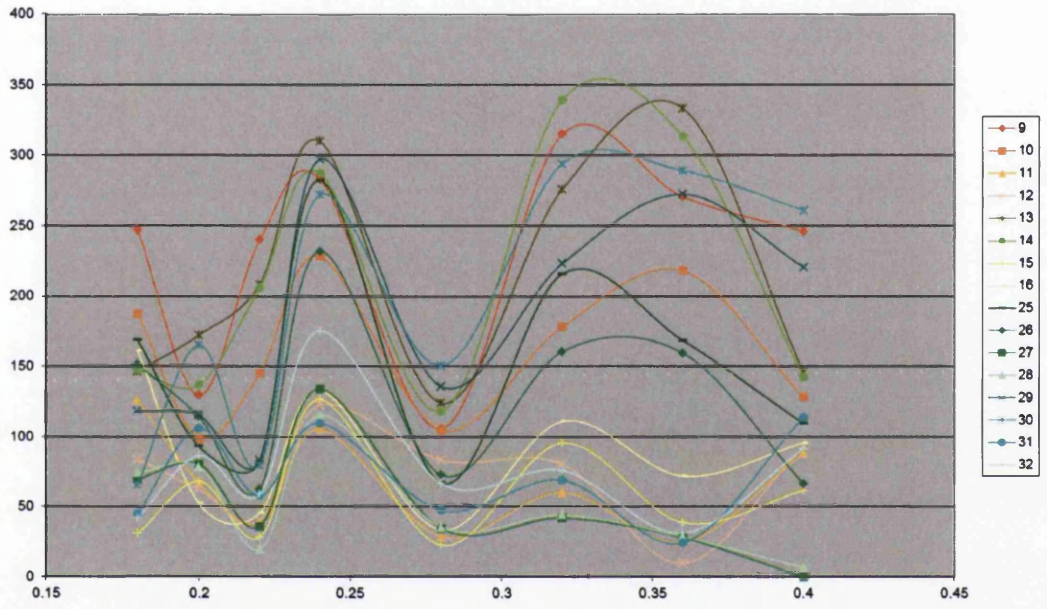

Figure 8.1: Typical Harmonic Pattern found in the Results

Appendix A

Tooling

A.1 Original Tram Rail Tooling

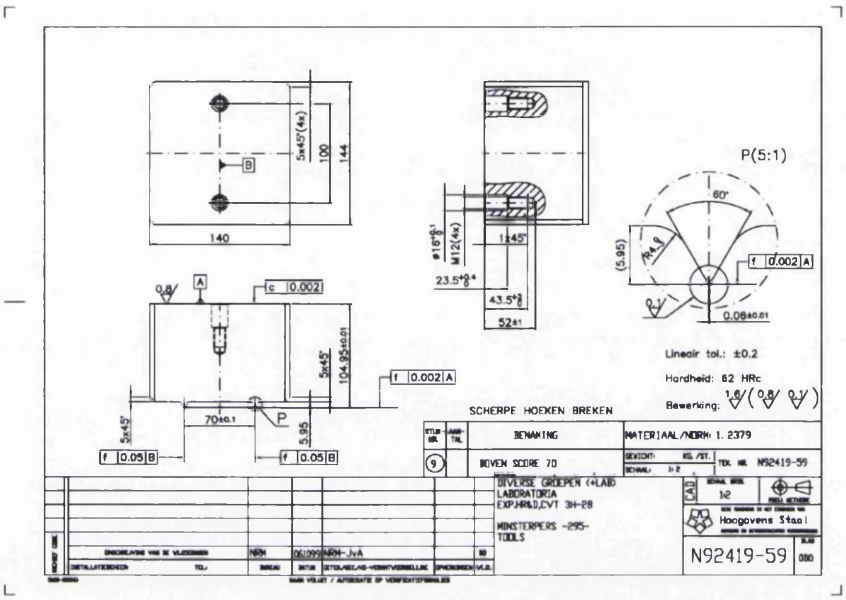

(a) Drg N92419-59 - Score 70

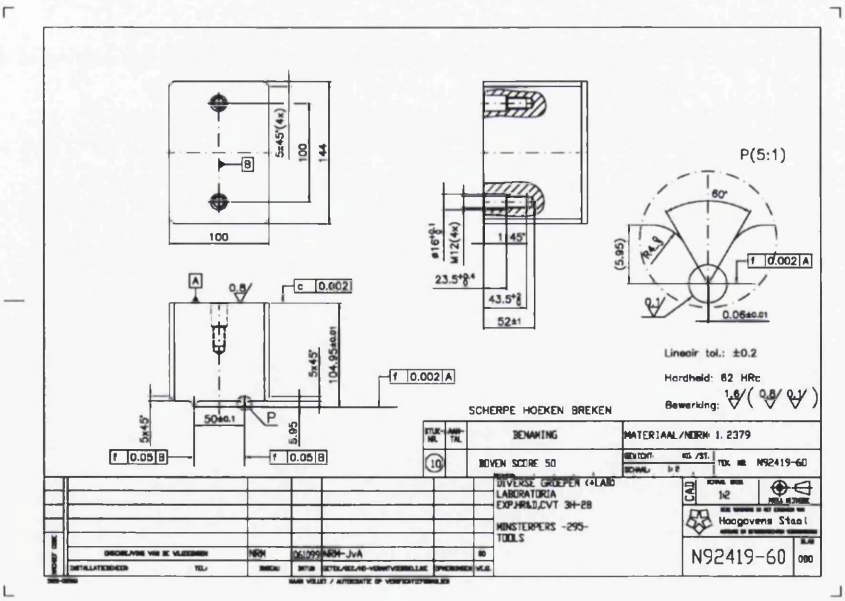

(b) Drg N92419-60 - Score 50

Figure A.1: Original Tram Rail Tooling

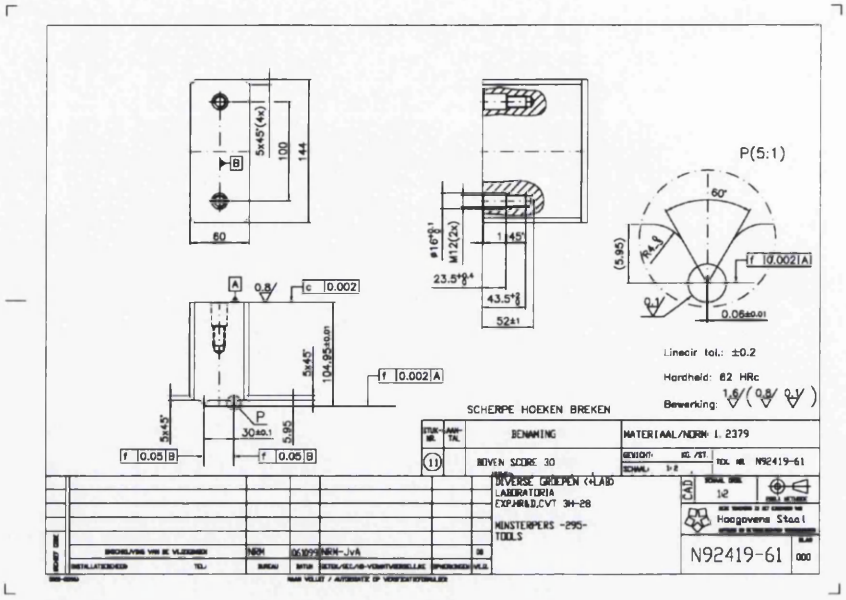

(a) Drg N92419-61 - Score 30

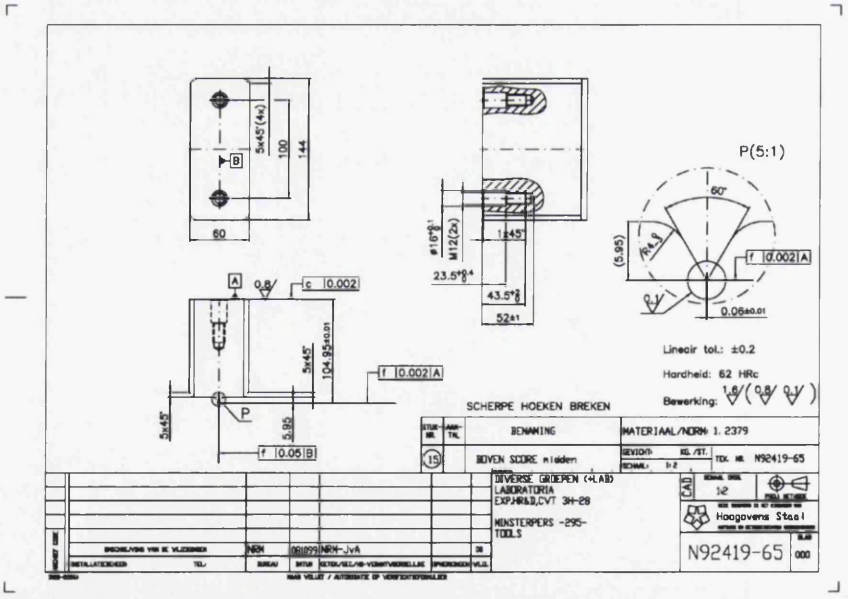

(b) Drg N92419-65 - Score Midden

Figure A.2: Original Tram Rail Tooling

A.2 New Tram Rail Tooling

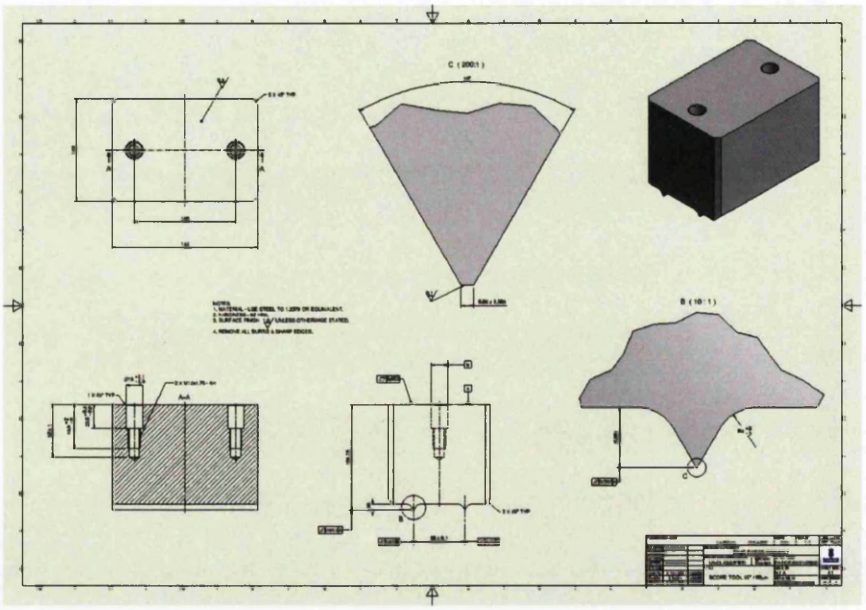

(a) 60°60μm Tool

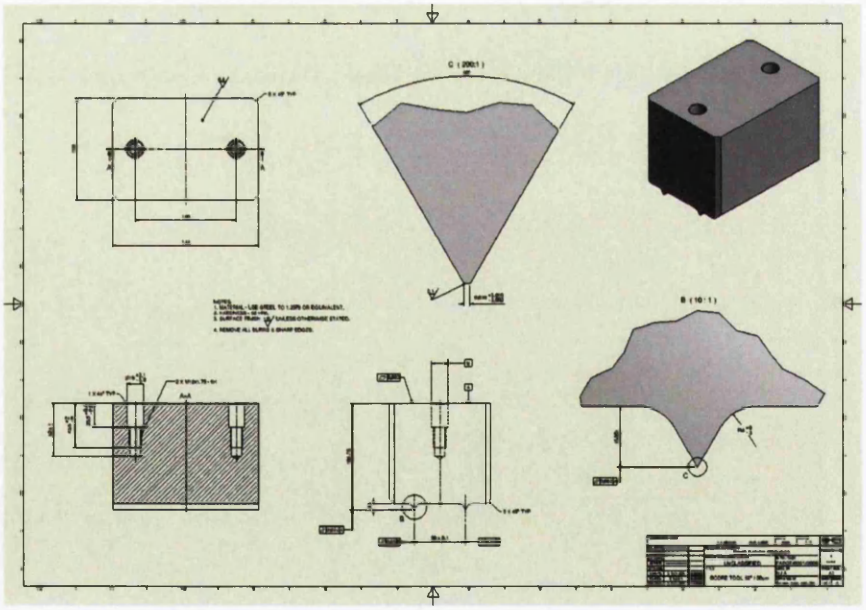

(b) 60°30μm Tool

Figure A.3: New 60°60μm and 60°30μm Tooling

A.3 Sample Holders

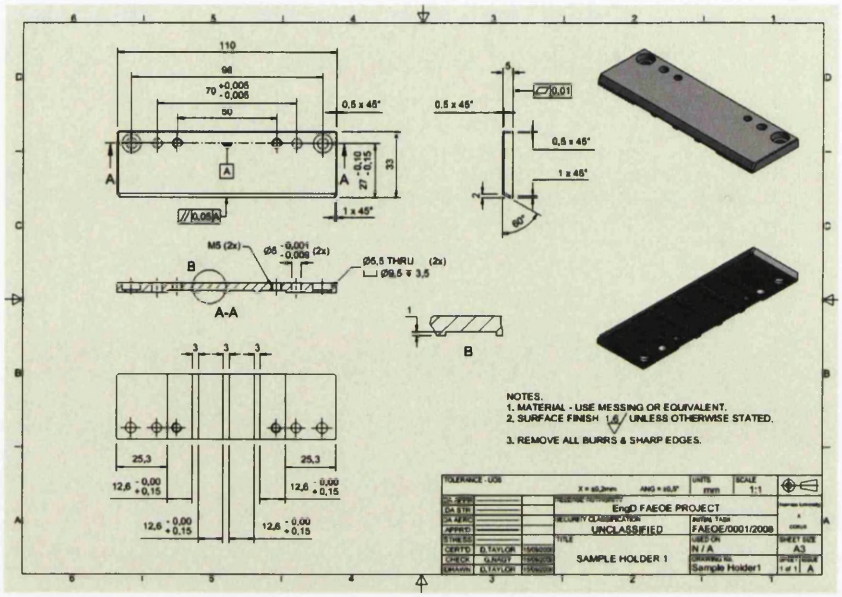

(a) RH Holder

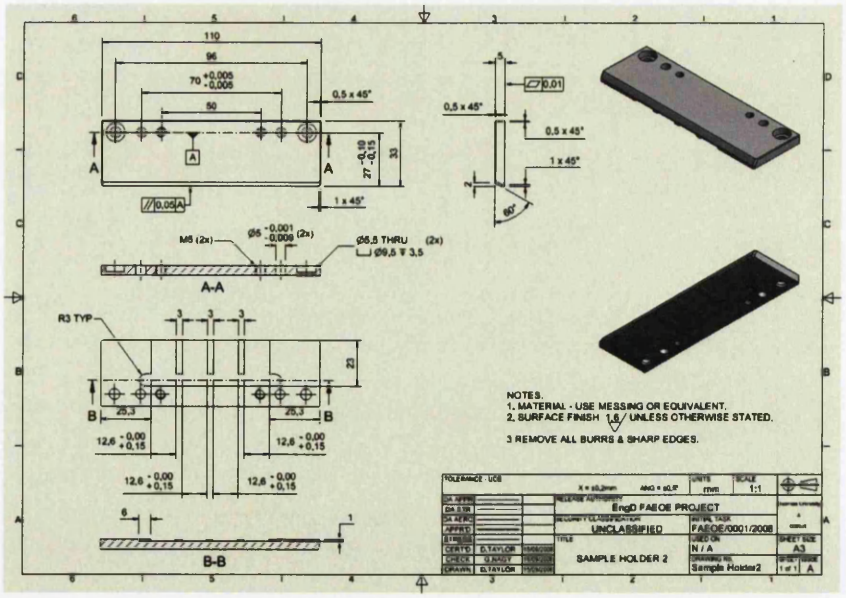

(b) LH Holder

Figure A.4: Production Drawings for Sample Holders

A.4 Mode II Tooling

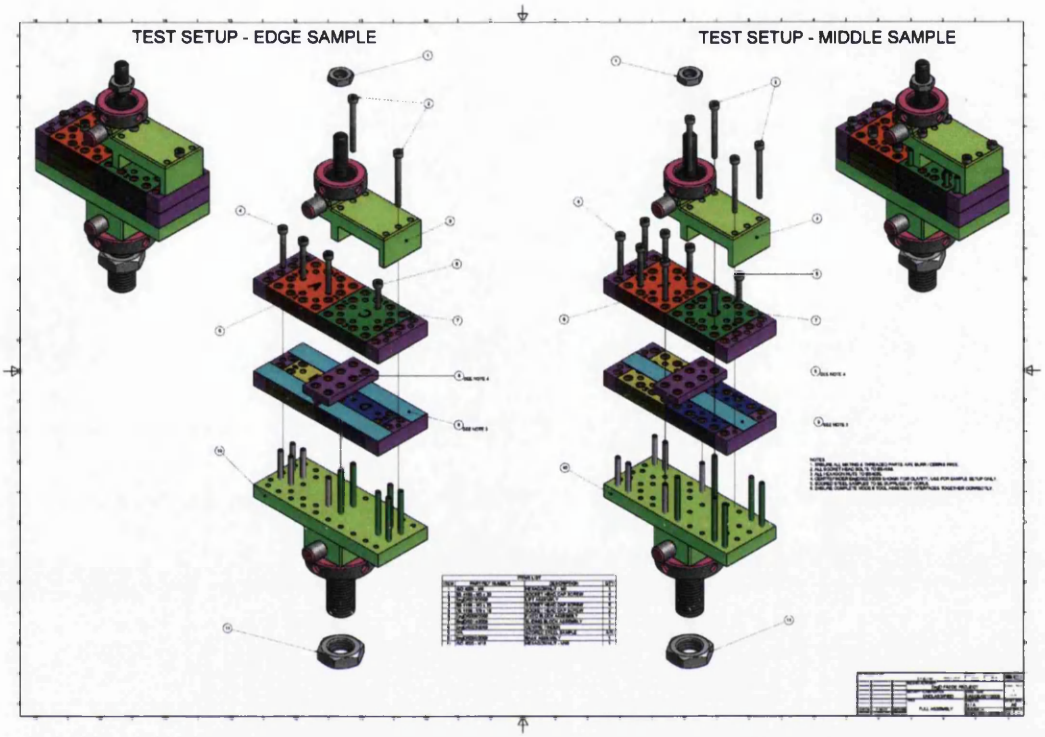

(a) Full Assembly - Sht 1

Figure A.5: Mode II Tooling Production Drawings

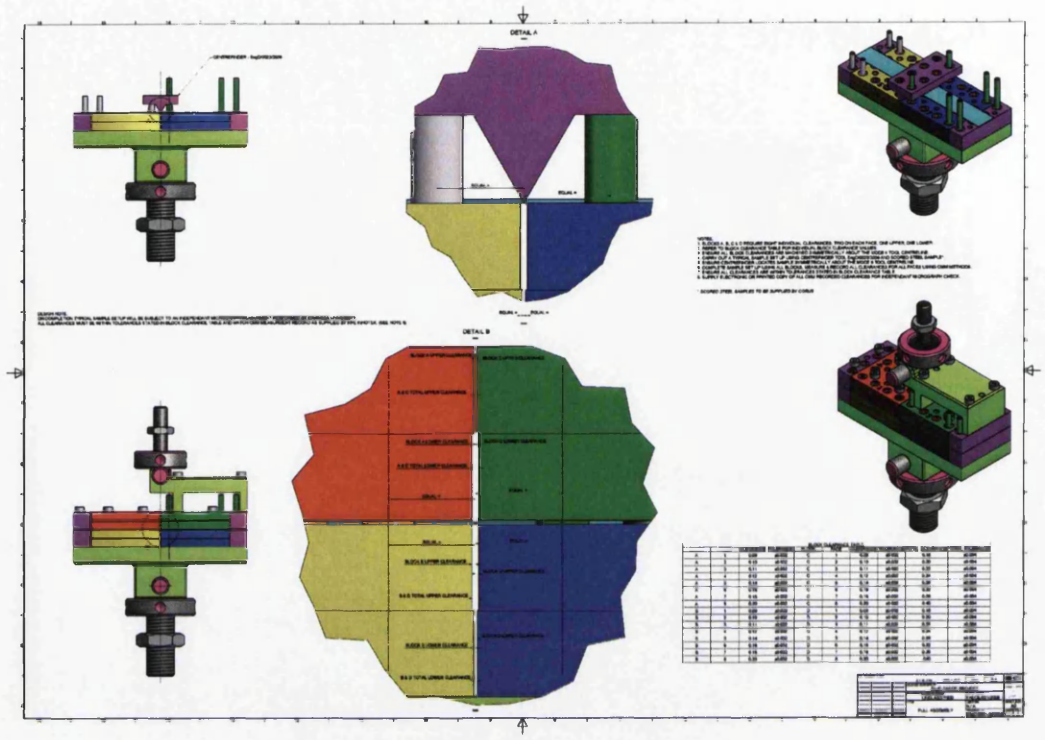

(a) Full Assembly - Sht 2

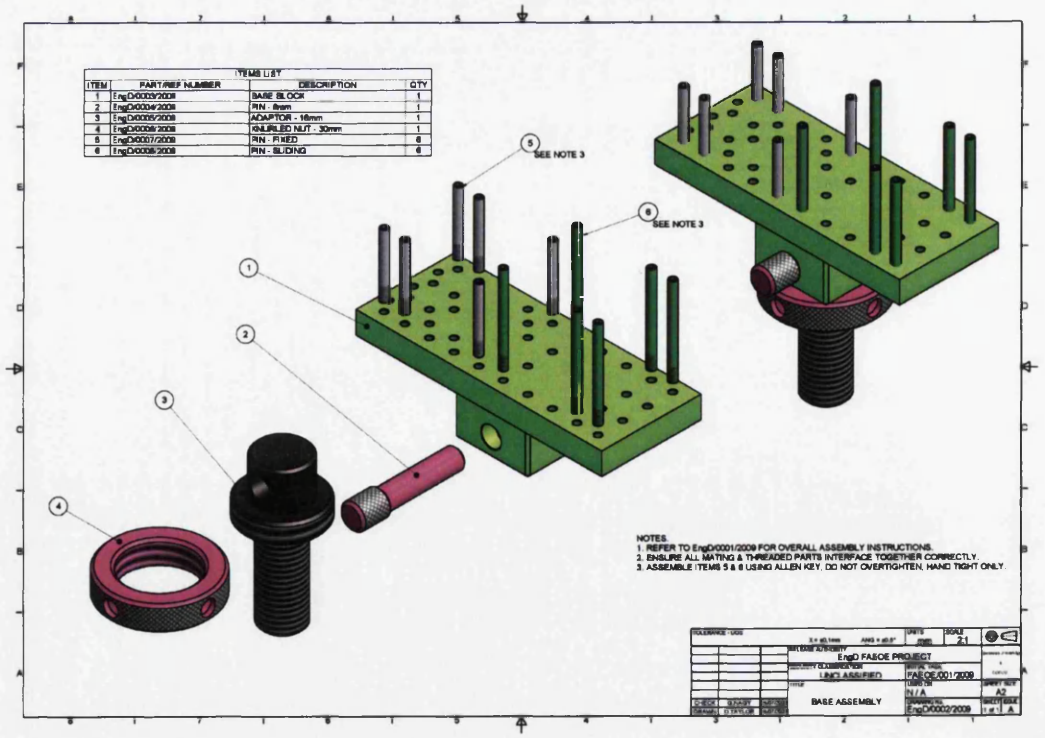

(b) Base Assembly

Figure A.6: Mode II Tooling Production Drawings

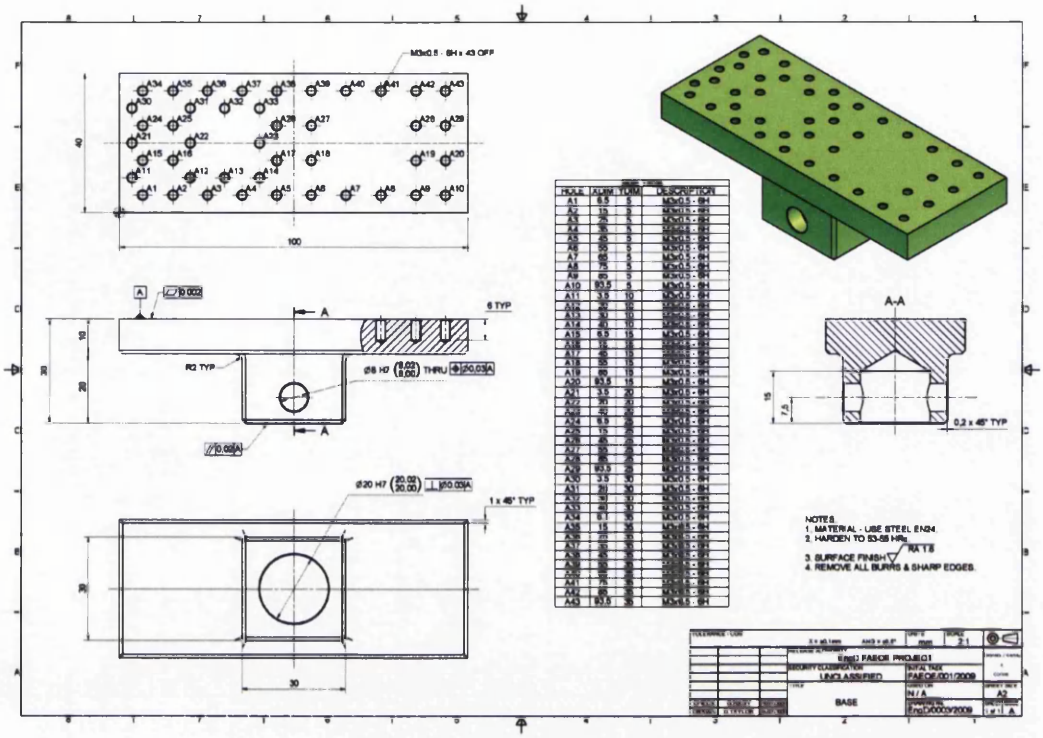

(a) Base

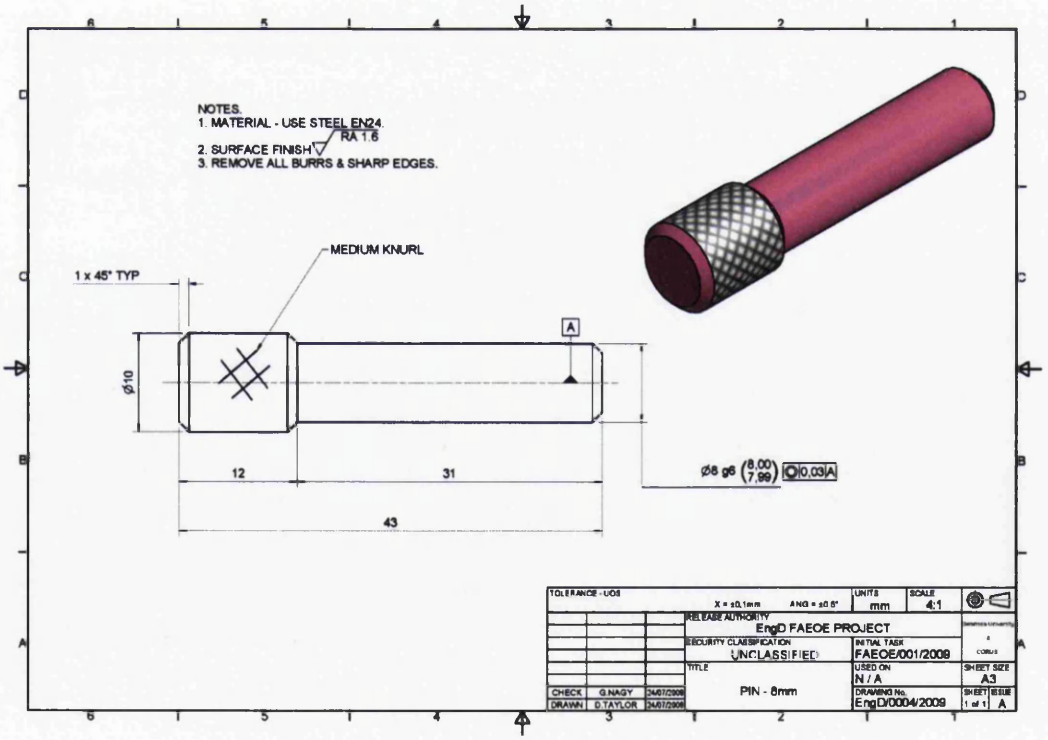

(b) Pin - 8mm

Figure A.7: Mode II Tooling Production Drawings

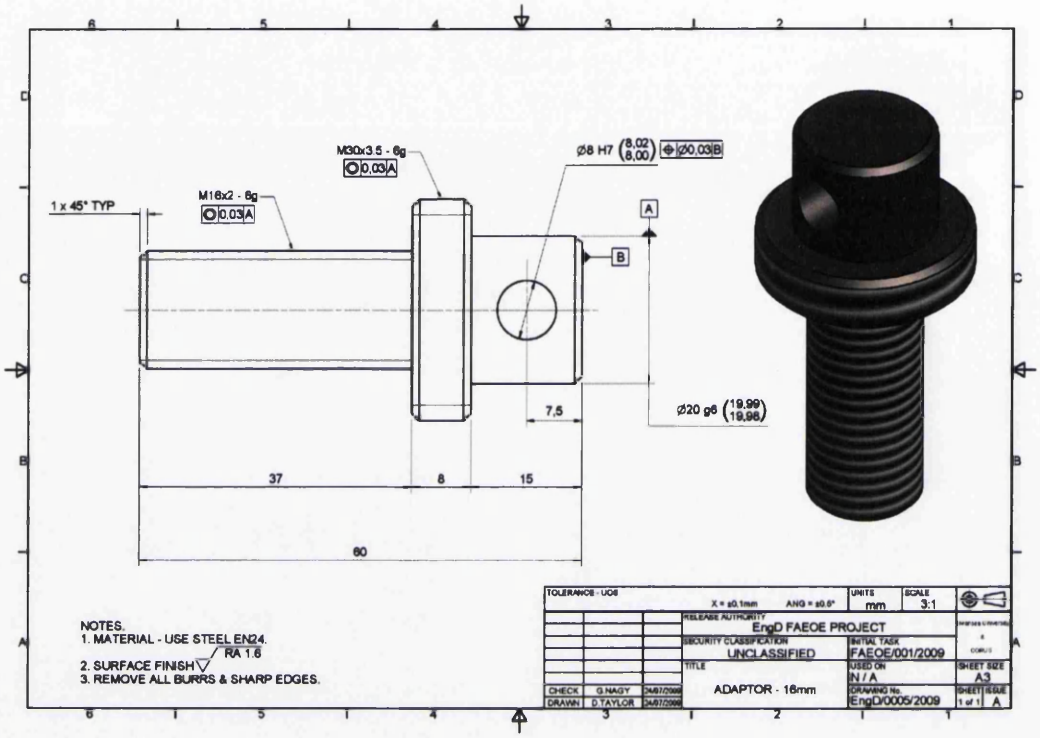

(a) Adaptor - 16mm

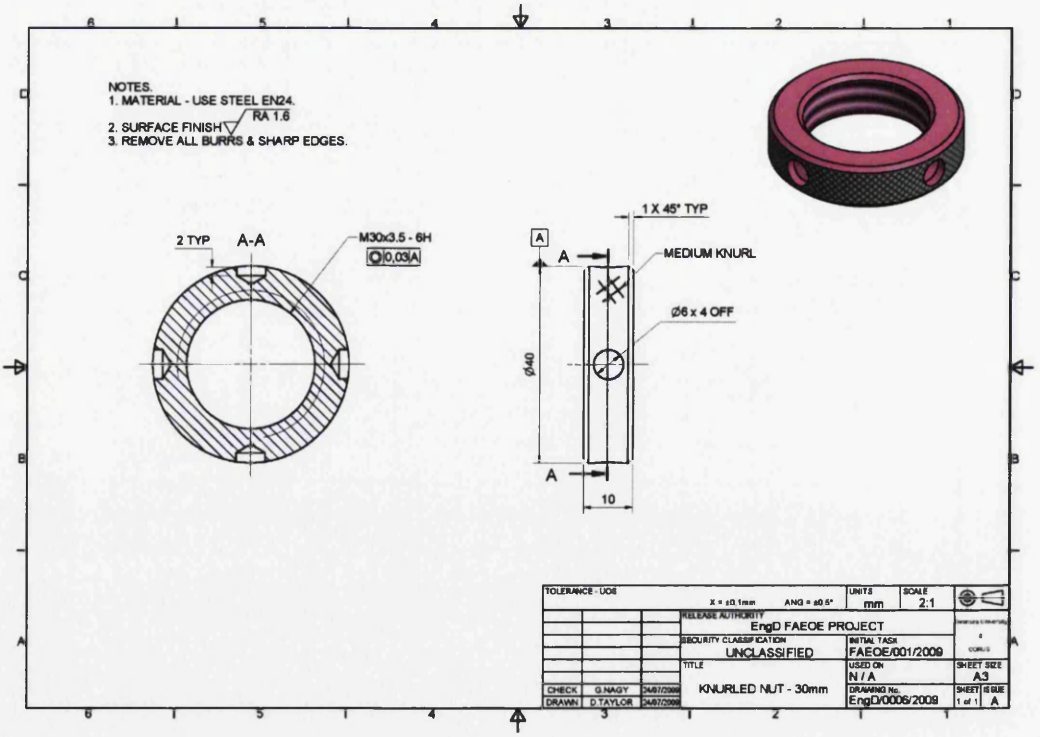

(b) Knurled Nut - 30mm

Figure A.8: Mode II Tooling Production Drawings

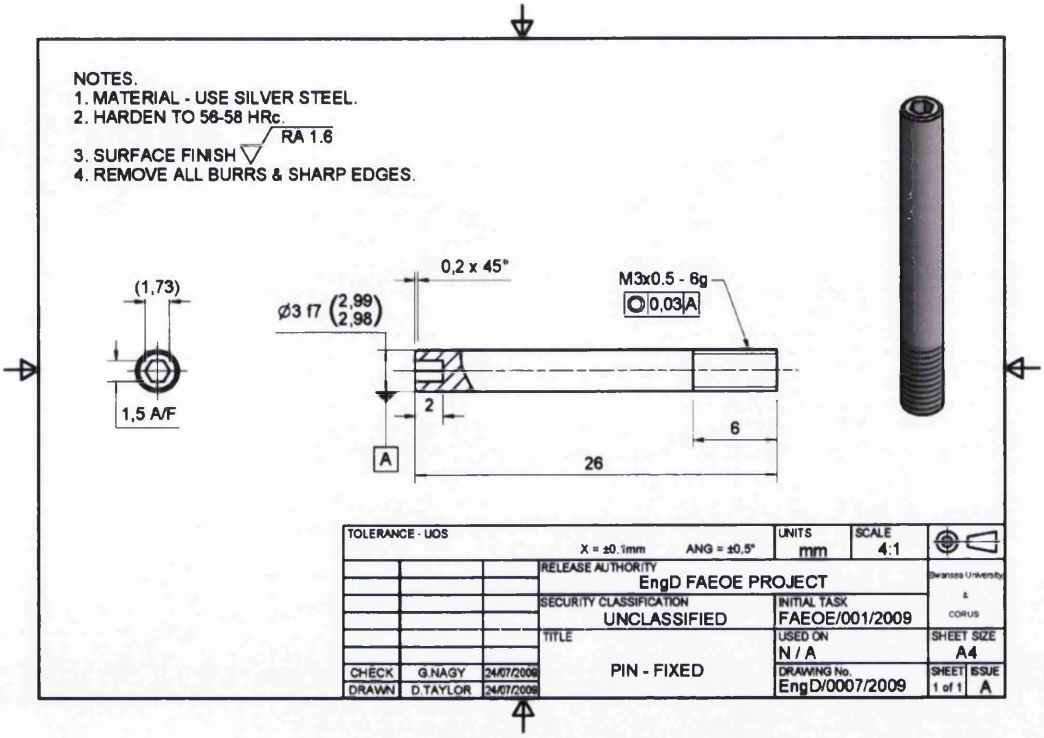

(a) Pin - Fixed

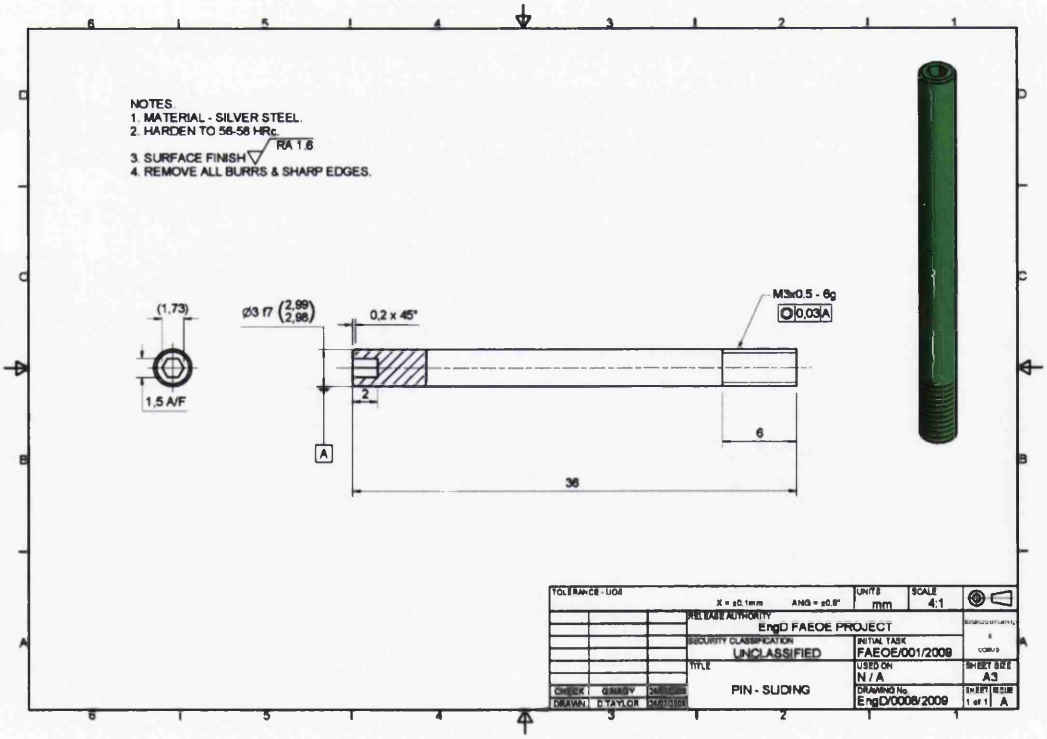

(b) Pin - Sliding

Figure A.9: Mode II Tooling Production Drawings

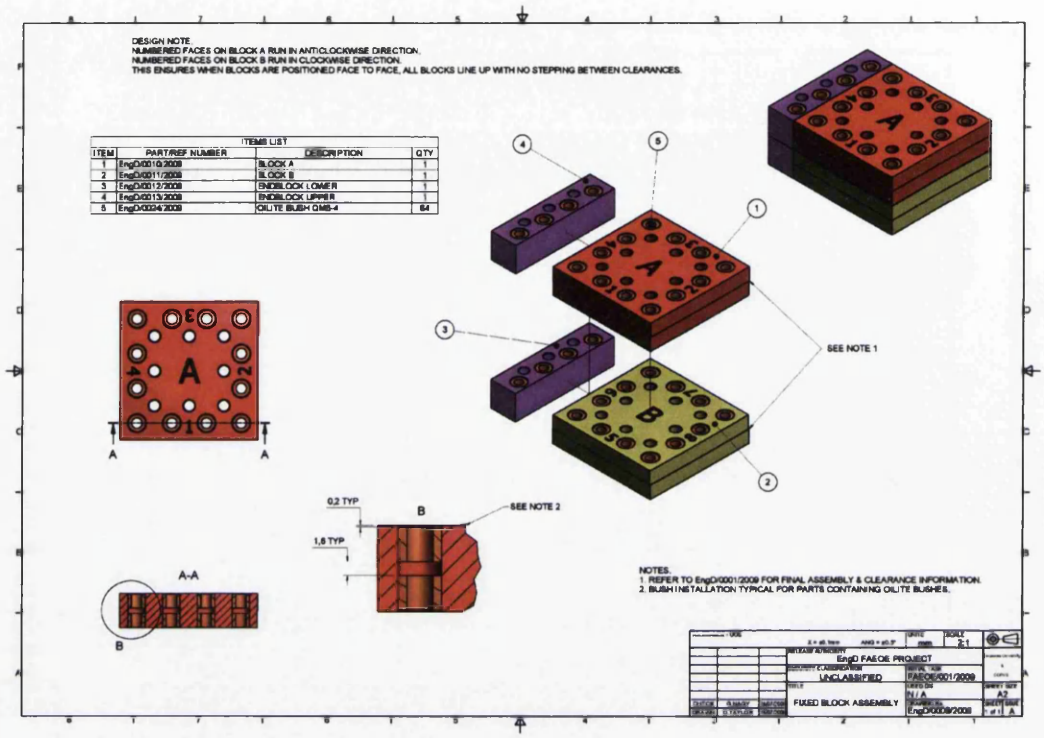

(a) Fixed Block Assembly

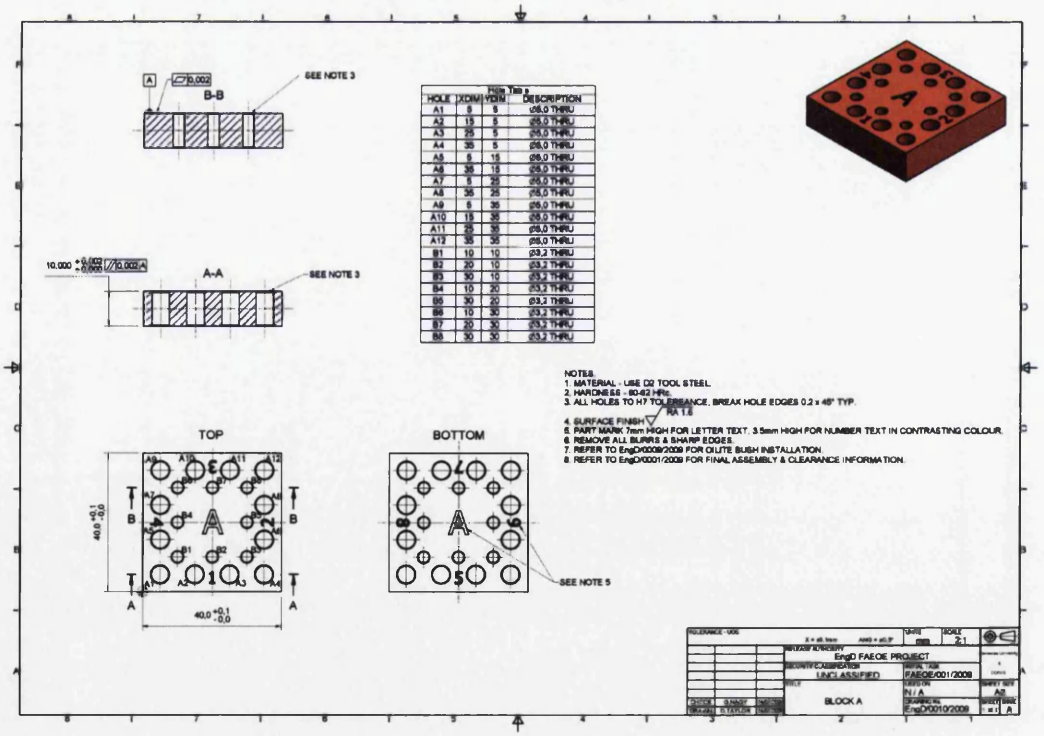

(b) Block A

Figure A.10: Mode II Tooling Production Drawings

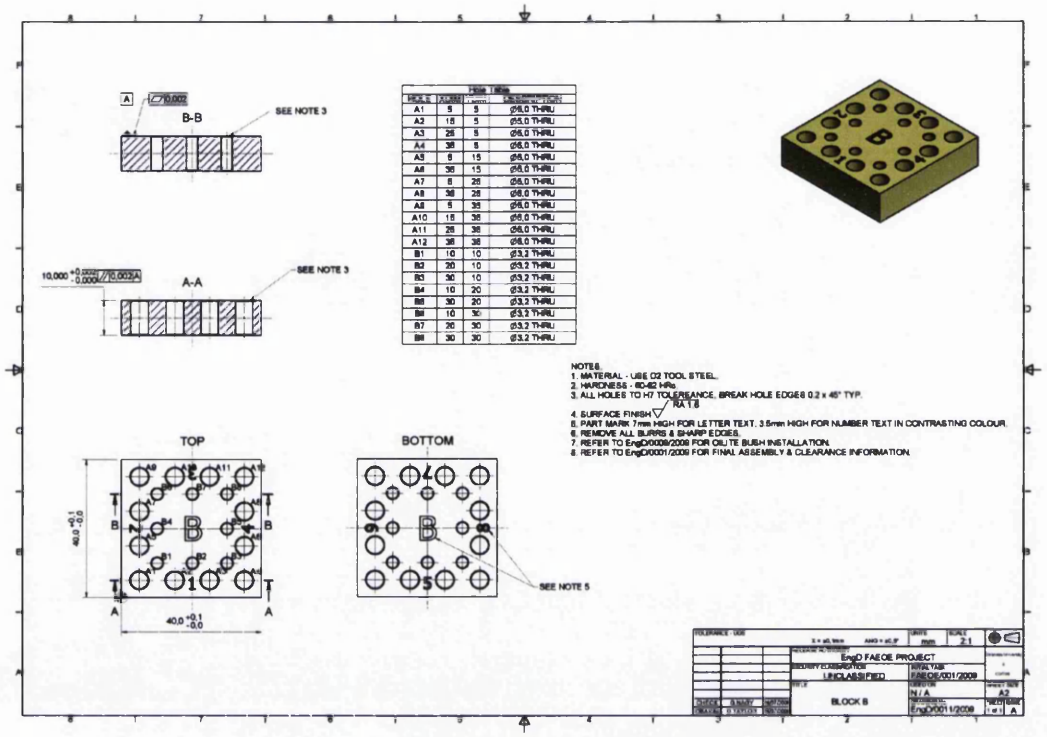

(a) Block B

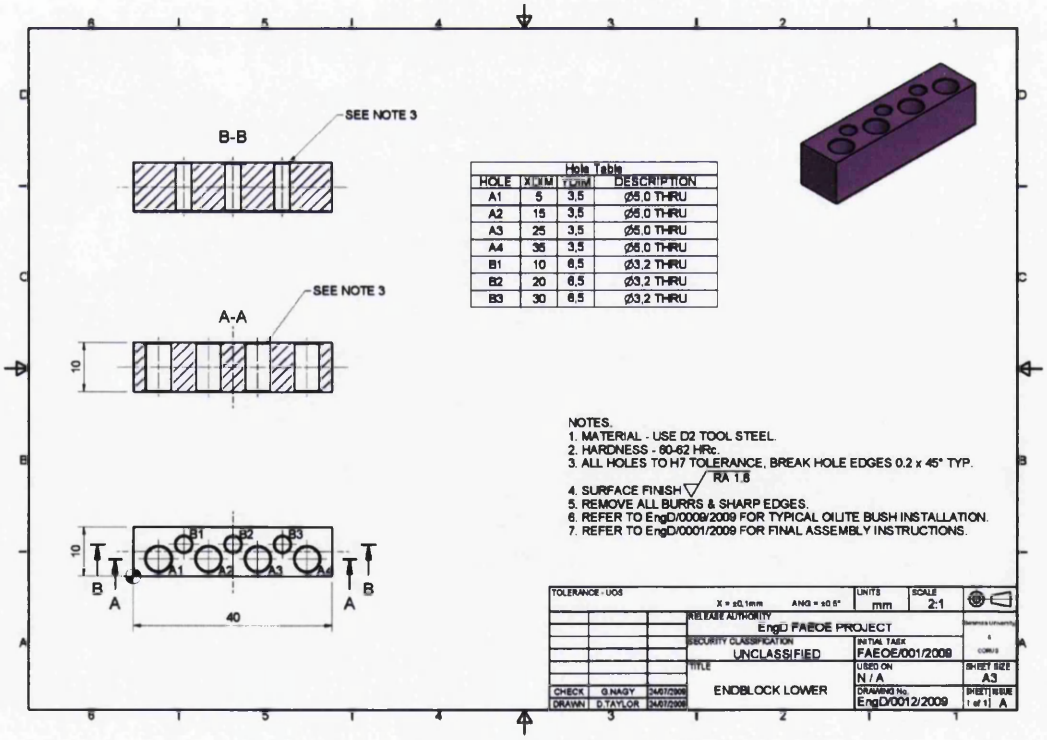

(b) EndBlock Lower

Figure A.11: Mode II Tooling Production Drawings

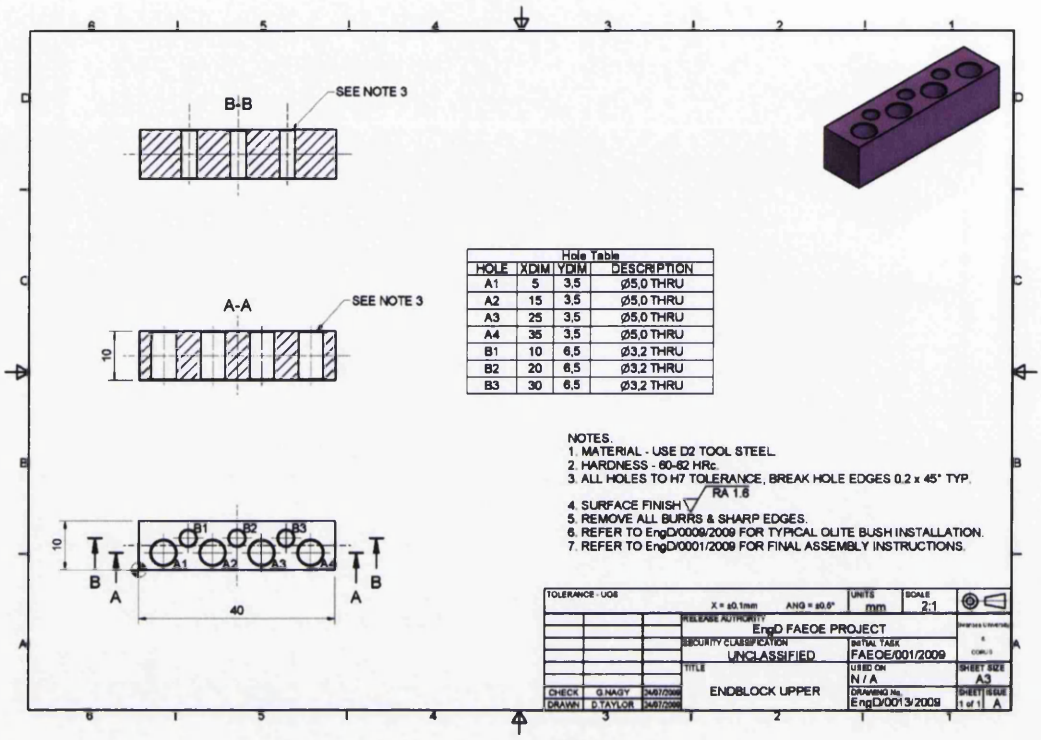

(a) EndBlock Upper

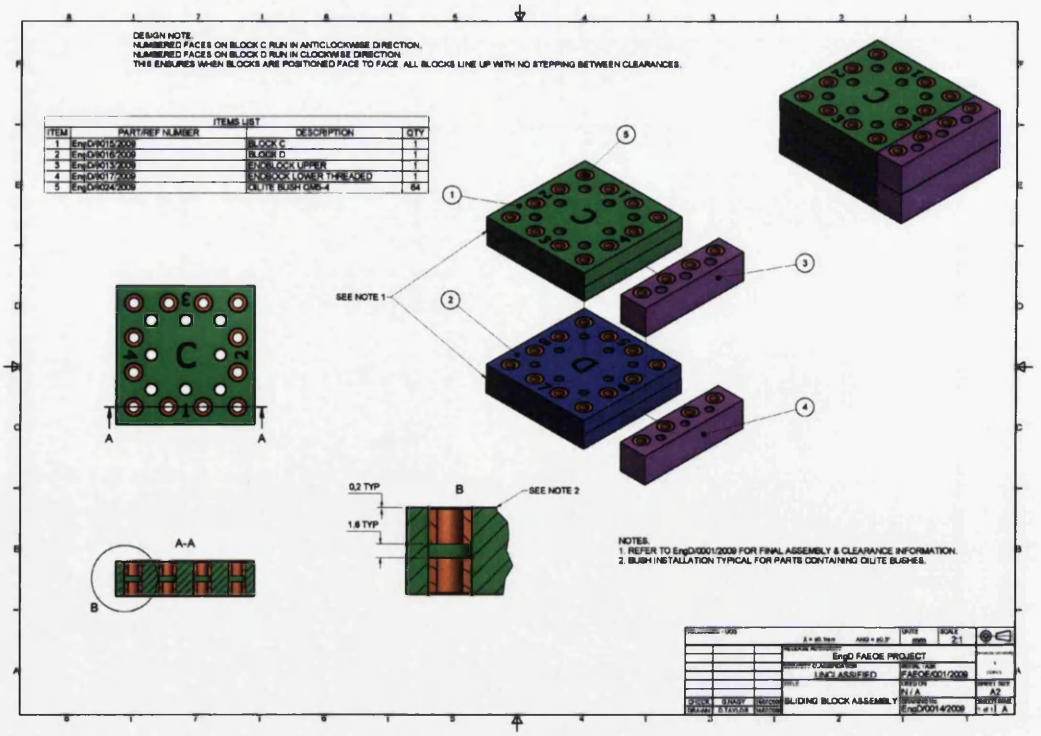

(b) Sliding Block Assembly

Figure A.12: Mode II Tooling Production Drawings

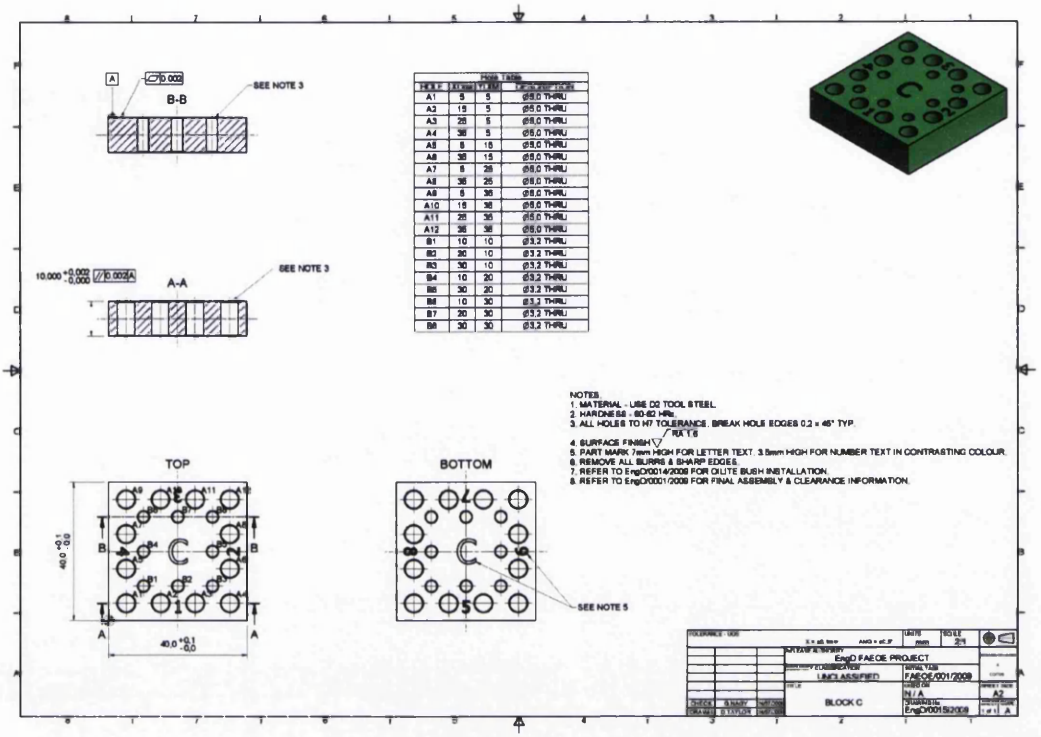

(a) Block C

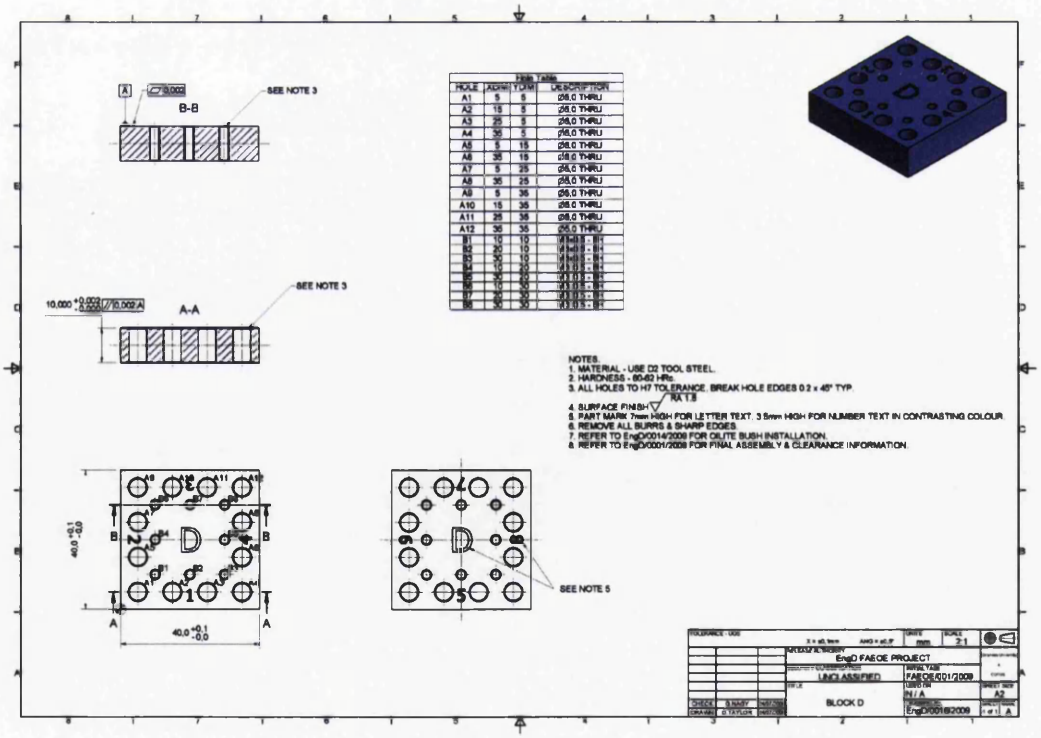

(b) Block D

Figure A.13: Mode II Tooling Production Drawings

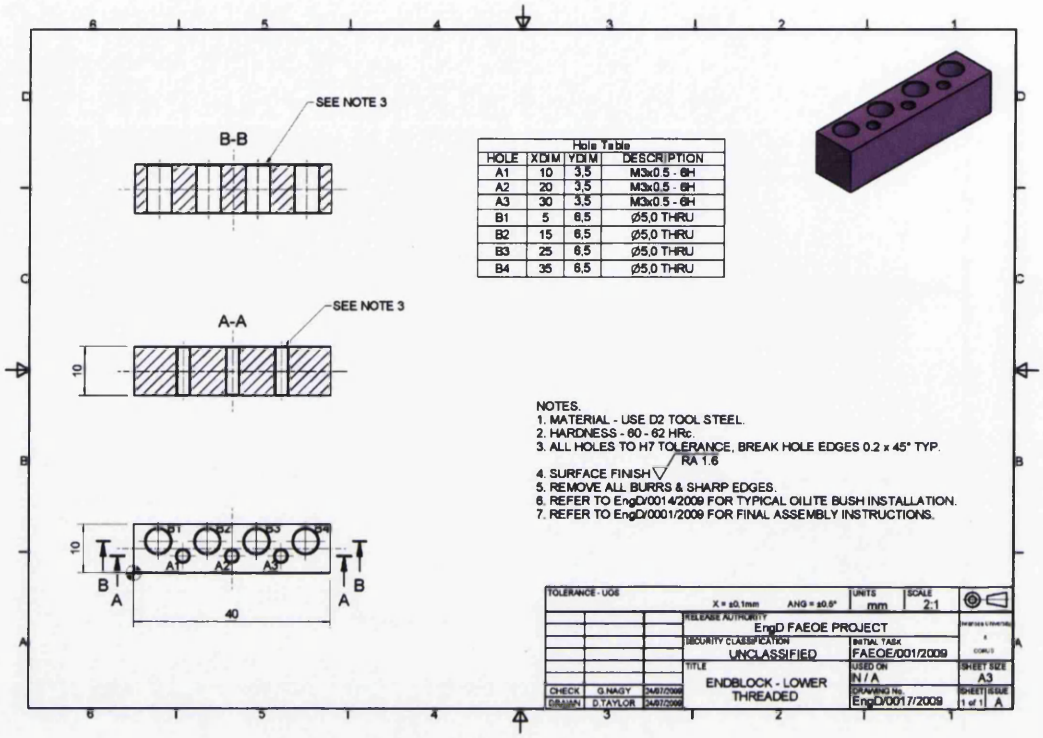

(a) EndBlock Lower Threaded

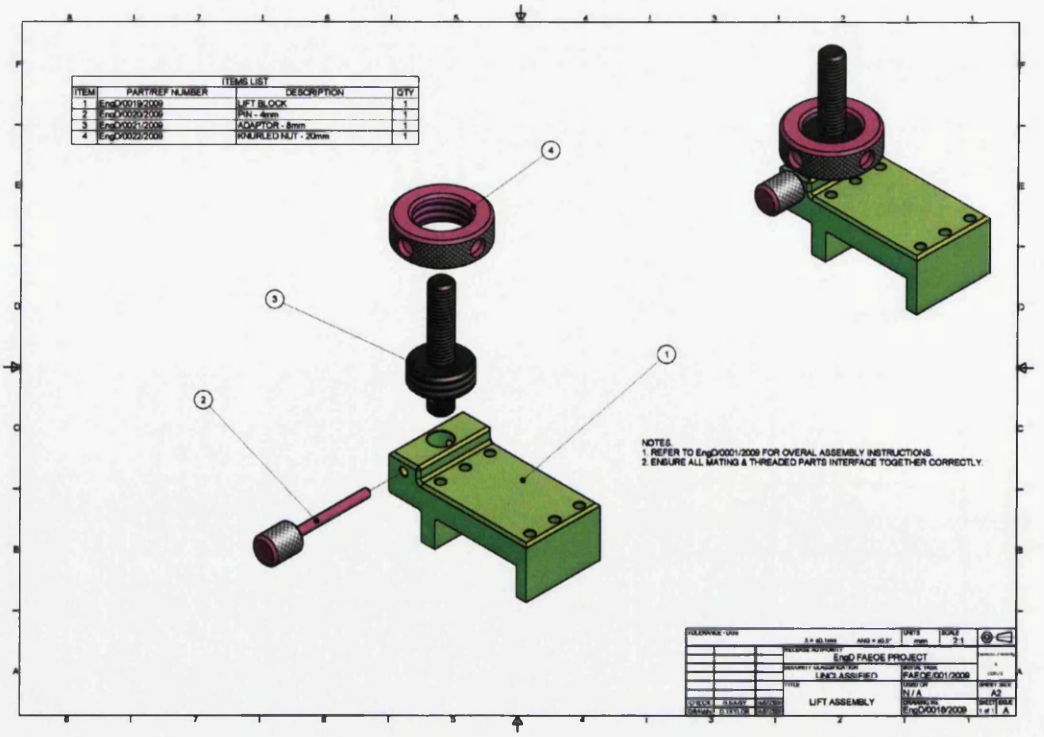

(b) Lift Assembly

Figure A.14: Mode II Tooling Production Drawings

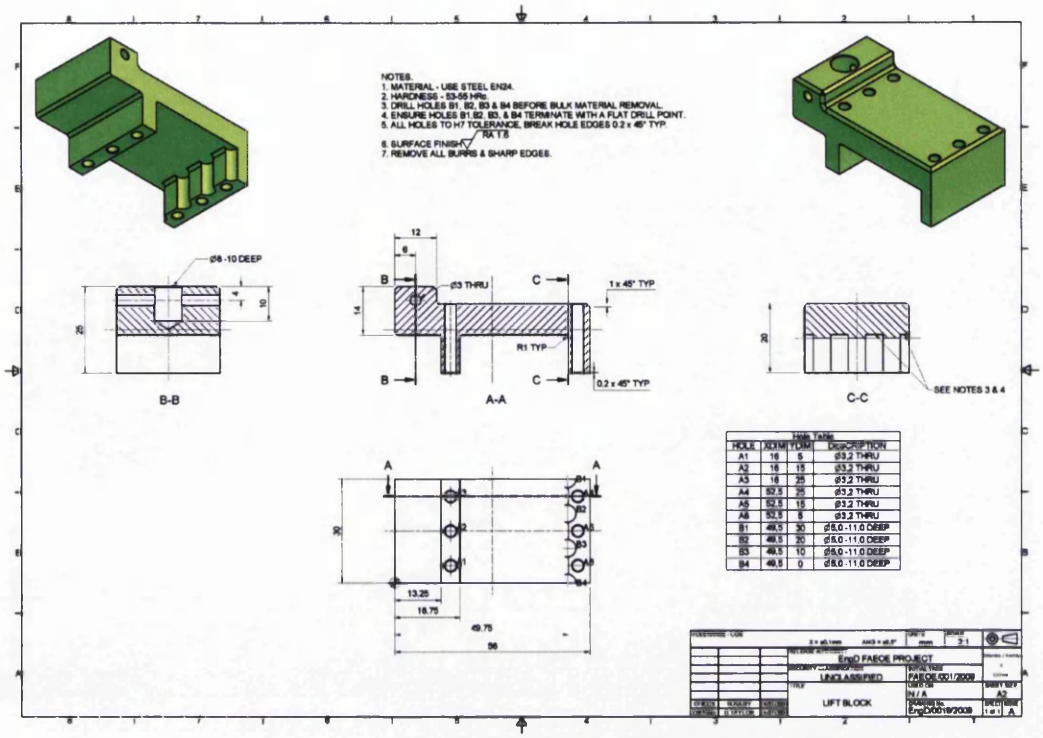

(a) Lift Block

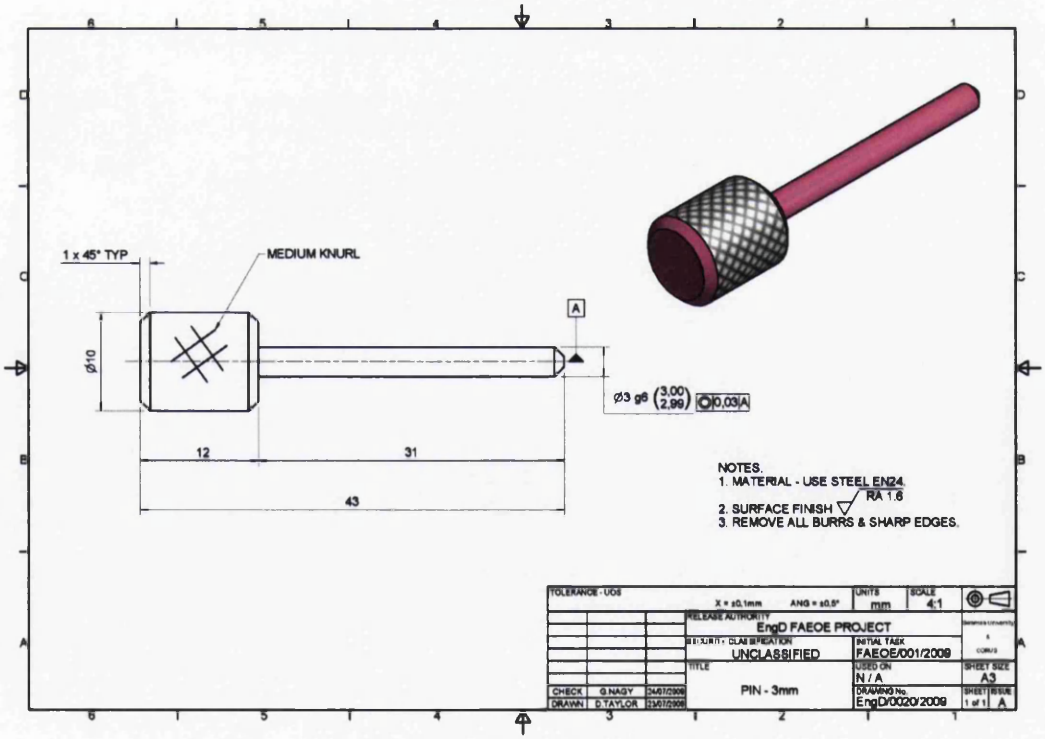

(b) Pin - 3mm

Figure A.15: Mode II Tooling Production Drawings

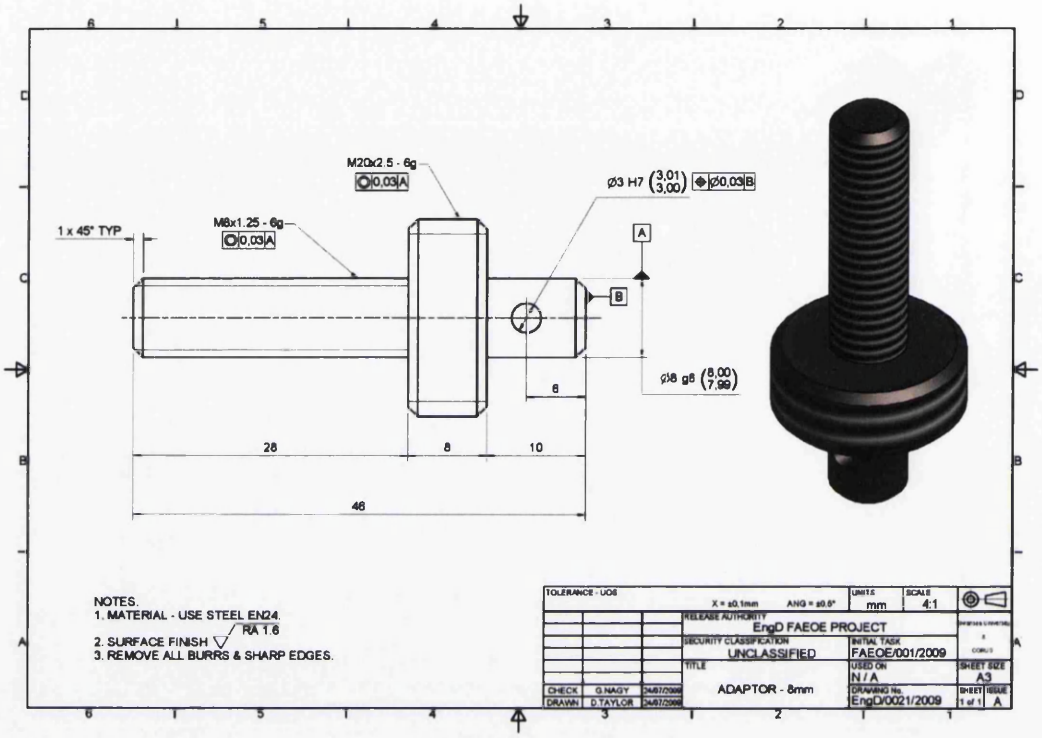

(a) Adaptor - 8mm

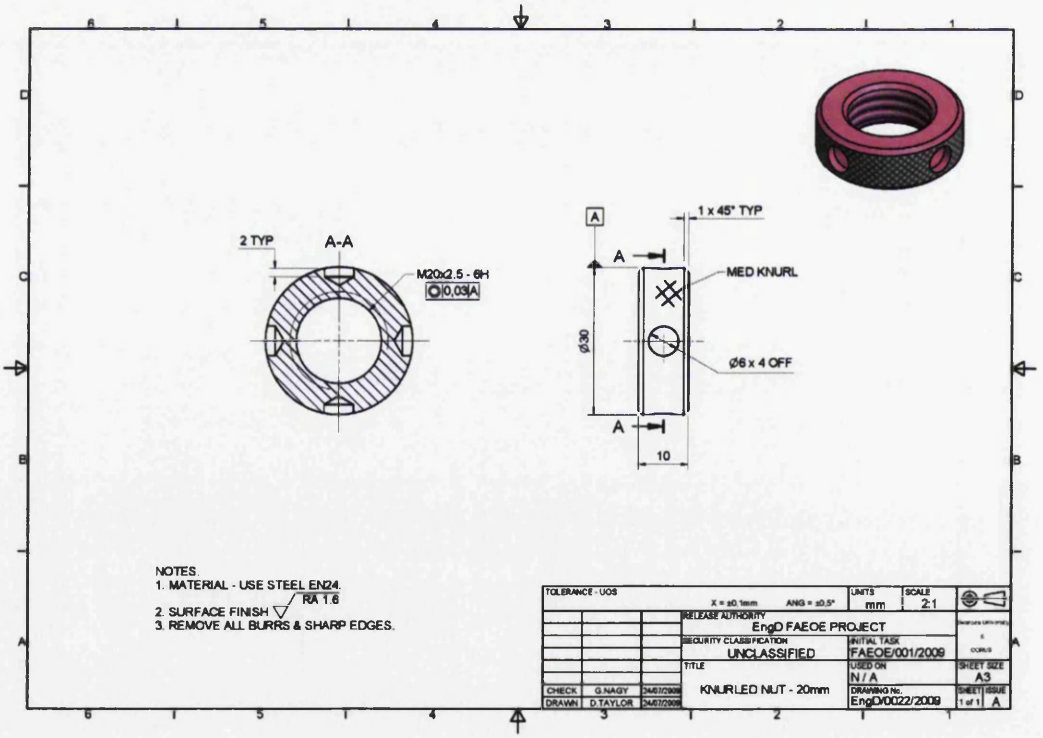

(b) Knurled Nut - 20mm

Figure A.16: Mode II Tooling Production Drawings

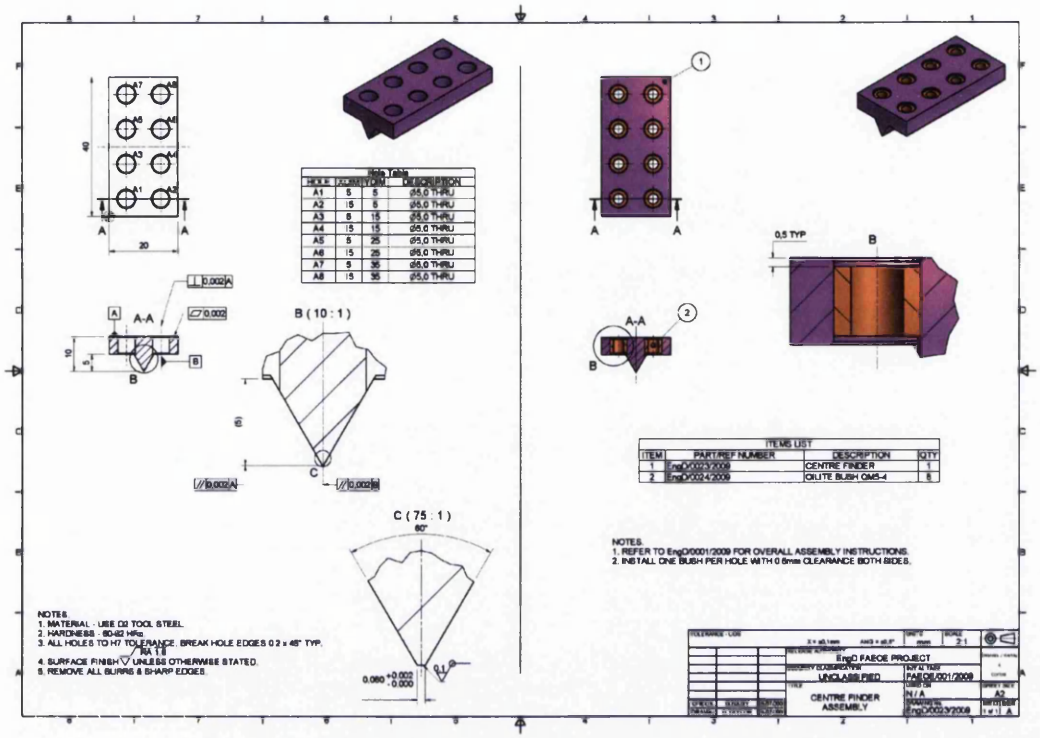

(a) Centre Finder Assembly

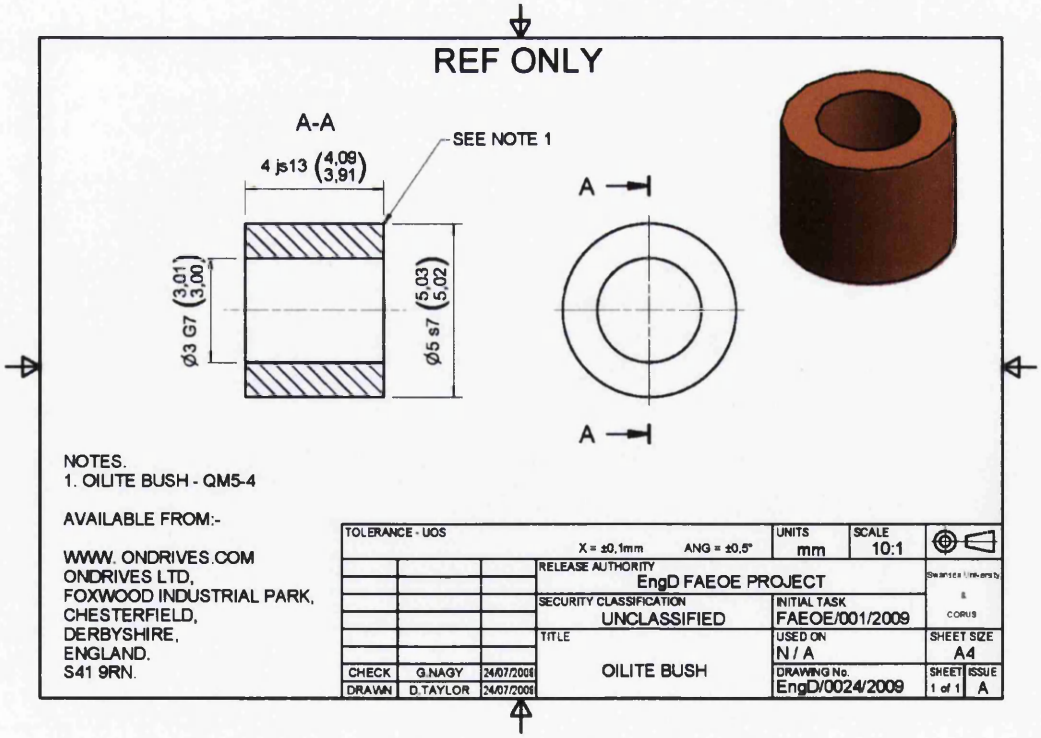

(b) Oilite Bush

Figure A.17: Mode II Tooling Production Drawings

A.5 Universal Tensile Tooling

Having investigated the capabilities of the press tool and its potential to manufacture scored samples, the process was extended with an examination into the different tensile test equipment available at both Corus RD&T and Swansea University. This investigation made clear that five tensile test machines were available for research use between facilities.

Location	Manufacture	Model No	Capacity
Corus RD&T IJmuiden	Instron	5567	30KN
Corus RD&T ECM2	Zwick	Z010	10KN
Swansea University	Hounsfield	H25KS	25KN
Swansea University	Hounsfield	H50KS	50KN

Table A.1: Tensile Test Machine Information

Looking at the projects material requirements it is clear from [21]that the materials considered have strengths in the following range.

Material Euronorm Designation	Yield Strength	Ultimate Strength
TS245	245 +/- 50	340 +/- 50
TS275	275 +/- 50	375+/- 50
TS300	300 +/- 40	325 +/- 40
TH340	340 +/- 50	395 +/- 50
TH415	415 +/- 50	435 +/- 50
TH435	435 +/- 50	460 +/- 50
TH550N	550 +/- 40	555 +/- 40

Table A.2: Material Strength Information

This information provides a method of calculating the maximum force required for sample manufacture, which in turn allows us to choose the correctly specified equipment.

Sample Size	Tool Profile	Max Deformed Area	Force to Deform Score
12.5mm	40/30	4.365mm	2.6KN
12.5mm	40/60	4.741mm	2.8KN
12.5mm	60/30	4.705mm	2.8KN
12.5mm	60/60	5.080mm	3.0KN
Tramrail	40/30	48.895mm	29.3KN
Tramrail	40/60	53.095mm	31.8KN
Tramrail	60/30	105.4mm	63.2KN
Tramrail	60/60	113.8mm	68.3KN

Table A.3: Max Force for Sample Manufacture

Tensile Machines at Corus RD&T ECM2

The following tensile test machines are available at Corus RD&T ECM2 in Port Talbot.

(a) Zwick Z010 (b) Zwick Z1474

Figure A.18: Tensile Test Machines at Corus RD&T ECM2

The Zwick model No Z010 is a bench mounted machine with an overall capacity of 10KN, which provides more than enough force to test and produce 12.5mm single score samples. The second machine is a Zwick model No 1474, a much

more heavy duty machine with a much larger overall capacity of 200KN, this machine is in constant use by Corus RD&T and was not be available for use when required.

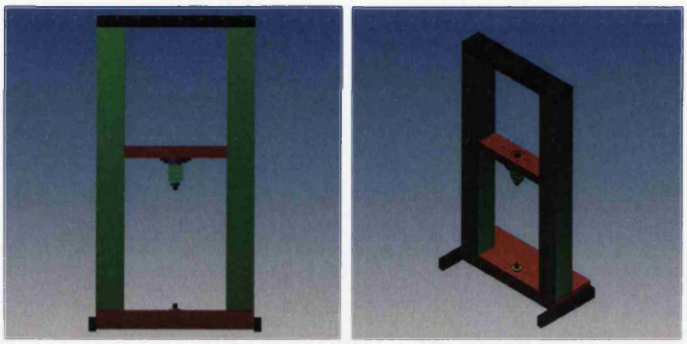

(a) Front View (b) Isometric View

Figure A.19: 3D Model of the Zwick Z010

A detailed 3D model of the Zwick Z010 was created, which enabled any tooling design to be tried and tested virtually before any manufacturing decision was made.

Tensile Machines at Swansea University

Swansea University houses two Hounsfield tensile testers in its Engineering Department. Both machines are identical with the exception of the load cells, which have 25KN and 50KN capacities respectively. In the event that the Zwick Z010 at Corus RD&T becomes unavailable or unserviceable then either of these machines will be more than capable of taking over the testing of the 12.5mm single score samples. Additionally, should there be a requirement for increased capacity then both of these machines are more powerful than the Z010, so provide a useful step up in available force. Again a detailed 3D model of the Hounsfield machine was created, which enabled the tooling design to be tried and tested virtually. The tooling required was made universal so that any tensile machine can be used to perform the tests if necessary.

(a) Hounsfield H25KS (b) Houndsfield H50KS

Figure A.20: Tensile Test Machines at Swansea University

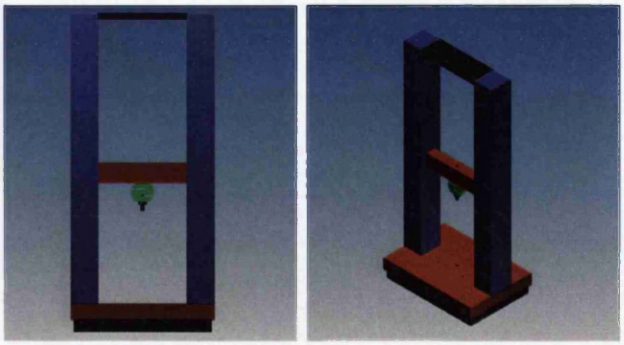

(a) Front View (b) Isometric View

Figure A.21: 3D Model of the Hounsfield

Tensile Testing Update

After reviewing the tensile test equipment available at both Corus RD&T and Swansea University, a further more detailed analysis was carried out that highlighted an additional tensile machine available at Swansea University.

(a) Hounsfield

Figure A.22: Hounsfield Tensile Tester at Swansea University

It is now believed that this machine will prove to be better suited for completing the experimental part of the project scheduled for this summer for the following reasons:-

(1) The tensile machine is available throughout August & September 2009.

(2) Machine is calibrated and all software is currently up to date.

(3) Load cells are available with 10KN, 1KN & 100N capacities.

(4) A temperature controlled cabinet is attached & available for use if required.

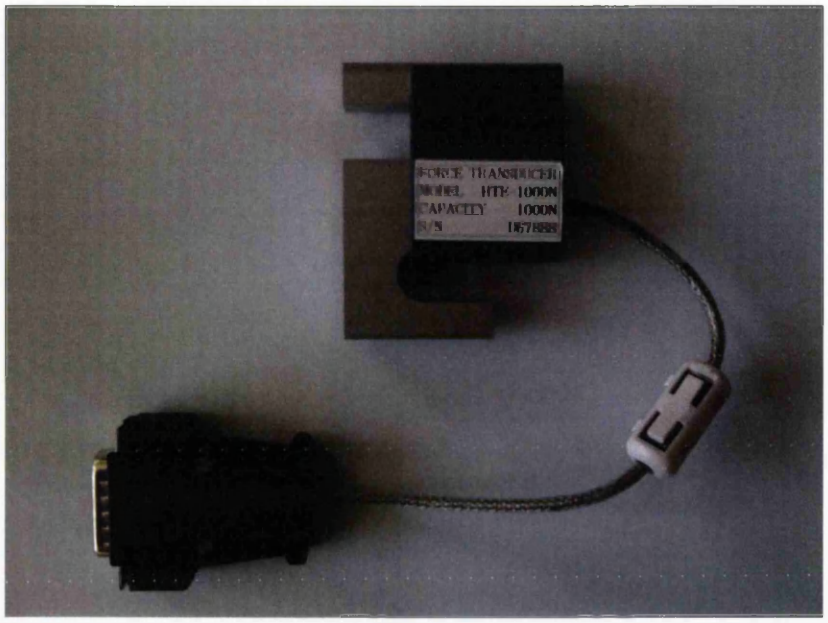

(a) 1000N Load Cell

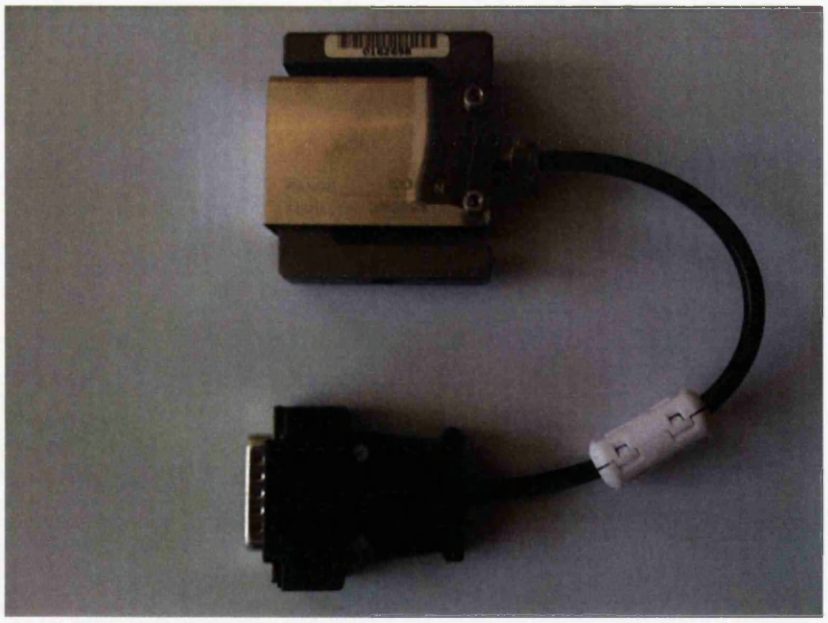

(b) 100N Load Cell

Figure A.23: 1000N & 100N Load Cells

Appendix B

Worked Example

B.1 Biaxial Deformation

A square element measuring 1 x 1mm in a sheet of 1mm thick packaging steel is deformed biaxially to become 1.284 x 1.284mm after forming, assuming that the the stress normal to the sheet is zero and the stress strain law for the material is:-

$$\bar{\sigma} = 744(0.16 + \bar{\varepsilon})^{0.27} \tag{B.1}$$

Determine:-

a. Principal Strains

b. Strain & Stress Ratios*(assumed constant)*

c. Effective Strain

d. Effective Stress

e. Principal Stress

f. Hydrostatic Stress

g. Deviatoric Stress

h. Flow Rule

i. Plastic Work of Deformation

Firstly, to find the thickness after forming:-

From incompressibility:-

$$l \times w \times t = l_o \times w_o \times t_o \tag{B.2}$$

$$t = \frac{l_o \times w_o \times t_o}{l \times w} = t = \frac{1 \times 1 \times 1}{1.284 \times 1.284} = t = 0.6065 \tag{B.3}$$

a. Principal Strains

$$\varepsilon_1 = \ln(\frac{l}{l_o}) = \ln(\frac{1.284}{1}) = 0.250 \tag{B.4}$$

$$\varepsilon_2 = \ln(\frac{w}{w_o}) \quad = \quad \ln(\frac{1.284}{1}) \quad = \quad 0.250 \tag{B.5}$$

$$\varepsilon_3 = \ln(\frac{t}{t_o}) \quad = \quad \ln(\frac{0.6065}{1}) \quad = \quad -0.500 \tag{B.6}$$

also, as a check

$$\varepsilon_3 = -(\varepsilon_1 + \varepsilon_2) \quad = \quad -(0.250 + 0.250) \quad = \quad -0.500 \tag{B.7}$$

b. Strain & Stress Ratios

$$\beta = \frac{\varepsilon_2}{\varepsilon_1} \quad = \quad \frac{0.250}{0.250} \quad = \quad 1 \tag{B.8}$$

$$\alpha = \frac{2\beta + 1}{2 + \beta} \quad = \quad \frac{3}{3} \quad = \quad 1 \tag{B.9}$$

c. Effective Strain

$$\bar{\varepsilon} = \sqrt{\frac{4}{3}(1 + \beta + \beta^2)}\varepsilon_1 \quad = \quad \sqrt{\frac{4}{3}(1 + 1 + 1^2)} \times 0.250 \quad = \quad 0.500 \tag{B.10}$$

d. Effective Stress

$$\bar{\sigma} = K(\varepsilon_0 + \bar{\varepsilon})^n \quad = \quad 744(0.16 + 0.5)^{0.27} \quad = \quad 665.043 \tag{B.11}$$

e. Principal Stress

$$\sigma_1 = \frac{\bar{\sigma}}{\sqrt{1 - \alpha + \alpha^2}} \quad = \quad \frac{665.043}{\sqrt{1 - 1 + 1^2}} \quad = \quad 665.043 \tag{B.12}$$

$$\sigma_2 = \alpha\sigma_1 \quad = \quad 1 \times 665.043 \quad = \quad 665.043 \tag{B.13}$$

$$\sigma_3 = 0 \tag{B.14}$$

f. Hydrostatic Stress

$$\sigma_h = \frac{\sigma_1 + \sigma_2 + \sigma_3}{3} \quad = \quad \frac{665.043 + 665.043 + 0}{3} \quad = \quad 443.362 \tag{B.15}$$

g. Deviatoric Stress

$$\sigma_1^{/} = \sigma_1 - \sigma_h \quad = \quad 665.043 - 443.362 \quad = \quad 221.681 \tag{B.16}$$

$$\sigma_2^{/} = \sigma_2 - \sigma_h \quad = \quad 665.043 - 443.362 \quad = \quad 221.681 \tag{B.17}$$

$$\sigma_3^{/} = \sigma_3 - \sigma_h \quad = \quad 0 - 443.362 \quad = \quad -443.362 \tag{B.18}$$

h. Flow Rule

$$\frac{\varepsilon_1}{\sigma_1^{/}} \quad = \quad \frac{0.250}{221.681} \quad = \quad 0.001128 \tag{B.19}$$

$$\frac{\varepsilon_2}{\sigma_2^{/}} \quad = \quad \frac{0.250}{221.681} \quad = \quad 0.001128 \tag{B.20}$$

$$\frac{\varepsilon_3}{\sigma_3^{/}} \quad = \quad \frac{-0.500}{-443.362} \quad = \quad 0.001128 \tag{B.21}$$

i. Plastic Work of Deformation

$$\frac{W}{vol} = \int_0^{\bar{\varepsilon}} \bar{\sigma} d\bar{\varepsilon} \quad = \quad \int_0^{0.5} 744(0.16 + \bar{\varepsilon})^{0.27} d\bar{\varepsilon} \tag{B.22}$$

$$= \quad \frac{744}{1.27}(0.66^{1.27} - 0.16^{1.27}) \quad = \quad 288.464 \tag{B.23}$$

The strains were applied incrementally up to a max effective strain of 0.5mm.

Appendix C

Factorial Analysis Results

C.1 Mode I - Force Results

Minitab™

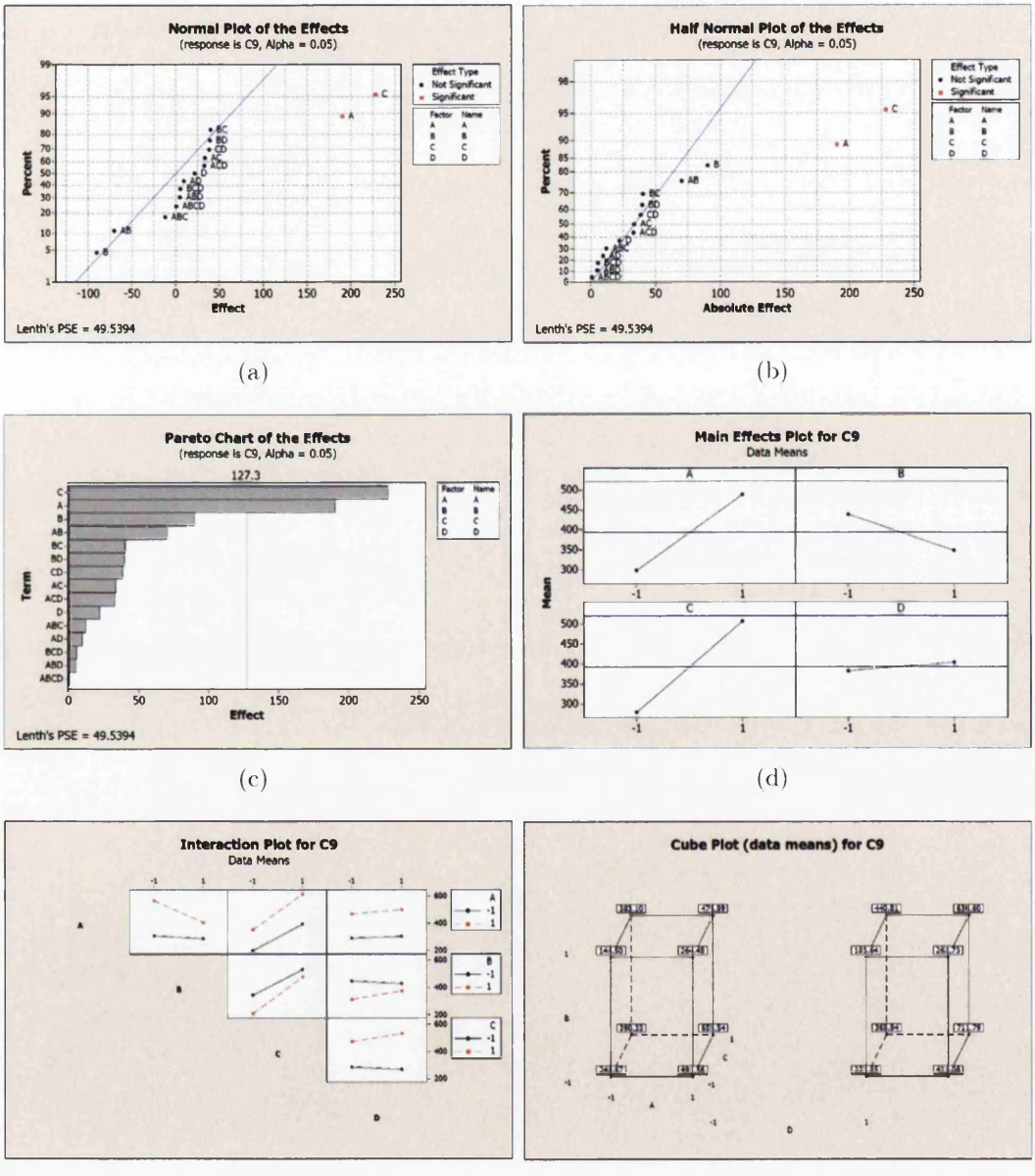

(a) (b)

(c) (d)

(e) (f)

Figure C.1: Mode I Force Results - Minitab™

Excel™

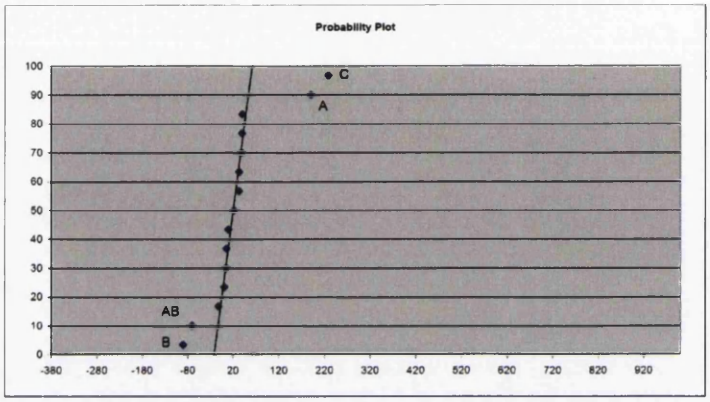

(a)

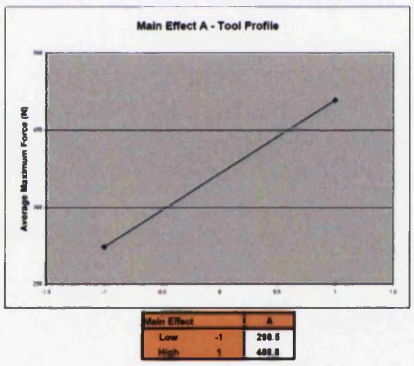

(b)

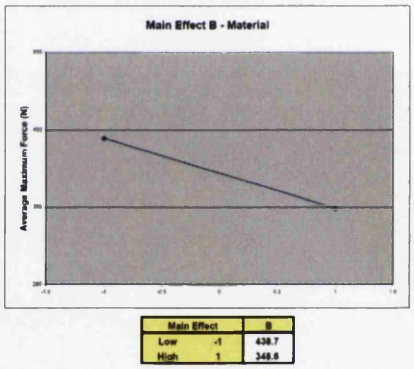

(c)

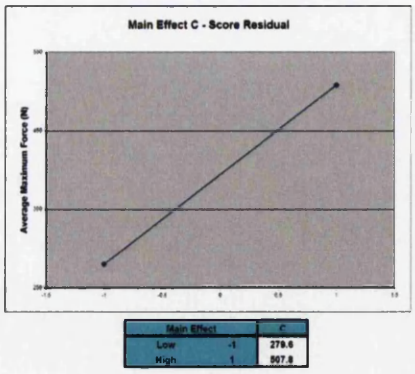

(d)

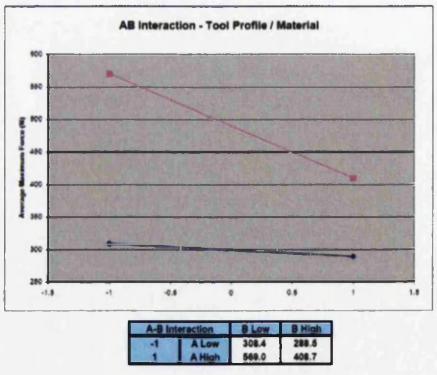

(e)

Figure C.2: Mode I Force Results - Excel™

C.2 Mode I - Displacement Results

Minitab™

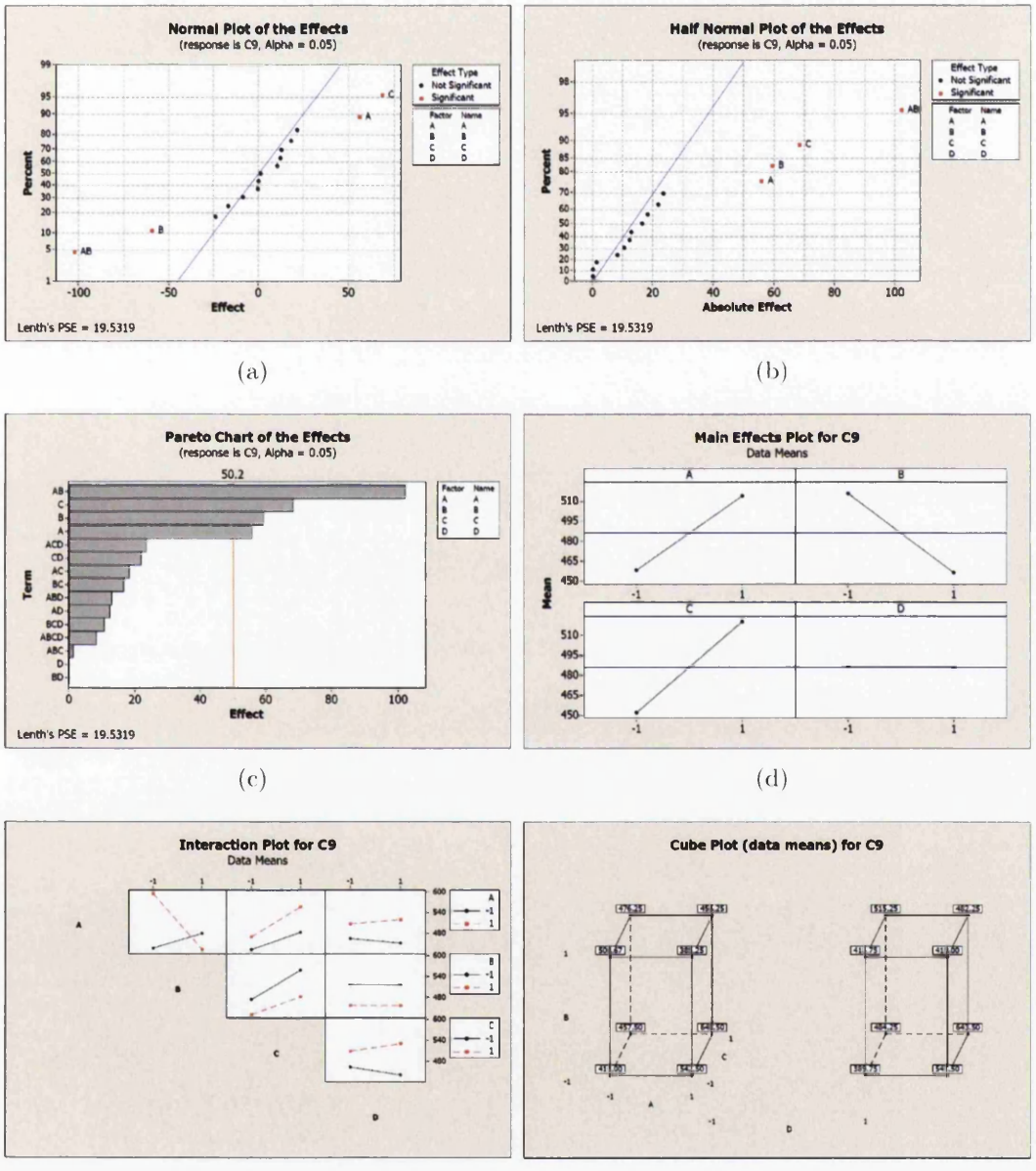

Figure C.3: Mode I Displacement Results - Minitab™

Excel™

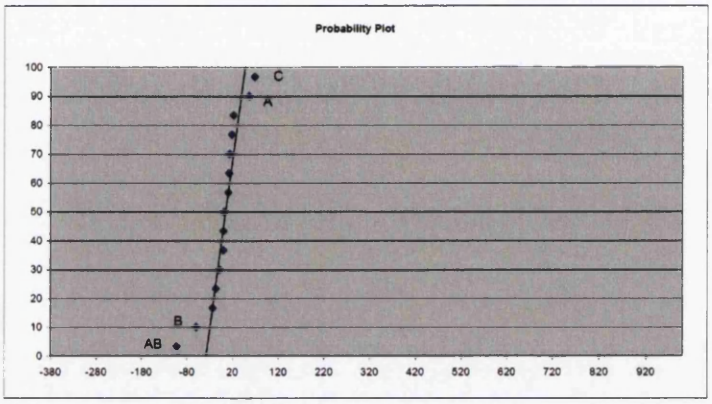

(a)

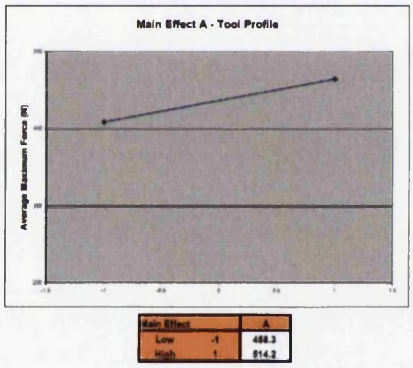

(b)

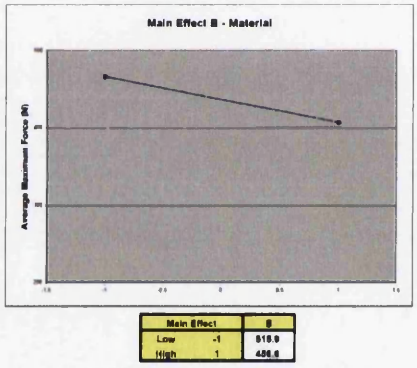

(c)

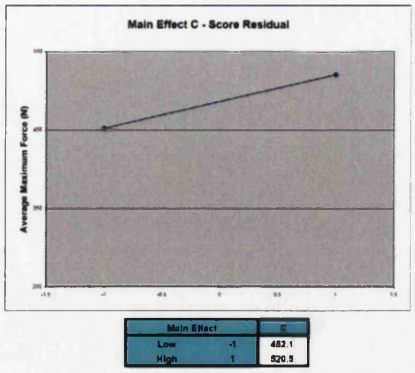

(d)

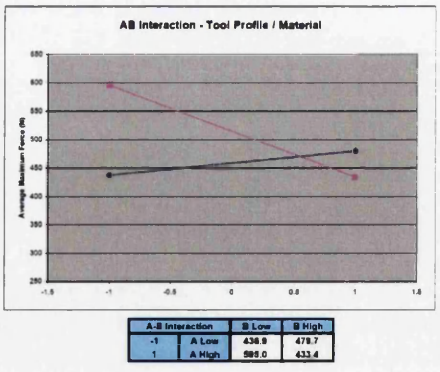

(e)

Figure C.4: Mode I Displacement Results - Excel™

C.3 Mode I -Stress Results

Minitab™

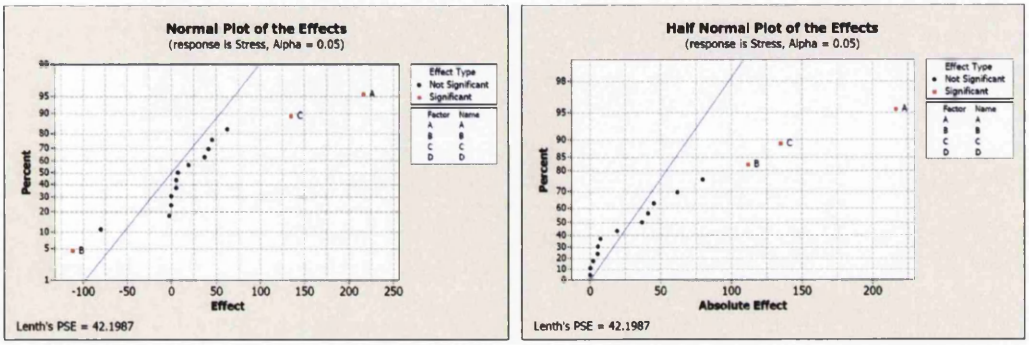

(a)

(b)

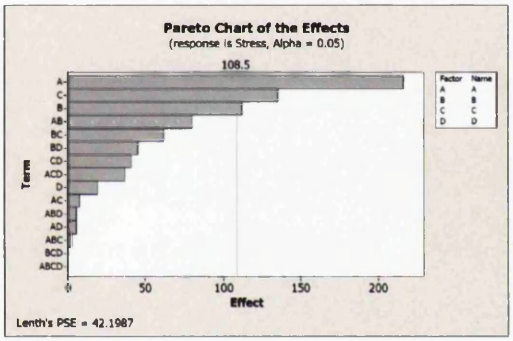

(c)

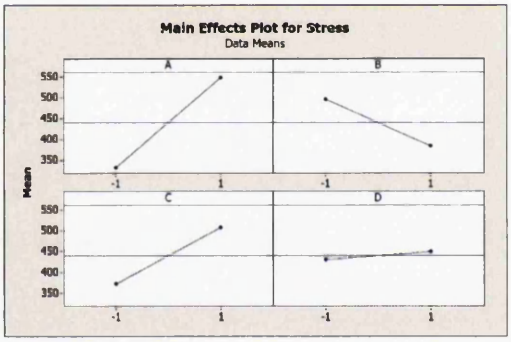

(d)

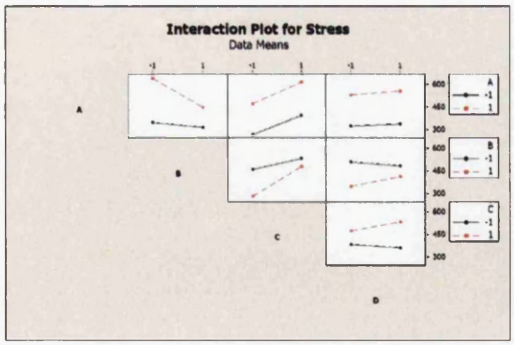

(e)

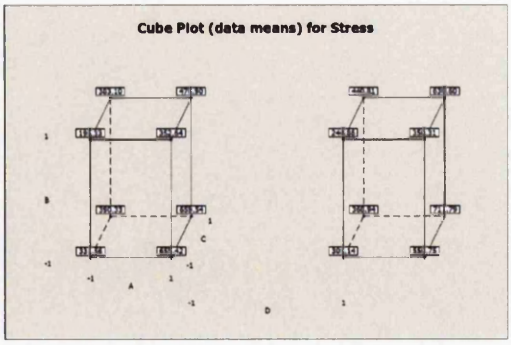

(f)

Figure C.5: Mode I Stress Results - Minitab™

Excel™

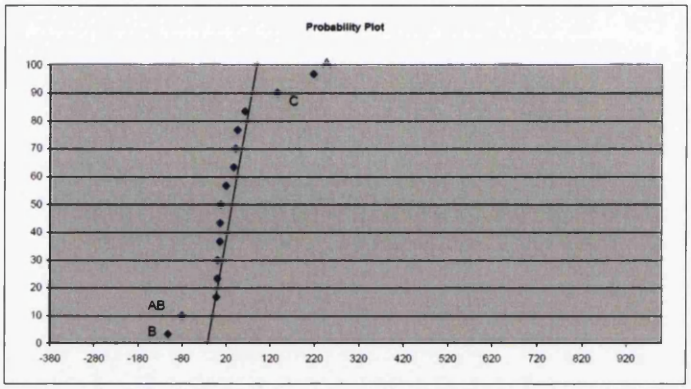

(a)

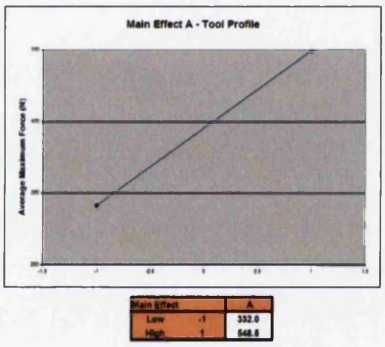

(b)

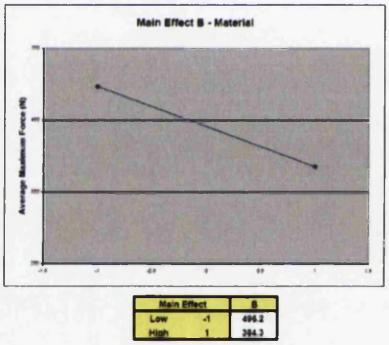

(c)

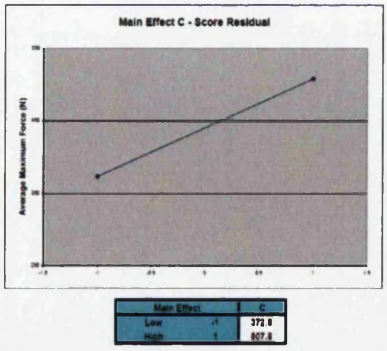

(d)

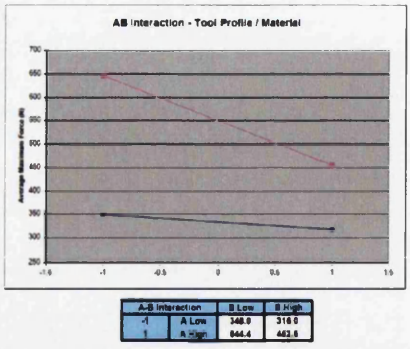

(e)

Figure C.6: Mode I Stress Results - Excel™

C.4 Mode II - Force Results

Minitab^{TM}: 0.18 - 0.20

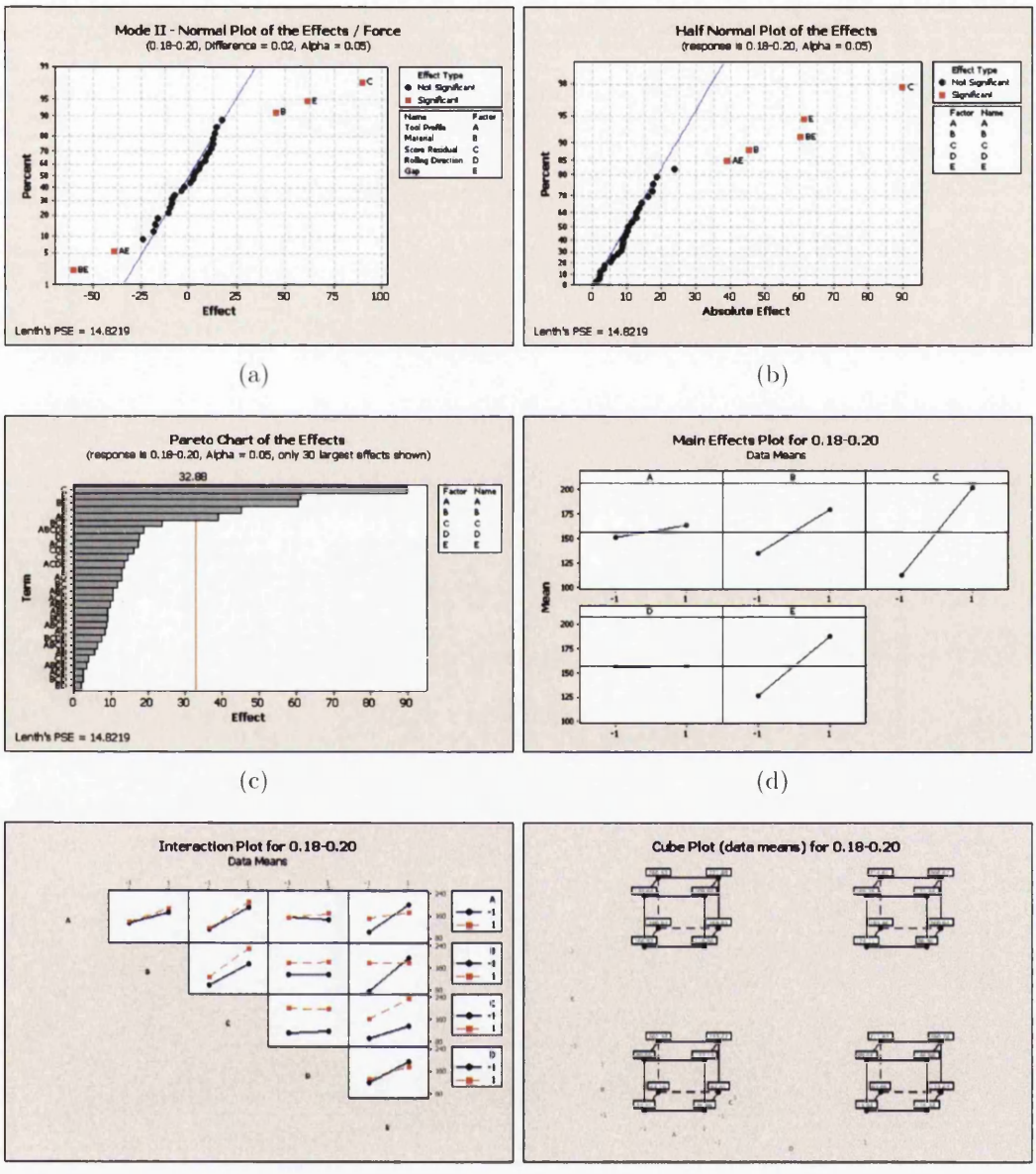

Figure C.7: Mode II Force Results - Minitab^{TM}0.18 - 0.20

Excel^{TM}: 0.18 - 0.20

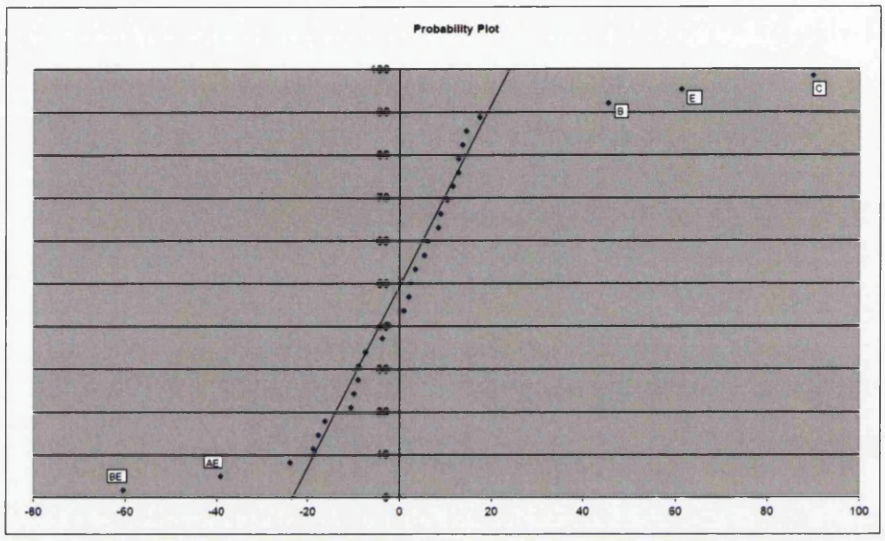

(a)

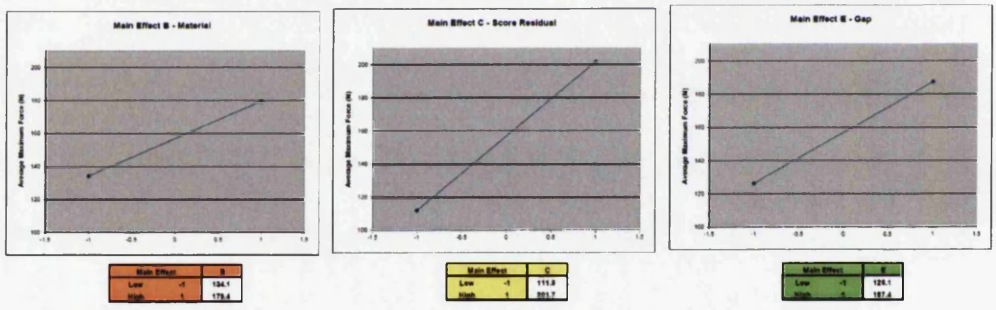

(b) (c) (d)

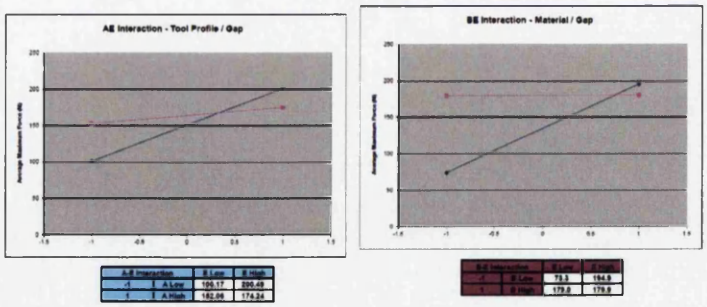

(e) (f)

Figure C.8: Mode II Force Results - Excel^{TM}0.18 - 0.20

Minitab^{TM}: 0.18 - 0.22

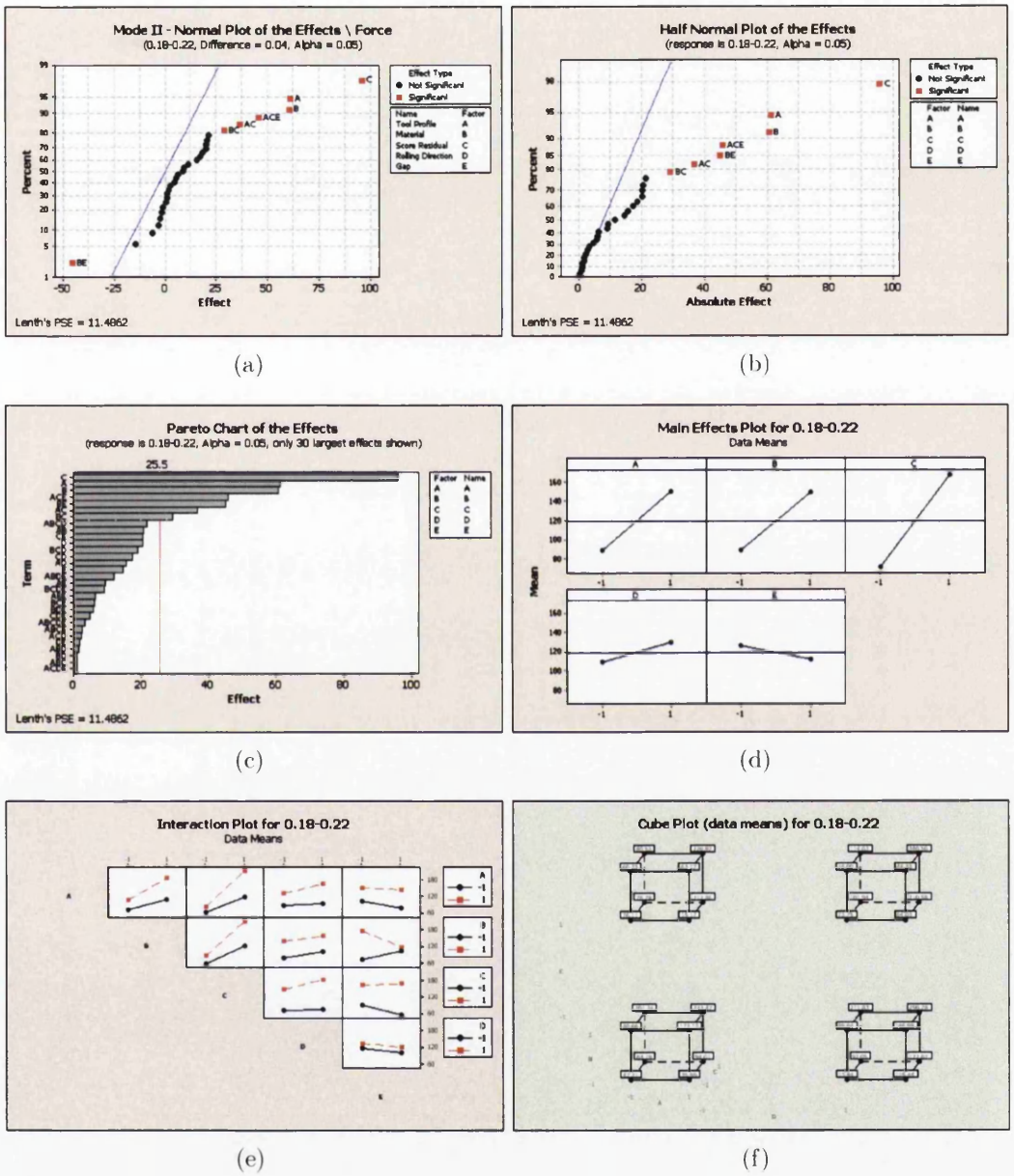

(a) (b)

(c) (d)

(e) (f)

Figure C.9: Mode II Force Results - Minitab^{TM}0.18 - 0.22

Minitab^{TM}: 0.18 - 0.24

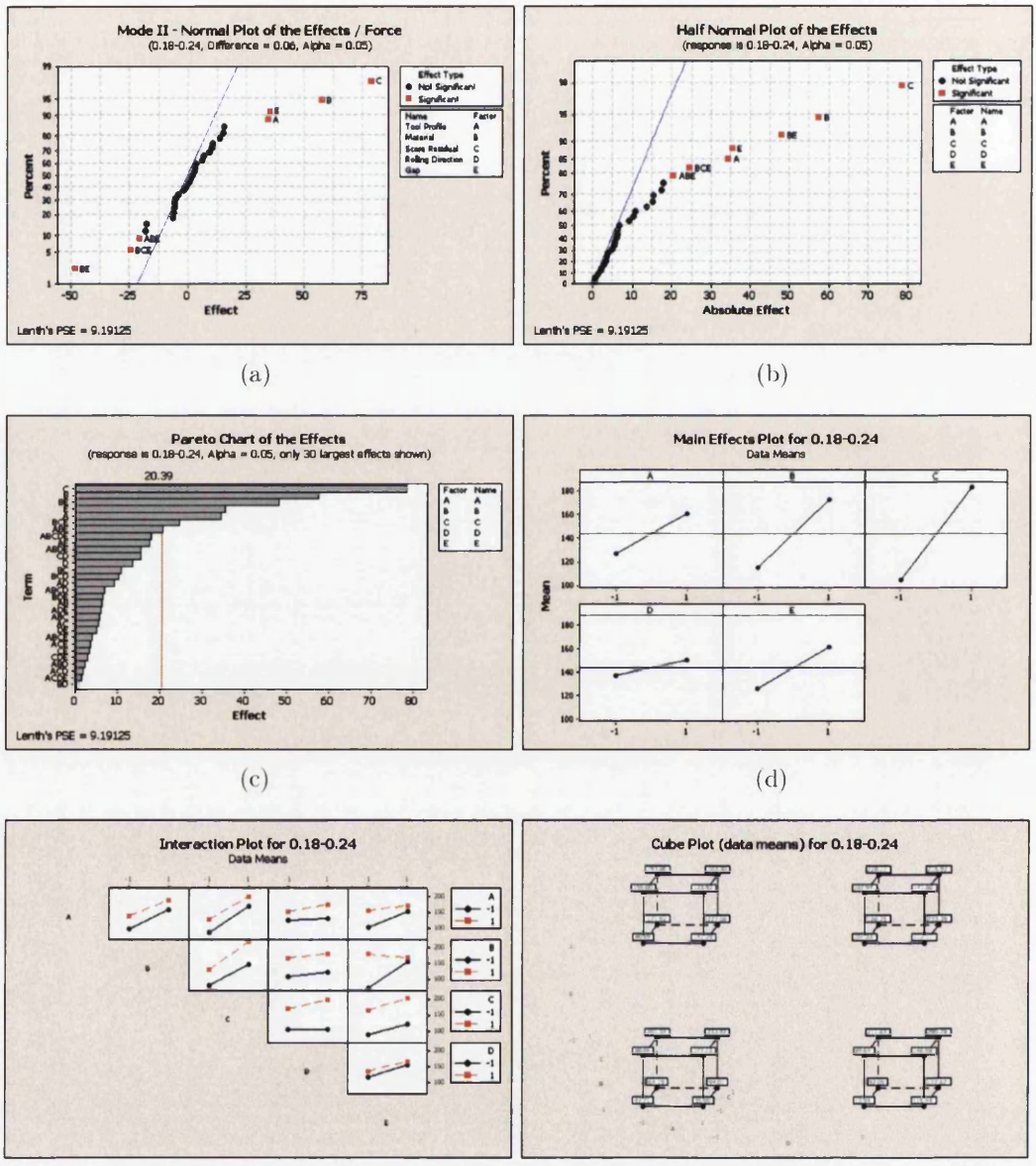

Figure C.10: Mode II Force Results - Minitab^{TM}0.18 - 0.24

Minitab^{TM}: 0.18 - 0.28

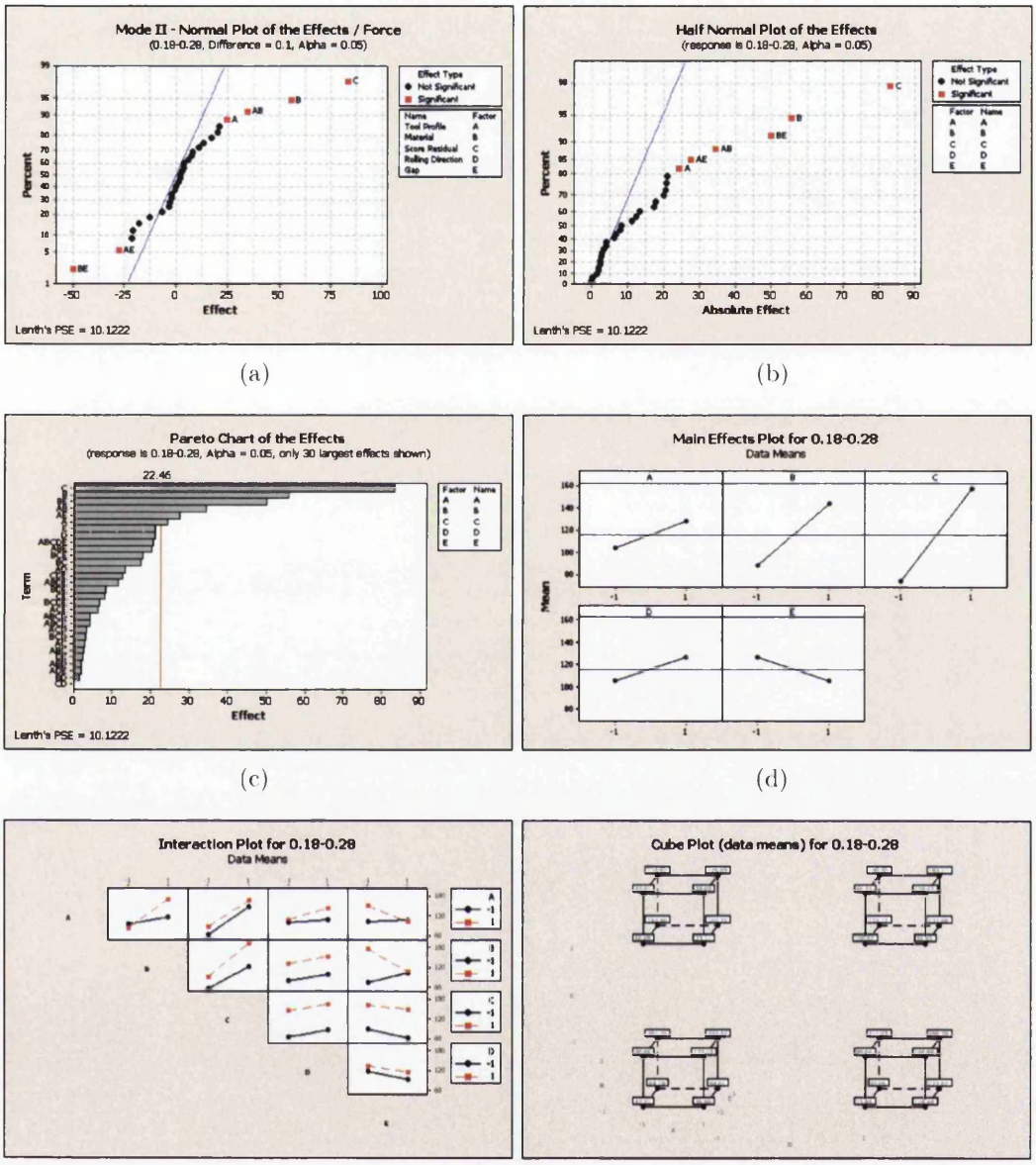

(a) (b)

(c) (d)

(e) (f)

Figure C.11: Mode II Minitab^{TM}0.18 - 0.28

Minitab^{TM}: 0.18 - 0.32

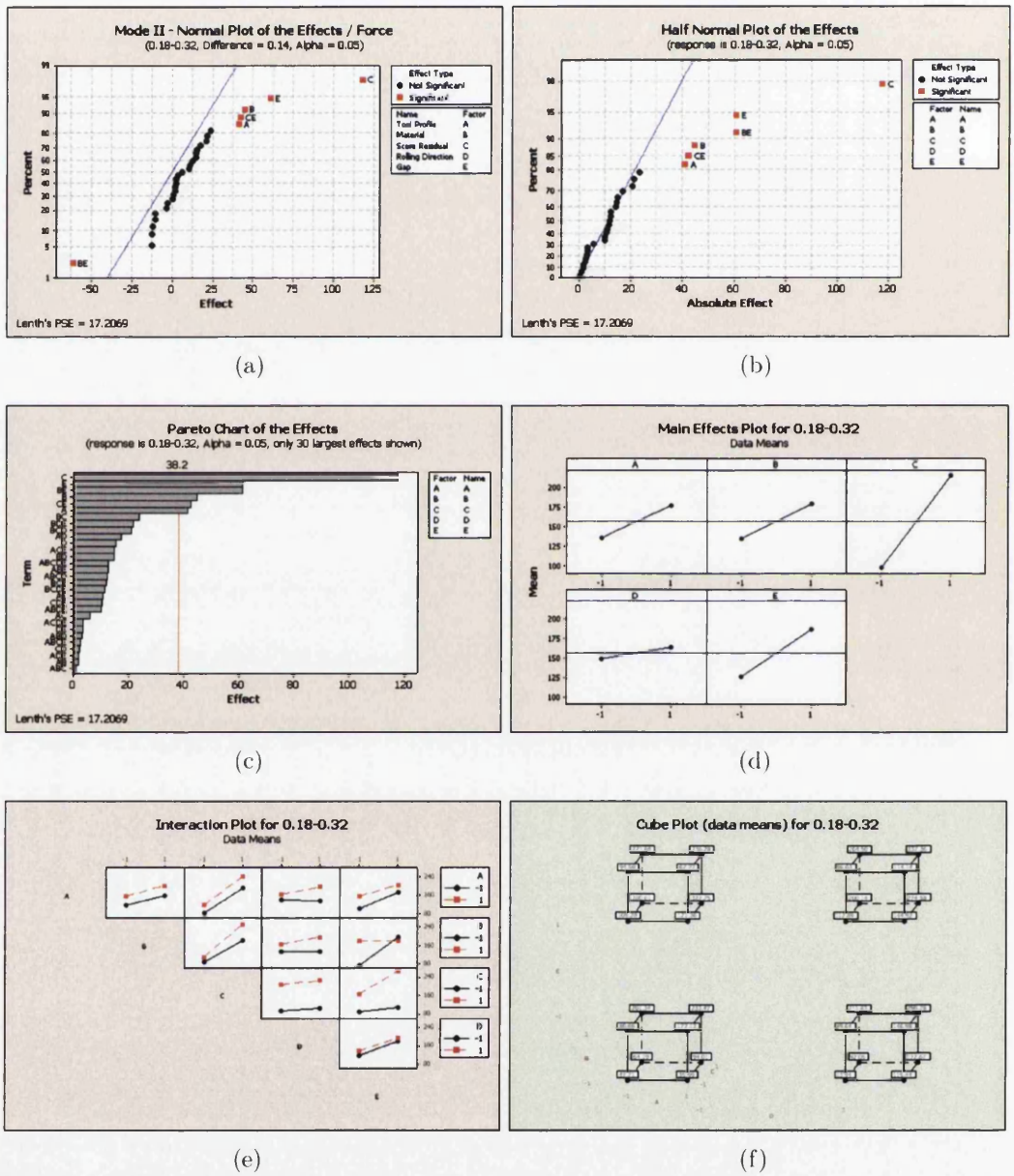

(a) (b)

(c) (d)

(e) (f)

Figure C.12: Mode II Force Results - Minitab^{TM}0.18 - 0.32

Minitab^{TM}: 0.18 - 0.36

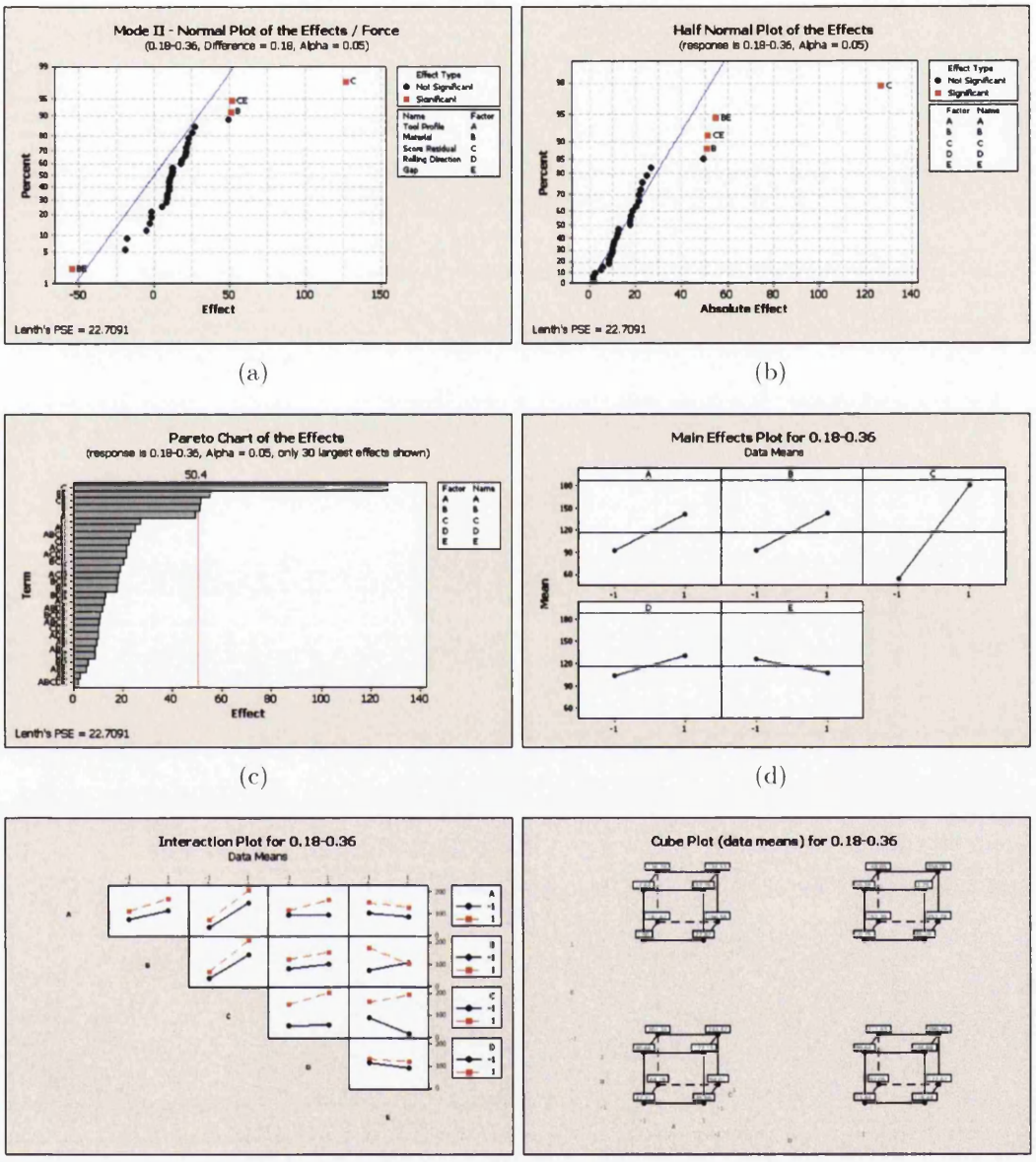

(a) (b)

(c) (d)

(e) (f)

Figure C.13: Mode II Force Results - Minitab^{TM}0.18 - 0.36

Minitab^{TM}: 0.18 - 0.40

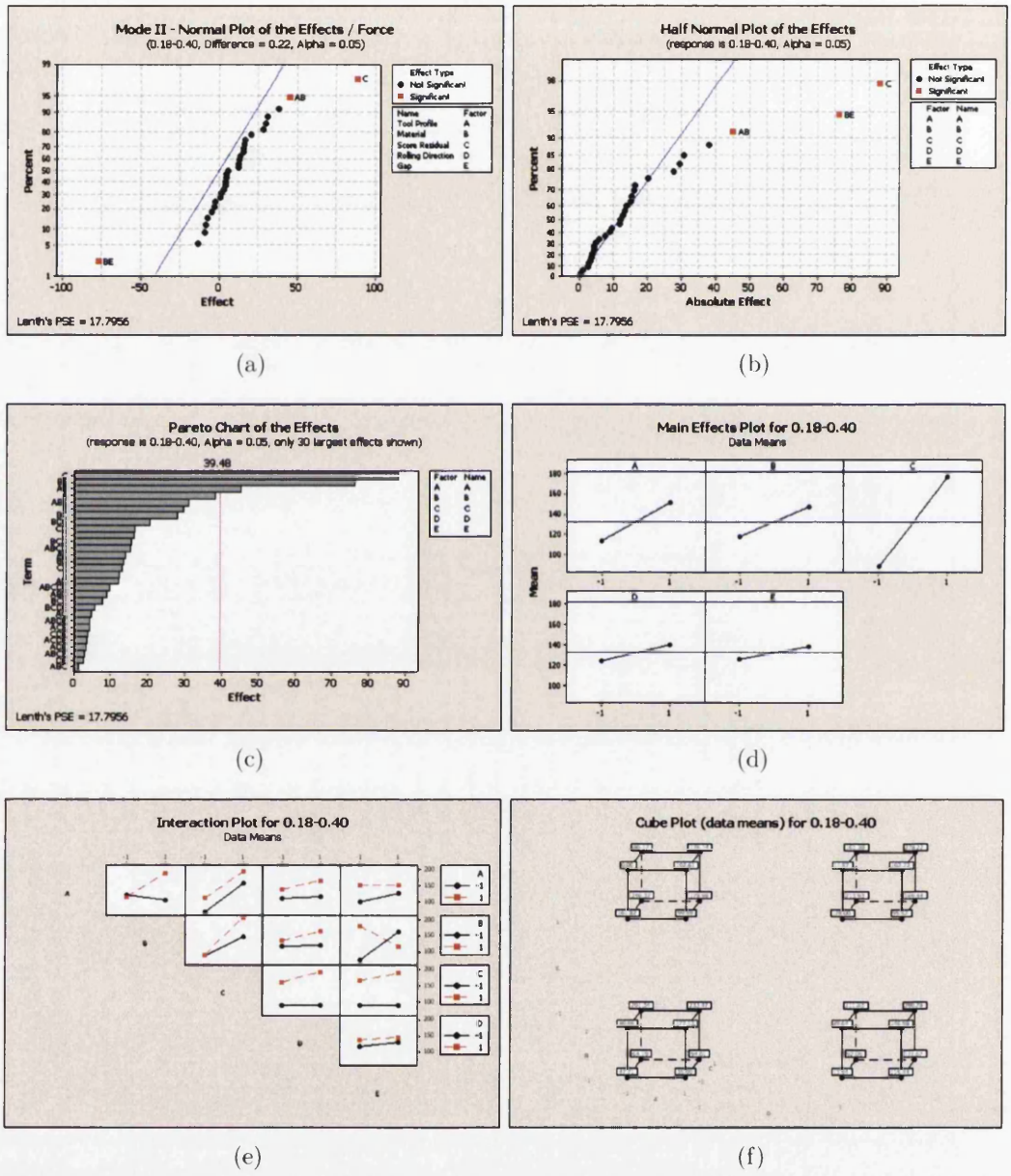

Figure C.14: Mode II Force Results - Minitab^{TM}0.18 - 0.40

Excel^{TM}: 0.18 - 0.40

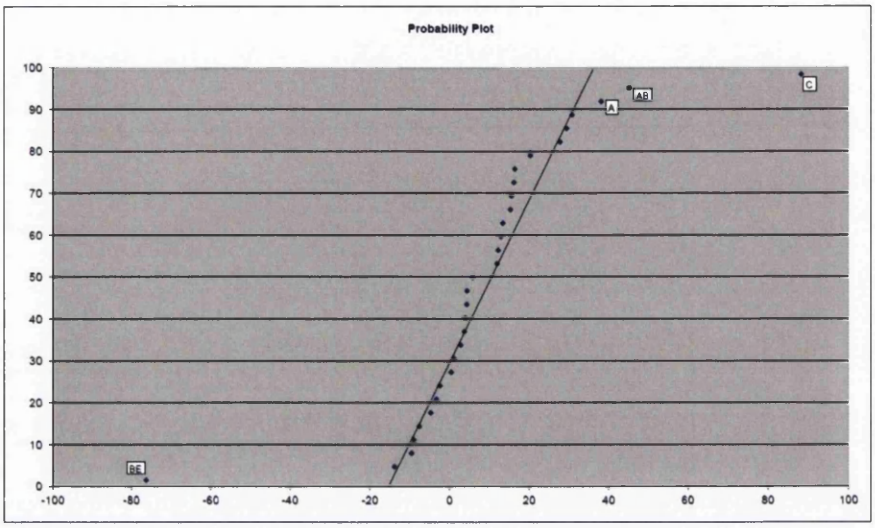

(a)

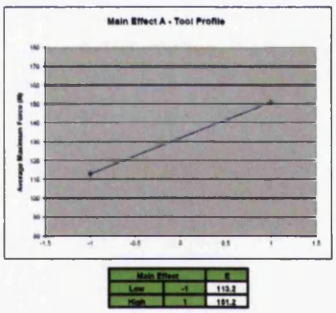

(b)

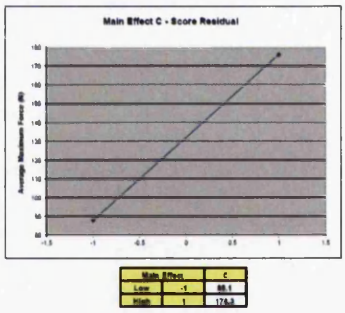

(c)

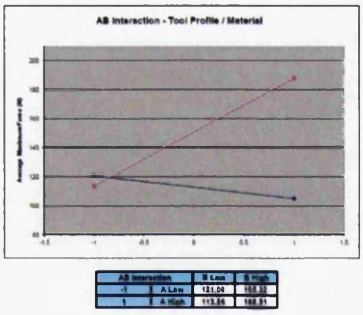

(d)

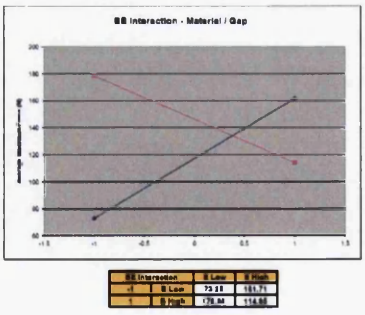

(e)

Figure C.15: Mode II Force Results - Excel^{TM}0.18 - 0.40

C.5 Mode II - Displacement Results

Minitab^{TM}: 0.18 - 0.20

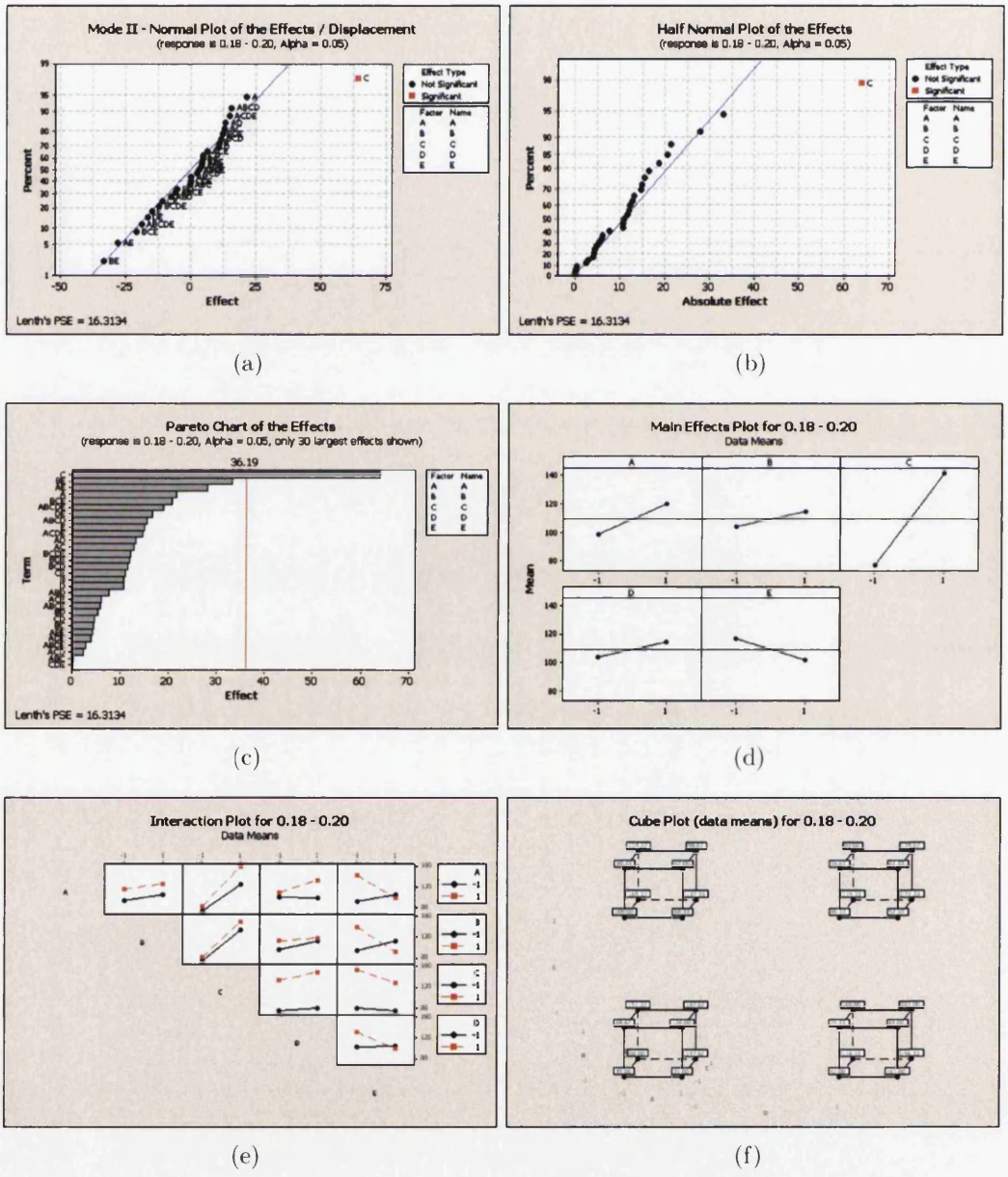

Figure C.16: Mode II Displacement Results - Minitab^{TM}0.18 - 0.20

Excel^{TM}: 0.18 - 0.20

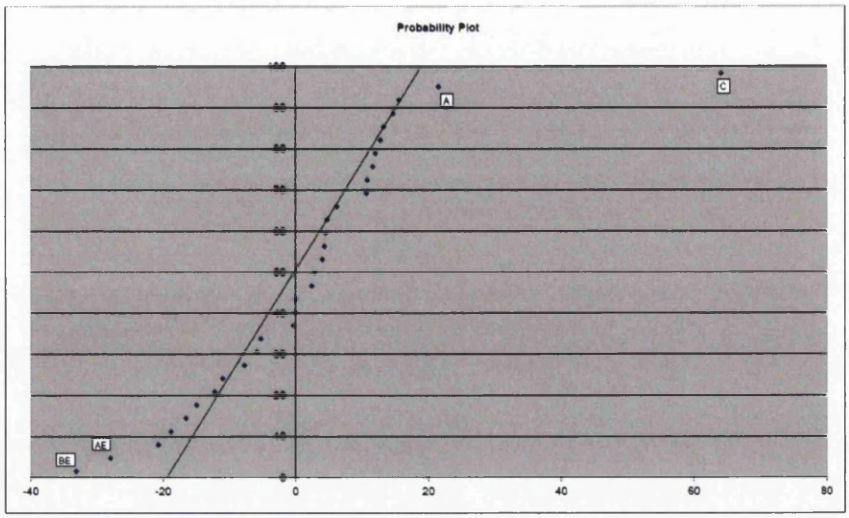

(a)

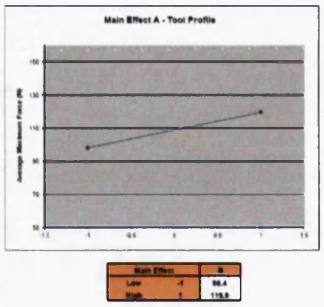

(b)

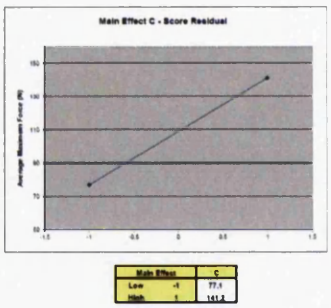

(c)

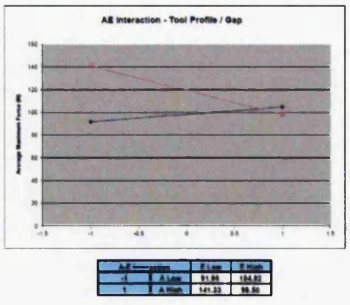

(d)

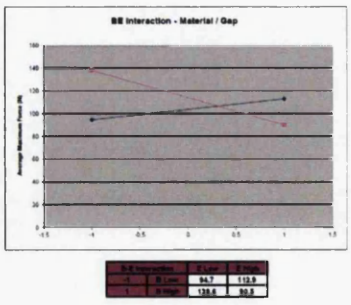

(e)

Figure C.17: Mode II Displacement Results - Excel^{TM}0.18 - 0.20

Minitab^{TM}: 0.18 - 0.22

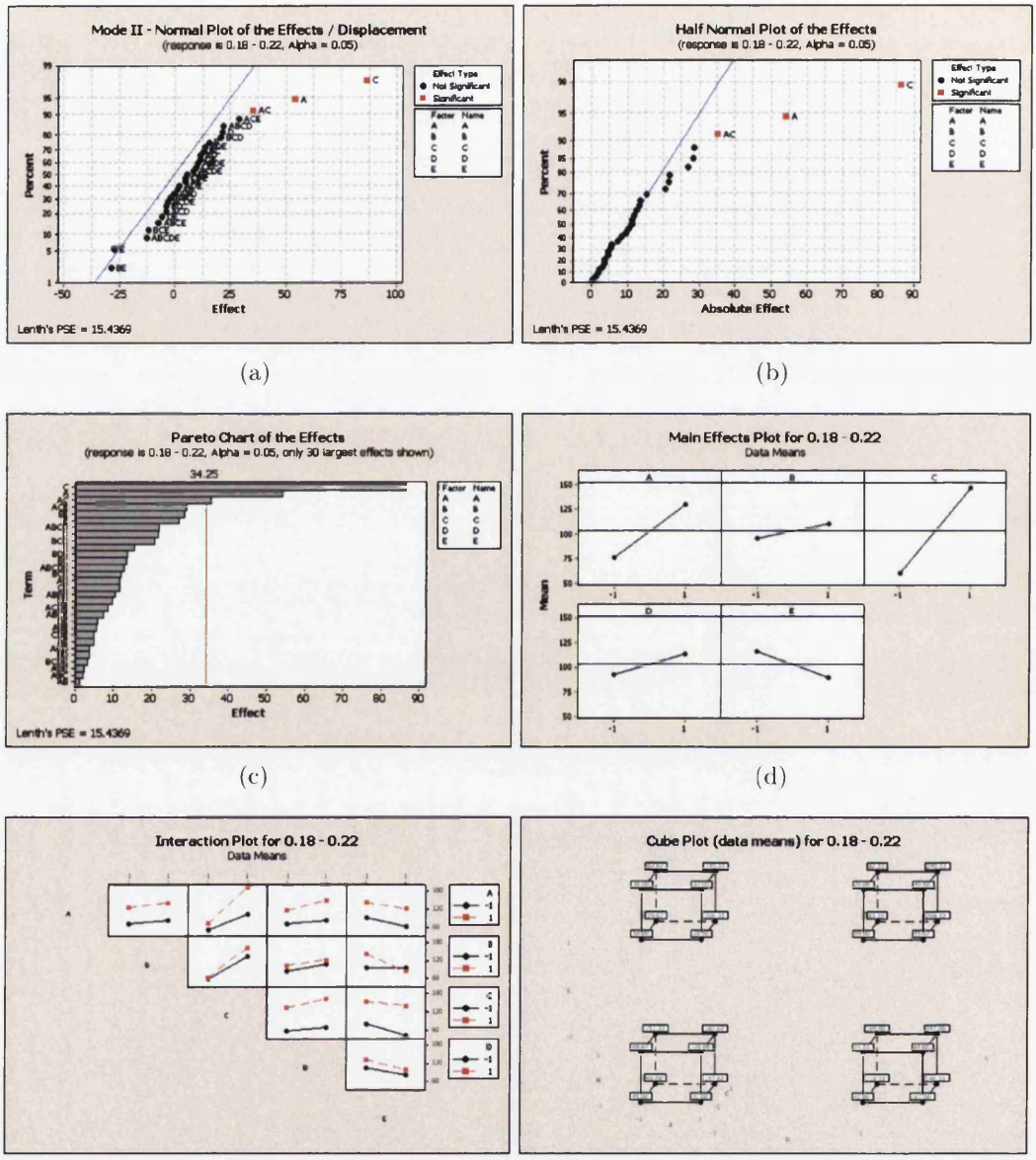

Figure C.18: Mode II Displacement Results - Minitab^{TM}0.18 - 0.22

Minitab^{TM}: 0.18 - 0.24

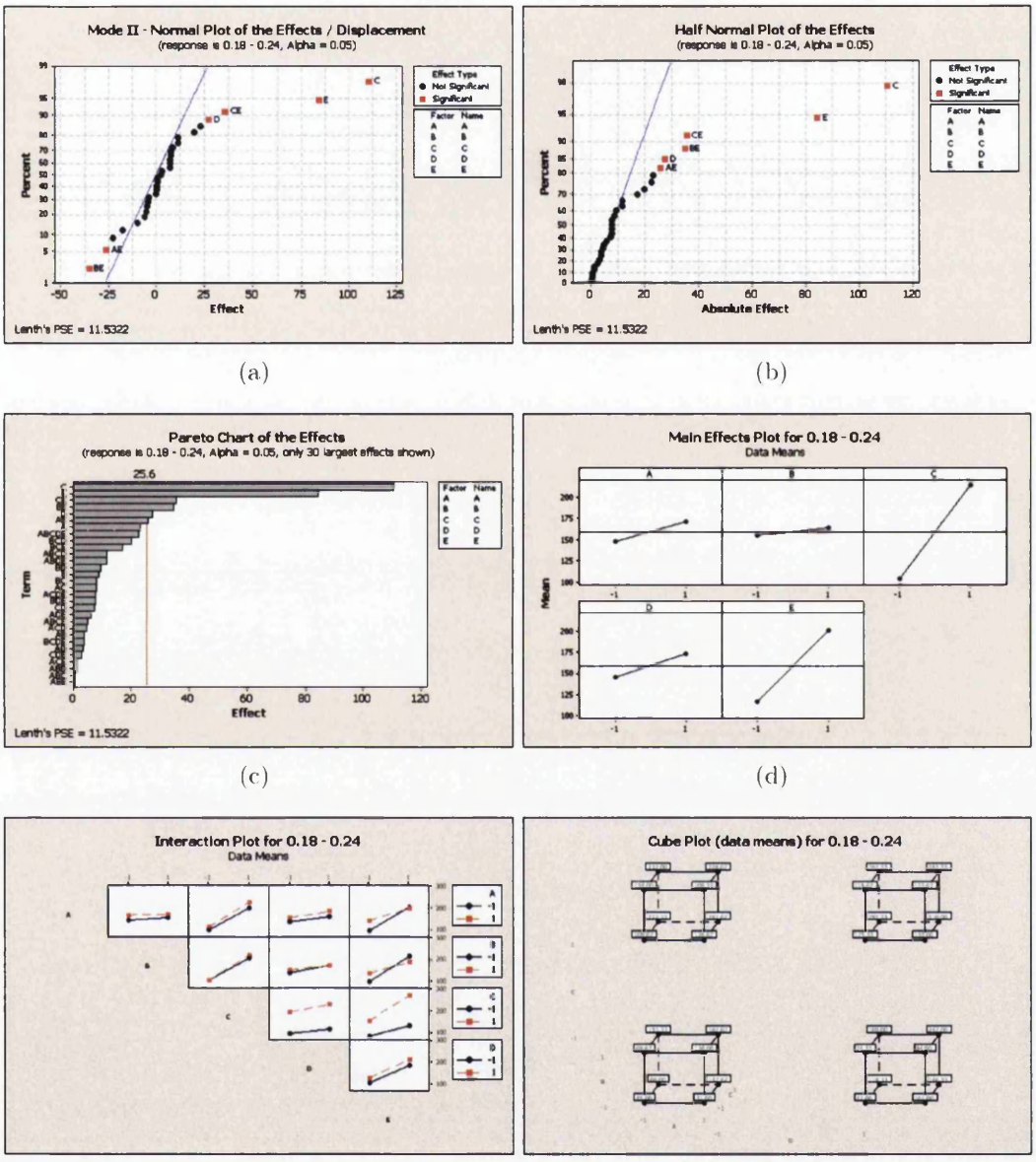

Figure C.19: Mode II Displacement Results - Minitab^{TM}0.18 - 0.24

Minitab^{TM}: 0.18 - 0.28

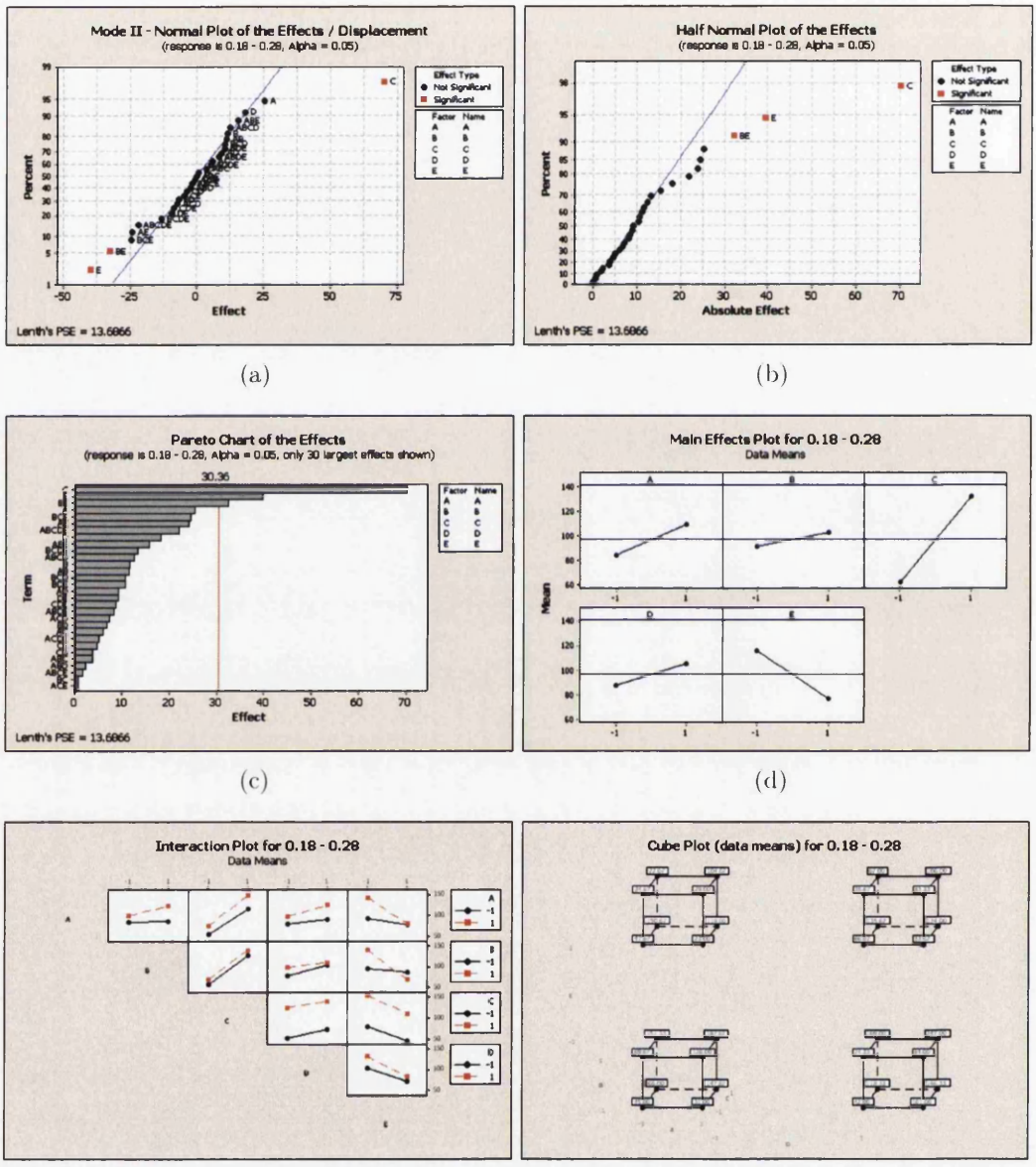

Figure C.20: Mode II Displacement Results - Minitab^{TM}0.18 - 0.28

Minitab^{TM}: 0.18 - 0.32

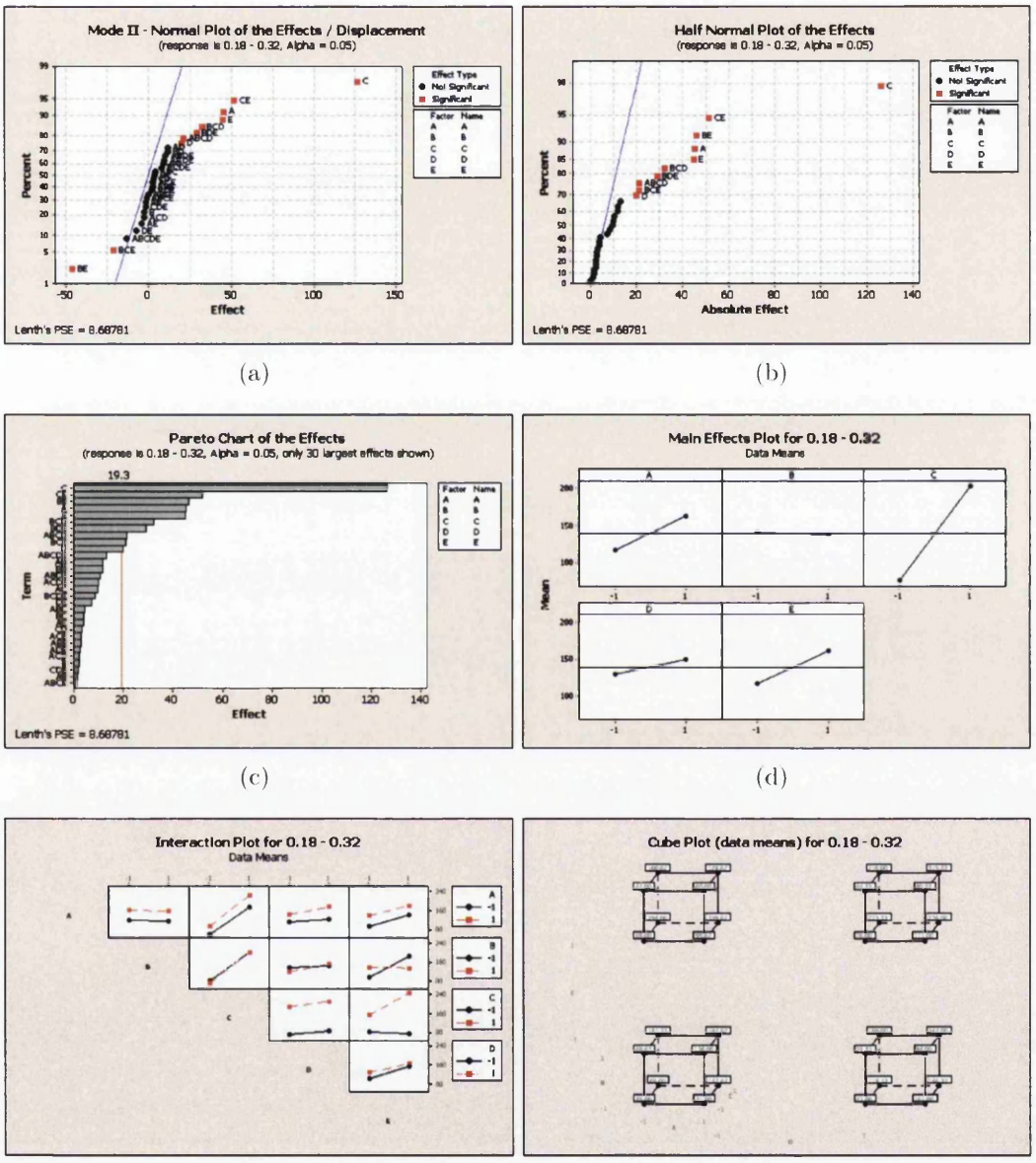

Figure C.21: Mode II Displacement Results - Minitab^{TM}0.18 - 0.32

Minitab^{TM}: 0.18 - 0.36

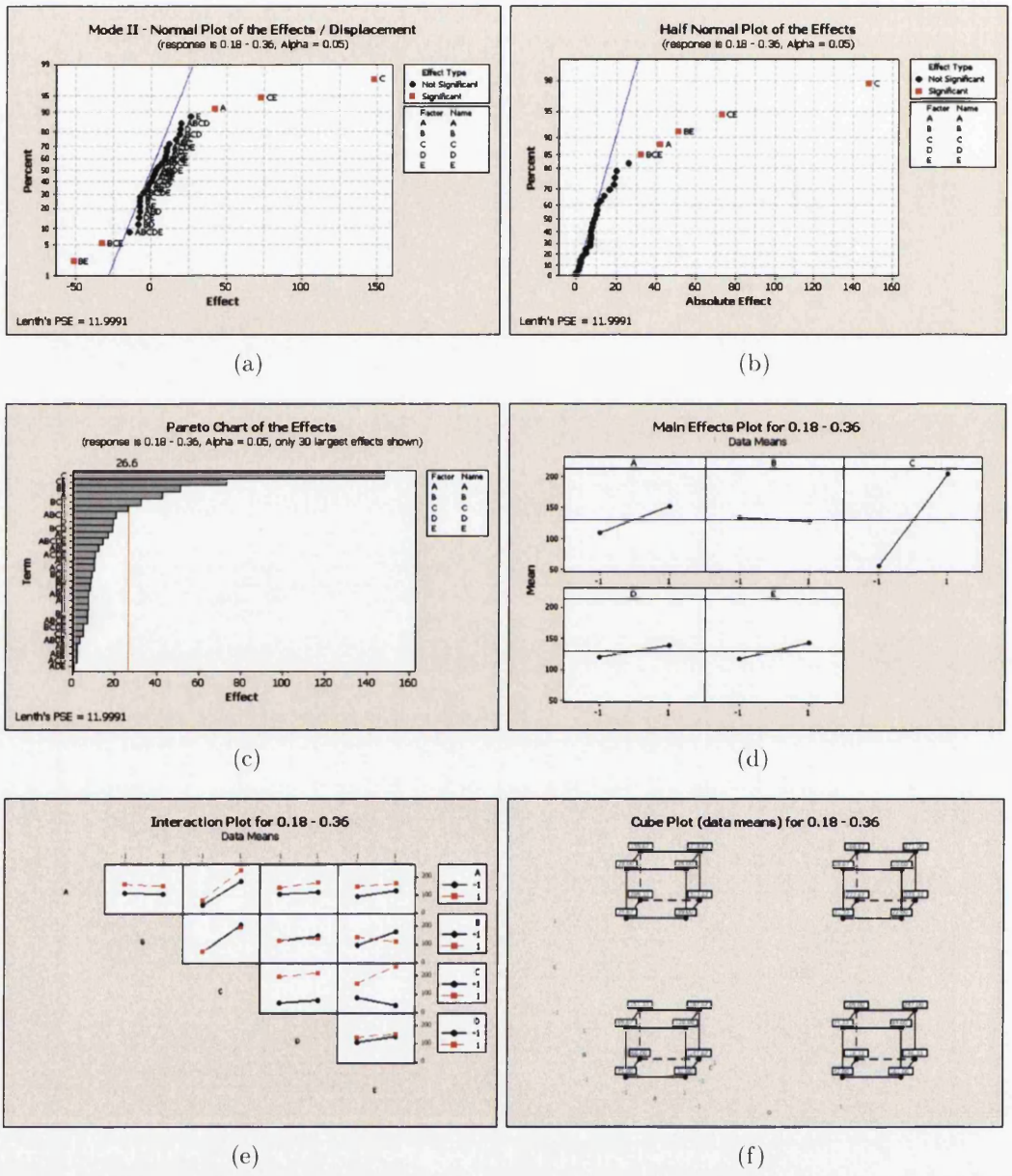

Figure C.22: Mode II Displacement Results - Minitab^{TM}0.18 - 0.36

Minitab^{TM}: 0.18 - 0.40

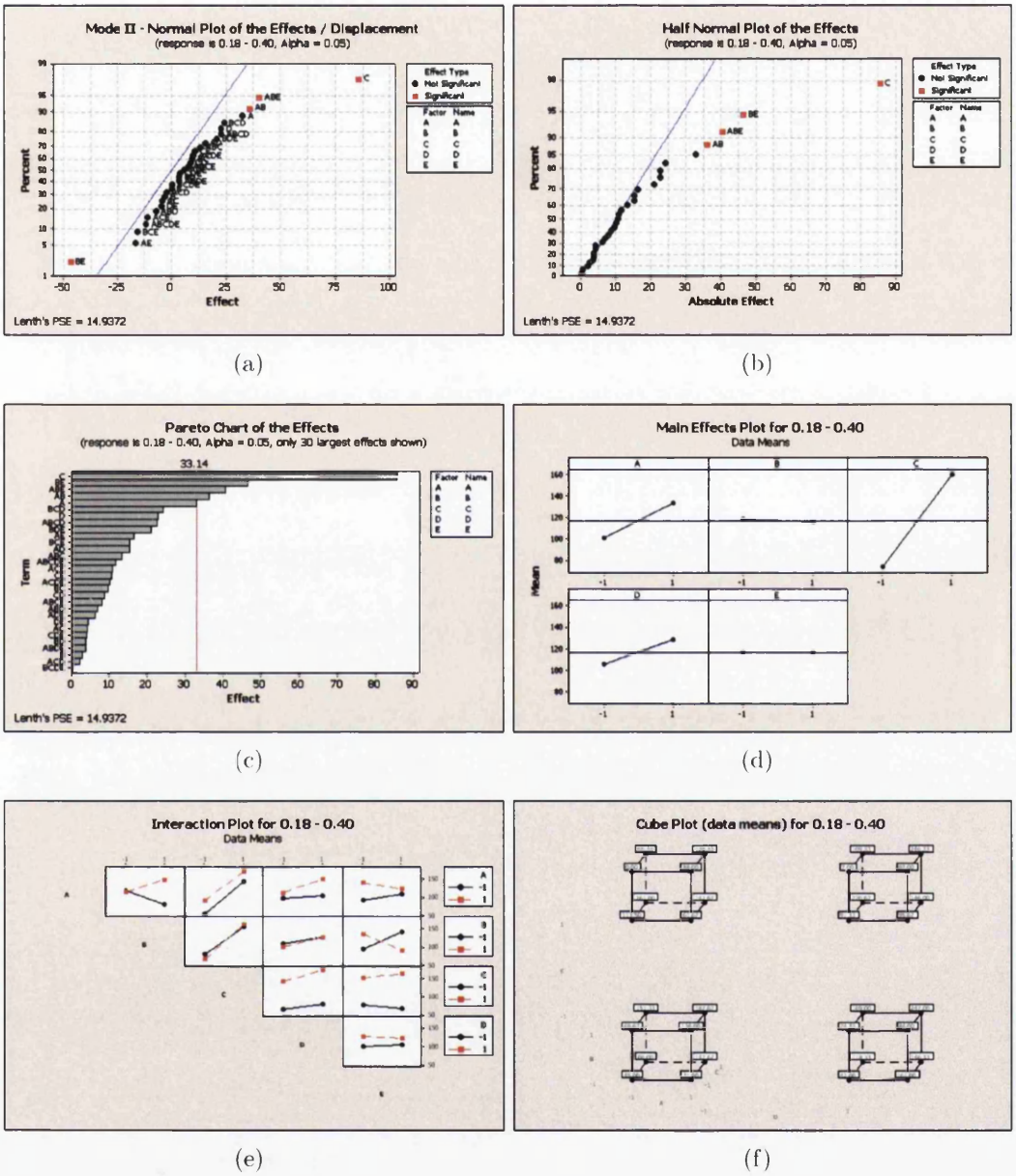

Figure C.23: Mode II Displacement Results - Minitab^{TM}0.18 - 0.40

Excel^{TM}: 0.18 - 0.40

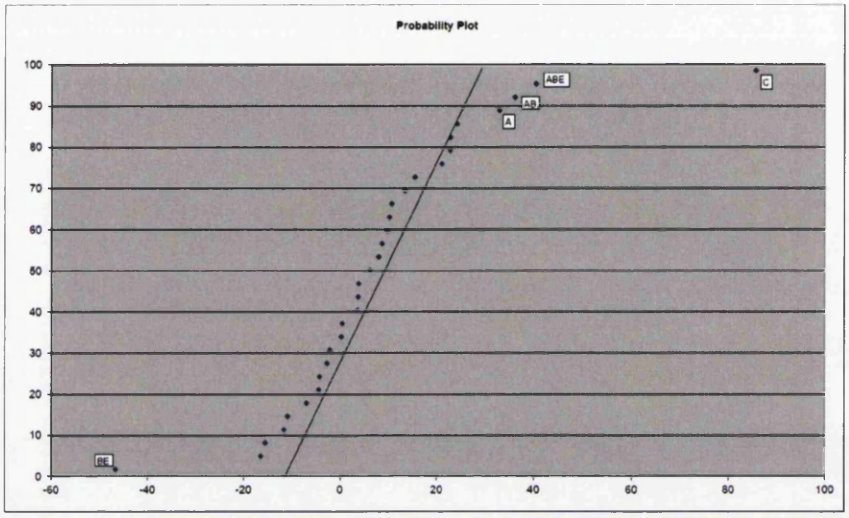

(a)

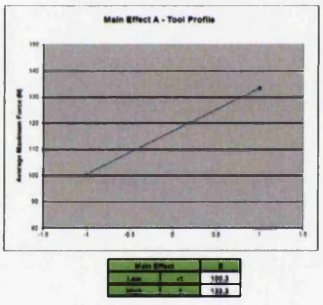

(b)

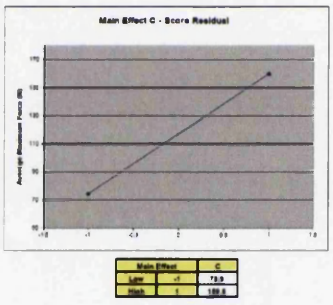

(c)

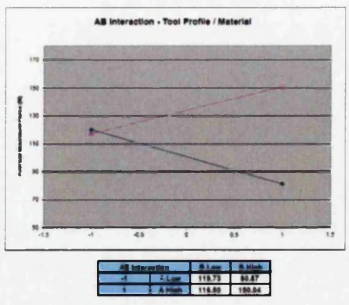

(d)

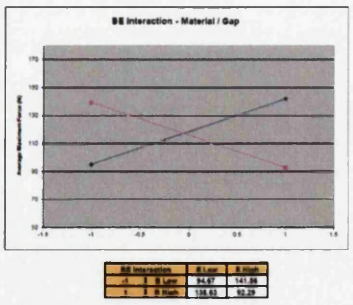

(e)

Figure C.24: Mode II Displacement Results - Excel^{TM}0.18 - 0.40

C.6 Mode III - Force Results

Minitab™

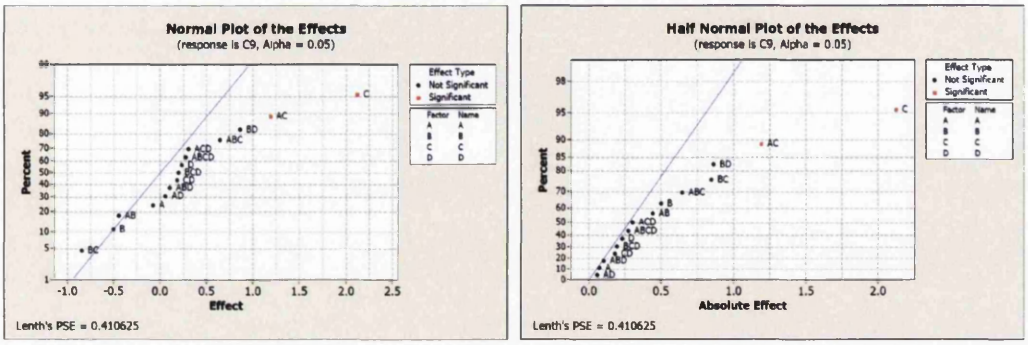

(a)

(b)

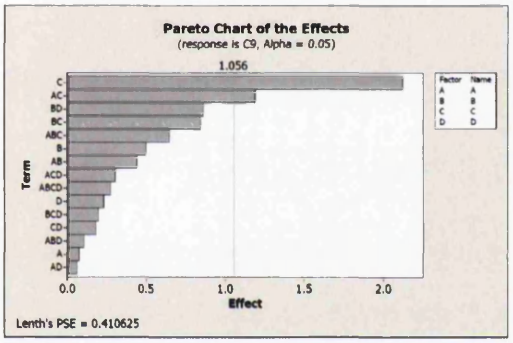

(c)

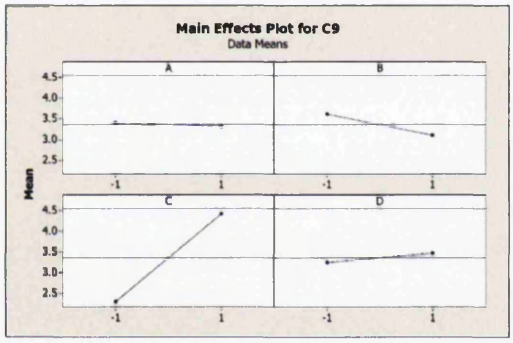

(d)

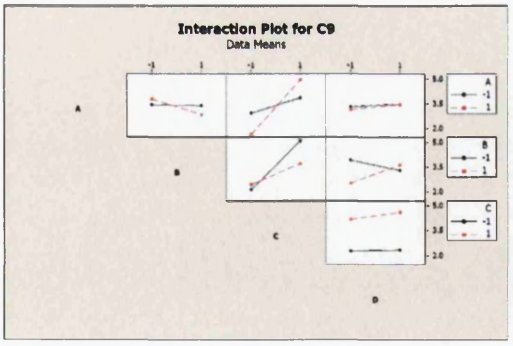

(e)

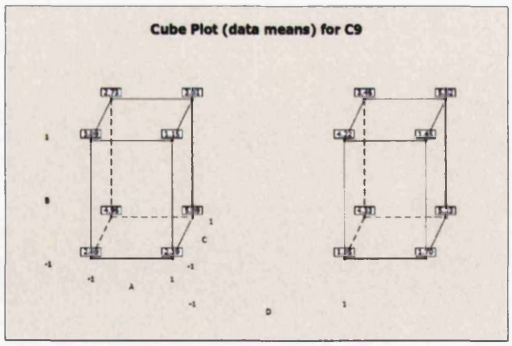

(f)

Figure C.25: Mode III Force Results - Minitab™

Excel^{TM}

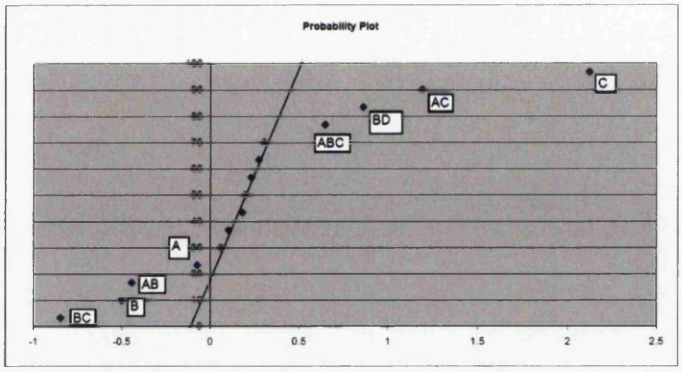

(a)

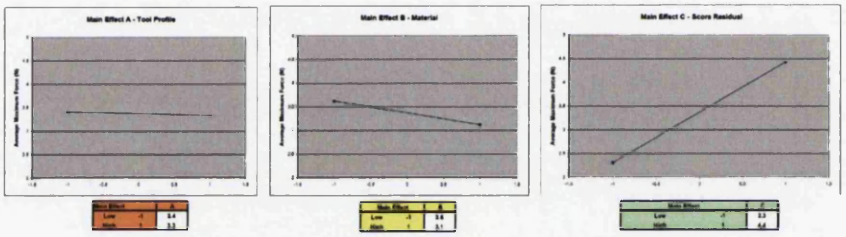

(b) (c) (d)

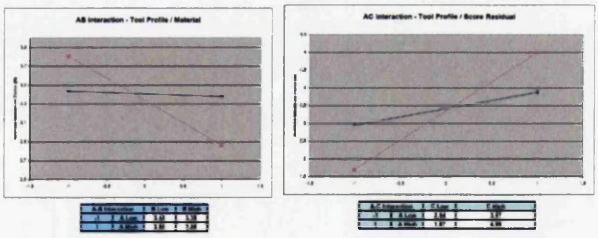

(e) (f)

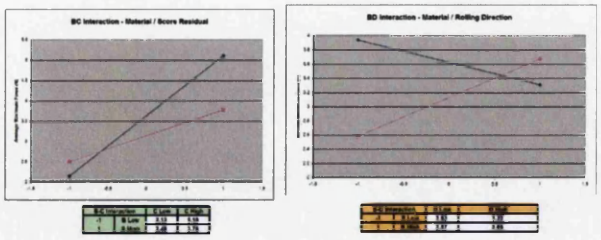

(g) (h)

Figure C.26: Mode III Force Results - Excel^{TM}

Appendix D

Damage Images

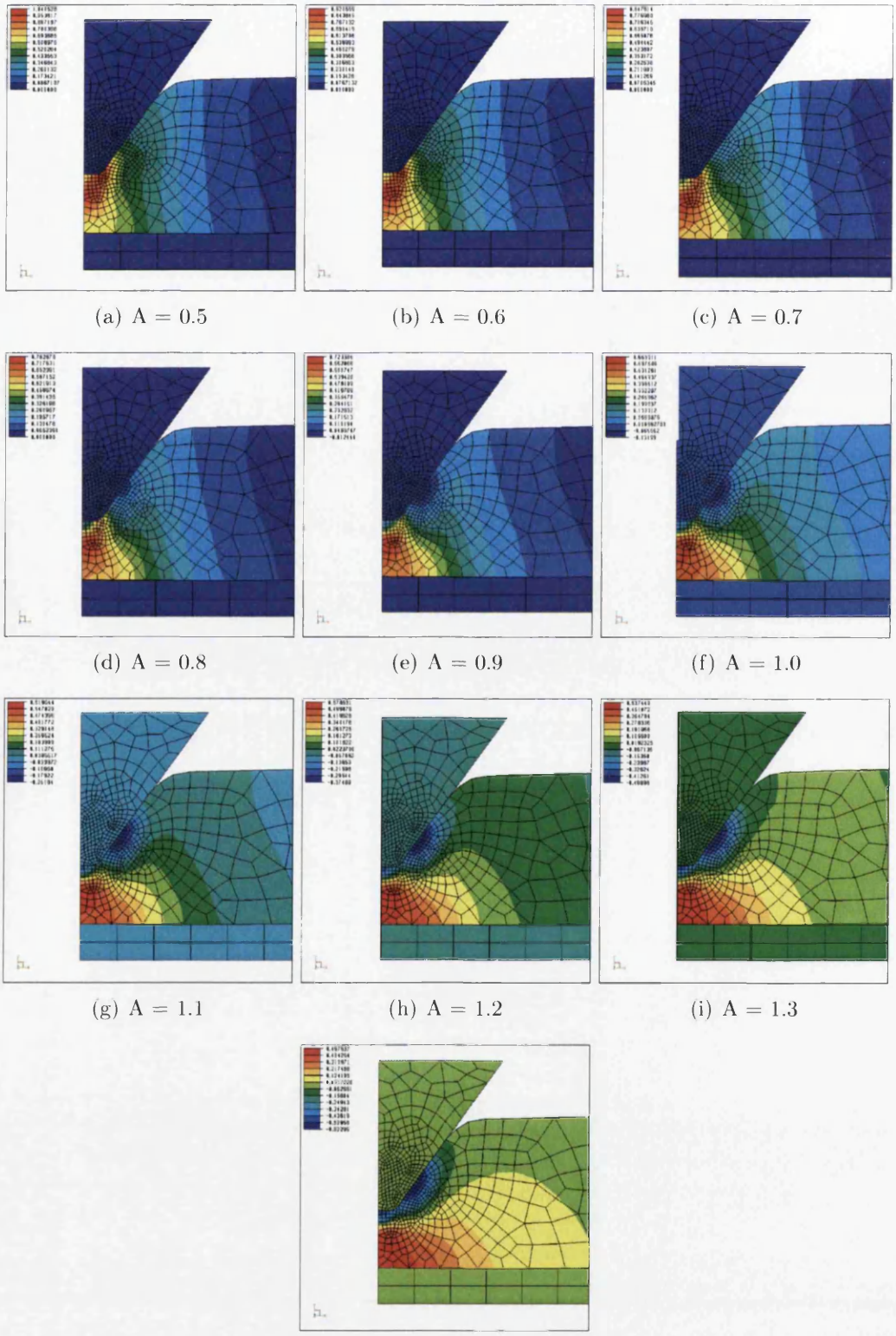

(a) A = 0.5 (b) A = 0.6 (c) A = 0.7

(d) A = 0.8 (e) A = 0.9 (f) A = 1.0

(g) A = 1.1 (h) A = 1.2 (i) A = 1.3

(j) A = 1.4

Figure D.1: PL1 - Oyane Damage with Score Residual at 78.4 μm

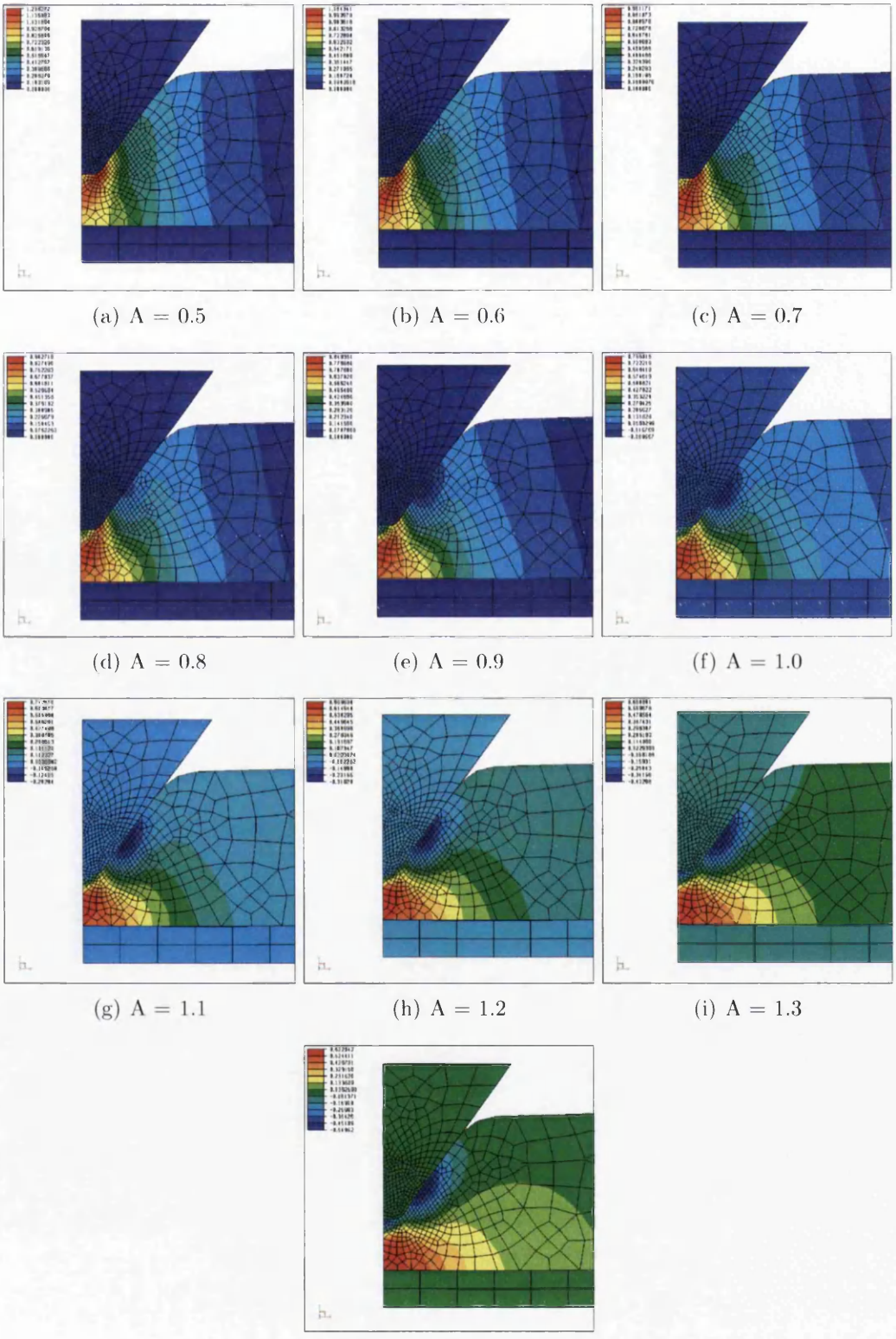

(a) A = 0.5 (b) A = 0.6 (c) A = 0.7

(d) A = 0.8 (e) A = 0.9 (f) A = 1.0

(g) A = 1.1 (h) A = 1.2 (i) A = 1.3

(j) A = 1.4

Figure D.2: PL2 - Oyane Damage with Score Residual at 68 μm

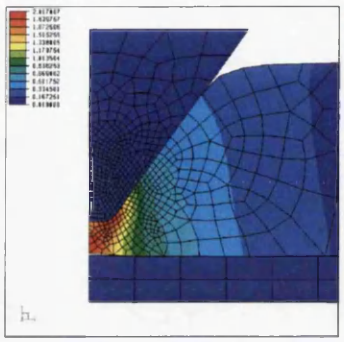

(a) A = 0.5

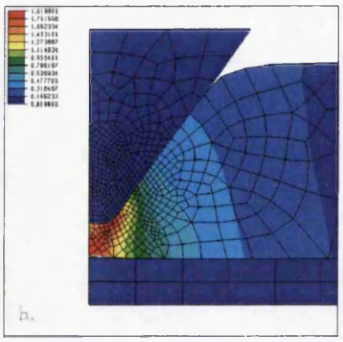

(b) A = 0.6

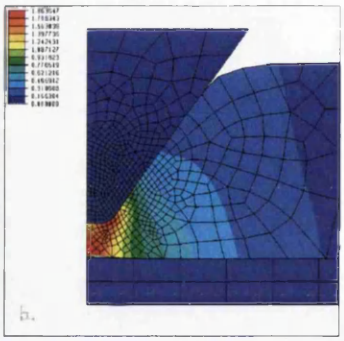

(c) A = 0.7

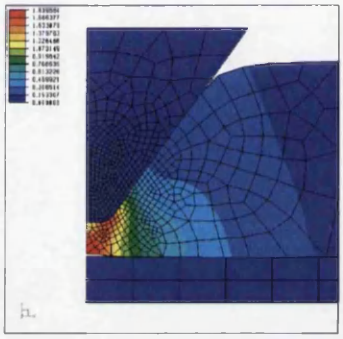

(d) A = 0.8

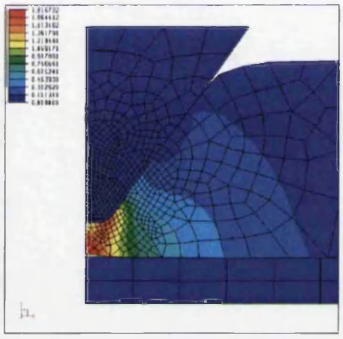

(e) A = 0.9

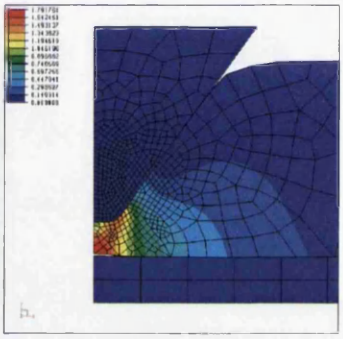

(f) A = 1.0

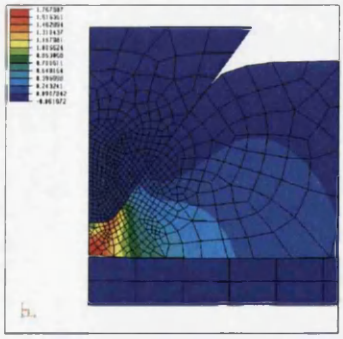

(g) A = 1.1

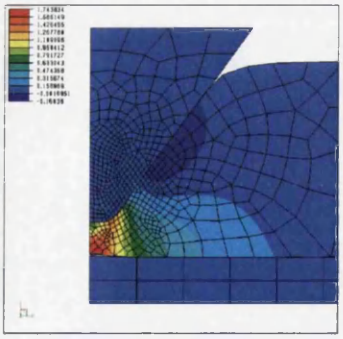

(h) A = 1.2

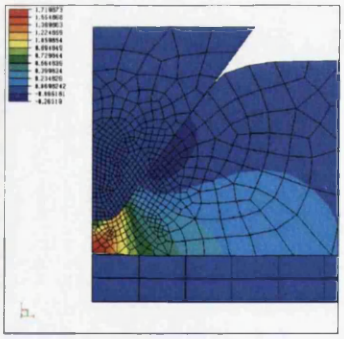

(i) A = 1.3

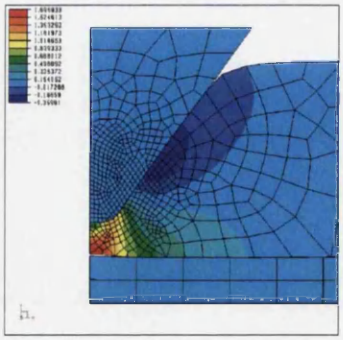

(j) A = 1.4

Figure D.3: PL4 - Oyane Damage with Score Residual at 36.3 μm

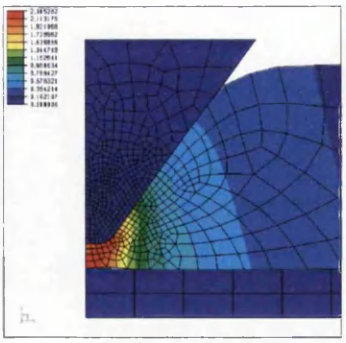

(a) A = 0.5

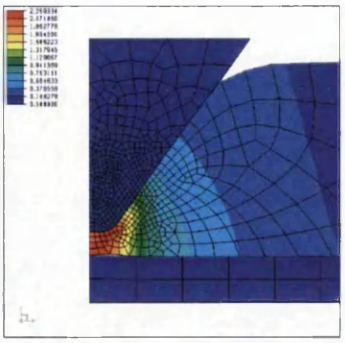

(b) A = 0.6

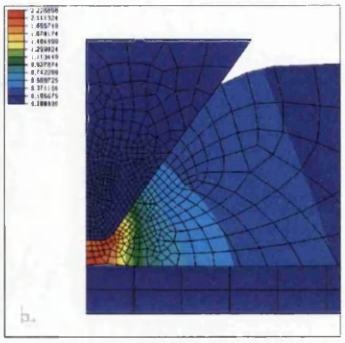

(c) A = 0.7

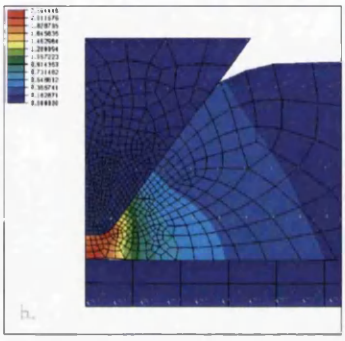

(d) A = 0.8

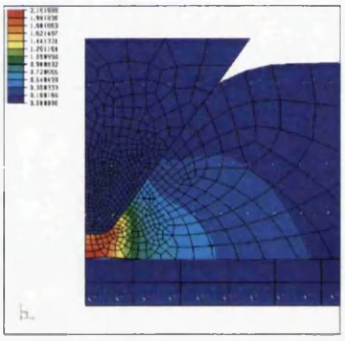

(e) A = 0.9

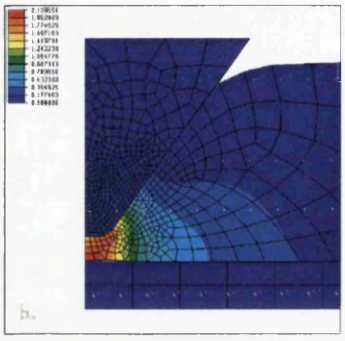

(f) A = 1.0

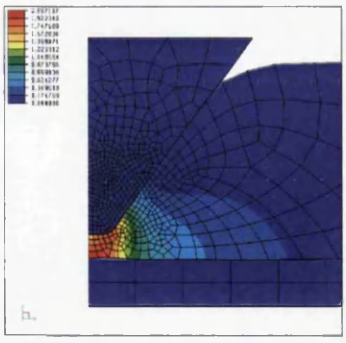

(g) A = 1.1

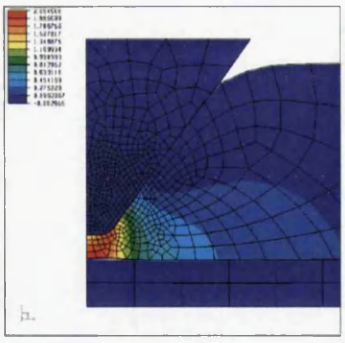

(h) A = 1.2

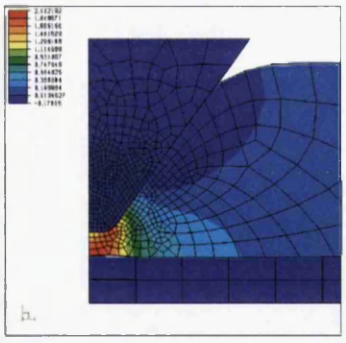

(i) A = 1.3

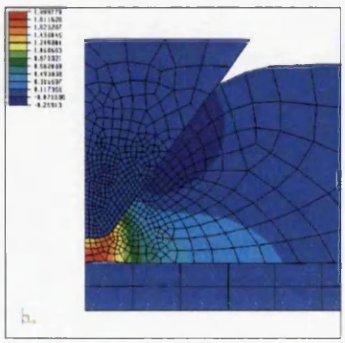

(j) A = 1.4

Figure D.4: PL3 - Oyane Damage with Score Residual at 25.9 μm

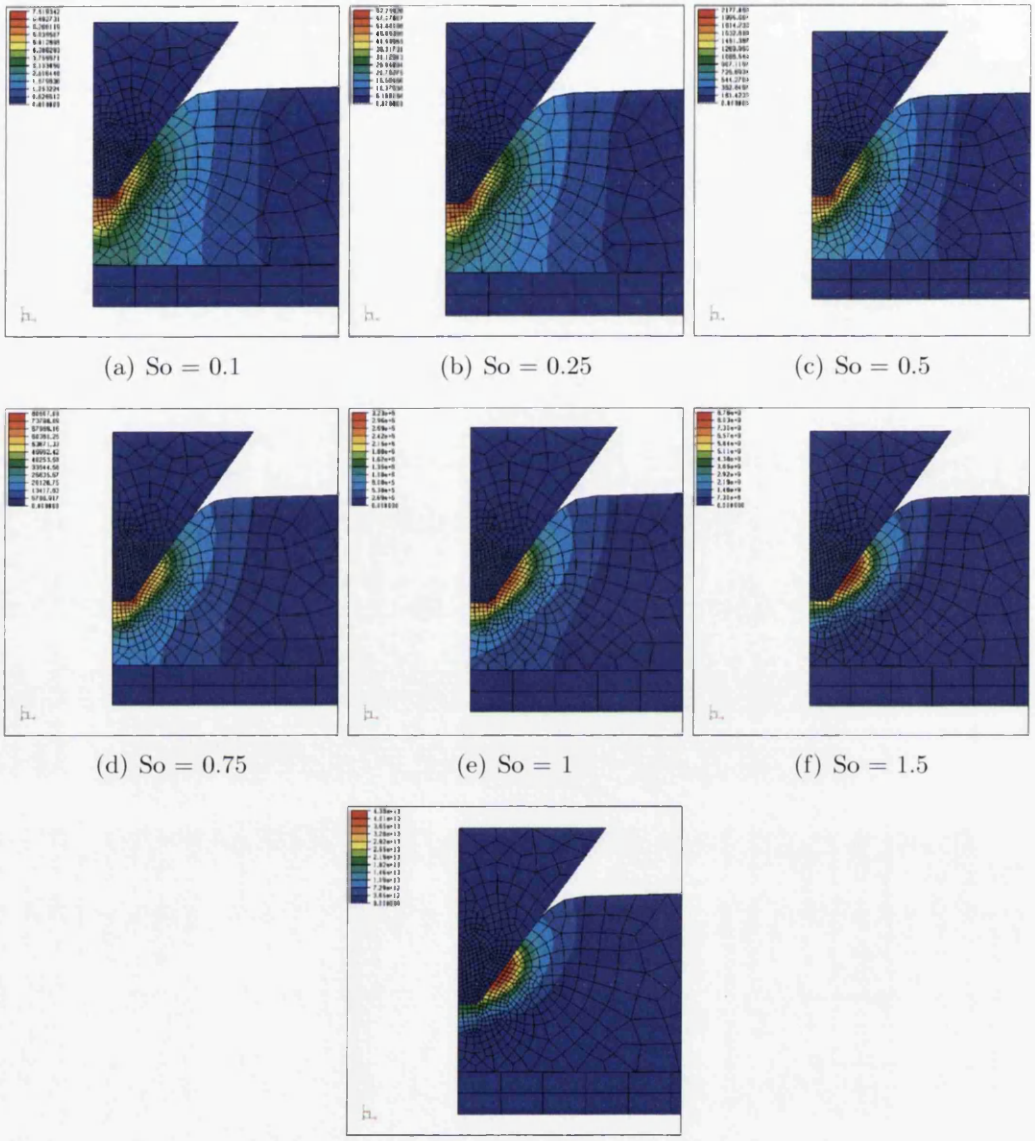

(a) So = 0.1 (b) So = 0.25 (c) So = 0.5

(d) So = 0.75 (e) So = 1 (f) So = 1.5

(g) So = 2

Figure D.5: PL1 - Gen Lemaitre Damage with Score Residual at 78.4 μm

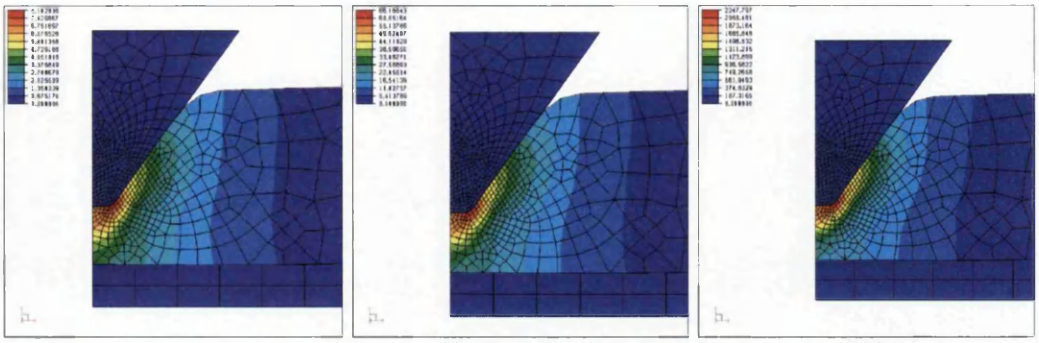

(a) So = 0.1 (b) So = 0.25 (c) So = 0.5

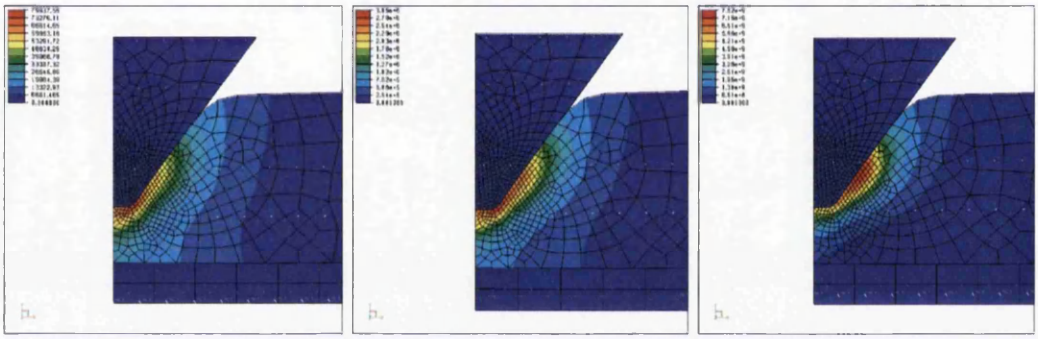

(d) So = 0.75 (e) So = 1 (f) So = 1.5

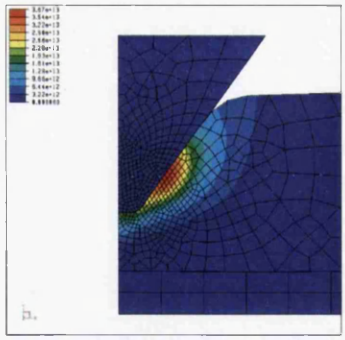

(g) So = 2

Figure D.6: PL2 - Gen Lemaitre Damage with Score Residual at 68 μm

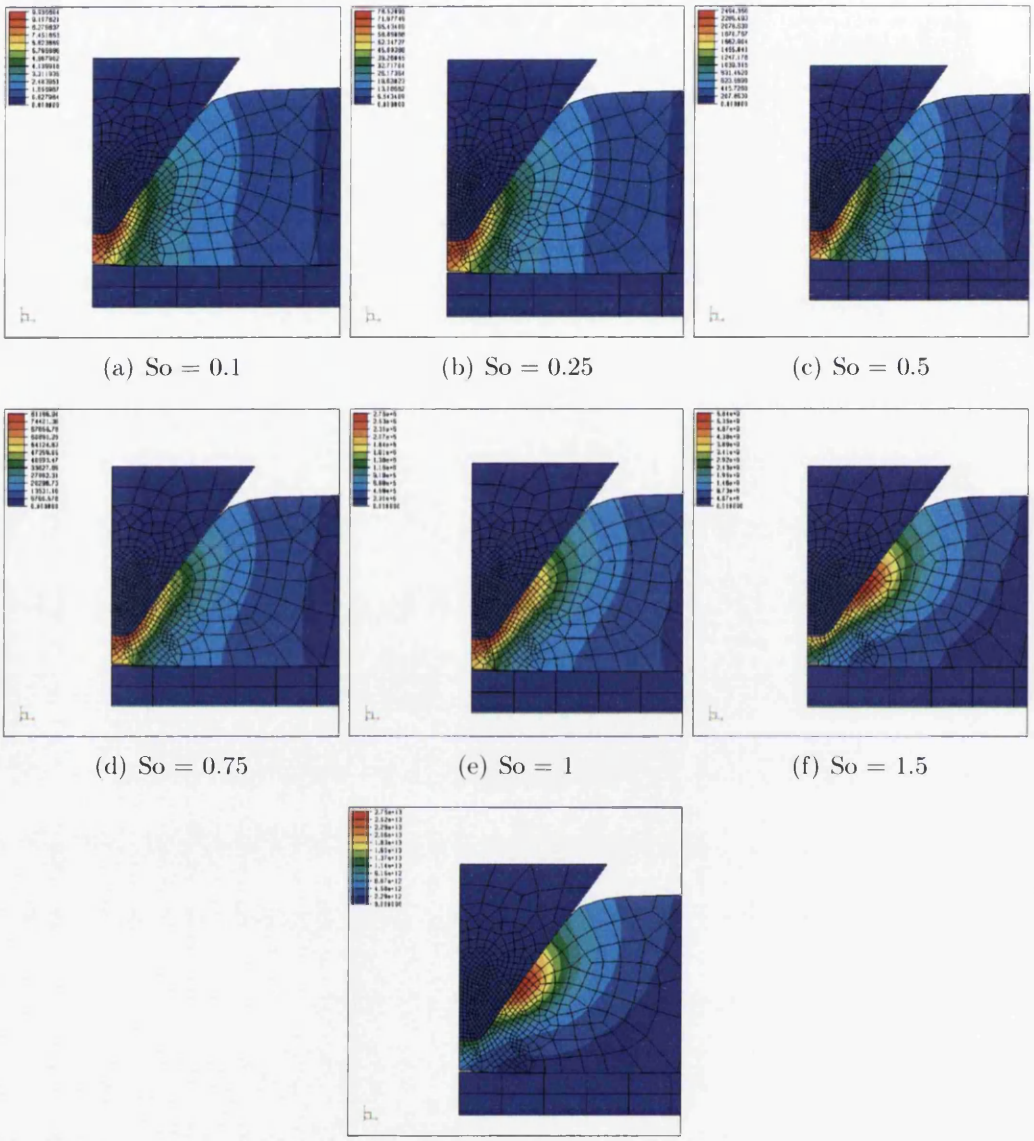

(a) So = 0.1 (b) So = 0.25 (c) So = 0.5

(d) So = 0.75 (e) So = 1 (f) So = 1.5

(g) So = 2

Figure D.7: PL4 - Gen Lemaitre Damage with Score Residual at 36.3 μm

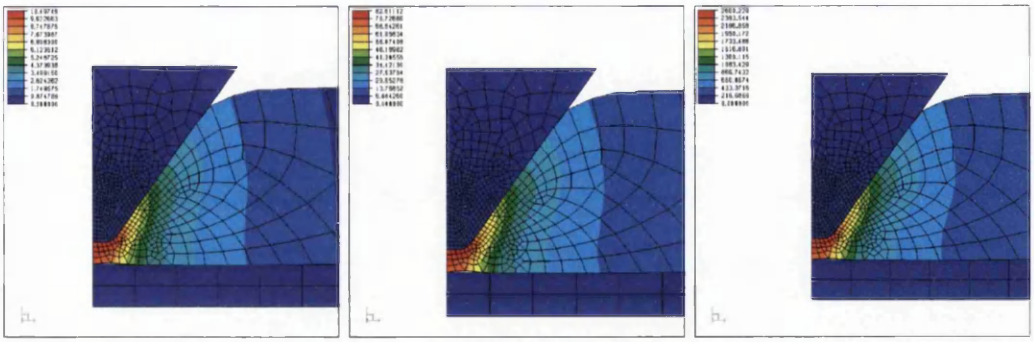

(a) So = 0.1 (b) So = 0.25 (c) So = 0.5

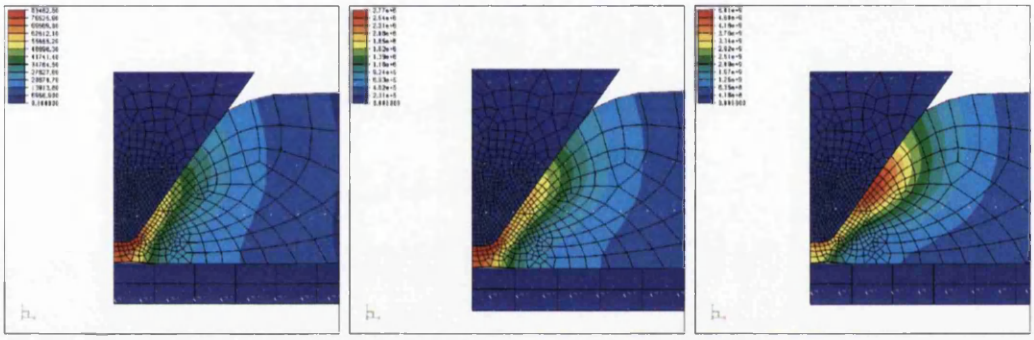

(d) So = 0.75 (e) So = 1 (f) So = 1.5

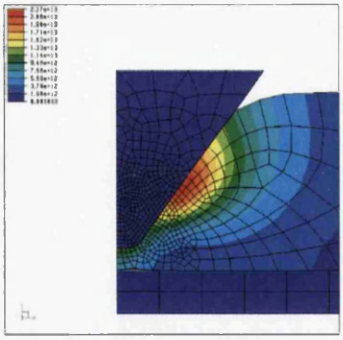

(g) So = 2

Figure D.8: PL3 - Gen Lemaitre Damage with Score Residual at 25.9 μm

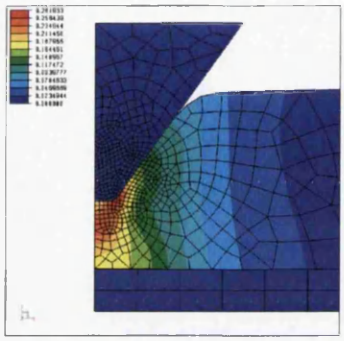

(a) SC = 78.4 μm : A = 0.5

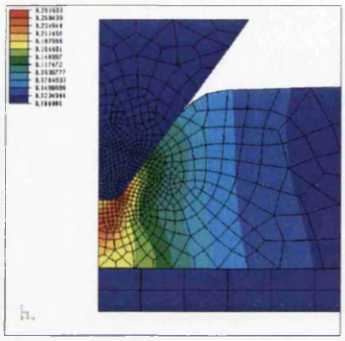

(b) SC = 78.4 μm : A = 1.4

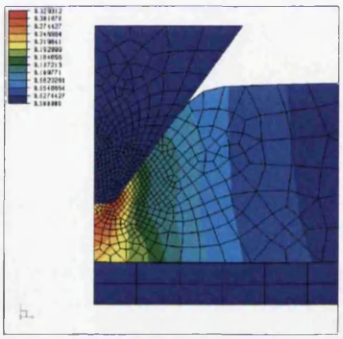

(c) SC = 68 μm : A = 0.5

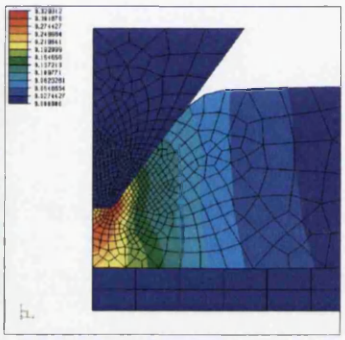

(d) SC = 68 μm : A = 1.4

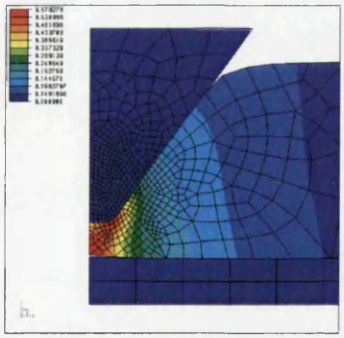

(e) SC = 36.3 μm : A = 0.5

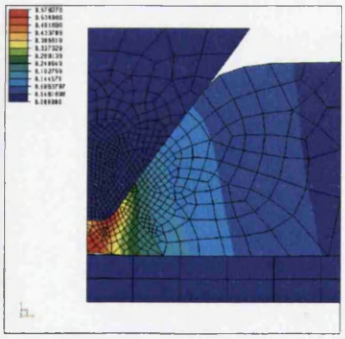

(f) SC = 36.3 μm : A = 1.4

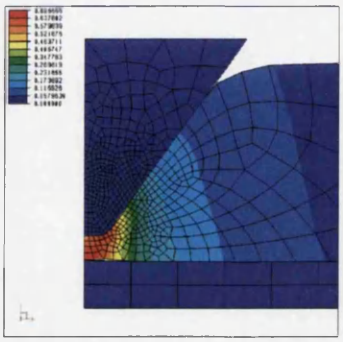

(g) SC = 25.9 μm : A = 0.5

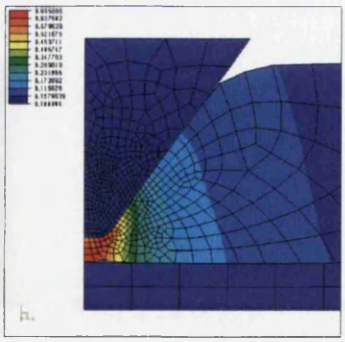

(h) SC = 25.9 μm : A = 1.4

Figure D.9: Rice & Tracy Damage

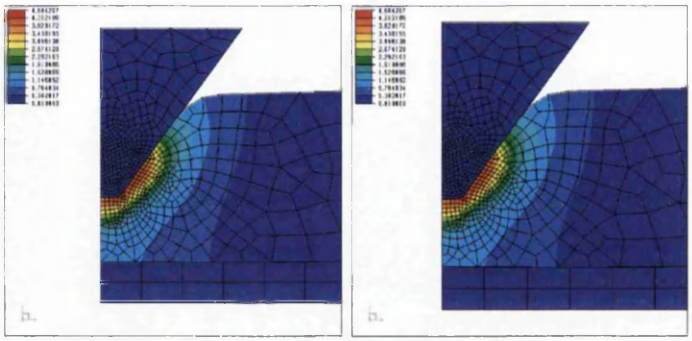

(a) SC = 78.4 μm : A = 0.5 (b) SC = 78.4 μm : A = 1.4

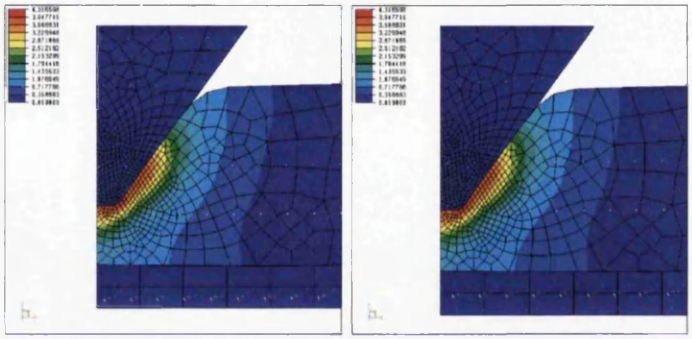

(c) SC = 68 μm : A = 0.5 (d) SC = 68 μm : A = 1.4

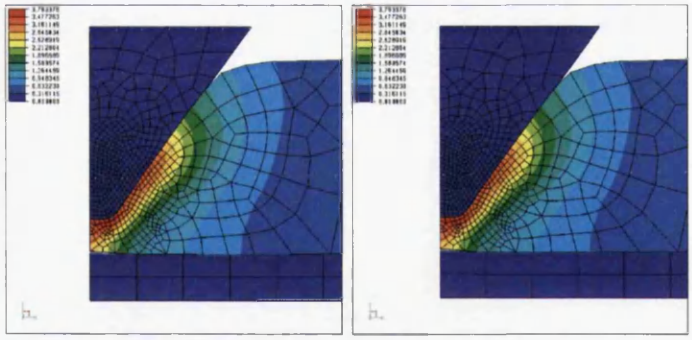

(e) SC = 36.3 μm : A = 0.5 (f) SC = 36.3 μm : A = 1.4

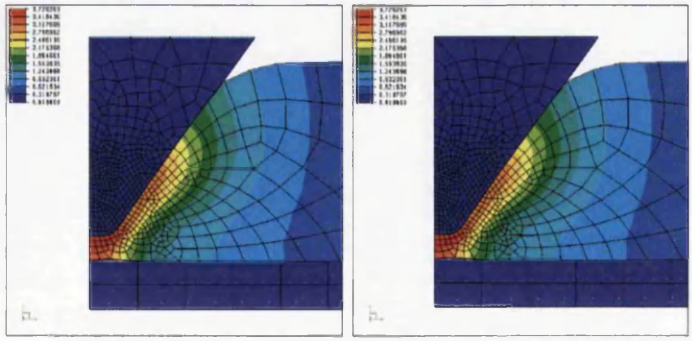

(g) SC = 25.9 μm : A = 0.5 (h) SC = 25.9 μm : A = 1.4

Figure D.10: Lemaitre Damage

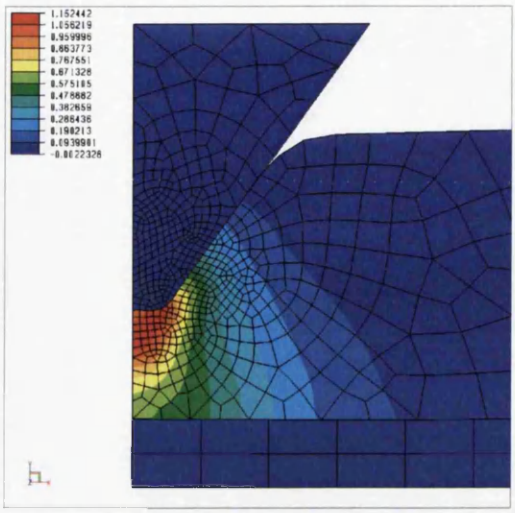

(a) SC = 78.4 μm : Strain XX

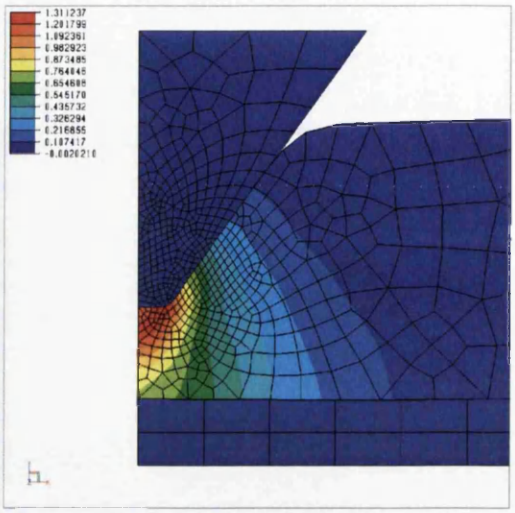

(b) SC = 68 μm : Strain XX

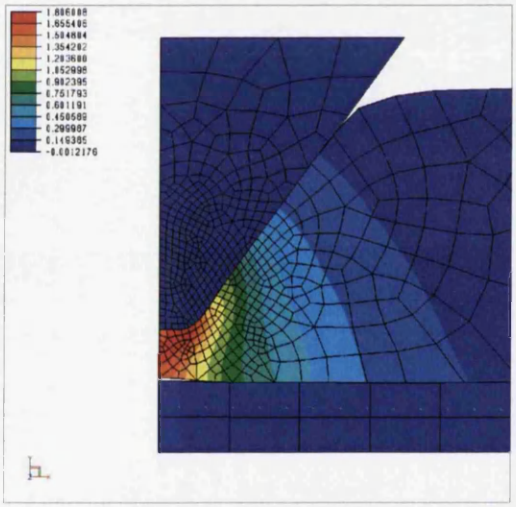

(c) SC = 36.3 μm : Strain XX

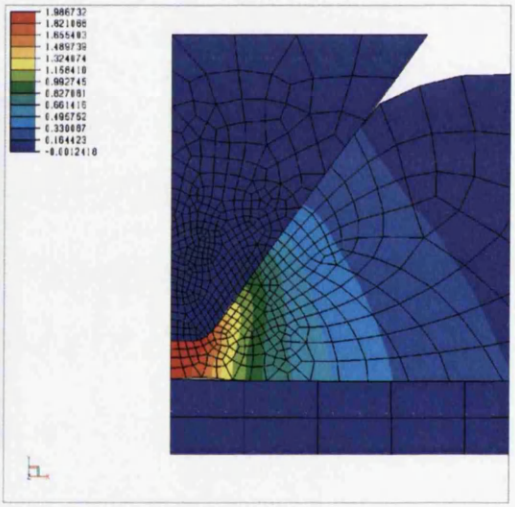

(d) SC = 25.9 μm : Strain XX

Figure D.11: Strain XX

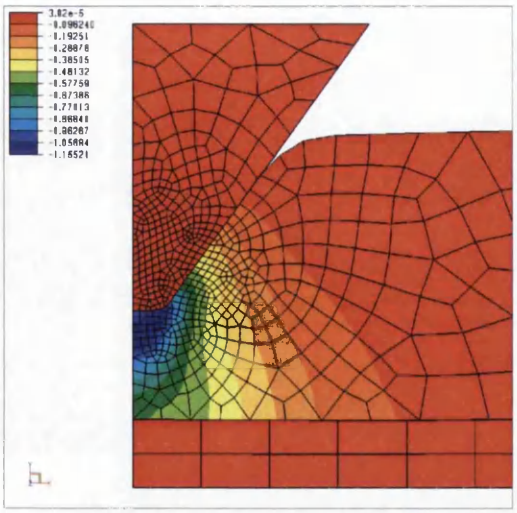

(a) SC = 78.4 μm : Strain YY

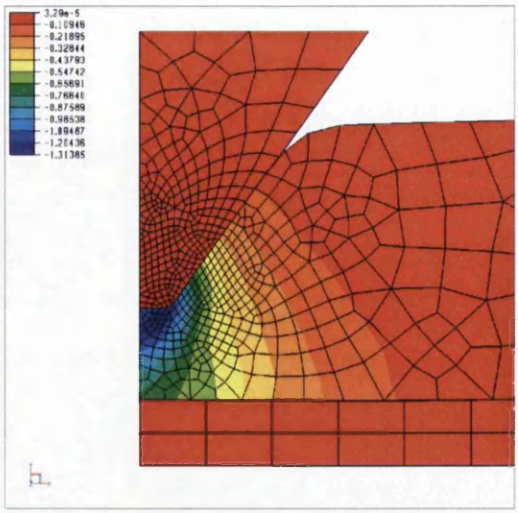

(b) SC = 68 μm : Strain YY

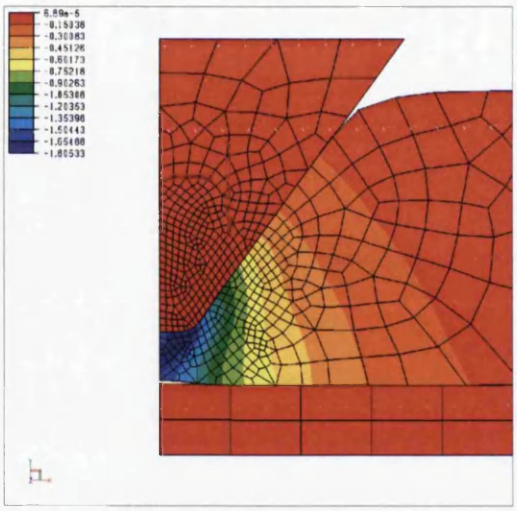

(c) SC = 36.3 μm : Strain YY

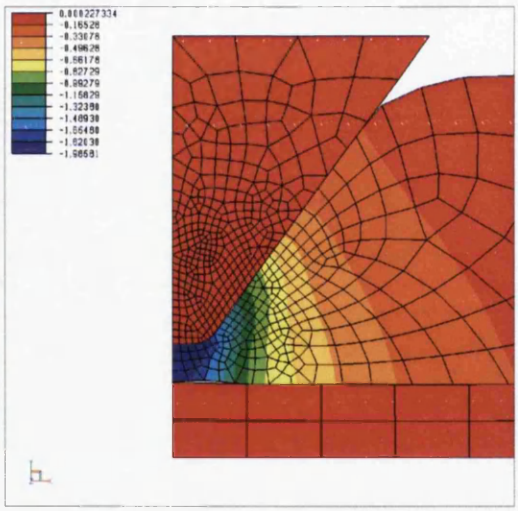

(d) SC = 25.9 μm : Strain YY

Figure D.12: Strain YY

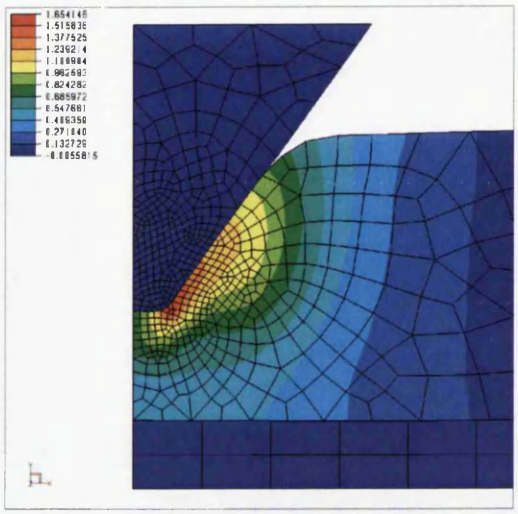

(a) SC = 78.4 μm : Strain XY

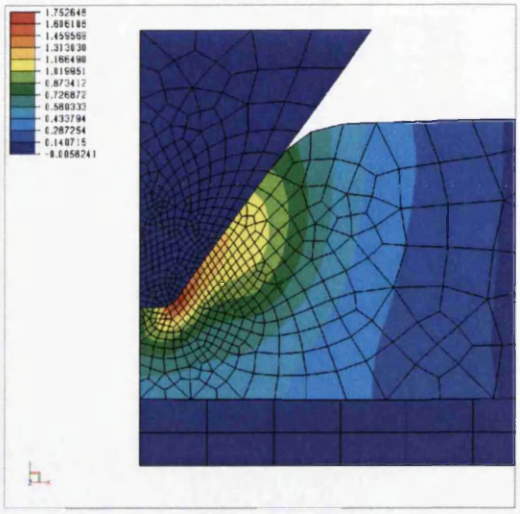

(b) SC = 68 μm : Strain XY

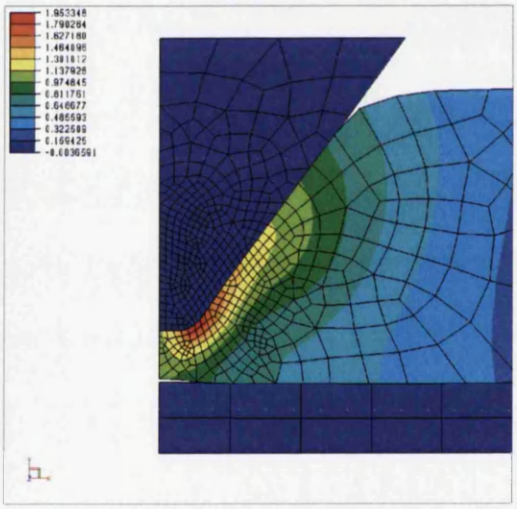

(c) SC = 36.3 μm : Strain XY

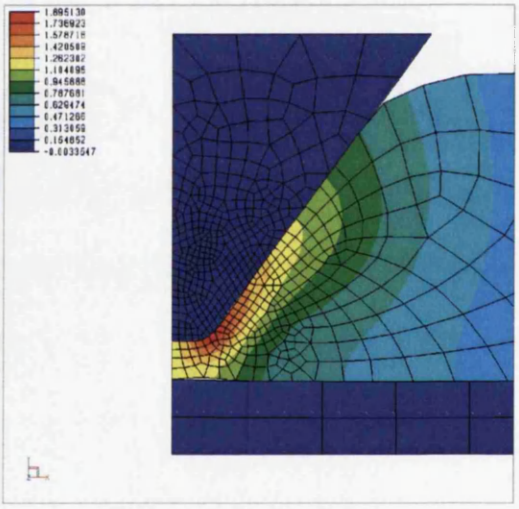

(d) SC = 25.9 μm : Strain XY

Figure D.13: Strain XY

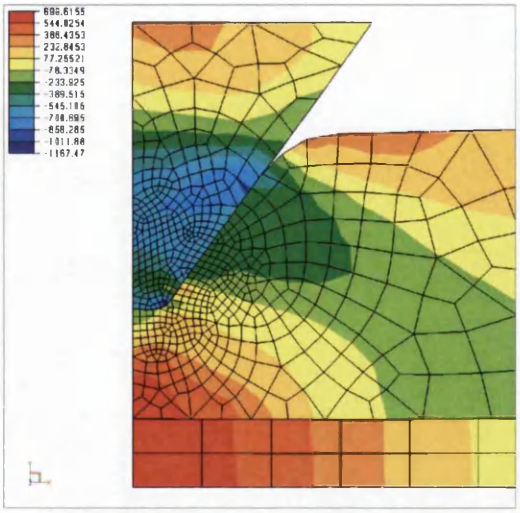

(a) SC = 78.4 μm : Stress XX

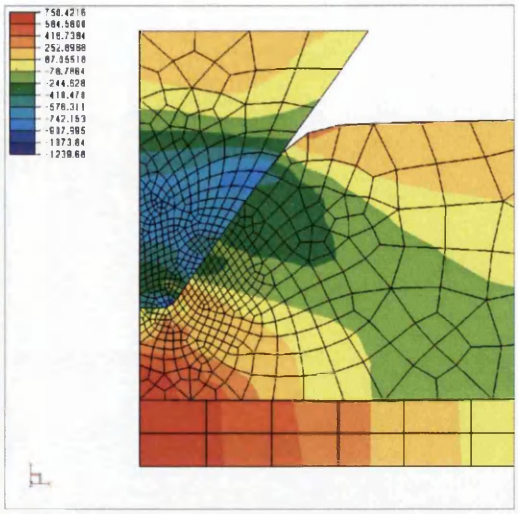

(b) SC = 68 μm : Stress XX

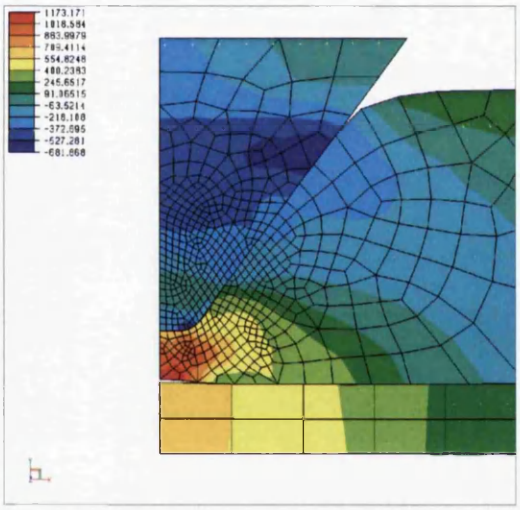

(c) SC = 36.3 μm : Stress XX

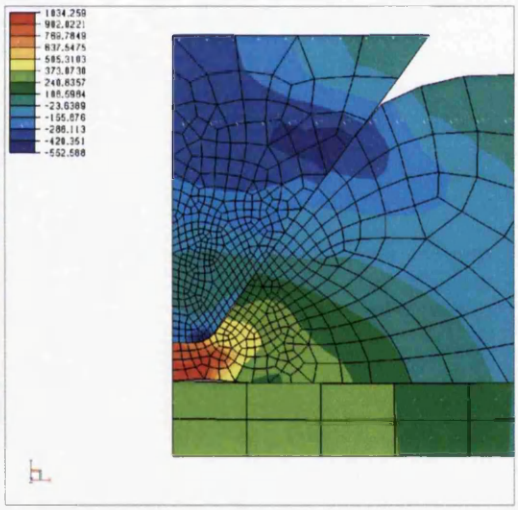

(d) SC = 25.9 μm : Stress XX

Figure D.14: Stress XX

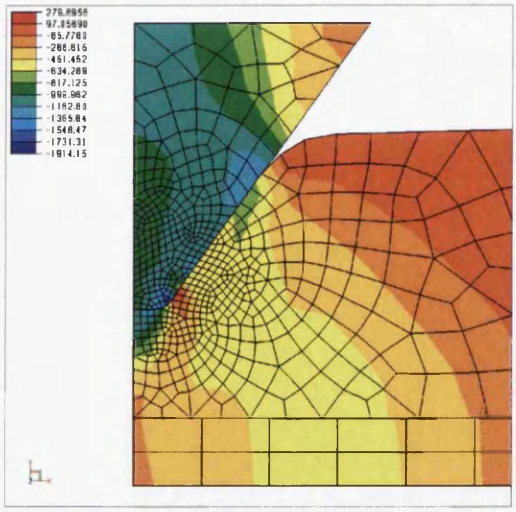

(a) SC = 78.4 μm : Stress YY

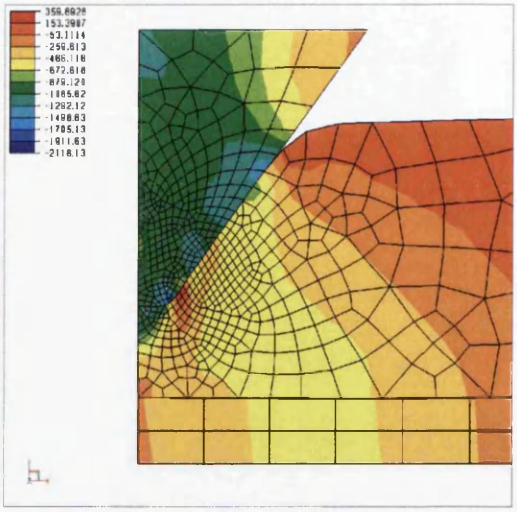

(b) SC = 68 μm : Stress YY

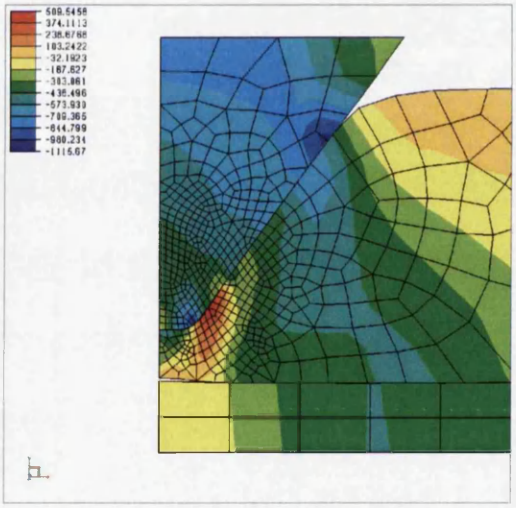

(c) SC = 36.3 μm : Stress YY

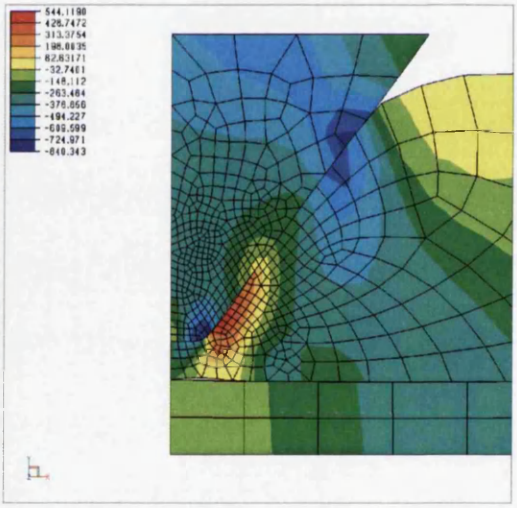

(d) SC = 25.9 μm : Stress YY

Figure D.15: Stress YY

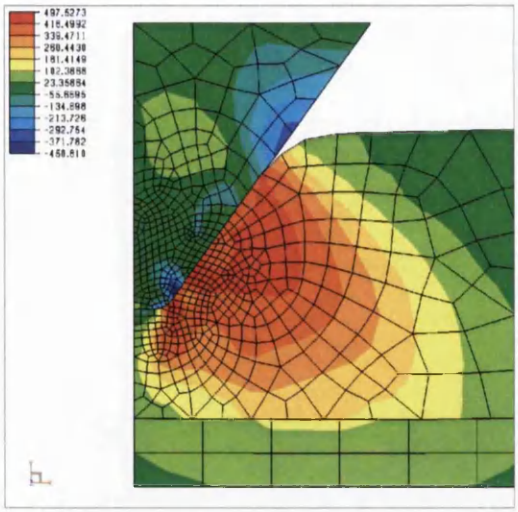

(a) SC = 78.4 μm : Stress XY

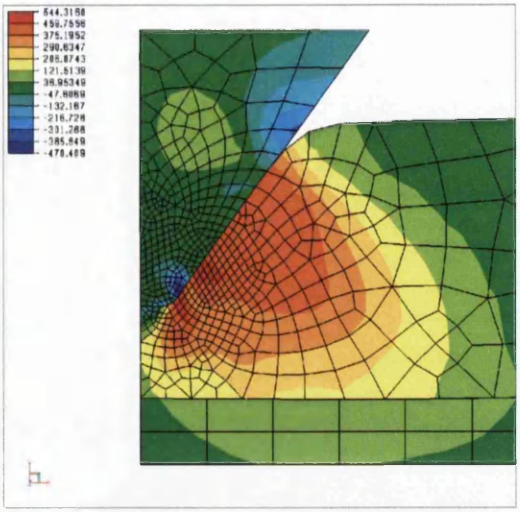

(b) SC = 68 μm : Stress XY

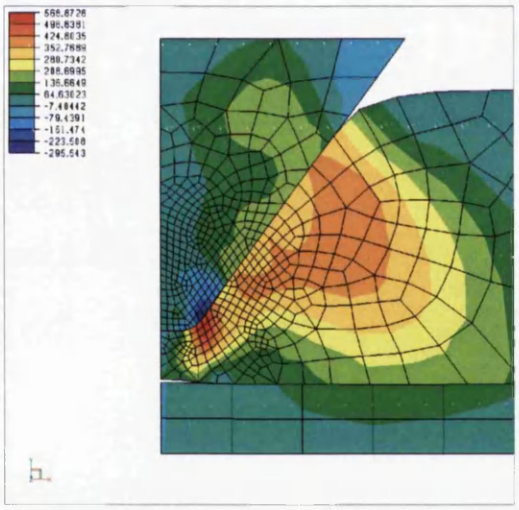

(c) SC = 36.3 μm : Stress XY

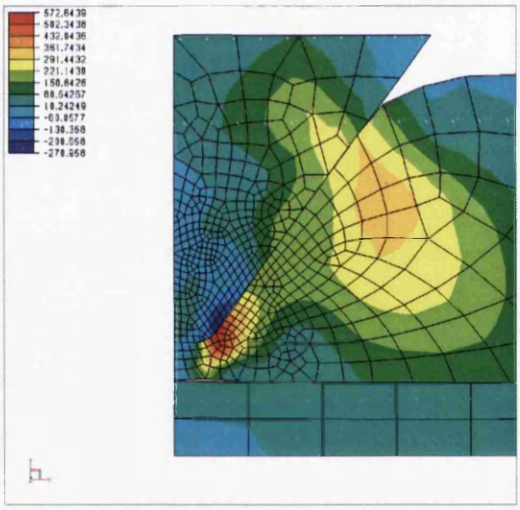

(d) SC = 25.9 μm : Stress XY

Figure D.16: Stress XY

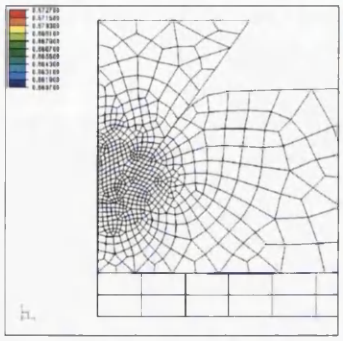

(a) Biaxial = 0.6667

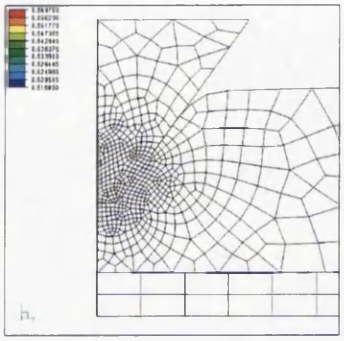

(b) Biaxial NU = 0.6547

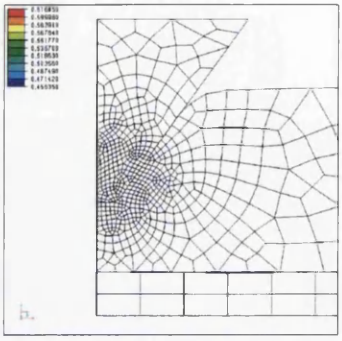

(c) Plane Strain = 0.5774

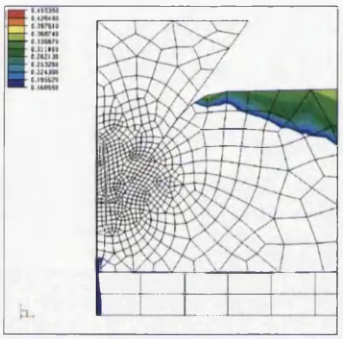

(d) Uniaxial Tension = 0.3333

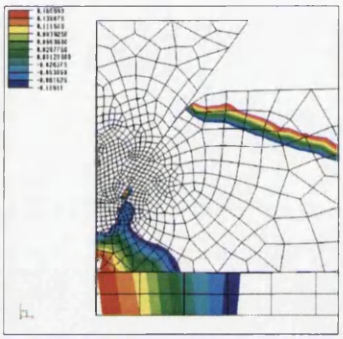

(e) Shear Pure = 0

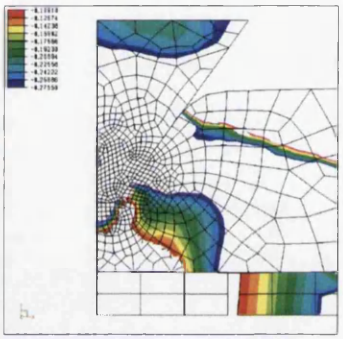

(f) Shear NU = -0.2182

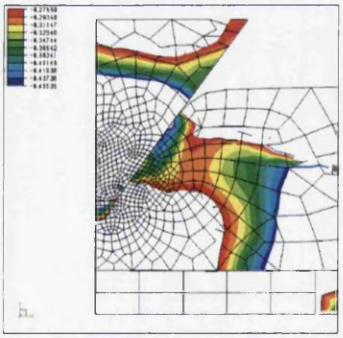

(g) Uniaxial Comp = -0.3328

Figure D.17: PL1 - Triaxiality : with Score Residual at 78.4 μm

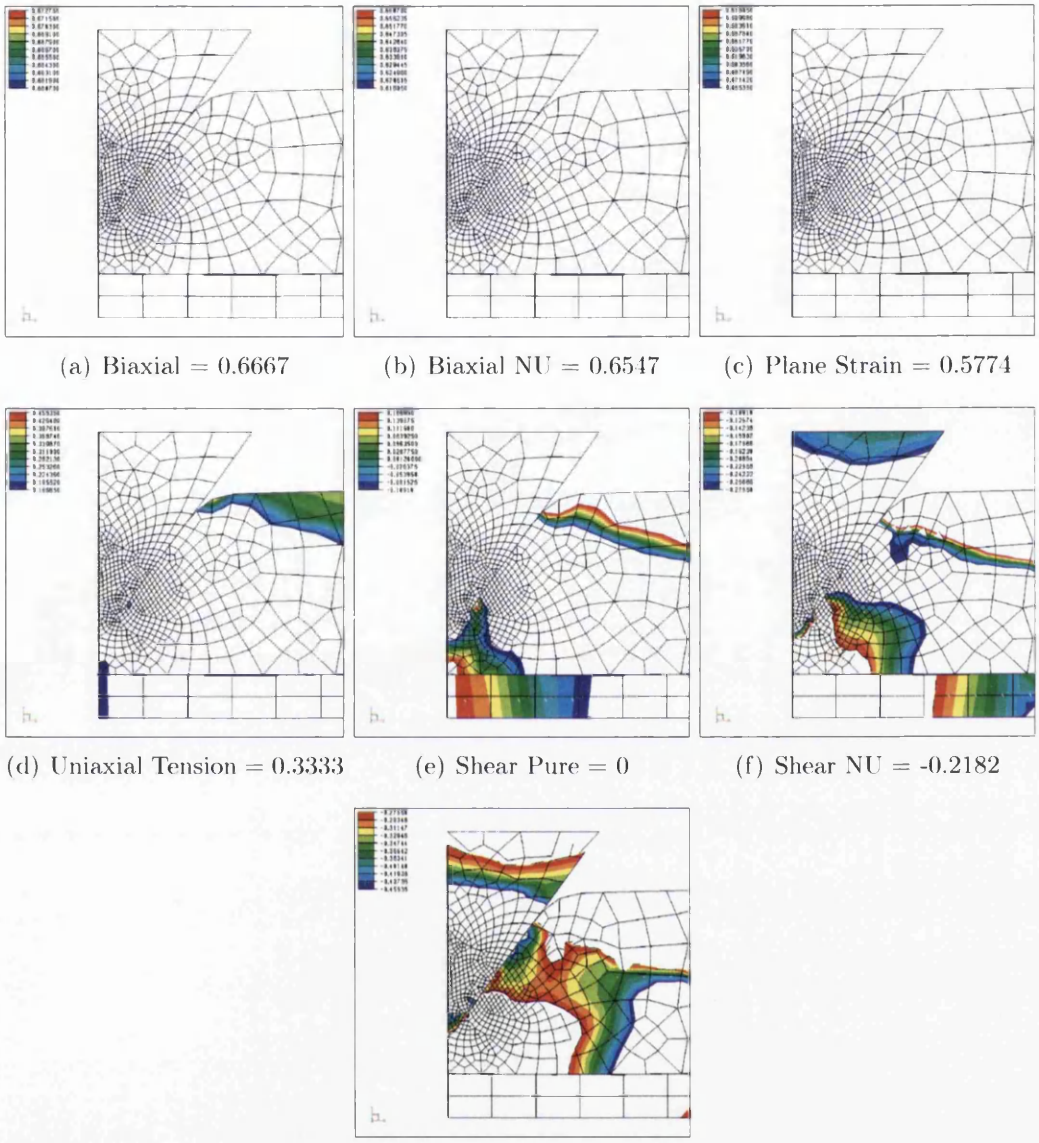

(a) Biaxial = 0.6667 (b) Biaxial NU = 0.6547 (c) Plane Strain = 0.5774

(d) Uniaxial Tension = 0.3333 (e) Shear Pure = 0 (f) Shear NU = -0.2182

(g) Uniaxial Comp = -0.3328

Figure D.18: PL2 - Triaxiality : with Score Residual at 68 μm

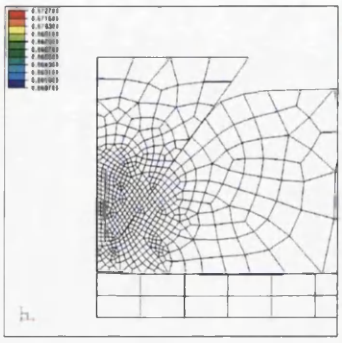

(a) Biaxial = 0.6667

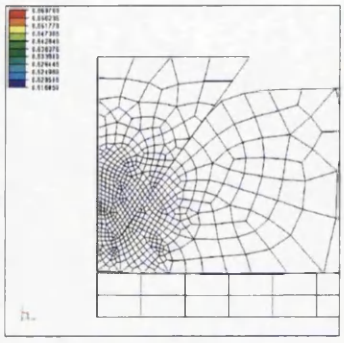

(b) Biaxial NU = 0.6547

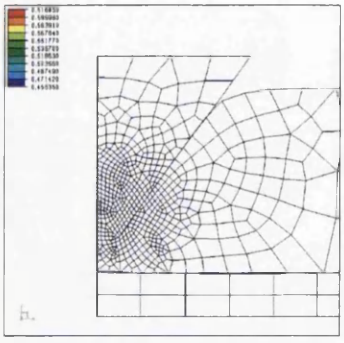

(c) Plane Strain = 0.5774

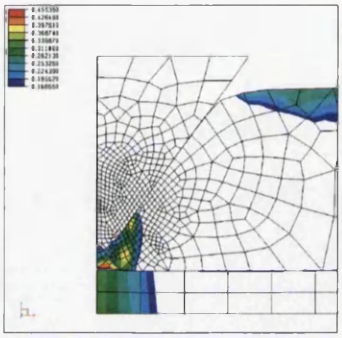

(d) Uniaxial Tension = 0.3333

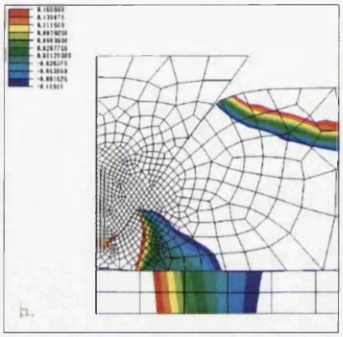

(e) Shear Pure = 0

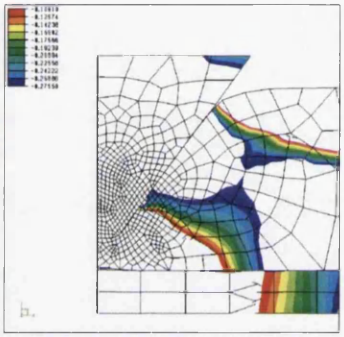

(f) Shear NU = -0.2182

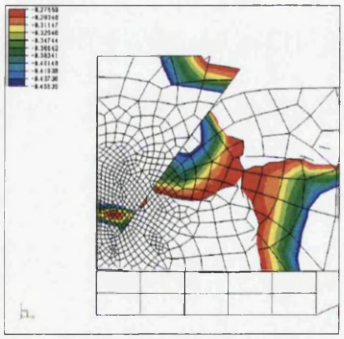

(g) Uniaxial Comp = -0.3328

Figure D.19: PL4 - Triaxiality : with Score Residual at 36.3 μm

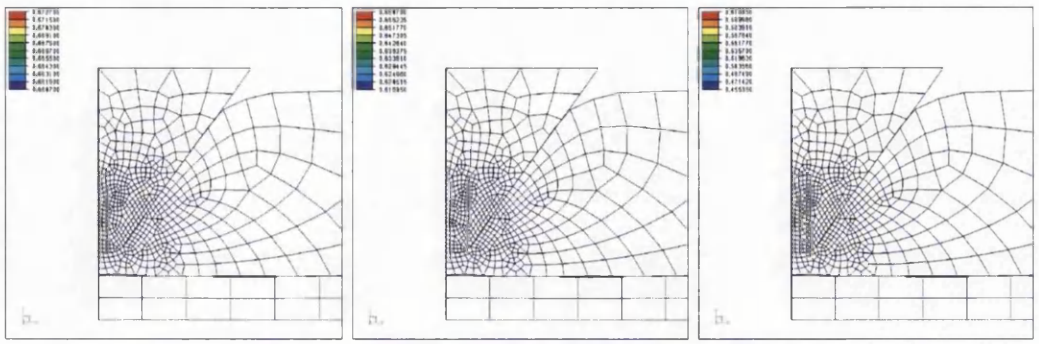

(a) Biaxial = 0.6667 (b) Biaxial NU = 0.6547 (c) Plane Strain = 0.5774

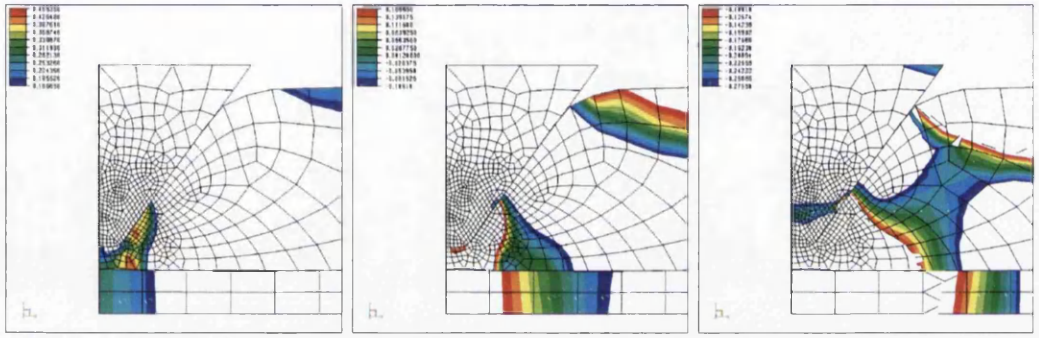

(d) Uniaxial Tension = 0.3333 (e) Shear Pure = 0 (f) Shear NU = -0.2182

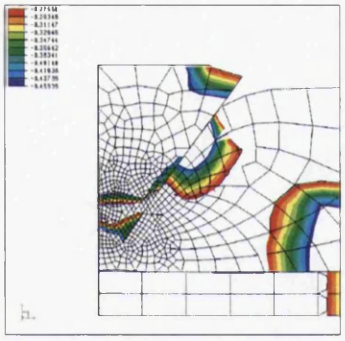

(g) Uniaxial Comp = -0.3328

Figure D.20: PL3 - Triaxiality : with Score Residual at 25.9 μm

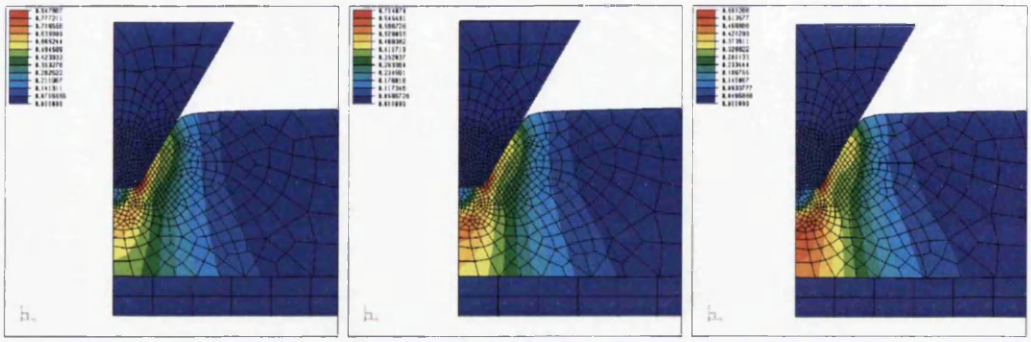

(a) A = 0.5 (b) A = 0.6 (c) A = 0.7

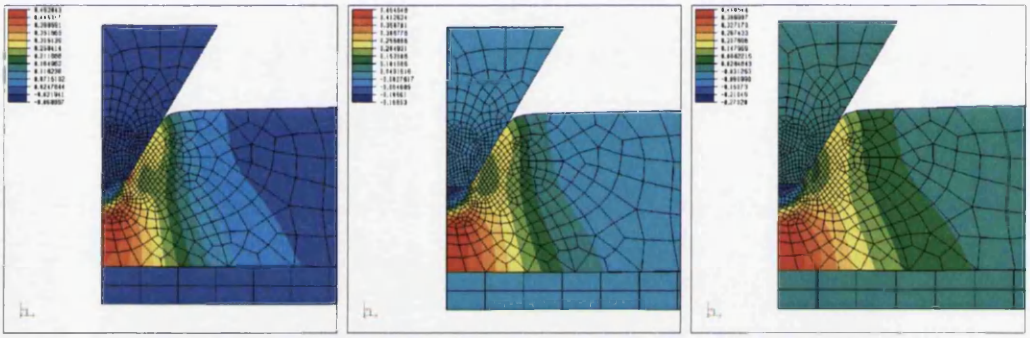

(d) A = 0.8 (e) A = 0.9 (f) A = 1.0

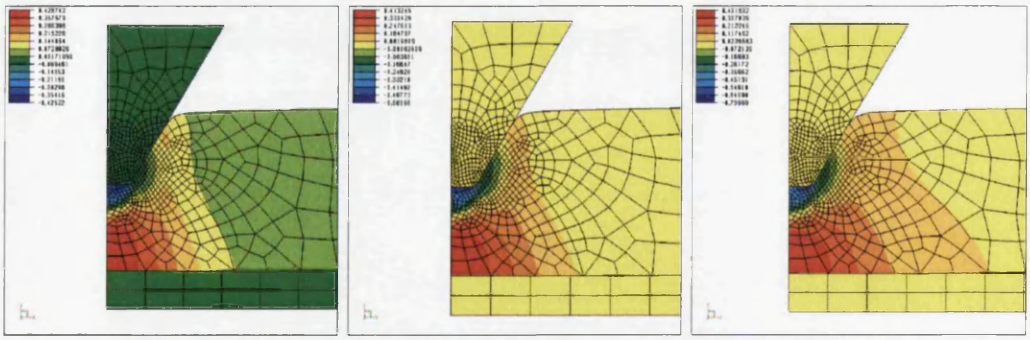

(g) A = 1.1 (h) A = 1.2 (i) A = 1.3

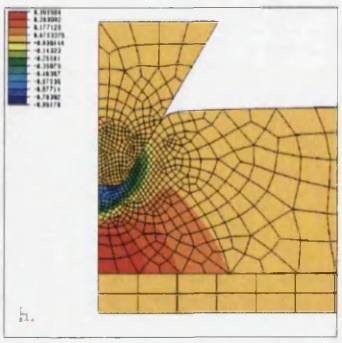

(j) A = 1.4

Figure D.21: PS107 - Oyane Damage with Score Residual at 107 μm

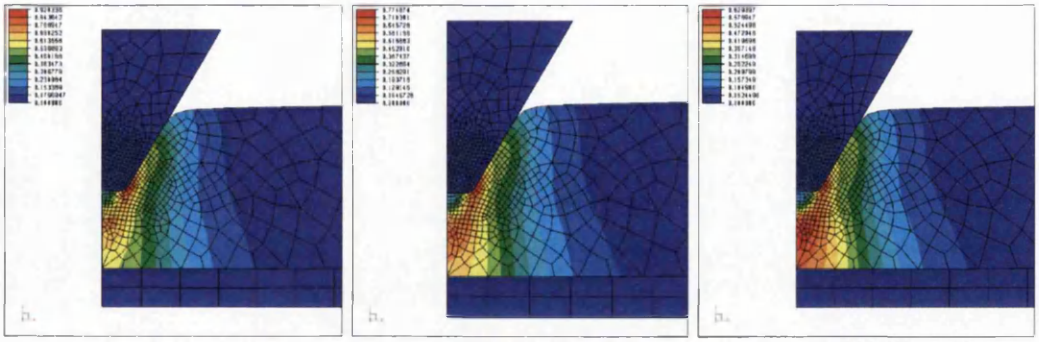

(a) A = 0.5 (b) A = 0.6 (c) A = 0.7

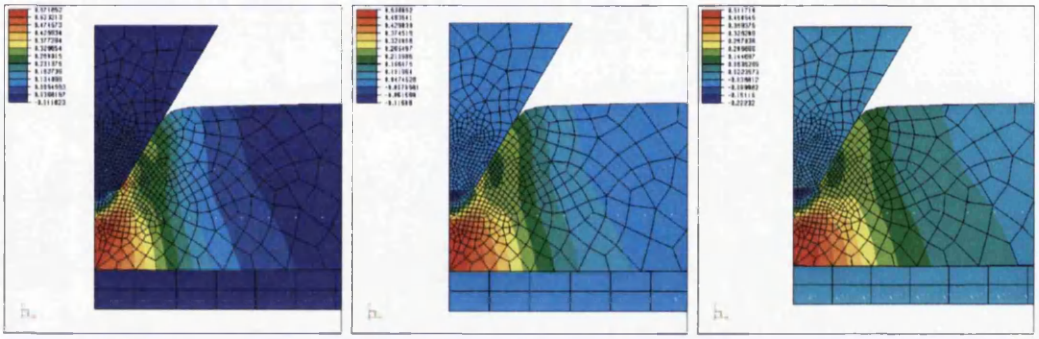

(d) A = 0.8 (e) A = 0.9 (f) A = 1.0

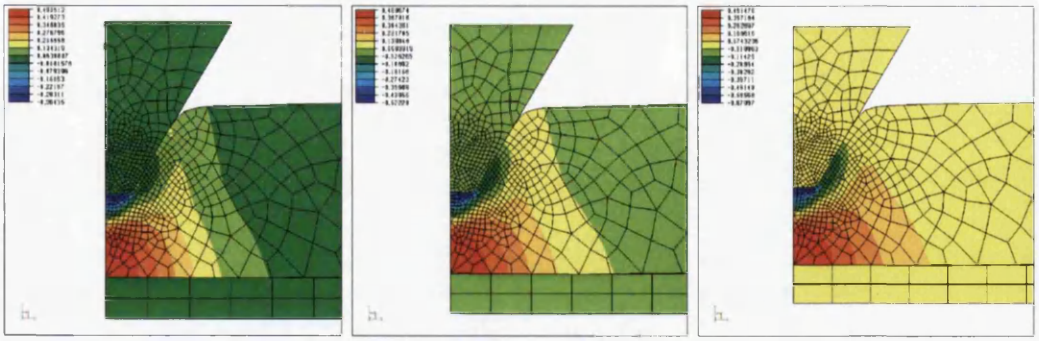

(g) A = 1.1 (h) A = 1.2 (i) A = 1.3

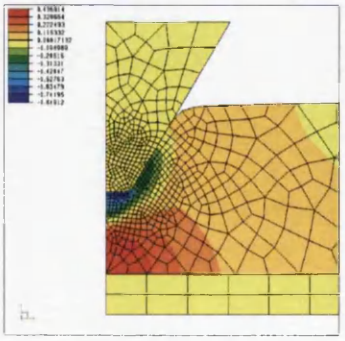

(j) A = 1.4

Figure D.22: PS91 - Oyane Damage with Score Residual at 91 μm

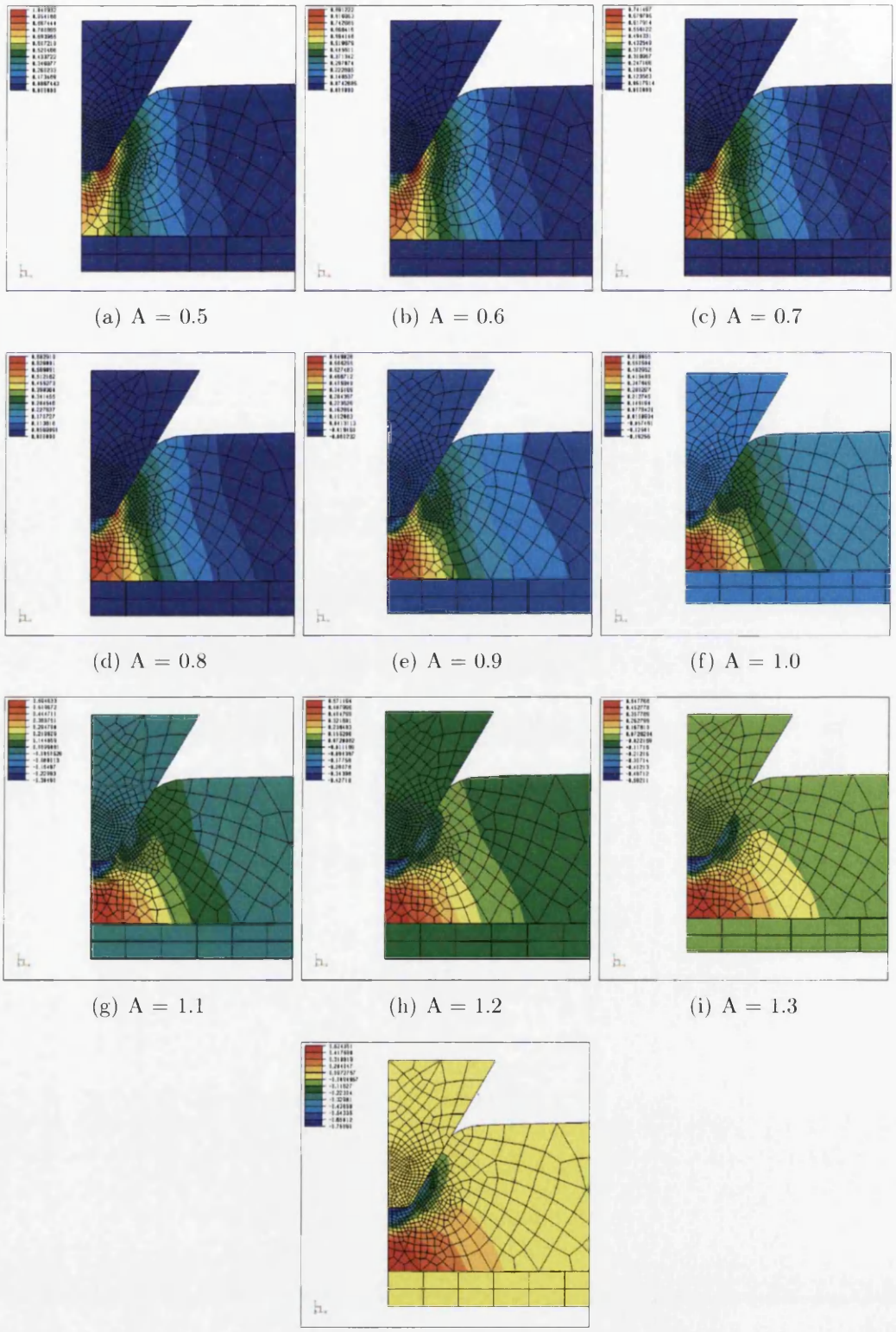

(a) A = 0.5 (b) A = 0.6 (c) A = 0.7

(d) A = 0.8 (e) A = 0.9 (f) A = 1.0

(g) A = 1.1 (h) A = 1.2 (i) A = 1.3

(j) A = 1.4

Figure D.23: PS83 - Oyane Damage with Score Residual at 83 μm

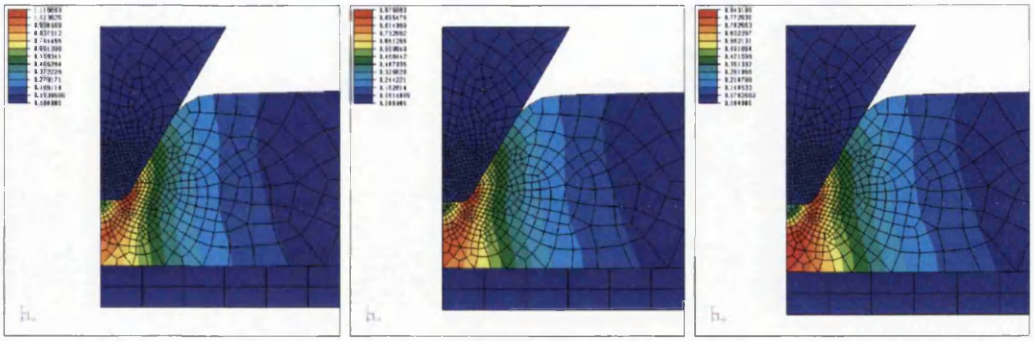

(a) A = 0.5 (b) A = 0.6 (c) A = 0.7

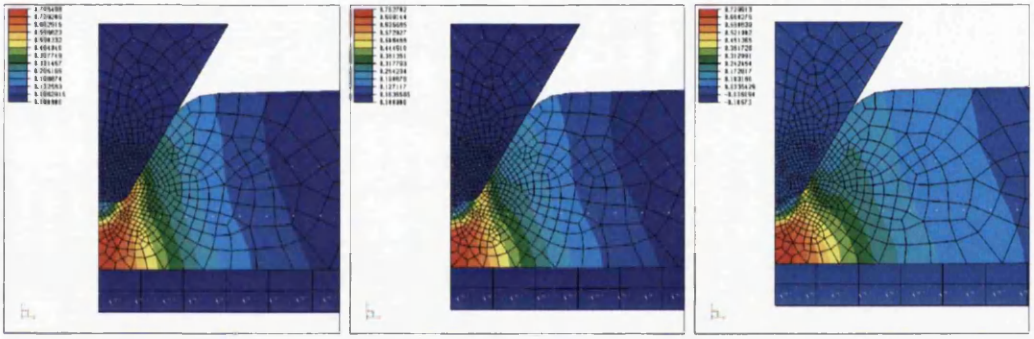

(d) A = 0.8 (e) A = 0.9 (f) A = 1.0

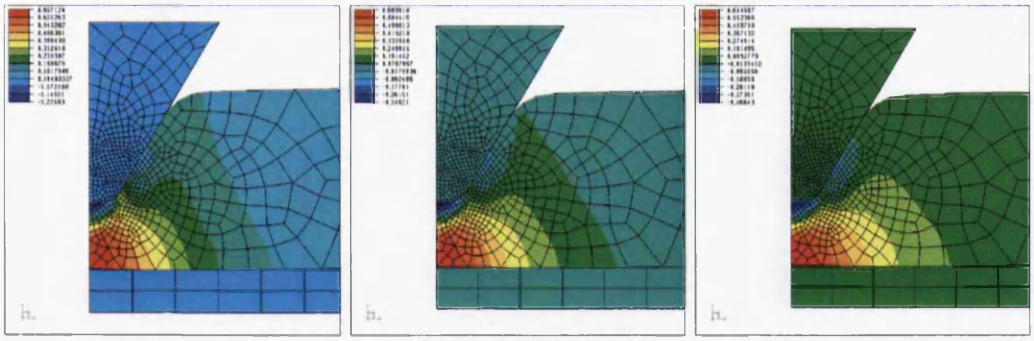

(g) A = 1.1 (h) A = 1.2 (i) A = 1.3

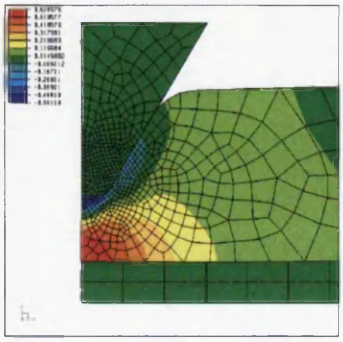

(j) A = 1.4

Figure D.24: PS72 - Oyane Damage with Score Residual at 72 μm

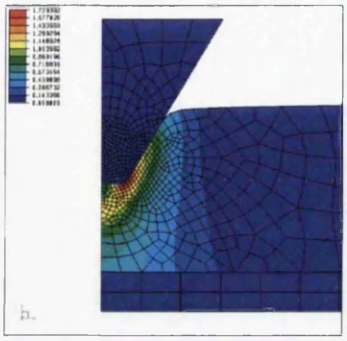

(a) So = 0.005

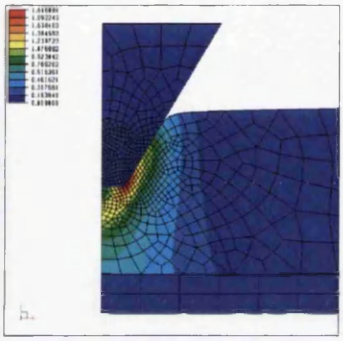

(b) So = 0.01

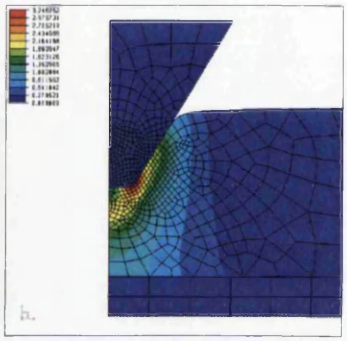

(c) So = 0.05

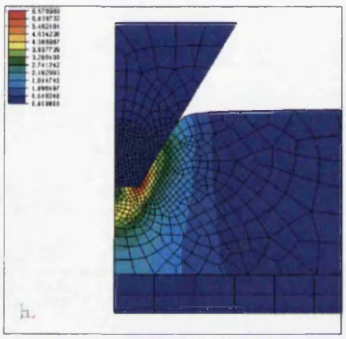

(d) So = 0.1

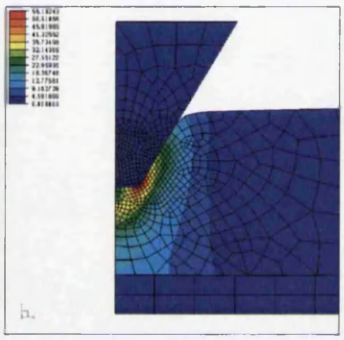

(e) So = 0.25

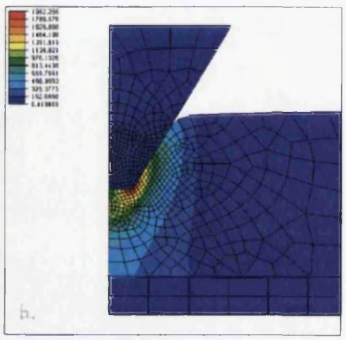

(f) So = 0.5

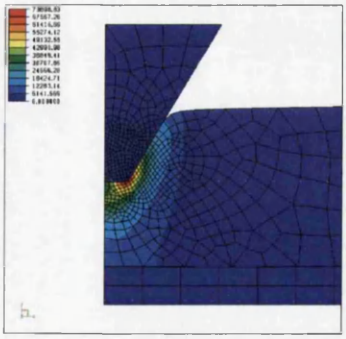

(g) So = 0.75

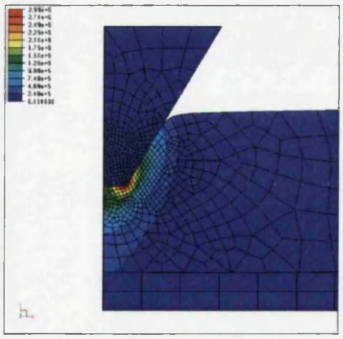

(h) So = 1

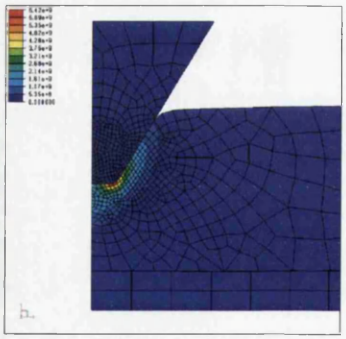

(i) So = 1.5

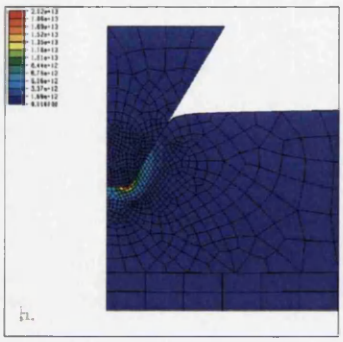

(j) So = 2

Figure D.25: PS107 - Gen Lemaitre Damage with Score Residual at 107 μm

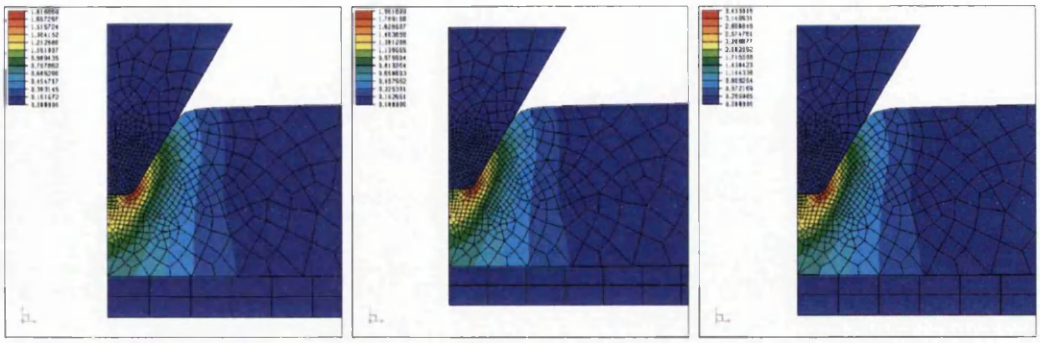

(a) So = 0.005 (b) So = 0.01 (c) So = 0.05

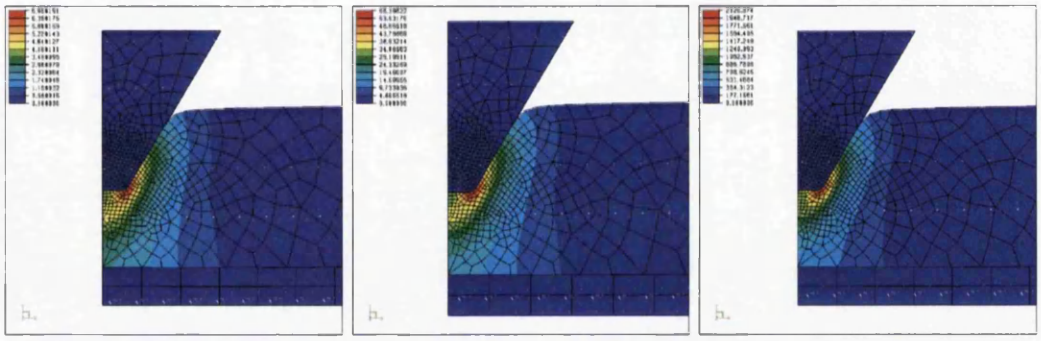

(d) So = 0.1 (e) So = 0.25 (f) So = 0.5

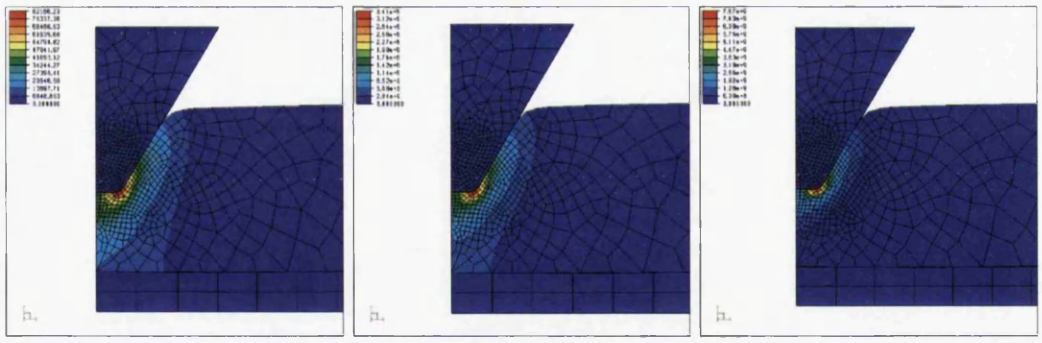

(g) So = 0.75 (h) So = 1 (i) So = 1.5

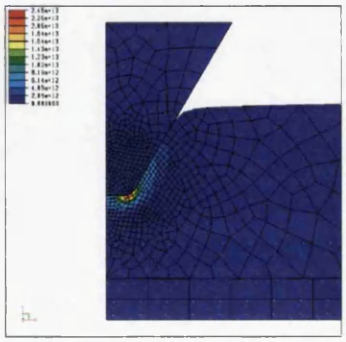

(j) So = 2

Figure D.26: PS91 - Gen Lemaitre Damage with Score Residual at 91 μm

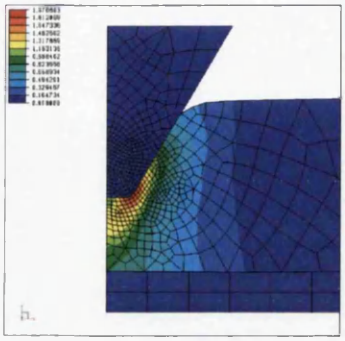

(a) So = 0.005

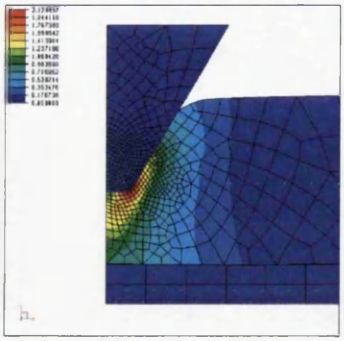

(b) So = 0.01

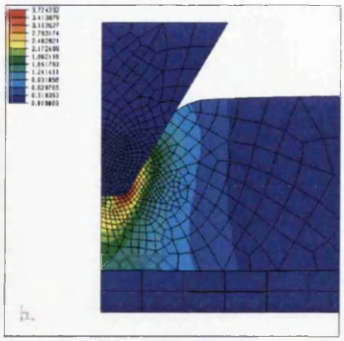

(c) So = 0.05

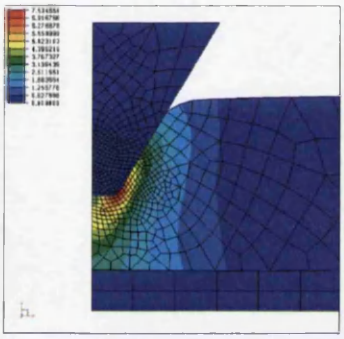

(d) So = 0.1

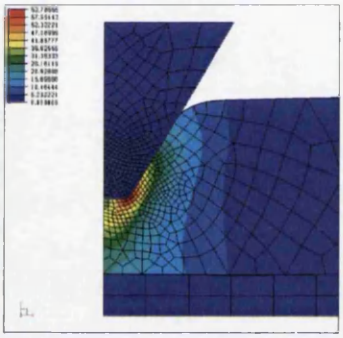

(e) So = 0.25

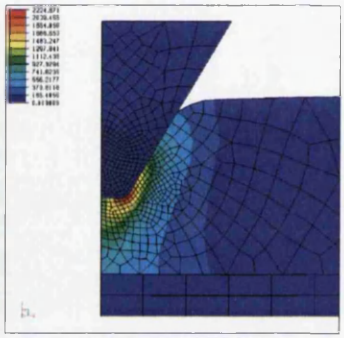

(f) So = 0.5

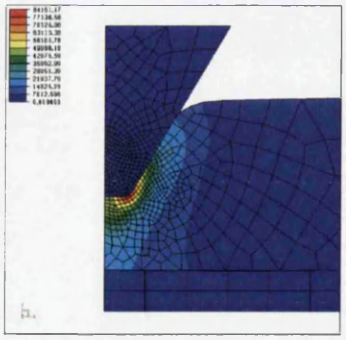

(g) So = 0.75

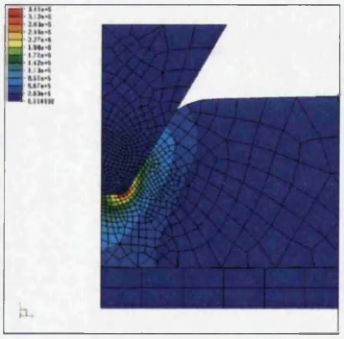

(h) So = 1

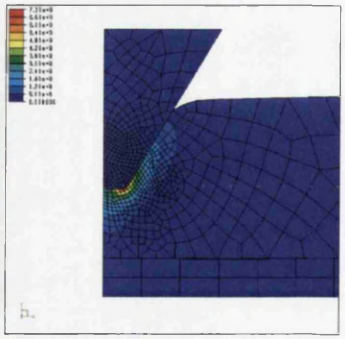

(i) So = 1.5

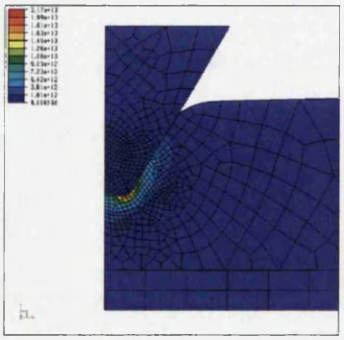

(j) So = 2

Figure D.27: PS83 - Gen Lemaitre Damage with Score Residual at 83 μm

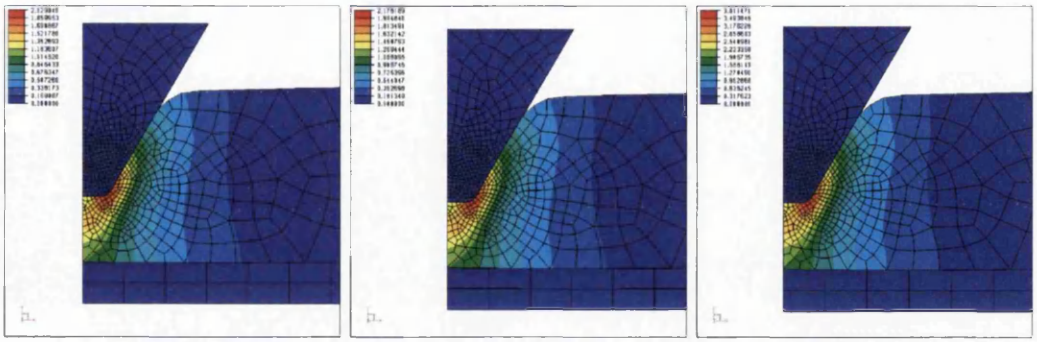

(a) So = 0.005 (b) So = 0.01 (c) So = 0.05

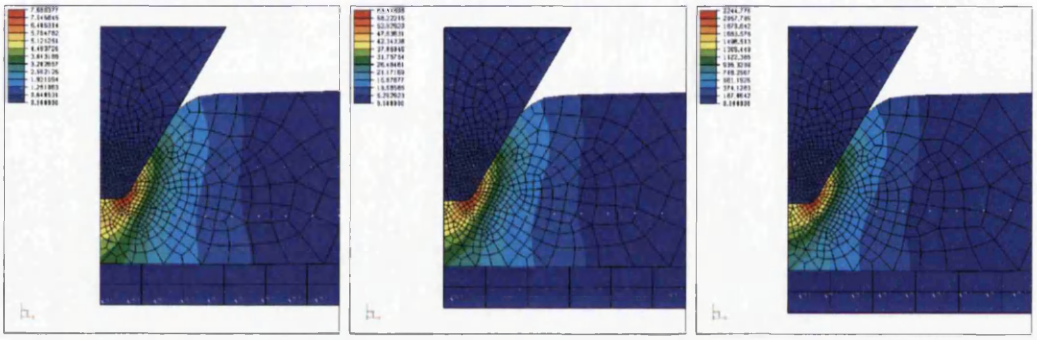

(d) So = 0.1 (e) So = 0.25 (f) So = 0.5

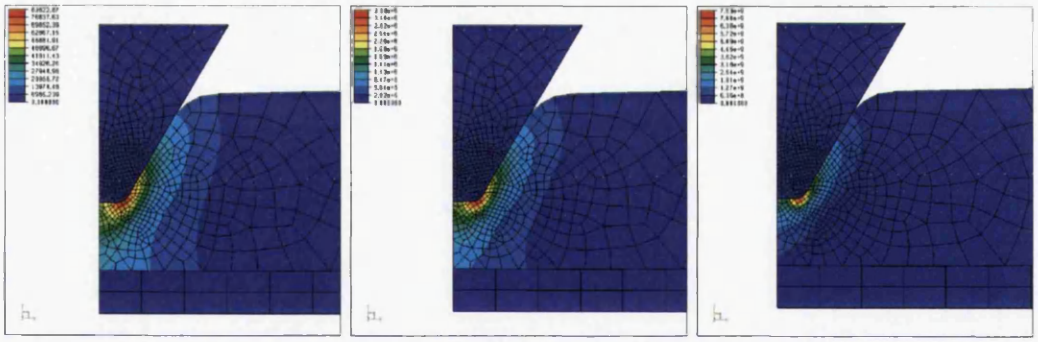

(g) So = 0.75 (h) So = 1 (i) So = 1.5

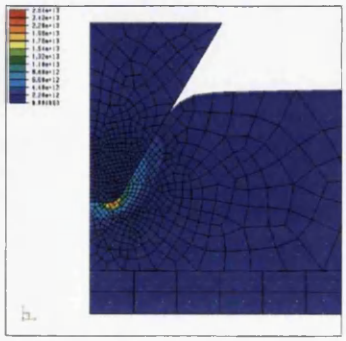

(j) So = 2

Figure D.28: PS72 - Gen Lemaitre Damage with Score Residual at 72 μm

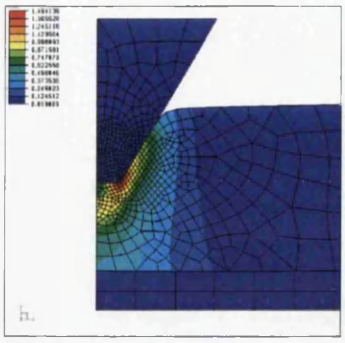

(a) So = -0.005

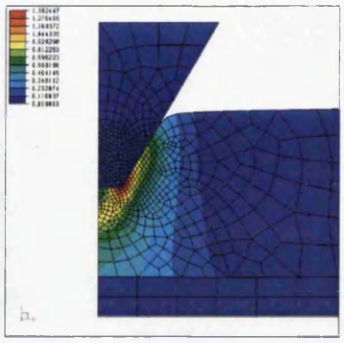

(b) So = -0.01

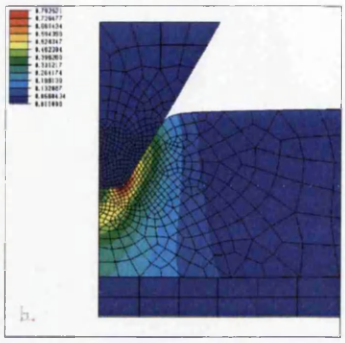

(c) So = -0.05

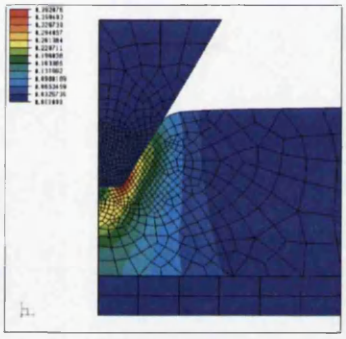

(d) So = -0.1

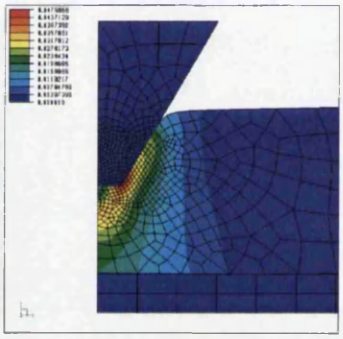

(e) So = -0.25

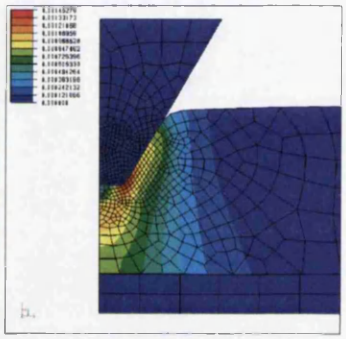

(f) So = -0.5

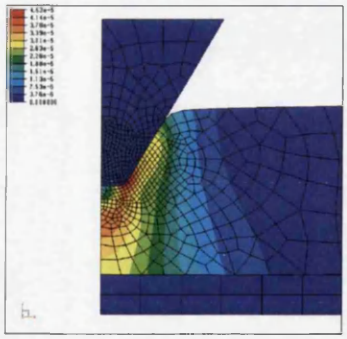

(g) So = -0.75

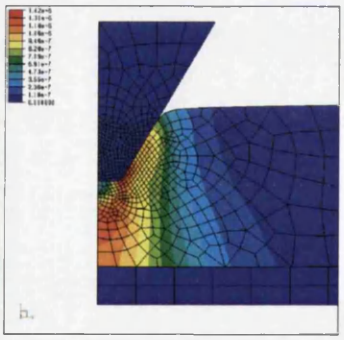

(h) So = -1

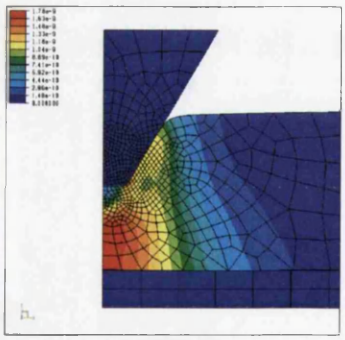

(i) So = -1.5

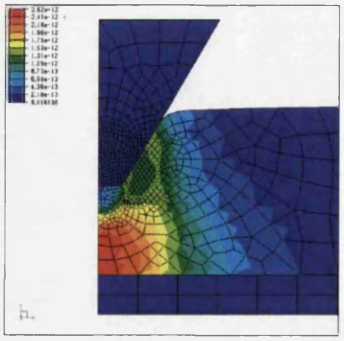

(j) So = -2

Figure D.29: PS107N - Neg Gen Lemaitre Damage with Score Residual at 107 μm

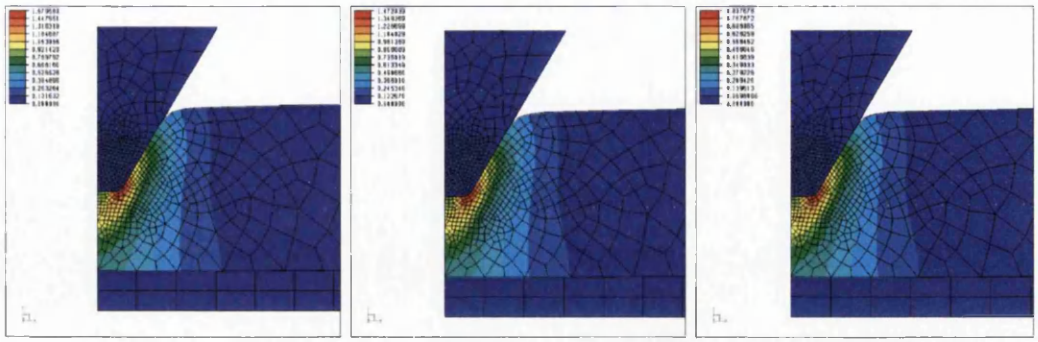

(a) So = -0.005 (b) So = -0.01 (c) So = -0.05

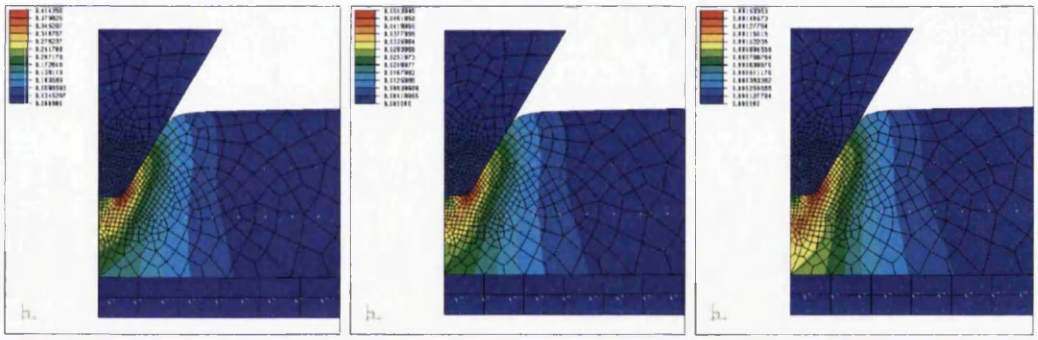

(d) So = -0.1 (e) So = -0.25 (f) So = -0.5

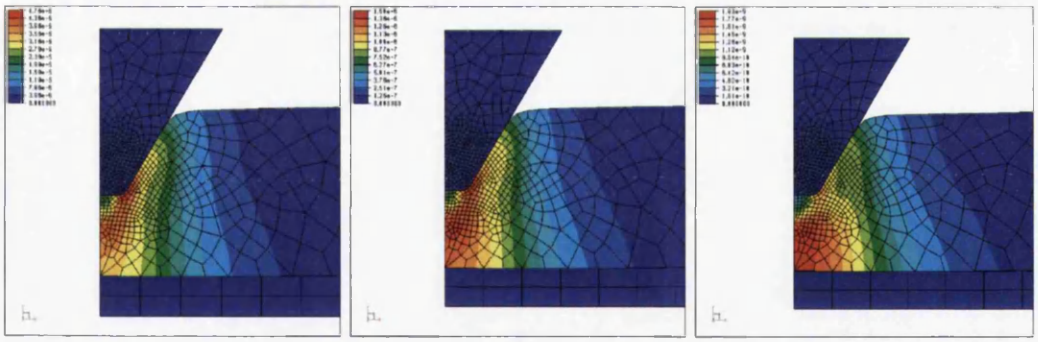

(g) So = -0.75 (h) So = -1 (i) So = -1.5

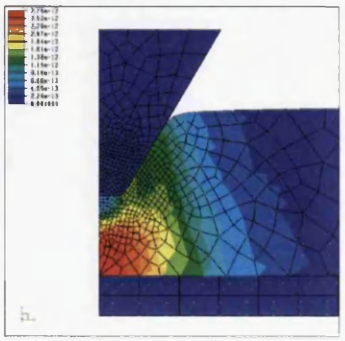

(j) So = -2

Figure D.30: PS91N - Neg Gen Lemaitre Damage with Score Residual at 91 μm

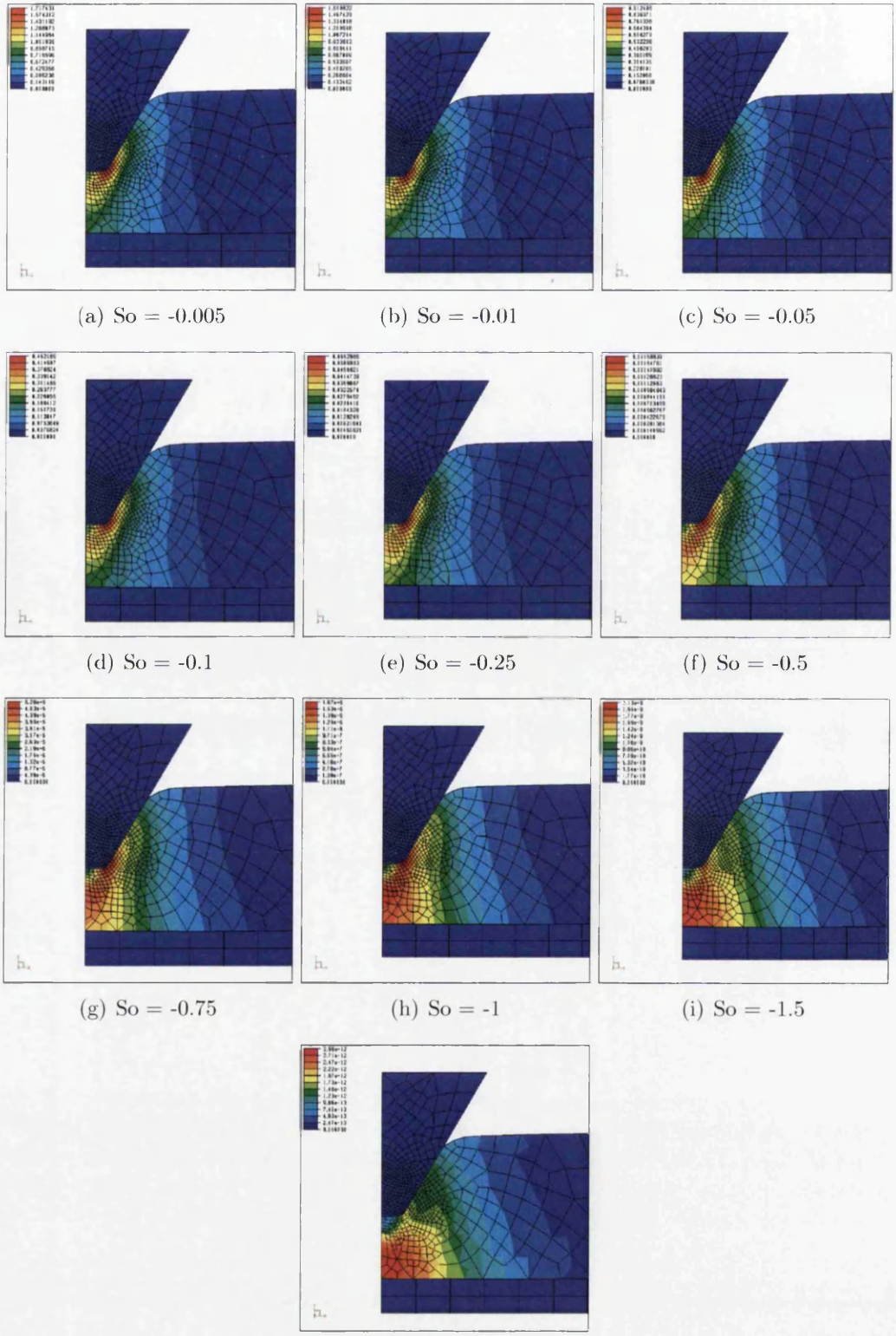

(a) So = -0.005 (b) So = -0.01 (c) So = -0.05

(d) So = -0.1 (e) So = -0.25 (f) So = -0.5

(g) So = -0.75 (h) So = -1 (i) So = -1.5

(j) So = -2

Figure D.31: PS83N - Neg Gen Lemaitre Damage with Score Residual at 83 μm

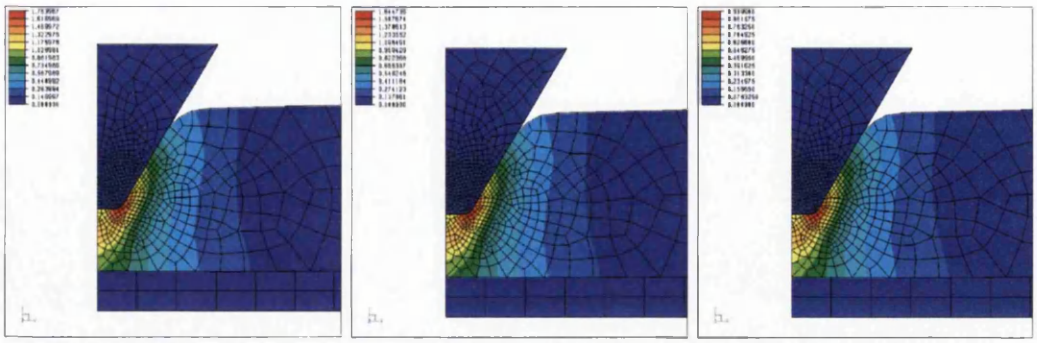

(a) So = -0.005 (b) So = -0.01 (c) So = -0.05

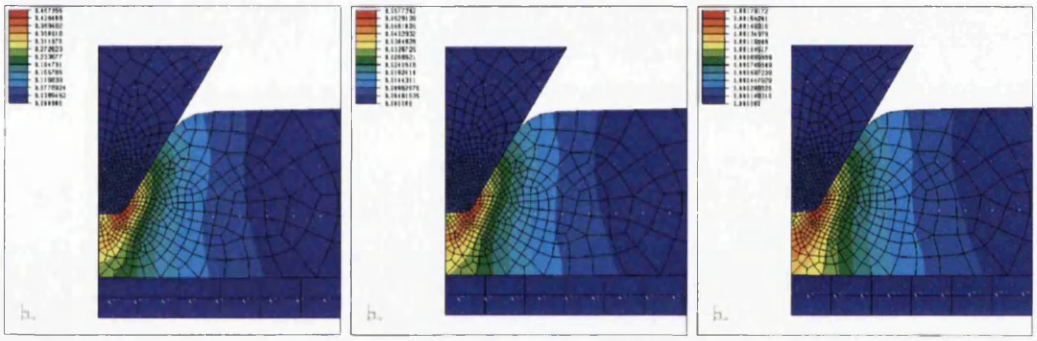

(d) So = -0.1 (e) So = -0.25 (f) So = -0.5

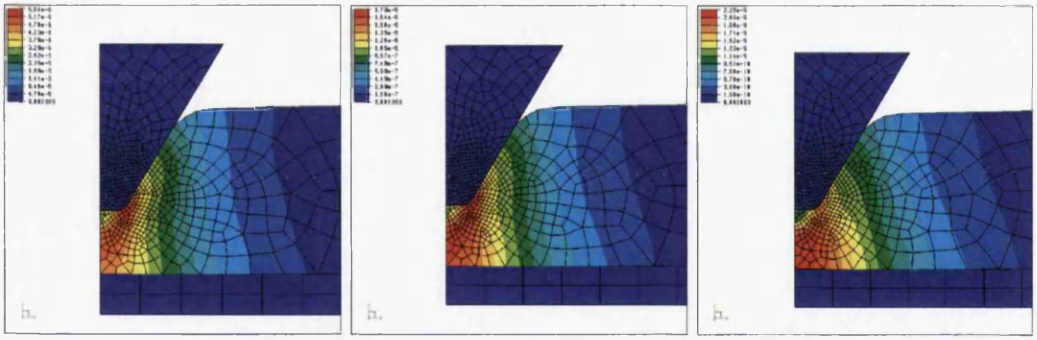

(g) So = -0.75 (h) So = -1 (i) So = -1.5

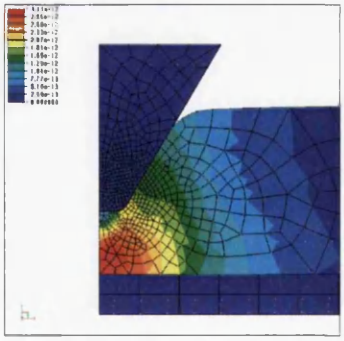

(j) So = -2

Figure D.32: PS72N - Neg Gen Lemaitre Damage with Score Residual at 72 μm

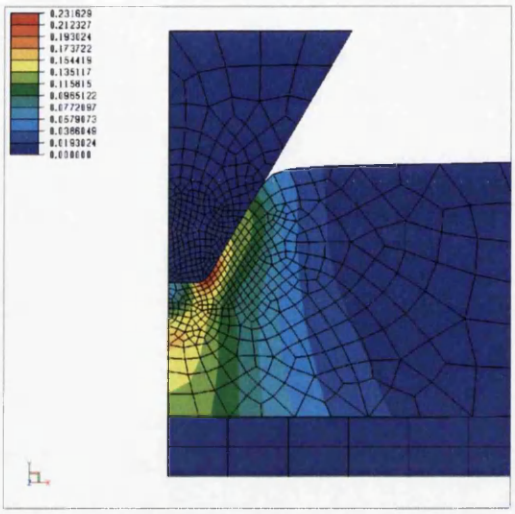

(a) SC = 107 μm

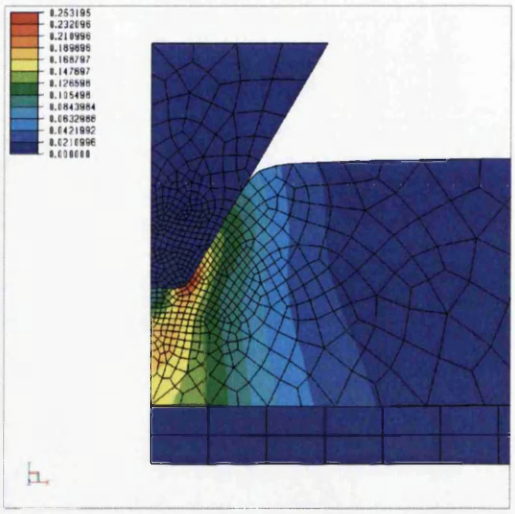

(b) SC = 91 μm

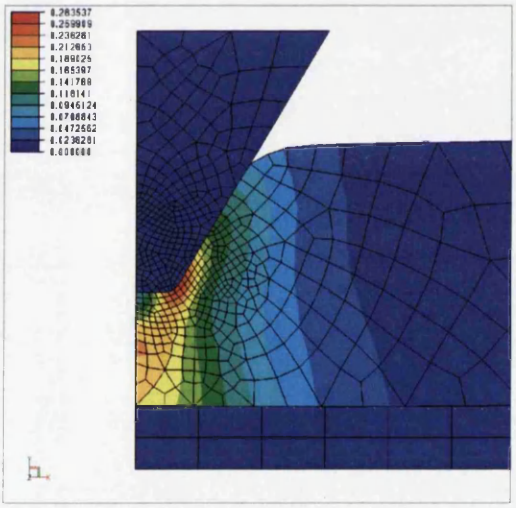

(c) SC = 83 μm

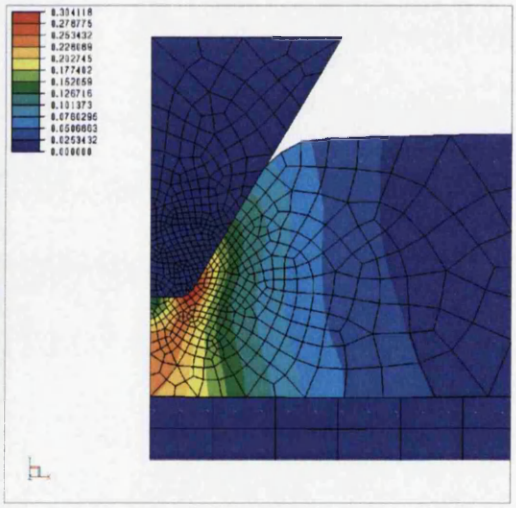

(d) SC = 72 μm

Figure D.33: Rice & Tracy Damage

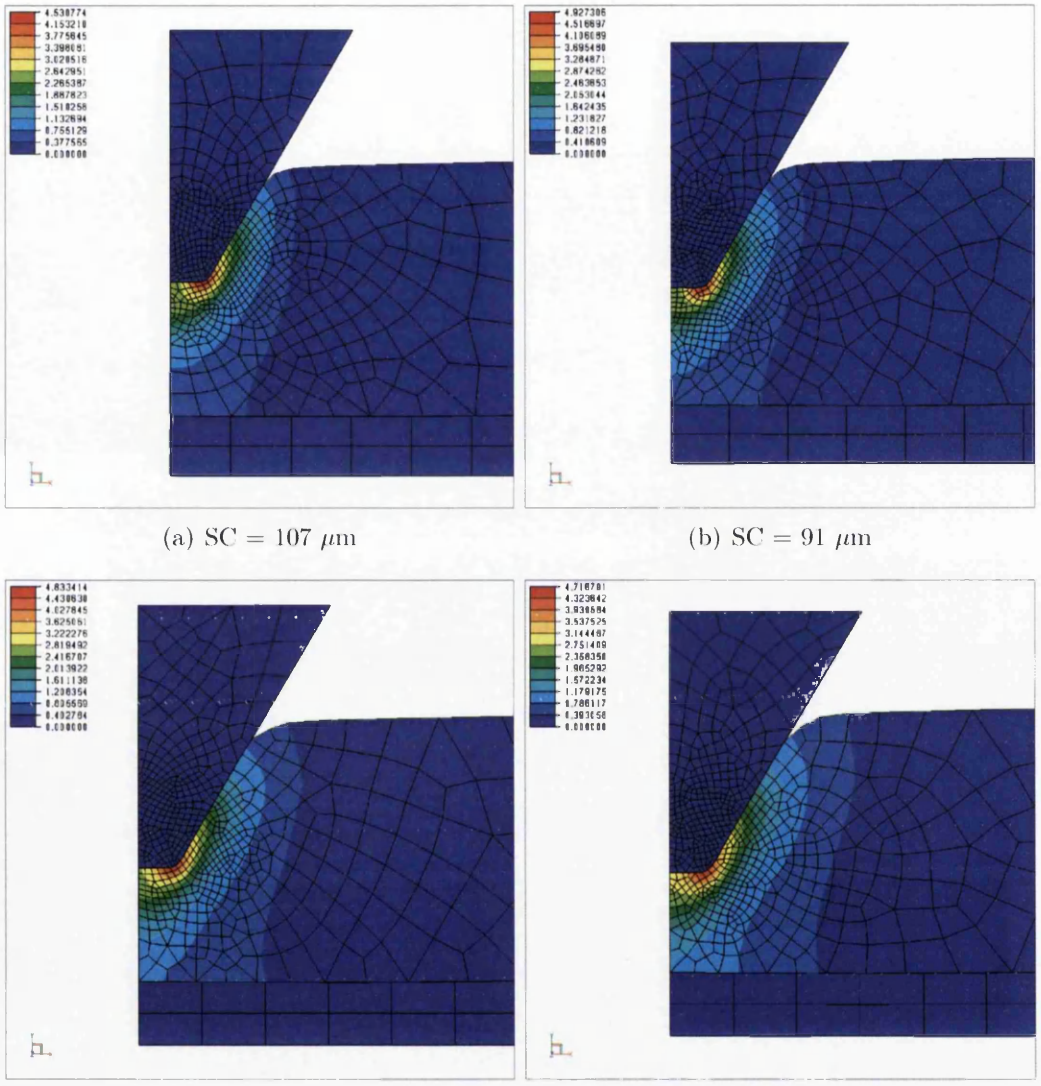

(a) SC = 107 μm

(b) SC = 91 μm

(c) SC = 83 μm

(d) SC = 72 μm

Figure D.34: Lemaitre Damage

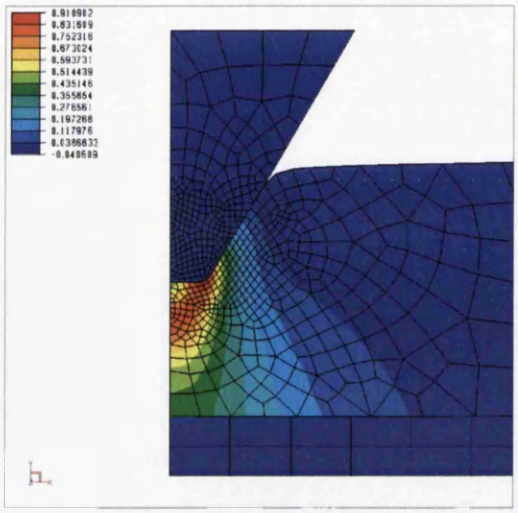

(a) SC = 107 μm : Strain XX

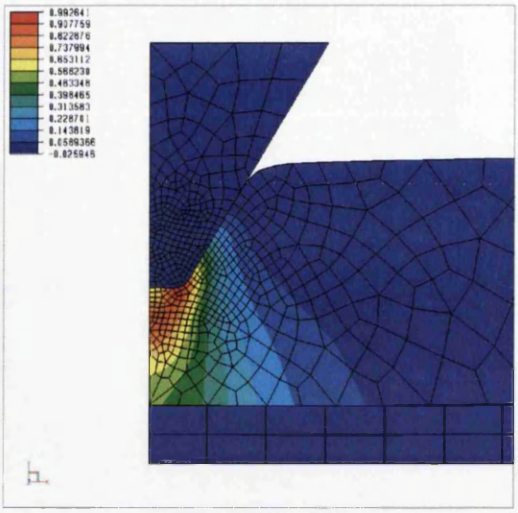

(b) SC = 91 μm : Strain XX

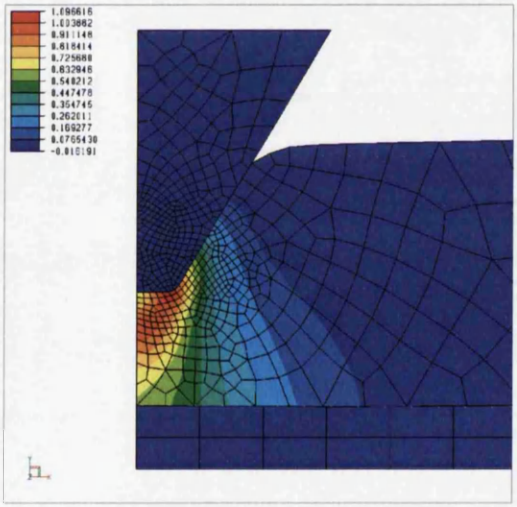

(c) SC = 83 μm : Strain XX

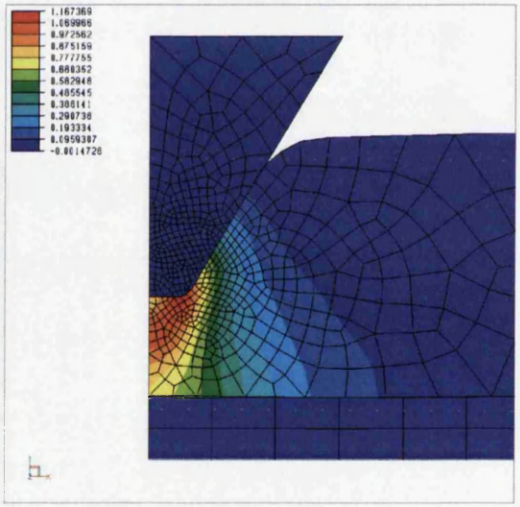

(d) SC = 72 μm : Strain XX

Figure D.35: PS Strain XX

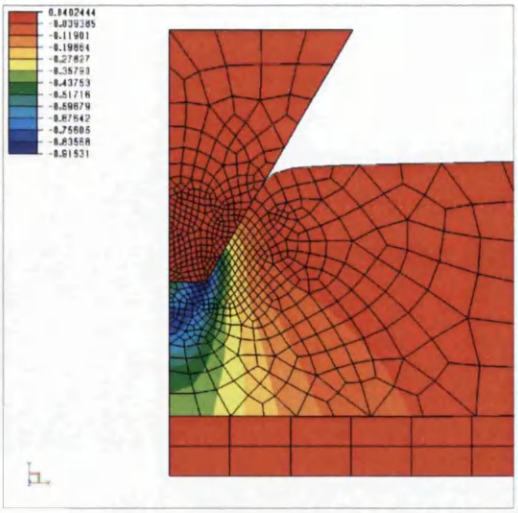

(a) SC = 107 μm : Strain YY

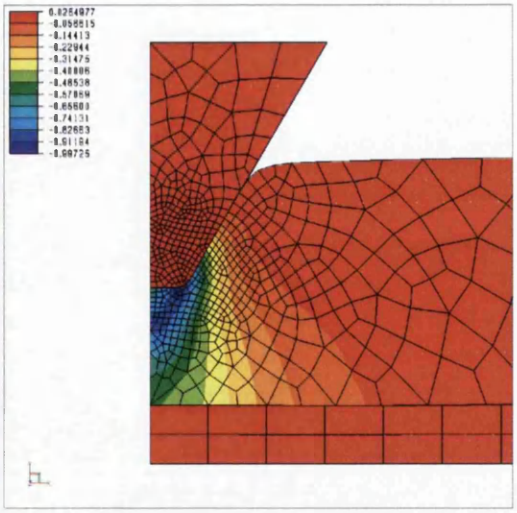

(b) SC = 91 μm : Strain YY

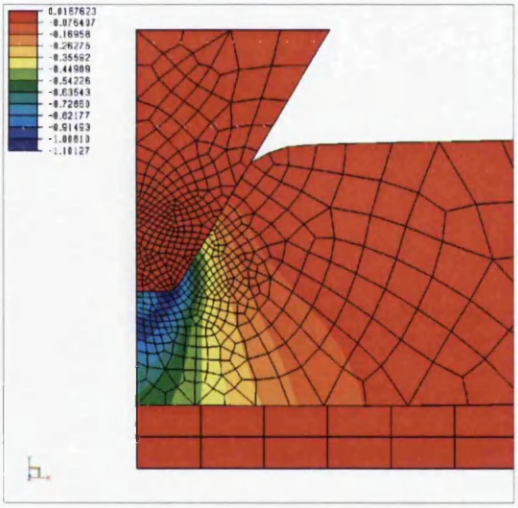

(c) SC = 83 μm : Strain YY

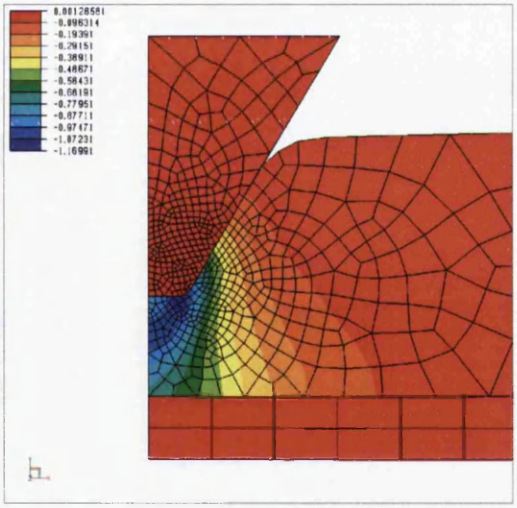

(d) SC = 72 μm : Strain YY

Figure D.36: PS Strain YY

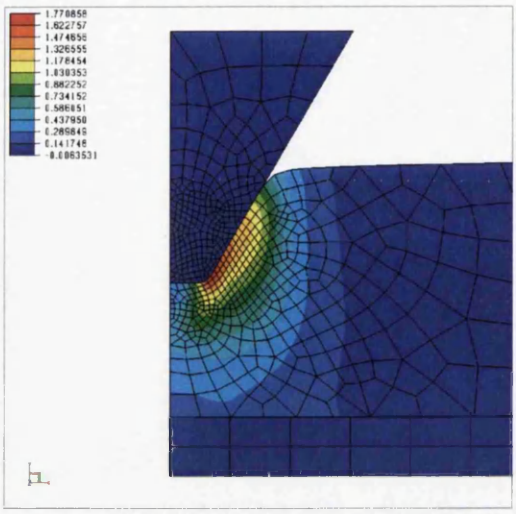

(a) SC = 107 μm : Strain XY

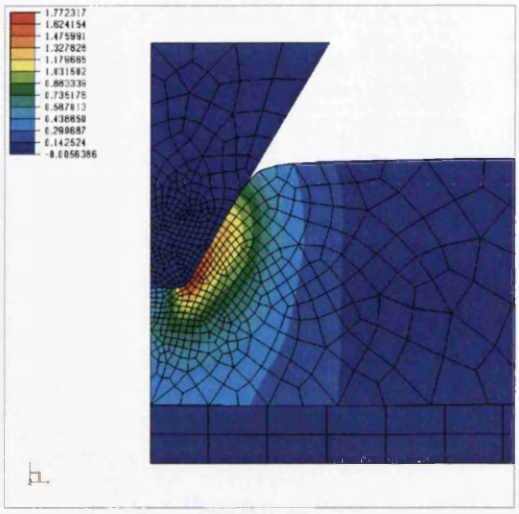

(b) SC = 91 μm : Strain XY

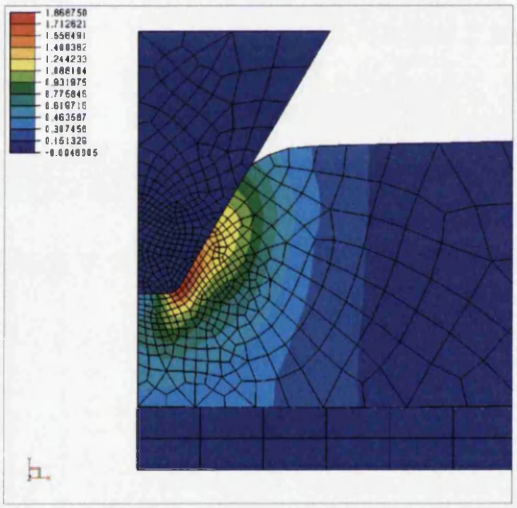

(c) SC = 83 μm : Strain XY

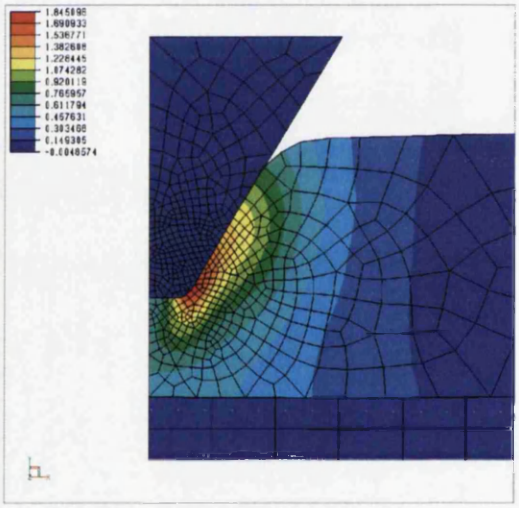

(d) SC = 72 μm : Strain XY

Figure D.37: PS Strain XY

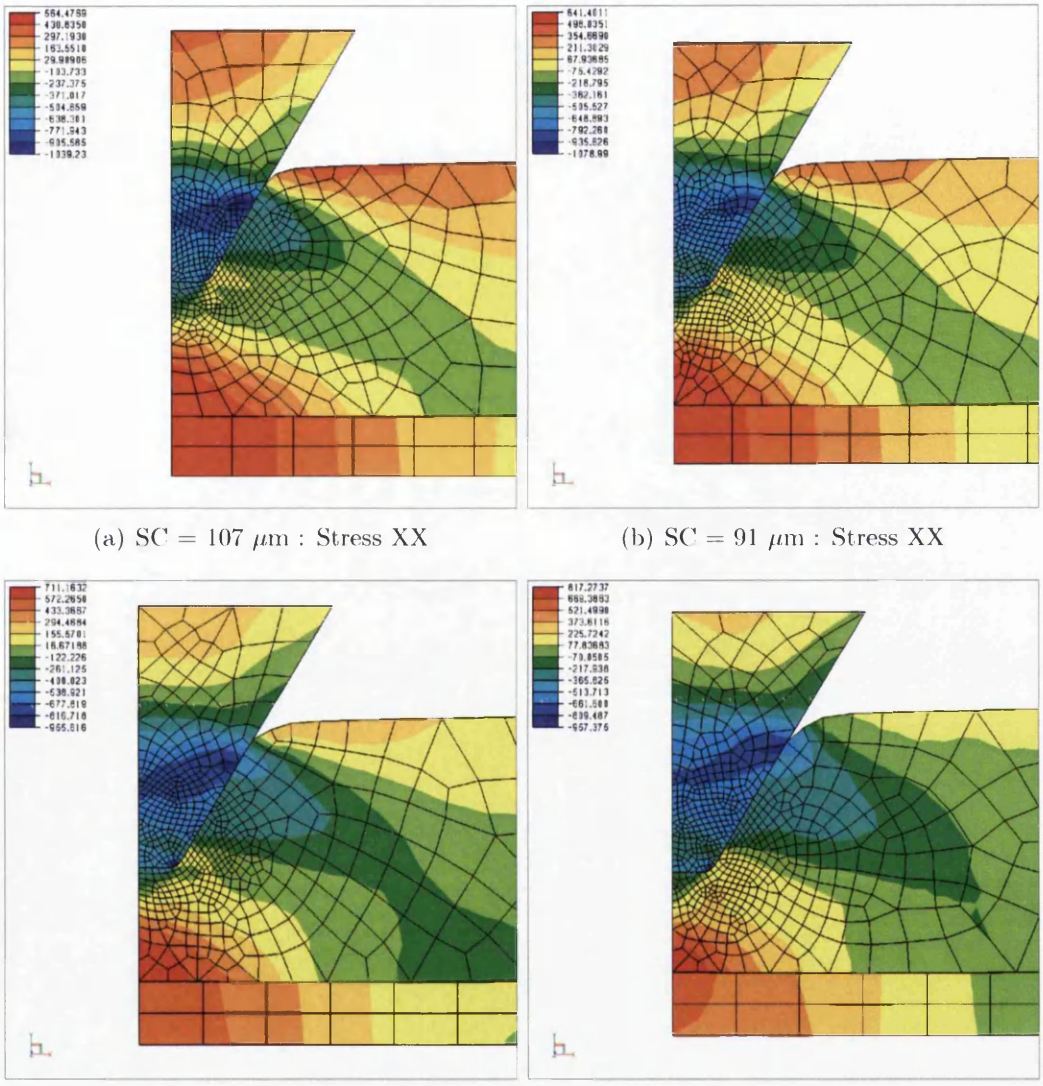

(a) SC = 107 μm : Stress XX

(b) SC = 91 μm : Stress XX

(c) SC = 83 μm : Stress XX

(d) SC = 72 μm : Stress XX

Figure D.38: PS Stress XX

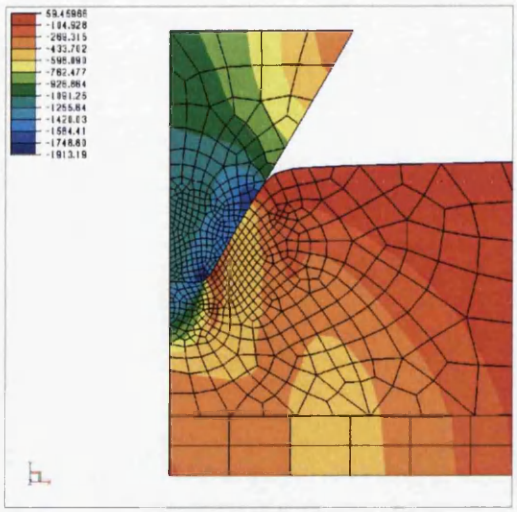

(a) SC = 107 μm : Stress YY

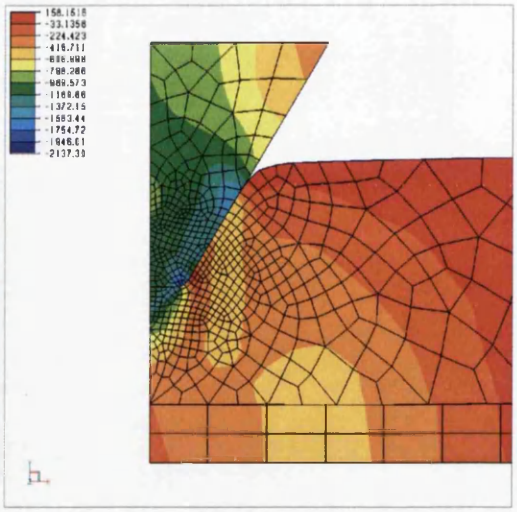

(b) SC = 91 μm : Stress YY

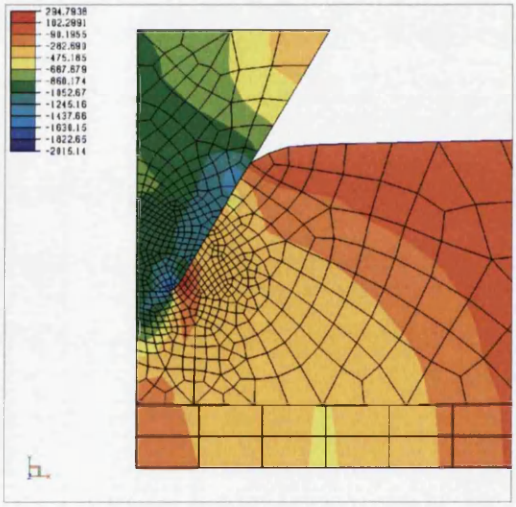

(c) SC = 83 μm : Stress YY

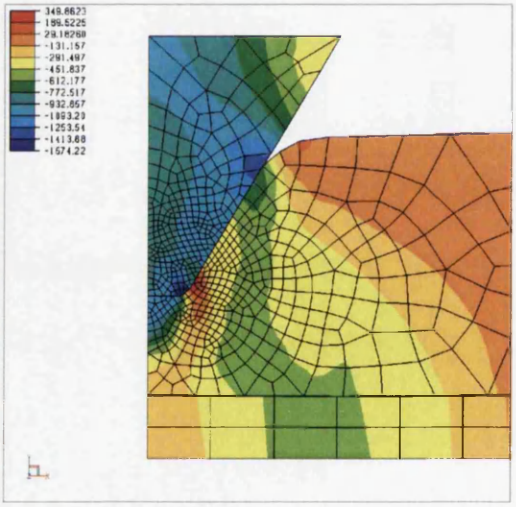

(d) SC = 72 μm : Stress YY

Figure D.39: PS Stress YY

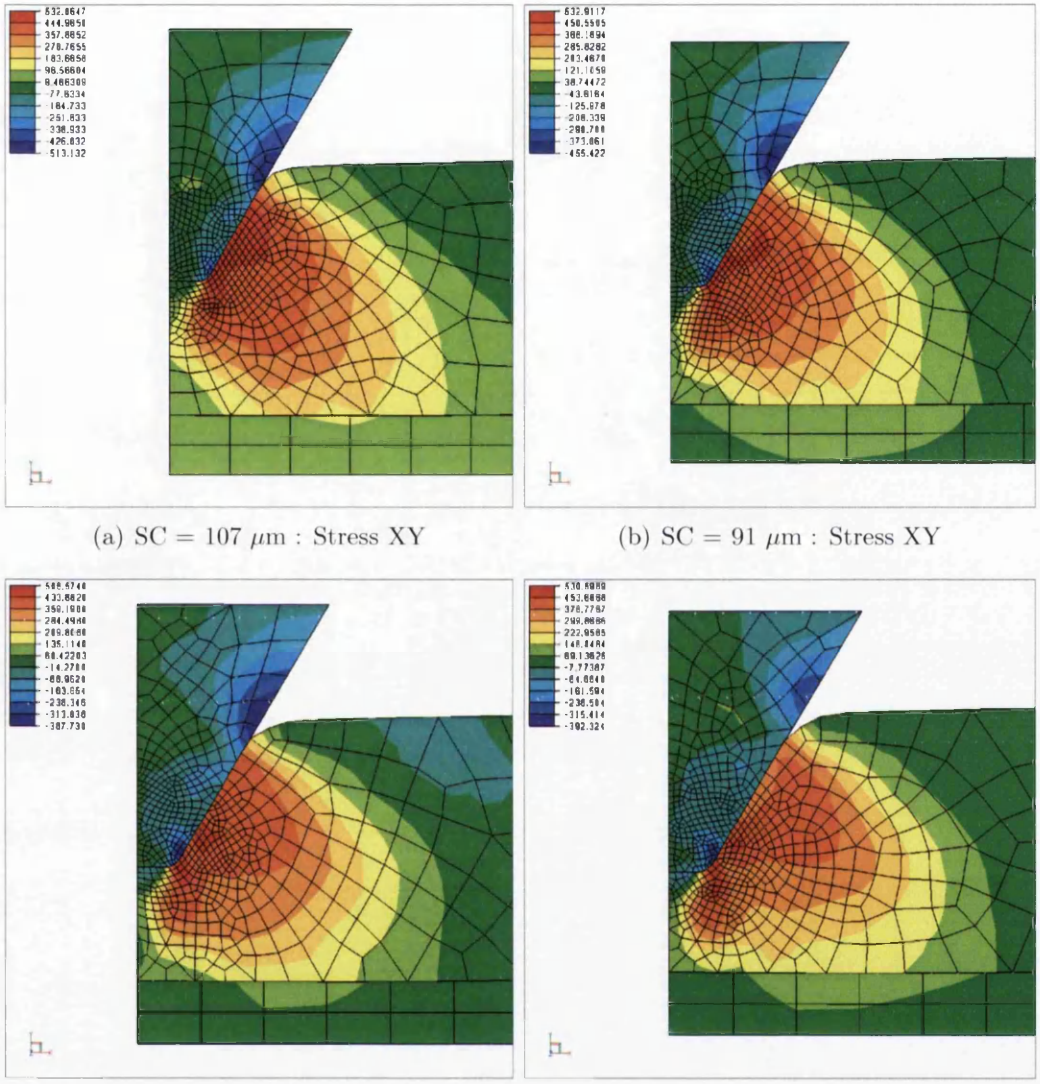

(a) SC = 107 μm : Stress XY

(b) SC = 91 μm : Stress XY

(c) SC = 83 μm : Stress XY

(d) SC = 72 μm : Stress XY

Figure D.40: PS Stress XY

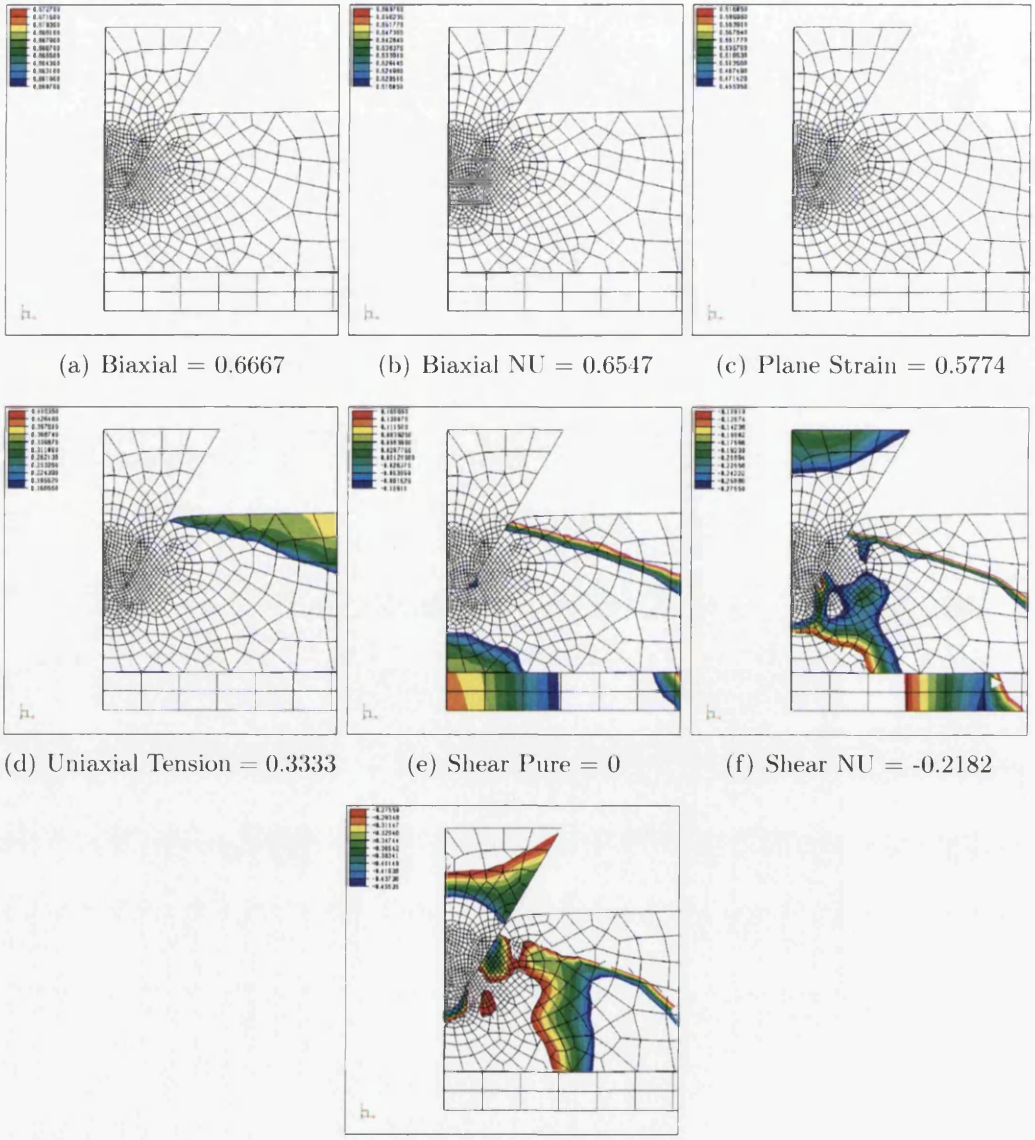

(a) Biaxial = 0.6667 (b) Biaxial NU = 0.6547 (c) Plane Strain = 0.5774

(d) Uniaxial Tension = 0.3333 (e) Shear Pure = 0 (f) Shear NU = -0.2182

(g) Uniaxial Comp = -0.3328

Figure D.41: PS107 - Triaxiality : with Score Residual at 107 μm

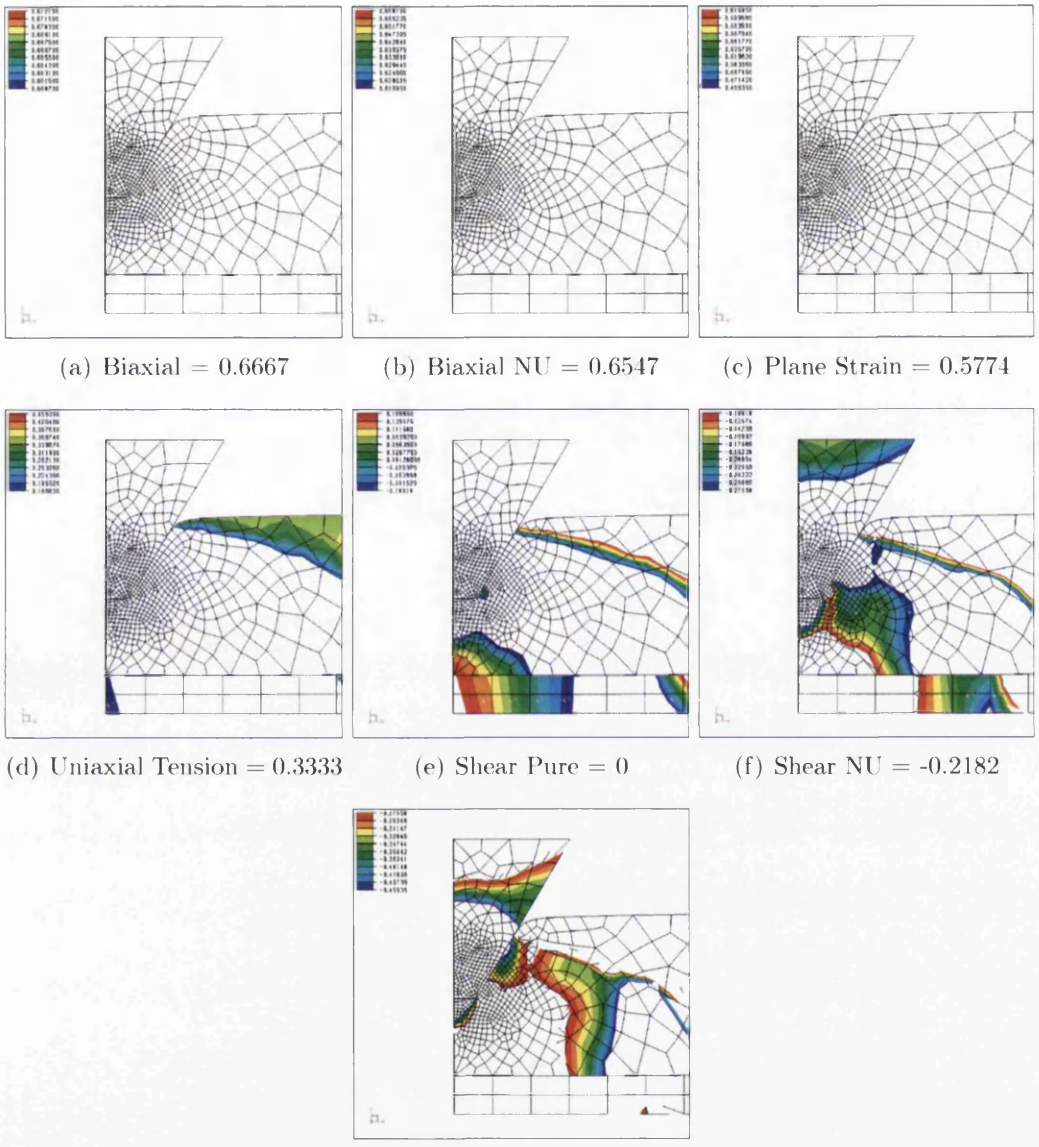

(a) Biaxial = 0.6667 (b) Biaxial NU = 0.6547 (c) Plane Strain = 0.5774

(d) Uniaxial Tension = 0.3333 (e) Shear Pure = 0 (f) Shear NU = -0.2182

(g) Uniaxial Comp = -0.3328

Figure D.42: PS91 - Triaxiality : with Score Residual at 91 μm

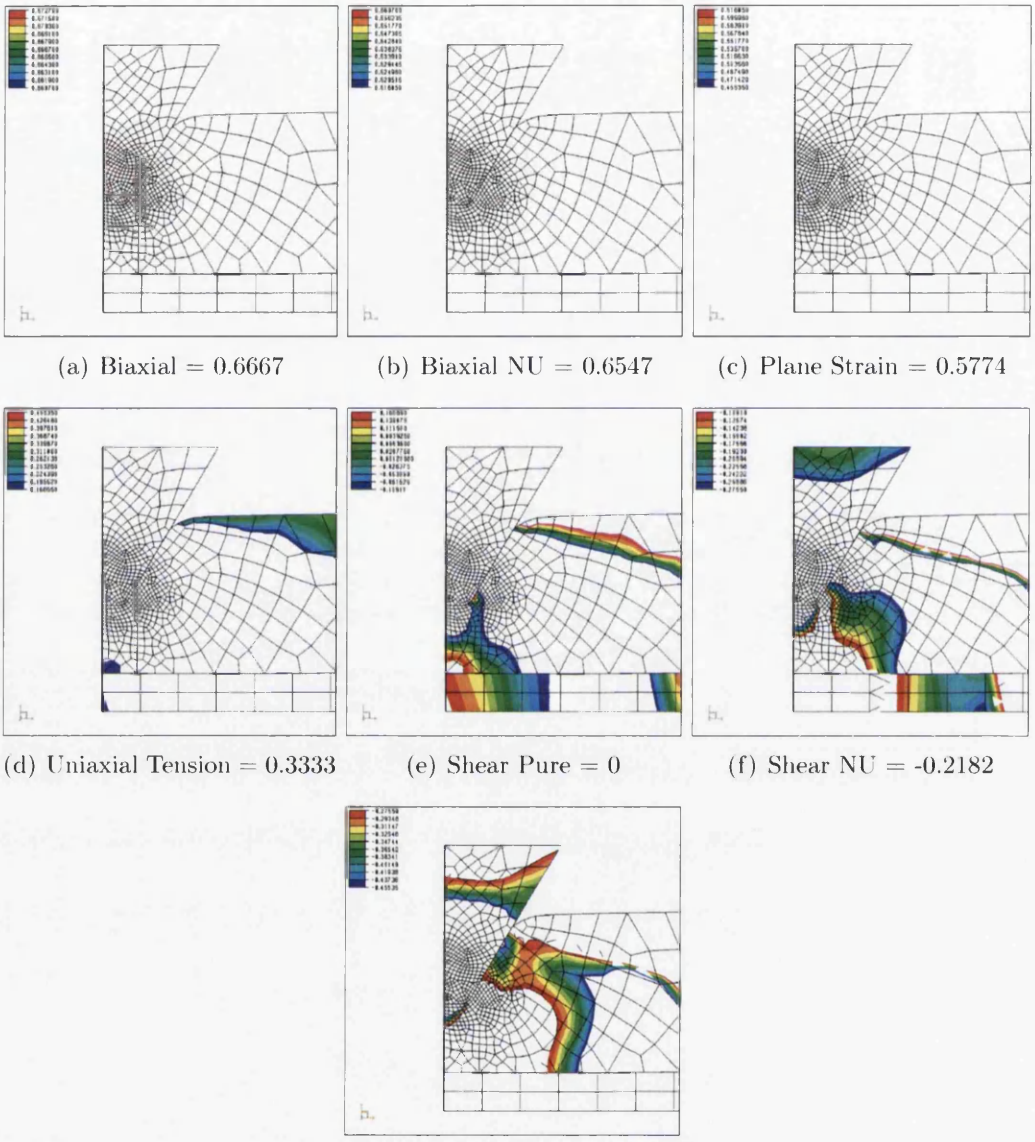

(a) Biaxial = 0.6667 (b) Biaxial NU = 0.6547 (c) Plane Strain = 0.5774

(d) Uniaxial Tension = 0.3333 (e) Shear Pure = 0 (f) Shear NU = -0.2182

(g) Uniaxial Comp = -0.3328

Figure D.43: PS83 - Triaxiality : with Score Residual at 83 μm

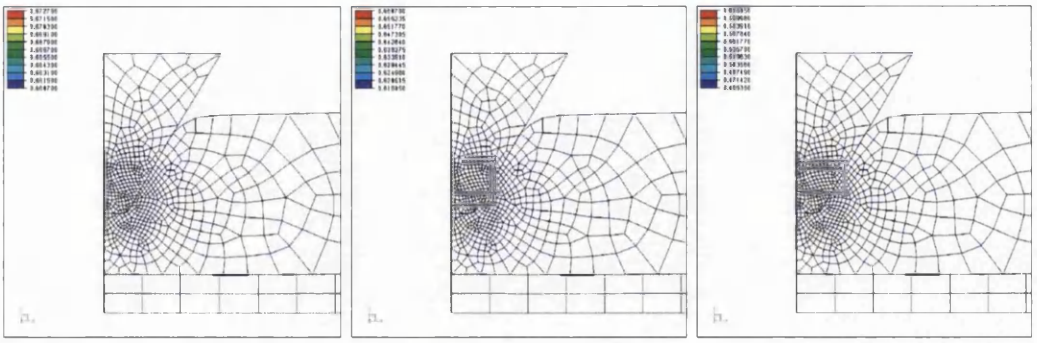

(a) Biaxial = 0.6667 (b) Biaxial NU = 0.6547 (c) Plane Strain = 0.5774

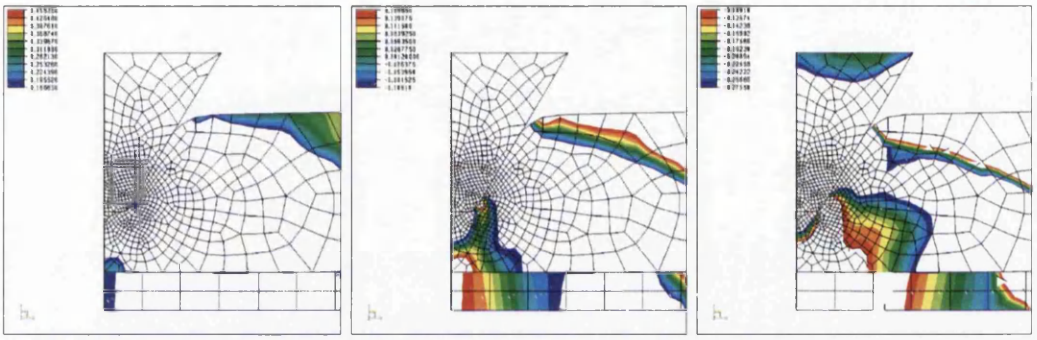

(d) Uniaxial Tension = 0.3333 (e) Shear Pure = 0 (f) Shear NU = -0.2182

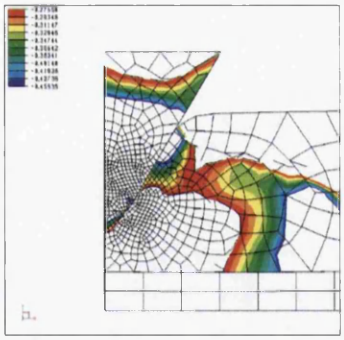

(g) Uniaxial Comp = -0.3328

Figure D.44: PS72 - Triaxiality : with Score Residual at 72 μm

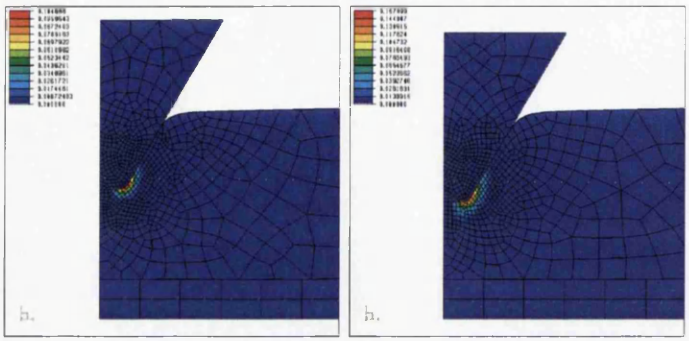

(a) SR = 107 μm (b) SR = 91 μm

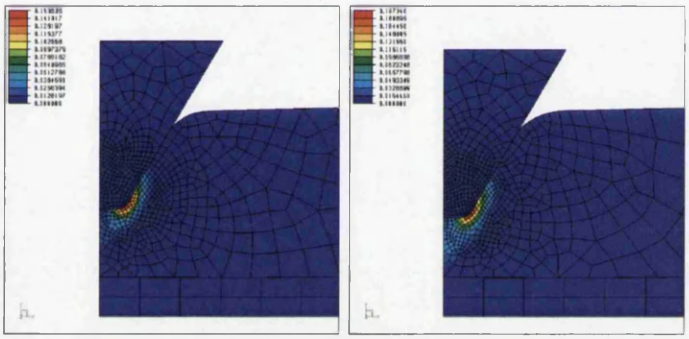

(c) SR = 83 μm (d) SR = 72 μm

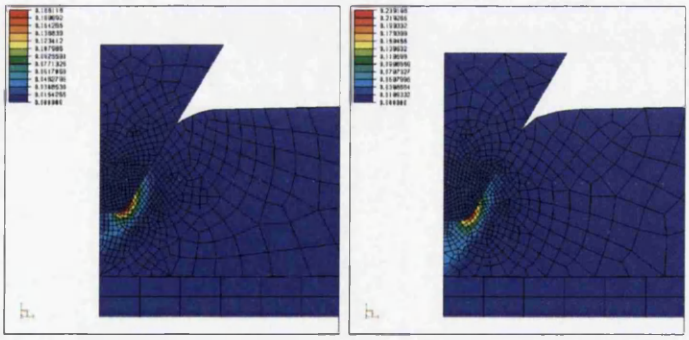

(e) SR = 78 μm (f) SR = 68 μm

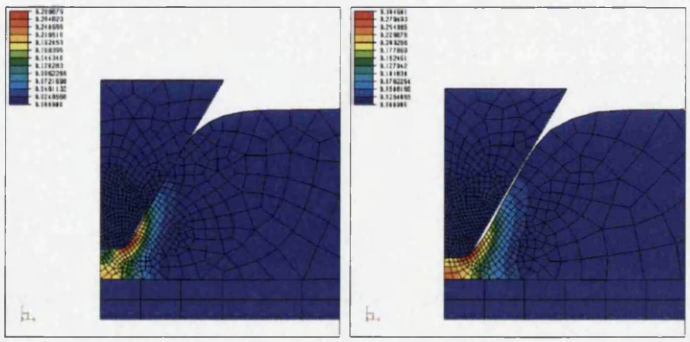

(g) SR = 36 μm (h) SR = 26 μm

Figure D.45: Coupled Lemaitre Damage: So = 0.8, R=8, PT=1.1, CC=0.2

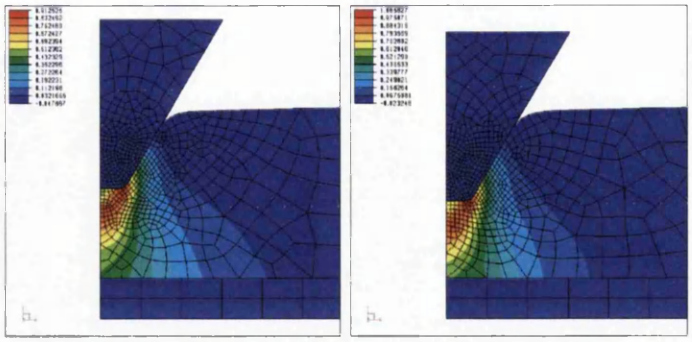

(a) SR = 107 μm (b) SR = 91 μm

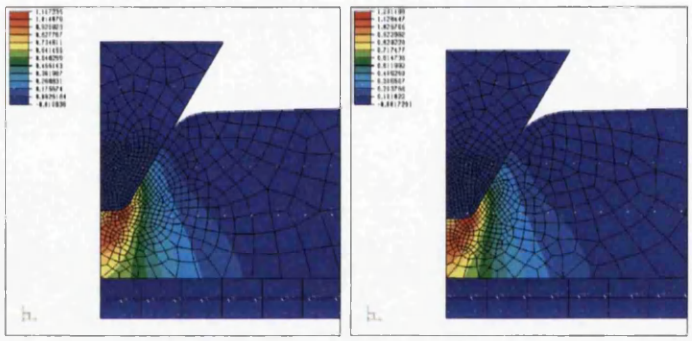

(c) SR = 83 μm (d) SR = 72 μm

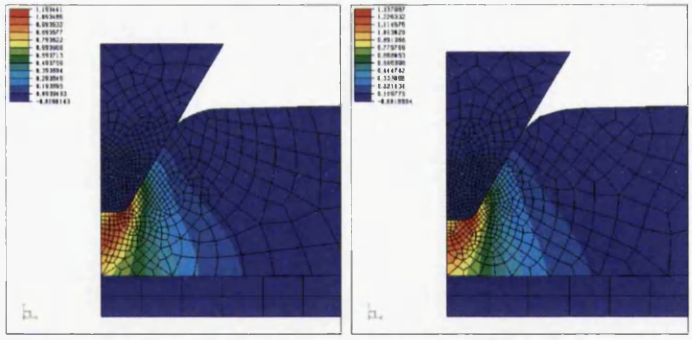

(e) SR = 78 μm (f) SR = 68 μm

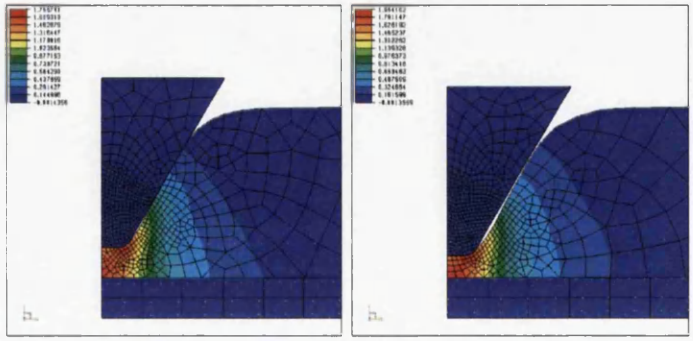

(g) SR = 36 μm (h) SR = 26 μm

Figure D.46: Direct Strain X-X: So = 0.8, R=8, PT=1.1, CC=0.2

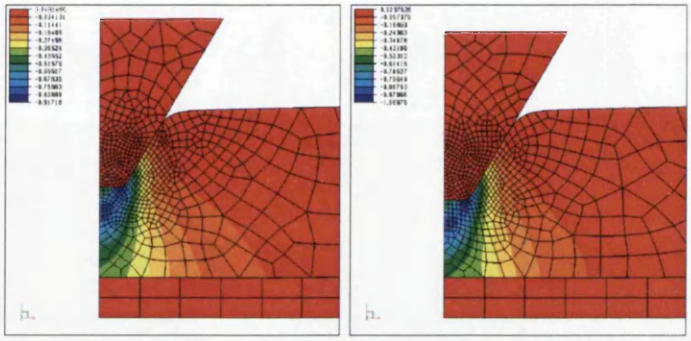

(a) SR = 107 μm (b) SR = 91 μm

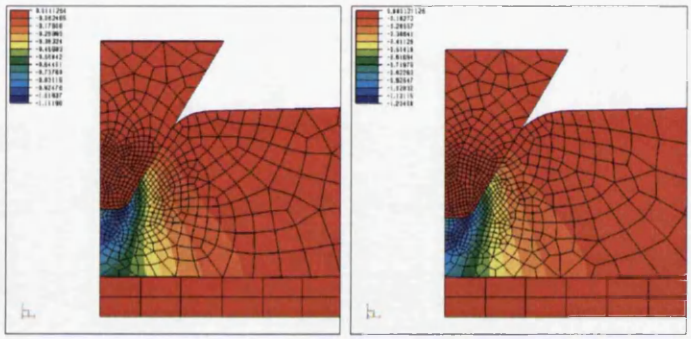

(c) SR = 83 μm (d) SR = 72 μm

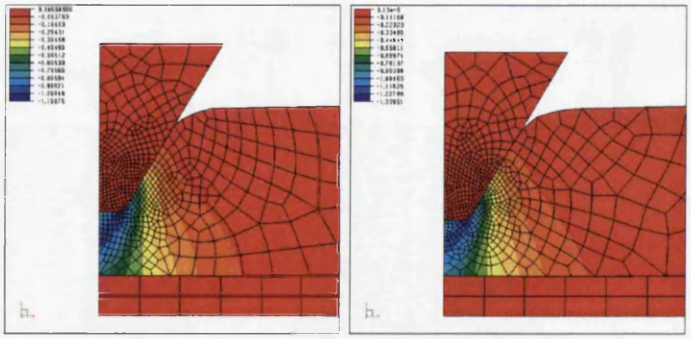

(e) SR = 78 μm (f) SR = 68 μm

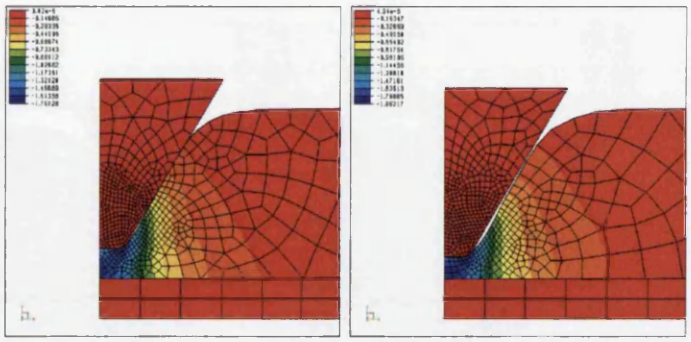

(g) SR = 36 μm (h) SR = 26 μm

Figure D.47: Direct Strain Y-Y: So = 0.8, R=8, PT=1.1, CC=0.2

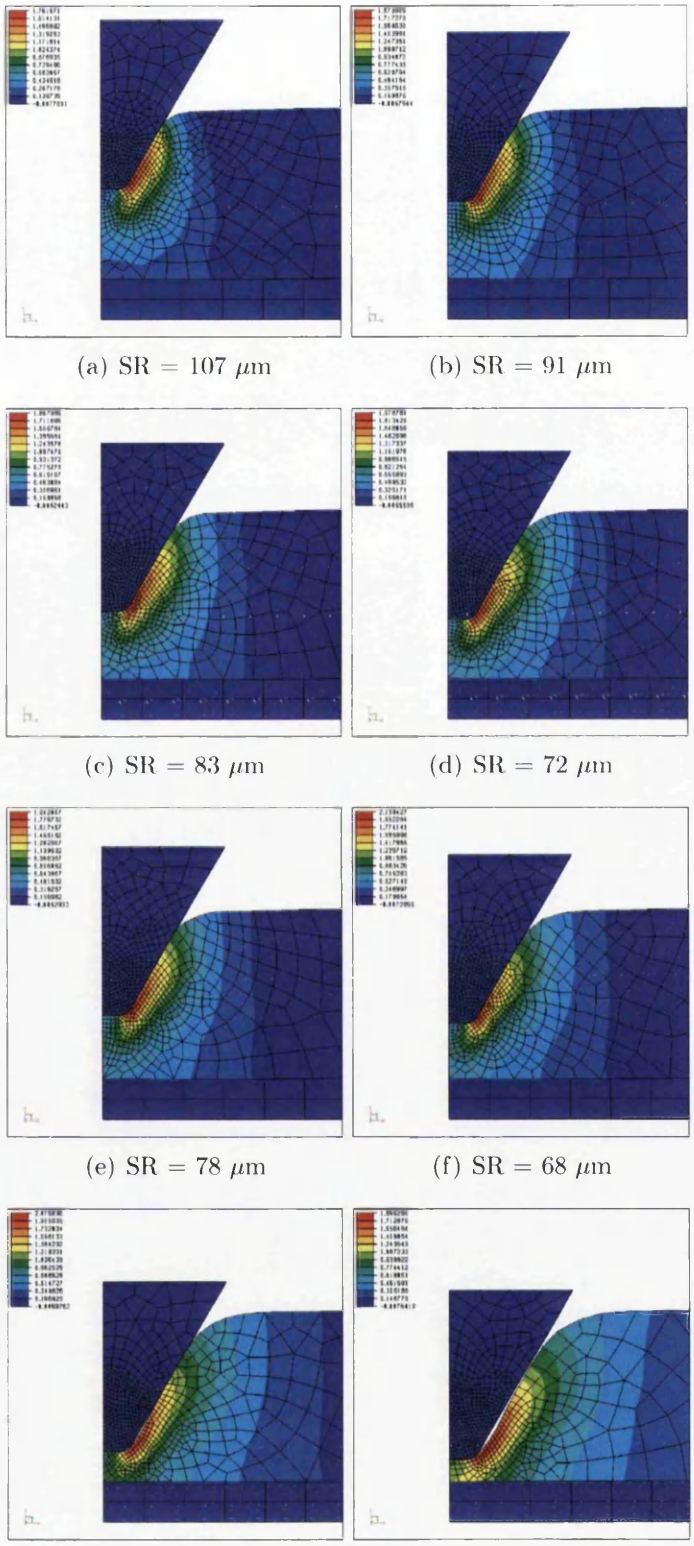

(a) SR = 107 μm (b) SR = 91 μm

(c) SR = 83 μm (d) SR = 72 μm

(e) SR = 78 μm (f) SR = 68 μm

(g) SR = 36 μm (h) SR = 26 μm

Figure D.48: Shear Strain X-Y: So = 0.8, R=8, PT=1.1, CC=0.2

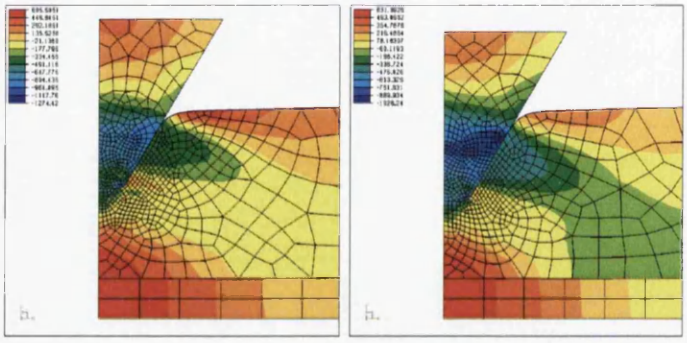

(a) SR = 107 μm (b) SR = 91 μm

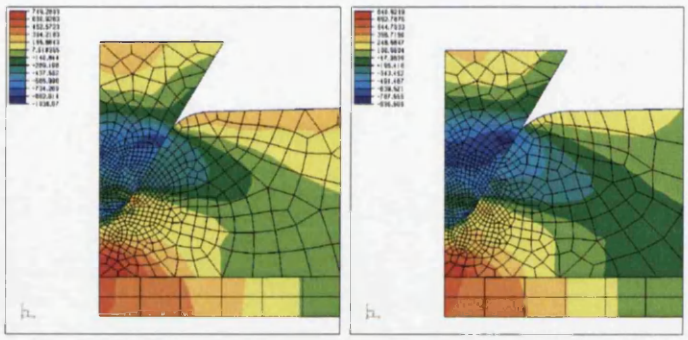

(c) SR = 83 μm (d) SR = 72 μm

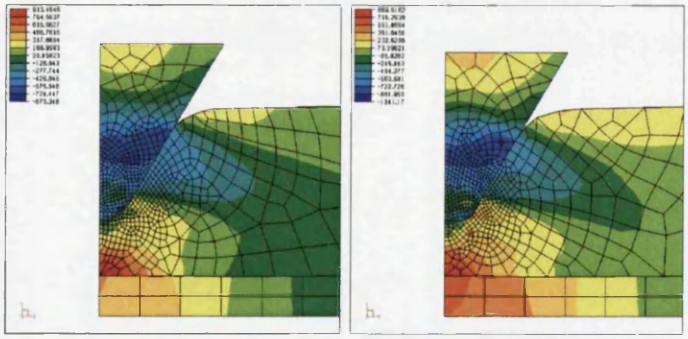

(e) SR = 78 μm (f) SR = 68 μm

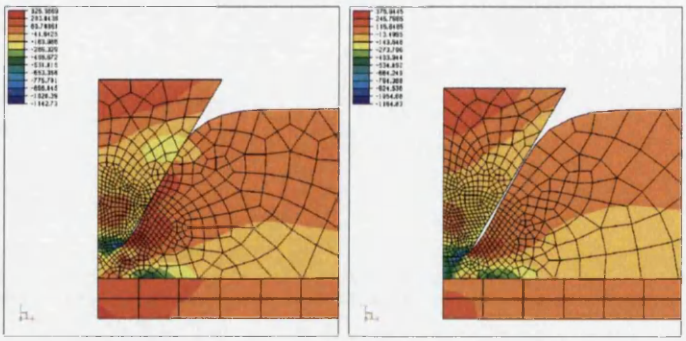

(g) SR = 36 μm (h) SR = 26 μm

Figure D.49: Direct Stress X-X: So = 0.8, R=8, PT=1.1, CC=0.2

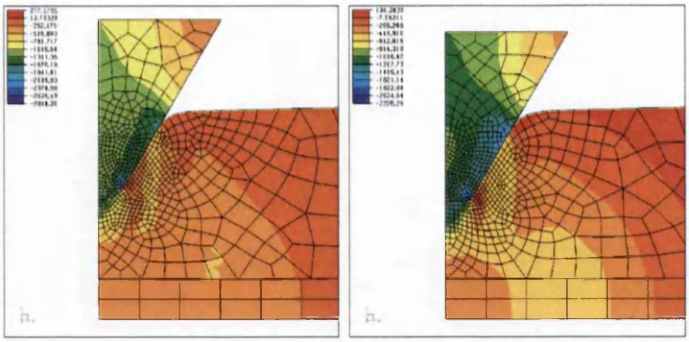

(a) SR = 107 μm (b) SR = 91 μm

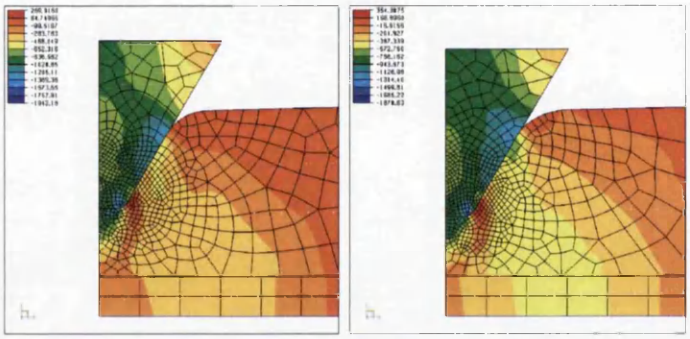

(c) SR = 83 μm (d) SR = 72 μm

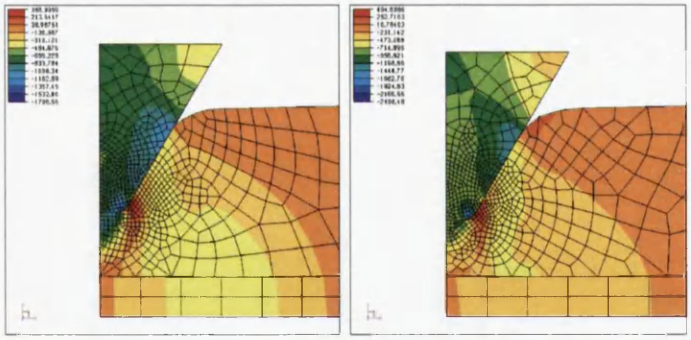

(e) SR = 78 μm (f) SR = 68 μm

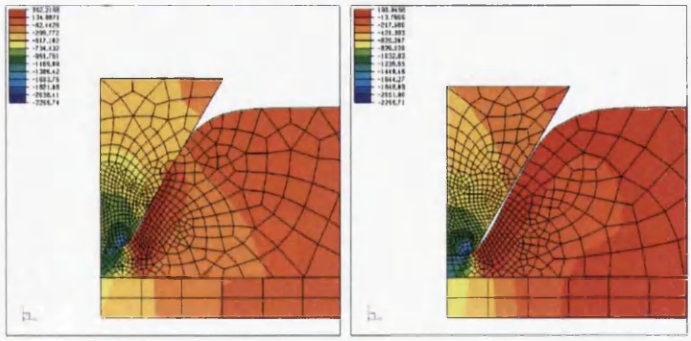

(g) SR = 36 μm (h) SR = 26 μm

Figure D.50: Direct Stress Y-Y: So = 0.8, R=8, PT=1.1, CC=0.2

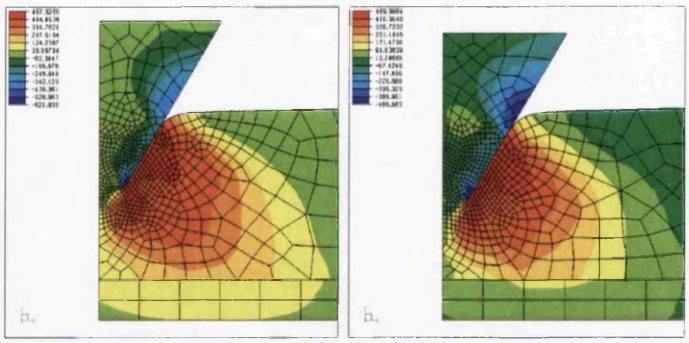

(a) SR = 107 μm (b) SR = 91 μm

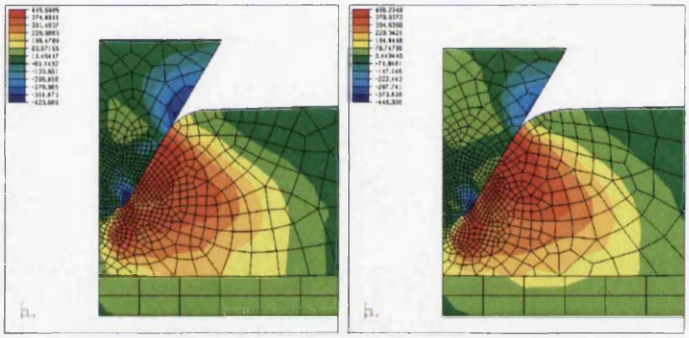

(c) SR = 83 μm (d) SR = 72 μm

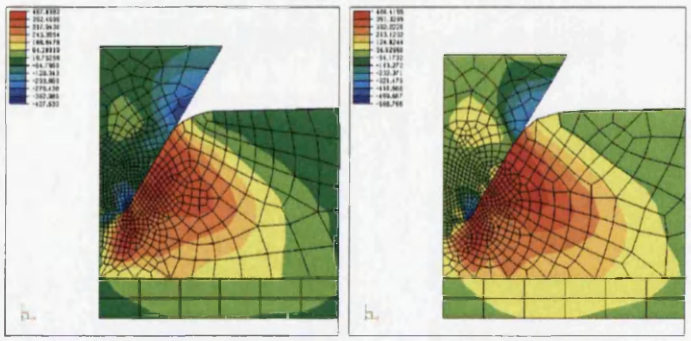

(e) SR = 78 μm (f) SR = 68 μm

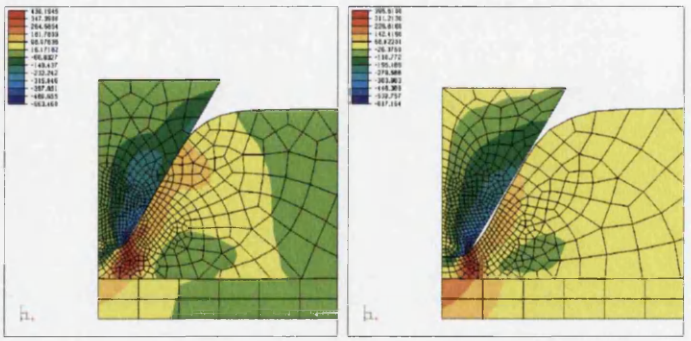

(g) SR = 36 μm (h) SR = 26 μm

Figure D.51: Shear Stress X-Y: So = 0.8, R=8, PT=1.1, CC=0.2

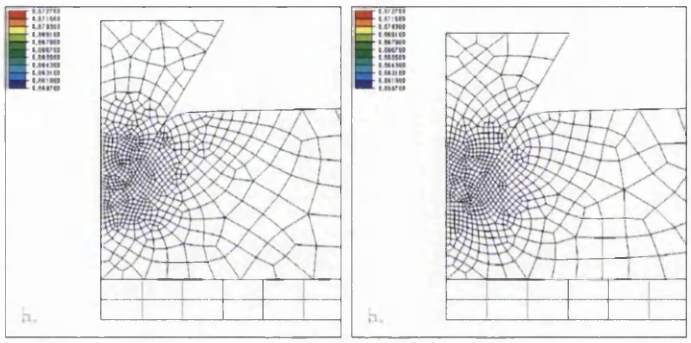

(a) SR = 107 μm

(b) SR = 91 μm

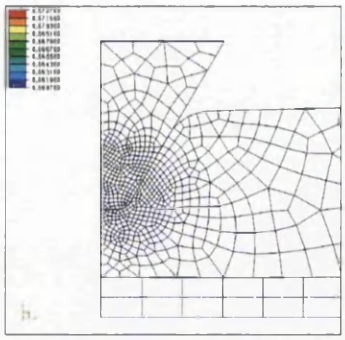

(c) SR = 83 μm

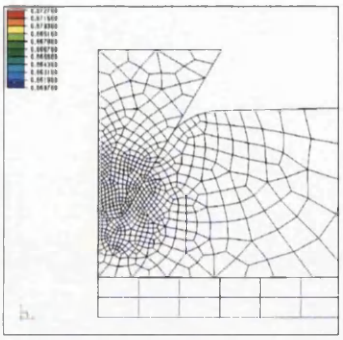

(d) SR = 72 μm

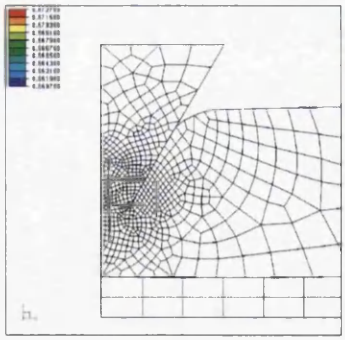

(e) SR = 78 μm

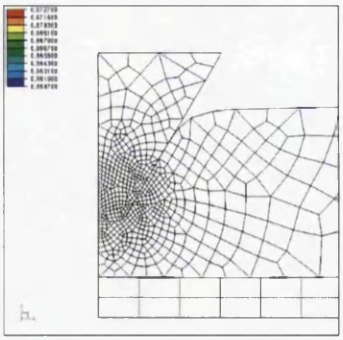

(f) SR = 68 μm

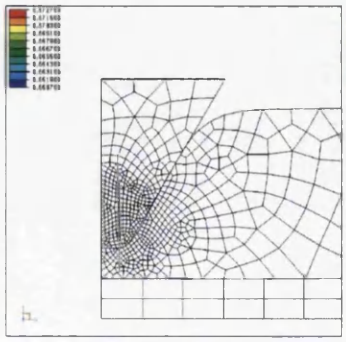

(g) SR = 36 μm

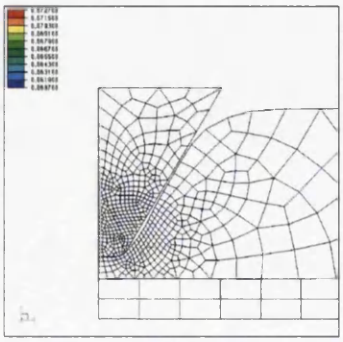

(h) SR = 26 μm

Figure D.52: Triaxiality - Biaxial: So = 0.8, R=8, PT=1.1, CC=0.2

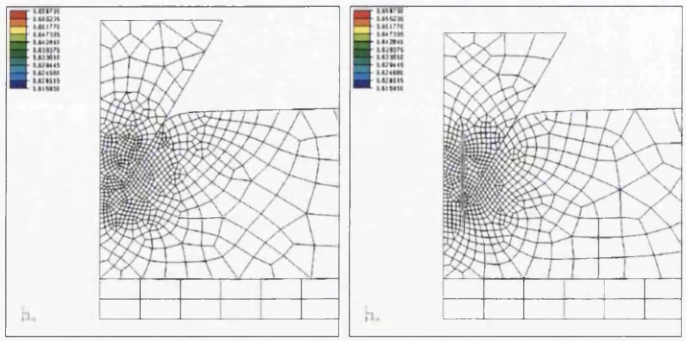

(a) SR = 107 μm (b) SR = 91 μm

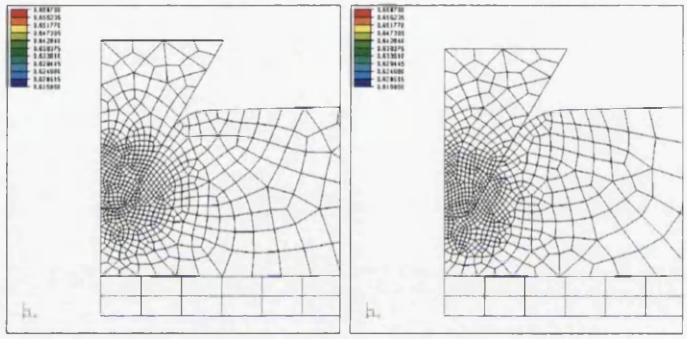

(c) SR = 83 μm (d) SR = 72 μm

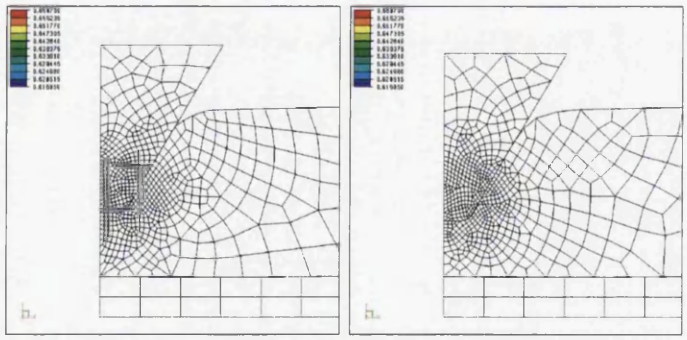

(e) SR = 78 μm (f) SR = 68 μm

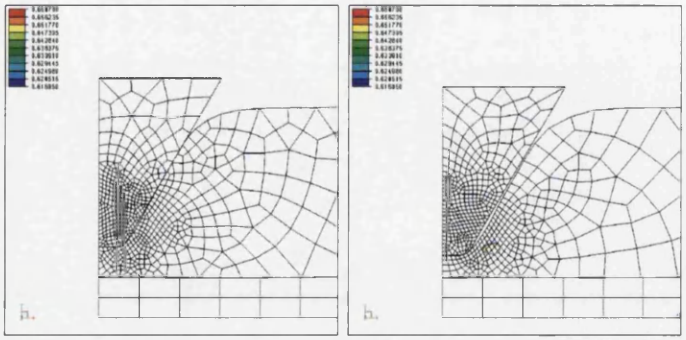

(g) SR = 36 μm (h) SR = 26 μm

Figure D.53: Triaxiality - Biaxial NU: So = 0.8, R=8, PT=1.1, CC=0.2

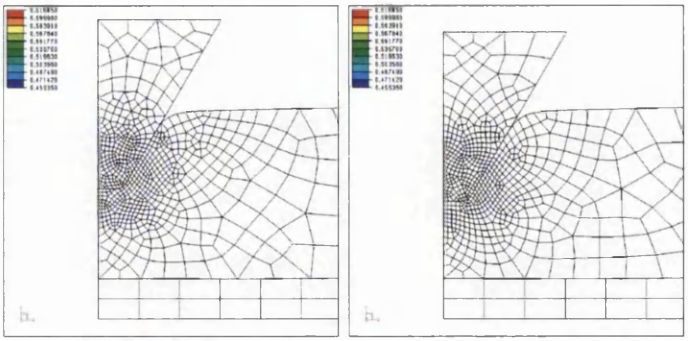

(a) SR = 107 μm (b) SR = 91 μm

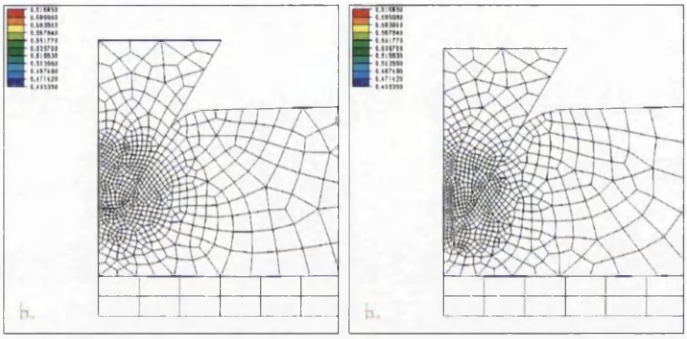

(c) SR = 83 μm (d) SR = 72 μm

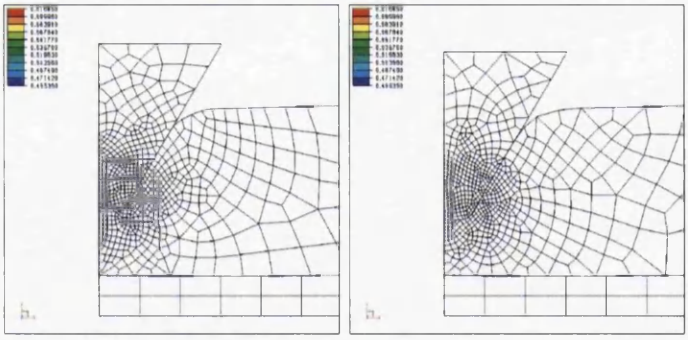

(e) SR = 78 μm (f) SR = 68 μm

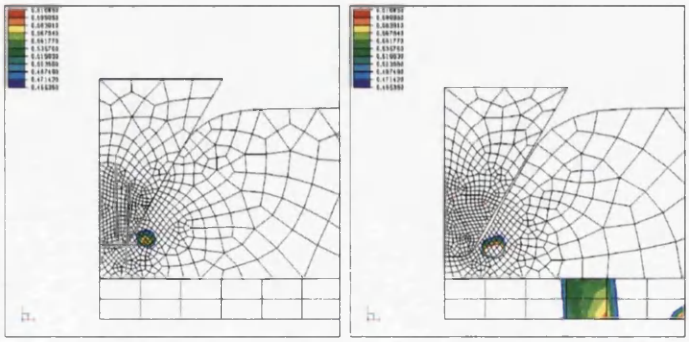

(g) SR = 36 μm (h) SR = 26 μm

Figure D.54: Triaxiality - Plane Strain: So = 0.8, R=8, PT=1.1, CC=0.2

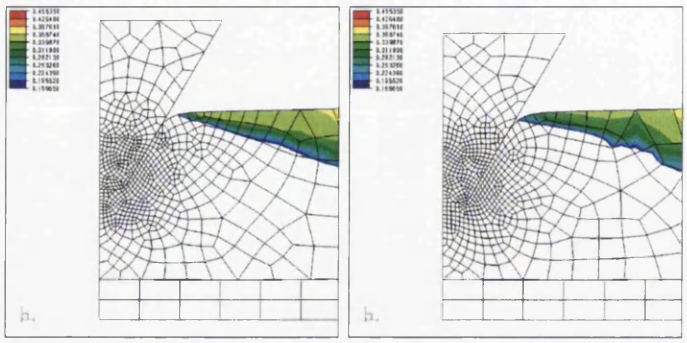

(a) SR = 107 μm (b) SR = 91 μm

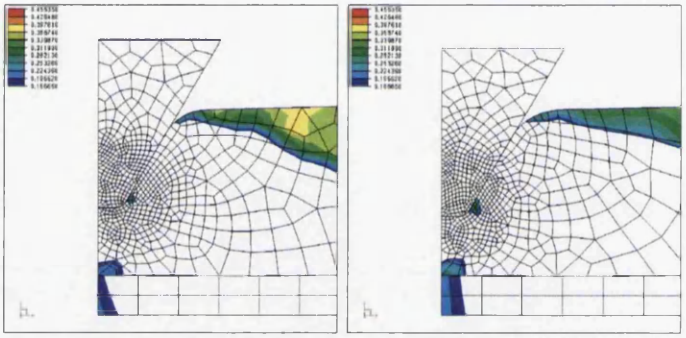

(c) SR = 83 μm (d) SR = 72 μm

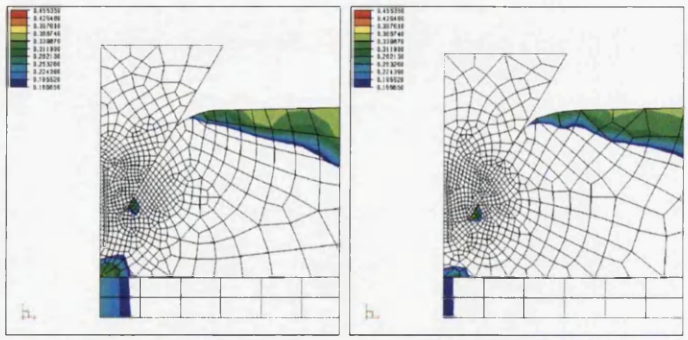

(e) SR = 78 μm (f) SR = 68 μm

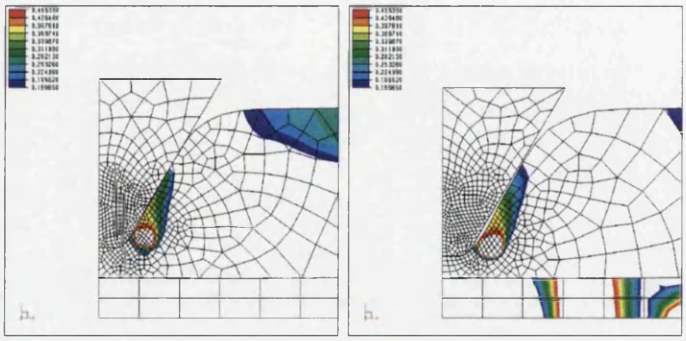

(g) SR = 36 μm (h) SR = 26 μm

Figure D.55: Triaxiality - Uniaxial Tension: So = 0.8, R=8, PT=1.1, CC=0.2

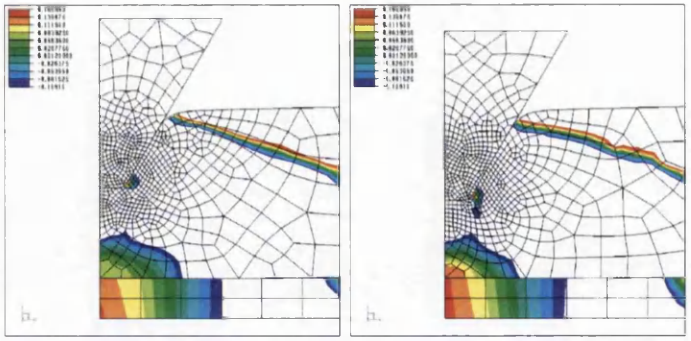

(a) SR = 107 μm (b) SR = 91 μm

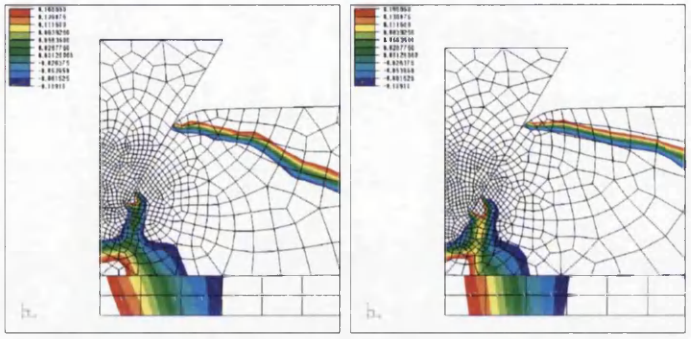

(c) SR = 83 μm (d) SR = 72 μm

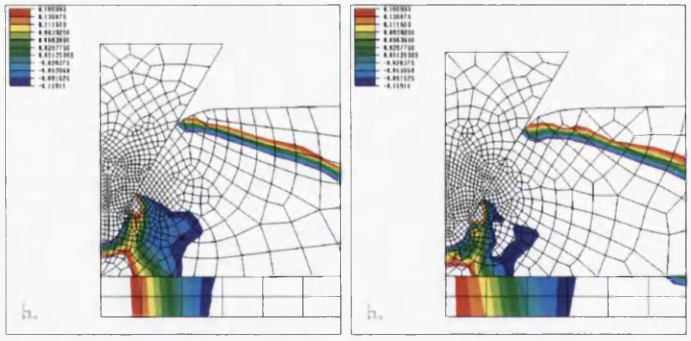

(e) SR = 78 μm (f) SR = 68 μm

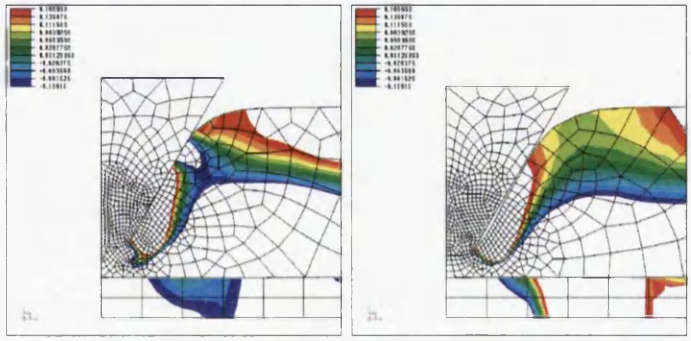

(g) SR = 36 μm (h) SR = 26 μm

Figure D.56: Triaxiality - Shear Pure: So = 0.8, R=8, PT=1.1, CC=0.2

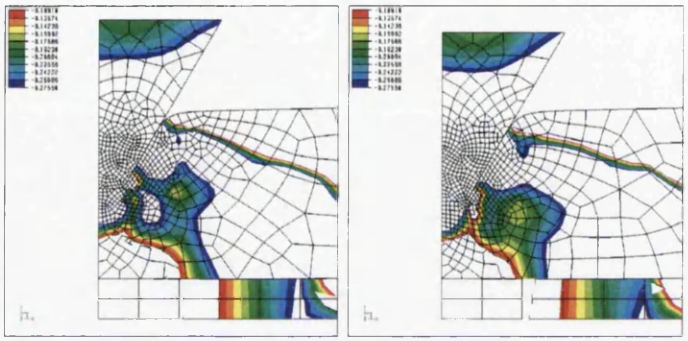

(a) SR = 107 μm (b) SR = 91 μm

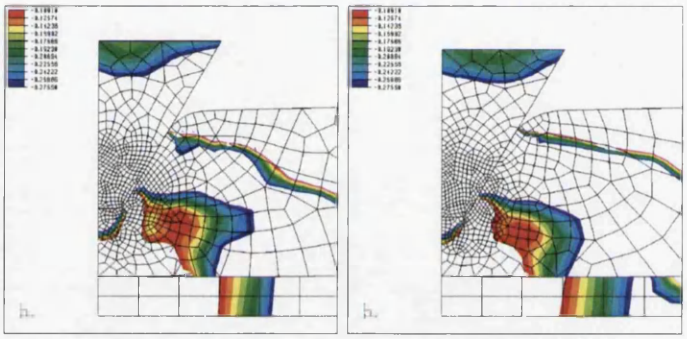

(c) SR = 83 μm (d) SR = 72 μm

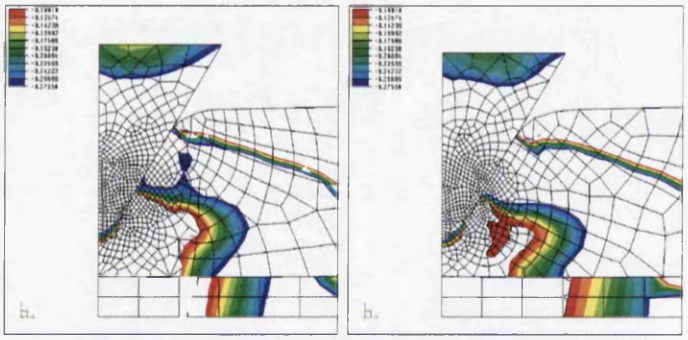

(e) SR = 78 μm (f) SR = 68 μm

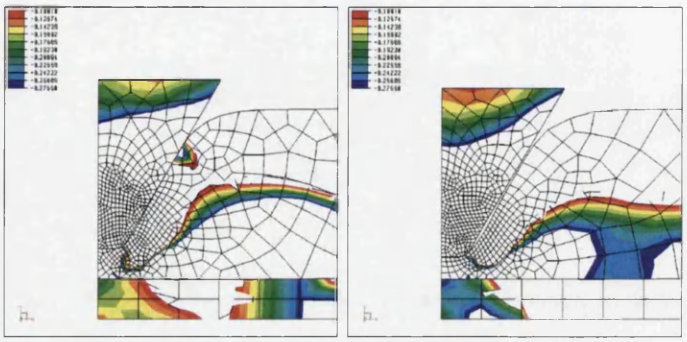

(g) SR = 36 μm (h) SR = 26 μm

Figure D.57: Triaxiality - Shear NU: So = 0.8, R=8, PT=1.1, CC=0.2

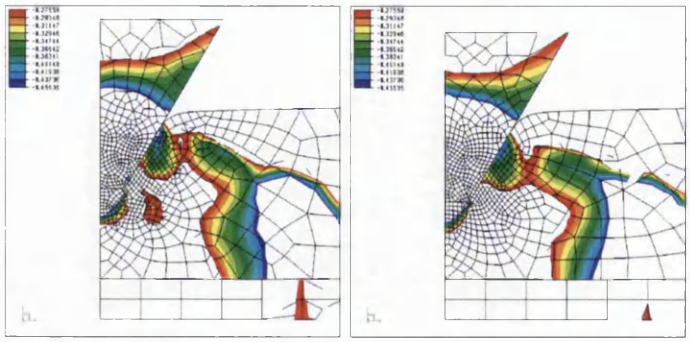

(a) SR = 107 μm (b) SR = 91 μm

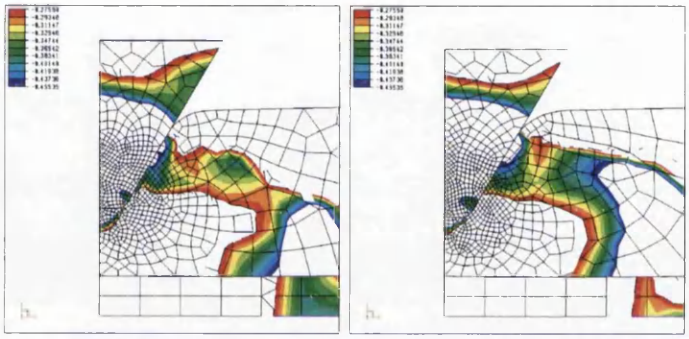

(c) SR = 83 μm (d) SR = 72 μm

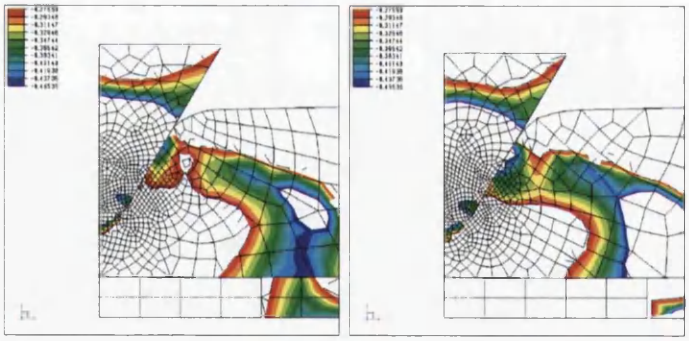

(e) SR = 78 μm (f) SR = 68 μm

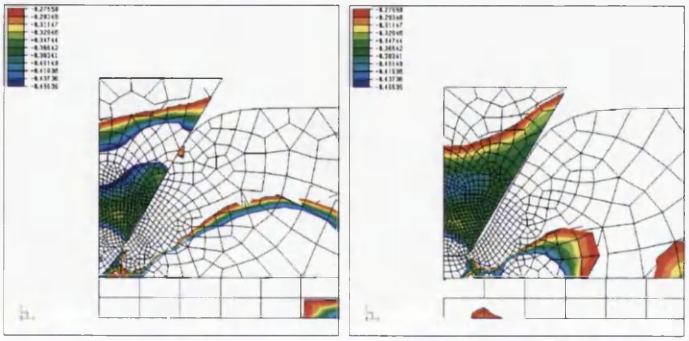

(g) SR = 36 μm (h) SR = 26 μm

Figure D.58: Triaxiality - Uniaxial Compression: So = 0.8, R=8, PT=1.1, CC=0.2

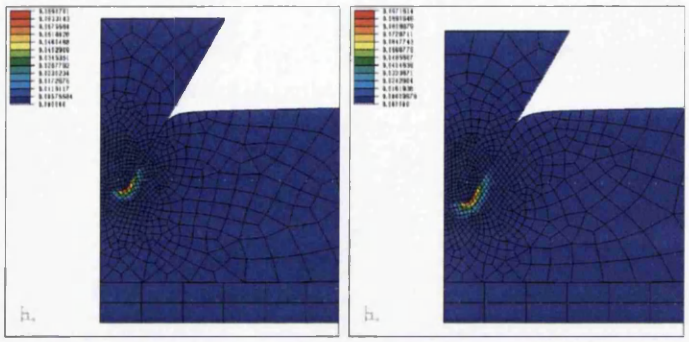

(a) SR = 107 μm (b) SR = 91 μm

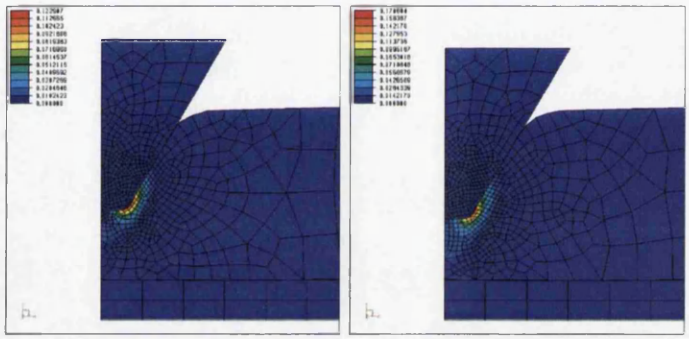

(c) SR = 83 μm (d) SR = 72 μm

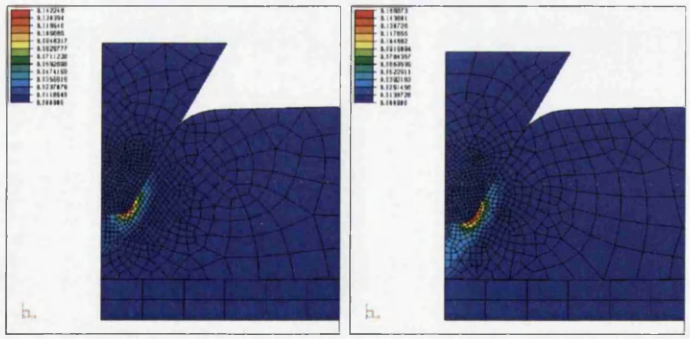

(e) SR = 78 μm (f) SR = 68 μm

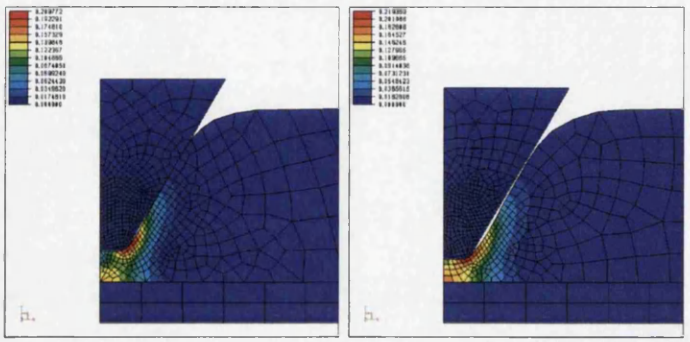

(g) SR = 36 μm (h) SR = 26 μm

Figure D.59: Coupled Lemaitre Damage: So = 1, R=8, PT=1.1, CC=0.2

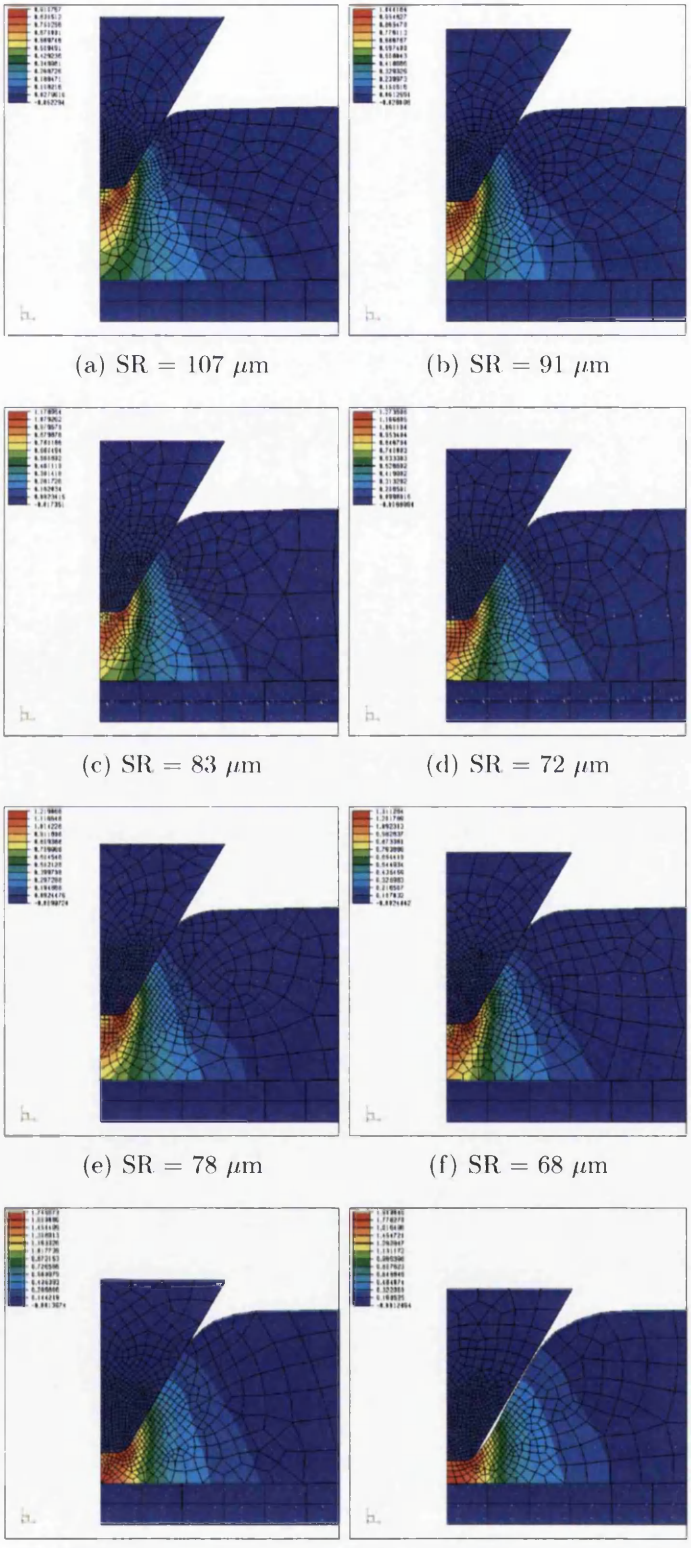

(a) SR = 107 μm (b) SR = 91 μm

(c) SR = 83 μm (d) SR = 72 μm

(e) SR = 78 μm (f) SR = 68 μm

(g) SR = 36 μm (h) SR = 26 μm

Figure D.60: Direct Strain X-X: So = 1, R=8, PT=1.1, CC=0.2

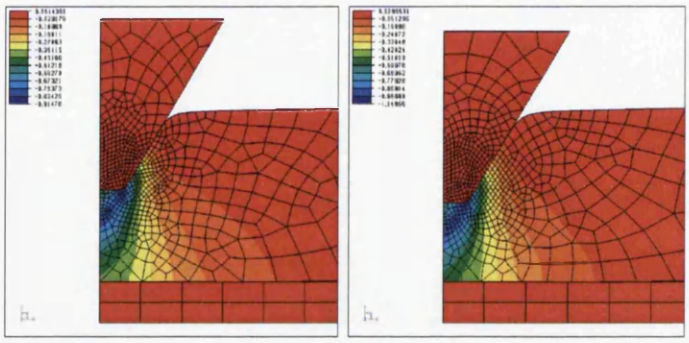

(a) SR = 107 μm (b) SR = 91 μm

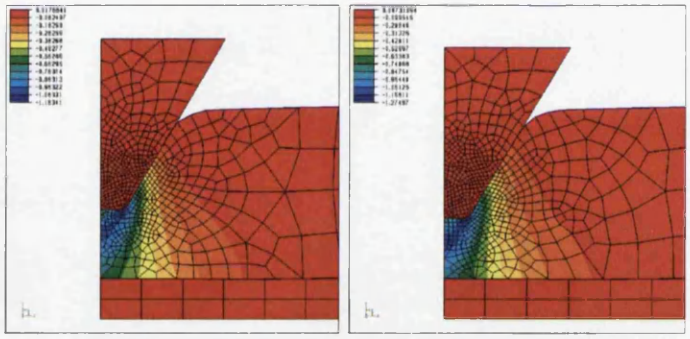

(c) SR = 83 μm (d) SR = 72 μm

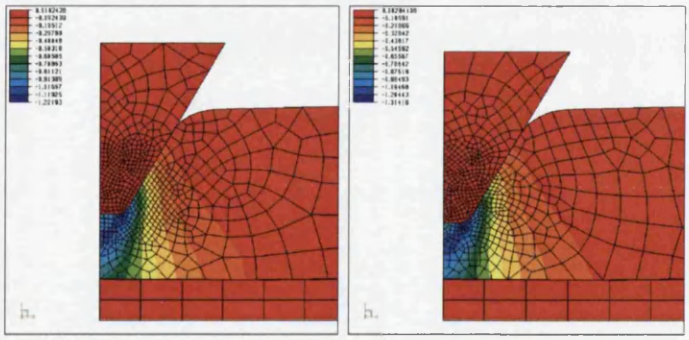

(e) SR = 78 μm (f) SR = 68 μm

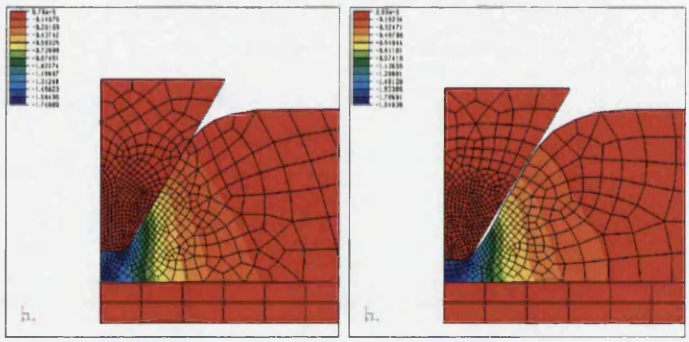

(g) SR = 36 μm (h) SR = 26 μm

Figure D.61: Direct Strain Y-Y: So = 1, R=8, PT=1.1, CC=0.2

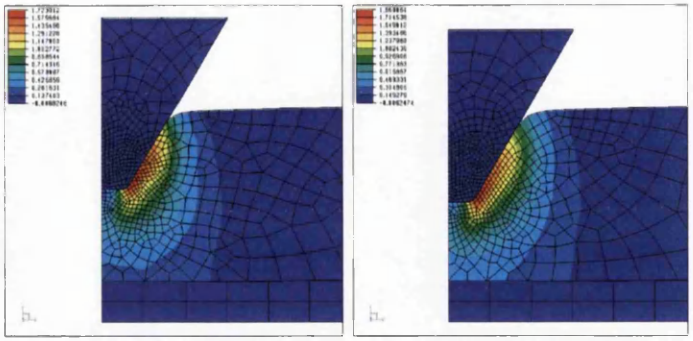

(a) SR = 107 μm (b) SR = 91 μm

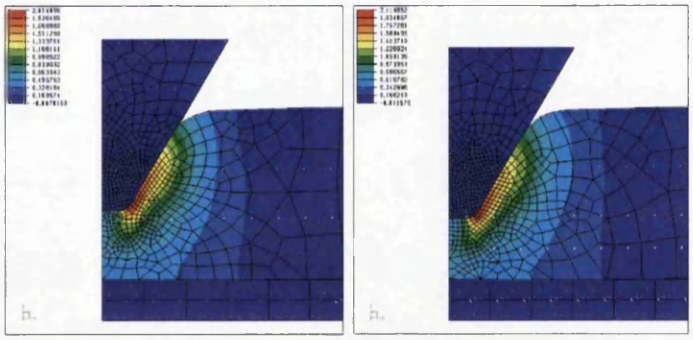

(c) SR = 83 μm (d) SR = 72 μm

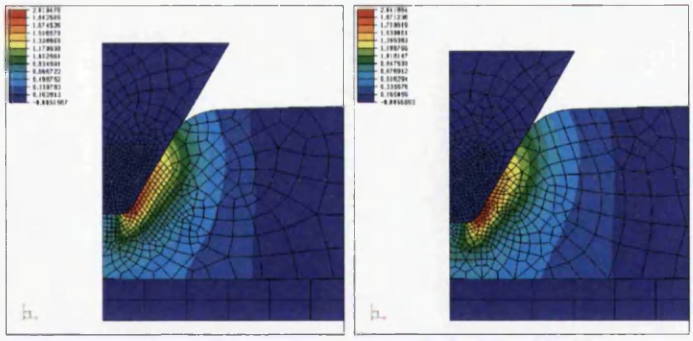

(e) SR = 78 μm (f) SR = 68 μm

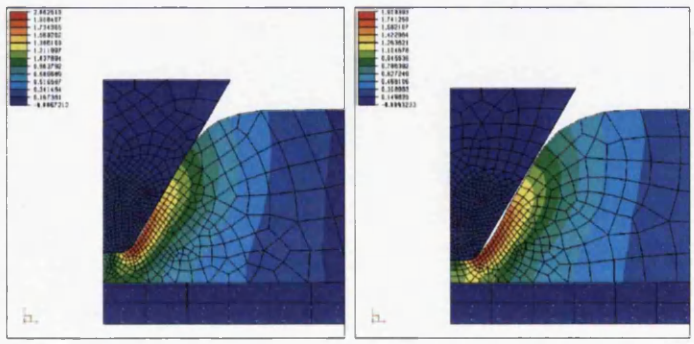

(g) SR = 36 μm (h) SR = 26 μm

Figure D.62: Shear Strain X-Y: So = 1, R=8, PT=1.1, CC=0.2

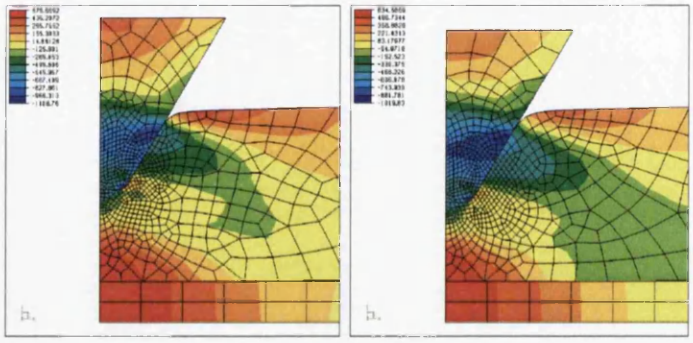

(a) SR = 107 μm (b) SR = 91 μm

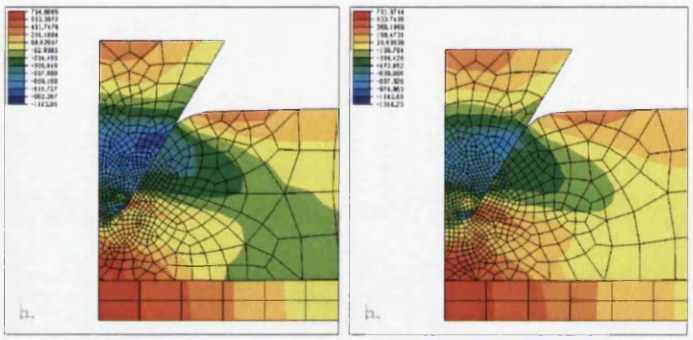

(c) SR = 83 μm (d) SR = 72 μm

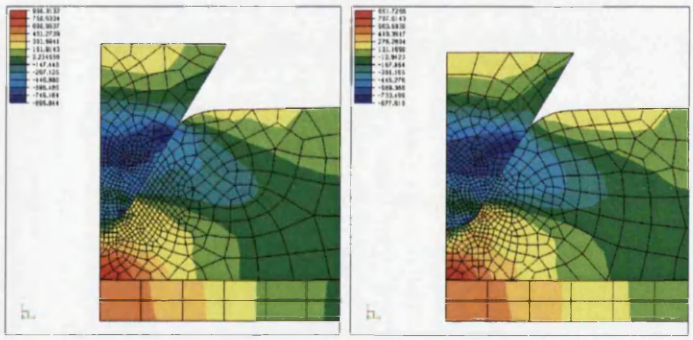

(e) SR = 78 μm (f) SR = 68 μm

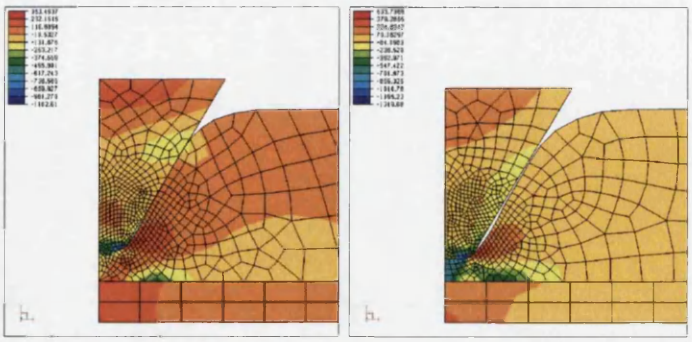

(g) SR = 36 μm (h) SR = 26 μm

Figure D.63: Direct Stress X-X: So = 1, R=8, PT=1.1, CC=0.2

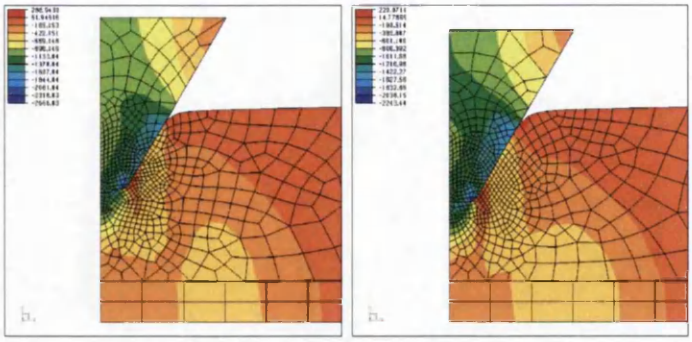

(a) SR = 107 μm (b) SR = 91 μm

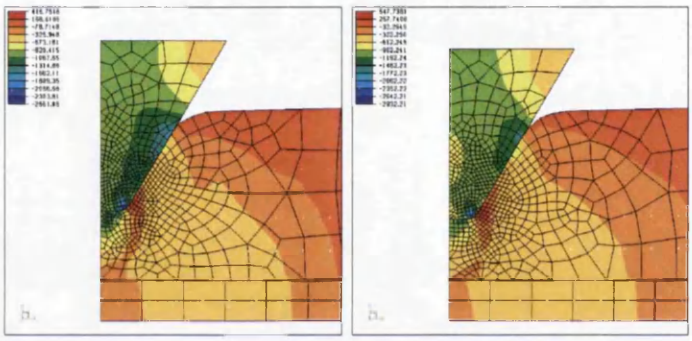

(c) SR = 83 μm (d) SR = 72 μm

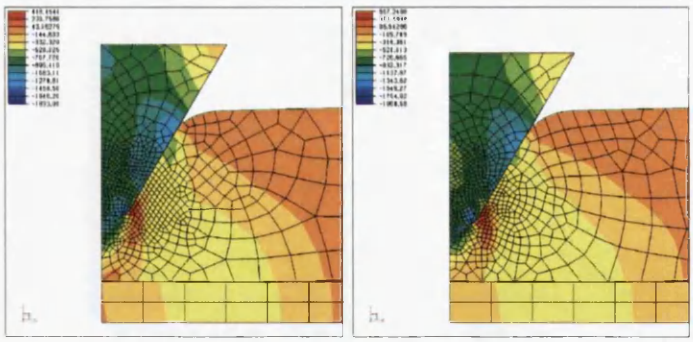

(e) SR = 78 μm (f) SR = 68 μm

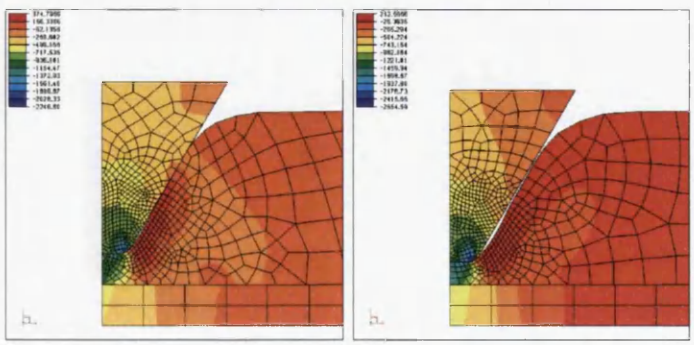

(g) SR = 36 μm (h) SR = 26 μm

Figure D.64: Direct Stress Y-Y: So = 1, R=8, PT=1.1, CC=0.2

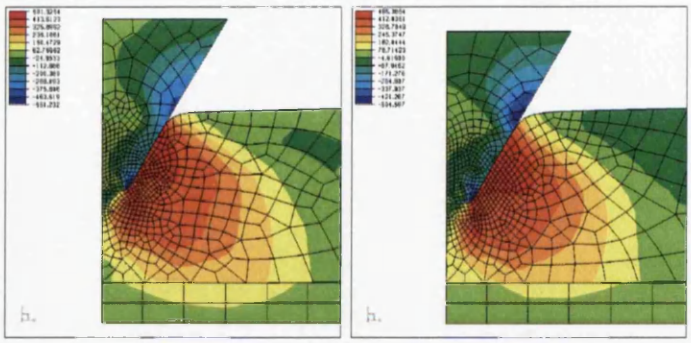

(a) SR = 107 μm (b) SR = 91 μm

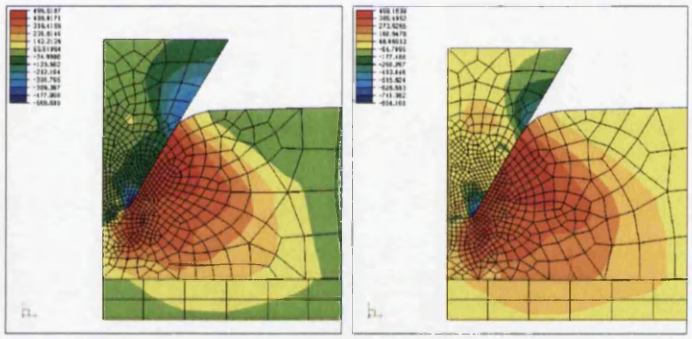

(c) SR = 83 μm (d) SR = 72 μm

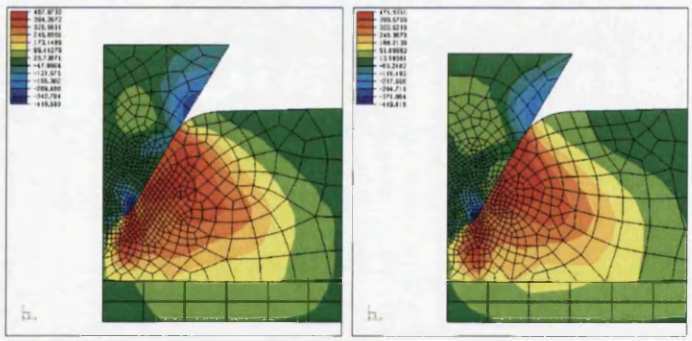

(e) SR = 78 μm (f) SR = 68 μm

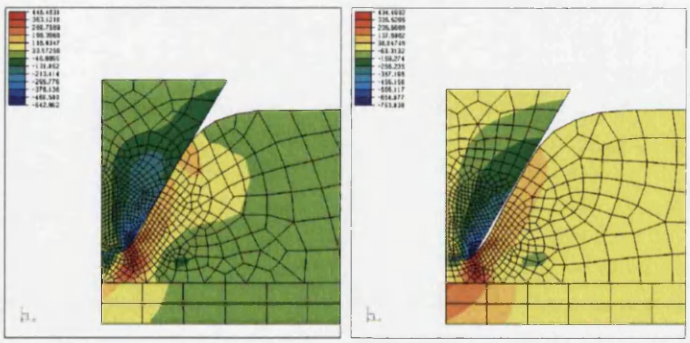

(g) SR = 36 μm (h) SR = 26 μm

Figure D.65: Shear Stress X-Y: So = 1, R=8, PT=1.1, CC=0.2

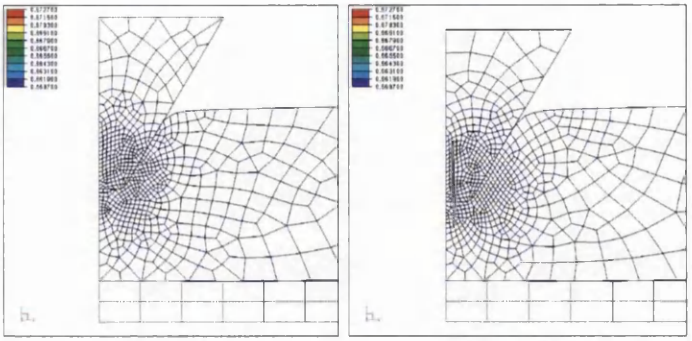

(a) SR = 107 μm (b) SR = 91 μm

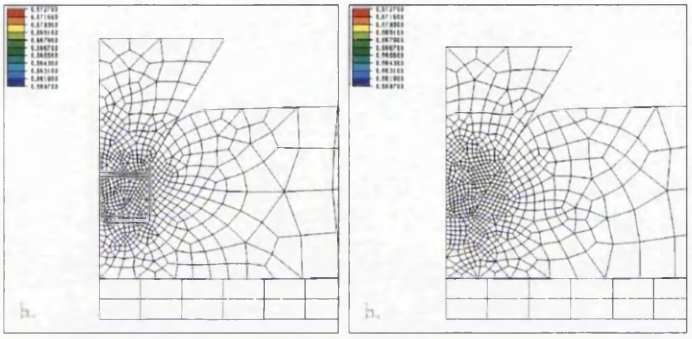

(c) SR = 83 μm (d) SR = 72 μm

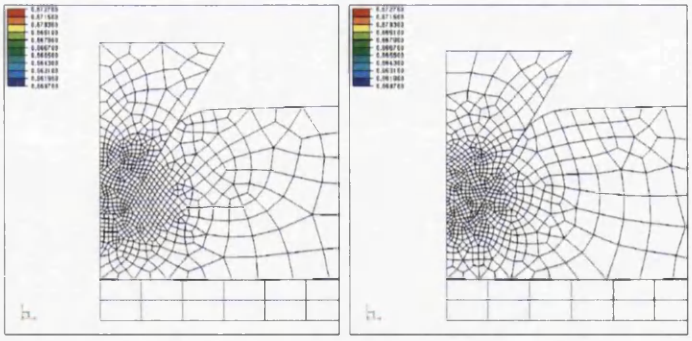

(e) SR = 78 μm (f) SR = 68 μm

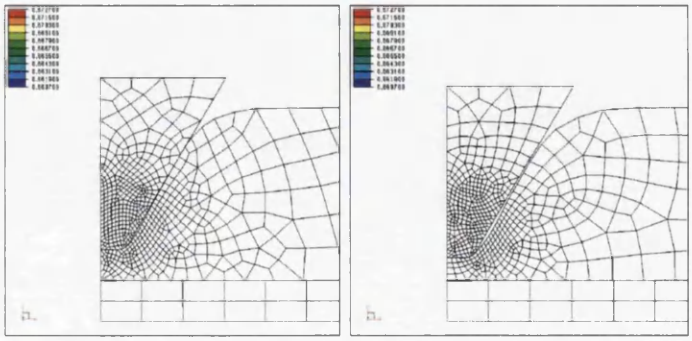

(g) SR = 36 μm (h) SR = 26 μm

Figure D.66: Triaxiality - Biaxial: So = 1, R=8, PT=1.1, CC=0.2

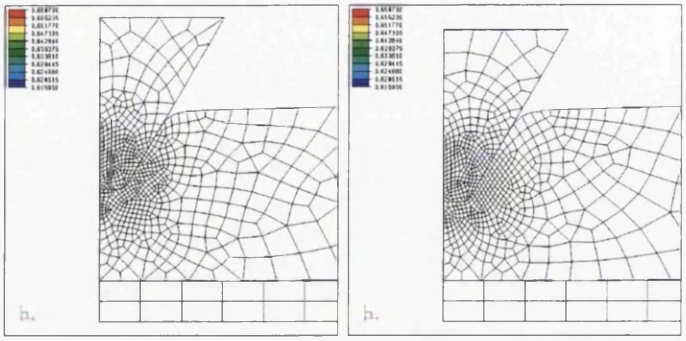

(a) SR = 107 μm (b) SR = 91 μm

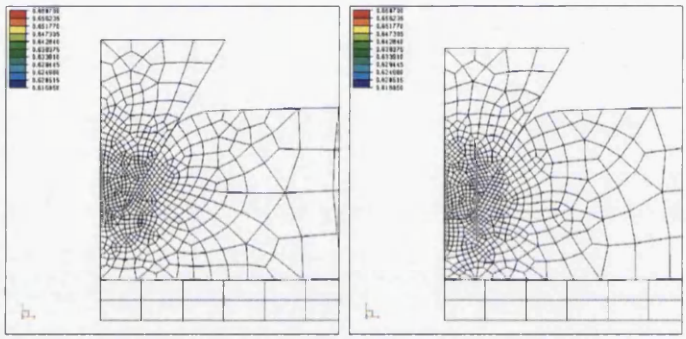

(c) SR = 83 μm (d) SR = 72 μm

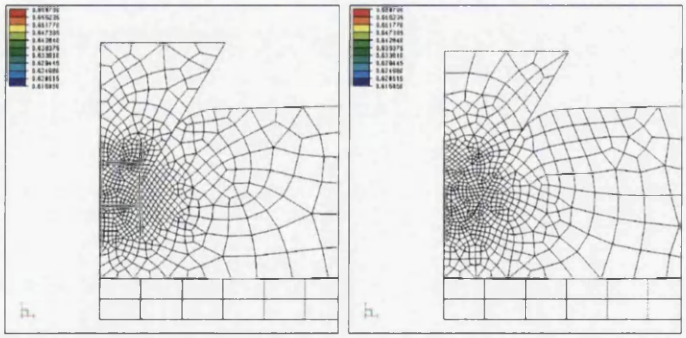

(e) SR = 78 μm (f) SR = 68 μm

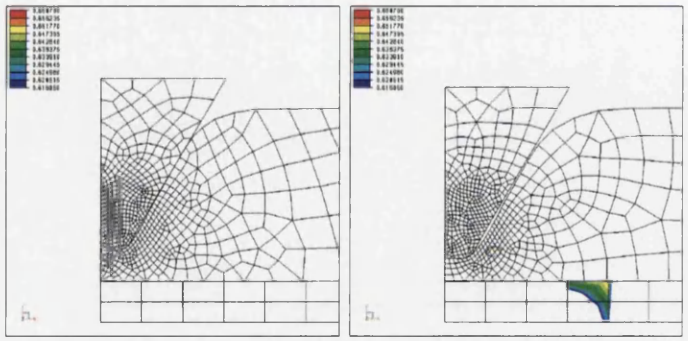

(g) SR = 36 μm (h) SR = 26 μm

Figure D.67: Triaxiality - Biaxial NU: So = 1, R=8, PT=1.1, CC=0.2

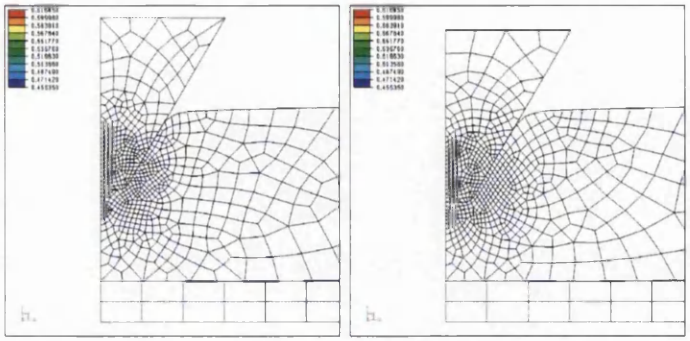

(a) SR = 107 μm (b) SR = 91 μm

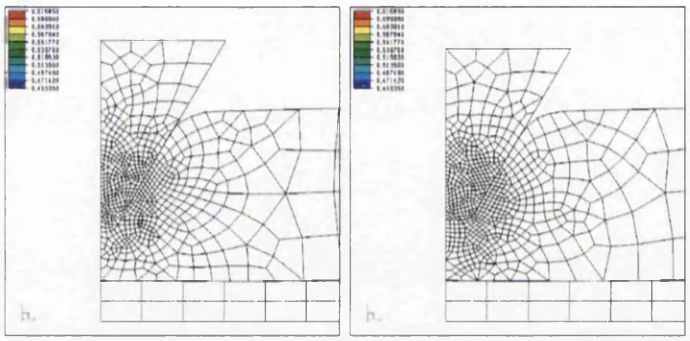

(c) SR = 83 μm (d) SR = 72 μm

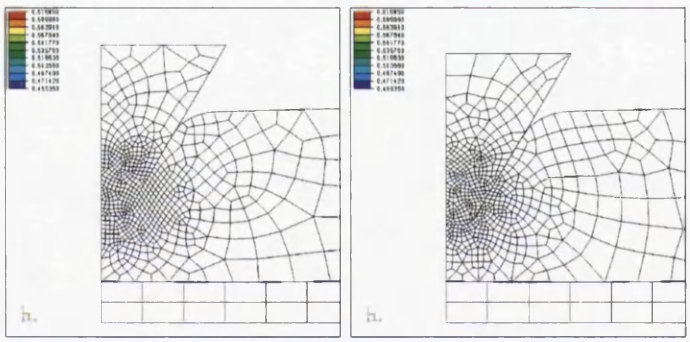

(e) SR = 78 μm (f) SR = 68 μm

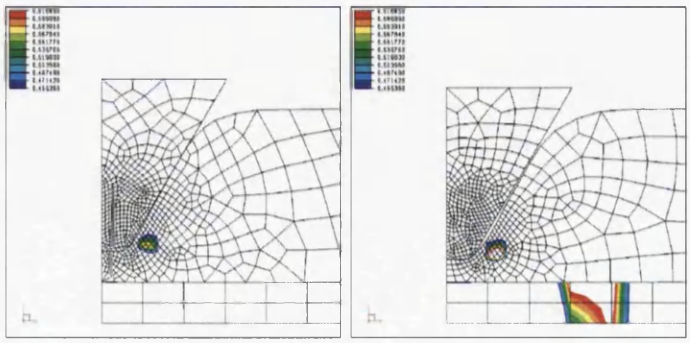

(g) SR = 36 μm (h) SR = 26 μm

Figure D.68: Triaxiality - Plane Strain: So = 1, R=8, PT=1.1, CC=0.2

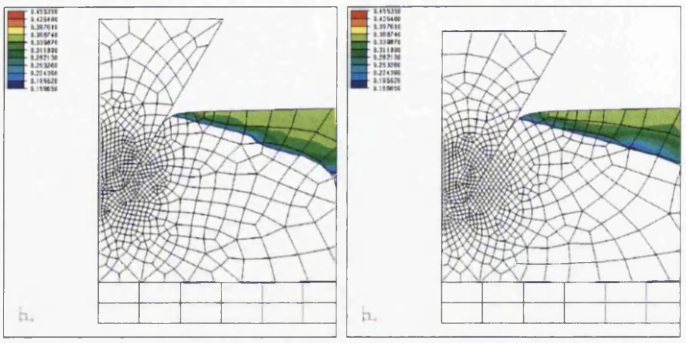

(a) SR = 107 μm (b) SR = 91 μm

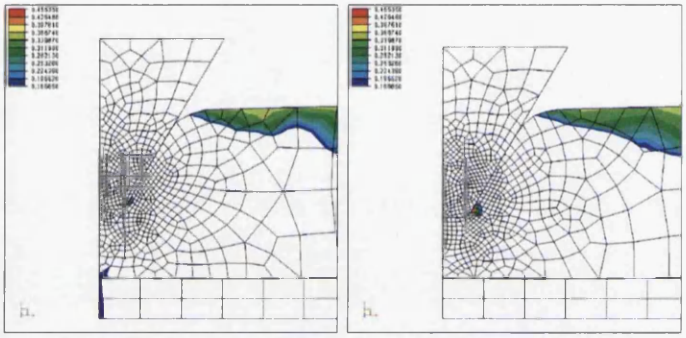

(c) SR = 83 μm (d) SR = 72 μm

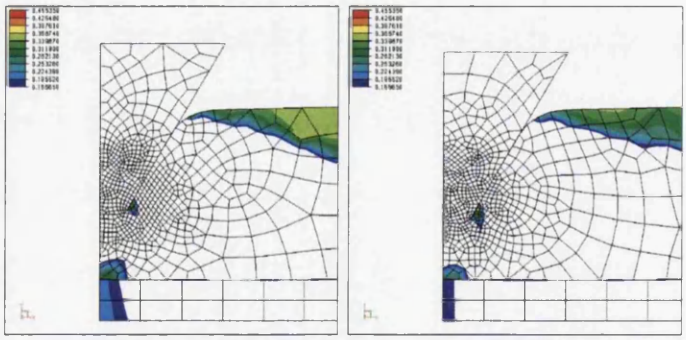

(e) SR = 78 μm (f) SR = 68 μm

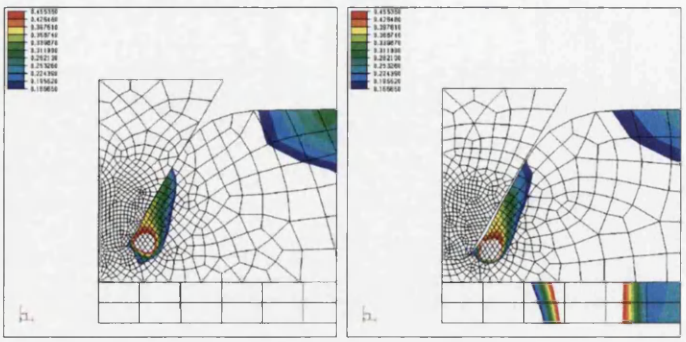

(g) SR = 36 μm (h) SR = 26 μm

Figure D.69: Triaxiality - Uniaxial Tension: So = 1, R=8, PT=1.1, CC=0.2

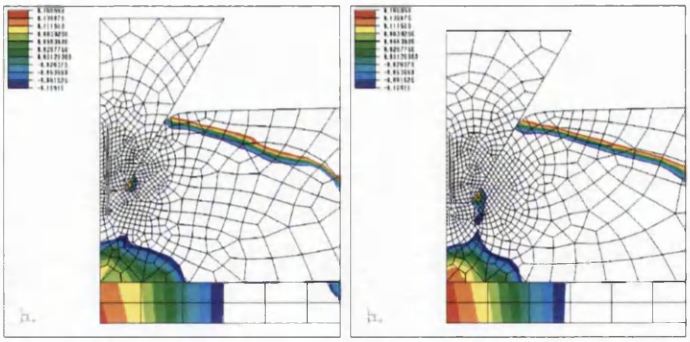

(a) SR = 107 μm (b) SR = 91 μm

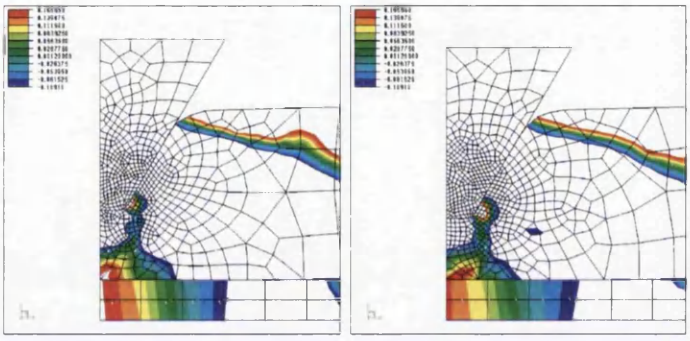

(c) SR = 83 μm (d) SR = 72 μm

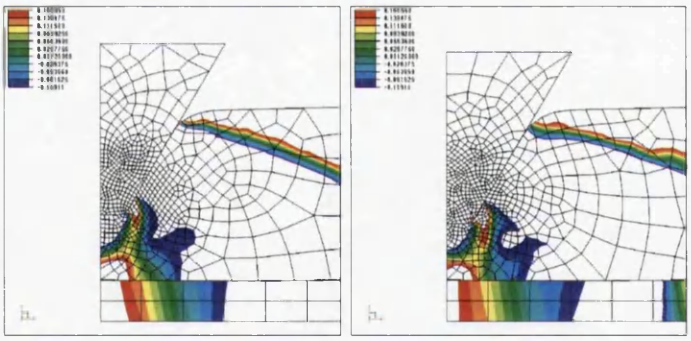

(e) SR = 78 μm (f) SR = 68 μm

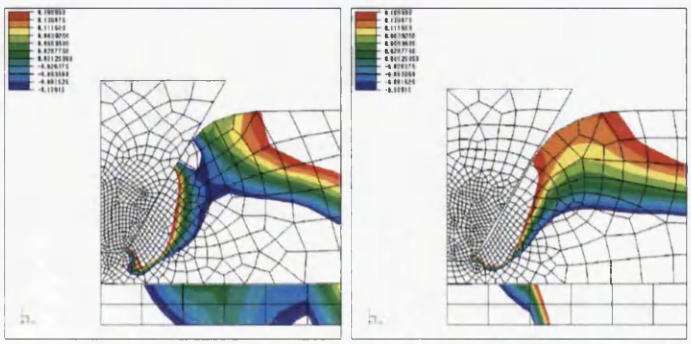

(g) SR = 36 μm (h) SR = 26 μm

Figure D.70: Triaxiality - Shear Pure: So = 1, R=8, PT=1.1, CC=0.2

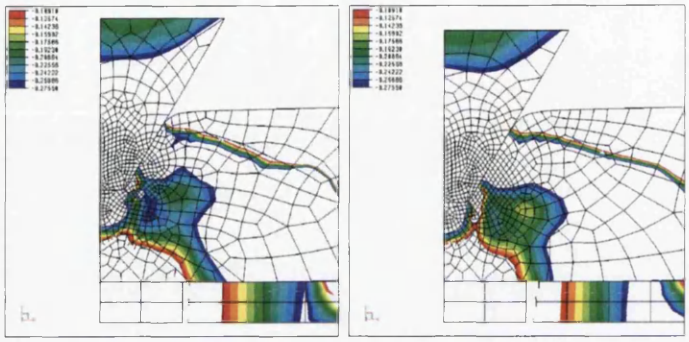

(a) SR = 107 μm (b) SR = 91 μm

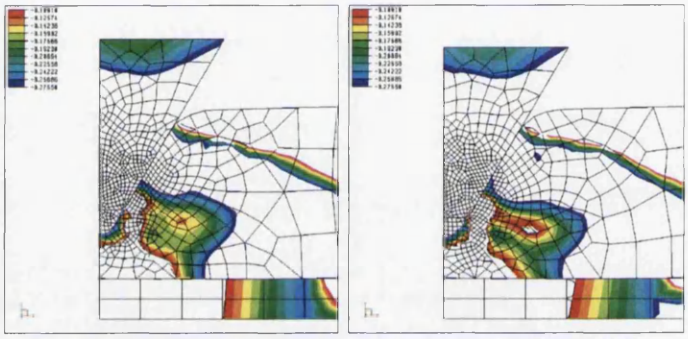

(c) SR = 83 μm (d) SR = 72 μm

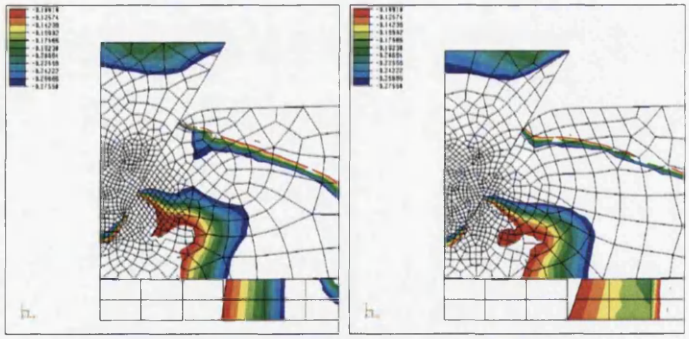

(e) SR = 78 μm (f) SR = 68 μm

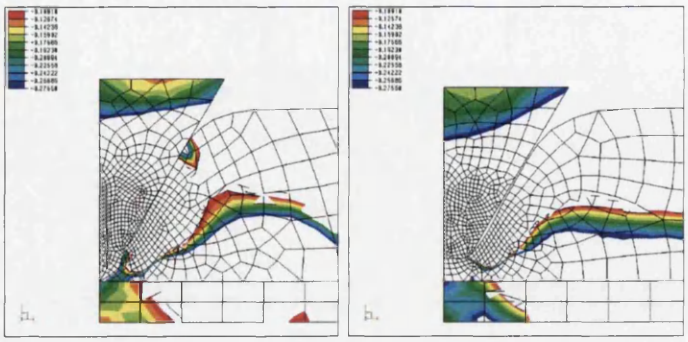

(g) SR = 36 μm (h) SR = 26 μm

Figure D.71: Triaxiality - Shear NU: So = 1, R=8, PT=1.1, CC=0.2

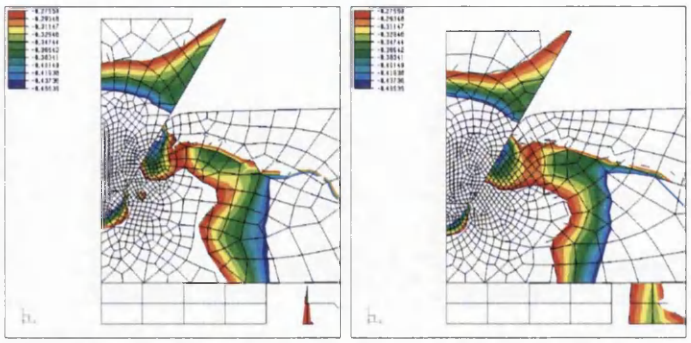

(a) SR = 107 μm (b) SR = 91 μm

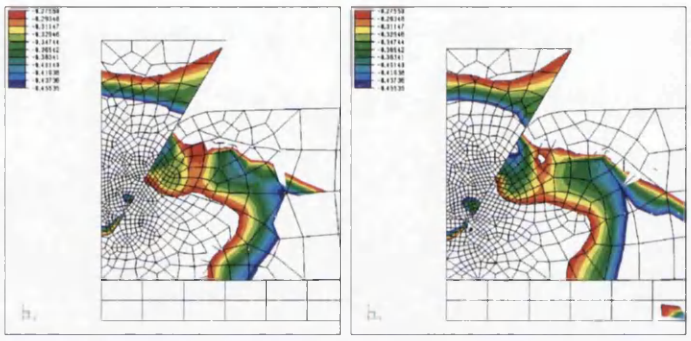

(c) SR = 83 μm (d) SR = 72 μm

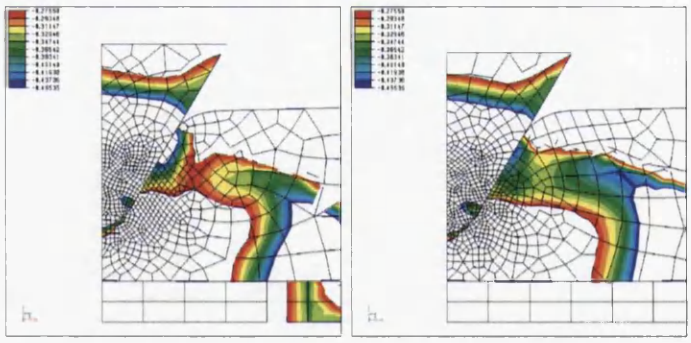

(e) SR = 78 μm (f) SR = 68 μm

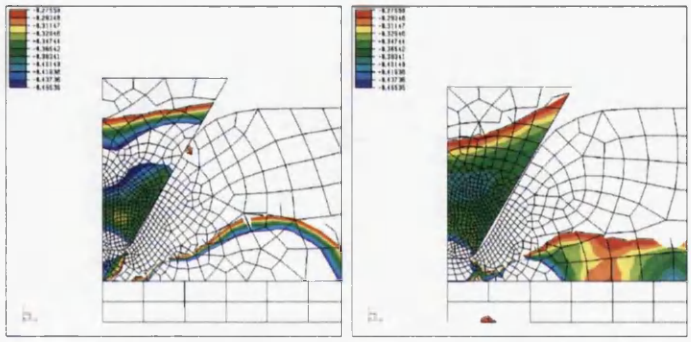

(g) SR = 36 μm (h) SR = 26 μm

Figure D.72: Triaxiality - Uniaxial Compression: So = 1, R=8, PT=1.1, CC=0.2

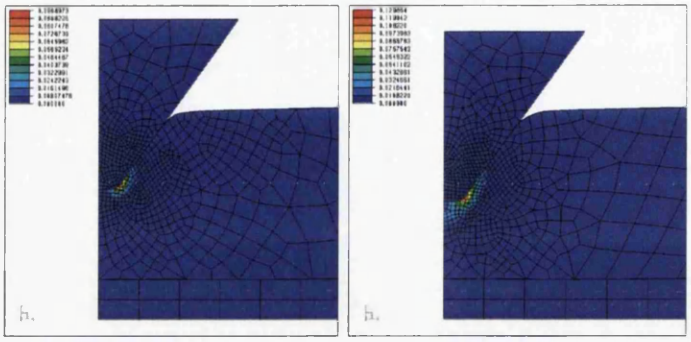

(a) SR = 107 μm (b) SR = 91 μm

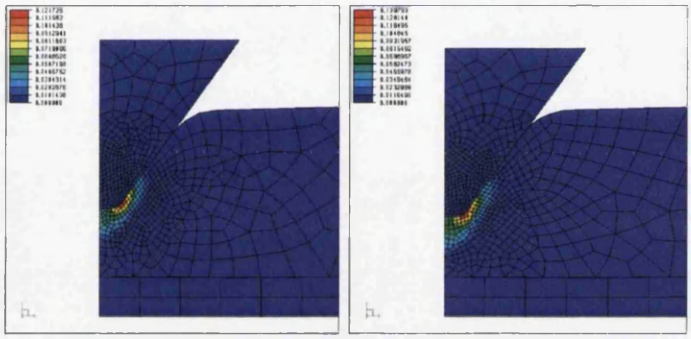

(c) SR = 83 μm (d) SR = 72 μm

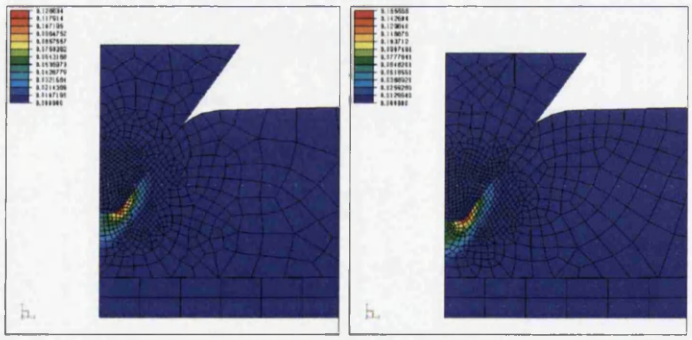

(e) SR = 78 μm (f) SR = 68 μm

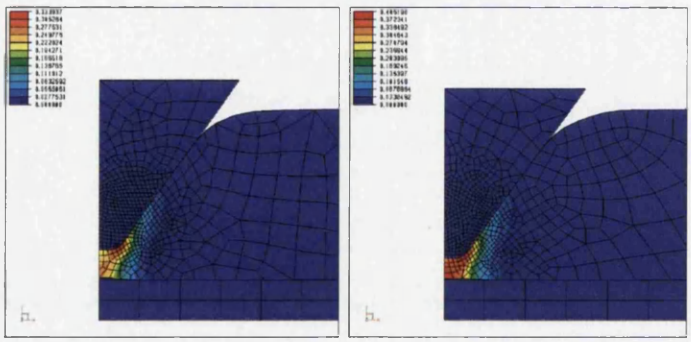

(g) SR = 36 μm (h) SR = 26 μm

Figure D.73: Coupled Lemaitre Damage: So = 0.8, R=8, PT=1.1, CC=0.2

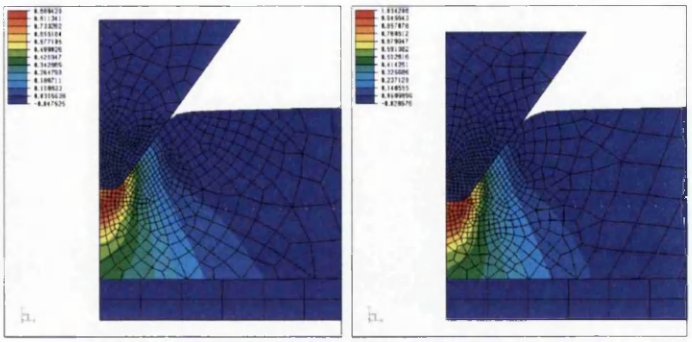

(a) SR = 107 μm (b) SR = 91 μm

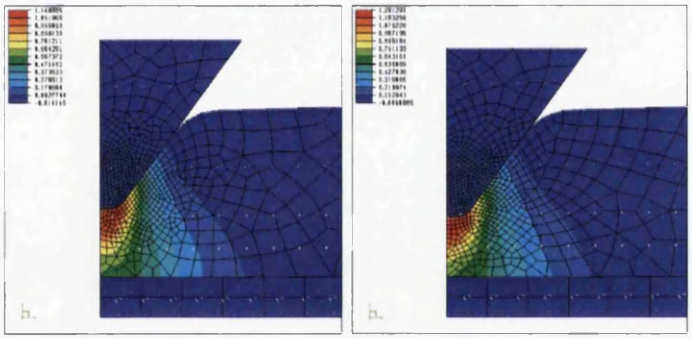

(c) SR = 83 μm (d) SR = 72 μm

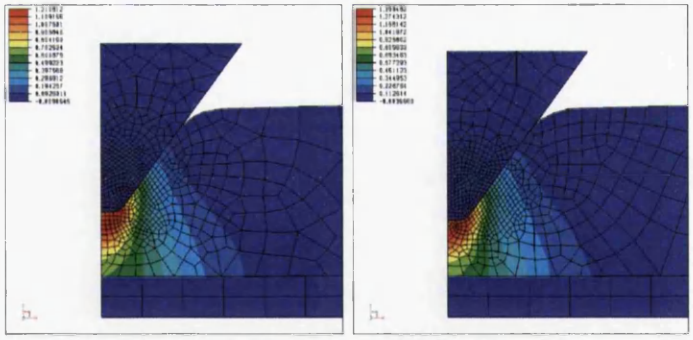

(e) SR = 78 μm (f) SR = 68 μm

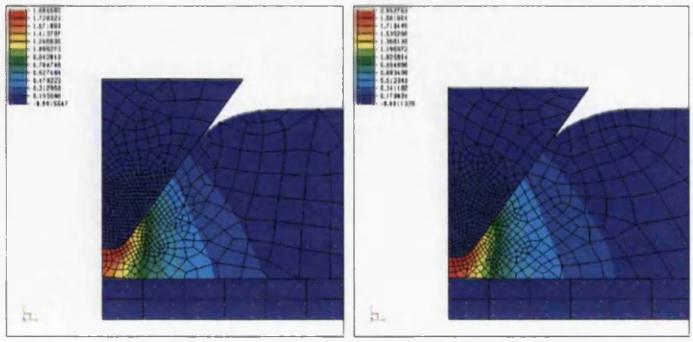

(g) SR = 36 μm (h) SR = 26 μm

Figure D.74: Direct Strain X-X; So = 0.8, R=8, PT=1.1, CC=0.2

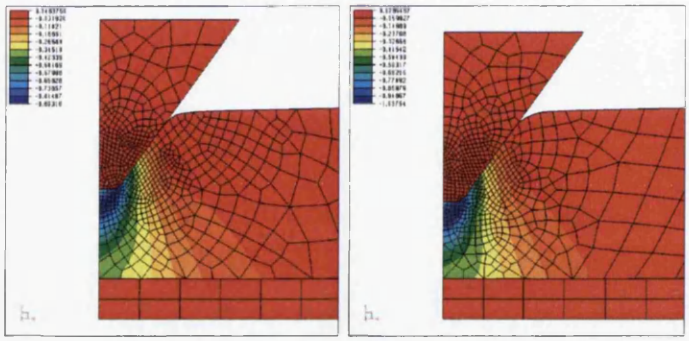

(a) SR = 107 μm (b) SR = 91 μm

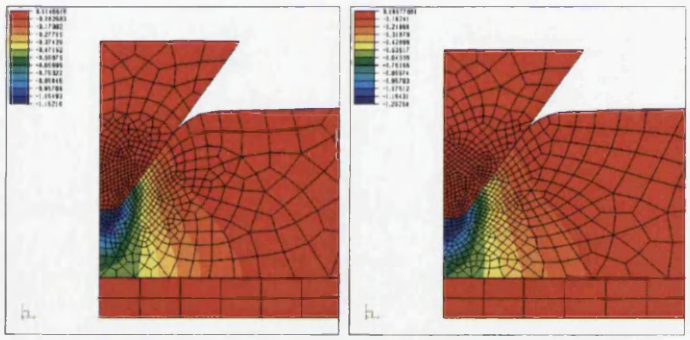

(c) SR = 83 μm (d) SR = 72 μm

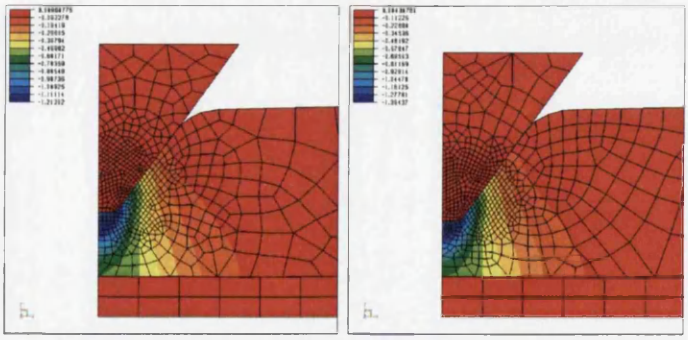

(e) SR = 78 μm (f) SR = 68 μm

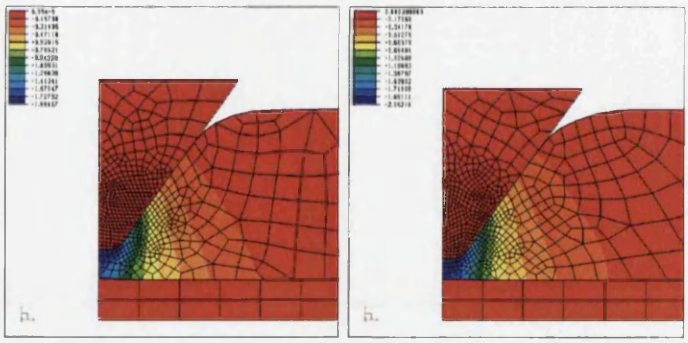

(g) SR = 36 μm (h) SR = 26 μm

Figure D.75: Direct Strain Y-Y: So = 0.8, R=8, PT=1.1, CC=0.2

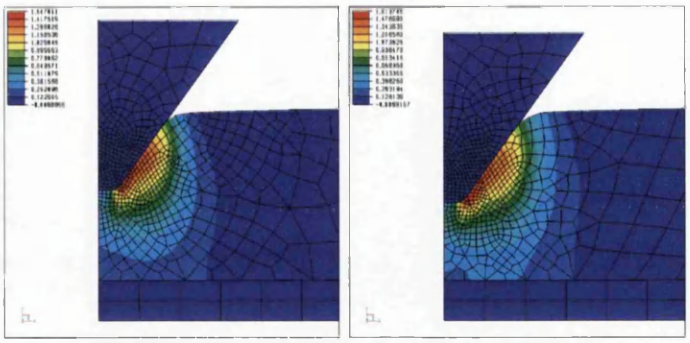

(a) SR = 107 μm (b) SR = 91 μm

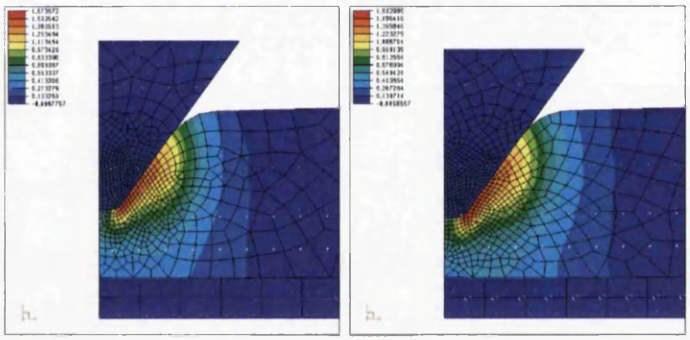

(c) SR = 83 μm (d) SR = 72 μm

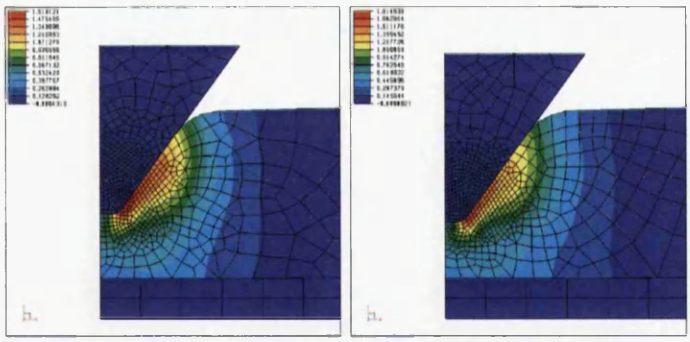

(e) SR = 78 μm (f) SR = 68 μm

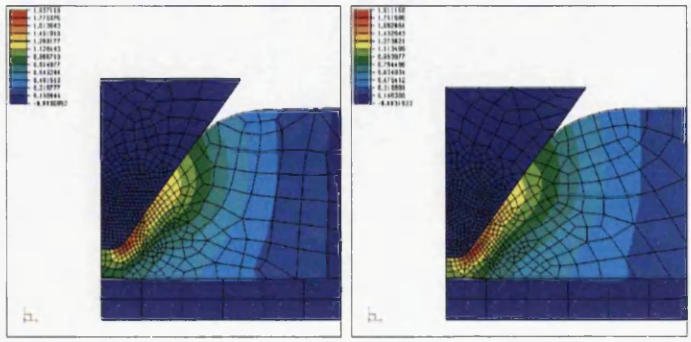

(g) SR = 36 μm (h) SR = 26 μm

Figure D.76: Shear Strain X-Y: So = 0.8, R=8, PT=1.1, CC=0.2

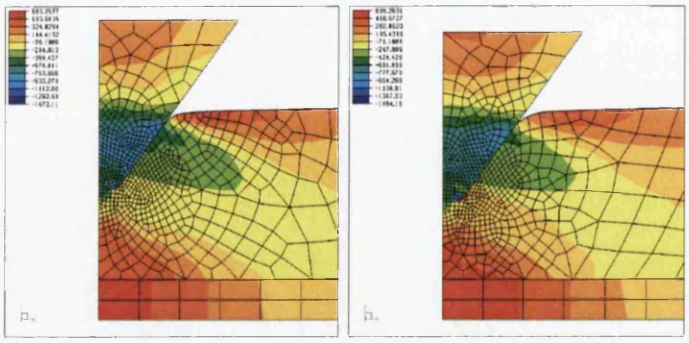

(a) SR = 107 μm (b) SR = 91 μm

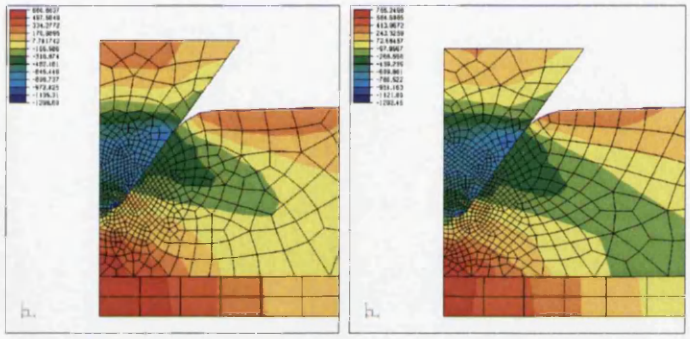

(c) SR = 83 μm (d) SR = 72 μm

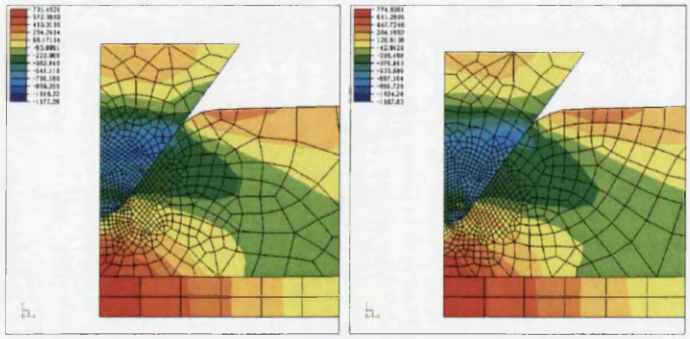

(e) SR = 78 μm (f) SR = 68 μm

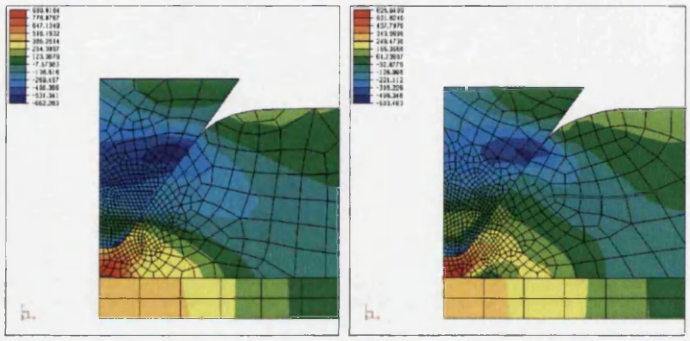

(g) SR = 36 μm (h) SR = 26 μm

Figure D.77: Direct Stress X-X; So = 0.8, R=8, PT=1.1, CC=0.2

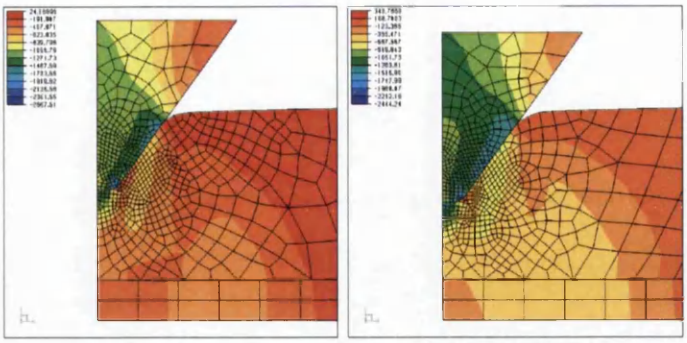

(a) SR = 107 μm (b) SR = 91 μm

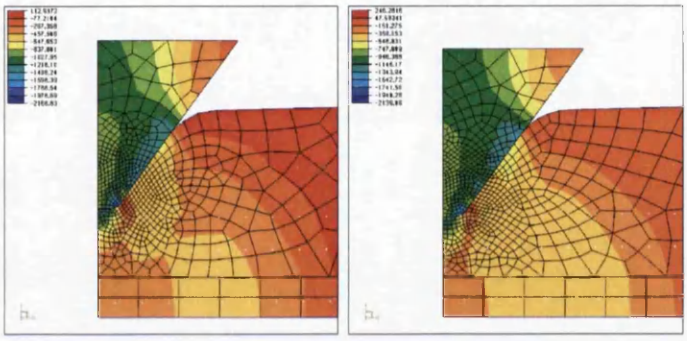

(c) SR = 83 μm (d) SR = 72 μm

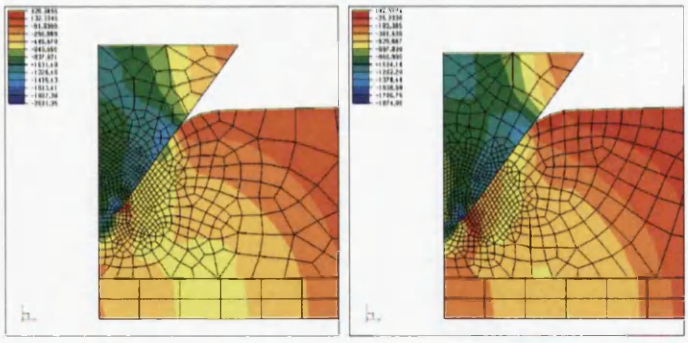

(e) SR = 78 μm (f) SR = 68 μm

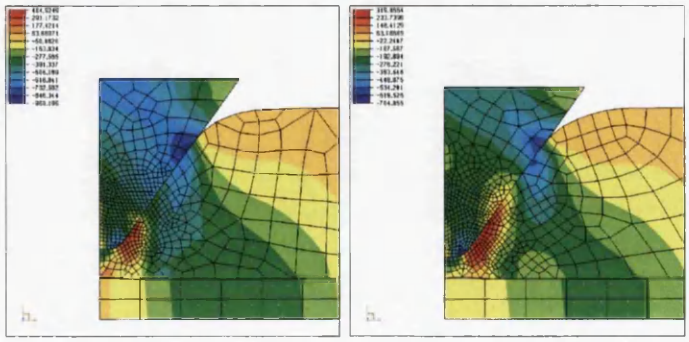

(g) SR = 36 μm (h) SR = 26 μm

Figure D.78: Direct Stress Y-Y: So = 0.8, R=8, PT=1.1, CC=0.2

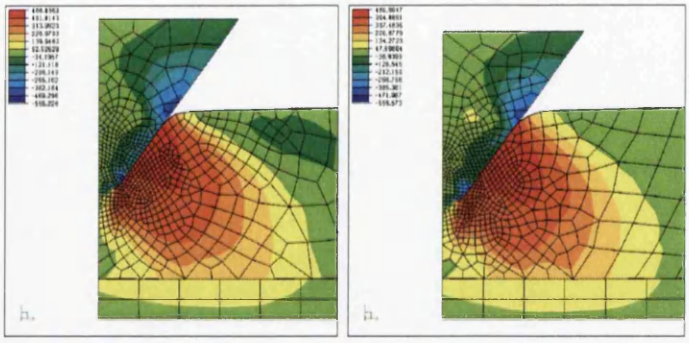

(a) SR = 107 μm (b) SR = 91 μm

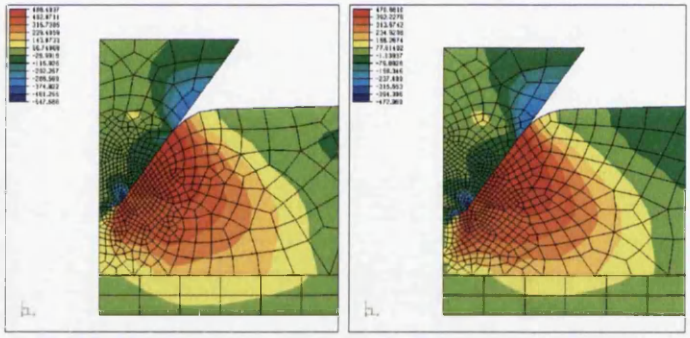

(c) SR = 83 μm (d) SR = 72 μm

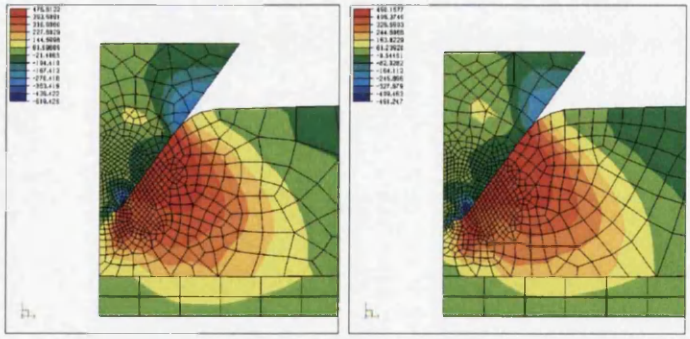

(e) SR = 78 μm (f) SR = 68 μm

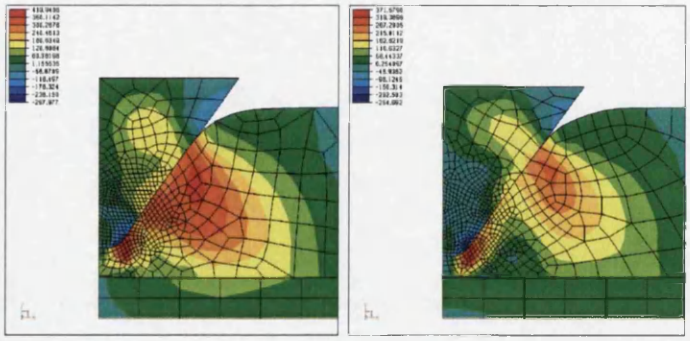

(g) SR = 36 μm (h) SR = 26 μm

Figure D.79: Shear Stress X-Y: So = 0.8, R=8, PT=1.1, CC=0.2

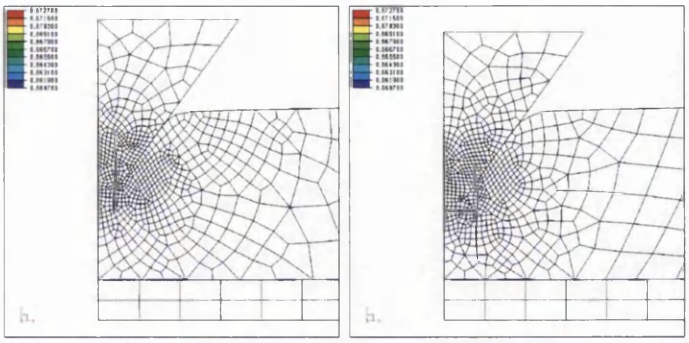

(a) SR = 107 μm (b) SR = 91 μm

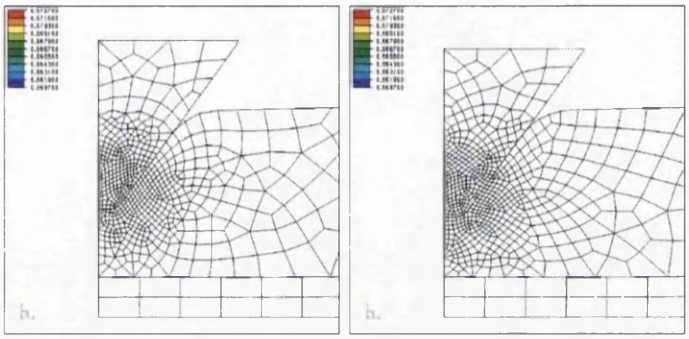

(c) SR = 83 μm (d) SR = 72 μm

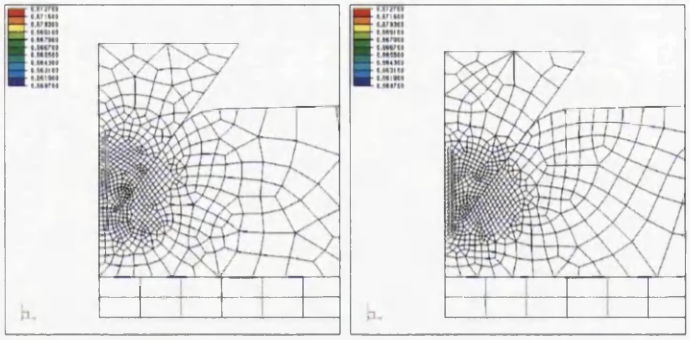

(e) SR = 78 μm (f) SR = 68 μm

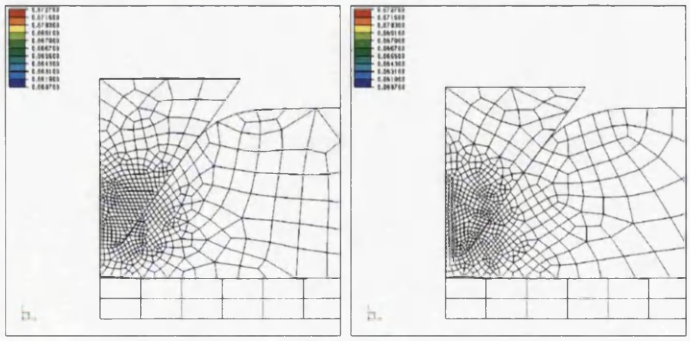

(g) SR = 36 μm (h) SR = 26 μm

Figure D.80: Triaxiality - Biaxial: So = 0.8, R=8, PT=1.1, CC=0.2

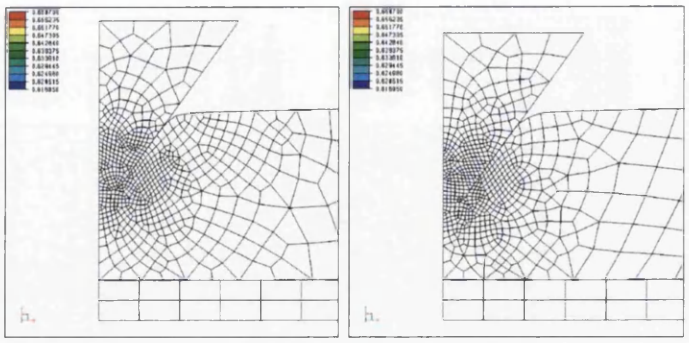

(a) SR = 107 μm (b) SR = 91 μm

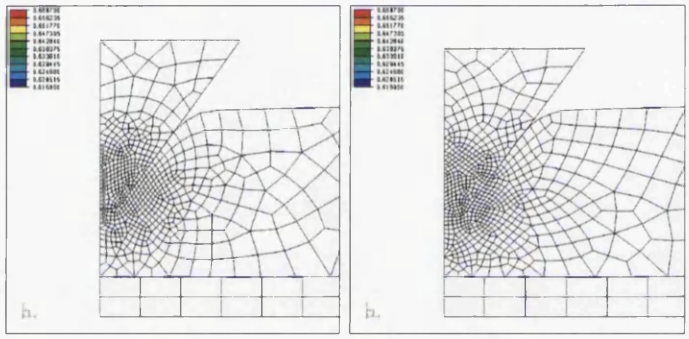

(c) SR = 83 μm (d) SR = 72 μm

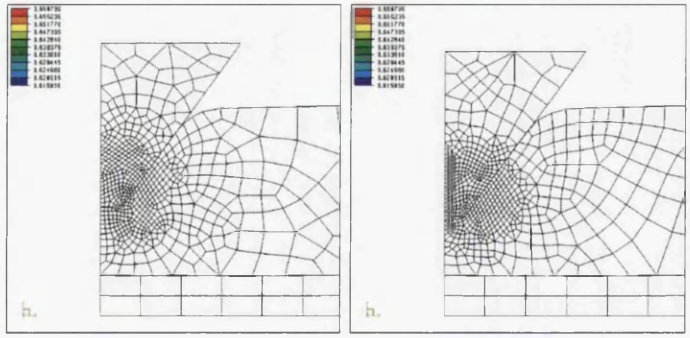

(e) SR = 78 μm (f) SR = 68 μm

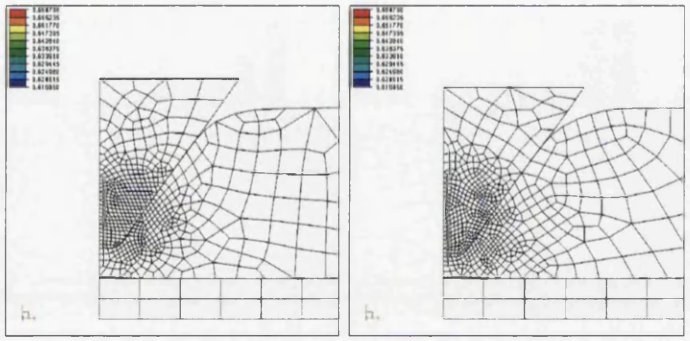

(g) SR = 36 μm (h) SR = 26 μm

Figure D.81: Triaxiality - Biaxial NU: So = 0.8, R=8, PT=1.1, CC=0.2

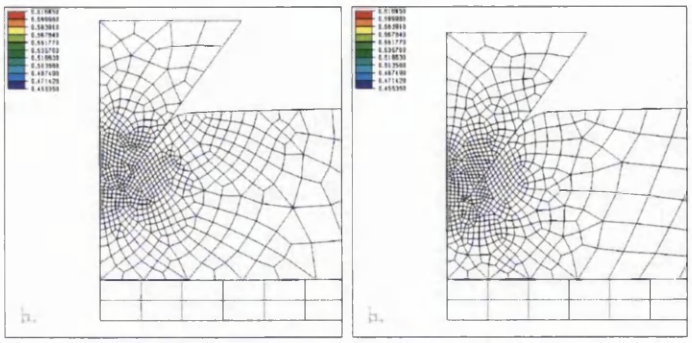

(a) SR = 107 μm (b) SR = 91 μm

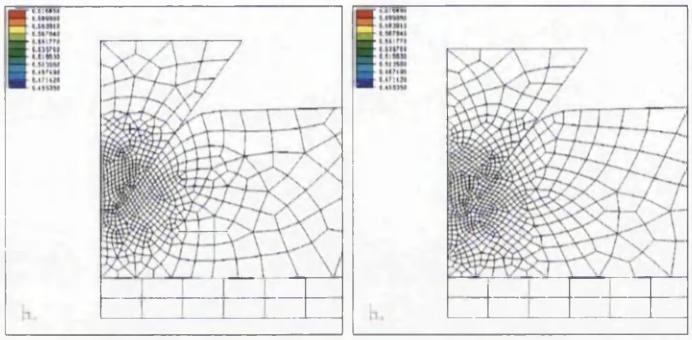

(c) SR = 83 μm (d) SR = 72 μm

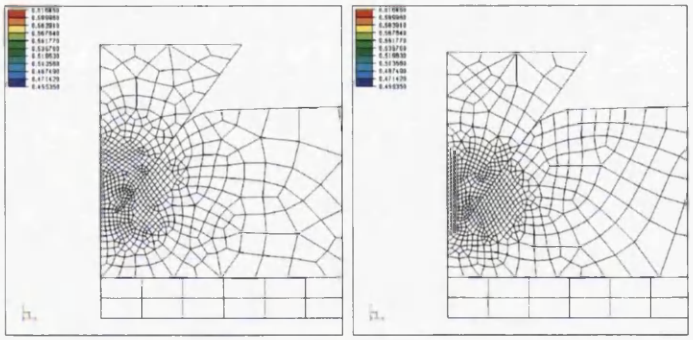

(e) SR = 78 μm (f) SR = 68 μm

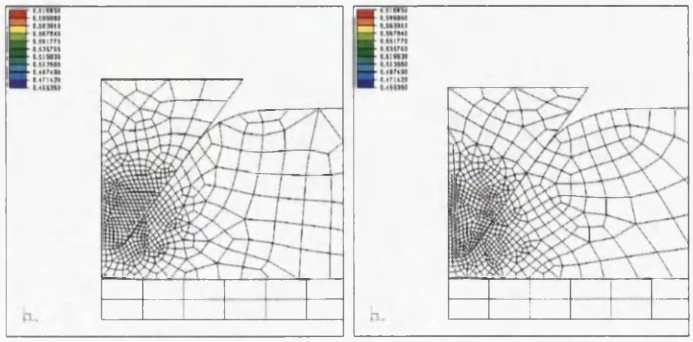

(g) SR = 36 μm (h) SR = 26 μm

Figure D.82: Triaxiality - Plane Strain: So = 0.8, R=8, PT=1.1, CC=0.2

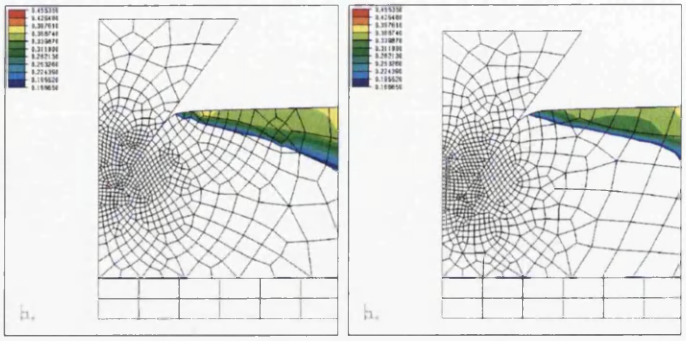

(a) SR = 107 μm (b) SR = 91 μm

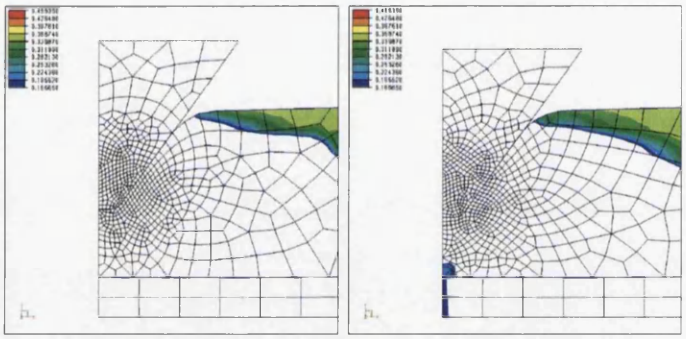

(c) SR = 83 μm (d) SR = 72 μm

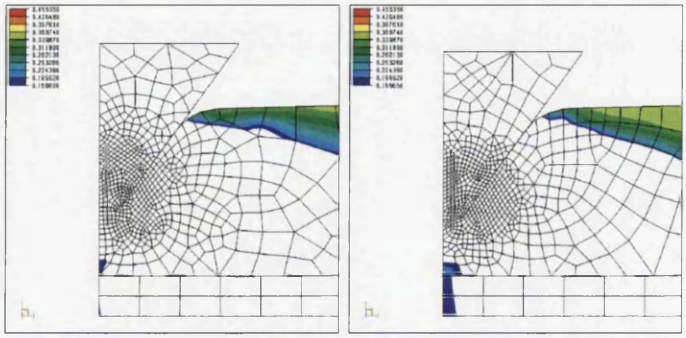

(e) SR = 78 μm (f) SR = 68 μm

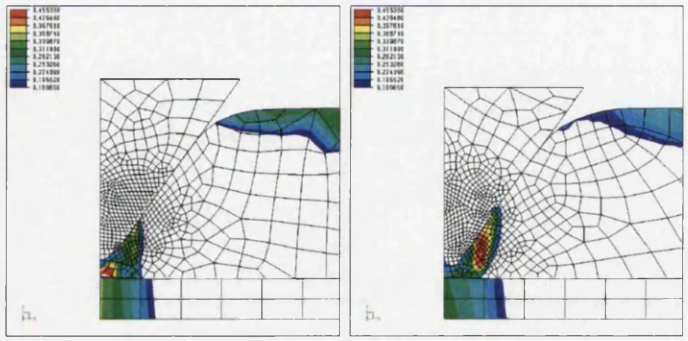

(g) SR = 36 μm (h) SR = 26 μm

Figure D.83: Triaxiality - Uniaxial Tension: So = 0.8, R=8, PT=1.1, CC=0.2

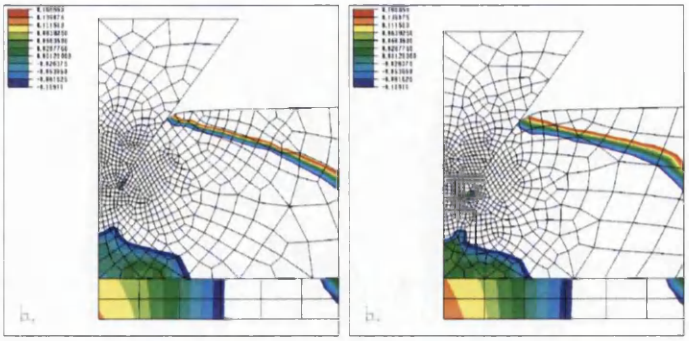

(a) SR = 107 μm (b) SR = 91 μm

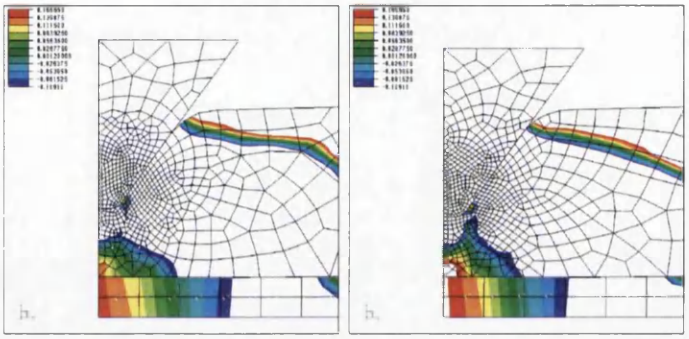

(c) SR = 83 μm (d) SR = 72 μm

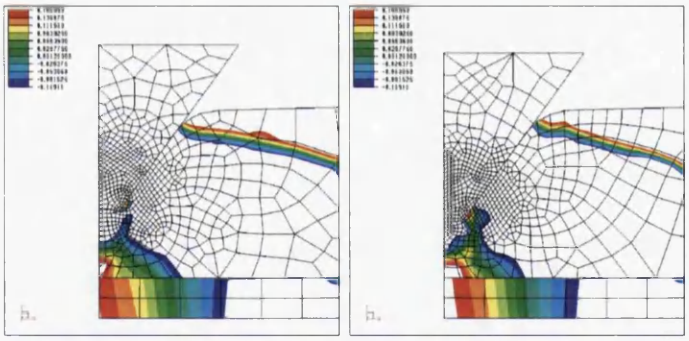

(e) SR = 78 μm (f) SR = 68 μm

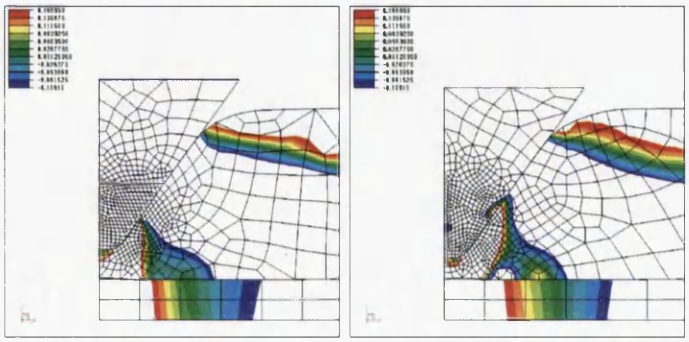

(g) SR = 36 μm (h) SR = 26 μm

Figure D.84: Triaxiality - Shear Pure: So = 0.8, R=8, PT=1.1, CC=0.2

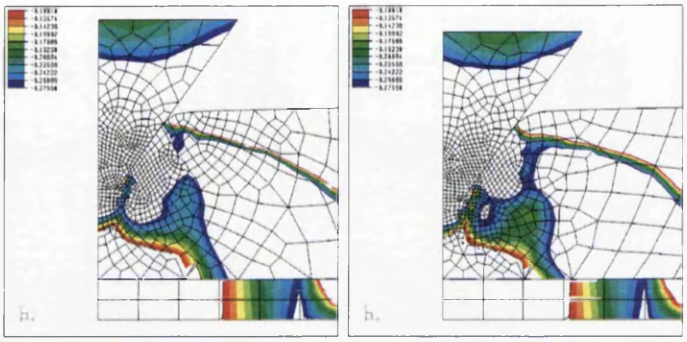

(a) SR = 107 μm (b) SR = 91 μm

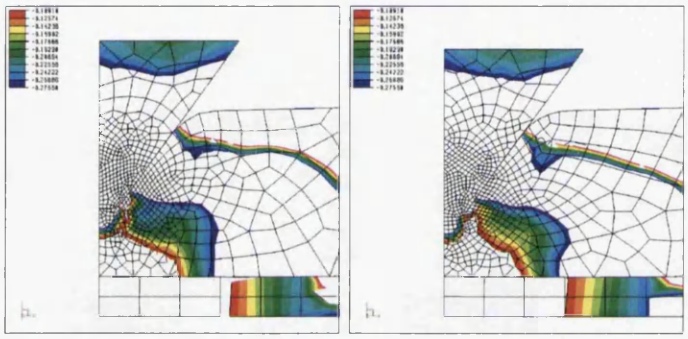

(c) SR = 83 μm (d) SR = 72 μm

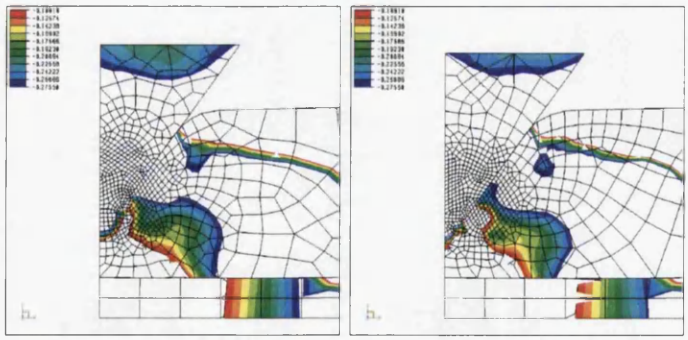

(e) SR = 78 μm (f) SR = 68 μm

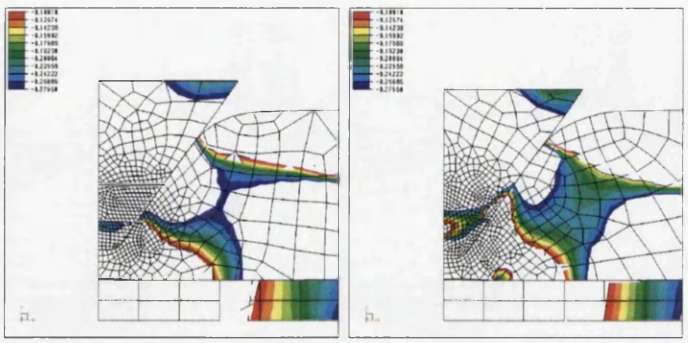

(g) SR = 36 μm (h) SR = 26 μm

Figure D.85: Triaxiality - Shear NU: So = 0.8, R=8, PT=1.1, CC=0.2

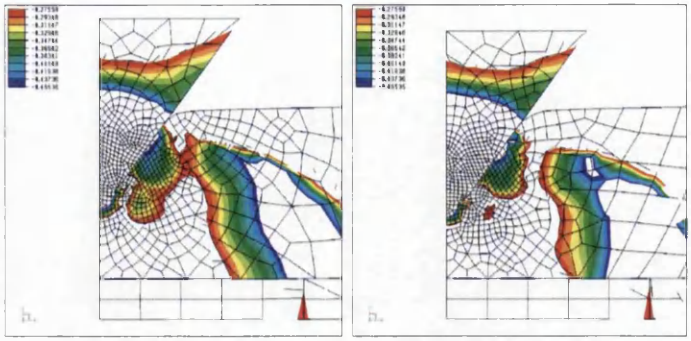

(a) SR = 107 μm (b) SR = 91 μm

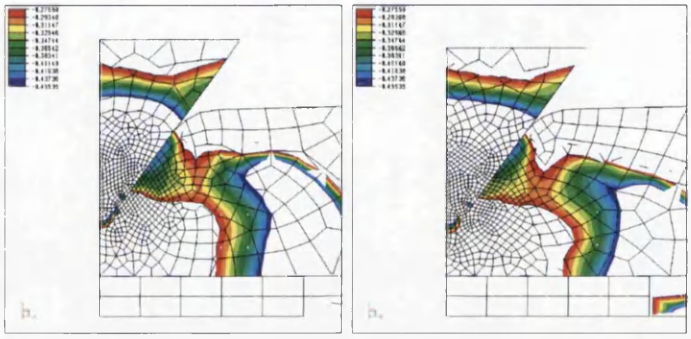

(c) SR = 83 μm (d) SR = 72 μm

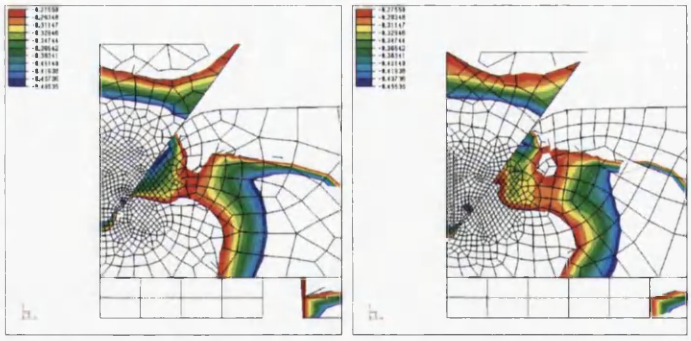

(e) SR = 78 μm (f) SR = 68 μm

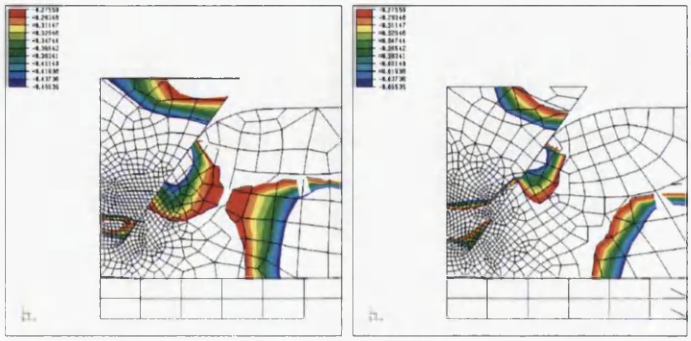

(g) SR = 36 μm (h) SR = 26 μm

Figure D.86: Triaxiality - Uniaxial Compression: So = 0.8, R=8, PT=1.1, CC=0.2

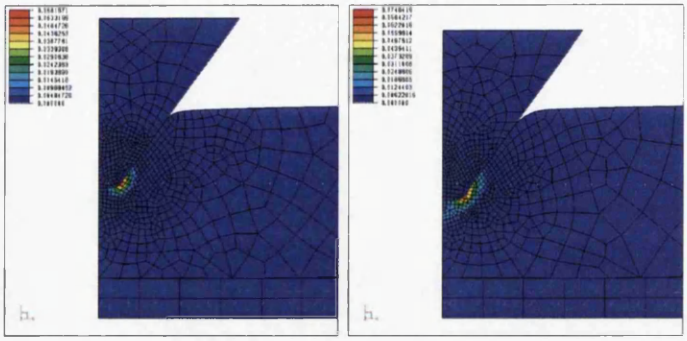

(a) SR = 107 μm (b) SR = 91 μm

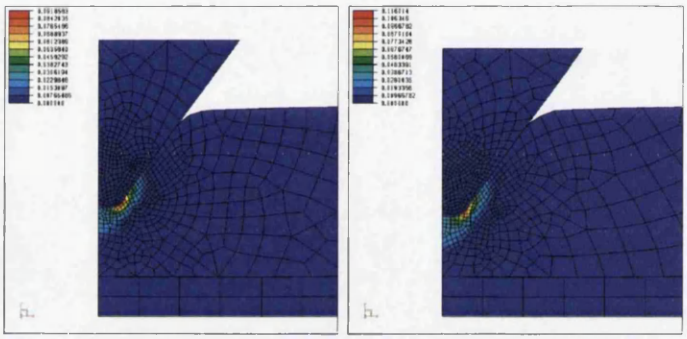

(c) SR = 83 μm (d) SR = 72 μm

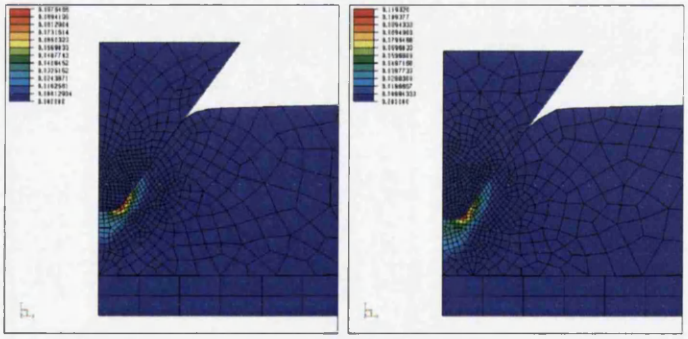

(e) SR = 78 μm (f) SR = 68 μm

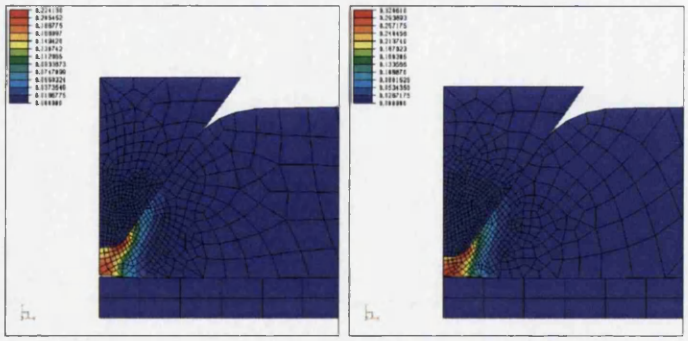

(g) SR = 36 μm (h) SR = 26 μm

Figure D.87: Coupled Lemaitre Damage: So = 1, R=8, PT=1.1, CC=0.2

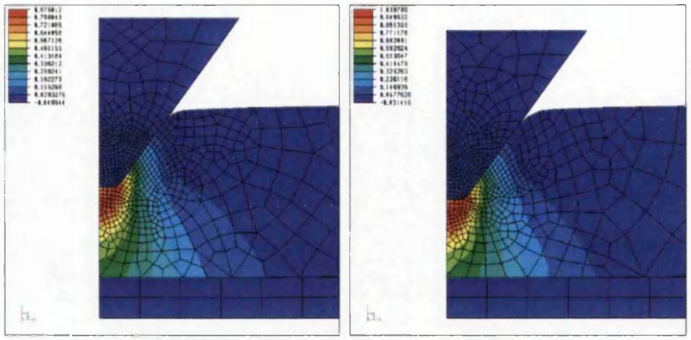

(a) SR = 107 μm (b) SR = 91 μm

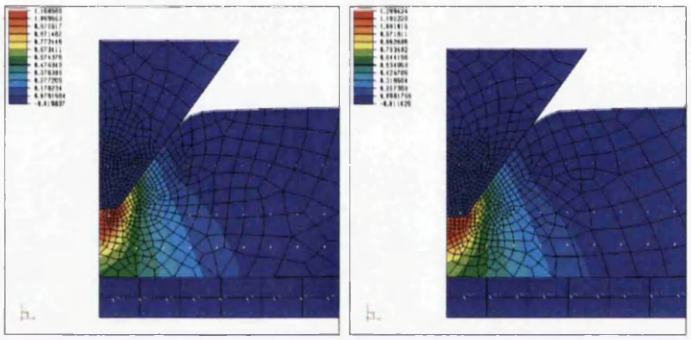

(c) SR = 83 μm (d) SR = 72 μm

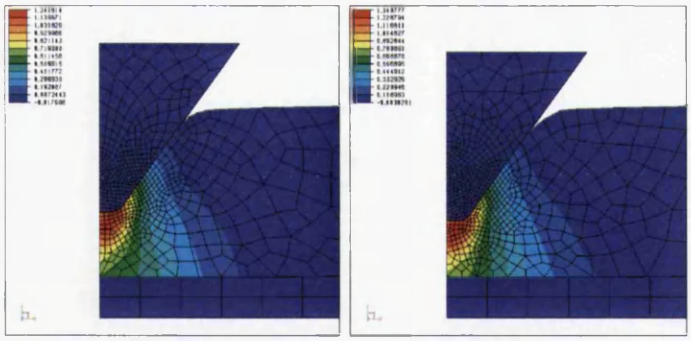

(e) SR = 78 μm (f) SR = 68 μm

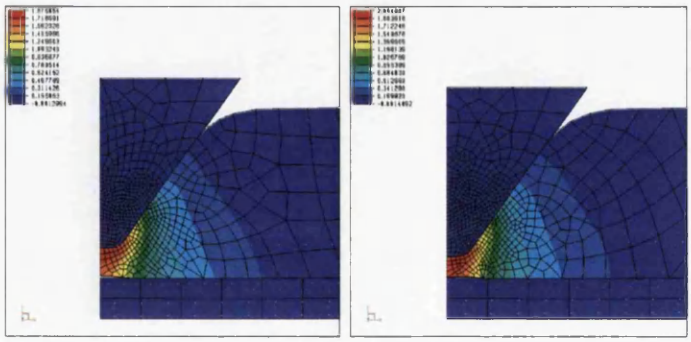

(g) SR = 36 μm (h) SR = 26 μm

Figure D.88: Direct Strain X-X: So = 1, R=8, PT=1.1, CC=0.2

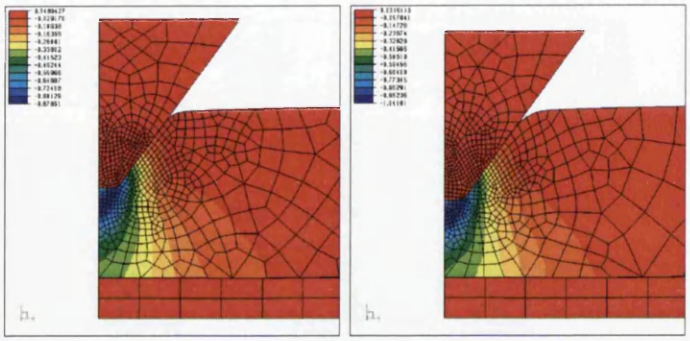

(a) SR = 107 μm (b) SR = 91 μm

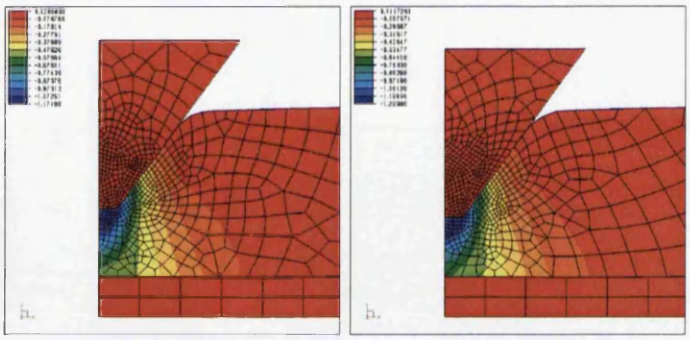

(c) SR = 83 μm (d) SR = 72 μm

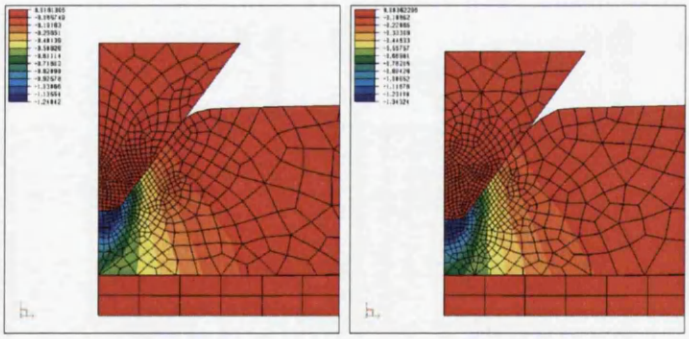

(e) SR = 78 μm (f) SR = 68 μm

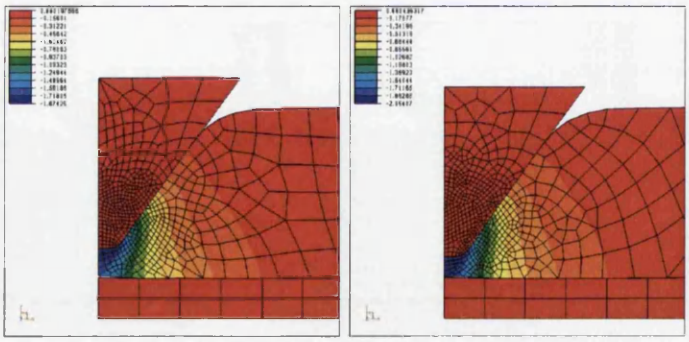

(g) SR = 36 μm (h) SR = 26 μm

Figure D.89: Direct Strain Y-Y: So = 1, R=8, PT=1.1, CC=0.2

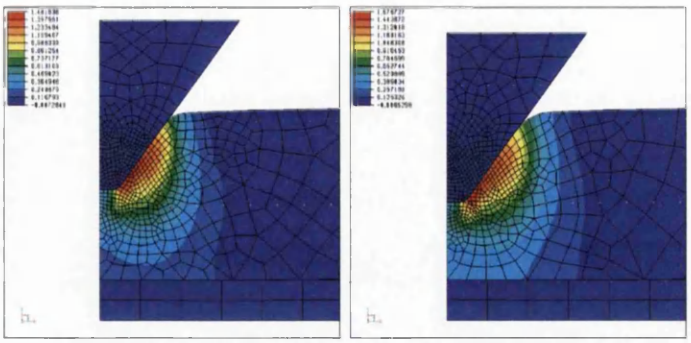

(a) SR = 107 μm (b) SR = 91 μm

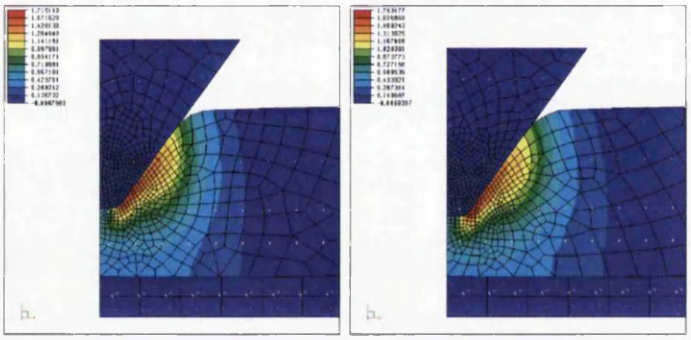

(c) SR = 83 μm (d) SR = 72 μm

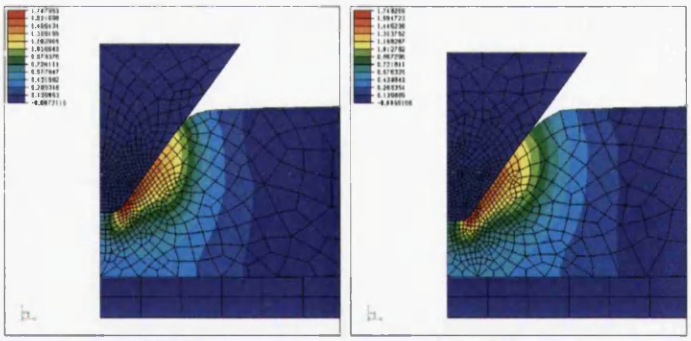

(e) SR = 78 μm (f) SR = 68 μm

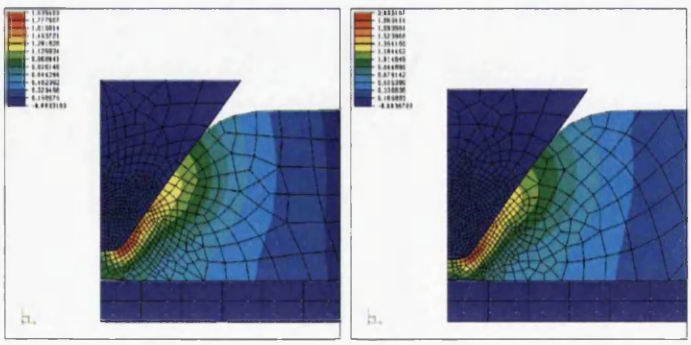

(g) SR = 36 μm (h) SR = 26 μm

Figure D.90: Shear Strain X-Y: So = 1, R=8, PT=1.1, CC=0.2

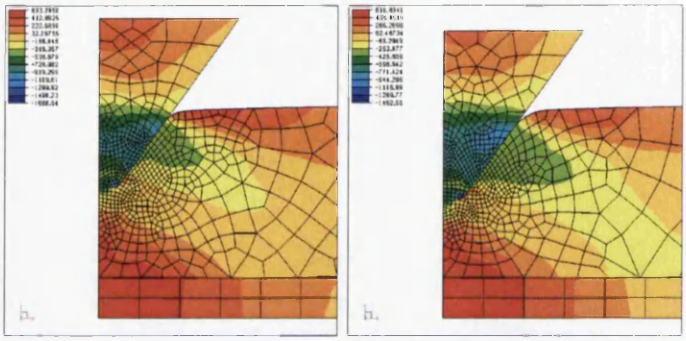

(a) SR = 107 μm (b) SR = 91 μm

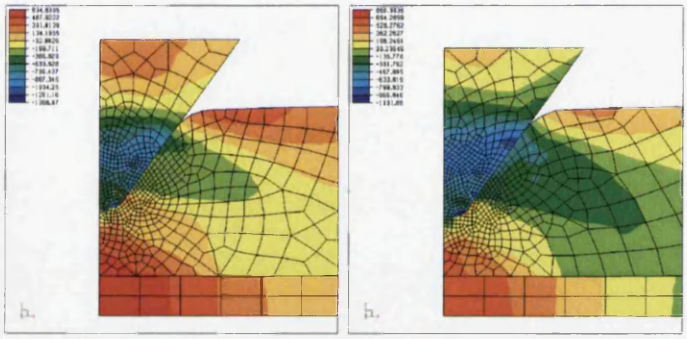

(c) SR = 83 μm (d) SR = 72 μm

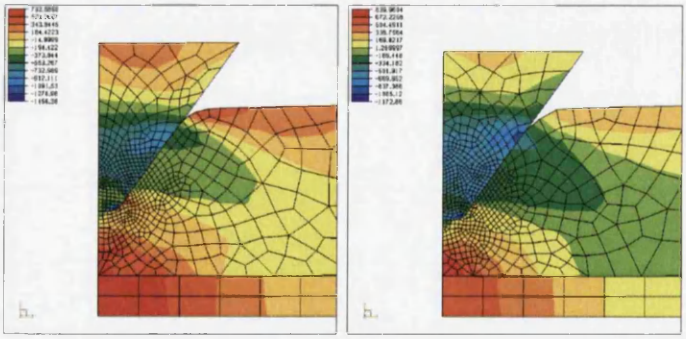

(e) SR = 78 μm (f) SR = 68 μm

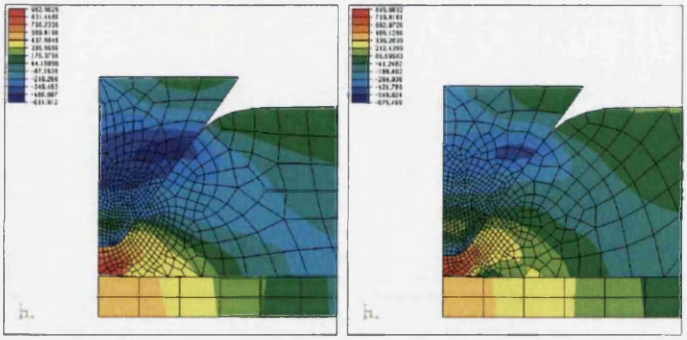

(g) SR = 36 μm (h) SR = 26 μm

Figure D.91: Direct Stress X-X: So = 1, R=8, PT=1.1, CC=0.2

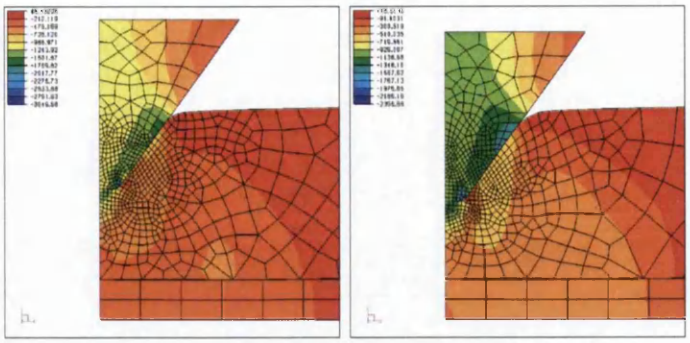

(a) SR = 107 μm (b) SR = 91 μm

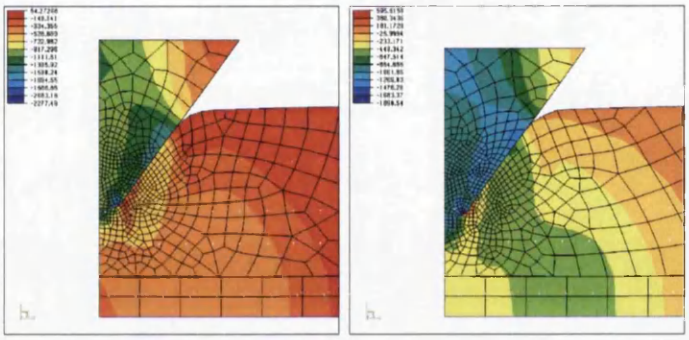

(c) SR = 83 μm (d) SR = 72 μm

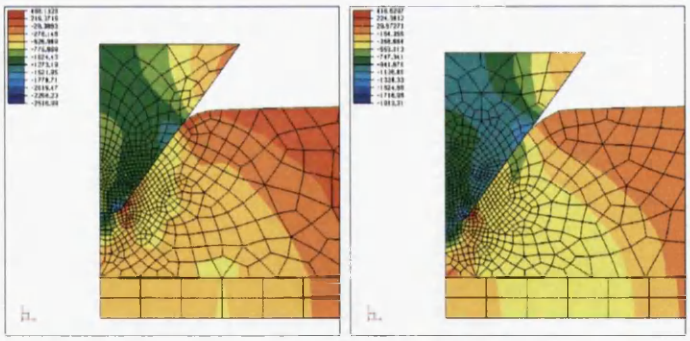

(e) SR = 78 μm (f) SR = 68 μm

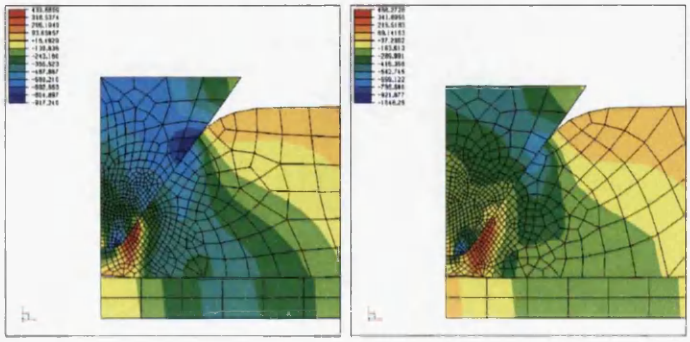

(g) SR = 36 μm (h) SR = 26 μm

Figure D.92: Direct Stress Y-Y: So = 1, R=8, PT=1.1, CC=0.2

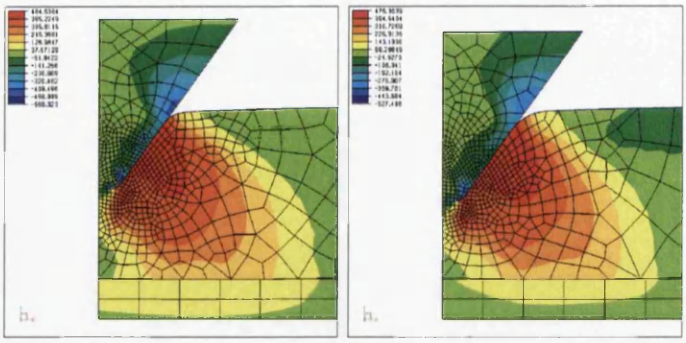

(a) SR = 107 μm (b) SR = 91 μm

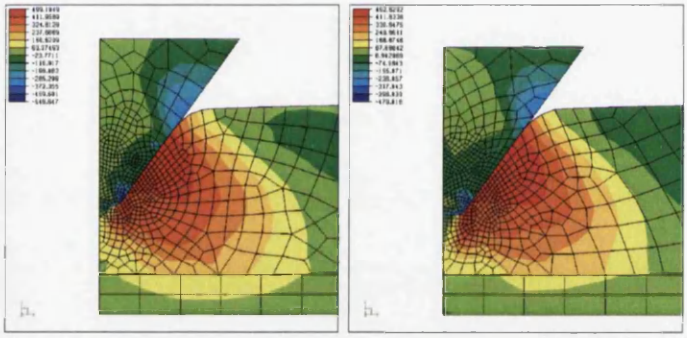

(c) SR = 83 μm (d) SR = 72 μm

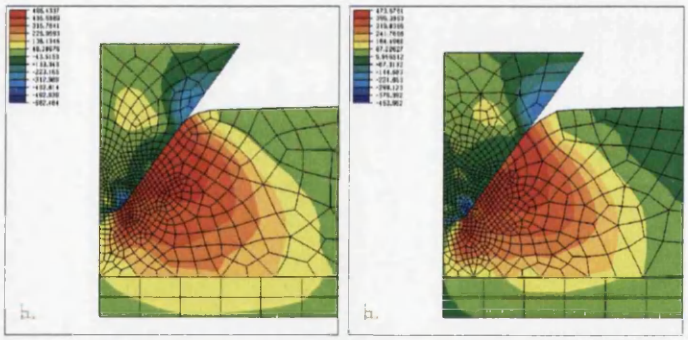

(e) SR = 78 μm (f) SR = 68 μm

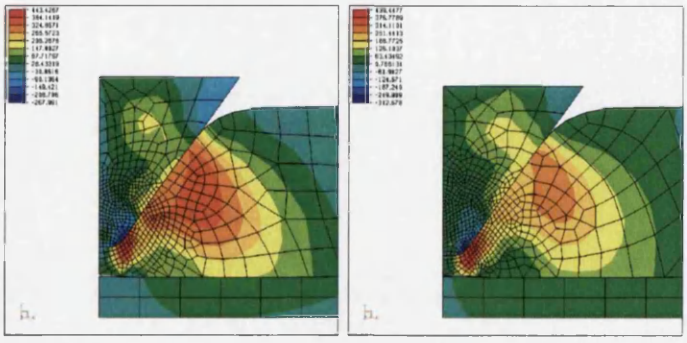

(g) SR = 36 μm (h) SR = 26 μm

Figure D.93: Shear Stress X-Y; So = 1, R=8, PT=1.1, CC=0.2

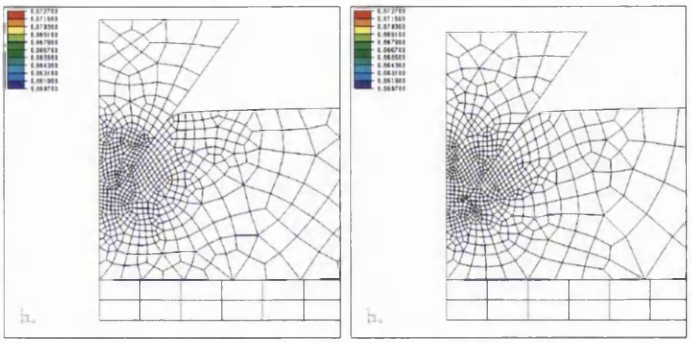

(a) SR = 107 μm (b) SR = 91 μm

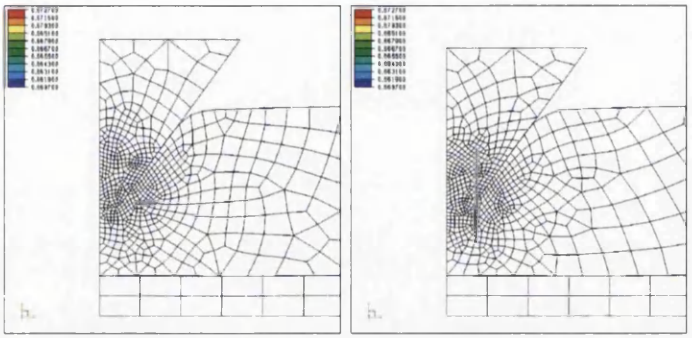

(c) SR = 83 μm (d) SR = 72 μm

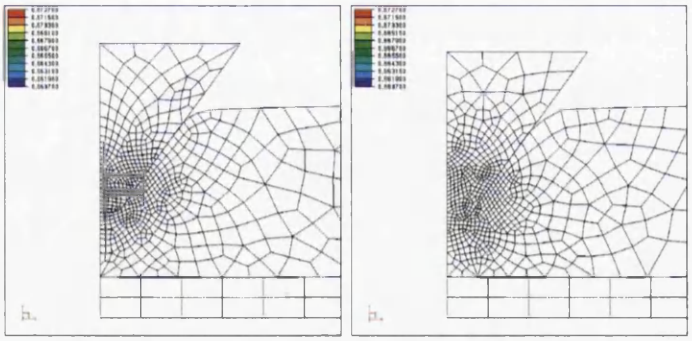

(e) SR = 78 μm (f) SR = 68 μm

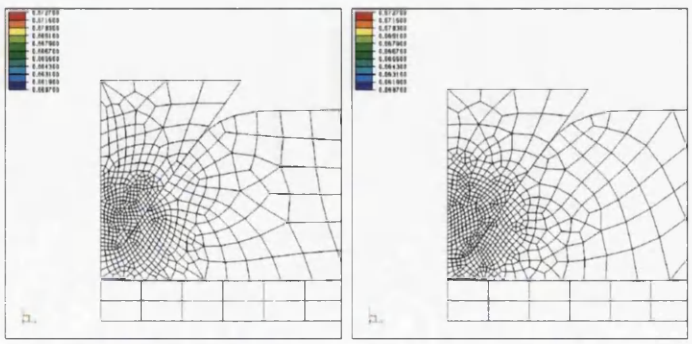

(g) SR = 36 μm (h) SR = 26 μm

Figure D.94: Triaxiality - Biaxial: So = 1, R=8, PT=1.1, CC=0.2

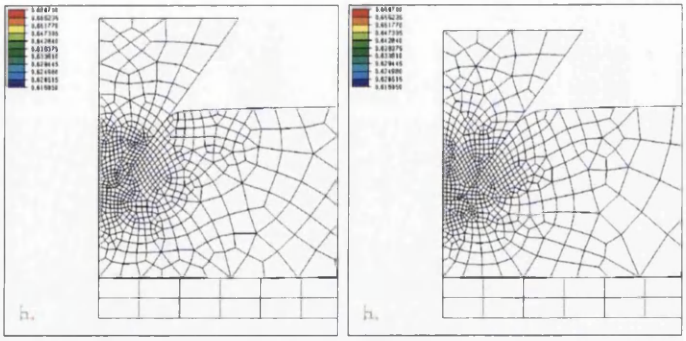

(a) SR = 107 μm (b) SR = 91 μm

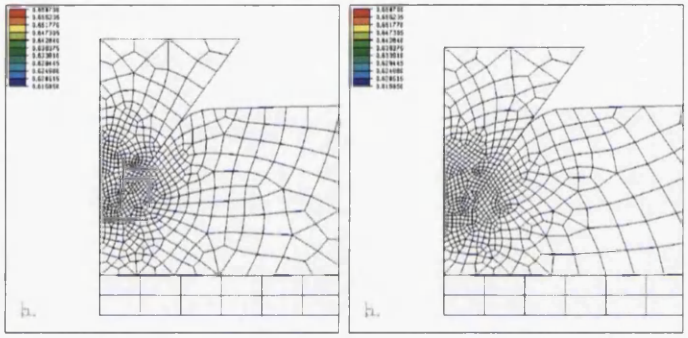

(c) SR = 83 μm (d) SR = 72 μm

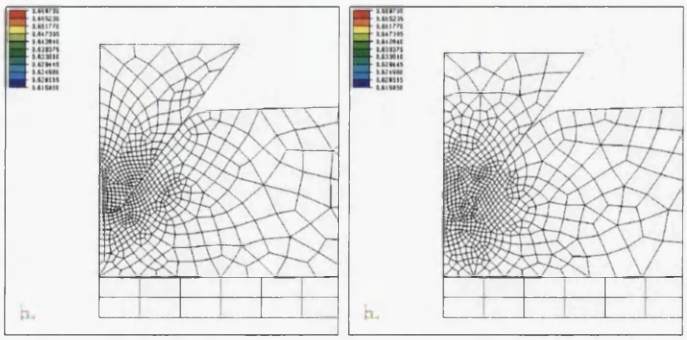

(e) SR = 78 μm (f) SR = 68 μm

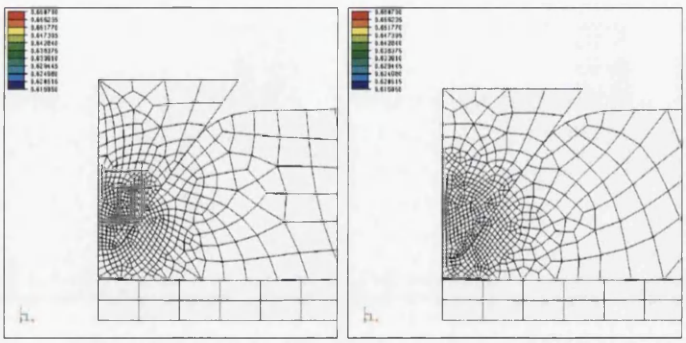

(g) SR = 36 μm (h) SR = 26 μm

Figure D.95: Triaxiality - Biaxial NU: So = 1, R=8, PT=1.1, CC=0.2

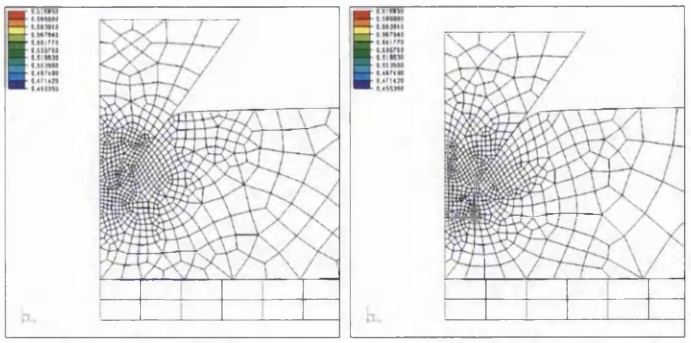

(a) SR = 107 μm (b) SR = 91 μm

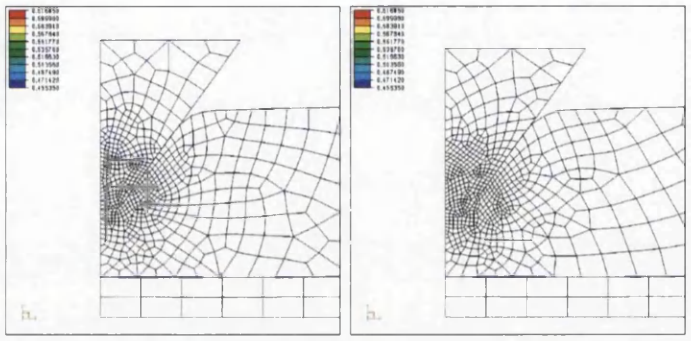

(c) SR = 83 μm (d) SR = 72 μm

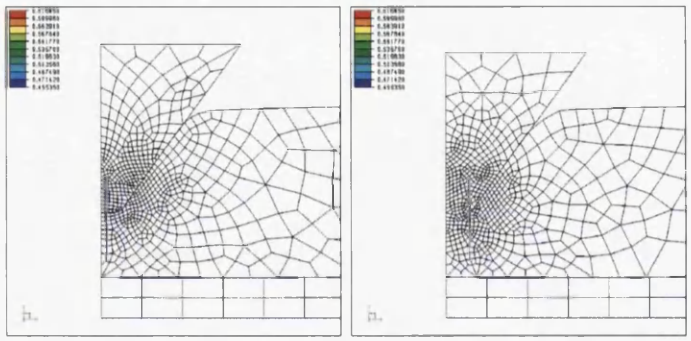

(e) SR = 78 μm (f) SR = 68 μm

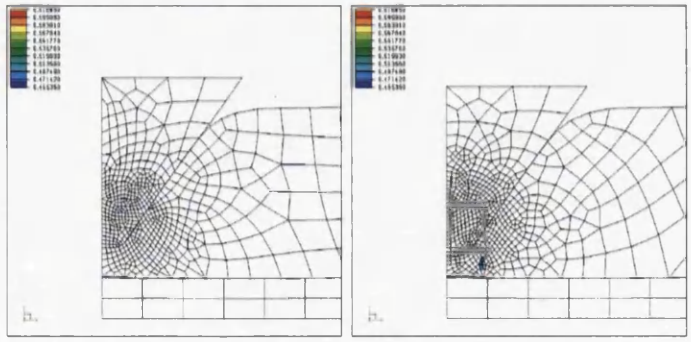

(g) SR = 36 μm (h) SR = 26 μm

Figure D.96: Triaxiality - Plane Strain: So = 1, R=8, PT=1.1, CC=0.2

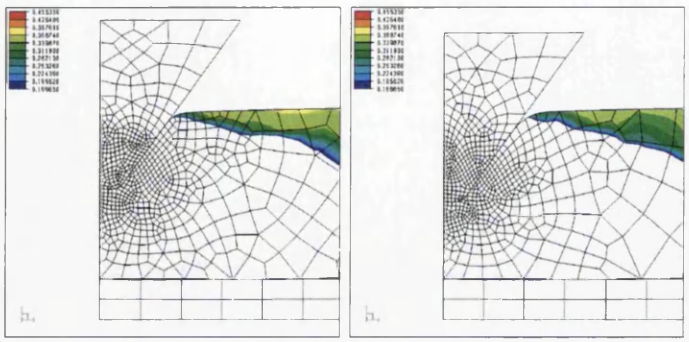

(a) SR = 107 μm (b) SR = 91 μm

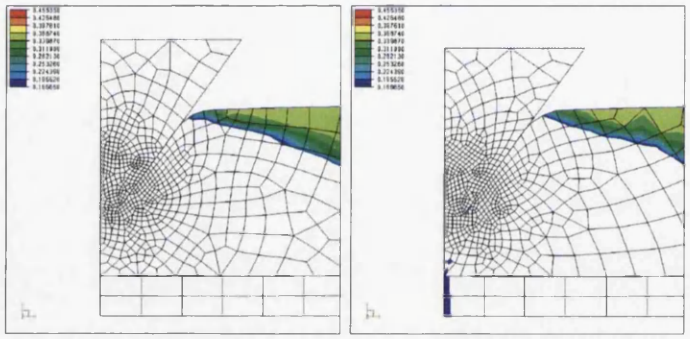

(c) SR = 83 μm (d) SR = 72 μm

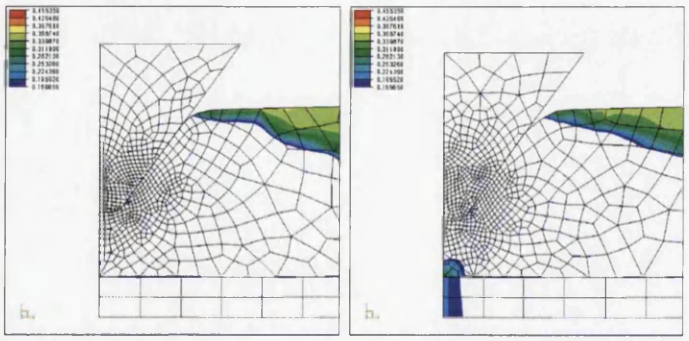

(e) SR = 78 μm (f) SR = 68 μm

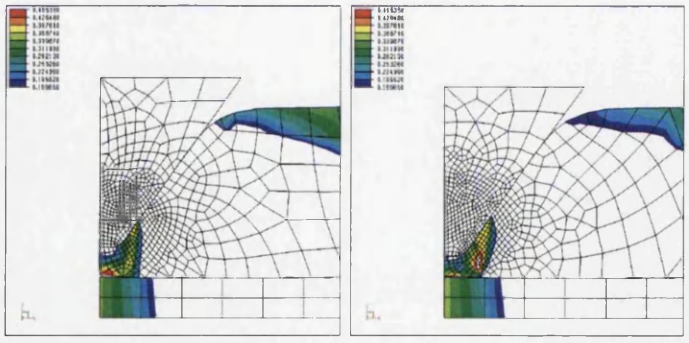

(g) SR = 36 μm (h) SR = 26 μm

Figure D.97: Triaxiality - Uniaxial Tension: So = 1, R=8, PT=1.1, CC=0.2

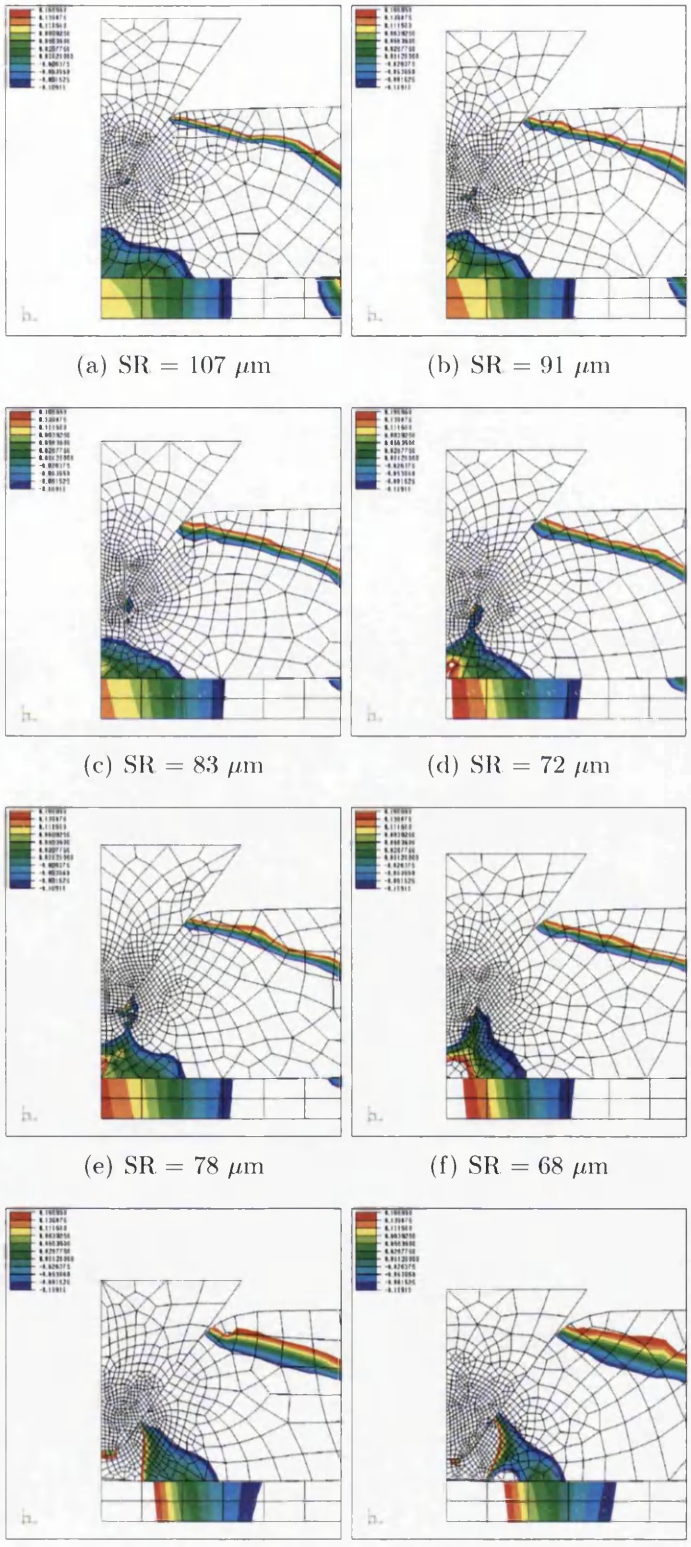

(a) SR = 107 μm (b) SR = 91 μm

(c) SR = 83 μm (d) SR = 72 μm

(e) SR = 78 μm (f) SR = 68 μm

(g) SR = 36 μm (h) SR = 26 μm

Figure D.98: Triaxiality - Shear Pure: So = 1, R=8, PT=1.1, CC=0.2

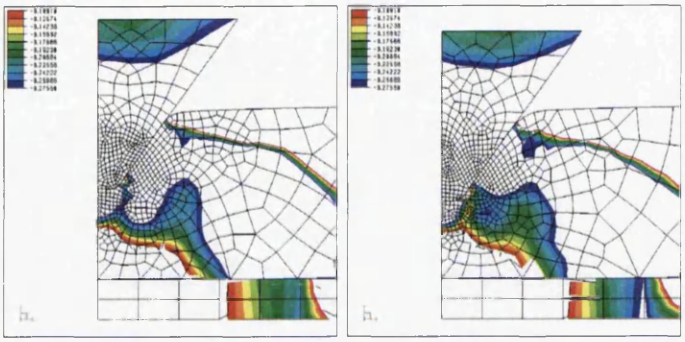

(a) SR = 107 μm (b) SR = 91 μm

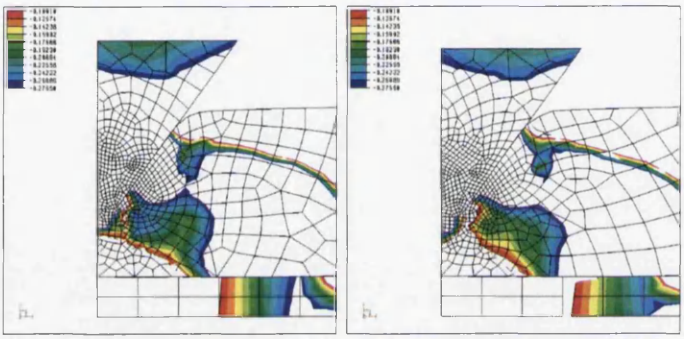

(c) SR = 83 μm (d) SR = 72 μm

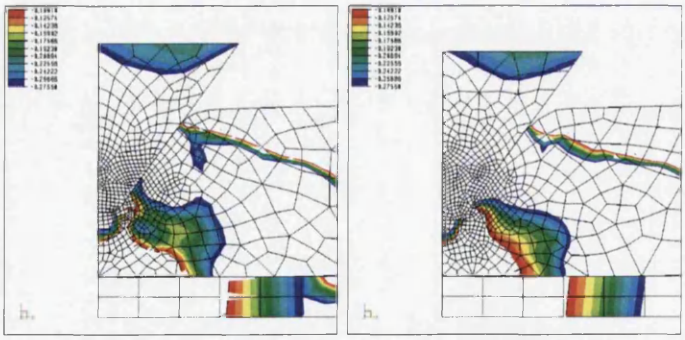

(e) SR = 78 μm (f) SR = 68 μm

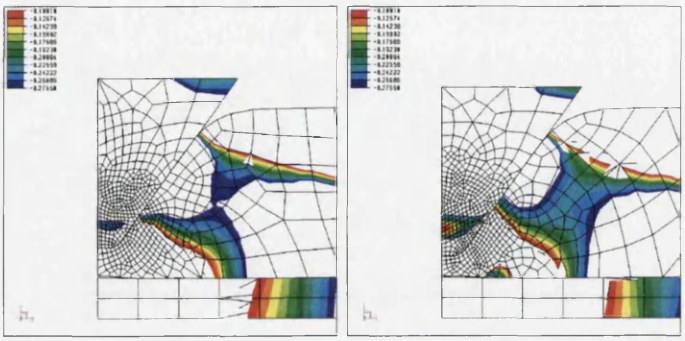

(g) SR = 36 μm (h) SR = 26 μm

Figure D.99: Triaxiality - Shear NU: So = 1, R=8, PT=1.1, CC=0.2

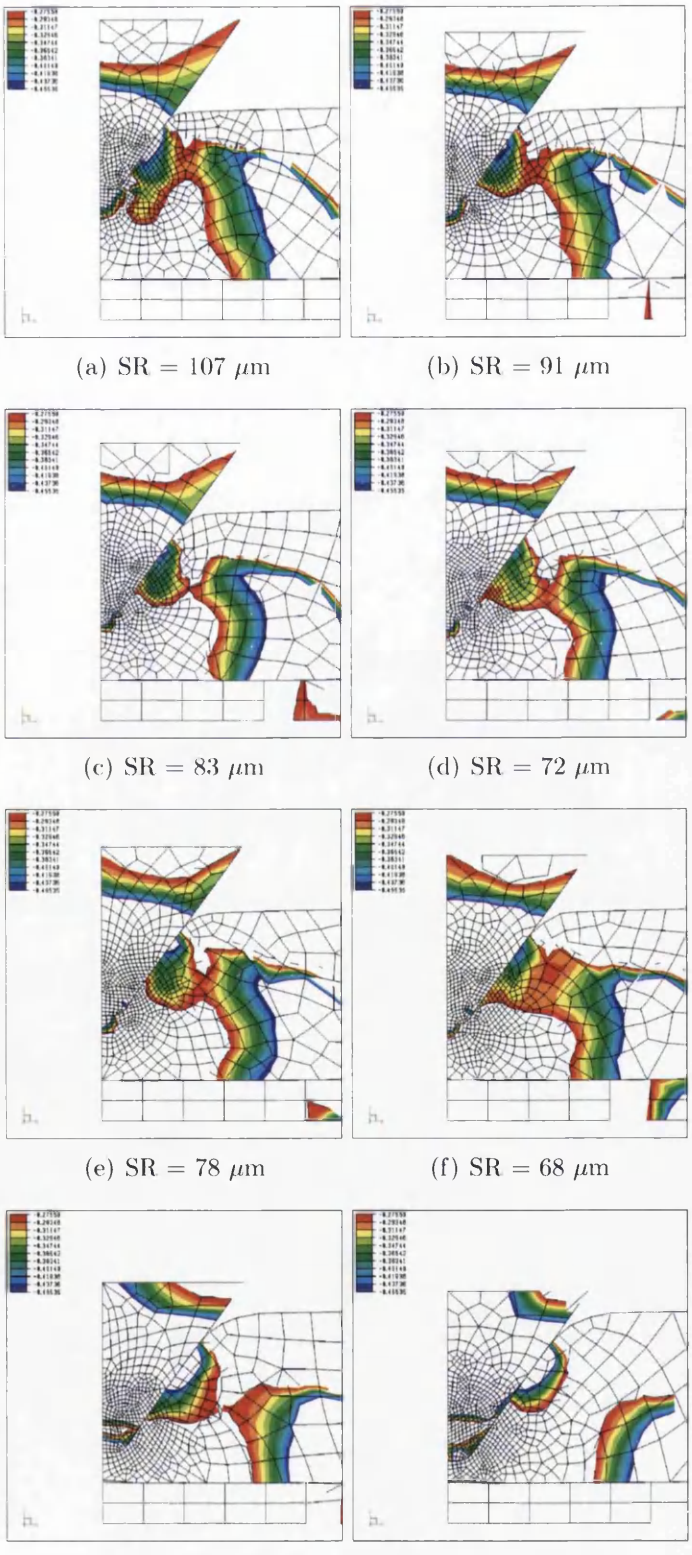

(a) SR = 107 μm (b) SR = 91 μm

(c) SR = 83 μm (d) SR = 72 μm

(e) SR = 78 μm (f) SR = 68 μm

(g) SR = 36 μm (h) SR = 26 μm

Figure D.100: Triaxiality - Uniaxial Compression: So = 1, R=8, PT=1.1, CC=0.2

References

[1] ANDERSON, P., FLECK, N. & JOHNSON, K. (1990). Localisation of plastic deformation in shear due to microcracks. *Journal of Mechanics & Physics of Solids*, **38(5)**, 681–699. 4

[2] ANDERSON, T. (1995). *Fracture Mechanics: Fundamentals and Applications*. CRC Press. 10, 105

[3] ANONYMOUS (2007). *The Food Can: A Time Saver*. Anonymous Article, cited 26th June 2007. 1

[4] APEAL (2007). Convenience. Article. 1

[5] ARMERO, F. & OLLER, S. (2000). A general framework for continuum damage models. i. infinitesimal plastic damage models in stress space. *International Journal of Solids and Structures*, **37**, 7409–7436. 101

[6] BAO, Y. & WIERZBICKI, T. (2004). On fracture locus in the equivalent strain and stress triaxiality space. *Int Journal of Mech. Sci.*, **46**, 81–98. 96

[7] BAO, Y. & WIERZBICKI, T. (2005). On the cut-off value of negative triaxiality for fracture. *Eng. Frac. Mech.*, **72**, 1049–1069. 96

[8] BAO, Y., TENG, X. & WIERZBICKI, T. (2009). On the application of stress triaxiality formula for plane strain fracture testing. *Journal of Eng. Mat. Tech.*, **131**. 96

[9] BOERS, S. (2000). An experimental and numerical study of the tearing behaviour of thin sheet metal. *Corus RD&T Reference Source*. 11, 12, 40, 178

[10] BOERS, S. & TEUNISSEN, R. (2002). Research on alternative score geometries in favour of faeoe closures. *Corus RD&T Reference Source*. 52, 61

[11] BOERS, S., SCHREURS, P. & GREERS, M. (2005). Operator-split damage-plasticity applied to groove forming in food can lids. *International Journal of Solids and Structures*, **42**, 4154–4178. 1, 15, 52, 61

[12] BRUNIG, M., CHYRA, O., ALBRECHT, D., DRIEMEIER, L. & ALVES, M. (2008). Ductile damage criterion at various stress triaxialities. *International Journal of Plasticity*, **24**, 1731–1755. 83

[13] CAMEY, K., DUBOIS, P., BUYUK, M. & KAN, S. (2008). A generalized, three dimensional definition, description and derived limits of the triaxial failure of metals. *Earth & Space*. 83

[14] CHABOCHE, J. (1978). Description thermodynamique et phnomnologique de la viscoplasticit cyclique avec endommagement. Technical Report 3, Office National dEtudes et de Recherches Arospatiales. 99

[15] CHABOCHE, J. (1981). Continuous damage mechanics a tool to describe phenomena before crack initiation. *Nucl. Engng. Des.*, **64**, 233–247. 99

[16] CHABOCHE, J. (1984). Anisotropic creep damage in the framework of continuum damage mechanics. *Nucl. Engng. Des.*, **79**, 309–319. 99

[17] CHABOCHE, J. (1988). Continuum damage mechanics: Part i general concepts and part ii damage growth, crack initiation and crack growth. *Journal Applied Mechanics*, **55**, 59–72. 101

[18] COPPOLA, T., CORTESE, L. & FOLGARAIT, P. (2009). The effect of stress invariants on ductile fracture limit in steels. *Engineering Fracture Mech.*, **76**, 1288–1302. 96

[19] CORDEBOIS, J. & SIDOROFF, F. (1979). Damage induced elastic anisotropy. *Euromech 115 Villard de Lans*, **Juin 1979**, 761–774. 102

[20] CORDEBOIS, J. & SIDOROFF, F. (1982). Endomagement anisotrope en lasticit et plasticit. *Journal de Mcanique Thorique et Applique*, **Numro spcial.**, 45–60. 101

[21] CORUS (2008). Product range & technical specifications. *CORUS Packaging Plus*. 202

[22] DE SOUZA NETO, E.A., PERIC, D. & OWEN, D.R.J. (2008). *Computational Methods for Plasticity: Theory and Applications*. Wiley: Chichester. 89, 91, 101, 102, 103, 109, 113, 120, 145, 153, 155

[23] ENGEL, L. & KLINGELE, H. (1981). *An Atlas of Metal Damage.*. Wolfe Science Books. 92

[24] FLECK, N. & HUTCHINSON, J. (1986). Void growth in shear. *Proc Royal Society*, **A-407**, 435–458. 4

[25] FLECK, N., HUTCHINSON, J. & TVERGAARD, V. (1989). Softening by void nucleation and growth in tension and shear. *J. Mech. Phys. Solids*, **37(4)**, 515–540. 76

[26] FLECK, N., ASHBY, M. & HUTCHINSON, J. (2003). The role of geometrically necessary dislocations in giving material strengthening. *Scripta Materialia*, **48**, 179–183. 86

[27] FONSEKA, G. & KRAJČINOVIĆ, D. (1981). The continuous damage theory of brittle materials part 2: Uniaxial and plane response modes. *J. Appl. Mech.*, **48**, 816–824. 101

[28] GHADBEIGI, H., PINNA, C., S.CELOTTO & YATES, J. (2010). Local plastic strain evolution in a high strength dual phase steel. *Journal of Materials Science and Engineering*, **A,527**, 5026–5032. 85

[29] GUPTA, V. & BERGSTROM, J. (2002). A progressive damage model for failure by shear faulting in polycrystalline ice under biaxial compression. *International Journal of Plasticity*, **18**, 507–530. 4

[30] GURSON, A. (1977). Continuum theory of ductile rupture by void nucleation and growth part i: Yield criteria and flow rule for porous media. *Journal of Engineering Materials and Technology*, **99**, 2–15. 100

[31] HOLZAPFEL, G. (2000). *Nonlinear Solid Mechanics*. John Wiley & Sons Ltd, Chichester. 90

[32] HORII, H. & NEMAT-NASSER, S. (1983). Overall moduli of solids with microcracks: Load induced anisotropy. *J. Mech. Phys. Solids*, **312**, 155–171. 102

[33] JANSON, J. (1978). A continuous damage approach to the fatigue process. *Engng. Fract. Mech.*, **10**, 651–657. 101

[34] JAVANI, H., PEERLINGS, R. & GEERS, M. (2009). 3d modelling of nonlocal ductile damage: element technology. *Int. Jnl. Mat. Form.*, **2**, 923–926. 180

[35] JAVANI, H., PEERLINGS, R. & GEERS, M. (2010). A remeshing strategy for 3d elasto-plasticity coupled with damage applicable to forming processes. *Int. Jnl. Mat. Form.*, **3**, 915–918. 180

[36] KACHANOV, L. (1958). Time of the rupture process under creep condition. *Izv. Akad. Nauk. SSSR, Otd. Tekhn. Nauk.*, **8**, 26–31, in Russian. 97, 98

[37] KACHANOV, L. (1977). Creep and rupture under complex loading. *Problemi Prochnosti*, **6**. 101

[38] KRAJČINOVIĆ, D. (1983). Constitutive equations for damaging materials. *J. Appl. Mech.*, **50**, 355–360. 101

[39] KRAJČINOVIĆ, D. (1985). Continuous damage mechanics revisited: Basic concepts and definitions. *J. Appl. Mech.*, **52**, 829–834. 101

[40] KRAJČINOVIĆ, D. (1996). *Damage Mechanics.*. North-Holland, Amsterdam. 97

[41] KRAJČINOVIĆ, D. & FONSEKA, G. (1981). The continuous damage theory of brittle materials part 1: General theory. *J. Appl. Mech.*, **48**, 809–815. 101

[42] KRUGLA, M. (2008). Sample preparation and investigation procedure of the cross section of the scores. *Corus RD&T Reference Source*. 7

[43] KRUGLA, M. (2008). Tinplated steel - investigation of the scores, msa 2081046. *Corus RD&T Reference Source*. 40

[44] LAI, W., RUBIN, D. & KREMPL, E. (1999). *Introduction to Continuum Mechanics:3rd Edition*. Butterworth Heinemann, USA. 90

[45] LECKIE, F. & HAYHURST, D. (1974). Creep rupture of structures. *Proc. Roy. Soc.*, **340**, 323–347. 99

[46] LECKIE, F. & ONAT, E. (1981). Tensorial nature of damage measuring internal variables. *Proc. of the IUTAM Symposium on Physical Nonlinearities in Structures*, 140–155. 103

[47] LEMAITRE, J. (1983). A three-dimensional ductile damage model applied to deep-drawing forming limits. *ICM*, **4**, 1047–1053. 100

[48] LEMAITRE, J. (1985). A continuous damage mechanics model for ductile fracture. *Journal of Engineering Materials and Technology*, **107**, 83–89. 100, 103, 105

[49] LEMAITRE, J. (1985). Coupled elasto-plasticity and damage constitutive equations. *Computational Methods Applied Mechanical Engineering*, **51**, 31–49. 100, 103

[50] LEMAITRE, J. (1987). Formulation and identification of damage kinetic constitutive equations. In D. Krajčinović & J. Lemaitre, eds., *Continuum Damage Mechanics: Theory and Applications.*, 37–89, Springer-Verlag. 101

[51] LEMAITRE, J. (1996). *A Course on Damage Mechanics*. Springer-Verlag Berlin Heidelberg, Berlin. 89, 111, 142, 145

[52] LEMAITRE, J. & CHABOCHE, J.L. (1990). *Mechanics of Solid Materials*. Cambridge University Press, Cambridge. 97, 101, 102, 103, 105, 107, 142, 144, 145

[53] LEMAITRE, J. & DESMORAT, R. (2005). *Engineering Damage Mechanics*. Springer-Verlag Berlin Heidelberg, Berlin. 5, 89, 142, 145, 153

[54] LEMAITRE, J. & DUFAILLY, J. (1987). Damage measurements. *Engineering Fracture Mechanics*, **28**, 643–661. 102, 142

[55] LEMAITRE, J., DESMORAT, R. & SAUZAY, M. (2000). Anisotropic damage law of evolution. *European Journal of Mechanics and Solids*, **19**, 187–208. 100, 102

[56] LI, R.C.L., CHEN, J. & ZHANG, J. (2010). Study on compression deformation, damage and fracture behaviour of tial alloys: Part ii. fracture behavior. *Material Science and Engineering*, **A-527**, 2468–2477. 4

[57] LI, R.C.L., CHEN, J., ZHANG, J. & HE, H. (2010). Study on compression deformation, damage and fracture behaviour of tial alloys: Part i. deformation and damage behavior. *Material Science and Engineering*, **A-527**, 2455–2467. 4, 83

[58] LI, Y., LUO, M., GERLACH, J. & WIERZBICKI, T. (2010). Prediction of shear induced frcature in sheet metal forming. *Journal of Mat. Proc Techn.*, **210**, 1858–1869. 96

[59] MALVERN, L. (1969). *Introduction to the Mechanics of a Continuous Medium*. Prentice Hall,Inc, New Jersy. 90

[60] MARCINIAK, Z., DUNCAN, J.L. & HU, S.J. (2002). *Mechanics of Sheet Metal Forming*. Butterworth-Heinemann, Oxford. 124, 125

[61] MARQUIS, D. & LEMAITRE, J. (1988). Constitutive equations for the coupling between elasto-plasticity damage and ageing. *Rev. Phys. Applic*, **23**, 615–624. 100

[62] MASE, G. & MASE, G. (1999). *Continuum Mechanics for Engineers:2nd Edition*. CRC Press, Boca Raton. 90

[63] MEDIAVILLA, J., PEERLINGS, R. & GREERS, M. (2006). An integrated continuous-discontinuous approach towards damage engineering in sheet metal forming processes. *Engineering Fracture Mechanics*, **73**, 895–916. 15, 52, 61

[64] MITCHELL, G. (1990). *Topics in the Numerical Analysis of Inelastic Solids.*. Phd, Department of Civil Engineering, University College of Swansea., Swansea. 101

[65] MONSALVE, A. (2006). Study and modelling of the opening and tearing-off process of tinplate lids. *Engineering Failure Analysis*, **13**, 210–225. 52, 61

[66] MONSALVE, A. & GUTIERREZ, I. (2000). Application of a modified rigid plastic model to the out-plane fracture of easy open end cans. *International Journal of Fracture*, **102**, 323–339. 52, 61

[67] MONTGOMERY, D. (2009). *Design and Analysis of Experiments, Seventh Edition*. John Wiley and Sons, Ltd. 41, 53, 62

[68] MURAKAMI, S. (1988). Mechanical modeling of material damage. *J. Appl. Mech.*, **55**, 280–286. 99

[69] MURAKAMI, S. & OHNO, N. (1981). A continuum theory of creep and creep damage. *Proceedings of the IUTAM Symposium on Creep in Structures.*, 422–443. 99

[70] NAHSON, K. & HUTCHINSON, J. (2008). Modification of the gurson model for shear failure. *Eur.J. Mech. & Solids*, **27**, 1–17. 76

[71] NIAZI, M., H.H.WISSELINK & MEINDERS, T. (2012). Validation of modified lemaitres anisotropic damage model with the cross die drawing test. *Key Engineering Materials*, **49-52**, 488. 181

[72] NIAZI, M., H.H.WISSELINK & MEINDERS, T. (2012). Viscoplastic regularization of local damage models: A latent solution. *Key Engineering Materials*, **845-850**, 504–506. 181

[73] NIAZI, M., H.H.WISSELINK & MEINDERS, T. (2012). Viscoplastic regularization of local damage models: revisited. *Computational Mechanics*. 181

[74] NIELSEN, K. & TVERGAARD, V. (2010). Ductile shear failure or plug failure of spot welds modelled by modified gurson model. *Eng. Frac. Mechs*, **77**, 1031–1047. 76

[75] OWEN, D.R.J. & HINTON, E. (1980). *Finite Elements in Plasticity*. Pineridge Press Ltd, Swansea. 120

[76] PILKEY, W. (2004). *Formulas for Stress, Strain and Structural Matrices: Second Edition*. John Wiley and Sons Inc. 10

[77] PIRES, F. (2005). *Issues on the Finite Element Modelling of Degradation and Prediction of Failure in Finitely Straining Ductile Materials*. Phd, School of Engineeing, University of Wales., Swansea. 113, 144, 153, 155

[78] PIRES, F., DESOUSA NETO, E., OWEN, D. & COTTRELL, M. (2003). A hybrid continuous/discrete representation of fracturing solids. *ASME International Mech Eng Congress and Exposition*. 113

[79] PIRES, F., DESOUSA NETO, E. & OWEN, D. (2004). On the finite element prediction of damage growth and fracture initiation in finitely deforming ductile materials. *Computer Methods in Applied Mechanics and Engineering*, 5223–5256. 113

[80] PUGH, S. (1990). *Total Design*. Addison-Wesley. 26

[81] RABOTNOV, Y. (1963). On the equations of state for creep. In *Progress in Applied Mechanics,Prager Anniversary Volume.*, 307, Macmillan., New York. 98

[82] RICE, J. (1968). A path independent integral and the approximate analysis of strain concentration by notches and cracks. *Journal of Applied Mechanics*, **35**, 379–386. 105

[83] SAANOUNI, K., CHABOCHE, J. & LESNE, P. (1989). Creep crack-growth prediction by a non-local damage formulation. In J. Mazars & Z. Bazant, eds., *Cracking and Damage, Strain Localization and Size Effect.*, 404–414, Elsevier., Amsterdam. 99

[84] SHIGLEY, J. & MISCHKE, C. (1996). *Standard Handbook of Machine Design*. McGraw Hill. 20

[85] SIMO, J. & JU, J. (1987). Strain and stress based continuum damage models i - formulation and ii - computational aspects. *International Journal of Solids and Structures*, **23**, 821–869. 101

[86] STOUGHTON, T. & YOON, J. (2011). A new approach for failure criterion for sheet metals. *International Journal of Plasticity*, **27**, 440–459. 85

[87] TANG, C., LEE, T. & RAO, B. (2003). An experimental study of shear damage and failure of alluminium alloy 2024t3. *Journal of Mat. Proc. Tech.*, **139**, 208–211. 96

[88] TAYLOR, D. (2008). Computer modelling of full aperture easy open ends for improved can end design - second year annual report. *CORUS RD&T Reference Source*. 7

[89] TAYLOR, D. (2009). Computer modelling of full aperture easy open ends for improved can end design - third year annual report. *CORUS RD&T Reference Source*. 7, 40

[90] TAYLOR, D., NAGY, G. & OWEN, D. (2011). Computational investigation of damage and fracture mechanisms controlling the performance of full aperture easy open ends for food containers. COMPLAS 2011 - Computational Plasticity XI - Fundamentals and Applications. 7

[91] TAYLOR, D., NAGY, G. & OWEN, D. (2011). Experimental investigation of damage and fracture mechanisms controlling the performance of full aperture easy open ends for food containers. ESAFORM 2011 - The 14th International Conference on Material Forming. 7

[92] TEUNISSEN, R. & E, V. (2000). Characterisation of the score crack in a popped easy open end lid. *Corus RD&T Reference Source*. 8

[93] TVERGAARD, V. (2008). Shear deformation of voids with contact modelled by internal pressure. *Int.J.of Mech. Sci.*, **50**, 1459–1465. 76

[94] TVERGAARD, V. & HUTCHINSON, J. (2002). Two mechanisms of ductile fracture: void by void growth versus multiple void interaction. *Int.J.of Solids & Structures*, **39**, 3581–3597. 88

[95] TVERGAARD, V. & K.L.NIELSEN (2010). Relations between a micro-mechanical model and a damage model for ductile failure in shear. *Eng. Frac. Mechs*, **58**, 1243–1252. 76

[96] VDAA, E. (2000). Impress visit to ijtc on closures research. *Corus RD&T Reference Source*. 10

[97] VDAA, E. & KESSELS, A. (1999). Influence of panel geometry on opening forces of faeoe's. *Corus RD&T Reference Source*. 8

[98] VOYIADJIS, G. & KATTAN, P. (2005). *Damage Mechanics*. Taylor & Francis, Boca Raton. 89

[99] WILSON, A. (1998). Can with easy open end. W.I.P. Organisation. 13

[100] ZIENKIEWICZ, O. & TAYLOR, R.L. (2000). *The Finite Element Method, Fifth Edition*. Butterworth-Heinemann. 120